Schlumberger

Cased Hole Log Interpretation Principles/Applications

1989

Schlumberger

Cased Hole Log Interpretation Principles/Applications

Schlumberger
Cased Hole Log Interpretation Principles/Applications

SCHLUMBERGER • EDUCATIONAL • SERVICES

Fourth printing, March 1997

Schlumberger Wireline & Testing
P.O. Box 2175
Houston, Texas 77252-2175

Printed in the United States of America
SMP-7025

An asterisk (*) is used throughout this document to denote a mark of Schlumberger.

Contents

1 Introduction 1-1

History 1-1
Well Logging 1-1
Cementing 1-1
Perforating 1-1
Correlation Logs 1-1
Formation Evaluation 1-3
Other Developments 1-3
The Field Operation 1-3
Log Data Acquisition 1-4
Data Processing 1-4
Data Transmission 1-5
References 1-6

2 Fundamentals of Quantitative Log Interpretation 2-1

Log Interpretation 2-1
Porosity 2-1
Saturation 2-1
Permeability 2-2
Reservoir Geometry 2-2
Temperature and Pressure 2-3
Log Interpretation 2-3
Determination of Saturation 2-4
References 2-4

3 Formation Evaluation in Cased Holes 3-1

Logs for Cased Hole Formation Evaluation 3-1
Natural Gamma Ray Logs 3-1
Properties of Gamma Rays 3-2
Equipment 3-3
Calibration 3-3
The NGS Log 3-3
Physical Principle 3-3
Measurement Principle 3-4
Log Presentation 3-4
Interpretation 3-4
Applications 3-5

Contents

Neutron Logs 3-6
Principle 3-6
Equipment 3-7
Log Presentation 3-7
Calibration 3-7
Investigation Characteristics 3-7
Tool Response 3-8
Hydrogen Index of Salt Water 3-8
Response to Hydrocarbons 3-8
Shales, Bound Water 3-10
Effect of Lithology 3-10
Determining Porosity from Neutron Logs 3-10
Thermal Neutron Measurement 3-10
Sonic Logs 3-10
Principle 3-10
Log Presentation 3-12
Sonic Velocities in Formations 3-12
Porosity Determination (Wyllie Time-Average Equation) 3-12
Log Quality 3-15
Applications 3-15
Thermal Decay Time Logs 3-16
Introduction 3-16
Principle 3-17
The TDT-K Tool 3-18
Log Presentation 3-18
Dual-Burst TDT Tool 3-20
Porosity Determination from TDT-K Logs 3-24
Porosity Determination from Dual-Burst TDT Logs 3-25
Gas Detection with TDT-K Logs 3-25
Gas Detection with Dual-Burst TDT Logs 3-25
TDT Interpretation 3-26
Matrix Capture Cross Sections 3-27
Gamma Ray Spectrometry Tool (GST) 3-32
Introduction 3-32
Principles of the Technique 3-32
Fast Neutron Interactions 3-32
Neutron Capture Interactions (Thermal Absorption) 3-34

Contents

Log Presentation 3-35
Carbon-Oxygen Interpretation 3-36
Capture Mode Interpretation 3-37
Applications 3-39
Reservoir Monitoring 3-41
Production Monitoring 3-41
Flood Monitoring 3-41
Injection Well Monitoring 3-43
Monitoring a Producing Well 3-44
References 3-45

4 Completion Evaluation 4-1
Production Logging Services 4-1
Production Logging Applications 4-1
Well Performance 4-2
Well Problems 4-2
Flow in Vertical Pipes 4-2
Single-Phase Flow 4-2
Multiphase Flow 4-3
Production Logging Tools and Interpretation 4-5
Flow Velocity 4-5
Spinner Flowmeter Tools 4-5
Interpretation in Single-Phase Flow 4-7
2-Pass Technique 4-8
Radioactive Tracer Tools 4-10
Fluid Density Tools 4-12
Temperature Tools 4-16
Noise Tools 4-18
Gravel Pack Logging 4-19
Production Logging Wellsite Quicklook Interpretation Program 4-21
Job Planning 4-22
Production Logging and Well Testing 4-23
Well Testing Basics 4-24
Modeling Radial Flow into a Well 4-25
Modeling Departures from Radial Flow 4-26
Downhole Flow Measurements Applies to Well Testing 4-28
Layered Reservoir Testing 4-31

Contents

Computerized Acquisition and Interpretation Features 4-32
References 4-35

5 Cement Evaluation 5-1
Cementing Technique 5-1
CBL-VDL Measurement 5-2
Compensated Cement Bond Tool 5-4
Cement Evaluation Tool 5-6
Microannulus 5-7
Third Interface Reflections 5-8
Gas Effect 5-8
Field Examples 5-9
Cement Evaluation Program 5-11
References 5-17

6 Corrosion Evaluation of Casing and Tubing 6-1
Predicting Corrosion 6-1
Corrosion Protection Evaluation Tool 6-2
Log Example 6-2
Monitoring Metal Loss 6-2
Multifrequency Electromagnetic Thickness Tool 6-3
Thickness Measurement 6-4
Casing Properties Ratio 6-4
Log Quality 6-4
Log in Test Well 6-5
Compensation for Permeability Change 6-6
Outside Casing Parted 6-6
Split Casing 6-6
Triple String 6-7
Double String 6-7
Cement Evaluation Tool 6-7
Internal and External Corrosion 6-8
Finding Leaks 6-8
Borehole Televiewer Tool 6-9
Expanded Depth Scale 6-10
Multifinger Caliper Tool 6-11
Pipe Analysis Tool 6-13

Contents

Electromagnetic Thickness 6-15
Multiple Casing Strings 6-16
Casing Hole and Pitting 6-16
Corrosion Protection Evaluation Tool 6-17
Multiple-Log Example 6-17
References 6-18

7 Perforating 7-1
Shaped Charge Theory 7-1
Gun System Design 7-3
Industry Testing of Perforating Systems 7-4
Gun System Performance under Downhole Conditions 7-5
Completion Design 7-6
Natural Completions 7-6
Guidelines for Selecting Optimum Underbalance 7-11
Sand Control Completions 7-12
Stimulated Completions 7-13
Schlumberger Perforation Analysis Program (SPAN) 7-13
General 7-13
Entrance Hole Diameter Prediction 7-13
Penetration Correction for Formation Characteristics 7-13
Productivity Calculation 7-14
Well Completion Techniques 7-15
Wireline Casing Gun Technique 7-15
Through-Tubing Perforating Technique 7-16
Tubing-Conveyed Perforating Technique 7-17
Completion Evaluation 7-17
References 7-19

8 Mechanical Rock Properties vs. Completion Design 8-1
Elastic Constants 8-1
Inherent Strength Computations and Their Relationship to Formation Collapse 8-2
Stresses around a Producing Cavity 8-2
Solution to the "Collapse" Problem 8-3
Griffith Failure Criterion 8-3
Mohr-Coulomb Failure Criterion 8-4
Stress Analysis in Relation to Hydraulic Fracturing 8-5

Contents

Calibration with Mini-Frac Data 8-6
Fracture Pressure Computations 8-7
Hydraulic Fracture Geometry Analysis 8-7
Fracture Height 8-8
The FracHite Program 8-9
Fracture Propagation Azimuth 8-9
References 8-10

9 Cased Hole Seismic 9-1
Cased Hole Seismic Equipment 9-1
Digital Check-Shot Survey Fracture Pressure Computations 9-3
Time-to-Depth Conversion and Velocity Profile 9-3
Geogram Processing 9-4
Vertical Seismic Profile 9-5
VSP Processing 9-8
Offset Vertical Seismic Profile 9-8
Walkaway Surveys 9-8
DSA Tool for VSP Acquisition 9-13
Primary Uses of the VSP Survey 9-14
Proximity Survey Interpretation 9-14
References 9-14

10 Other Cased Hole Services 10-1
Guidance Continuous Tool (GCT) 10-1
Measurement Theory 10-2
Calibration 10-3
Log Quality Control 10-3
Accuracy 10-3
Wellsite Processing 10-3
Presentation of Results 10-4
Freepoint Indicator Tool 10-5
Hydraulic Sealing 10-7
Through-Tubing Bridge Plug 10-7
PosiSet Mechanical Plugback Tool 10-8
Cased Hole Wireline Formation Tester 10-9
Cased Hole Wireline Formation Tester Tools 10-9
Formation Interval Tester (FIT) 10-9

Contents

Dual Shot Kit with Repeat Formation Tester 10-10
Interpretation 10-10
Correlated Electromagnetic Retrieval (CERT) Tool 10-10
Subsidence Monitoring 10-10
Introduction 10-10
Subsidence Measurement Techniques 10-11
The Formation Subsidence Monitor Tool (FSMT) 10-11
Cable Motion Measurement 10-11
Radioactive Bullet Placement 10-12
Measurement Theory 10-12
FSMT Tool Calibrations 10-13
Logging Procedure 10-14
Log Data Processing 10-14
Presentation of Results 10-14
References 10-15

1 Introduction

HISTORY

Well Logging

Electrical well logging was introduced to the oil industry over a half century ago. The first log was recorded on September 5, 1927, in a well in the small oil field of Pechelbronn, in Alsace, a province of northeastern France. This log, a single graph of the electrical resistivity of the rock formations cut by the borehole, was recorded by the "station" method. The downhole tool (called a sonde) was stopped at periodic intervals in the borehole, measurements were made, and the calculated resistivity was hand-plotted on a graph. This procedure was repeated from station to station until the entire log was recorded.

In 1929, electrical resistivity logging was introduced on a commercial basis in Venezuela, the United States, and Russia, and soon afterwards in the Dutch East Indies. The usefulness of the resistivity measurement for correlation purposes and for identification of potential hydrocarbon-bearing strata was quickly recognized by the oil industry.

It was a natural move for the Schlumberger brothers to extend their experience and expertise from openhole operations into the cased hole wireline service area that evolved a decade later.

Cementing

The procedure of cementing a casing string in the wellbore to isolate the productive interval was introduced in Oklahoma in 1920 by E. P. Halliburton. Cementing soon became the standard completion technique and the need for a method to evaluate the cement quality became obvious. In 1933 Schlumberger offered the continuous thermometer log and one of the primary applications was to pick the cement top by recording the heat anomalies from the curing cement. Other cement evaluation techniques were tried later but were found to be unsuccessful, until the development of the sonic tool which led to the Cement Bond Log (CBL*) introduced in 1961. Cementing techniques have evolved from the early simple efforts into highly scientific operations. Cement evaluation services have evolved in a similar manner with the Cement Bond Log and Cement Evaluation Tool (CET*) coupled with digital recording and processing techniques.

Perforating

Success with early cementing operations required the development of a method to perforate the casing for production. Wireline bullet guns were introduced in the mid 1930s to allow the casing to be set through the producing interval and later perforated. Wireline perforating soon became the standard. Shaped charge guns, based on explosive techniques developed during World War II, were introduced by Welex in 1947, with Schlumberger entering the field in 1949. These shaped charge perforators were so much more effective than the bullet guns that by 1960 the large majority of perforating operations were performed with shaped charge guns. A wireline perforating setup is shown in Fig. 1-1.

Schlumberger introduced the through-tubing perforating gun system and high-pressure wireline wellhead control equipment in 1950. This allowed zones to be perforated safely with a pressure differential into the wellbore and for a well to be recompleted without shutting the well in. A schematic of a wireline pressure control system is depicted in Fig. 1-2.

The need for underbalanced perforating operations for more effective completions was recognized early on. Johnston Testers promoted this technique in the early 1940s with a shoot-and-test, tubing-conveyed bullet gun, but, due primarily to operational and safety considerations, the promotion was relatively unsuccessful. The tubing-conveyed technique didn't really catch on until the 1970s after Roy Vann reintroduced the system using large, shaped charge guns. Today, tubing-conveyed perforating is a popular system for large intervals or multiple zones and is easily combined with well testing.

Correlation Logs

Success with the perforated completion method led to several attempts to eliminate depth control problems associated with

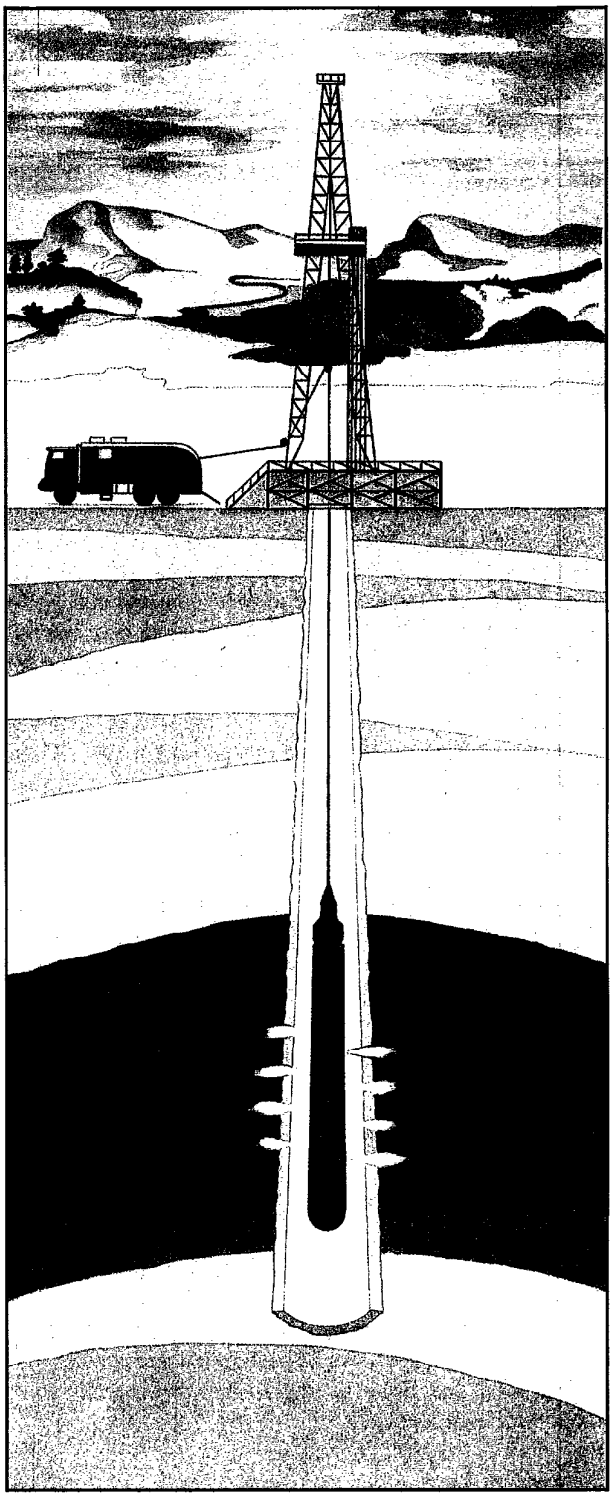

Fig. 1-1—Wireline perforating operation

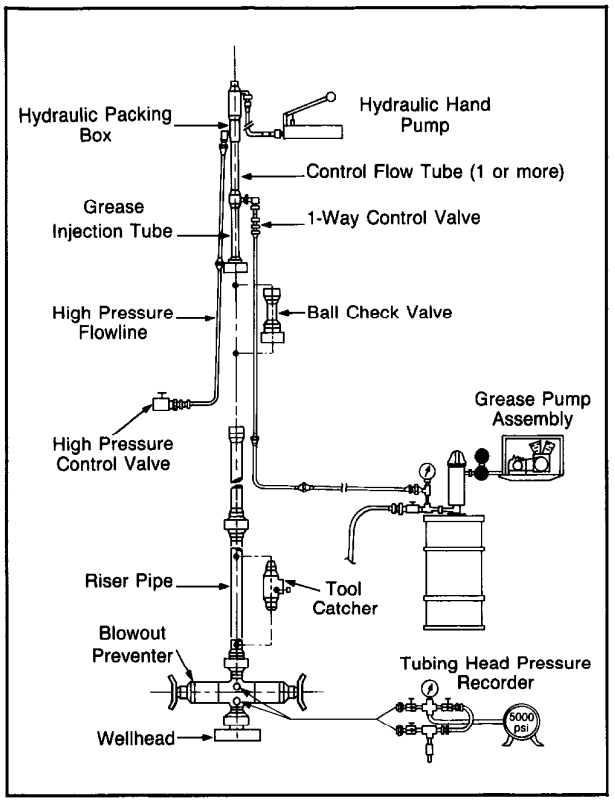

Fig. 1-2—Wireline pressure control equipment

the operation. This resulted in sensors that could "see" through casing for correlation with the electrical logs recorded in open hole. Worth Wells introduced the gamma ray log in the United States in 1939 and the neutron log in 1941.

The gamma ray and neutron tools represented the first use of radioactive properties in well logging and the first use of downhole electronics. Unlike resistivity tools, gamma ray and neutron tools are used to log formations through steel casing, as well as in air- or gas-filled holes or in oil-based muds.

One significant early Schlumberger contribution to good depth control was the development of the magnetic casing collar locator. When combined with a gamma ray and/or neutron log, this tool provided a technique to tie the casing collars to specific depths in relation to the formations. This provided positive depth control for subsequent wireline operations such as perforating. The magnetic casing collar locator quickly made the mechanical type locators obsolete and today is part of the wireline tool string in virtually every trip into a cased hole. The development of the gamma ray scintillation detector in the late 1950s was another major breakthrough for better correlation with openhole logs and therefore better depth control.

Formation Evaluation

In combination with the gamma ray log, a neutron log enhances lithological interpretations and well-to-well stratigraphic correlations. After about 1949, attention was given to the neutron log as a porosity indicator. This was the first serious attempt to evaluate formations through casing. However, the early neutron logs were greatly influenced by the casing and wellbore environment. It was not until the introduction of the Compensated Neutron Log (CNL*) in 1970 that the neutron gained wide acceptance as a porosity measurement.

The pulsed neutron log was introduced by Lane Wells in 1964 and Schlumberger followed with the Thermal Decay Time (TDT*) tool soon after. These 3⅝-in. tools had limited success due to size limitations, and it wasn't until the 1 11/16-in. TDT-K through-tubing tool was available and interpretation techniques developed that the service became popular to evaluate reservoirs behind casing. The tool records the rate of decay of thermal neutrons in the formation. The decay rate responds primarily to the amount of chlorine present in the formation water. The log, therefore, resembles the openhole resistivity log and is used in a similar manner. The tool provides a good estimate of porosity and fluid saturations through casing in reservoirs where resistivity techniques work well and when borehole environmental conditions are reasonable. The Dual-Burst Thermal Decay Time (TDT*-P) tool was introduced in 1986 to minimize the wellbore environmental effects.

The Gamma Ray Spectrometry Tool (GST*) was introduced in the late 1970s and makes a measurement of oil saturation in zones where conditions are not favorable for the TDT tool.

Other Developments

Many other types of cased hole wireline services, both mechanical and electrical, were developed throughout the years. A system for setting bridge plugs and packers on wireline was developed in the late 1940s. Sophisticated tools for setting plugs below tubing are now available.

In 1957 a complete series of production logging tools was introduced to measure the nature and behavior of downhole fluids. Today, these sensors can be combined into one tool and recorded simultaneously.

This historical sketch has not, by any means, covered all of the cased hole wireline developments. Other measurements include testing, corrosion evaluation, directional information, borehole seismic, and many other special purpose devices.

THE FIELD OPERATION

Wireline cased hole operations are performed from a production services unit (Fig. 1-3). The truck carries the downhole tools, the electrical cable and winches needed to lower the instruments into the borehole, the surface instrumentation needed to power the downhole tools and to receive and process their signals, and the equipment needed to make a permanent recording of the "log".

The downhole tool string is usually composed of two or more components. One component, called the sonde, contains the sensors used in making the measurement. The type

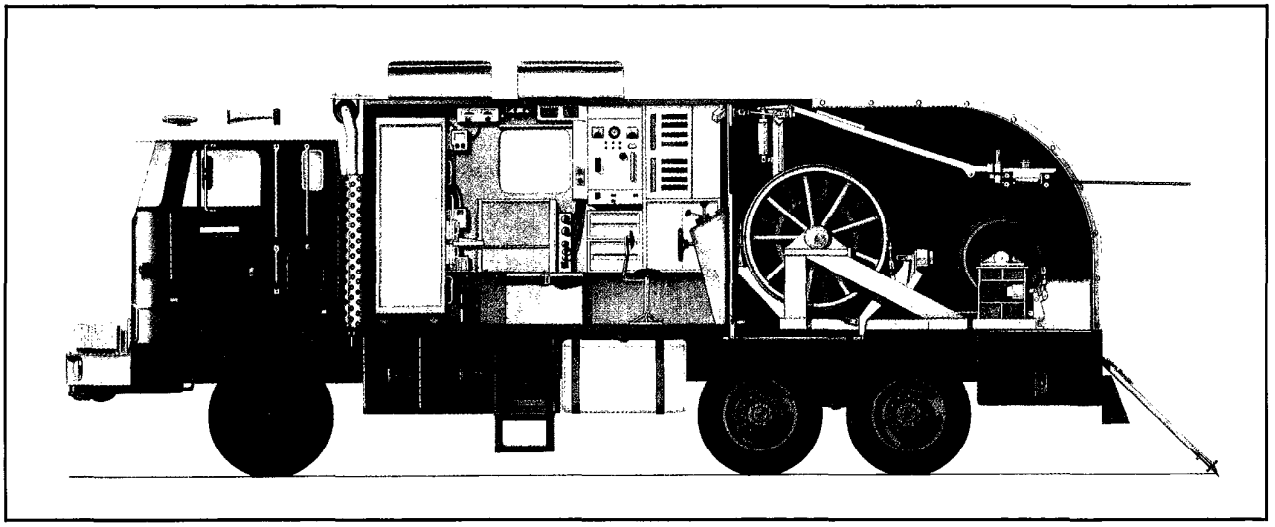

Fig. 1-3—A typical CSU cased hole truck. The large winch contains up to 30,000 ft of 7-conductor cable for casing operations and the small winch contains up to 24,000 ft of slim monoconductor cable for work in producing wells under pressure. For offshore/remote locations, the cab and winch assemblies are mounted on a skid.

of sensor used depends, of course, upon the nature of the measurement. Acoustic sensors use transducers; radioactivity sensors use detectors sensitive to radioactivity.

Another component of the downhole tool string is the cartridge. The cartridge contains the electronics that power the sensors, process the resulting measurement signals, and transmit the signals up the cable to the truck. The cartridge may be a separate component screwed to the sonde to form the total tool, or it may be combined with the sensors in the sonde to form a single tool. A collar locator tool is almost always included in any tool string regardless of the operation.

Today, most wireline tools are readily combinable. In other words, the sensors of several tools can be connected to form one tool and thereby make many measurements and logs on a single descent into and ascent from the well. The Production Logging Tool (PLT*) may combine eight or more sensors depending on the answers needed.

The production services logging unit usually carries a main winch and an auxiliary winch to lower and retrieve wireline tools from the well. The main winch usually contains 7-conductor cable that is required for some logging tools. The small winch contains small monoconductor cable for servicing producing wells under pressure.

Well depths are measured with a calibrated measuring wheel system. Logs are normally recorded during the ascent from the well to assure a taut cable and better depth control. Both up and down logging passes are usually recorded with production logs.

Signal transmission over the cable may be in analog or digital form; modern trends favor digital. The cable is also used, of course, to transmit the electrical power from the surface to the downhole tools.

The surface instrumentation (Fig. 1-4) provides electrical power to downhole tools. More importantly, the surface instrumentation receives the signals from the downhole tools, processes and/or analyzes those signals, and responds accordingly. The desired signals are output to magnetic tape in digital form and to a cathode-ray tube and photographic film in analog form.

The photographic film is processed on the logging unit, and paper prints are made from the film. This continuous recording of the downhole measurement signals is referred to as the log.

Log Data Acquisition

Wireline-logging technology is being changed by the rapid advancements in digital electronics and data-handling methods. These new technologies have changed our thinking about existing logging techniques and remolded our ideas about the direction of future developments. Affected are the sensors, the downhole electronics, the cable, the cable telemetry, and the signal processing at the surface.

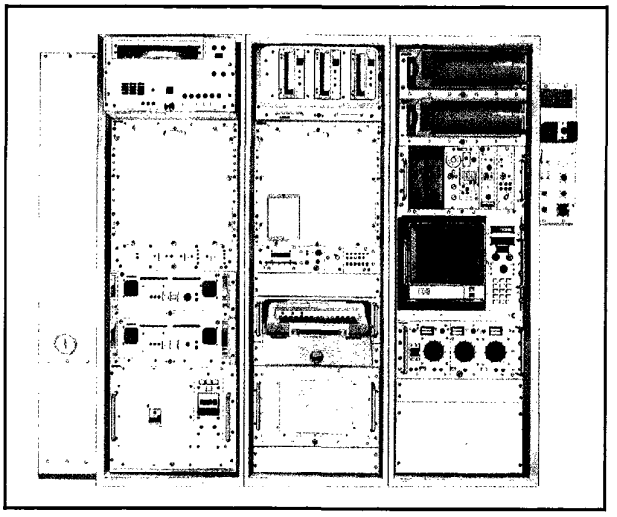

Fig. 1-4—The CSU wellsite unit is a computer-based integrated data acquisition and processing system.

Basic logging measurements may contain large amounts of information. In the past, some of this data was not recorded because of the lack of high data-rate sensors and electronics downhole, the inability to transmit the data up the cable, and the inability to record it in the logging unit. Similarly, those limitations have prevented or delayed the introduction of some new logging measurements and tools. With digital telemetry, there has been a tremendous increase in the data rate that can be handled by the logging cable. Digital recording techniques within the logging unit provide a substantial increase in recording capability. The use of digitized signals also facilitates the transmission of log signals by radio, satellite, or telephone line to computer centers or base offices.

Data Processing

Signal processing can be performed on at least three levels: downhole in the tool, uphole in the truck, and at a central computing center. Where the processing is done depends on where the desired results can most efficiently be produced, where the extracted information is first needed, where the background expertise exists, or where technological considerations dictate.

Whenever it seems desirable, the logging tool is designed so that the data are processed downhole and the processed signal is transmitted to the surface. This is the case when little future use is envisioned for the raw data or when the amount of raw data precludes its transmission. In most cases, however, it is desirable to bring measured raw data to the surface for recording and processing. The original data are thus available for any further processing or display purposes and are permanently preserved for future use.

A wellsite digital computer system, called Schlumberger's Cyber Service unit (CSU*), is now standard on most Schlumberger wireline units throughout the world (Fig. 1-4). The system provides the capability to handle large amounts of data. It overcomes many of the past limitations of combination tool systems (the stacking or combination of many measurement sensors into a single logging tool string). It also expedites field operations. Tool calibration is performed much more quickly and accurately, and tool operation is more efficiently and effectively controlled.

The CSU system provides the obvious benefit of wellsite processing of data. Processing of sonic waveforms for compressional and shear velocities is already being done, as is the processing of nuclear energy spectra for elemental composition and, then, chemical composition. More sophisticated deconvolution and signal filtering schemes are practical with the CSU system.

Nearly all the common log interpretation models and equations can be executed on the CSU unit. Although not quite as sophisticated as the log interpretation programs available in computer centers, the wellsite programs significantly exceed what can be accomplished manually. Wellsite programs exist to determine porosity and saturations in simple and complex lithology, to identify lithology, to calculate downhole flow rates, to calculate perforator performance, to analyze well tests, and to determine the quality of cement jobs. In addition, data (whether recorded, processed, or computed) can be reformatted in the form most appropriate for the user. The demand for wellsite formation evaluation processing will undoubtedly increase and programs will become more sophisticated.

The computer center offers a more powerful computer, expert log analysts, more time, and the integration of more data. Schlumberger computer centers are located in major oil centers throughout the world. They provide more sophisticated signal processing and formation analysis than the wellsite CSU system. Evaluation programs range in scope from single-well evaluation programs to reservoir description services that evaluate entire fields. Statistical techniques can be employed more extensively, both in the selection of parameters and in the actual computations.

Log processing seems to be moving more and more toward the simultaneous integration of all log measurements. Programs are being designed to recognize that the log parameters of a given volume of rock are interrelated in predictable ways, and these relationships are given attention during processing. New programs can now use data from more sources, such as cores, pressure and production testing, and reservoir modeling.

Data Transmission

The CSU system is able to transmit logs from the wellsite with a suitable communication link. The receiving station can be another CSU system, a transmission terminal, or a central computer center. Data can be edited or reformatted before transmission to reduce the transmission time or to tailor the data to the recipient. Built-in checks on the transmission quality ensure the reliability and security of the transmitted information.

With the LOGNET* communications network, graphic data or log tapes can be transmitted via satellite from the wellsite to multiple locations (Fig. 1-5). This service is available in the continental United States and Canada, onshore and offshore. Virtually any telephone is a possible receiving station.

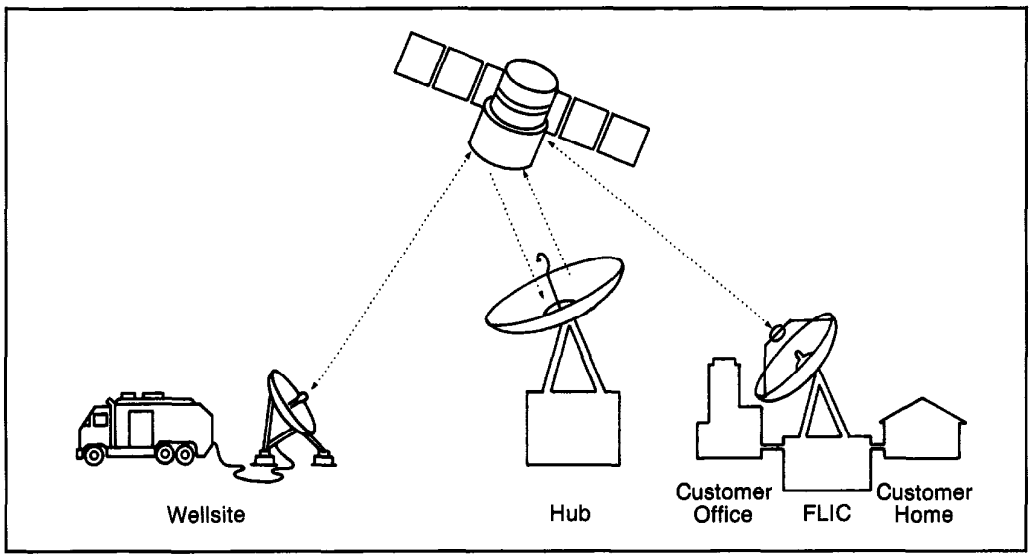

Fig. 1-5—Schematic of LOGNET communications system

A small transportable communications antenna at the wellsite permits transmission of the well log data via satellite to a Schlumberger computing center and then by telephone to the client's office or home. Since the system is 2-way, offset logs or computed logs can be transmitted back to the wellsite. The system also provides normal 2-way voice communication. There are several receiving station options:

- A standard digital FAX machine will receive log graphic data directly at the office.
- A Pilot 50* portable telecopier plugged into a standard telephone outlet at the office or at home allows clients to take advantage of the 24-hr service.
- A Pilot 100* log station can be installed in the client's office to receive tape and log graphics and to make multiple copies of the log graphics. Since this station is automatic, it can receive data unattended.
- An ELITE 1000* workstation can be installed in the client's office to receive data from the LOGNET communications network. A complete library of environmental corrections as well as the entire range of Schlumberger advanced answer products are available with this new workstation.
- A Elite 2000* computer center, staffed with a Schlumberger log analyst and log data processor, can be installed in the client's office for onsite computer interpretation of well log data. This center has access to all of the standard Schlumberger log interpretation programs.

Encrypted data provides security during transmission.

Other local transmission systems exist elsewhere in the world using telephone, radio, and/or satellite communications. In some instances, transmission from the wellsite is possible. In others, transmission must originate from a more permanent communication station. With some preplanning, it is possible to transmit log data to and from nearly any point in the world.

REFERENCES

Alger, R.P., Locke, S., Nagel, W.A., and Sherman, H.: "The Dual-Spacing Neutron Log—CNL," *JPT* (Sept., 1972) **24**, No. 9.

Allan, T.O. and Atterbury, J.H., Jr.: "Effectiveness of Gun Perforating," AIME *Trans.* (1954) **201**, 8-14.

Allen, L.S., Tittle, C.W., Mills, W.R., and Caldwell, R.L.: "Dual-Spaced Neutron Logging for Porosity," *Geophysics* (Jan., 1967) **32**, No. 1.

Bush, R.E. and Mardock, E.S.: "The Quantitative Interpretation of Radioactivity Logs," *JPT* (1951) **3**, No. 7; AIME *Trans.*, 192.

Cementing Technology, Dowell Schlumberger (1984).

Froelic, B., Pittman, D., and Seeman, B.: "Cementing Evaluation Tool - A New Approach to Cement Evaluation," paper 10207 presented at the 1981 SPE Annual Technical Conference and Exhibition.

Grosmangin, M., Kokesh, F.P., and Majani, P.: "The Cement Bond Log - A Sonic Method for Analyzing the Quality of Cementation of Borehole Casings," paper 1512 presented at the 1960 SPE Annual Technical Conference and Exhibition.

Krueger, R.F.: "Joint Bullet and Jet Perforation Tests Progress Report," *API Drilling and Production Practices* **156** 126.

Lock, G.A. and Hoyer, W.A.: "Natural Gamma Ray Spectral Logging," *The Log Analyst* (Sept.-Oct., 1971) **12**, No. 5.

Pontecorvo, B.: "Neutron Well Logging - A New Geological Method Based on Nuclear Physics," *OGJ* (Sept., 1941) **40**, No. 18.

Russell, J.H. and Bishop, B.O.: "Quantitative Evaluation of Rock Porosity by Neutron-Neutron Method," *JPT* (April, 1954).

Russell, W.L.: "Interpretation of Neutron Well Logs," *AAPG Bulletin* (1952) **36**, No. 2.

Schlumberger, C., Schlumberger, M., and Leonardon, E.G.: "Electrical Coring: A Method of Determining Bottom-Hole Data by Electrical Measurements," AIME T. P. 462, *Geophys. Prosp. Trans.*, AIME (1932) 110.

Schlumberger Log Interpretation Principles/Applications, Schlumberger Educational Services, Houston (1987).

Serra, O., Baldwin, J., and Quirein, J.: "Theory, Interpretation, and Practical Applications of Natural Gamma Ray Spectroscopy," *Trans.*, 1980 SPWLA Annual Logging Symposium.

Tittle, C.W., Faul, H., and Goodman, C.: "Neutron Logging of Drill Holes: The Neutron-Neutron Method," *Geophysics* (April, 1951) **16**, No. 4.

Wahl, J.S., Nelligan, W.B., Frentrop, A.H., Johnstone, C.W., and Schwartz, R.J.: "The Thermal Neutron Decay Time Log," *JPT* (Dec., 1970).

Westaway, P., Hertzog, R., and Plasek, R.E.: "The Gamma Spectrometer Tool Inelastic and Capture Gamma Ray Spectroscopy for Reservoir Analysis," paper 9461 presented at the 1980 SPE Annual Technical Conference and Exhibition.

Youmans, A.H., Hopkinson, E.C., Bergan, R.A., and Oshry, H.L.: "Neutron Lifetime - A New Nuclear Log," *JPT* (March, 1964) 319-328.

2 Fundamentals of Quantitative Log Interpretation

LOG INTERPRETATION

Almost all oil and gas produced today comes from accumulations in the pore spaces of reservoir rocks—usually sandstones, limestones, or dolomites. The amount of oil or gas contained in a unit volume of the reservoir is the product of its porosity by the hydrocarbon saturation.

In addition to the porosity and the hydrocarbon saturation, the volume of the formation containing hydrocarbons is needed in order to estimate total reserves and to determine if the accumulation is commercial. Knowledge of the thickness and the area of the reservoir is needed for computation of its volume.

To evaluate the producibility of a reservoir, it is necessary to know how easily fluid can flow through the pore system. This property of the formation rock, which depends on the manner in which the pores are interconnected, is its permeability.

The main petrophysical parameters needed to evaluate a reservoir, then, are its porosity, hydrocarbon saturation, thickness, area, and permeability. In addition, the reservoir geometry, formation temperature and pressure, and lithology can play important roles in the evaluation, completion, and production of a reservoir.

Porosity

Porosity is the pore volume per unit volume of formation; it is the fraction of the total volume of a sample that is occupied by pores or voids. The symbol for porosity is ϕ. A dense, uniform substance, such as a piece of glass, has almost zero porosity; a sponge, on the other hand, has a very high porosity.

Porosities of subsurface formations can vary widely. Dense carbonates (limestones and dolomites) and evaporites (salt, anhydrite, gypsum, sylvite) may show practically zero porosity; well-consolidated sandstones may have 10 to 15% porosity; unconsolidated sands may have 30%, or more, porosity. Shales or clays may contain over 40% water-filled porosity, but the individual pores are usually so small that the rock is impervious to the flow of fluids.

Porosities are classified according to the physical arrangement of the material that surrounds the pores and to the distribution and shape of the pores. In a clean sand, the rock matrix is made up of individual sand grains, more or less spherical in shape, packed together in some manner where the pores exist between the grains. Such porosity is called intergranular, sucrosic, or matrix porosity. Generally, it has existed in the formations since the time they were deposited. For this reason, it is also referred to as primary porosity.

Depending on how they were actually deposited, limestones and dolomite may also exhibit intergranular porosity. They may also have secondary porosity in the form of vugs or small caves. Secondary porosity is caused by the action of the formation waters or tectonic forces on the rock matrix after deposition. For instance, slightly acidic percolating waters may create and enlarge the pore spaces while moving through the interconnecting channels in limestone formations, and shells of small crustaceans trapped therein may be dissolved and form vugs. Conversely, percolating waters rich in minerals may form deposits that partially seal off some of the pores or channels in a formation, thereby reducing its porosity and/or altering the pore geometry. Waters rich in magnesium salts can seep through calcite with a gradual replacement of the calcium by magnesium. Since the replacement is atom for atom, mole for mole, and the volume of one mole of dolomite is 12% less than that of calcite, the result is a reduced matrix volume and corresponding increase in pore volume.

Stresses in the formation may also occur and cause networks of cracks, fissures, or fractures, which add to the pore volume. In general, however, the actual volume of the fractures is usually relatively small. They do not normally increase the porosity of the rock significantly, although they may significantly increase its permeability.

Saturation

The saturation of a formation is the fraction of its pore volume occupied by the fluid considered. Water saturation, then, is the fraction (or percentage) of the pore volume that

contains formation water. If nothing but water exists in the pores, a formation has a water saturation of 100%. The symbol for saturation is S; various subscripts are used to denote saturation of a particular fluid (S_w for water saturation, S_o for oil saturation, S_h for hydrocarbon saturation, S_g for gas saturation).

Oil, or gas, saturation is the fraction of the pore volume that contains oil or gas. The pores must be saturated with some fluid. Thus, the summation of all saturations in a given formation rock must total 100%. Although there are some rare instances of saturating fluids other than water, oil, and hydrocarbon gas (such as carbon dioxide or simply air), the existence of a water saturation less than 100% generally implies a hydrocarbon saturation equal to 100% less the water saturation (or $1-S_w$).

The water saturation of a formation can vary from 100% to a quite small value, but it is seldom, if ever, zero. No matter how "rich" the oil or gas reservoir rock may be, there is always a small amount of capillary water that cannot be displaced by the oil; this saturation is generally referred to as irreducible or connate water saturation.

Similarly, for an oil- or gas-bearing reservoir rock, it is impossible to remove all the hydrocarbons by ordinary fluid drives or recovery techniques. Some hydrocarbons remain trapped in parts of the pore volume; this hydrocarbon saturation is called the residual hydrocarbon saturation.

In a reservoir that contains water in the bottom and oil in the top, the demarcation between the two is not always sharp; there is a more or less gradual transition from 100% water to mostly oil. If the oil-bearing interval is thick enough, water saturation at the top approaches a minimum value, the irreducible water saturation, S_{wirr}. Because of capillary forces, some water clings to the grains of the rock and cannot be displaced. A formation at irreducible water saturation will produce water-free hydrocarbons. Within the transition interval some water will be produced with the oil, the amount increasing as S_w increases. Below the transition interval, water saturation is 100%. In general, the lower the permeability of the reservoir rock the longer the transition interval. Conversely, if the transition interval is short, permeability will usually be high.

Permeability

Permeability is a measure of the ease with which fluids can flow through a formation. For a given sample of rock and for any homogeneous fluid, the permeability will be a constant provided the fluid does not interact with the rock itself.

The unit of permeability is the darcy (which is very large), so the thousandth part or the millidarcy (md) is generally used. The symbol for permeability is k.

In order to be permeable, a rock must have some interconnected pores, capillaries, or fractures. Therefore some rough relationship between porosity and permeability exists. Greater permeability, in general, corresponds to greater porosity, but this is far from being an absolute rule.

Shales and some sands have high porosities, but the grains are so small that the paths available for the movement of fluid are quite restricted and tortuous; thus, their permeabilities may be very low.

Other formations, such as limestone, may be composed of a dense rock broken by a few small fissures or fractures of great extent. The porosity of such a formation can be low, but the permeability of a fracture can be enormous. Therefore, fractured limestones may have low porosities but extremely high permeabilities.

Reservoir Geometry

Producing formations (reservoirs) occur in an almost limitless variety of shapes, sizes, and orientations. Figure 2-1 shows some of the major reservoir types; almost any combination of these is also possible.

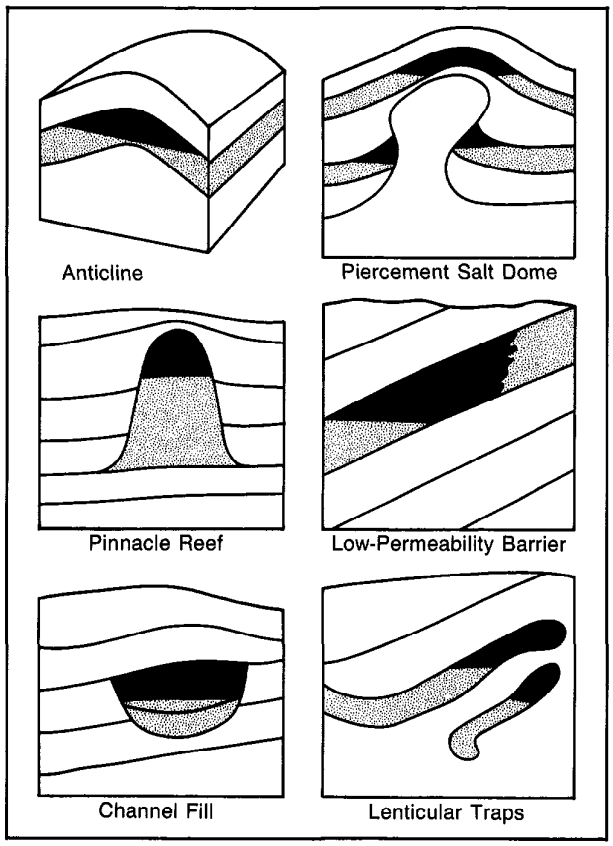

Fig. 2-1—Some typical reservoir shapes and orientations

The physical shape and orientation of a reservoir can bear heavily on its producibility. Reservoirs can be wide or narrow, thick or thin, large or small. Giant reservoirs, such as some in the Middle East, can cover hundreds of square miles and be thousands of feet thick. Others are tiny, far too small for a well completion. Configurations vary from a simple lens shape to tortuously complex shapes.

Most reservoir-forming rocks were supposedly laid down in layers like blankets or pancakes. Their physical characteristics thus tend to be quite varied in different directions, a condition called anisotropy. This nonuniformity is a very important consideration in reservoir engineering and completion design.

Normally, the permeability of such formations is much higher parallel to rather than perpendicular to the layering, and the permeabilities of the various layers can also vary widely.

Reservoirs that did not originate as deposited layers of grains do not conform to this laminar model of anisotropy. Carbonate rocks that originated as reefs, rocks subjected to extensive fracturing, or rocks with vuggy porosity are examples.

Temperature and Pressure

Temperature and pressure also affect hydrocarbon production in several ways. In the reservoir rock, temperature and pressure control the viscosities and mutual solubilities of the three fluids—oil, gas, and water. As a result, the phase relationship of the oil/gas solution may be subject to highly significant variations in response to temperature and pressure changes. For example, as pressure drops gas tends to come out of solution. If this happens in the reservoir rock, the gas bubbles can cause a very substantial decrease in the effective permeability to oil.

The relationships between pressure, temperature, and the phase of hydrocarbon mixtures are extremely variable, depending on the specific types and proportions of the hydrocarbons present. Figure 2-2 is a simple, 2-component phase diagram that illustrates those relationships.

Ordinarily, the temperature of a producing reservoir does not vary much, although certain enhanced-recovery techniques (such as steam flood or fire flood) create conspicuous exceptions to this rule. However, some pressure drop between the undisturbed reservoir and the wellbore is inevitable. This pressure drop is called the pressure drawdown; it can vary from a few pounds per square inch (psi) up to full reservoir pressure. These relationships will be addressed in Chapter 4.

Log Interpretation

Unfortunately, few petrophysical parameters can be measured directly. Instead, they must be derived or inferred from the measurement of other physical parameters of the formations. A large number of these physical parameters can now be measured through casing. They include, among others, the thermal decay time, the natural radioactivity, the hydrogen content, the elemental yields, and in some cases the interval transit time of the rock.

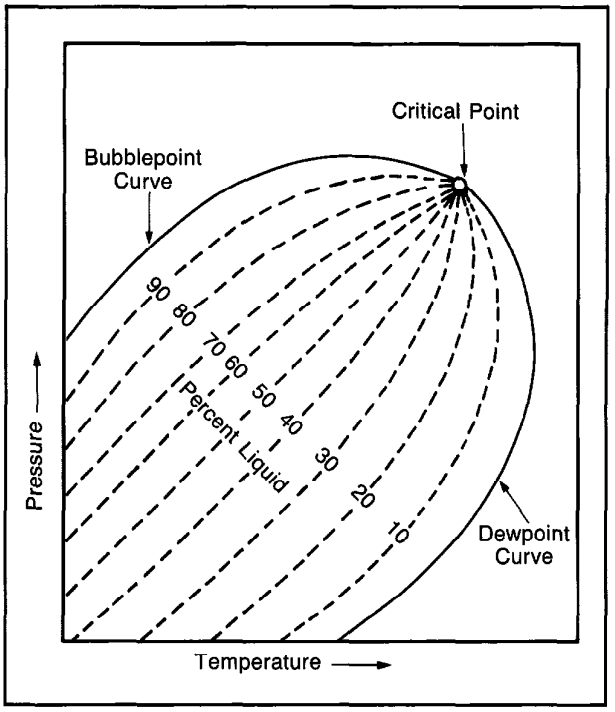

Fig. 2-2—2-component diagram

Log interpretation is the process by which these measurable parameters are translated into the desired petrophysical parameters of porosity, hydrocarbon saturation, producibility, lithology, and mechanical rock properties.

Since the petrophysical parameters of the virgin formation are usually needed, the well logging tool must be able to "see" beyond the casing and cement into the virgin formation, or the interpretation techniques must be able to compensate for these environmental effects. An elaborate environmental test facility and computer modeling programs are used to design correction algorithms for these environmental effects.

It is the purpose of the various well logging tools to provide measurements from which the petrophysical characteristics of the reservoir rocks can be derived or inferred. It is the purpose of quantitative log interpretation to provide the equations and techniques with which these translations can be accomplished.

Determination of Saturation

Determining water and hydrocarbon saturation is one of the basic objectives of well logging. Most of the cased hole water saturation equations are based on proven openhole interpretation models. In open hole, the models use resistivity values while sigma measurements are used in most cased hole evaluations.

Actually, the basic fundamental premises of cased hole log interpretation are few in number and simple in concept. These will be covered in Chapter 3.

REFERENCES

Archie, G.E.: "Classification of Carbonate Reservoir Rocks and Petrophysical Considerations," AAPG *Bulletin* (February, 1952) **36**, No. 2.

Jones, P.J.: "Production Engineering and Reservoir Mechanics (Oil Condensate and Natural Gas)," *OGJ* (1945).

Log Interpretation Charts, Schlumberger Educational Services, Houston (1989).

Log Interpretation Principles/Applications, Schlumberger Educational Services, Houston (1987).

Timur, A.: "An Investigation of Permeability, Porosity, and Residual Water Saturation Relationships for Sandstone Reservoirs," *The Log Analyst* (July-Aug., 1968) **9**, No. 4.

3 Formation Evaluation in Cased Holes

LOGS FOR CASED HOLE FORMATION EVALUATION

Cased hole logs for formation evaluation are principally those from the radiation-measuring tools; e.g., the Thermal Decay Time (TDT), Gamma Ray Spectrometry (GST), Compensated Neutron (CNL), standard gamma ray (GR), and Natural Gamma Ray Spectrometry (NGS*) tools. In addition the Array-Sonic* or Long-Spaced Sonic (LSS*) tools provide porosity data in well-cemented casings and the density log is also useful in special cases.

- The standard gamma ray log is the basic log used for correlation and gives lithology control; in particular it provides an estimate of shaliness. In many old wells where the produced waters contain dissolved radioactive salts the use of the gamma ray log may be unreliable for this purpose because of the accumulation of radioactive deposits on the casing, particularly in the perforated interval. In these situations the NGS log or openhole log data are required.
- The NGS tool can be used to help identify clay type and to calculate clay volumes. The thorium and potassium responses are usually much better shale indicators than the total gamma ray log. The NGS log combined with the GST log permits the volumetric mineral analysis of complex lithological mixtures.
- The CNL neutron log provides a porosity index which depends primarily on the hydrogen content of the formation. When cementation conditions permit, the Array-Sonic log combined with the CNL log can be used to detect gas zones through casing. Under ideal conditions, the density/neutron log combination can also be used.
- In well-bonded casing the Array-Sonic log provides formation compressional and shear travel times for porosity information and data for mechanical rock property calculations.
- The TDT log provides water saturation through discrimination between saline water and hydrocarbon. Additional measurements also provide information for calculating apparent porosity and apparent formation water salinity. In some cases the presence of gas may be detected. The TDT log is also an excellent shale indicator.
- The GST tool provides a measurement of the gamma ray yields of common minerals corresponding to the fluids, porosity, and lithology of the formation. The water/oil saturation determination is independent of formation water salinity so the tool is applicable in formations of unknown water salinity or zones with formation water too fresh for TDT logs.

The principles, characteristics, and interpretation of these logs will be covered in this chapter. Porosity, lithology, and shaliness information from openhole logs or core data are always helpful for interpretation of cased hole logs.

NATURAL GAMMA RAY LOGS

The natural gamma ray (GR) log is a recording of the natural radioactivity of the formations. There are two types of GR logs. One, the standard GR log, measures only the total radioactivity. The other, the NGS (Natural Gamma Ray Spectrometry) log, measures the total radioactivity and the concentrations of potassium, thorium, and uranium producing the radioactivity.

The GR log is generally recorded in track 1 (left track) of the log. It is usually recorded in conjunction with some other log—such as the cement evaluation log or thermal decay time log. Indeed, nearly every cased hole log now includes a recording of the GR log.

Among the GR and NGS uses are the following:

- differentiate potentially porous and permeable reservoir rocks (sandstone, limestone, dolomite) from nonpermeable clays and shales
- define bed boundaries
- tie cased hole to openhole logs
- give a qualitative indication of shaliness
- monitor radioactive tracers
- aid in lithology (mineral) identification

- in the case of the NGS log, detect and evaluate deposits of radioactive minerals
- in the case of the NGS log, define the concentrations of potassium, thorium, and uranium
- in the cases of the NGS log, monitor multiple isotope tracers.

In sedimentary formations the GR log normally reflects the shale content of the formations. This is because the radioactive elements tend to concentrate in clays and shales. Clean formations have a low level of radioactivity, unless radioactive contaminant such as volcanic ash or granite wash is present or the formation waters contain dissolved radioactive salts. An example of the standard gamma ray log is shown in Fig. 3-1.

Properties of Gamma Rays

Gamma rays are bursts of high-energy electromagnetic waves that are emitted spontaneously by some radioactive elements. Nearly all of the gamma radiation encountered in the earth is emitted by the radioactive potassium isotope of atomic weight 40 (K^{40}) and by the radioactive elements of the uranium and thorium series.

The number and energies of the emitted gamma rays are distinctive of each element (Fig. 3-2): potassium (K^{40}) emits gamma rays of a single energy at 1.46 MeV, whereas the uranium and thorium series emit gamma rays of various energies.

In passing through matter, gamma rays experience successive Compton-scattering collisions with atoms of the formation material, losing energy with each collision. After the gamma ray has lost enough energy, it is absorbed via the photoelectric effect by an atom of the formation. Thus, natural gamma rays are gradually absorbed and their energies degraded (reduced) as they pass through the formation.

The rate of absorption varies with formation density. Two formations having the same amount of radioactive material per unit volume but having different densities will show different radioactivity levels; the less dense formations will appear to be slightly more radioactive. The GR log response, after appropriate corrections for borehole environments, is proportional to the weight concentrations of the radioactive material in the formation:

$$GR = \frac{\Sigma \rho_i V_i A_i}{\rho_b} , \qquad \text{(Eq. 3-1)}$$

where:

ρ_i = the densities of the radioactive minerals

V_i = the bulk volume factors of the minerals

A_i = proportionality factors corresponding to the radioactivity of the mineral

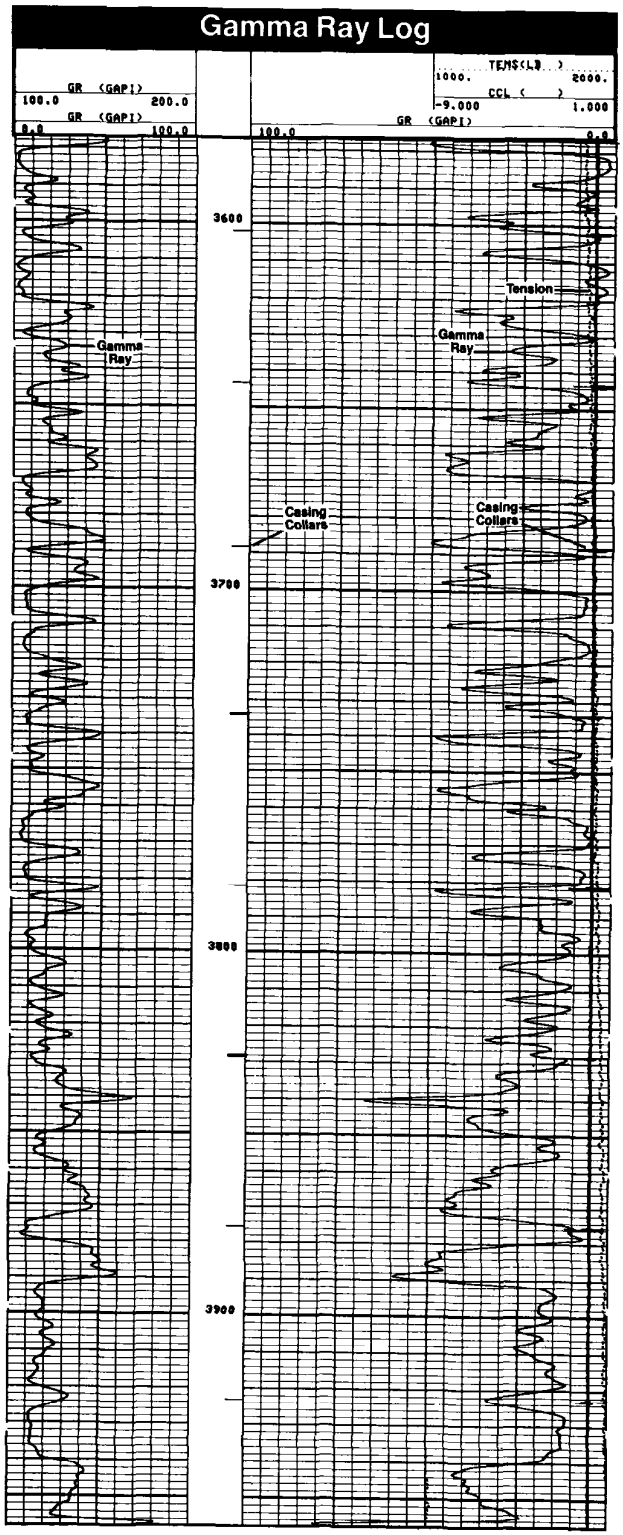

Fig. 3-1—Standard gamma ray log

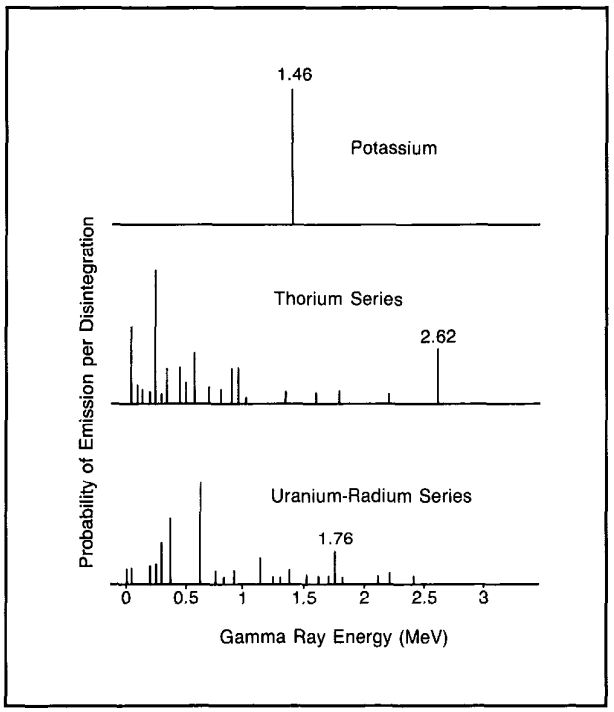

Fig. 3-2—Gamma ray emission spectra of radioactive minerals

ρ_b = the bulk density of the formation.

In sedimentary formations, the depth of investigation of the GR log is about 1 ft.

Equipment

The GR sonde contains a detector to measure the gamma radiation originating in the volume of formation near the sonde. Scintillation counters are now generally used for this measurement. They are much more efficient than the Geiger-Mueller counters used in the past. Because of its higher efficiency, a scintillation counter need only be a few inches in length; therefore, good vertical formation detail is obtained. The GR log may be, and usually is, run in combination with most cased hole services.

Calibration

The primary calibration standard for GR tools is set at the American Petroleum Institute (API) test facility in Houston. A field calibration standard (radioactive source) is used to normalize each tool to the API standard and the logs are calibrated in API units. The radioactivities in sedimentary formations generally range from a few API units in anhydrite or salt to 200 or more in shales.

Prior to the API calibration procedure, GR logs were scaled in micrograms of radium equivalent per ton of formation. Conversions from these units to API units are shown in Table 3-1.

Equipment	Old Unit	API Units Per Old Unit
GNT-F or G Gamma Ray	1 μgm Ra-eq/ton	16.5
GNT-J, K Gamma Ray, GLD-K	1 μgm Ra-eq/ton	11.7

Table 3-1—Conversion from old units to API units for Schlumberger GR logs

The NGS Log

Like the GR log, the NGS log measures the natural radioactivity of the formations. Unlike the GR log, which measures only the total radioactivity, this log measures both the number of gamma rays and the energy level of each and permits the determination of the concentrations of radioactive potassium, thorium, and uranium in formation rocks.

Physical Principle

Most of the gamma ray radiation in the earth originates from the decay of three radioactive isotopes: potassium 40 (K^{40}), with a half-life of 1.3×10^9 years; uranium 238 (U^{238}), with a half-life of 4.4×10^9 years; and thorium 232 (Th^{232}), with a half-life of 1.4×10^{10} years.

Potassium 40 decays directly to stable argon 40 with the emission of a 1.46-MeV gamma ray. However, uranium 238 and thorium 232 decay sequentially through various daughter isotopes before arriving at stable lead isotopes. As a result, gamma rays of many different energies are emitted and fairly complex energy spectra are obtained, as Fig. 3-2 shows. The characteristic peaks in the thorium series at 2.62 MeV and the uranium series at 1.76 MeV are caused by the decay of thallium 208 and bismuth 214, respectively.

It is generally assumed that formations are in secular equilibrium; that is, the daughter isotopes decay at the same rate as they are produced from the parent isotope. This means that the relative proportions of parent and daughter elements in a particular series remain fairly constant; so, by looking at the gamma ray population in a particular part of the spectrum it is possible to infer the population at any other point. In this way, the amount of parent isotope present can be determined.

Once the parent isotope population is known, the amount of nonradioactive isotope can also be found. The ratio of potassium 40 to total potassium is very stable and constant on the earth. Apart from thorium 232, the thorium isotopes are very rare and so can be neglected. The relative proportions of the uranium isotopes depend somewhat on their

environment, and there is also a gradual change because of their different half-lives; at present, the ratio of uranium 238 to uranium 235 is about 137.

Measurement Principle

The NGS tool uses a sodium iodide scintillation detector. Gamma rays emitted by the formation rarely reach the detector directly. Instead, they are scattered and lose energy through three possible interactions with the formation: the photoelectric effect, Compton scattering, and pair production. Because of these interactions and the response of the sodium iodide scintillation detector, the original spectra of Fig. 3-2 are degraded to the rather "smeared" spectra shown in Fig. 3-3.

The high-energy part of the detected spectrum is divided into three energy windows, W1, W2, and W3, each covering a characteristic peak of the three radioactivity series (Fig. 3-3). Knowing the response of the tool and the number of counts in each window, it is possible to determine the amounts of thorium 232, uranium 238, and potassium 40 in the formation.

There are relatively few counts in the high-energy range where peak discrimination is best; therefore, measurements are subject to large statistical variations, even at low logging speeds. By including a contribution from the high-count rate, low-energy part of the spectrum (windows W1 and W2), these high statistical variations in the high-energy windows can be reduced by a factor of 1.5 to 2. The statistics are further reduced by another factor of 1.5 to 2 by using a filtering technique that compares the counts at a particular depth with

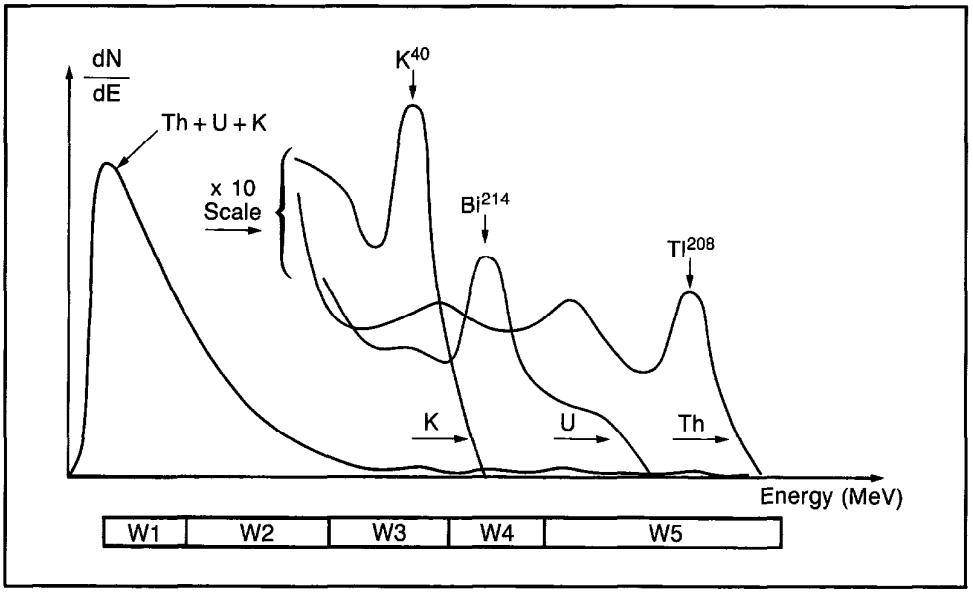

Fig. 3-3—Potassium, thorium, and uranium response curves (NaI crystal detector)

the previous values in such a way that spurious changes are eliminated while the effects of formation changes are retained. Normally, only the final filtered data are presented on film, but the unfiltered raw data are always recorded on tape.

Log Presentation

The NGS log provides a recording of the amounts (concentrations) of potassium, thorium, and uranium in the formation. These are usually presented in tracks 2 and 3 of the log (Fig. 3-4). The thorium and uranium concentrations are presented in parts per million (ppm) and the potassium concentration in percent (%).

In addition to the concentrations of the three individual radioactive elements, a total (standard) GR curve is recorded and presented in track 1. The total response is determined by a linear combination of the potassium, thorium, and uranium concentrations. This standard curve is expressed in API units. If desired, a "uranium-free" measurement (CGR) can also be provided. It is simply the summation of gamma rays from thorium and potassium only.

Interpretation

The major occurrences of the three radioactive families are as follows:

- potassium: micas, feldspars, micaceous clays (illite), radioactive evaporites

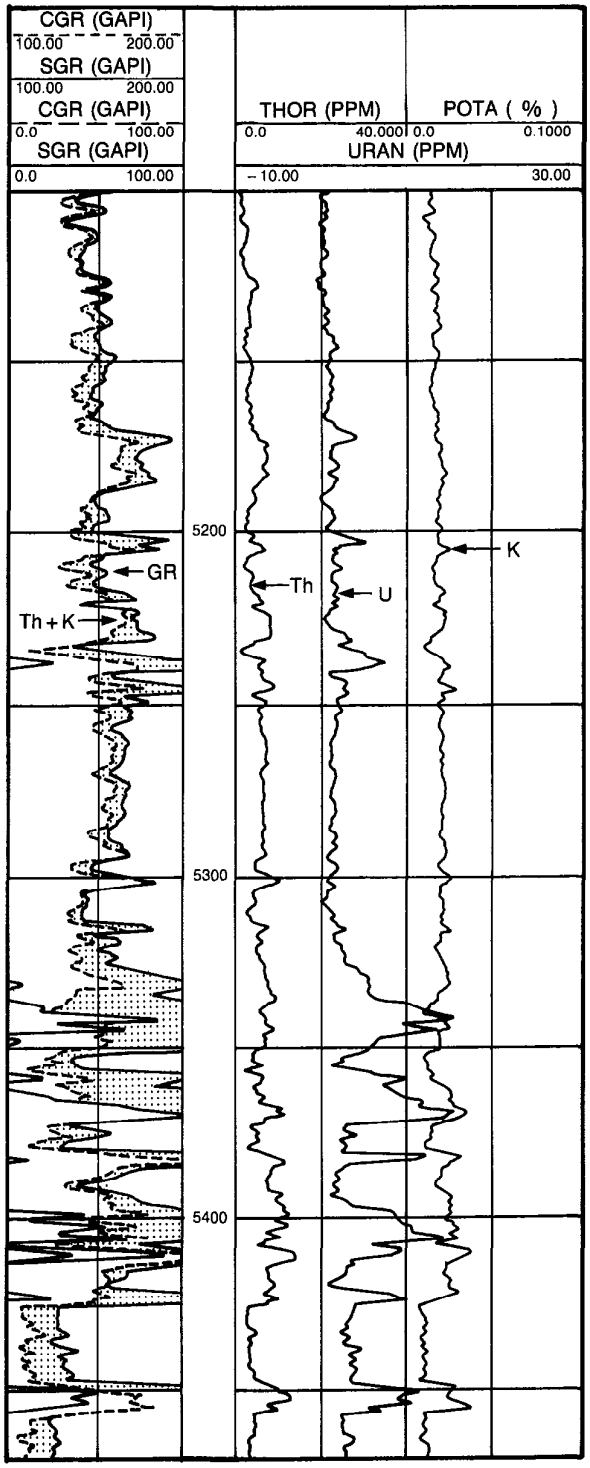

Fig. 3-4—Natural gamma ray spectrometry log

- thorium: shales, heavy minerals
- uranium: phosphates, organic matter.

The significance of the type of radiation depends on the formation in which it is found. In carbonates, uranium usually indicates organic matter, phosphates, and stylolites. The thorium and potassium levels are representative of clay content. In sandstones, the thorium level is determined by heavy minerals and clay content, and the potassium is usually contained in micas and feldspars. In shales, the potassium content indicates clay type and mica, and the thorium level depends on the amount of detrital material or the degree of shaliness.

High uranium concentrations in a shale suggest that the shale is a hydrocarbon source rock. In igneous rock the relative proportions of the three radioactive families are a guide to the type of rock, and the ratios Th/K and Th/U are particularly significant.

The radioactive minerals found in a formation are, to some extent, dependent on the mode of sedimentation or deposition. The mode of transportation and degree of reworking and alteration are also factors. As an example, because thorium has very low solubility, it has limited mobility and tends to accumulate with the heavy minerals. On the other hand, uranium has a greater solubility and mobility, and so high uranium concentrations are found in fault planes, fractures, and formations where water flow has occurred. Similarly, high concentrations of uranium can build up in the permeable beds and on the tubing and casing of producing oil wells. Marine deposits are characterized by their extremely low radioactive content, with none of the three families making any significant contribution. Weathered zones are often indicated by pronounced changes in the thorium and potassium content of the formation but a more or less constant Th/K ratio.

Applications

The NGS log can be used to detect, identify, and evaluate radioactive minerals. It also can be used to help identify clay type and to calculate clay volumes. This, in turn, can provide insight into the source, the depositional environment, the diagenetic history, and the petrophysical characteristics (such as surface area, pore structure) of the rock.

The thorium and potassium response or the thorium-only response of the NGS log is often a much better shale indicator than the simple GR log or other shale indicators. Shaly-sand interpretation programs can thereby benefit from its availability. The NGS log can also be used for correlation where beds of thorium and potassium content exist.

The combination of the NGS log with other lithology-sensitive measurements (such as the GST and neutron logs)

permits the volumetric mineral analysis of very complex lithological mixtures. In less complex mixtures, it allows the minerals to be identified with greater certainty and volumes to be calculated with greater accuracy.

NEUTRON LOGS

Cased hole neutron logs are used principally for the delineation of porous formations and the determination of their porosity. They respond primarily to the amount of hydrogen in the formation. Thus, in clean formations whose pores are filled with water or oil, the neutron log reflects the amount of liquid-filled porosity. The neutron log is also useful for correlation with openhole logs in areas where the gamma ray log does not give good definition (i.e., thick, clean carbonate zones as shown in Fig. 3-5).

Gas zones can often be identified by comparing the neutron log with a sonic porosity log or core porosity.

Principle

Neutrons are electrically neutral particles, each having a mass almost identical to the mass of a hydrogen atom. High-energy (fast) neutrons are continuously emitted from a radioactive source in the sonde. These neutrons collide with nuclei of the formation materials in what may be thought of as elastic "billiard-ball" collisions. With each collision, the neutron loses some of its energy.

The amount of energy lost per collision depends on the relative mass of the nucleus with which the neutron collides. The greater energy loss occurs when the neutron strikes a nucleus of practically equal mass—i.e., a hydrogen nucleus. Collisions with heavy nuclei do not slow the neutron very much. Thus, the slowing of neutrons depends largely on the amount of hydrogen in the formation.

Within a few microseconds these epithermal neutrons have been slowed by successive collisions to thermal velocities, corresponding to energies of around 0.025 eV. They then diffuse randomly, without losing more energy, until they are captured by the nuclei of atoms such as chlorine, hydrogen, or silicon.

The capturing nucleus becomes intensely excited and emits a high-energy gamma ray of capture. Depending on the type of neutron tool, either these capture gamma rays or the neutrons themselves are counted by a detector in the sonde.

When the hydrogen concentration of the material surrounding the neutron source is large, most of the neutrons are slowed and captured within a short distance of the source. On the contrary, if the hydrogen concentration is small, the neutrons travel farther from the source before being captured. Accordingly, the counting rate at the detector increases for decreased hydrogen concentration, and vice versa.

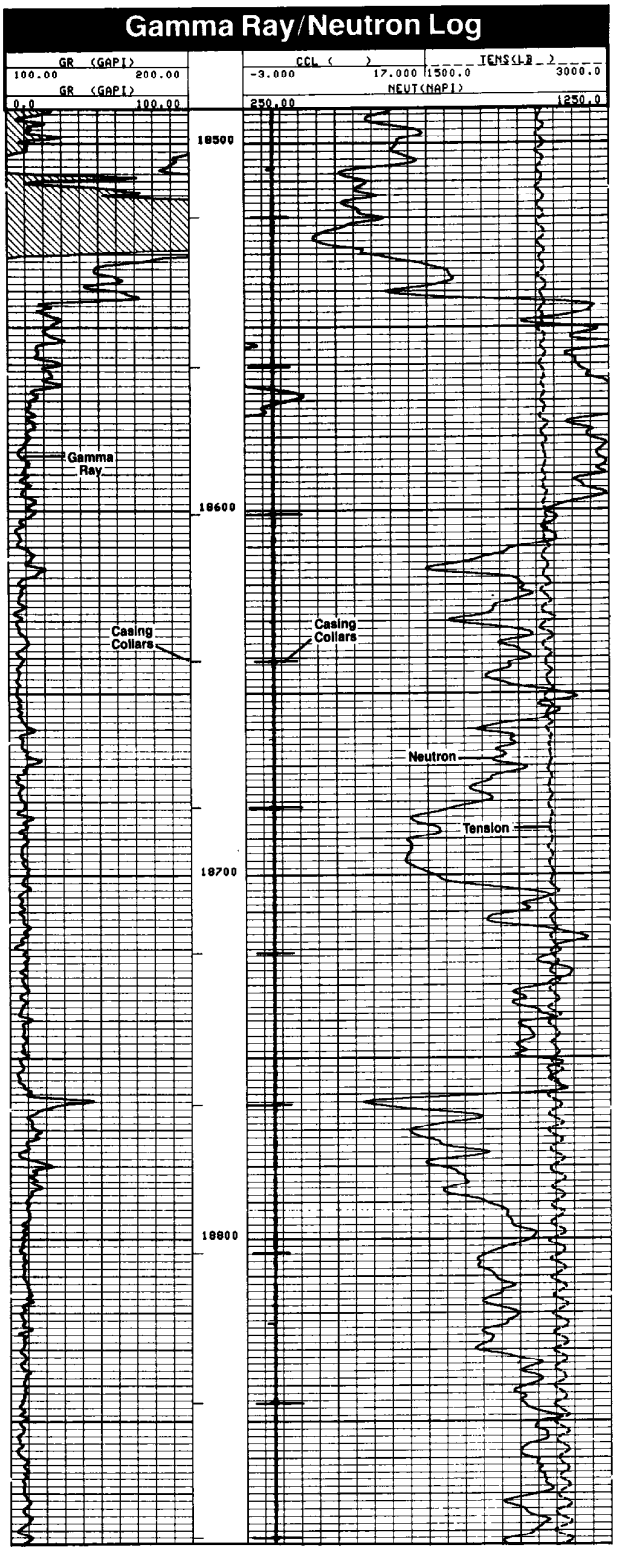

Fig. 3-5—Neutron Log

Equipment

Neutron logging tools run in casing include the neutron (GNT) tool series (no longer in use) and the CNL tool. The current tools use Americium-Beryllium (AmBe) sources to provide neutrons with initial energies of 4.2 MeV electron volts.

The GNT tools were nondirectional devices that employed a single detector sensitive to both high-energy capture gamma rays and thermal neutrons. Although the GNT tools responded primarily to porosity, their readings were greatly influenced by fluid salinity, temperature, pressure, and by the casing and cement.

The CNL tool is a mandrel-type tool especially designed for combination with any of several other tools to provide a simultaneous neutron log (Fig. 3-6). The CNL tool is a dual-spacing, thermal neutron-detection instrument. The ratio of counting rates from the two detectors is processed by the surface equipment to produce a linearly scaled recording of neutron porosity index. The effects of wellbore parameters are greatly reduced by taking the ratio of two counting rates similarly affected by these perturbations. The CNL tool can be run in liquid-filled holes but cannot be used in gas-filled holes.

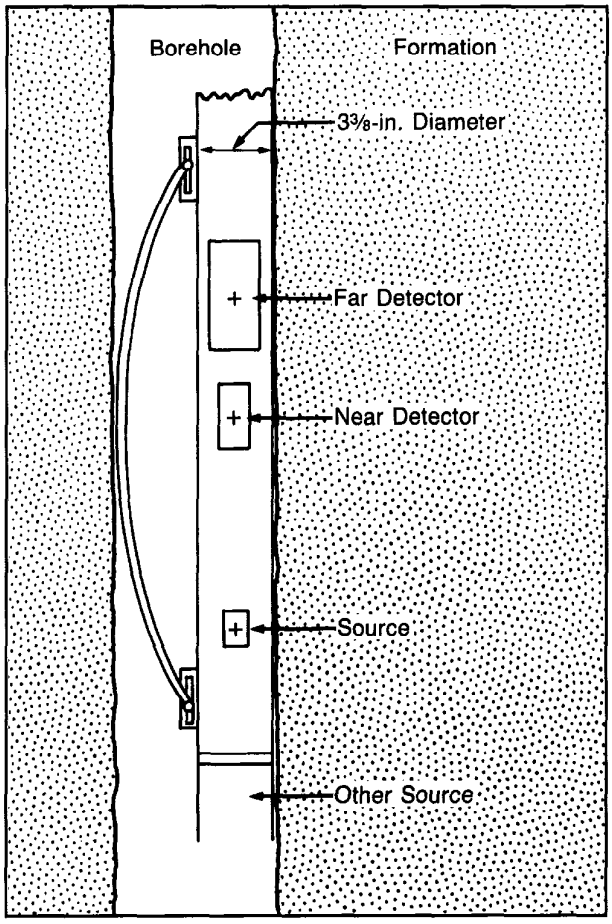

Fig. 3-6—CNT tool configuration

Since thermal neutrons are measured in the CNL tool, the response is affected by elements having a high thermal neutron capture cross section. Also the tool is sensitive to shale in the formation because of the hydroxyls associated with the clay mineral structure. The large apparent porosity values are due largely to the hydrogen concentration associated with the shale matrix. This effect can mask the tool response to gas in shaly formations.

Log Presentation

The CNL neutron log is recorded in linear porosity units for a particular matrix lithology. Figure 3-7 is an example of a combination CNL-GR log.

Calibration

The primary calibration standard for GNT neutron logs was the API neutron pit in Houston. The response of the logging tool in a 19% porosity, water-filled limestone was defined as 1000 API units. Secondary calibrating devices (radioactive source), accurately related to the API pit, were used for the field calibration.

Prior to the API calibration procedure, neutron logs were scaled in counts per second. Conversion factors are provided in Table 3-2 to rescale them for comparison with neutron logs scaled in API units. At present, neutron logs are scaled directly in porosity units.

The primary calibration standard for CNL tools is a series of water-filled laboratory formations. The porosities of these controlled formations are known within ± 0.5 porosity units. The secondary (shop) standard is a water-filled calibrating tank. A wellsite check is made by using a fixture that reproduces the count rate ratio obtained in the tank.

Investigation Characteristics

The typical vertical resolution of the CNL tool is 2 ft. However, a new method of processing the count rates is now available. This method improves the vertical resolution to 1 ft by exploiting the better vertical resolution of the near detector.

The radial investigation depends on the porosity of the formation. Very roughly, at zero porosity the depth of investigation is about 1 ft. At higher porosity the depth of investigation is less because neutrons are slowed and captured closer to the borehole. For average conditions, the depth of investigation is about 10 in. for the CNL tool.

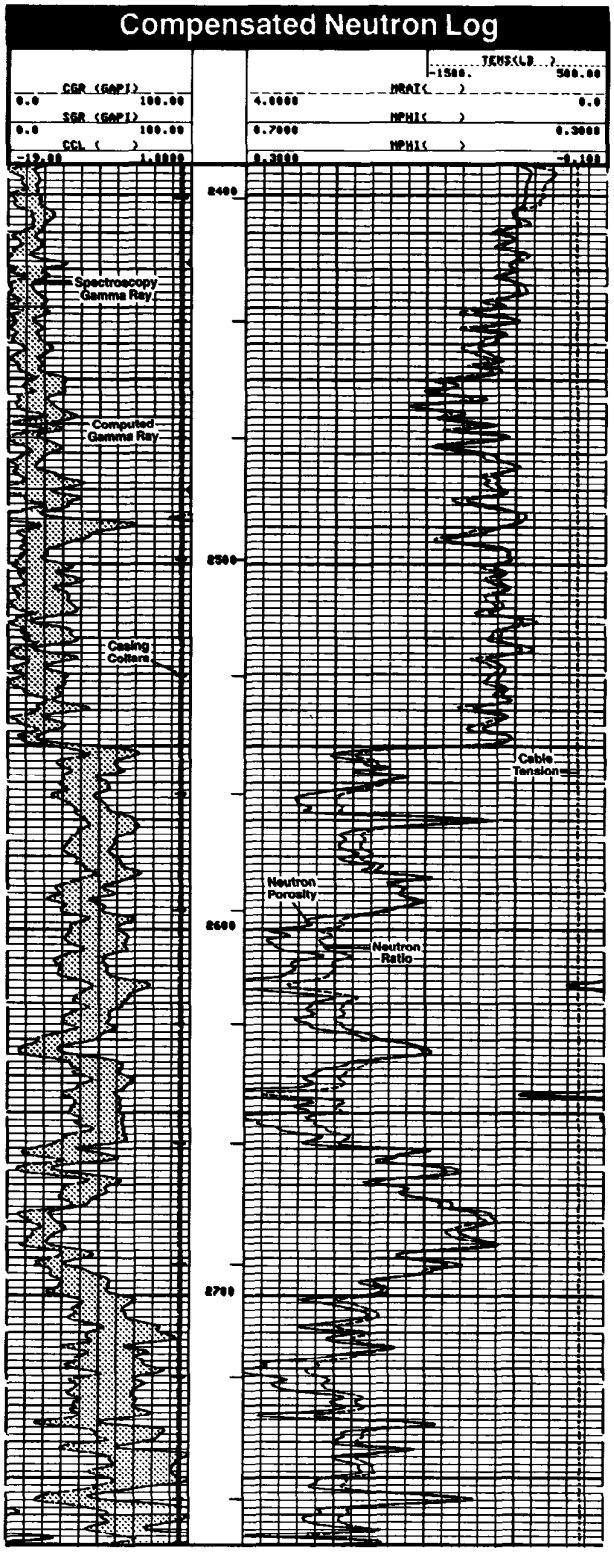

Fig. 3-7—Compensated neutron log

Tool Type Source: PuBe or AmBe	Spacing (in.)	API Units per Std. CPS
GNT-F, G, H	15.5	1.55
GNT-F, H	19.5	5.50
GNT-G	19.5	5.70
GNT-J, K	16	2.70

Table 3-2—Conversion from standard CPS units to API units for old Schlumberger neutron logs

Tool Response

As already stated, the responses of the neutron tools primarily reflect the amount of hydrogen in the formation. Since oil and water contain practically the same amount of hydrogen per unit volume, the responses reflect the liquid-filled porosity in clean formations. However, the tools respond to all the hydrogen atoms in the formation, including those chemically combined in formation matrix minerals. Thus, the neutron reading depends mostly on the hydrogen index of the formation. The hydrogen index is proportional to the quantity of hydrogen per unit volume, with the hydrogen index of fresh water at surface conditions taken as unity.

Hydrogen Index of Salt Water

Dissolved sodium chloride (NaCl) takes up space and thereby reduces the hydrogen density. An approximate formula for the hydrogen index of a saline solution at 75° F is:

$$H_w = 1 - 0.4P \quad , \qquad \text{(Eq. 3-2a)}$$

where P is the NaCl concentration in parts per million. More generally, independent of temperatures,

$$H_w = \rho_w (1 - P) \quad . \qquad \text{(Eq. 3-2b)}$$

In openhole logging, formations are generally invaded and the water in the zone investigated by the neutron logs is considered to have the same salinity as the borehole fluid. For cased holes, the invaded zone usually disappears with time, and the water salinity is that of the formation water. The correction to the CNL log is provided by Chart Por-14a in the Log Interpretation Charts book.

Response to Hydrocarbons

Liquid hydrocarbons have hydrogen indices close to that of water. Gas, however, usually has a considerably lower hydrogen concentration that varies with temperature and pressure. Therefore, when gas is present near enough to the wellbore to be within the tool's zone of investigation, a neutron log reads too low a porosity. This characteristic allows the neutron log to be used with other porosity logs to detect gas zones and identify gas/liquid contacts.

The quantitative response of the neutron tool to gas or light hydrocarbon depends primarily on the hydrogen index and another factor—the "excavation effect". The hydrogen index can be estimated from the composition and density of the hydrocarbon. The hydrogen index of heavier hydrocarbons (oils) can be approximated by the equation:

$$H_o = (18/14)\ \rho_o = 1.28\ \rho_o \ . \qquad \text{(Eq. 3-3)}$$

This equation assumes the chemical composition of the oil is $n(CH_2)$. H_o is derived from the comparison of the hydrogen density and molecular weight of water to those of oil.

Another set of equations can be used to estimate the hydrogen index of hydrocarbon fluids:

For light hydrocarbons ($\rho_h < 0.25$) ,

$$H_h \approx 2.2\ \rho_h \ . \qquad \text{(Eq. 3-4a)}$$

For heavy hydrocarbons ($\rho_h > 0.25$) ,

$$H_h \approx \rho_h + 0.3 \ . \qquad \text{(Eq. 3-4b)}$$

Still another proposal suggests the equation

$$H_h = 9 \left(\frac{4 - 2.5\ \rho_h}{16 - 2.5\ \rho_h} \right) \rho_h \ . \qquad \text{(Eq. 3-5)}$$

Physics indicate that the effect of gas in the formation near the borehole is greater than would be expected by taking into account only its smaller hydrogen density. Previous calculations had been made as if the gas-filled portion of the porosity were replaced by rock matrix. The new calculations show that when this additional rock matrix is "excavated" and replaced with gas, the formation has a smaller neutron-slowing characteristic. The calculated difference in the neutron log readings has been termed the excavation effect. If this effect is ignored, too-high values of flushed-zone gas saturation and too-low values of porosity are given. In cased holes, this excavation effect is exaggerated since there are no invasion fluids present to flush the gas away from the borehole.

Figure 3-8 shows the corrections needed for excavation effect. The values of porosity for sandstone, limestone, and dolomite lithologies are plotted. Intermediate porosity values can be interpolated. The ordinate scale is used to correct neutron log porosities. An additional ordinate scale is provided for correcting porosities derived from a neutron-density crossplot that does not contain the excavation effect correction. Excavation effect corrections have already been incorporated into Chart CP-5 in the Log Interpretation Charts book.

The corrections for excavation effect given by Fig. 3-8 can be approximated by the formula:

$$\Delta\phi_{Nex} = K[2\phi^2\ S_{wH} + 0.04\ \phi](1 - S_{wH}) \ , \qquad \text{(Eq. 3-6)}$$

where $\Delta\phi_{Nex}$, ϕ, and S_{wH} are in fractional units. For sandstone the coefficient, K, is 1; for limestone it is about 1.046, and for dolomite it is about 1.173. Note that the second term of this equation is rather small and can often be disregarded.

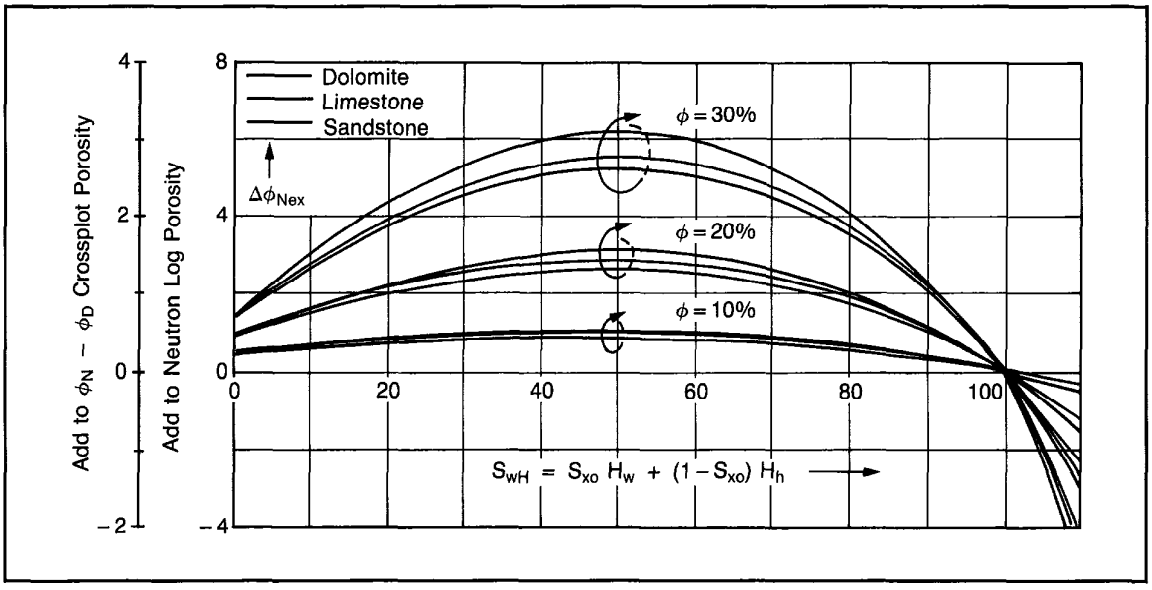

Fig. 3-8—Neutron correction for excavation effect

Shales, Bound Water

Neutron tools see all hydrogen in the formation even if some is not associated with the liquids saturating the formation porosity. For example, it sees bound water associated with the shales. Shales in general have an appreciable hydrogen index; in shaly formations the apparent porosity derived from the neutron response will be greater than the actual effective porosity of the reservoir rock. Also, the neutron tool measures water of crystallization. For example, nonporous gypsum ($CaSO_4 + 2H_2O$) has a large apparent porosity because of its significant hydrogen content.

Effect of Lithology

The readings of all neutron logs are affected to some extent by the lithology of the matrix rock. CNL logs are usually scaled for a limestone matrix. Porosities for other lithologies are obtained from Chart Por-13 (Fig. 3-9).

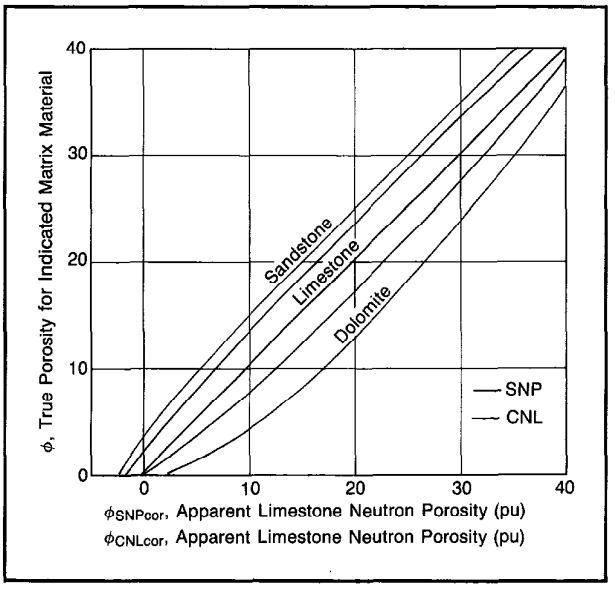

Fig. 3-9—Neutron porosity equivalence curves

Determining Porosity from Neutron Logs

Subject to the various assumptions and corrections, values of apparent porosity can be derived from any neutron log. However, certain effects, such as lithology, clay content, and amount and type of hydrocarbon, can be recognized and corrected for only if additional porosity information—from sonic and/or openhole porosity logs—is available. Any interpretation of a neutron log alone should be undertaken with a realization of the uncertainties involved.

Thermal Neutron Measurement

Neutron tools are designed to minimize the environmental effects on the thermal neutron measurement. The standard conditions for calibration are:

- 8¾-in. borehole diameter,
- casing thickness, 0.304 in.,
- cement thickness, 1.62 in.,
- fresh water in borehole and formation,
- no standoff,
- 75 °F temperature,
- atmospheric pressure, and
- tool eccentered in hole.

If there are departures from these conditions, the logs will require corrections. The combined correction for all factors, usually small, yields a value of corrected neutron porosity index. Chart Por-14 provides the corrections to the neutron measurements.

SONIC LOGS

In a well-bonded, fluid-filled, cased hole, rock acoustic travel times can be obtained with the Array-Sonic tool or the Long-Spaced Sonic (LSS) tool. When the casing and formation are acoustically coupled the casing signal attenuates rapidly and the formation signals dominate.

In its simplest form, a sonic tool consists of a transmitter that emits a sound pulse and a receiver that picks up and records the pulse as it passes the receiver. The sonic log is simply a recording versus depth of the time, t, required for a sound wave to traverse 1 ft of formation. Known as the interval transit time, transit time, Δt, or slowness, t is the reciprocal of the velocity of the sound wave. The interval transit time for a given formation depends upon its lithology, porosity, and texture. This dependence upon porosity makes the sonic log very useful as a porosity log.

Principle

The propagation of sound in a borehole is a complex phenomenon. It is governed by the mechanical properties of several separate acoustical domains. These include the formation, the borehole fluid column, and the logging tool itself.

The sound emanated from the transmitter impinges on the borehole wall. This establishes compressional and shear waves within the formation, surface waves along the borehole wall, and guided waves within the fluid column.

In the case of well logging, the borehole wall, formation bedding, borehole rugosity, and fractures can all represent significant acoustic discontinuities. Therefore, the phenomena of wave refraction, reflection, and conversion lead to the presence of many acoustic waves in the borehole when a sonic log is being run. It is not surprising, in view of these considerations, that many acoustic energy arrivals are seen by the receivers of a sonic logging tool. The more usual

energy arrivals in well-bonded casing are shown in the acoustic waveform displays of Fig. 3-10. These waveforms were recorded with an array of eight receivers located 8 to 11½ ft from the transmitter. The various wave packets have been labeled. Although the wave packets are not totally separated in time at this spacing, the distinct changes corresponding to the onset of the formation compressional and shear arrivals and the Stoneley arrival can be observed.

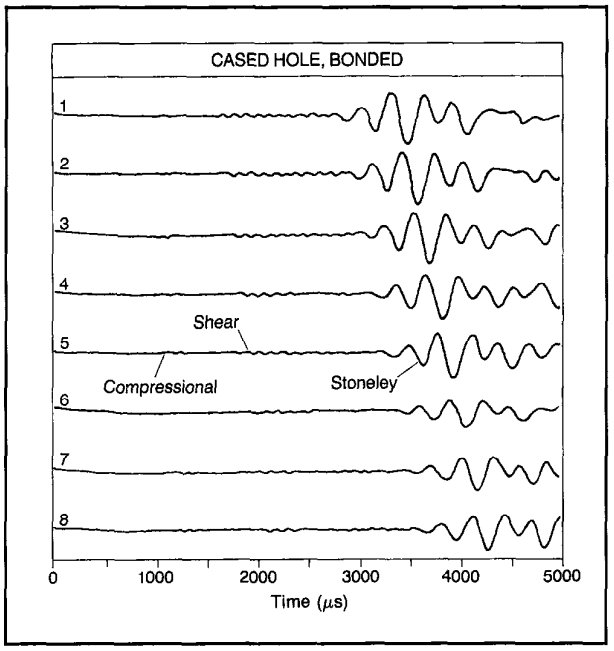

Fig. 3-10—Sonic waveforms in cased hole with good cement bonding

The compressional wave is one that has traveled from the transmitter to the formation as a fluid pressure wave, has been refracted at the borehole wall, has traveled within the formation at the compressional wave velocity of the formation, and has traveled back to the receiver as a fluid pressure wave.

The shear wave is one that has traveled from the transmitter to the formation as a fluid pressure wave, has traveled within the formation at the shear wave velocity of the formation, and has traveled back to the receiver as a fluid pressure wave.

The Stoneley wave is one of large amplitude that has traveled from transmitter to receiver with a velocity less than that of the compressional waves in the borehole fluid. The velocity of the Stoneley wave is dependent upon the frequency of the sound pulse, hole diameter, formation shear velocity, densities of the formation, and fluid and fluid compressional wave velocity. Casing also affects the Stoneley wave, but it has virtually no effect on the compressional and shear waves.

The casing arrival is the first component on the acoustic waveform so the first energy detection cannot be used to measure formation arrival times. Therefore, a sonic tool with long spacing is required to provide a correct measurement of the velocity through casing. The 8, 10, or 12-ft spacing separates the arrival times of the components of the acoustic waveform and permits their identification as shown in Fig. 3-10.

LSS sonic tools, with transmitter-receiver spacings of 8 ft and 10 ft or 10 ft and 12 ft, are available, although the Array-Sonic tool is preferable. Using the standard BHC system for borehole compensation with an LSS sonde would make the tool excessively long. Therefore, an alternate solution called "depth-derived" borehole compensation is used.

The LSS sonde has two transmitters and two receivers arranged as shown in Fig. 3-11. Readings are taken at two different depth positions of the sonde: once when the two receivers straddle the measure point depth and once when the two transmitters straddle the measure point depth.

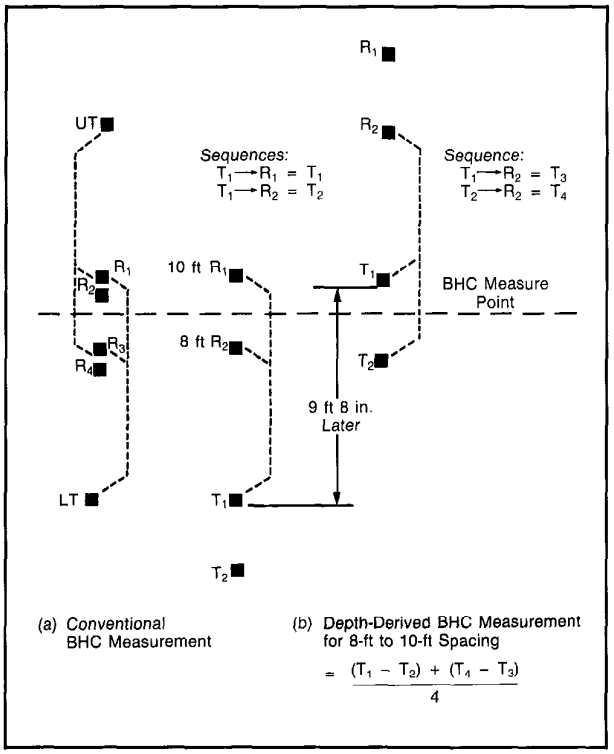

Fig. 3-11—Depth-derived borehole compensation for long-spaced sonic tools

First t reading = $T_1 \rightarrow R_1 - T_1 \rightarrow R_2$

Second t reading = $T_1 \rightarrow R_2 - T_2 \rightarrow R_2$

The first t reading is memorized until the sonde has reached the position to make the second t reading, then both are averaged to obtain the borehole-compensated measurement.

$$t = \frac{\text{memorized first } t \text{ reading} + \text{second } t \text{ reading}}{2 \times \text{span}},$$

where span is the distance (2 ft) between a pair of receivers.

Assuming that the two sonde position depths are accurately known and the sonde tilting is similar for the two positions, the depth-derived borehole compensated system is equivalent to the standard BHC system. Use of the upper transmitter and receiver yields an 8 to 10-ft sonic t measurement, and use of the lower transmitter and receiver yields a 10 to 12-ft sonic t measurement.

The Array-Sonic service is the preferred tool for cased hole velocity measurements. The tool contains two broadband (5 to 18 kHz) piezoelectric transmitters spaced 2 ft apart. Two piezoelectric receivers are located 3 ft and 5 ft from the upper transmitter. In cased wells, these receivers are used to make standard 3-ft Cement Bond Logs (CBL) and 5-ft Variable Density* logs (VDL). Figure 3-12 shows the Array-Sonic tool in the cement bond mode.

The Array-Sonic tool also contains an array of eight wideband piezoelectric receivers. The receivers are spaced 6 in. apart with the closest receiver 8 ft from the upper transmitter. Two of these receivers, receivers 1 and 5, spaced 2 ft apart, can be used for making standard long-spaced, 8 to 10-ft and 10 to 12-ft, depth-derived, borehole-compensated t logs. Measurement hardware consisting of a closely spaced transmitter-receiver pair also exists to make a continuous mud t log. Borehole fluid is drawn through this measurement section as the tool is moved during logging.

The 8-array receiver outputs and the two from the sonic sonde are multiplexed with the mud t receiver output and transmitted to the surface in either analog or digital form. The array waveforms are processed at the wellsite with the CSU* surface instrumentation and array processor or at the computing center using a true full-waveform technique. A signal processing algorithm follows the components as they sweep past the array and calculates speeds and equivalent travel times.

Log Presentation

Sonic velocities in common formation lithologies range from about 6000 to 23,000 ft/sec. To avoid small decimal fractions, the reciprocal of velocity, t, is recorded (English scale) in microseconds per foot (μs/ft) over a range from about 44 μs/ft for zero-porosity dense dolomite to about 190 μs/ft for water. The interval transit time is usually recorded on a linear scale in tracks 2 and 3 of the log (Fig. 3-13).

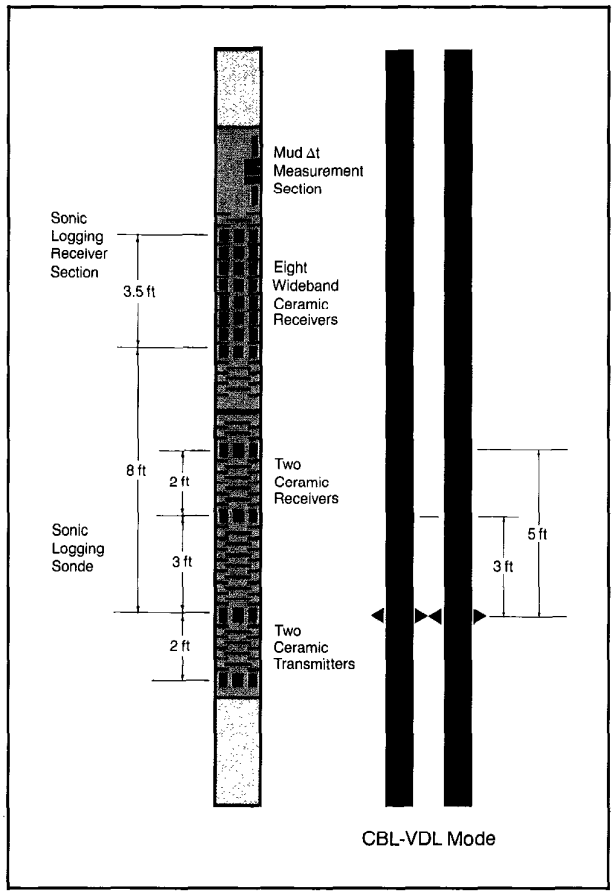

Fig. 3-12—Array-Sonic tool in cement bond log mode

Sonic Velocities in Formations

In sedimentary formations the speed of sound depends on many parameters; principally, it depends on the rock matrix material (sandstone, limestone, dolomite) and on the distributed porosity. Ranges of values of sonic velocity and transit time for common rock matrix materials and casing are listed in Table 3-3.

The values listed are for nonporous substances. Porosity decreases the velocity of sound through the rock material and, correspondingly, increases the interval transit time.

Porosity Determination (Wyllie Time-Average Equation)

Consolidated and Compacted Sandstones

After numerous laboratory determinations, Wyllie proposed, for clean and consolidated formations with uniformly distributed small pores, a linear time-average or weighted-average relationship between porosity and compressional transit time:

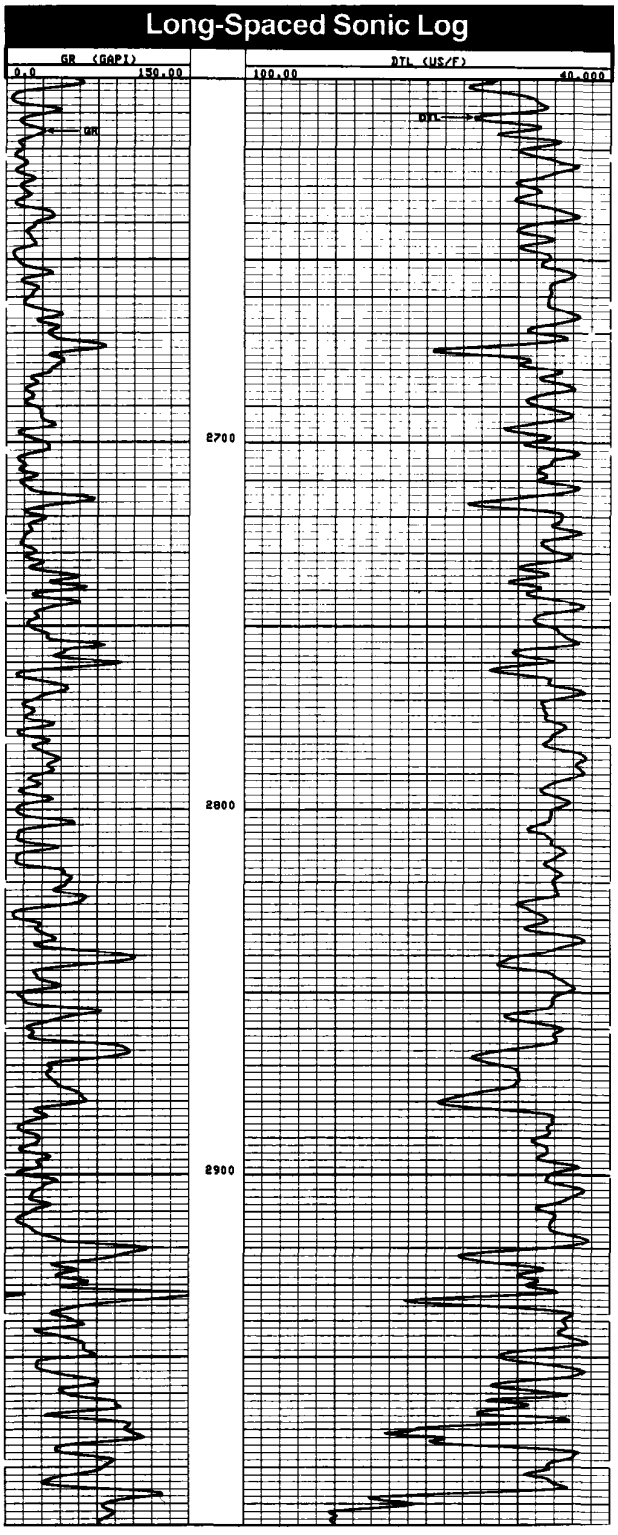

Fig. 3-13—Sonic log presentation

	v_{ma}(ft/sec)	Δt_{ma}(μs/ft)	Δt_{ma}(μs/ft) (commonly used)
Sandstones	18,000-19,500	55.5-51.0	55.5 or 51.0
Limestones	21,000-23,000	47.6-43.5	47.5
Dolomites	23,000	43.5	43.5
Anhydrite	20,000	50.0	50.0
Salt	15,000	66.7	67.0
Casing (iron)	17,500	57.0	57.0

Table 3-3—Sonic velocities in formations

$$t_{LOG} = \phi\, t_f + (1 - \phi)\, t_{ma} \qquad \text{(Eq. 3-7a)}$$

or

$$\phi_{SV} = \frac{t_{LOG} - t_{ma}}{t_f - t_{ma}}\,, \qquad \text{(Eq. 3-7b)}$$

where:

t_{LOG} = reading on the sonic log in μs/ft

t_{ma} = transit time of the matrix material

t_f = is the transit time of the saturating fluid (about 189 μs/ft for freshwater mud systems).

Generally, consolidated and compacted sandstones have porosities from 15 to 25%. In such formations, the response of the sonic log seems to be relatively independent of the exact contents of the pores: water, oil, gas, or even disseminated shale. However, in some higher porosity sandstones (30% or greater) that have very low water saturation, high hydrocarbon saturation, and very shallow invasion, the t values may be somewhat greater than those in the same formations when water saturated.

If any shale laminae exist within the sandstone, the apparent sonic porosity values are increased by an amount proportional to the bulk volume fraction of laminae. The t readings are increased because t_{sh} is generally greater than t_{ma} of the sandstone matrix.

Carbonates

In carbonates having intergranular porosity the time-average formula still applies, but, sometimes, pore structure and pore size distribution are quite different from that of sandstones. There is often some secondary porosity consisting of vugs and/or fractures with much larger dimensions than the pores of the primary porosity. In vuggy formations, the velocity of sound seems to depend mostly on the primary intergranular porosity, and the porosity derived from the sonic reading through the time-average formula will tend to be too low by

an amount approaching the secondary porosity. Thus, if the total porosity (ϕ_t) of a formation exhibiting primary and secondary porosity is available (from a neutron and/or density log, for example), the amount of secondary porosity can be estimated:

$$\phi_2 = \phi_t - \phi_{SV} . \qquad \text{(Eq. 3-8)}$$

Uncompacted Sands

Direct application of the time-average equation gives values of porosity that are too high in unconsolidated and insufficiently compacted sands. Uncompacted sands are most prevalent in the geologically younger formations, particularly at shallow depths. However, even at deeper depths these younger sands are often uncompacted when the overburden-to-formation fluid pressure differentials are less than about 4000 to 5000 psi. Such lack of compaction may be indicated when adjacent shales exhibit t values greater than 100 μs/ft.

When the formations are not sufficiently compacted, the observed t values are greater than those that correspond to the porosity according to the time-average formula, but the ϕ versus t relationship is still approximately linear. In these cases, an empirical correction factor, B_{Cp}, is applied to Eq. 3-7 to give a corrected porosity, ϕ_{SVcor}:

$$\phi_{SVcor} = \frac{t - t_{ma}}{t_f - t_{ma}} \times \frac{1}{B_{Cp}} . \qquad \text{(Eq. 3-9)}$$

The value of B_{cp} is given approximately by dividing the sonic velocity in nearby shale beds by 100. However, the compaction correction factor is best determined by comparing ϕ_{SV} as obtained from Eq. 3-7, with the true porosity obtained from another source.

Neutron Method: The previous two methods require a clean sand. If the sands are shaly, neither method can be safely used. If a CNL neutron log is available, ϕ_N may be compared with ϕ_{SV} (or t) using Chart Por-3. Differences between ϕ_N and ϕ_{SV} in water-filled sands are due to lack of compaction. For such sands, $B_{Cp} = \phi_{SV}/\phi_N$.

In some shallowly invaded, high-porosity rocks with high hydrocarbon saturation, sonic-derived porosity may be too high because of fluid effect. Both oil and gas transmit sound at lower velocities (higher transit times) than does water. Therefore, the transit time-to-porosity transform, which assumes water as the saturating pore fluid, sometimes overstates rock porosity. In these cases, the time-average-derived porosity is multiplied by 0.9 in oil-bearing formations and by 0.7 in gas-bearing formations. These fluid corrections are applied only when the time average-derived porosity is obviously too high.

Empirical Equation Based on Field Observations

The long-standing problems with using the time-average equation, coupled with numerous comparisons of sonic transit time versus porosity, led to the proposal of an empirical transit time-to-porosity transform. The transform is also shown in Chart Por-3. The transform is empirical, being based entirely on comparisons of sonic transit time versus an independent porosity measurement.

The empirical transform exhibits several salient features. First, it appears that all pure quartz sandstones may be characterized by a unique matrix velocity, slightly less than 18,000 ft/sec. A value of 17,850 ft/sec (or t_{ma} = 56 μs/ft) is suggested. Limestone and dolomite also seem to exhibit unique matrix velocities: 20,500 ft/sec (or t_{ma} = 49 μs/ft) for limestone and 22,750 ft/sec (or t_{ma} = 44 μs/ft) for dolomite.

In sandstone, the transform yields slightly greater porosity values over the low-to-medium-porosity range (i.e., the 5 to 25% range) than does the time-average equation using an 18,000 ft/sec matrix velocity. In fact, at 15% porosity the transform indicates a porosity similar to that given by the time-average equation using a matrix velocity of 19,500 ft/sec. Thus, it appears that the higher matrix velocities used in sonic interpretation in the past have been selected to force the time-average equation to yield a truer porosity over the low-to-medium range; this is true for both carbonates and sandstones.

For moderately high porosity sands (30%), the proposed empirical transform generally corresponds to the time-average equation using v_{ma} = 18,000 ft/sec. Above 35% porosity, however, sonic transit time increases much more rapidly than porosity, and its response quickly departs from that predicted by the time-average equation. This is the region in which the time-average equation would require a "lack of compaction" correction. The new transform eliminates the need for the correction factor and yields porosity directly.

This empirical transform can be approximated over the range of normally encountered porosities by the following equation:

$$\phi_{SV} = \frac{C(t_{LOG} - t_{ma})}{t_{LOG}} . \qquad \text{(Eq. 3-10)}$$

The value of the constant C has a range of 0.625 to 0.7 depending upon the investigator. Chart Por-3 uses the originally proposed value of 0.7 for C. However, more recent transit time-to-porosity comparisons indicate the value 0.67 is more appropriate.

For the case of a gas-saturated reservoir rock, C becomes 0.6. It should be used when the rock investigated by the sonic tool contains an appreciable amount of hydrocarbon in the gassy (vapor) phase. Because of the very shallow depth of investigation, this condition normally exists only in higher porosity sandstones (greater than 30%).

Correlations with t Curve

Variations of velocity in different types of rock produce a sonic curve with a correlatable character. In addition, the very good vertical definition of the sonic log and the reduced hole effect because of borehole compensation make this log excellent for correlation. It is very helpful in some cases where other logs give poor results (thick shale sections and evaporites). Moreover, some types of formations, evaporites in particular, can be easily identified from their t values.

Shear-Wave Interpretation

All of the preceding discussion has concerned compressional transit time interpretation. With the Array-Sonic tool and full-waveform recording, it is now possible to obtain shear-wave transit time measurements on a more routine basis. Application of the shear wave in formation evaluation is only now beginning to be explored. It is obvious that shear-wave velocity data will be useful in calculating rock elastic or inelastic properties and as an adjunct to shear seismic data.

Shear-wave transit time data are also useful in identifying matrix minerals and pore fluids (Fig. 3-14). For example, a crossplot of compressional transit time, t_c, and shear transit time, t_s, can be used to identify the mineral content of the various rocks traversed by the wellbore. The technique is similar to other porosity log crossplotting techniques (e.g., sonic-neutron).

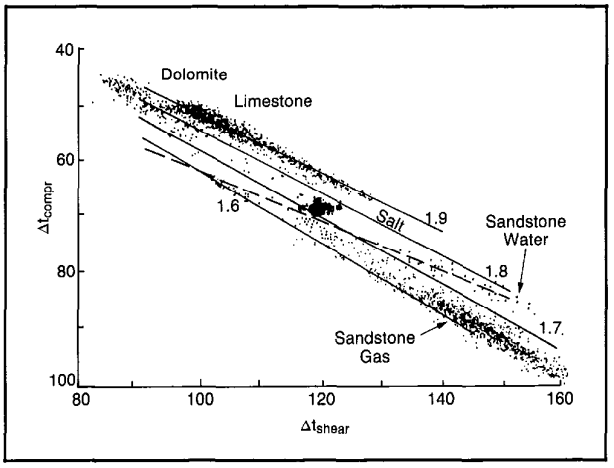

Fig. 3-14—Sonic-derived compressional and shear crossplots

There is evidence that the shear-wave transit time may be useful for fluid identification. Laboratory observations suggest that light hydrocarbon saturation decreases the velocity of the compressional wave (relative to brine saturation) through the porous rock and increases the velocity of the shear wave.

A relationship between porosity and shear velocity (or interval transit time) has also been noted. Indeed, the time-average relationship (Eq. 3-7) and the empirical relationship (Eq. 3-10) that relate compressional transit time to porosity appear to apply to shear transit time as well. Of course, appropriate matrix and fluid parameters must be used. For shear-wave propagation, the parameters are approximately:

sandstone, $t_{ma} \approx 86$ μs/ft
limestone, $t_{ma} \approx 90$ μs/ft
dolomite, $t_{ma} \approx 76$ μs/ft
anhydrite, $t_{ma} \approx 100$ μs/ft
water, $t_{ma} \approx 350$ μs/ft.

These values are tentative. Further experience with the shear transit time may lead to some refinement. Also, the listing of a shear transit time value for water is somewhat imaginary since water does not support shear-wave propagation. However, the use of the listed value for water in the time-average equation does seem to yield acceptable porosity values.

Log Quality

The log quality of sonic logs through casing depends on the acoustic coupling of the casing and formation. In zones with no cement bond, the acoustic energy is trapped in the casing and no formation parameters are measured. But even marginal bonding can produce enough acoustic coupling for reliable formation measurements.

Figure 3-15 shows a comparison of a BHC log run in open hole with an Array-Sonic log run after the well was cased with 7-in. casing. Cement bond was evaluated with the Cement Evaluation Tool (CET). The cement map, a picture of the cement bond as if the casing were split vertically and flattened, shows a good bond as black and no bond as white.

The top interval has a good bond, so the openhole and cased hole sonics agree as expected. The middle interval shows a fairly severe cement channel, yet there is enough cement bond to transfer acoustic energy and the two compressional measurements agree. The bottom interval shows a zone with no bonding and the cased hole log is not measuring formation parameters.

The openhole and cased hole sonic logs in Fig. 3-16 agree very well even though the Variable Density log, run with the Array-Sonic tool, shows some zones with poor and intermediate bonding.

Applications

Sonic logs in cased holes provide the same information as in open holes so the applications are similar. Compressional travel times are converted to porosity and integrated for correlation with borehole seismic measurements.

When combined with a CNL neutron log, a through-casing sonic log can reveal lithology and the presence of gas. Figure

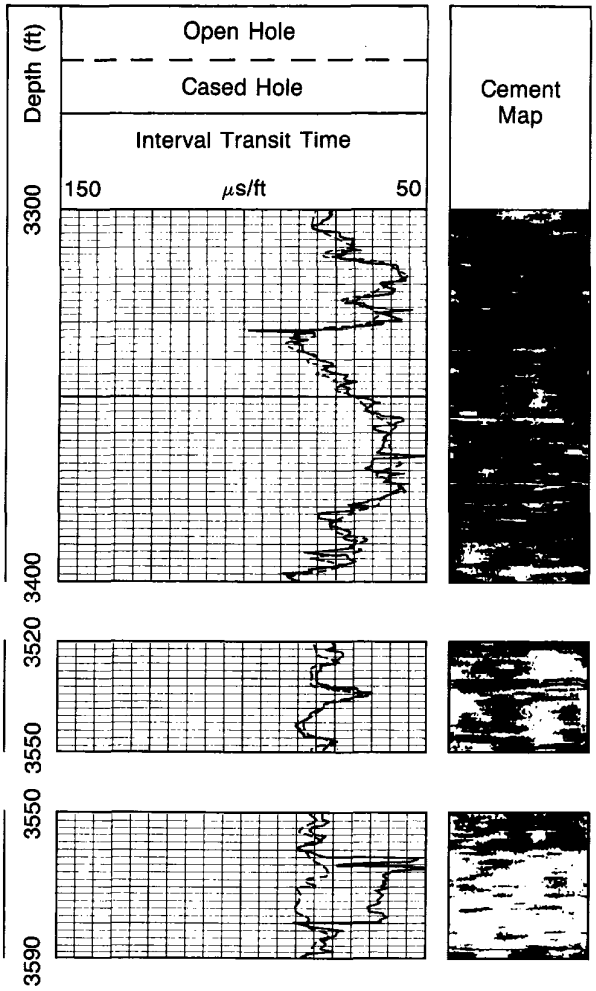

Fig. 3-15—Comparison of openhole and cased hole sonic logs with "cement map" from CET tool

3-17 shows cased hole sonic/CNL porosity logs run through a gas-bearing formation. The zone from 3424 to 3432 ft was perforated and produced 2 million ft³/D of gas.

THERMAL DECAY TIME LOGS

Introduction

There are two thermal decay time tools currently in use. The new Dual-Burst TDT* tool and the TDT-K tool which has been the industry standard for many years. Both tools have 1 11/16-in. diameters for through-tubing operations. The Dual-Burst TDT tool uses a diffusion model to analyze the decay of a burst of fast neutrons in the downhole environment. This method uses a better approximate solution to the neutron diffusion equation than the exponential decay model used by

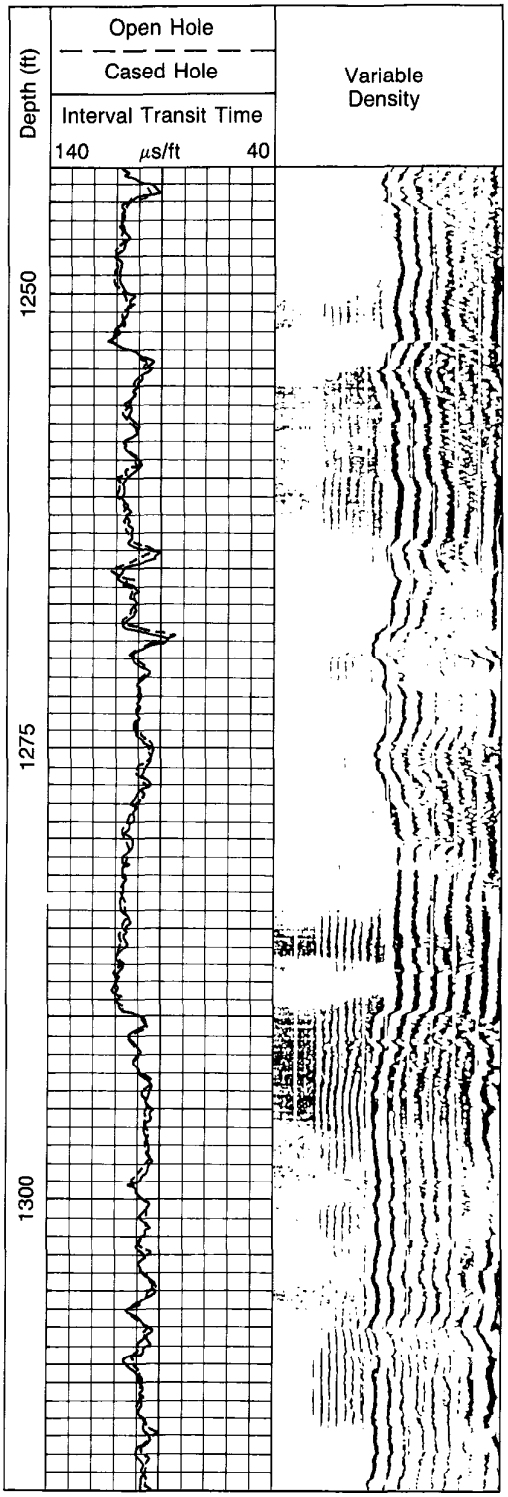

Fig. 3-16—Comparison of openhole and cased hole sonic logs with a VDL display of the acoustic waveforms

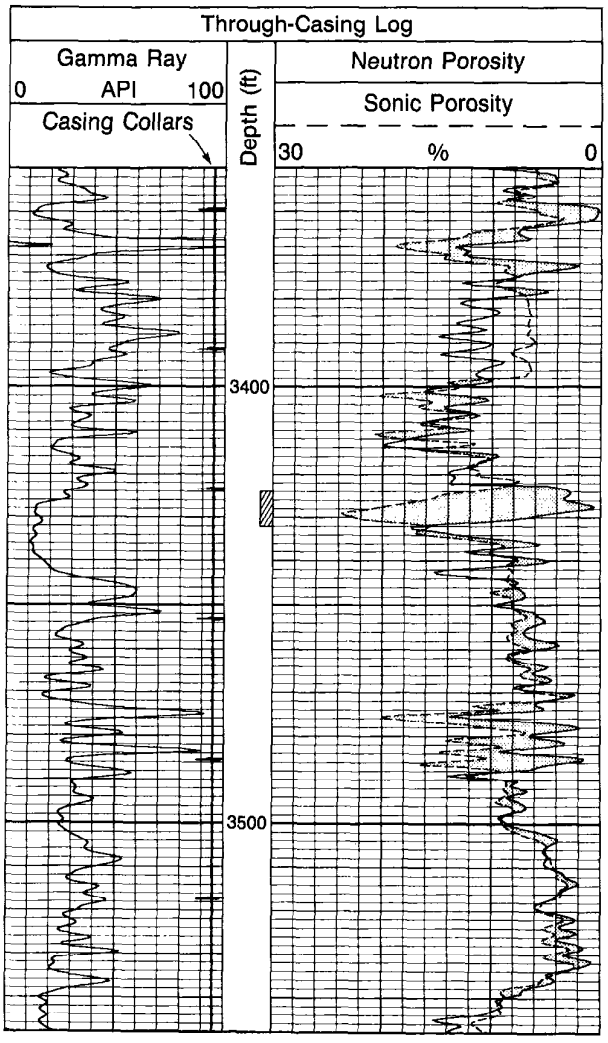

Fig. 3-17—Cased hole sonic and CNL logs showing an 8-ft thick gas zone

the TDT-K tool. The principle of operation for both tools will be covered later.

The Thermal Decay Time (TDT) log records the thermal neutron capture cross section of the formation by measuring the thermal neutrons' rate of decay. Because chlorine is by far the strongest neutron absorber of the common earth elements, the response of the TDT log is determined primarily by the chlorine present (as sodium chloride) in the formation water. Since the effects of water salinity, porosity, and shaliness on the thermal neutron decay rate are similar to those on resistivity logs, the TDT log resembles the usual openhole resistivity logs and is easily correlated with them. But the TDT differs in that it can be run in cased holes. Consequently, when formation water salinity permits, TDT logging provides the means to recognize the presence of hydrocarbons in formations which have been cased, and to detect changes in water saturation during the production life of the well. The TDT log is thus useful for the evaluation of old wells, for diagnosing production problems, and for monitoring reservoir performance.

As in the case of the resistivity log, the most important parameter values needed for quantitative interpretation are porosity and water salinity. Information is also required on shaliness, lithology, and the nature of the hydrocarbon. Modern openhole logging programs and crossplot techniques usually provide such information.

Principle

A neutron generator in the TDT sonde repeatedly emits pulses of high-energy neutrons. Following each burst the neutrons are rapidly slowed down in the borehole and formation to thermal velocities. They are then captured by nuclei with a corresponding emission of gamma rays. Relative changes in the thermal neutron population in the media are sampled by gamma ray detectors placed at a short distance from the source. During the period of measurement the thermal neutron population decreases exponentially. This decrease is due to either neutron capture or neutron migration (diffusion).

At every point in the formation, a certain fraction of the thermal neutrons locally present is absorbed per unit time. This fraction is $v\Sigma_{abs}$, where v is the neutron velocity and Σ_{abs} is the macroscopic absorption (capture) cross section in the medium. Σ_{abs} is the summation of the cross sections of all the individual atomic nuclei in a unit volume of formation for a mean thermal neutron velocity of 2200 m/s (corresponding to a temperature of 77 °F). For most chemical elements of interest in logging, Σ_{abs} is inversely proportional to the neutron velocity. Thus, the quantity $v\Sigma_{abs}$ is a constant which characterizes the formation. Since Σ varies inversely, and v varies directly with the square root of temperature, the quantity $v\Sigma$ is independent of temperature (as is also the intrinsic decay time, τ_{int}).

Consider, now, the thermal neutron density at a point in a formation. Let N_o be the thermal neutron density after a delay time, t_o, following the neutron burst. Let t_o be long enough to permit the neutrons to reach thermal equilibrium. Then if neutron capture is the only process occurring, the neutron density, N, decays according to the equation:

$$N = N_o e^{-t/\tau_{int}} , \qquad \text{(Eq. 3-11)}$$

where t is the time measured from t_o.

If capture were the only process by which neutrons disappear, the measured decay time would be equal to the intrinsic decay time, τ_{int}. The τ_{int} of a formation is related to its capture properties by:

$$\tau_{int} = \frac{4.545}{\Sigma_{abs}} \quad \text{(Eq. 3-12)}$$

However, neutron capture is not the only process occurring. The neutron diffusion effect is an important aspect in the actual measurement. In a homogeneous medium, the diffusion of neutrons arises from spatial variation in the neutron density. Therefore, the apparent decay time of the local neutron population contains both intrinsic decay time and diffusion time components. Without correction, the measured decay time is shortened below τ_{int}. This effect will be greater at low porosities. The methods used to handle the diffusion component will be covered under the tool sections.

Figure 3-18 shows schematically how the gamma ray count rate might typically vary with time after a fast neutron burst. At the extreme left, there is a rapid decay due to high absorption rates in the borehole fluid and casing. Next, there is a practically straight line position corresponding to the region of formation decay of the neutron density. Finally, at the right, the curve flattens out; the readings here correspond to induced radioactivity in the formation and the sonde.

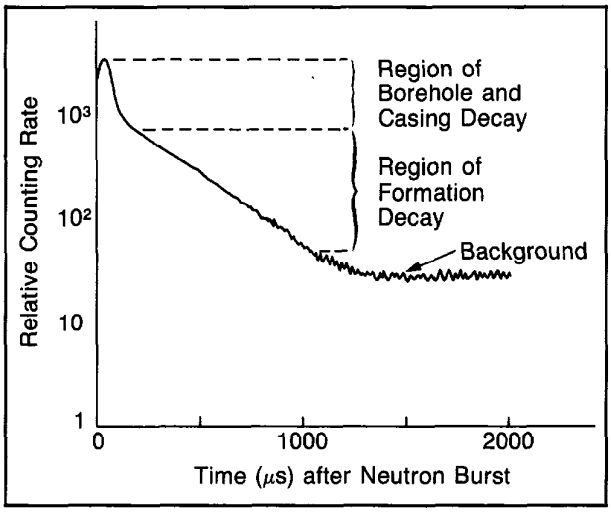

Fig. 3-18—Decay of capture gamma ray counting rate

The TDT-K Tool

The TDT-K tool provides values of thermal decay time and a ratio curve derived from the count rates of the two detectors. After the end of a tau-wide neutron burst the tool has a hardware delay of twice tau-formation to allow the borehole signal to decay, and an updated value of tau is determined using the mainly borehole free count rates after delay.

In Fig. 3-18, the "straight-line" part of the curve corresponds primarily to exponential decay of the neutron density. This part of the curve represents formation response, and it is here that the decay time must be measured.

Figure 3-19 shows the thermal neutron decay for a 38% porous quartz sand containing water with 95,000 ppm salinity. Time zero represents the end of the neutron burst. The initial rapid decay is due to borehole effects. When the background counting rate is subtracted from the values of curve A, curve B with extended straight-line portion results.

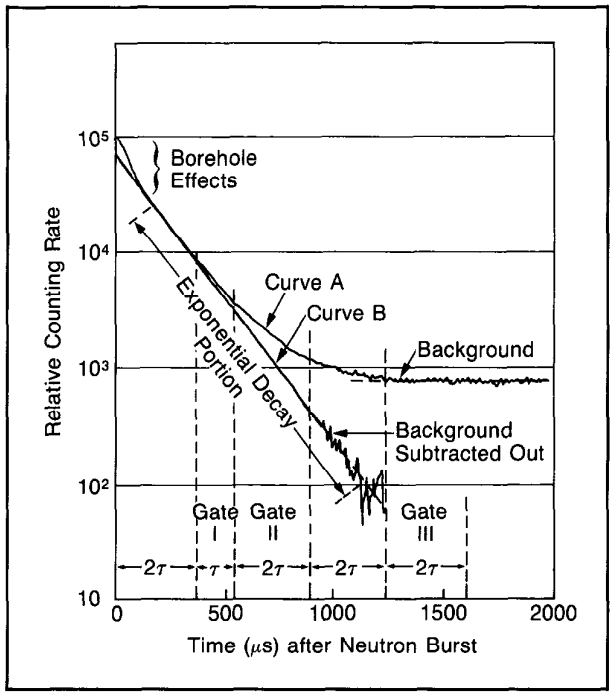

Fig. 3-19—Background counts are subtracted from total to give true exponential decay curve

To measure the decay rate, the gamma rays detected at the sonde are counted over two discrete time intervals, or gates, which are chosen to fall within the exponential decay time. These detection gates are variable in time (after the neutron burst) and in duration. A third and later gate provides the background count rate which is automatically subtracted from the counts of curve A.

Log Presentation

An illustrative log from this tool is shown in Fig. 3-20. Some of the data provided for formation evaluation are:

- Σ, which is the thermal neutron capture cross section. The measurement is derived from the count rates of the near detector:

$$\Sigma_{LOG} = \frac{4.545}{\tau_{LOG}} .$$

- a Ratio curve, which is computed from near (N) and far (F) count rates of the two detectors:

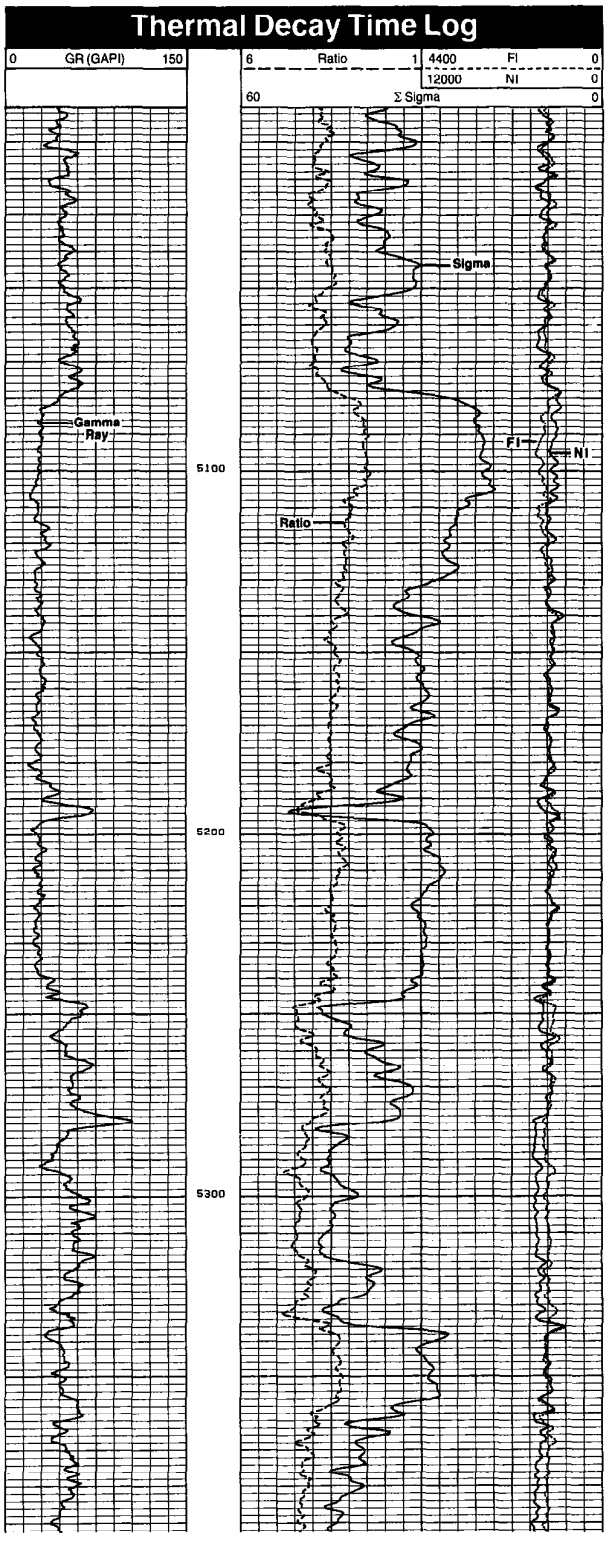

Fig. 3-20—A typical TDT-K log presentation

$$\text{Ratio} = \frac{N_1 - \frac{1}{3} N_3}{F_1 + F_2 - F_3} .$$

The TDT-K ratio and Σ data can be used in charts such as those in Fig. 3-21 (Tcor-3, -4 or -5) to obtain an apparent porosity (ϕ_K) and an apparent water salinity.

- a count rate display, which is a recording of the counting rates, N_1 and F_1, from Gate 1 of near and far detectors. N_1 and F_1 are uncorrected for background. The two curves are scaled to facilitate direct comparison. In some cases, as will be discussed, this display is useful for detecting gas.

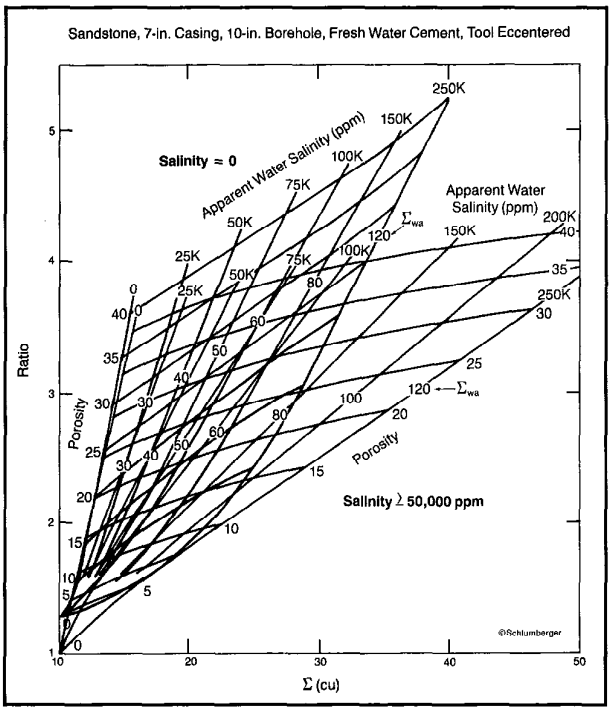

Fig. 3-21—Chart to derive apparent porosity and apparent water salinity from sigma and ratio values

Factors Influencing TDT-K τ Measurements

With the TDT-K tool the recorded values, τ_{LOG}, may differ from τ_{int} because of the borehole environment, diffusion, and the geometry of the formation. The limitations imposed by these factors are discussed below.

Diffusion Effect

The detector of the TDT-K tool is located within the zone where, for homogeneous media, diffusion contributes to some decrease in neutron density during the measuring period. Accordingly the measured decay time is shortened below τ_{int}.

For practical TDT-K interpretation, the effect of diffusion must be compensated by using an apparent capture cross section equal to 1.6 times the true value for the rock matrix. This empirical rule results from the study of many logs.

Effects of Inhomogeneity and Borehole Environment

A formation appears homogeneous to the TDT tool whenever the size of its heterogeneities is less than 1 in. (i.e., small compared to the distance the thermal neutrons travel before being captured). This is typically the case of rocks with intergranular porosity.

However, the zone investigated by the tool also includes large-size heterogeneities (borehole fluid, cement sheath, casing). These all have some effect on the TDT-K measurement.

When salt water is in the casing, the formation decay time is always much longer than the casing-fluid decay time. In this case, little borehole effect on the measured decay time is expected. When the saltwater-filled casing is large (9 in. or more), the counting rate is low, and the statistical variations may be large.

Freshwater and oil muds have long decay times, but not long enough to affect the measurement of hydrocarbon-bearing formations. On the other hand, the decay time of shales and saltwater-bearing formations may be significantly lengthened, particularly in a large sized hole.

Oil wells logged while producing have less borehole effect, probably as a result of the presence of either formation water (short τ) or large amounts of gas (weak signal) in the oil column, and, at times, centralization of the tool by the tubing.

It is difficult to set a practical limit on hole sizes required for reliable τ measurements with the TDT-K tool because hole size is dependent on both the casing size and the nature of borehole fluid.

Dual-Burst (TDT) Tool

The Dual-Burst Thermal Decay Time tool uses a new method of analyzing the decay of a burst of fast neutrons in the downhole environment. This method, called the diffusion model, uses a better approximate solution to the neutron diffusion equation than the exponential decay model. The benefit of this approach is that the algorithm solves for the actual formation sigma and the measurement is independent of the borehole fluid without the need for Log Interpretation Charts book corrections. This capability is of obvious benefit in time lapse logging where the composition of the borehole fluid can change over time and in a log-inject-log program where the borehole fluid is changed deliberately. In addition to the correct formation sigma, the Dual-Burst TDT tool also provides a measure of the thermal neutron diffusion coefficient plus a neutron porosity measurement.

The Dual-Burst TDT tool has an improved neutron generator with doubled neutron output. The dual burst neutron generator system provides a short neutron burst and a long neutron burst to optimize the counting of capture gamma rays. The count rate after the short burst is low enough to permit counting gates to be placed very near to it in order to obtain a maximum borehole-to-formation-signal contrast. The count rate from the long burst remains high long afterwards so there is good statistical precision for the long formation decay component. This system permits high neutron output while controlling the effects of counting losses resulting from dead time. The Dual-Burst TDT tool also provides improved formation-to-borehole signal ratio and vice-versa.

The dual-burst timing is shown in Fig. 3-22. It illustrates the arrangement of the neutron burst and counting gates. The neutron bursts are shown by the cross hatch and the gates are shown in the dotted areas. The tool has 16 time gates for each detector, and a full measurement cycle includes 128 repetitions of the dual burst plus a background check.

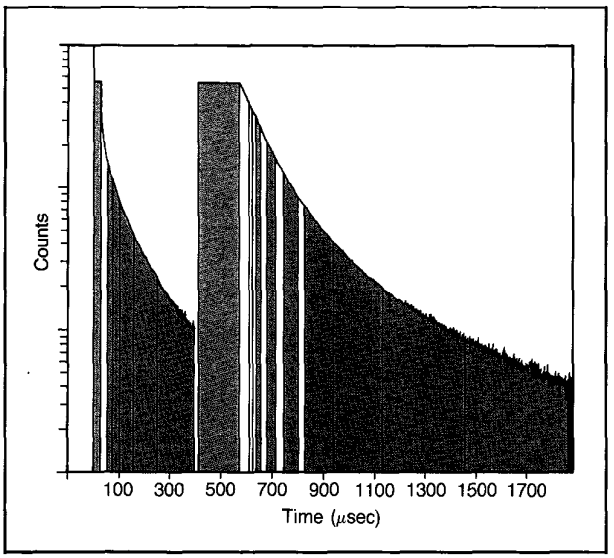

Fig. 3-22—Dual-Burst TDT timing

Diffusion Model

The standard model describes the decay of thermal neutrons following a burst of fast neutrons in a borehole and surrounding formation. The time-dependent neutron diffusion equation,

$$-D\,\nabla^2\,\phi(\vec{r},t) + \Sigma_a\phi = -\frac{1}{v}\,\frac{\partial\phi}{\partial t} + S(\vec{r},t), \quad \text{(Eq. 3-13)}$$

where:

D = thermal diffusion constant
∇^2 = the LaPlacian operator
$\phi\ (\vec{r},t)$ = neutron flux
$\Sigma_a\phi$ = macroscopic absorption cross section of the medium
v = speed of a thermal neutron
$S\ (\vec{r},t)$ = thermal neutron source,

is an approximation to the Boltzmann transport equation. This relationship can not be solved analytically in the logging environment without several approximations.

An analytical form of the solutions of the diffusion equation was developed by solving it in a spherical geometry for two regions and two groups of neutrons—an adequate approximation as proven by the results. The purpose of this calculation was to establish a trend for interpretation of measurements in laboratory formations. The time-dependent part of the solutions has the form:

$$d(t) = \frac{A_f}{\tau_f}\, t^{-\gamma_f} e^{-t/\tau_f} + \frac{A_b}{\tau_b}\, t^{-\gamma_b} e^{-t/\tau_b}, \qquad \text{(Eq. 3-14)}$$

where $d(t)$ is the count rate in a gamma ray detector at time t, the impulse amplitudes A_f and A_b are functions only of the neutron slowing properties of the borehole and formation materials, the borehole geometry, and the neutron source intensity. γ_f and γ_b are diffusion parameters. Diffusion parameters are included in database measurements. In the Dual-Burst TDT tool software there are different parameters in the diffusion functions for the near- and far-spaced detectors. Diffusion effects are smaller in the response of the far detector than in the near.

For the full 2-component processing, the interpolated diffusion coefficients from the data base are used as a starting point for a level-by-level interactive fine tuning of these coefficients in order to obtain the best fit between measured count rates and count rates reconstructed from the diffusion model. This approach, although slow and computer intensive, provides an actual measure of the thermal neutron diffusion coefficient which is beneficial for unknown or unusual borehole geometries and/or formation lithologies.

The real-time wellsite computation uses a single component diffusion model. A correction is applied to compensate for any remaining contribution from the second component. The parameters that determine γ_f and γ_b in Eq. 3-14 for the near- and far-spaced detectors are interpolated from results obtained in laboratory test formations for different borehole geometries, for various formation lithologies, porosities, and contrast between formation and borehole cross sections. These database results were obtained by fitting the diffusion model to laboratory test formation data characterized in terms of matrix cross sections, porosities, and formation fluid salinities.

Data Base

A data base was developed from laboratory measurements to test the diffusion model and to develop its parameterization for the Dual-Burst TDT tool. Currently, the data base consists of over 2500 measurements that covers 6-in., 8-in., 10-in., and 12-in. boreholes for sandstone, limestone, and dolomite formations. There are porous formations of 15, 33, and zero pu for each borehole size. The 6-in. borehole had a 4.5-in., 9.5 lb/ft casing. Two casing sizes were used for the 8-in. borehole formations: 6⅝ in., 24 lb/ft and 5.5 in., 14 lb/ft. One casing size was used for the 10-in. boreholes, 7⅝ in., 26.4 lb/ft and for 12-in. boreholes, 9 5/8 in., 40 lb/ft. There are five formation salinities and six borehole salinities for each of the porous test formations. In each borehole, measurements were made at four angles around the circumference and one measurement was made with a 1-in. standoff. The circumferential measurements were made so that azimuthal inhomogeneities in the test formations could be averaged. Over one million counts were acquired in the far detector in each measurement. At this level, biases in the parameter estimates are much less than the uncertainties in the formation characteristics.

Analysis shows the results of the diffusion model to be independent of the value of the delay time after the neutron burst and it is possible to simultaneously use the data from all gates, even the ones following the short burst, to compute the formation capture cross section. An immediate benefit of this is the improved statistics of the measurement since the count rates from more gates can be used. This allows the Dual-Burst TDT answer to be derived from the far detector, less influenced by borehole effects, without the need for heavy vertical averaging detrimental to the vertical resolution of the measurement. Another benefit of the independence of the formation sigma measurement to the tool timing system lies in the stability of the answer regardless of possible hardware design improvements modifying the timing of the measurement. This is particularly important in the case of reservoir monitoring projects spanning over several years, where consistency over the complete duration of the project is required.

The full 2-component processing, with its fine tuning of the diffusion coefficients to fit the measured data, is also independent of the source-detector spacing. This independence of the diffusion model upon the spacing offers a valuable redundancy of the system; if one of the near or far measuring devices fails during logging, the data obtained by the second system is still valid. Usually, with both systems operational, comparison of the answers provided by the near and the far spacing detectors is a valuable log quality control tool.

Tests with varying borehole salinities of zero to 220,000 ppm show a maximum borehole fluid effect of 5% of the true value with the diffusion model independent of the detector spacing (Fig. 3-23). The independence to borehole fluid of the formation sigma from the diffusion model is a large improvement over previous techniques and is particularly beneficial to log-inject-log and reservoir monitoring applications, where differences of formation sigma are monitored under varying borehole fluid conditions.

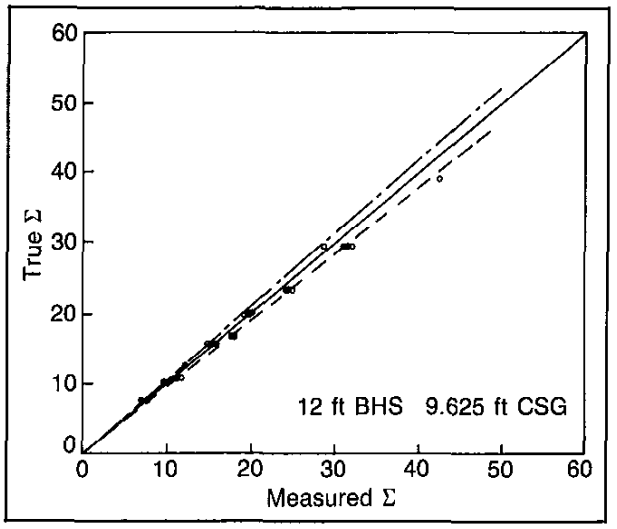

Fig. 3-23—2-component diffusion model, sensitivity to borehole fluid

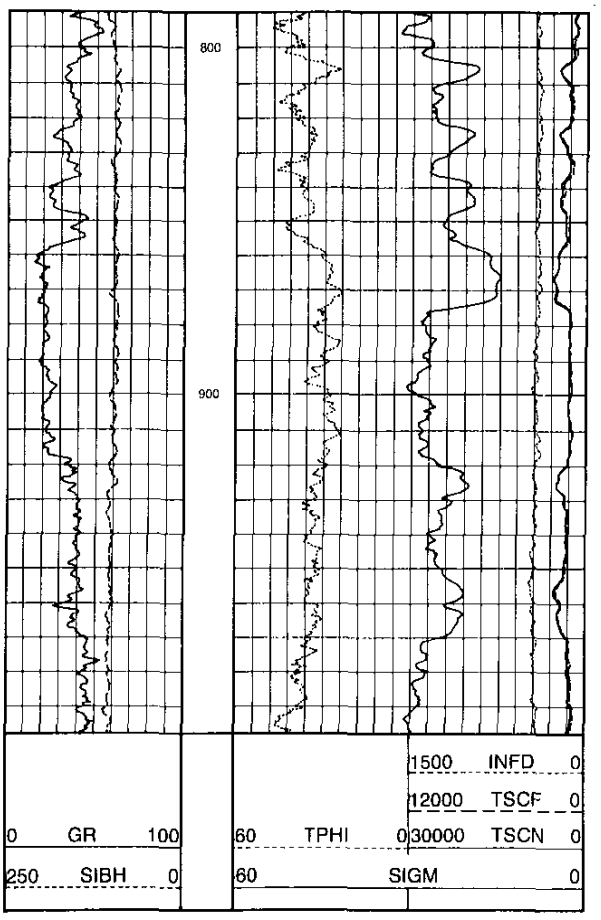

Fig. 3-24—Typical Dual-Burst TDT log presentation

Log Presentation

A typical log presentation for the Dual-Burst TDT tool is shown in Fig. 3-24. The curves presented are as follows:

track 1	GR	Gamma Ray
	CCL	Casing Collar Locator
	SIBH	Corrected Borehole Sigma
track 2	TPHI	Porosity from the Dual-Burst TDT
track 3	TSCF	Total Selected Counts Far Detector
	TSCN	Total Selected Counts Near Detector
	INFD	Inelastic Counts Far Detector
tracks 2-3	SIGM	Borehole Corrected Formation Sigma.

The corrected borehole sigma (SIBH) is derived from the intermediate values of near borehole sigma (SBHN), which are from a fit to the early gate counts following the short burst.

The porosity (TPHI) is derived from a ratio of formation gate counts and sigma; a borehole salinity correction has been made.

TSCF and TSCN are gate counts that respond similarly to the overlay used in the TDT-K to show gas in the formation.

INFD is the inelastic count gate during the long burst of the far detector. It will be affected by borehole environment, gas in the formation, and gas in the borehole. It should be reasonably independent of the formation sigma and porosity. INFD helps to distinguish gas-filled formations from tight porosity.

The corrected formation sigma (SIGM) is derived from near formation sigma, far formation sigma, and borehole sigma. The near and far sigmas, SFND and SFFD respectively, are diffusion model fits to the late gates following the long burst.

Quality Control

Data from a second film is used for quality control. A typical display is shown on Fig. 3-25 and the output is identified as follows:

track 1	GR	Gamma Ray
	FBAC	Far Detector Background Counts
	MMOF†	Minitron Monitor Far Detector
depth track	ISHU	Shunt Current
track 2	SFFD	Diffusion Corrected Formation Sigma Far
	SFND	Diffusion Corrected Formation Sigma Near
	TCAF†	Total Counts Analyzed Far Detector
track 3	SDSI	Standard Deviation of Sigma
	SIGC	Borehole Correction to SFFD

† Denotes items that appear only as flags.

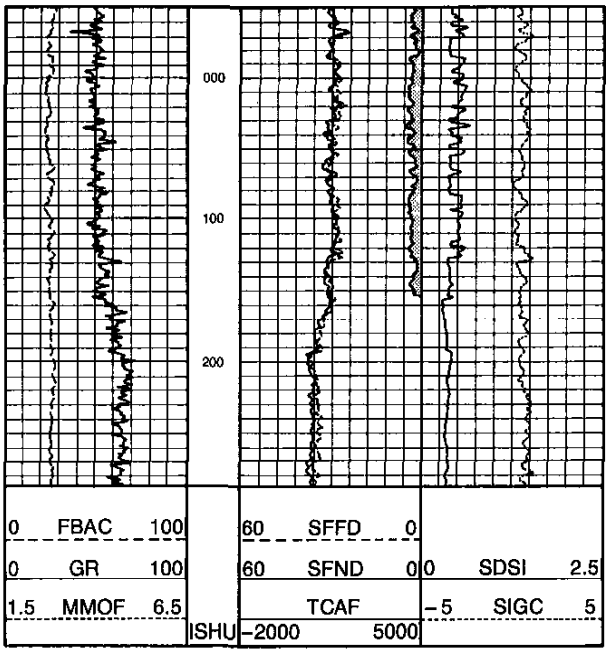

Fig. 3-25—Dual-Burst TDT quality control log

The MMOF and ISHU flags are indicators that the minitron is operating in the correct pressure mode.

TCAF is the total number of analyzed counts in a given depth frame and will be affected by logging speed and the amount of filtering applied. A minimum of 5000 counts for TCAF is required for good log repeatability. A flag will appear on the quality control film whenever TCAF is less than 5000 counts. Typical shale values to expect when the minitron is functioning properly are TCAF > 5000, INFD > 300, TSCF > 1200, and TSCN > 3000.

The standard deviation of SIGM is computed and output as SDSI and will reflect logging speed and filtering. The value of SDSI is one standard deviation, which means that SIGM will repeat to within plus or minus SDSI 67% of the time, or to within plus or minus two times SDSI 95% of the time. The repeatability of multiple passes will be worse by some amount due to depth mismatching, tool orientation variances, etc.

Log Example

Figure 3-26 shows a 4-pass Dual-Burst TDT field log run through a carbonate reservoir overlain by anhydrite. The oil producer was completed in a 6¼-in. open hole drilled through 7-in. casing. The borehole sigma values indicate that the oil water contact level had changed between the four log runs. However, the repeatability of sigma formation values are better than 0.5 c.u. throughout the zone, showing little effect from the borehole environment.

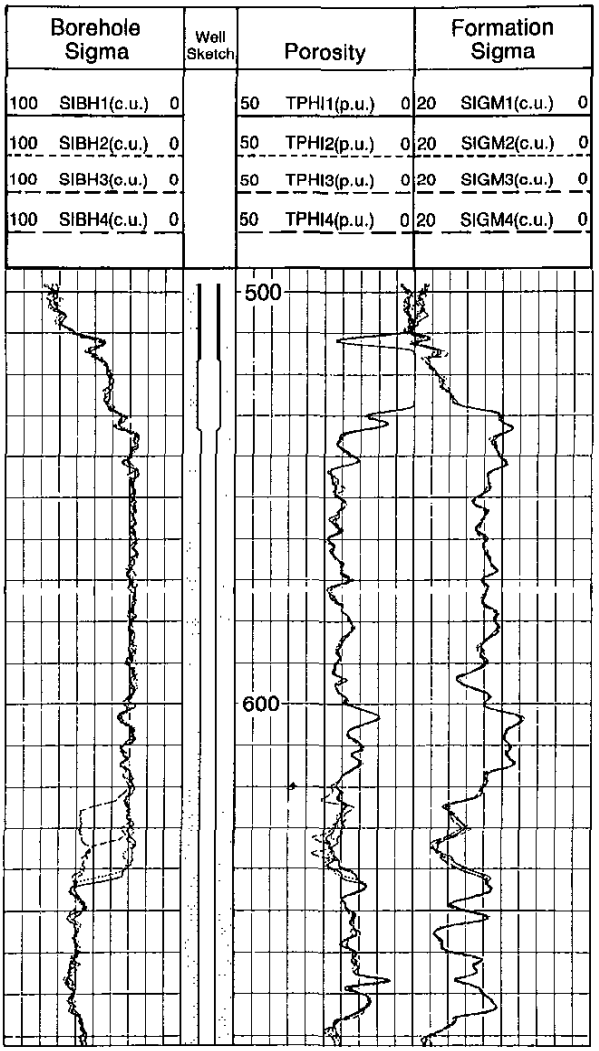

Fig. 3-26—Dual-Burst TDT wellsite computation, 4-pass overlay

Dual-Burst TDT Computer Processing

The full 2-component diffusion model is implemented as an offsite computation, since it is extremely computer intensive. For real-time wellsite computation, a simplified model was developed.

The wellsite calculation is based on a single component diffusion model. The decay is treated as a single nonexponential decay as described by the diffusion model. Thus, in very saline boreholes the sigmas from both the near and far spacing detectors are nearly correct. A single-component diffusion algorithm fit to the counts immediately following the short burst provides a borehole sigma. In addition, the code has a set of environmental corrections for specific wellbore geometry. The inputs required from the logging engineer are minimal: only hole size, casing size, and casing weight. Figure 3-27 shows an example comparison between wellsite (single-component) and offsite (2-component) processing.

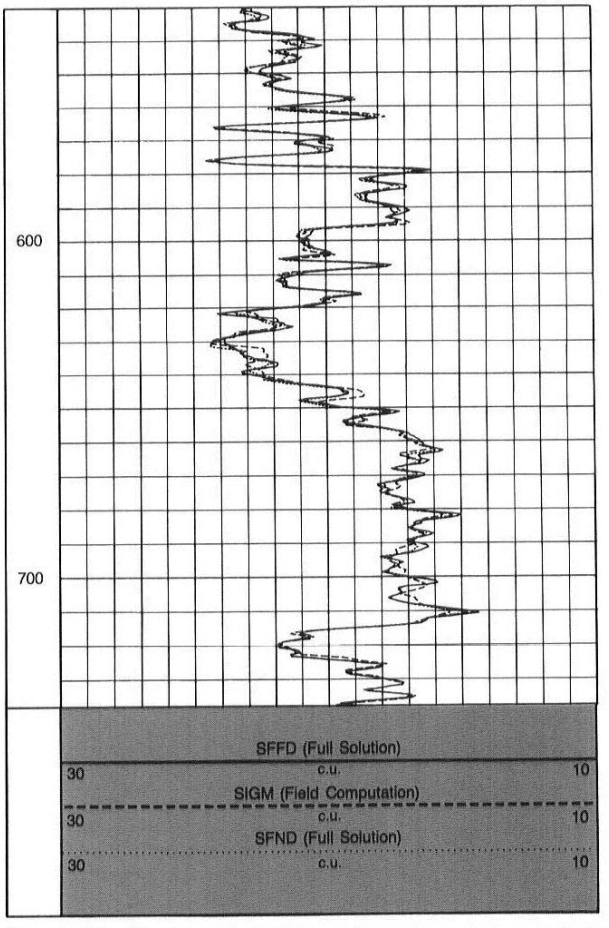

Fig. 3-27—Overlay of wellsite processing and computer center processing of Dual-Burst TDT log data

The wellsite calculation results in accurate sigma values in standard environments, but will lose some accuracy whenever the tool encounters conditions for which the diffusion parameters have not been calibrated, such as shale.

Vertical Resolution

The best repeatability between multiple passes will be obtained when the output of a nuclear logging tool is vertically averaged or smoothed. However, if the smoothing is applied too heavily, thin-bed resolution may be lost.

The Dual-Burst TDT data may be recorded with a choice of depth-frame averaging (Table 3-4). Normally, recording would be made with constant TPDC set at 1. This provides repeatability of the same quality as that of the TDT-K tool but with better vertical resolution. Figure 3-28 shows three separate logging passes recorded at 500 fph and processed with the full range of TPDC settings. It can be seen that as the vertical averaging is increased the repeatability improves —at the expense of vertical resolution. The value of TPDC can be set according to client priorities.

Depth Constant (TPDC) Setting	Interval Depth Averaged (in.)
none	6
1	18
2	30
3	42
4	54
5	66

Table 3-4—Choice of depth-frame averaging with Dual-Burst TDT tool

Porosity Determination from TDT-K Logs

Ratio and Σ, entered into Chart Tcor-3, -4, or -5, yield an apparent porosity, ϕ_K, and an apparent formation-water salinity (Fig. 3-21), which permits a quick evaluation (as will be illustrated later in this section).

The porosity index (ϕ_K) found in this manner is a neutron porosity. Like other neutron porosities it is influenced by shaliness, gas, and matrix lithology.

The TDT-K ratio curve can itself sometimes serve as a qualitative porosity curve in clean formations where Σ is constant. Under these conditions it may, when appropriately scaled, be used like other neutron curves as an overlay curve with sonic or density porosity for the detection of gas. For quantitative use of ratio in water-bearing formations as a porosity curve the ratio curve would have to be calibrated for the given conditions versus known porosities from another source.

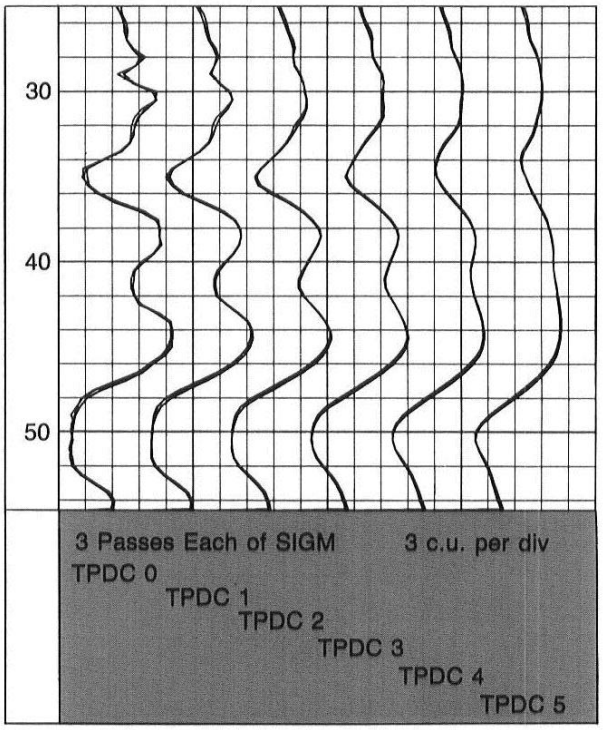

Fig. 3-28—Vertical resolution vs. TPDC setting

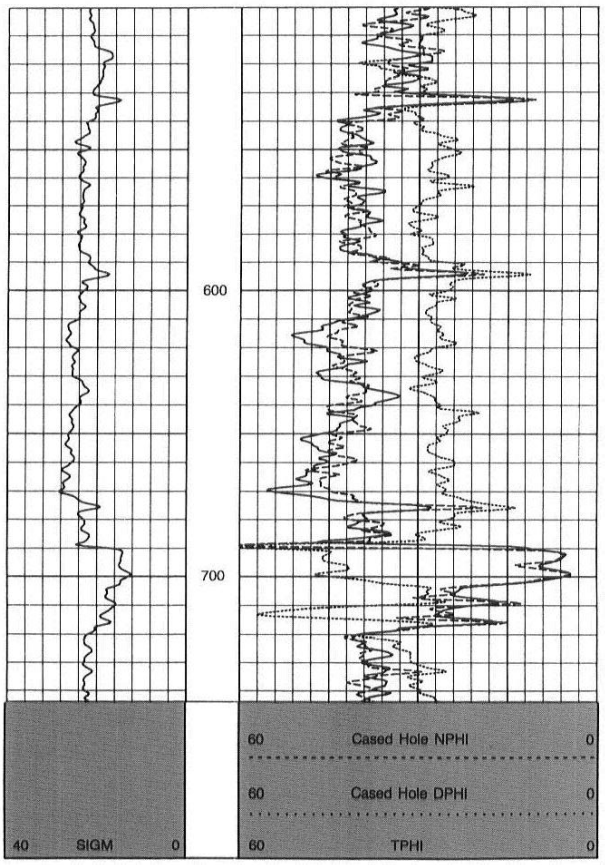

Fig. 3-29—Porosity comparison of TPHI (Dual-Burst TDT porosity), NPHI (CNL porosity), and DPHI (density porosity)

Porosity Determination from Dual-Burst TDT Logs

The Dual-Burst TDT tool provides an improved porosity output, labeled TPHI, that is derived from a near-to-far count rate ratio, formation sigma, and borehole sigma. It is corrected for borehole size, casing size, and borehole and formation fluid salinity. The Dual-Burst TDT porosity is similar to CNL porosity, as shown by the field log in Fig. 3-29. The porosity algorithms were constructed assuming casings to be fully cemented and centered in the borehole. The tool is presumed to have zero standoff from the casing.

Above 40% porosity, the TDT ratio becomes insensitive to porosity. At that point the TPHI output is deliberately attenuated to avoid false readings.

Gas Detection with TDT-K Logs

The relative sensitivities of the Gate 1 count rates, N_1 (from the near detector) and F_1 (from the far detector), are set so that the count rate curves overlay in water-bearing zones with little or no separation. The $N_1 - F_1$ count rate display is useful for detection of gas zones in clean, high-porosity formations by the separation of the two curves, with F_1 moving strongly to the left and N_1 slightly to the right (5100 ft zone of Fig. 3-20). In oil zones, F_1 often reads slightly to the left of N_1 and the curves tend to be parallel.

In relatively low-porosity zones ($\phi \approx 15 - 20$ pu), particularly if the zone is limy, both N_1 and F_1 decrease to the right. There may be no separation or F_1 may be slightly to the left with the two curves parallel in a manner similar to the oil saturation. Further decreases in porosity may make the zone look like gas. Knowledge of lithology and porosity is needed to distinguish gas in these cases.

The N_1 and F_1 levels are also affected by hole and annulus fluids. The lowest count rates occur in salt water, increasing slightly for oil and fresh water. The count rates increase markedly in gas-filled holes and the ratio curve is useless for porosity derivation.

Gas Detection with Dual-Burst TDT Logs

The Dual-Burst TDT log provides a method for porosity-independent gas identification. A typical field log presentation is shown in Fig. 3-30. Gamma ray (GR) and borehole sigma (SIBH) are presented in track 1, TDT porosity (TPHI) in track 2, and formation sigma (SIGM) over tracks 2 and 3.

Also shown in track 3 are three count rate curves used for gas identification. Scaled presentations for far-detector count

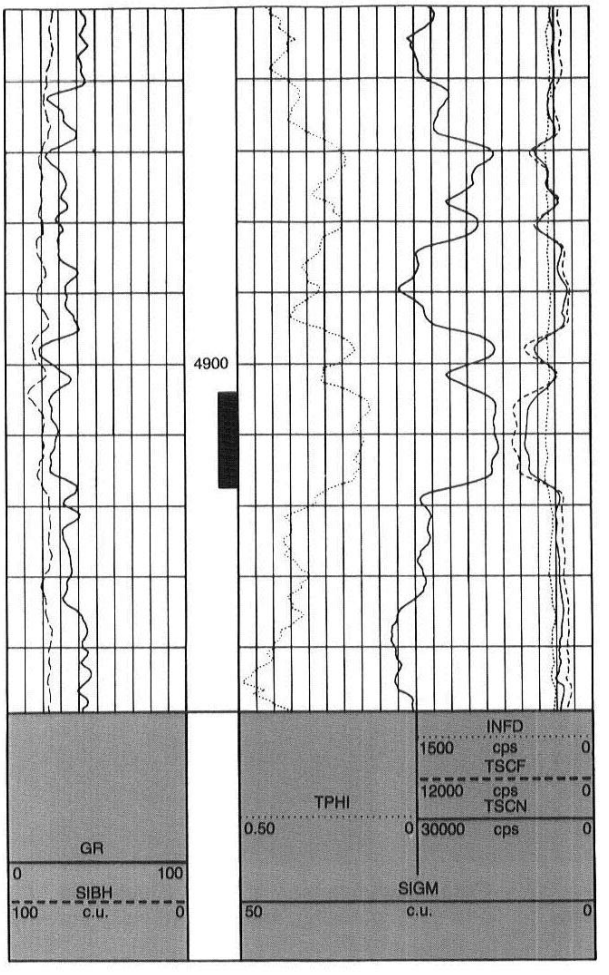

Fig. 3-30—Gas identification resolved with a new output, INFD

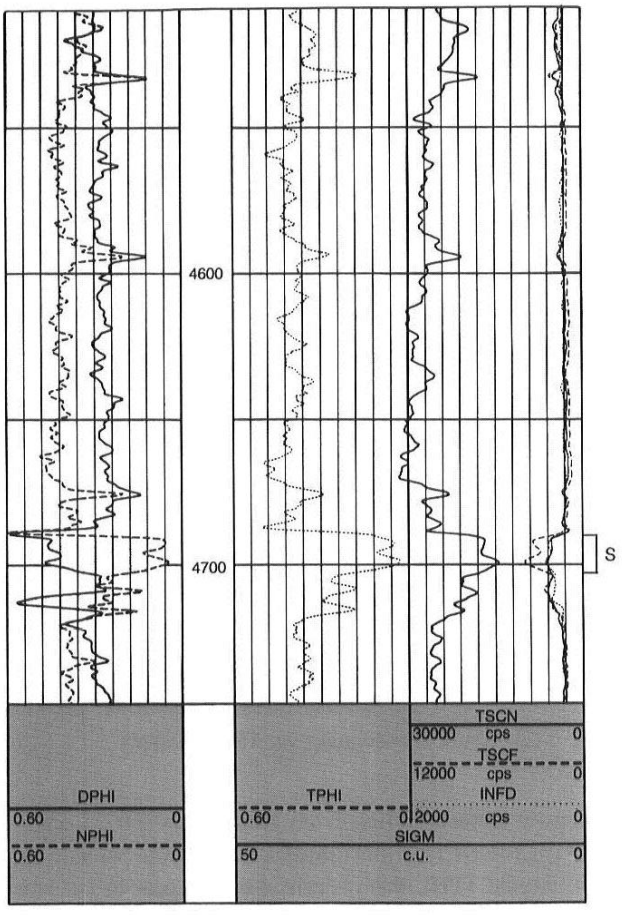

Fig. 3-31—Gas detection with Dual-Burst TDT log vs. openhole logs

rate (TSFC) and near-detector count rate (TSCN) are similar to the TDT-K N_1 and F_1 count rates that are used to indicate gas. Porosity and lithology changes can cause count rate profiles similar to those encountered in gas zones. The inelastic count rate from the Dual-Burst TDT tool far detector (INFD) curve helps to solve this problem. The INFD is sensitive to gas but not to porosity.

Conventionally, the zone at 4910 ft would be interpreted as gas from the far/near count separation. However, INFD does not increase, indicating no gas effect. Openhole logs show that the interval is a 15% porosity limestone bed which appears between higher porosity sandstones.

Openhole density/neutron logs through a sand/shale sequence are displayed in track 1 of a Dual-Burst TDT log in Fig. 3-31. The zone "S" clearly shows gas effect on the density/neutron porosities, and is also defined by the three count-rate curves of the Dual-Burst TDT tool.

TDT Interpretation

Interpretation procedures of the Dual-Burst TDT logs are similar to those for the TDT-K logs except that diffusion and borehole corrections are not required on Dual-Burst logs.

In the general case of a shaly, porous formation containing water and hydrocarbon, one may write:

$$\Sigma_{LOG} = \underline{(1 - V_{sh} - \phi)\,\Sigma_{ma}} + \underline{V_{sh}\Sigma_{sh}} + \underline{\phi S_w \Sigma_w} + \underline{\phi\,(1 - S_w)\,\Sigma_h}\,, \qquad \text{(Eq. 3-15)}$$

where:

ϕ = formation porosity
V_{sh} = volume of shale per unit volume of formation
S_w = volume fraction of porosity occupied by water

Σ_{ma}, Σ_{sh}, Σ_w, Σ_h = a capture cross section of rock matrix, shales, water, and hydrocarbon, respectively.

In Eq. 3-15 each highlighted group represents the relative volume of the corresponding component. In particular, the relative volume of rock matrix includes everything which is not shale or fluid; therefore, Σ_{ma} must represent not only the main rock minerals but also their impurities and cementing material.

The expression for S_w is as follows:

$$S_w = \frac{(\Sigma_{LOG}-\Sigma_{ma}) - \phi(\Sigma_h-\Sigma_{ma}) - V_{sh}(\Sigma_{sh}-\Sigma_{ma})}{\phi(\Sigma_w-\Sigma_h)} . \quad \text{(Eq. 3-16)}$$

In the simpler case of a clean (shale-free) formation:

$$\Sigma_{LOG} = (1-\phi)\Sigma_{ma} + \phi S_w\Sigma_w + \phi(1-S_w)\Sigma_h \quad \text{(Eq. 3-17)}$$

and

$$S_w = \frac{(\Sigma_{LOG}-\Sigma_{ma}) - \phi(\Sigma_h-\Sigma_{ma})}{\phi(\Sigma_w-\Sigma_h)} . \quad \text{(Eq. 3-18)}$$

To obtain the value of S_w, Eq. 3-16 or 3-18 can be solved directly by use of Chart Sw-12. In both cases the determination of S_w requires the knowledge of six independent parameters: ϕ, V_{sh}, Σ_{ma}, Σ_{sh}, Σ_w, and Σ_h.

Matrix Capture Cross Sections

The capture cross section of minerals can be computed from their chemical composition. Table 3-5 lists the computed capture cross sections for most minerals of interest.

Material	τ_{int} (μs)	Σ_{int} @ 20° C (c.u.)
Pure Materials*		
Quartz (SiO_2)	1070	4.25
Calcite ($CaCO_3$)	630	7.2
Dolomite ($CaCO_3 \cdot MgCO_3$)	944	4.8
Anhydrite ($CaSO_4$)	367	12.4
Gypsum ($CaSO_4 \cdot 2H_2O$)	350	13.0
Magnesite ($MgCO_3$)	3160	1.4
Rock Salt (NaCl)	6.3	726.0
Iron	23	198.0
Water (H_2O)	205	22.2

*Values computed from nuclear cross sections of constituent elements.

Table 3-5—Matrix capture cross sections

Formation lithology is usually expressed in terms of relative amount of sandstone, limestone, and dolomite. This information (from log interpretation or local knowledge) usually establishes the value of Σ_{ma}. However, the actual cross sections of sandstone, limestone, and dolomite encountered in practice may differ from the computed values for quartz, calcite, and dolomite due to the presence of associated minerals and impurities.

In practice, the average log-derived values listed in Table 3-6, which take into account both the impurities and the diffusion effect, may be used for TDT-K logs. Preferably, however, Σ_{ma} should be determined by crossplot techniques described later.

Formation	Apparent Capture Cross Section
Orthoquartzitic sand	8.0 c.u.
Subarkosic sand	10.0 c.u.
Limestone	12.0 c.u.
Dolomite	8.0 c.u.

Table 3-6—TDT-K log-derived values for capture cross sections

Formation Water Capture Cross Sections

Pure water has a capture cross section of 22.2 c.u. at 77 °F. Formation waters, however, contain salt in solution so that their capture cross sections are primarily a function of their salinities. Only slight effects are caused by pressure and temperature variations, since they affect only the density of the water.

Chart Tcor-2 (top) shows Σ_w as a function of total sodium chloride content at temperatures of 75 ° and 200 °F. Formation water may contain other elements in addition to sodium chloride. Normally, only two of these are important in TDT interpretation: boron and lithium. Equivalent NaCl salinity may be computed by adding to the ppm of the chloride ion, 80 times the ppm of boron, and 11 times the ppm of lithium. This sum is multiplied by 1.65 before entering Chart Tcor-2 (top).

Analysis of a water sample obtained during production usually provides the best determination of water salinity. When the salinity is not too high, water resistivity computed from openhole logs may also be used to evaluate the salinity. However, when the salinity is high a small error in R_w produces a large error in salinity.

Finally, Σ_w can be determined graphically from crossplots (as will be explained later).

Hydrocarbons

The capture cross section of a hydrocarbon is essentially a function of its hydrogen atom content, since hydrogen is the principal neutron capturing element. Hydrocarbon hydrogen content depends on the chemical composition of the oil and solution-gas and on the formation volume factor.

Σ_h for the liquid phase can be derived from Chart Tcor-1 (bottom) when the API oil gravity and the solution GOR are known. It can be seen from this figure that a value of Σ_h = 21 c.u. should be a good approximation for most field conditions.

The capture cross section of free gas varies greatly depending on gas composition, pressure, and temperature. Chart Tcor-1 (top) shows the capture cross section of methane as a function of temperature and pressure. A good approximation of capture cross sections of other hydrocarbon gases is given by:

$$\Sigma_g = \Sigma_{methane} \times (0.23 + 1.4\ \gamma_g)\ , \quad \text{(Eq. 3-19)}$$

where γ_g is the specific gravity of gas, taking γ_{air} = 1.0.

Shales

The capture cross section of shales is usually in the range from 35 to 55 c.u. The chemical composition of an average shale shows that boron or other thermal absorbers is the main reason for these large capture cross sections. Boron accounts for 34 c.u. or two-thirds of the total capture cross section. The balance is essentially due to hydrogen and iron.

Influence of Fluid Invasion

TDT logs run in open holes are influenced by invasion and therefore can only be used for evaluation of the flushed zone saturation. In a cased hole, the invading mud filtrate from drilling usually disappears from the porous and permeable water-bearing zones in a few days or weeks after completion.

Invasion in wells which have been killed or shut in prior to TDT logging can give misleading results. In such a case, the invading fluid (salt water or oil in the casing) contains no water-loss control material; due to capillary or differential pressure, it penetrates into the open or perforated intervals of sufficient permeability and quickly extends into and beyond the zone investigated by the TDT tool.

Uncertainty due to invasion by casing fluids is eliminated by logging the well while it is producing so that there is no danger of contaminating the producing zones. If the well has been shut in, it is advisable to produce it for several days before running the log. Even this may not ensure that the entire section is producing normally; oil zones contaminated by capillarity may still be nonproducing and appear wet on the TDT log. A flowmeter survey may be necessary to differentiate between these and the producing zones.

Saturation Analysis Using TDT Logs

Saturation computations from TDT logs depend upon the following conditions:

- water salinities of about 30,000 ppm or higher,
- porosities greater than about 10%,
- reasonably shale-free formations,
- known lithology (i.e., known Σ_{ma}), and
- known hydrocarbon type (i.e., known Σ_h).

In addition, because of the relatively shallow investigation of the TDT tool, it is necessary that any invaded zones shall have disappeared at the time the log is run.

The porosity from TDT ratio can be used, but openhole logs or a cased hole CNL or sonic log are preferred. If the formation is shaly, the shale formation, V_{sh}, must be estimated. In addition, the values of matrix and fluid capture cross sections must be known or determined by analysis in water zones.

Clean Formations

Level-by-level determination of S_w in clean formations is made using Chart Sw-12, Eq. 3-18, or by use of various crossplots.

$\Sigma-\phi$ and $\Sigma-\phi_N$ Crossplots

When readings are available from several levels over a clean interval of constant lithology and water salinity, a $\Sigma-\phi$ crossplot (Fig. 3-32) may be used. If there are several water-bearing levels with enough spread in porosity, these may

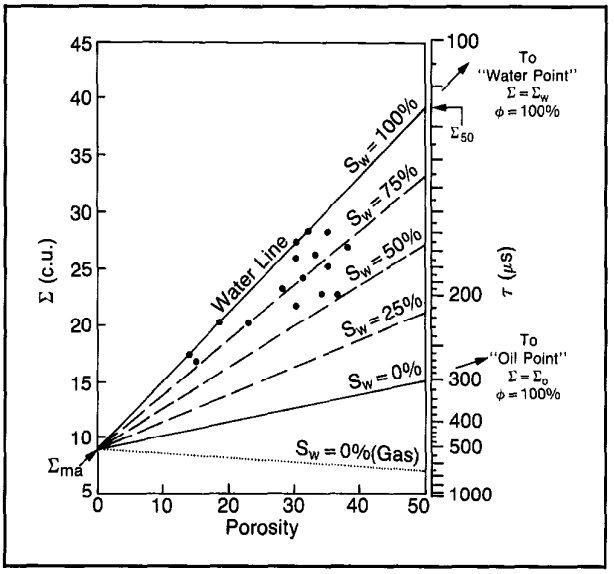

Fig. 3-32—Crossplot of sigma and porosity for determining Σ_{ma}, Σ_w, and S_w

serve to establish the water line as the line through the most northwesterly plotted points. The water line, when clearly defined, will yield the value of Σ_{ma} (from the intercept with $\phi=0$) and the value of Σ_w (from the intercept with $\phi=100\%$ or from $[2\times\Sigma_{50}-\Sigma_{ma}]$). Knowledge of Σ_{ma} and/or Σ_w from other sources will help confirm the position of the line.

The S_w = 0 line for oil is drawn to join the matrix point ($\Sigma = \Sigma_{ma}$, ϕ = 0) with the oil point (Σ_o = 21, ϕ = 100%). Intermediate S_w lines are drawn in by dividing the ordinate distances between S_w = 0 and S_w = 100 proportionately.

Shaliness

Additional information needed for shaly formations includes:

- V_{sh}: Estimated from the gamma ray (Fig. 3-33) or from other logs if available.
- Σ_{sh} and ϕ_{Nsh}: Estimated from TDT and neutron log readings in adjacent shales.

Shaly formations may be evaluated by use of Chart Sw-12, by Eq. 3-16, or by use of the $\Sigma-\phi_N$ crossplot entered with the modified values ϕ_{corr} and Σ_{corr} defined as:

$$\phi_{corr} = \phi_N - V_{sh} \times \phi_{Nsh} \qquad \text{(Eq. 3-20)}$$

and

$$\Sigma_{corr} = \Sigma_{LOG} - V_{sh}(\Sigma_{sh} - \Sigma_{ma}) \; . \qquad \text{(Eq. 3-21)}$$

As shown in Fig. 3-34, the corrected points on the $\Sigma-\phi_N$ plot should be translated in a direction parallel to the line joining the shale point to the matrix point.

It must be remembered that the presence of shale affects both the TDT and neutron logs rather unpredictably. Σ_{sh} varies between about 35 and about 55 c.u. and the figure read from the log in nearby pure shales may or may not be representative of the shale within the zones of interest. The determination of V_{sh} from the gamma ray log is subject to variation. Thus accuracy decreases rapidly with increasing V_{sh}. Observe in Fig. 3-34 that most of the corrected points are still above the S_w = 100% line. In addition, use of the cased hole gamma ray log as a shale indicator may be inaccurate because of deposition of radioactive deposits on or near the casing. It may also be affected, to some extent, if the original hole diameter was not constant. Preferably V_{sh} should be determined from clay (shale) indicators using open-hole logs.

In favorable cases the Σ curve itself can be used as a shale indicator. If a Σ_{min}, corresponding to clean, hydrocarbon-bearing sands at irreducible water saturation and a Σ_{sh}, corresponding to shales, can be picked from the log, then

$$V_{sh} \approx \frac{\Sigma_{LOG} - \Sigma_{min}}{\Sigma_{sh} - \Sigma_{min}} \; . \qquad \text{(Eq. 3-22)}$$

The amount of shale in water-bearing formations will be overestimated except in cases where $\Sigma_h \approx \Sigma_w$. Then the log will read Σ_{min} in clean sands and the Σ curve can be scaled directly in terms of V_{sh}.

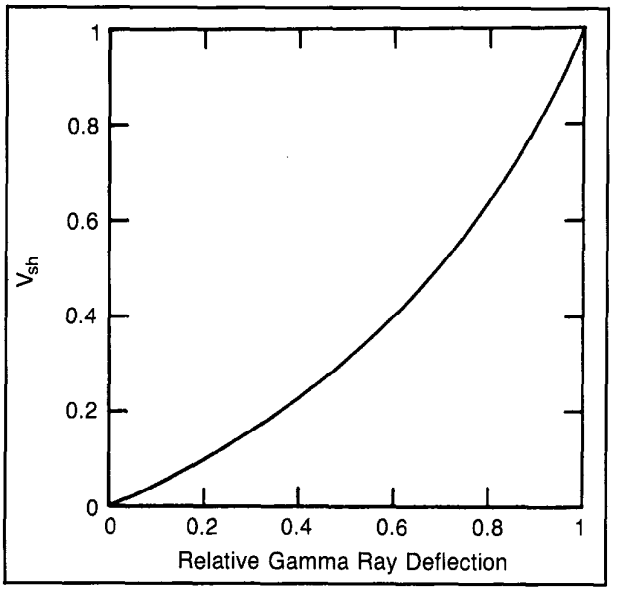

Fig. 3-33—Empirical V_{sh} vs. gamma ray deflection

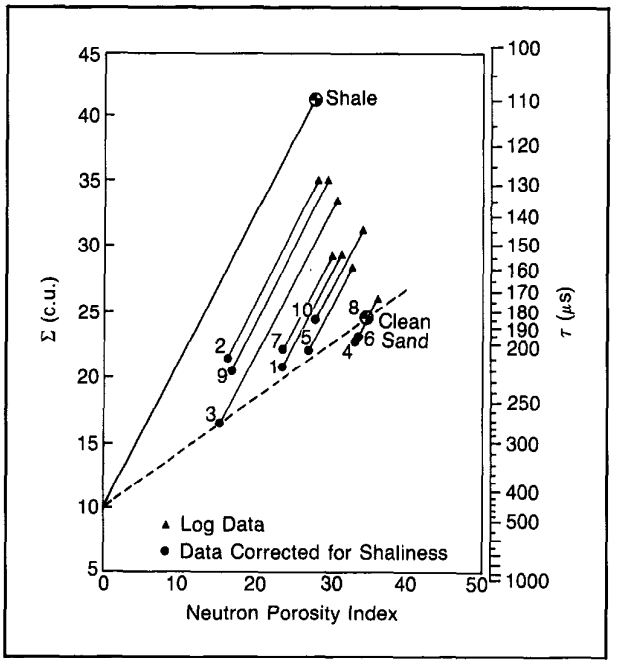

Fig. 3-34—Shale corrections applied in $\Sigma-\phi_d$ crossplot

Extended Crossplot, Σ_{eq} vs. ϕ_{eq}

It was pointed out earlier that to determine Σ_{ma} and Σ_w from the $\Sigma-\phi$ crossplot there must be some water-bearing zones and some large variations of porosity in the section under

study. When these conditions are not met, the extended crossplot offers one alternative method. It consists of entering the crossplot with "equivalent" values obtained in the following manner:

$$\phi_{eq} = \frac{\phi S_w}{1-\phi\ (1-S_w)} \qquad \text{(Eq. 3-23a)}$$

and

$$\Sigma_{eq} = \frac{\Sigma_{LOG} - (1-S_w) \times \phi\Sigma_h}{1-\phi\ (1-S_w)} . \qquad \text{(Eq. 3-23b)}$$

S_w and ϕ are determined from openhole logs. Σ_{LOG} is corrected for shaliness, if necessary, using Eqs. 3-20 and 3-21.

It can be shown that Eq. 3-17 may be written in the form:

$$\Sigma_{eq} = (1-\phi_{eq})\ \Sigma_{ma} + \phi_{eq} \times \Sigma_w . \qquad \text{(Eq. 3-24)}$$

This equation is identical in form to the one for a water-bearing formation of the same lithology (same Σ_{ma}). Consequently any point (Σ_{eq}, ϕ_{eq}) will plot along a straight line (100% water line). Variations in S_w will produce the variations in ϕ_{eq} needed to define the line in order that Σ_{ma} and Σ_w can be determined.

This procedure is reliable only when the values of S_w and ϕ computed from openhole logs are reasonably accurate and when water saturation has not changed between the times of resistivity and TDT loggings.

Σ_{ma} *Calibration*

When there are no extensive, clean, water-bearing zones in the interval logged by the TDT, determination of Σ_w and Σ_{ma} from the $\Sigma-\phi$ and $\Sigma-R_t$ crossplots is unreliable. In such a case the following approach may sometimes be useful.

Rearrange Eq. 3-16 to put it in the proper form for calculating a value of Σ_{ma}:

$$\Sigma_{ma}(\text{calculated}) = \frac{\Sigma_{LOG} - V_{sh}\Sigma_{sh} - \phi S_w\ \Sigma - \phi\ (1-S_w)\Sigma_h}{1-\phi-V_{sh}} . \qquad \text{(Eq. 3-25)}$$

Values of ϕ, S_w, and V_{sh} are derived from the interpretation of openhole logs. The value of Σ_{sh} is taken from the TDT reading in adjacent shale beds. Σ_w is estimated from formation-water salinity or from known values in the area. The calculation assumes that the values of ϕ and V_{sh} have not been changed by acidizing or treating and that the saturation response (S_w, Σ_w) of the TDT corresponds to the R_w, S_w value from the openhole logs. This latter condition will not be satisfied for a TDT run too soon after the start of production, where the filtrate of the invaded zone has not had time to dissipate. However, the TDT log used must have been run before any appreciable depletion has taken place.

The calculated values of Σ_{ma} are crossplotted versus corresponding values of $V_{ma} = (1-\phi-V_{sh})$ over the reservoir.

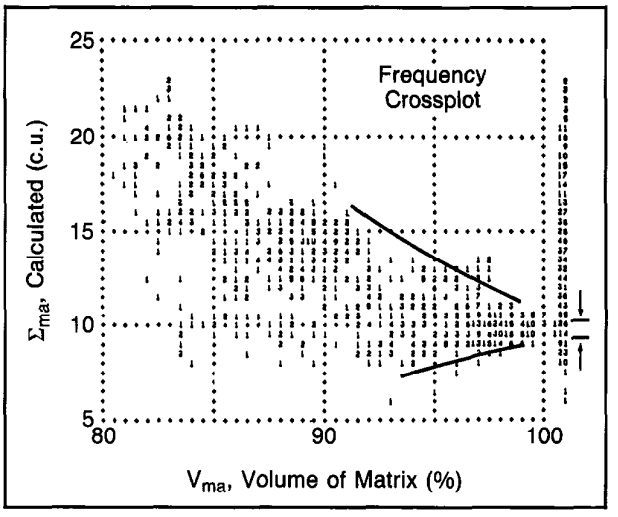

Fig. 3-35—Determination of Σ_{ma} from crossplot

Figure 3-35 shows this done in a frequency crossplot. Subject to the above conditions, the crossplot usually shows a "funneling" of points with increasing V_{ma}, toward a reliable value of Σ_{ma} at 100% volume of matrix. The column of numbers in the right margin of the chart also help in this determination. These numbers show the total number of plotted points for each value of Σ_{ma} (calculated). On Fig. 3-36 a value of Σ_{ma} around 9.5 c.u. is indicated.

Once Σ_{ma} is established, a $\Sigma-\phi$ plot (where Σ has been corrected for shaliness according to Eq. 3-21) can be used for estimation of Σ_w. (Or, more effectively, a $\Sigma-\phi$ Z-plot, with S_w as the Z variable, may be used.) The TDT water saturation can then be computed.

Dual Water Model

The current interpretation model used for S_w calculations from TDT data is the Dual Water Model. The model assumes that water in clean reservoir rock (movable plus irreducible, or free water) may or may not have the same salinity as the water bound to clay particles in shales (bound water), due to various geophysical and/or petrophysical processes such as depositional environment and diagenesis. Non-zero differences between bound and free water salinities must be accounted for before a final S_w determination can be made from TDT data.

Thus, the response equation is written:

$$\Sigma_{LOG} = V_{ma}\Sigma_{ma} + V_{wf}\Sigma_{wa} + V_{wb}\Sigma_{wb} + V_h\Sigma_h + V_k\Sigma_k . \qquad \text{(Eq. 3-26)}$$

The following terms may be written:

$$V_h = \phi_t - S_{wt} = \phi_t\ (1 - S_{wt})$$

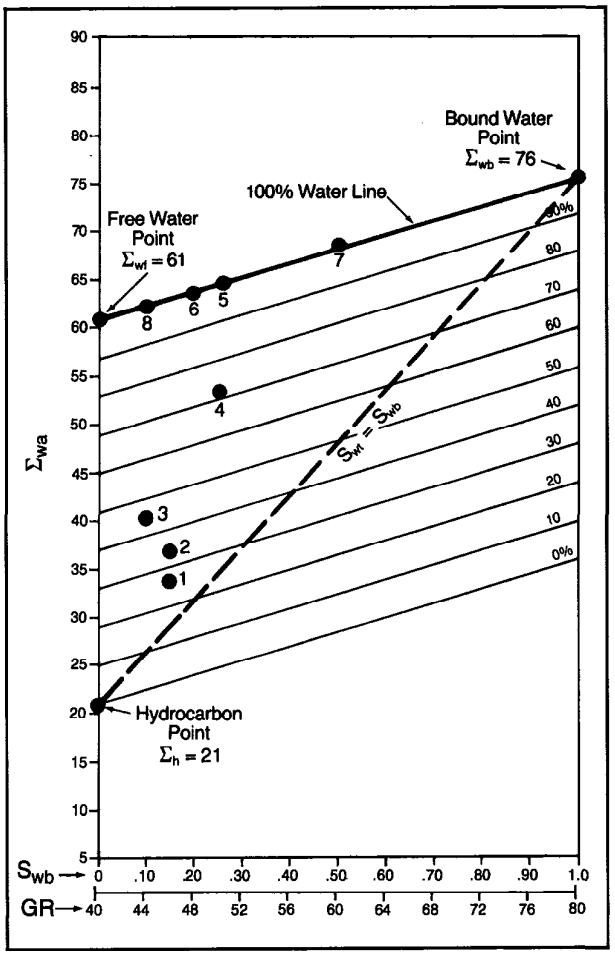

Fig. 3-36—Graphical determination of S_{wt}

$$V_k = (1 - \phi_t)\, V_{sh}$$

$$V_{wf} = \phi_t\, S_{wt} - \phi_t\, S_{wb} = \phi_t\, (S_{wt} - S_{wb})$$

$$V_{wb} = \phi_t\, S_{wb}$$

$$V_{ma} = 1 - \phi_t - V_k\ .$$

An assumption is now made: $\Sigma_{ma} = \Sigma_k$. In other words, the thermal neutron capture cross section of the reservoir rock matrix is approximately the same as that of a dry shale matrix, *K*. This assumption may or may not be correct, but is probably valid where the shales consist predominantly of silts and rock type material (e.g., calcite cementation of silts) and where dry clay colloids appear to be silty. It must be noted that some dry clay colloids, notably chlorite, have high capture cross sections. Fortunately, the volumes of high Σ colloids are small, thus the above assumption may be valid for most shales and shaly reservoir rock.

Using the assumption $\Sigma_{ma} = \Sigma_k$, it follows that:

$$\Sigma_{LOG} = \Sigma_{ma}\,(1 - \phi_t) + \Sigma_{wf}\,\phi_t\,(S_{wt} - V_{sh}) + \Sigma_{wb}\,\phi_t\,V_{sh} + \Sigma_h\phi_t\,(1 - S_{wt})\ . \quad \text{(Eq. 3-27)}$$

Conventional S_w and ϕ_e are obtained from:

$$S_w = \frac{S_{wt} - V_{sh}}{1 - V_{sh}} \quad \text{(Eq. 3-28)}$$

and

$$\phi_t = \phi_t\,(1 - V_{sh})\ . \quad \text{(Eq. 3-29)}$$

Graphical Determination of S_w

Chart Sw-17 in the Log Interpretation Charts book can be used for graphical interpretation of the TDT-K log. In one technique, applicable in shaly as well as clean sands, Σ_{wa}, is plotted versus bound water saturation on a specially constructed grid. To construct this grid three fluid points must be located: a free water point (Σ_{wf}), a hydrocarbon point (Σ_h), and a bound water point (Σ_{wb}) (Fig. 3-36). The free (or formation) water point can be measured from a formation water sample, from Chart Tcor-2 if water salinity is known, or from the TDT-K log in a clean, water-bearing sand using Chart Tcor-3, -4, or -5.

The hydrocarbon point, also located on the left side of the grid, can be determined from Chart Tcor-1 based upon the known or expected hydrocarbon type. The bound water point can be obtained from the TDT-K log in shale zones using Chart Tcor-3, -4, or -5. This point is located on the right side of the grid.

The distance between the free water and hydrocarbon points is linearly divided into constant water saturation lines drawn parallel to a line connecting the free water and bound water points.

Apparent water capture cross section, Σ_{wa}, is determined from Chart Tcor-3, -4, or -5 and then plotted versus bound water saturation S_{wb} to determine S_{wt}. S_{wb} can be estimated from the gamma ray log or other bound water indicator logs.

Knowing the total water saturation and the bound water saturation, the effective water saturation can be determined using Chart Sw-14.

Apparent water salinity, as obtained from Charts Tcor-3, -4, or -5, can also be plotted on Chart Sw-17 instead of the apparent capture cross section. Construction of the chart and its use are similar.

Computer-Processed Interpretation

Figure 3-37 is an illustrative example of computer-processed TDT interpretation. The Cyberscan* log is a wellsite evaluation based on the dual water interpretation model. Essential log measurements come from the TDT log, but, as with all cased hole log interpretations, the results can be enhanced with additional input from other logs such as NGS and total

porosity from openhole logs. The presentation shown is as follows:

- in track 1, the V_{sh} curve;
- in track 2, Sigma Water Apparent (SIWA), Sigma Water Wet (WSIG), and Gas Indicator; and
- in track 3, water saturation (SWC), porosity (PHIE), and ϕS_w (water content) curves. The separation between them (dark shaded) is ϕS_h (hydrocarbon bulk volume).

A TDT Cased Reservoir Analysis log is shown in Fig. 3-38. The program for this computing center evaluation is also based on the dual water interpretation model. The TDT data supports a limited standalone interpretation, but more reliable results are achieved when other cased hole and openhole log data are also available. Three levels of presentations are available depending on the data available: Level 1—only TDT-GR data; Level 2—openhole porosity data; Level 3—results from VOLAN* or GLOBAL* openhole programs. The Level 3 presentation shown in Fig. 3-38 is as follows:

- on the left side, the depth column and a well sketch showing the tubing, packer, perforations, etc. The sketch utilizes openhole caliper data when available;
- in track 1, cased hole GR log, openhole SP curve;
- in track 2, openhole porosity (PHI), gas indicator flag;
- in track 3, cased hole and openhole water saturation curves; and
- in track 4, bulk volume analysis.

The bulk volume of water comparison from the openhole and cased hole data shows how the reservoir is depleting.

GAMMA RAY SPECTROMETRY TOOL (GST)

Introduction

The GST gamma spectrometry tool measures the gamma rays resulting from interactions of neutrons with the different elements in the formations. The number of gamma rays and their energies form a spectrum which is recorded versus depth. These spectra are compared to signatures of the elements most commonly found in sedimentary rocks and their pore fluids. The number of gamma rays attributed to each of these common elements is presented as a percentage of the total gamma ray spectrum (relative yield). These elemental yields are used to calculate basic petrophysical parameters: namely lithology, shale volume, porosity, pore fluid types, and saturations.

The GST tool is operated in two modes: inelastic and capture-tau. In the inelastic mode, the tool is operated in either a stationary position at predetermined depth settings or in a continuous mode. Statistical precision is improved by averaging repeat passes. The gamma rays detected are the result of high-energy neutron interactions and occur during the neutron burst. Common elements detected are carbon (C), oxygen (O), silicon (Si), calcium (Ca), sulfur (S), and iron (Fe).

The capture-tau mode measurements are made with the tool in motion. The gamma rays detected are the result of thermal neutron absorption. This reaction occurs after the neutrons have slowed to the thermal energy level. Common elements detected are hydrogen (H), silicon (Si), calcium (Ca), chlorine (Cl), iron (Fe), and sulfur (S). A formation capture cross section (sigma) is also computed.

The GST elemental yields can be related to specific minerals or fluids found in the formations. GST yields and corresponding minerals or fluids are:

H	H_2O, clays, oil
Ca	$CaCO_3$, $CaMg(CO_3)_2$, $CaSO_4$, $CaSO_4(H_2O)_2$
Si	SiO_2, clays
Cl	NaCl
S	S, $CaSO_4$, $CaSO_4(H_2O)_2$
Fe	FeS_2, clays
C	Hydrocarbon, $CaCO_3$, $CaMg(CO_3)_2$.

By using the relationship between GST elemental yields and these minerals and fluids, formation characteristics such as lithology, porosity, fluid salinity, and hydrocarbon saturation can be calculated.

Principles of the Technique

The GST tool consists of a pulsed-neutron accelerator 14 MeV neutron source and a complete spectrometer system using an NaI detector and a multichannel data acquisition system. Gamma ray spectral intensities are analyzed in 256 channels covering an energy range of 0-8 MeV. All spectral information is sent uphole to a CSU unit for processing.

There are two major categories of gamma-ray-producing interactions used by the GST tool: fast neutron interactions and neutron capture interactions.

Fast Neutron Interactions

- This group involves inelastic scattering and neutron reactions (Fig. 3-39).
- Inelastic scattering involves the scattering of a neutron by the formation nuclei. The neutron energy is then reduced. Energy conservation is then accomplished by the release of gamma rays of specific energy.
- Fast neutron reactions can be the emission of an alpha particle leaving the nucleus in a temporarily excited state, followed by delayed gamma ray emission. Some of these resulting nuclei can be relatively long lived, emitting the so-called activation gamma rays.

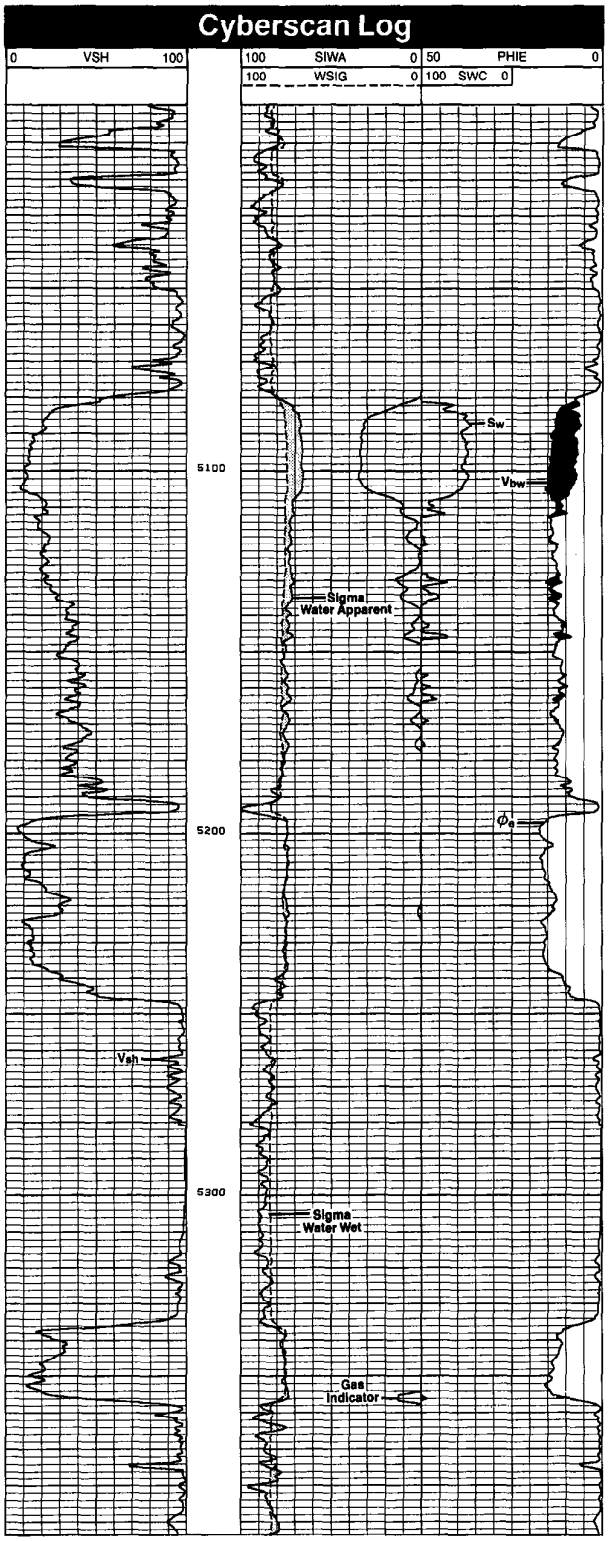

Fig. 3-37—Cyberscan wellsite computation of TDT data

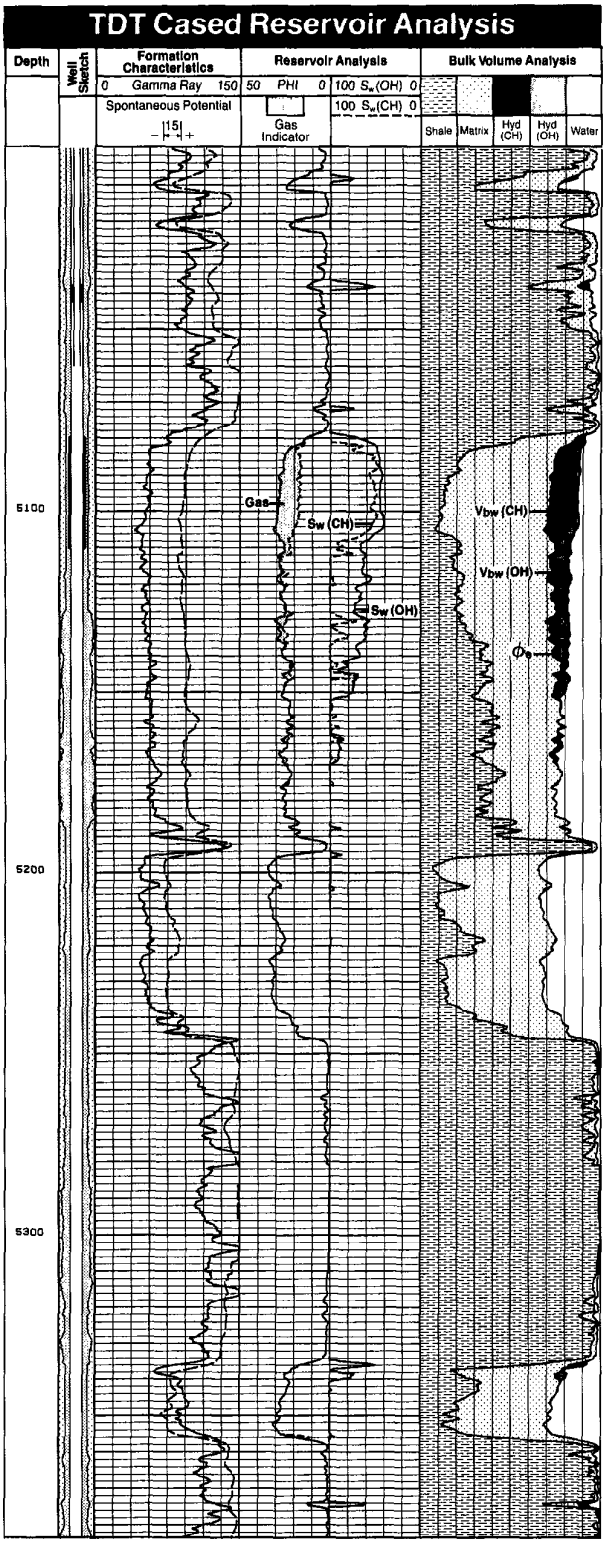

Fig. 3-38—TDT Cased Reservoir Analysis Log

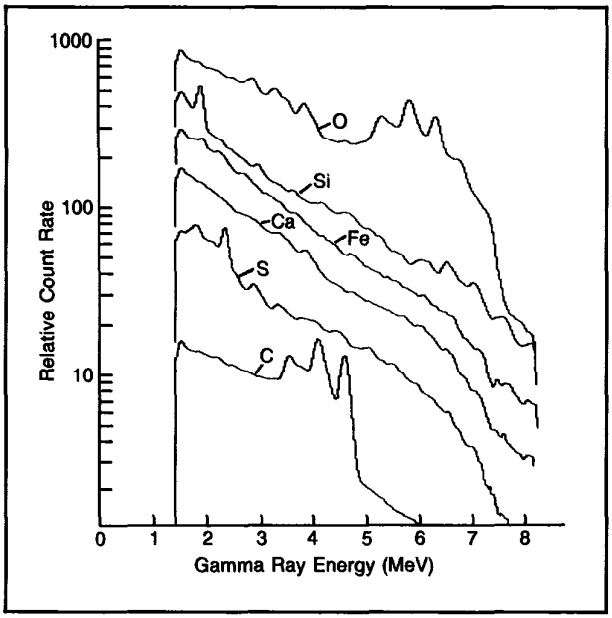

Fig. 3-39—Inelastic standards

Neutron Capture Interactions (also Called Thermal Absorption)

- This is a relatively slow process which generally occurs after the fast interactions. Neutrons from the tool are slowed to thermal levels through collisions. The thermal neutrons are absorbed by the formation nuclei. The resulting nucleus becomes excited and emits characteristic gamma rays (Fig. 3-40).

Among the commonly occurring elements giving detectable gamma ray yields from fast neutron interactions (primarily inelastic scattering) are C, Ca, Fe, O, S, and Si. Some elements that contribute to capture reactions are Ca, Cl, Fe, H, S, and Si.

The gamma rays emitted from formation nuclei are limited to specific well-defined energies. Each element (isotope) has a characteristic set of gamma rays that can be emitted from a given neutron interaction. Therefore, an element can be identified by its gamma ray signature, or spectrum, if the type of neutron interaction is known. The energies of the neutrons emitted from the source are known and, consequently, the type of neutron interaction taking place in the formation can be determined.

The GST tool can be operated in either of two timing modes. The modes are "inelastic," responding to fast reactions and "capture," which responds to the thermal absorption process. Lithological and reservoir information are then defined from the tool's response. Since the energies associated with gamma ray emission are unique to individual elements, the presence of an element can be established by the

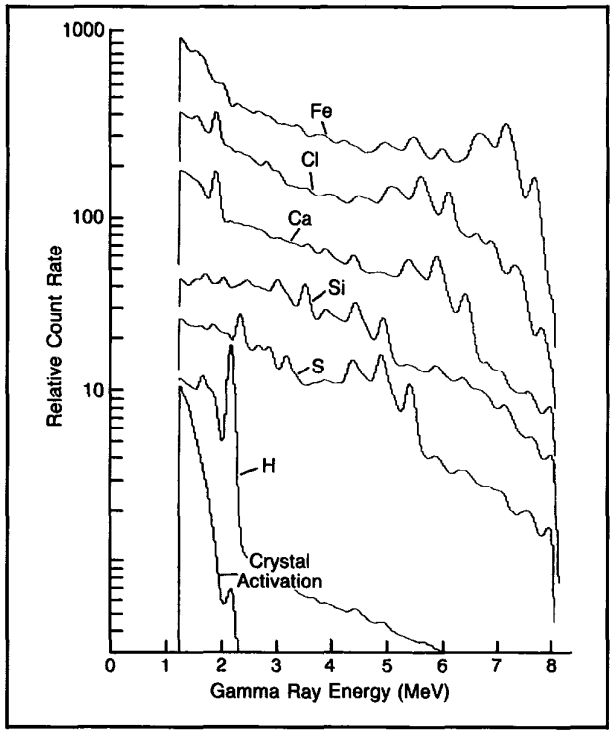

Fig. 3-40—Capture standards

presence of a set of gamma rays of characteristic energy. The concentration of that element is related to the intensity of emission (count rate).

The inelastic mode has a fixed timing cycle (Fig. 3-41). Gamma rays from fast neutron interactions are detected during the neutron burst itself. A short "capture background" gate is used to measure capture events that may have corrupted the inelastic spectrum. A "late capture" gate is also used to record capture spectrum during inelastic mode.

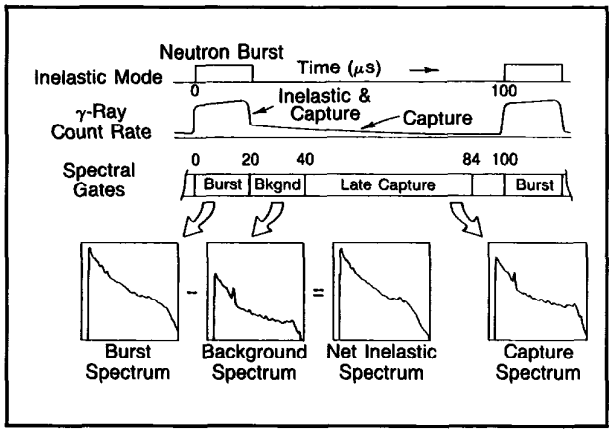

Fig. 3-41—GST inelastic mode timing program

These three spectra are digitized downhole and sent up to the surface computer by telemetry. The capture background is subtracted from the inelastic spectrum to give a "net inelastic" spectrum. At regular sampling intervals, a weighted least squares spectral fitting analysis is performed. The spectra are simultaneously recorded on magnetic tape.

In capture mode, the delay between the neutron burst and the measurement of the capture gamma ray spectrum is increased to allow borehole contributions to die away. The timing is varied continuously according to a simultaneous measurement of decay time, τ.

As an example, the spectra in Fig. 3-42 were obtained in a laboratory, oil-saturated (ϕ = 36%) sandstone with a 7-in. (17.8 cm) saltwater-filled casing cemented in a 10-in. (25.4 cm) hole. The characteristic peaks of the constituent elements are seen superimposed on a background of Compton-scattered gamma rays.

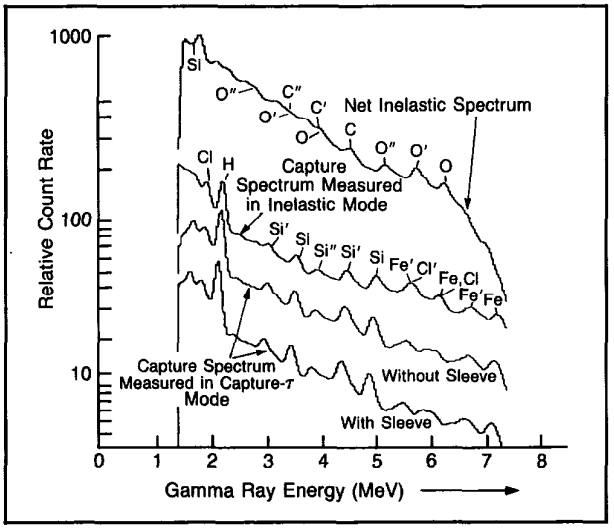

Fig. 3-42—Inelastic and capture spectra measured in laboratory formation

Several features of the different modes are shown in Fig. 3-42. Working from top to bottom, the top spectrum is a capture-background-corrected, inelastic spectrum. The second is the capture spectrum available from inelastic mode. The third and fourth spectra are both capture spectra. Notice the reduction in the borehole effect due to the capture tau timing mode. Further reduction is obtained by use of the (boron) fluid excluder sleeve. This is particularly noticeable on the chlorine yield, which, since we know the sample is oil-saturated sandstone, is entirely a borehole signal. The reduction in chlorine yield gives improved sensitivity to all the formation yields.

Log Presentation

The relationship between the GST yields and common elements in minerals and fluids found in formations are shown in Table 3-7. Several elements are indicative of more than one mineral or fluid, as is the case for carbon. Knowledge of lithology and porosity is required to predict hydrocarbon and water content.

C	=	Hydrocarbons, Limestone ($CaCO_3$), Dolomite ($CaMg(CO_3)_2$)
H	=	Water (H_2O), Clays, Hydrocarbons
Ca	=	Limestone ($CaCO_3$), Dolomite ($CaMg(CO_3)_2$), Anhydrite ($CaSO_4$)
Si	=	Quartz (SiO_2), Clays, Silts
Cl	=	Chloride Salts (NaCl)
S	=	Sulphur (S), Anhydrite ($CaSO_4$), Pyrite (FeS_2)
Fe	=	Pyrite (FeS_2), Clays

Table 3-7—Yield-mineralogy and fluid relations

In order to present log curves that can be related to formation parameters, several ratios of the measured yields are presented. These ratios are shown in Table 3-8.

Yield Ratio	Interaction	Name	Label
C/O	Inelastic	Carbon-Oxygen Ratio	COR
Cl/H	Capture	Salinity-Indicator Ratio	SIR
H/(Si + Ca)	Capture	Porosity-Indicator Ratio	PIR
Fe/(Si + Ca)	Capture	Iron-Indicator Ratio	IIR
Si/(Si + Ca)	Capture & Inelastic	Lithology-Indicator Ratio	LIR

Table 3-8—GST logging curves presented

Figure 3-43 shows a GST log recorded in both capture-tau and inelastic modes. The sigma curve is displayed along with the indicator ratios and the sulfur yields.

A Gradiomanometer (fluid density) log was run before the GST log to locate the oil/water contact. The shifts on the SIR, PIR, and Carbon/Oxygen (COR) ratio curves indicate that the oil/water contact was moving up during the logging runs.

The lithology indicating ratio (LIR) is near zero in the dolomitic limestone. There is an increase in sulfur yield above 4942 ft, accompanied by a higher sigma as the anhydrite caprock is approached.

The major oil/water contact is at 4986 ft. The contact is clearly detected by a COR increase from about 0.20 in the depleted section to 0.27 just above. This is accompanied by a large decrease in sigma and a decrease in SIR, which indicates that water salinity is still high.

Above the wellbore fluid interface, high COR (good porosity) corresponds to the undepleted part of the reservoir. This correlates with low sigma and SIR. However, in this section, from 4970 to 4959 ft, a premature breakthrough has

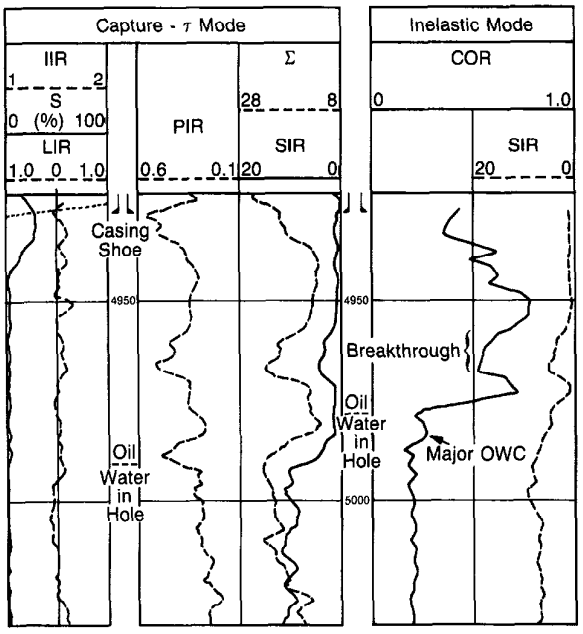

Fig. 3-43—Continuous capture logging and stationary inelastic logging in a clean carbonate reservoir

occurred along a high permeability layer. It is characterized by a marked dip in the COR readings. The associated increase in sigma and SIR suggests that this is an influx of relatively saline water.

Figure 3-44 is the computed hydrocarbon interpretation of COR. It is compared with the evaluation of sigma made assuming a sigma water representing the original high connate water salinity. In the comparison with initial hydrocarbon in place, the shaded area represents total depletion since drilling in 1976.

The close agreement between the COR and sigma results suggest that the incoming water is still at or near its original salinity. A computation of salinity was made from SIR (capture-tau), and is shown on the left of the figure. There appears to be some freshening of the water at the breakthrough; however, the response of SIR here is due primarily to the increase in water saturation.

Carbon/Oxygen Interpretation

The ratio of the carbon and oxygen yields from weighted-least-squares processing can be related to formation parameters from the following equation:

$$\text{COR} = \frac{\text{Spectral Carbon Yield}}{\text{Spectral Oxygen Yield}} = \frac{A\propto (1-\phi) + \beta\phi S_o + B_C}{\gamma (1-\phi) + \delta\phi S_w + B_O} \quad \text{(Eq. 3-30)}$$

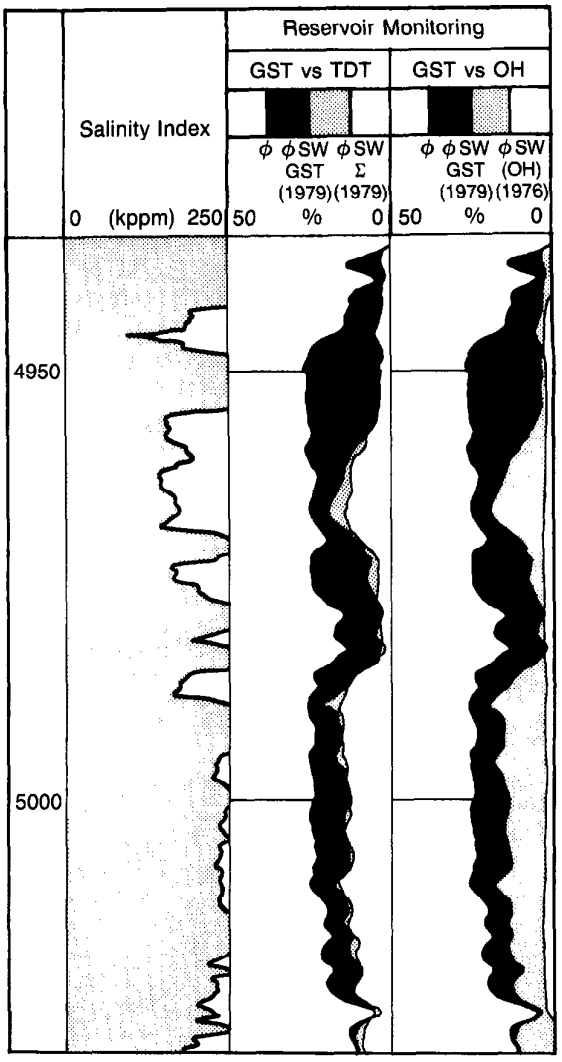

Fig. 3-44—Cased Reservoir Analysis of log in Fig. 3-43

Since inelastic reactions occur rapidly and close to the tool, the equation contains borehole contribution terms as well as atomic concentration and relative cross-sectional constants. The definition of these constants is:

A = ratio of average carbon and oxygen fast neutron (gamma ray-producing) cross sections

$$= \frac{\overline{\sigma}_C}{\overline{\sigma}_O}$$

B_C, B_O = carbon and oxygen contributions from the borehole

S_w = water saturation

$\propto$ = atomic concentration (moles per cubic centimeter) for carbon in matrix (lithology dependent)

β = atomic concentration of carbon in formation fluid
γ = atomic concentration of oxygen in matrix (lithology dependent)
δ = atomic concentration of oxygen in formation fluid
ϕ = porosity
S_o = oil saturation = $(1-S_w)$.

With a knowledge of lithology and porosity from external sources or calculations from capture yields (see later) minimum and maximum expected values for COR may be calculated by assuming S_w = 1 and 0, respectively.

This gives the two simplified versions of Eq. 3-30:

For S_w = 1,

$$C/O_{min} = A\,\frac{\propto (1-\phi) + B_C}{\gamma(1-\phi) + \delta\phi + B_O} \quad \text{(Eq. 3-31)}$$

For S_w = 0 and S_o = 1,

$$C/O_{max} = A\,\frac{\propto (1-\phi) + \beta\phi + B_C}{\gamma(1-\phi) + B_O} \quad \text{(Eq. 3-32)}$$

Lithology, C/O_{min}, and C/O_{max} may be plotted before recording the inelastic stations (Fig. 3-45). The measured C/O at each station is then plotted and interpolation between C/O_{min} and C/O_{max} provides a quick estimate of water saturation:

$$S_w = \frac{C/O_{max} - C/O_{LOG}}{C/O_{max} - C/O_{min}} \quad \text{(Eq. 3-33)}$$

Because the value of C/O_{max} and C/O_{min} are in constant flux they must be read from the log at each station.

The measurement at 730 ft gives:

$$S_w = \frac{1.25 - 0.80}{1.25 - 0.13} = 40\% \ .$$

Since S_w appears in both numerator and denominator of the C/O equation, this interpolation is not truly linear; therefore this technique should be used only as a "quicklook" estimation.

Charts GST-1 or GST-2 in the Log Interpretation Charts book permit the determination of S_w from COR measurements made with the GST tool (Fig. 3-46). The COR and porosity are entered on the appropriate chart (dependent upon borehole and casing size). Water saturation is defined by the location of the plotted point within the appropriate matrix "fan chart".

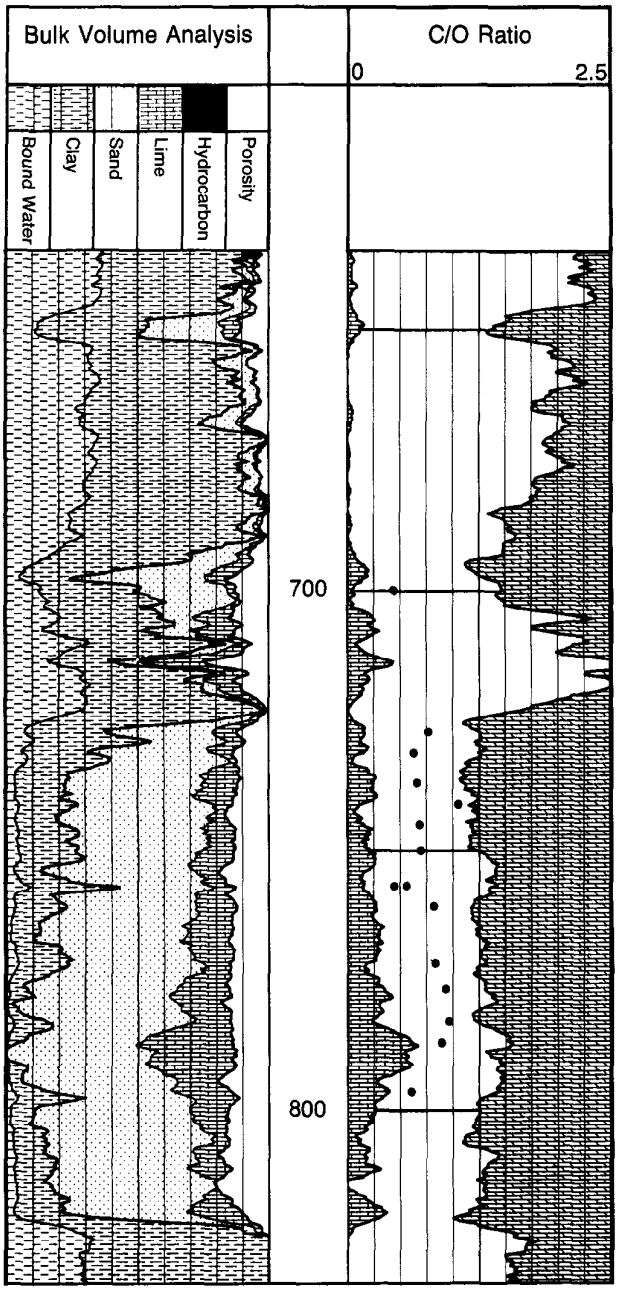

Fig. 3-45—Water saturation from COR ratio

Capture Mode Interpretation

In capture-tau logging porosity, lithology and formation fluid salinity can be determined in real time, or at a later stage in the computing center. These computations require input of hole size, casing grade, approximate cement thickness, and borehole salinity. Gamma ray, sigma, and some synthetic sigma curves are also plotted.

A Dual Water Model is used for the sigma interpretation. This is shown schematically in Fig. 3-47, where the total capture cross section Σ_{LOG} is the sum of the various sigmas.

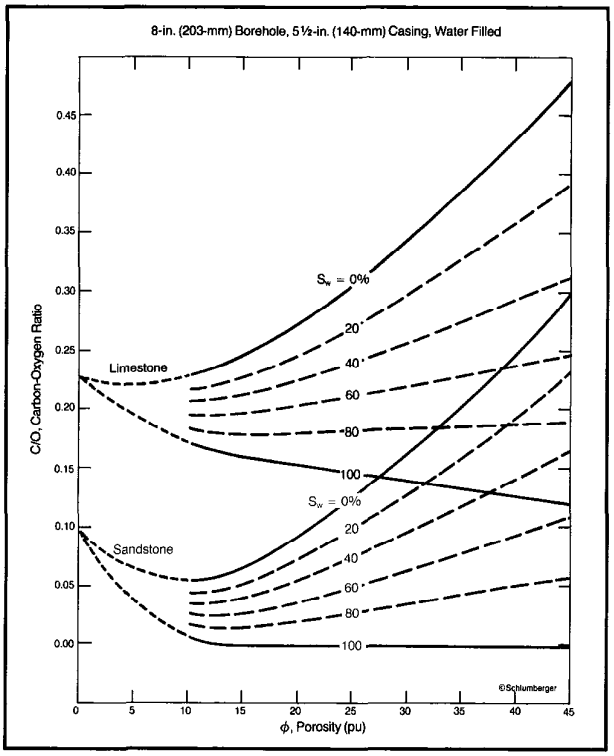

Fig. 3-46—GST-1 chart for determining S_w from COR and porosity data

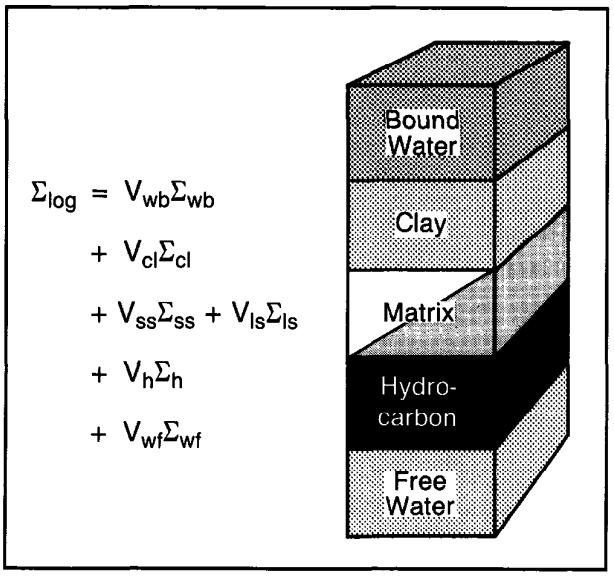

Fig. 3-47—Dual Water Model for capture mode interpretation

$V_{vf}\,\Sigma_{wf}$ = product of the volume and cross section of free water

$V_h\,\Sigma_h$ = product of the volume and cross section of hydrocarbon

$V_{ma}\,\Sigma_{ma}$ = product of the volume and cross section of matrix

$V_{cl}\,\Sigma_{cl}$ = product of the volume and cross section of dry clay

$V_{wb}\,\Sigma_{wb}$ = product of the volume and cross section of bound water

The example in Fig. 3-48 is the preliminary interpretation (pass 1).

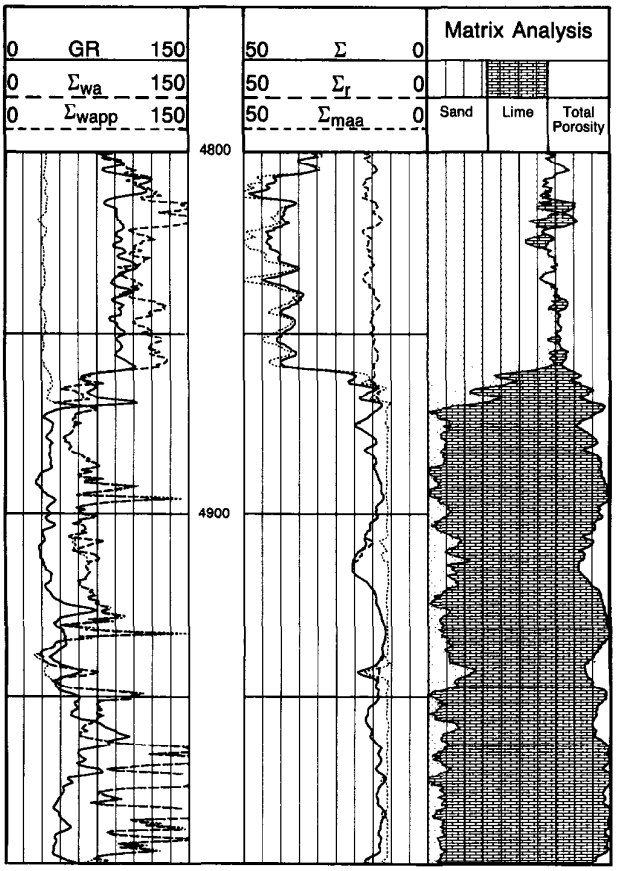

Fig. 3-48—Sigma computations from Dual Water Model

The synthetic sigma curves are computed using a sigma matrix (Σ_{ma}) calculated from GST lithology data. The apparent fluid cross section, Σ_{wapp}, is computed from GST chlorine measurement and Σ_{wa} from Σ_{LOG} and ϕ_t.

An apparent clean formation cross section (Σ_r) can be reconstructed as follows:

$$\Sigma_r = \phi_t\,\Sigma_{wapp} + (1-\phi_t)\,\Sigma_{ma}\ . \qquad \text{(Eq. 3-34)}$$

The lithology analysis indicates a calcite base with silicon base lithology above. Comparison of the measured (Σ_{LOG}) and reconstructed (Σ_r) cross sections shows a good overlay in the limestone, but a divergence in the shallower zone. Clearly, this is shale rather than sandstone. This is supported by the gamma ray data.

The apparent water cross sections (Σ_{wapp}, Σ_{wa}) also agree in clean limestone but differ in the shale. The curve (Σ_{wapp}) having the lower value in the shale is computed from GST salinity. This indicates that the relatively high reading of Σ_{wapp} computed from Σ_{LOG} in the shale is due to nonchlorine absorbers in the clay and not chlorine in bound water.

Using the reconstructed sigma curve displayed in Fig. 3-48 allows calculation of clay content:

$$V_{cl} = \frac{(\Sigma_{LOG} - \Sigma_r)}{(\Sigma_{cl} - \Sigma_{ma})} . \qquad \text{(Eq. 3-35)}$$

V_{cl} can also be calculated from the gamma ray and the $\Sigma_{max}-\Sigma_{min}$ approach.

The following "picks" are made from the pass 1 log:

Σ_{cl} = capture cross section of clay
Σ_{wb} = capture cross section for bound water
Σ_{wf} = capture cross section for free water
Σ_{min} = minimum sigma (clean formations)
Σ_{max} = maximum sigma (shales)
GR_{min} = minimum GR (clean formations)
GR_{max} = maximum GR (shales).

The shale corrected results are displayed in Fig. 3-49 with free water, bound water, and hydrocarbon volumes also indicated. The method has been found to give good results for porosity and V_{cl}. S_w can only be computed from capture data if there is a sizable difference between Σ_{wf} and Σ_h (when the formation water is relatively saline). Σ_h, the capture cross section of the hydrocarbon, is assumed to be known.

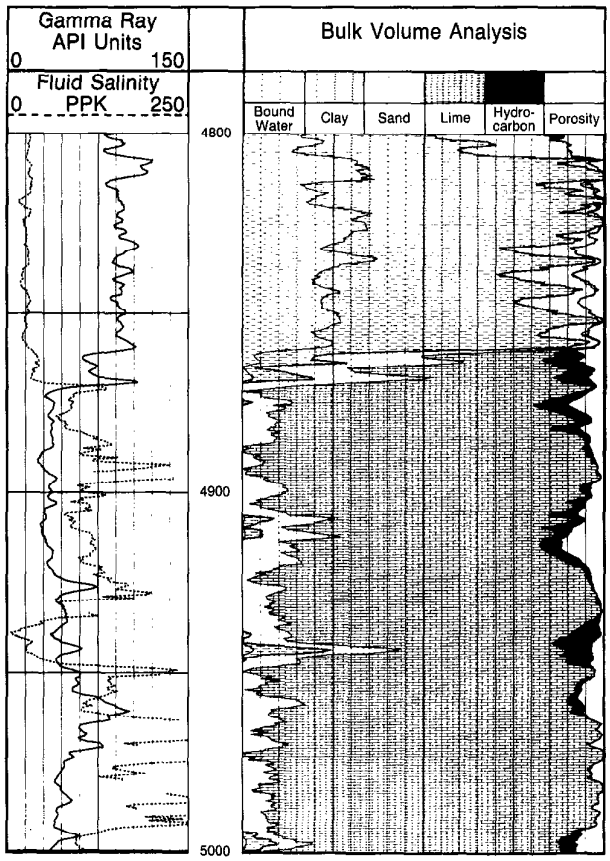

Fig. 3-49—Bulk volume analysis of log data from Fig. 3-50

Applications

Combinations of elemental yields measured with the GST tool are used to evaluate:

- oil saturation behind casing
- hydrocarbon depletion and waterfront movement, independent of salinity
- formation and/or flood water salinity
- development of gas caps
- formation characteristics such as porosity, lithology, and shaliness
- identification of special minerals
- steam front and CO_2 front monitoring
- coal quality

The service is particularly applicable in formations where the analysis of Thermal Decay Time logs may not provide needed answers such as:

- low-salinity or unknown-salinity formation waters
- monitoring sweep efficiency of waterflood projects
- mixed or complex lithologies.

The example in Fig. 3-50 shows an analysis of bulk volume matrix calculated from data acquired in the capture-tau mode and measured COR plots made through a freshwater, shaly sand zone. The 45 to 50% water saturations, calculated from CO data located a productive oil zone at 2280 ft.

The well shown in Fig. 3-51 is part of an active waterflood project. The well, when first drilled and completed, had no evidence of a floodwater breakthrough. The connate water salinities were known; therefore, accurate water saturation calculations from resistivity and porosity data in the open hole were possible (shown as the solid line in track 3).

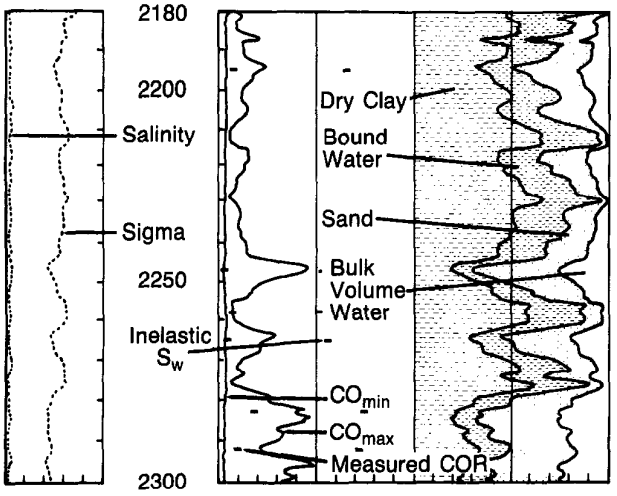

Fig. 3-50—COR data reveal oil in freshwater zone

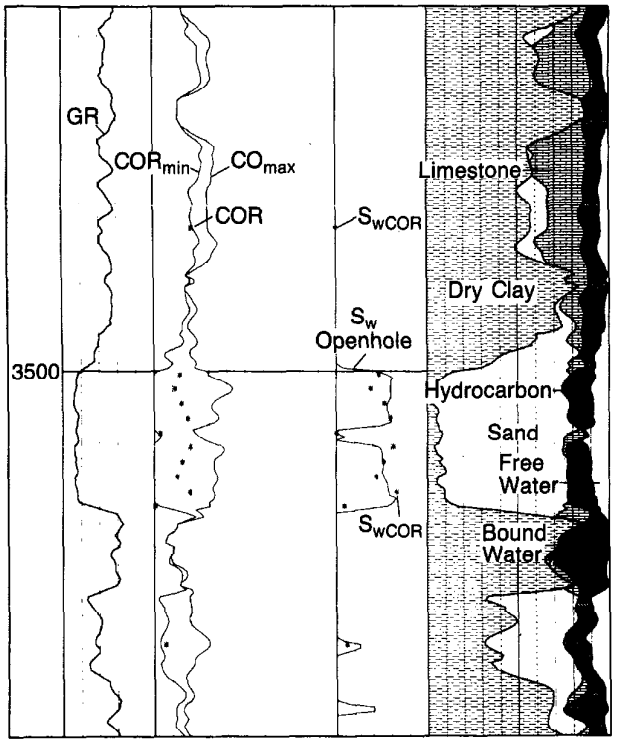

Fig. 3-51—GST computation in a water flood project

There is no indication of high water saturation in the zone of interest between 3499 and 3518 ft, as shown by the openhole logs.

The well was perforated above and below the lime stringer at 3508 ft. However, soon after completion, water production increased sharply and oil production decreased. The water analysis indicated a mixture of natural and flood waters.

A cased hole logging program was needed to detect the water-producing zone. Since the salinity of the naturally occurring waters was only about 20,000 ppm, the salinity of the flood waters was 3000 ppm, and the salinity of the commingled waters was unknown, an analysis using sigma from a conventional pulsed-neutron tool was not possible. Therefore, COR data was recorded for use in detecting water breakthrough.

Station measurements were recorded every 2 ft through the sand, and, as can be seen by comparing the water saturations computed from openhole resistivity with the CO data, the water was coming from the lower part of the lower sand lobe. A bridge plug between the two sets of perforations was all that was needed to correct the problem.

Proper modeling of the formation into the COR analysis is essential to achieve quality water saturation computations. The GST lithology data indicate the zone at 3480 ft to be a sandy, limy shale. A higher than normal COR was measured opposite this interval. Modeling in the correct amount of carbon associated with the volume of limestone causes the calculation of CO_{min} to be high also and to agree with the recorded value. Therefore, the resultant computation of high water saturation indicates no hydrocarbons.

The example shown in Fig. 3-52 is from a well with mixed lithologies. The minerals identified by the different logging tool include carbonates, sandstone, and anhydrite, and, as a complicating factor, the zones are quite shaly.

GST cased hole data and openhole data from the Litho-

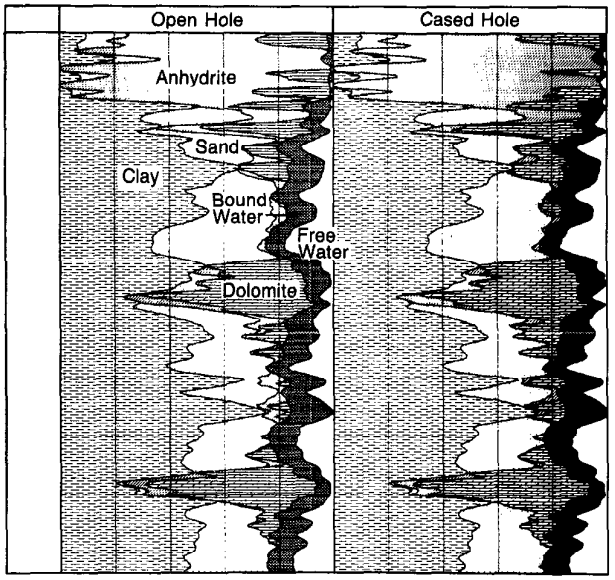

Fig. 3-52—Comparison of openhole and cased hole GST lithology

Density*, compensated neutron, borehole compensated sonic, and gamma ray logs were used. The GST, sonic, neutron, and gamma ray data can be obtained in cased hole and used for interpretation when insufficient openhole data are available.

The interpretation program used for the other examples is a fixed, deterministic model. A different model and interpretation driver has been used in this example for both the openhole and cased hole data. A set of linear tool response equations with linear inequality constraints was used for the computation. Various logging tools are selected by the analyst so that an overdetermined situation exists—more tools than minerals selected. Certain logging measurements are weighed according to their statistics, confidence, and relevance to the interpretation. The unknown volume of minerals is solved by a quadratic algorithm that minimizes the incoherence among the different tool readings.

This program allows the analyst to easily add or substract minerals and other logging measurements as necessary. Thus, for a traditional openhole lithology computation, the GST data can supplement the openhole data as it is added to the interpretation model. In this example, the openhole data are computed without the GST data; the sonic, neutron, and gamma ray measurements are used with the GST data for a separate computation. The openhole computation is presented in the left half of the plot and the cased hole computation is presented in the right half.

Although the openhole and cased hole computations are made separately, the same tool response equations and parameters are used when there is a duplication of data, such as for the neutron. Both programs have the same minerals: sandstone, dolomite, anhydrite, illite clay, and porosity (water). No hydrocarbon saturation determination was attempted in this computation so all the porosity is water filled.

In the openhole computation, there are sufficient data to accurately extract the mineral volumes. The correct description of anhydrite and dolomite is somewhat complicated by the large volume of clay. The ρ_b and U values for these three minerals are not sufficiently unique to keep the incoherence from a greater than minimum value. However, the less weighted tools of sonic and gamma ray are useful for calculation of the clay volumes.

The GST computation produces a close match to the openhole data with only slightly greater incoherence. In fact, anhydrite zones show smaller incoherence than the openhole computation because of the measurement of sulfur. Elemental sulfur as measured by the GST tool is unique to anhydrite for all the minerals allowed in this computation. The GST computation also provides a lithology indicator ratio (LIR), which is a measurement of the ratio of silicates and calcites. In this example, this ratio is useful in distinguishing sand and clay from dolomite and anhydrite.

The GST gamma spectrometry tool makes a valuable contribution to the expansion and reliability of cased hole logging techniques for the detection and recovery of hydrocarbons.

Reservoir Monitoring

The monitoring of reservoirs with cased hole logs can be accomplished with the CNL, TDT, or GST tools depending on the information needed and the mechanical constraints involved. In most cases the Dual-Burst TDT tool is the best choice because of the $1^{11}/_{16}$-in. size and the absence of borehole environmental effects.

Production Monitoring

In the time-lapse technique each TDT log is compared with one or more TDT logs run earlier in the life of the well. Differences between successive logs will reflect either changes in water saturation, or salinity or changes in the nature of the hydrocarbon. Preferably a "reference" log is run soon after production has begun, but after a sufficient period of time has elapsed for the filtrate-invaded zone behind casing to dissipate. For this reference log, then, formation conditions in terms of fluid levels and saturations should be similar to those for the openhole logs.

Multiple logging TDT-K runs were made in the well shown in Fig. 3-53 over a 5-yr period. Of these, four are presented which represent logs made when the well's water cut was 0, 5, 16, and 39%. For time-lapse measurements, changes in water saturation can be calculated as:

$$\Delta S_w = \frac{\Delta \Sigma}{\phi (\Sigma_w - \Sigma_h)} . \qquad \text{(Eq. 3-36)}$$

(The terms represent matrix contribution in a single-pass interpretation drop out, since these parameters do not change with time.) For this reservoir, Σ_w is 54, Σ_h 21, and ϕ about 0.26. For these conditions, it can be shown, with the above equation, that an uncertainty of 0.5 c.u. in the measured formation sigma will cause an uncertainty of 6 saturation units. For repeatability of 0.2 c.u., such as can be attained with Dual-Burst TDT measurements, the uncertainty is only 2 saturation units.

The increased gamma ray level with time at the bottom of the perforations shows that radioactive material was being deposited during production. In addition, the last run gamma ray shows an increase above 212 m, indicating oxygen activation from the water influx.

Flood Monitoring

In water flood or CO_2 flood projects, reservoir nonuniformities have a significant effect on both the areal and vertical sweep efficiency. In addition, gravity tonguing of the CO_2 over the oil bank, viscous fingering of CO_2 through the oil bank, and changes in mobility and injectivity due to relative

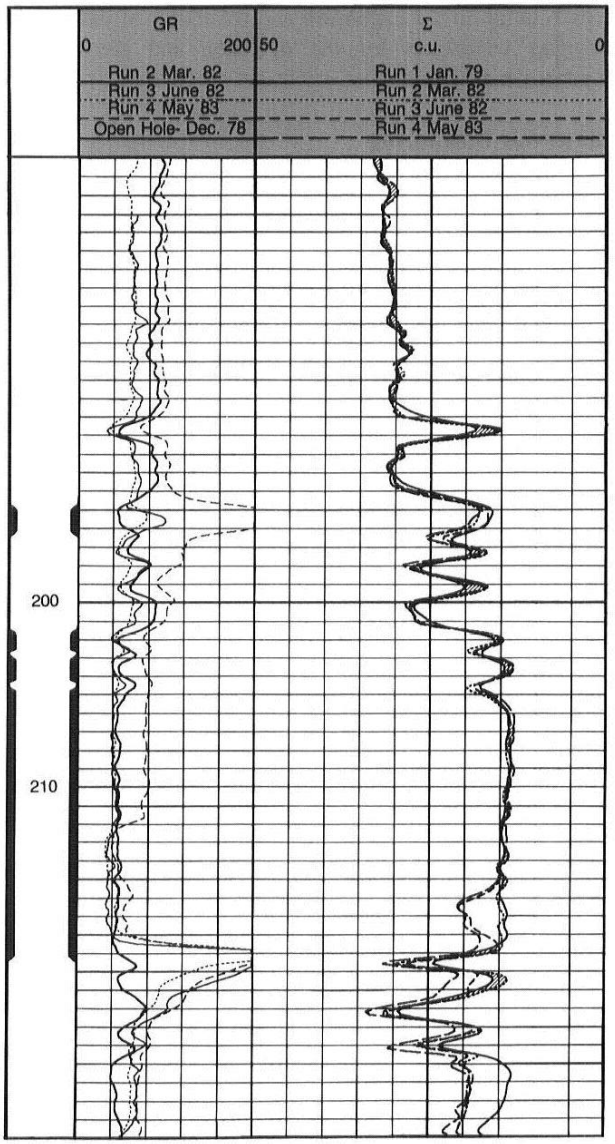

Fig. 3-53—TDT logs in a production monitoring project

permeability changes create additional problems. In water floods, the salinity of the commingled waters is unknown so an analysis using sigma from a TDT measurement is not possible. Therefore, COR data is required as was demonstrated in Fig. 3-51.

The FLOOD program is designed for monitoring the fluid saturations present in a CO_2 flood by means of cased hole logs. Through the use of monitor wells, logging measurements are made to quantify the presence of oil, water, and CO_2 at particular locations in the field. Monitoring can be performed in an injector, a producer, or an observation well. The type of and number of measurements are varied depending on the formation properties, cased hole environments, and availability of openhole log data. The program uses a simultaneous or least squares solution to quantify the changes in saturation at the wellbore. This is accomplished by a calibration of the cased hole base logs to established lithology, porosity, and water saturation information from open or cased hole volumetric analysis. Parameters from this calibration are applied to subsequent monitor log data which are then used to calculate the three phases.

The FLOOD program will accept measurements from TDT, CNL, GST tools, and also induction logs in wells that have fiberglass casing. Because of its small diameter, the TDT tool has the largest application of the neutron-emitting tools for through-tubing operations, which comprise much of the monitoring work.

The CNL log is accepted as the most reliable porosity through casing. Since it responds primarily to the hydrogen content in the formation, it is an excellent device for detecting the presence of CO_2. However, lack of cement has an adverse effect on the measurement, causing porosity values that are too high. Porosity from the TDT ratio is preferred in this situation.

The carbon/oxygen measurement from the GST tool is used in reservoirs that have fresh or variable salinity formation waters, but is limited to porosities greater than 15%.

Resistivity measurements can be used in wells that have fiberglass casing or in openhole completions. Resistivity and sigma measurements can be used in reservoirs with fresh or variable salinity waters when porosities are too low for carbon/oxygen ratio techniques.

Figure 3-54 is a flow diagram showing the program's three stages of computation points. The first stage is a computation of the standard volumetric analysis which provides the volume of each major rock type (dolomite, limestone, sand, shale, and evaporites), effective and secondary porosity, and bulk volume of water. This information is best obtained by openhole logs with nearby core and water sample data to support the parameters that go into this computation. In absence of this data, a cased hole volumetric analysis is needed from GST data. These volumes are important to minimize the assumptions that could result in systematic errors in the computed saturations.

The second stage is the determination of cased hole parameters that give the best agreement between the openhole and cased hole porosity and water saturation. Since only two phases (oil and water) should exist at the time of these measurements, the solution is

$$\Sigma_{fluid} = \left(\Sigma_{water} \times S_{water}\right) + \left(\Sigma_{oil} \times S_{oil}\right)$$
$$1 = S_{water} + S_{oil} , \qquad \text{(Eq. 3-37)}$$

where:

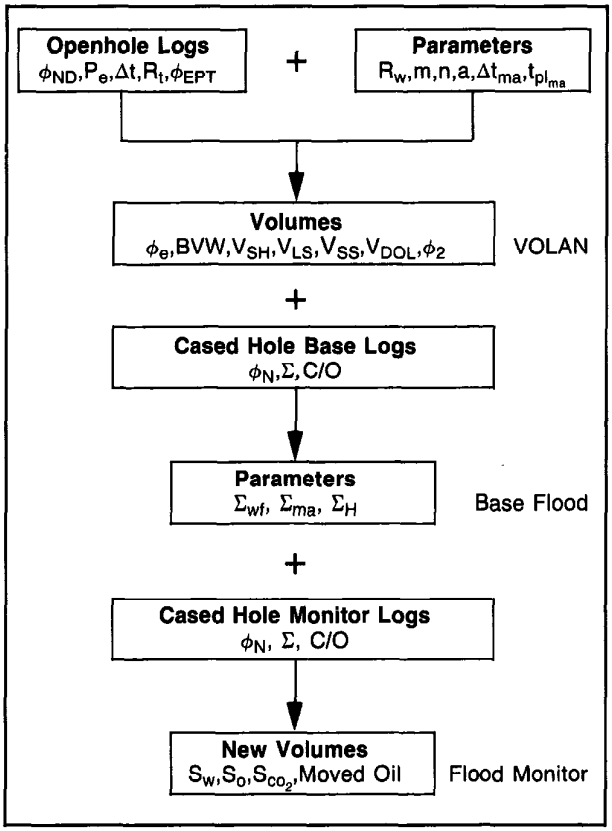

Fig. 3-54—CO_2 FLOOD monitor program

$$\Sigma_{fluid} = \frac{\Sigma_{LOG} - \Sigma_{matrix}\,(1-\phi_{ND})}{\phi_{ND}} \quad \text{(Eq. 3-38)}$$

The calibration is accomplished by slight adjustments to water, oil, matrix, and lithology correction for neutron porosity to obtain the best fit with the base data. All future monitoring of this well is compared to this base condition.

The third computation is the solution of the following equations using the base cased hole parameters with the new monitor data:

$$1 = S_{CO_2} + S_{oil} + S_{water} \quad \text{(Eq. 3-39)}$$

$$\Sigma_{fluid} = S_{CO_2}\Sigma_{CO_2} + \Sigma_{oil}S_{oil} + \Sigma_{water}S_{water} \quad \text{(Eq. 3-40)}$$

$$HI_{fluid} = S_{CO_2}HI_{CO_2} + HI_{oil}S_{oil} + HI_{water}S_{water} \quad \text{(Eq. 3-41)}$$

$$\frac{C}{O} = \frac{C_{matrix} + (S_{oil}C_{oil}+S_{CO_2})\,\phi_t + C_{borehole}}{O_{matrix} + (S_{water}O_{water} + S_{CO_2}O_{CO_2})\,\phi_t + O_{borehole}} \quad \text{(Eq. 3-42)}$$

If logging conditions are ideal, such as in an injector well during the water injection cycle with high salinity water (or sigma water greater than 50 c.u.), Eqs. 3-39, 3-40, and 3-41, are needed for the solution. In cases of fresh or variable water salinities, the carbon/oxygen ratio and Eq. 3-42 are required.

Injection Well Monitoring

Figure 3-55 is the base (2-phase) FLOOD log in an injector well. The monitoring program objective was to determine the amount and vertical distribution of oil moved by CO_2 injection through one cycle. The TDT log was used since the pre-CO_2 brine flush was sufficient to move any movable fluids beyond its depth of investigation, allowing a reliable

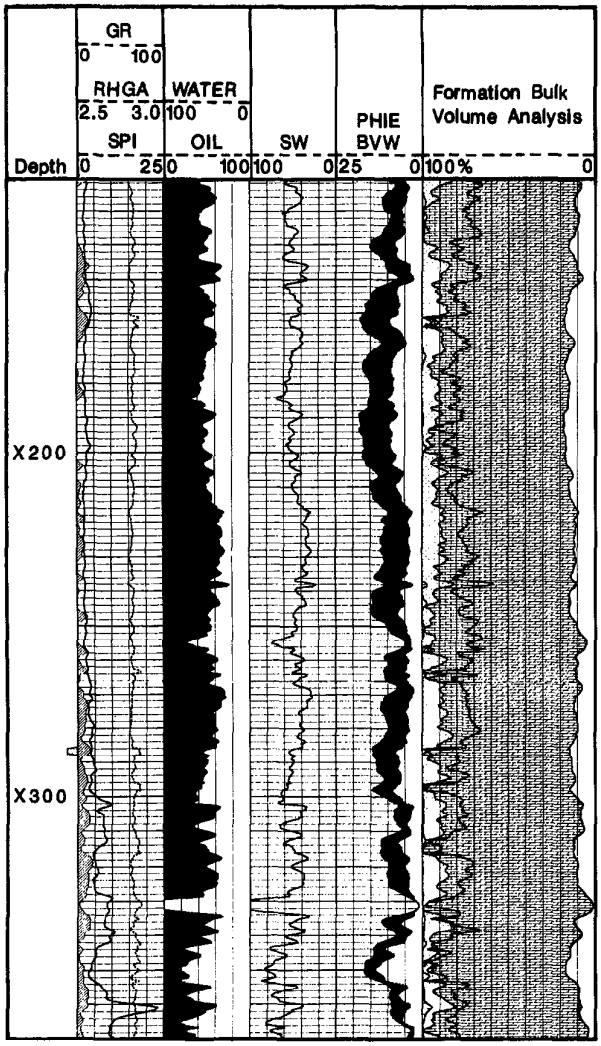

Fig. 3-55—FLOOD base log in an injection well

calibration of S_w from TDT data with S_{xo} from openhole Electromagnetic Propagation Tool (EPT*) computations. Also, the TDT was preferred because monitoring could take place while injecting through tubing to avoid crossflow after shut-in.

After one CO_2 slug was injected the TDT monitor log was run during brine injection to provide the data for the 3-phase solution shown in Fig. 3-56. Moved oil is indicated in the upper zones with the higher porosity but they also show the highest residual CO_2 saturation, indicating a mobility problem. The moved oil profile shows that the water is also going into the lower porosity zones.

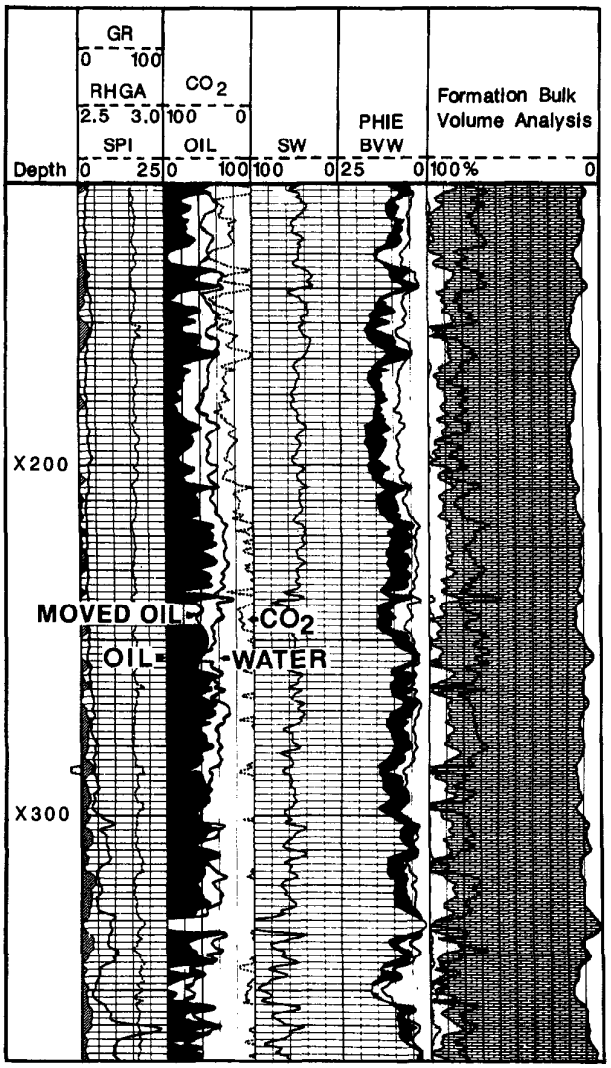

Fig. 3-56—FLOOD monitor log on well in Fig. 3-52 showing the 3-phase solution

Monitoring a Producing Well

The base FLOOD log (from a producing well) shown in Fig. 3-57 is the result of normalizing TDT porosity to density-neutron logs run in open hole. Water saturation was not calibrated to openhole data because of an incomplete logging program. The high formation water salinity, however, provides high confidence in the cased hole saturations. The Wolfcamp lime formation is virtually clay free, despite the appearance of the gamma ray log.

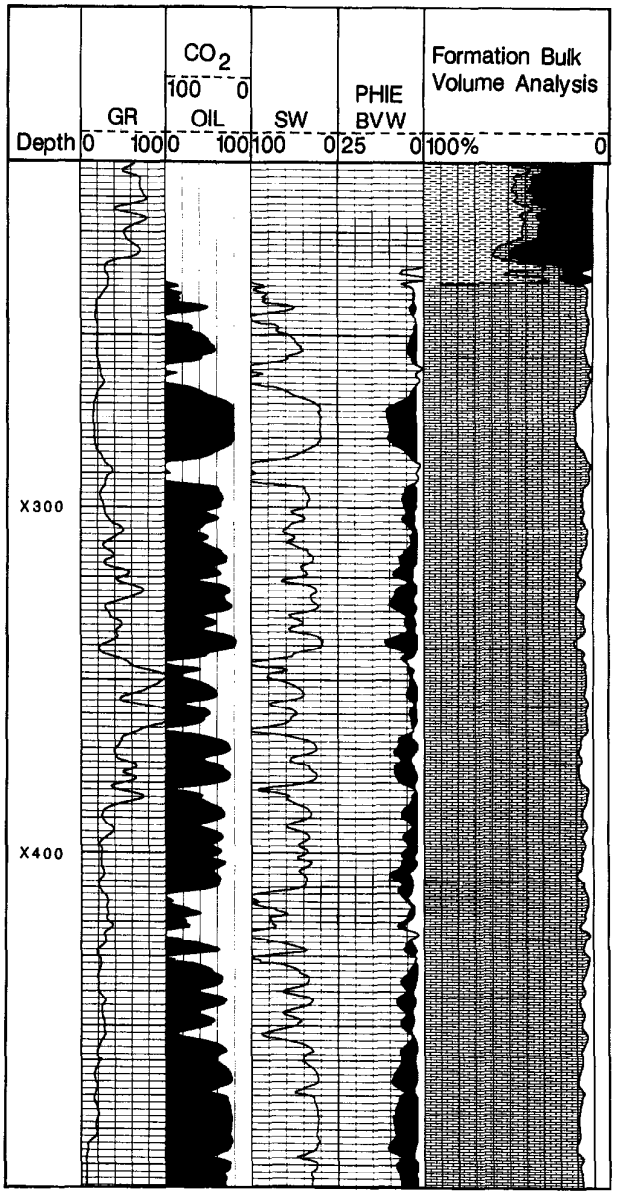

Fig. 3-57—FLOOD base log in a producing well

Figure 3-58 is the FLOOD monitor log showing the CO_2 breakthrough. This is a rare vertical flood started in 1980 to sweep oil ahead of a forming gas cap that is now at 9285 ft. CO_2 reached the perforations in this well years before the reservoir model predicted, possibly due to vertical permeability anomalies such as fractures. Once a breakthrough has been detected by the monitor log, the actual fluid entry can be determined with production logs.

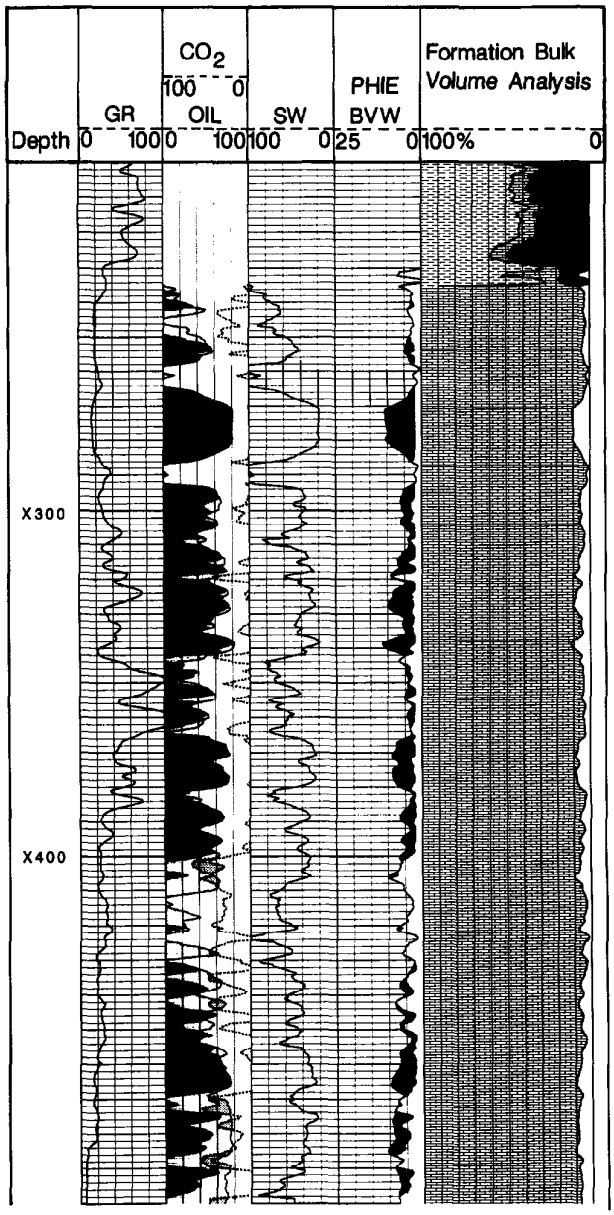

Fig. 3-58—FLOOD monitor log showing CO_2 breakthrough

REFERENCES

Alger, R.P., Locke, S., Nagel, W.A., and Sherman, H.: "The Dual Spacing Neutron Log," paper SPE 3565 presented at the 1971 SPE Annual Technical Conference and Exhibition.

American Petroleum Institute, "Recommended Practice for Standard Calibration and Form for Neutron Logs," API RP33 (Sept., 1959).

Armistead, F.C.: "Radioactivity Bore Hole Fluid Logging," United States Patent No. 3,164,720, 1965.

Blanchard, A. and Dewan, J.T.: "Calibration of Gamma Ray Logs," *Pet. Eng.* (Aug., 1953).

Baldwin, J.L., Quirein, J.A., and Serra, O.: "Theory and Practical Application of Natural Gamma Ray Spectroscopy," *Trans.*, 1980 SPWLA Annual Logging Symposium.

Culver, R.B., Hopkinson, E.C., and Youmans, A.H.: "Carbon/Oxygen (C/O) Logging Instrumentation," *SPEJ* (Oct., 1974) 463-470.

Davis, R.R., Hall, J.E., Flaum, C., and Boutemy, Y.L.: "A Dual Porosity CNL Logging System," paper 10296 presented at the 1981 SPE Annual Technical Conference and Exhibition.

Dewan, J.T., Johnstone, C.W., Jacobson, L.A., Wall, W.B., and Alger, R.P.: "Thermal Neutron Decay Time Logging Using Dual Detection," *The Log Analyst* (Sept.-Oct., 1973) **XIV**, No. 5, 13-26.

Dual-Burst TDT Logging*, Schlumberger Educational Services, Houston (1988).

Edmundson, H. and Raymer, L.L.: "Radioactive Logging Parameters for Common Minerals," *The Log Analyst* (Sept.-Oct., 1979).

Felder, R.D. and Hoyer, W.A.: "The Use of Well Logs to Monitor a Surfactant Flood Pilot Test," paper SPE 11147 presented at the 1982 SPE Annual Technical Conference and Exhibition, New Orleans.

Flaum, C. and Pirie, G.: "Determination of Lithology from Induced Gamma-Ray Spectroscopy," *Trans.*, 1981 SPWLA Annual Logging Symposium, paper H, 1.

Gaymard, R. and Poupon, A.: "Response of Neutron and Formation Density Logs in Hydrocarbon-Bearing Formations," *The Log Analyst* (Sept.-Oct., 1968).

Gilchrist, W.A., Jr., Quirein, J.A., Boutemy, Y.L., and Tabanou, J.R.: "Application of Gamma-Ray Spectroscopy of Formation Evaluation," presented at the 1982 SPWLA Annual Logging Symposium, Corpus Christi.

Gilchrist, W.A., Jr., Rogers, L.T., and Watson, J.T.: "Carbon/Oxygen Interpretation — A Theoretical Model," *Trans.*, 1983 SPWLA Annual Logging Symposium, Calgary.

Gilchrist, W.A., Jr., Galford, J.E., Flaum, C., and Soran, P.D.: "Improved Environmental Corrections for Compensated Neutron Logs," paper SPE 15540 presented at the SPE 1986 Annual Technical Conference and Exhibition.

Grau, J.A. and Schweitzer, J.S.: "Elemental Analysis of Oil Wells Using NaI (Tl) and 14-MeV Neutrons," *Trans.*, American Nuclear Society (1982) **43**, 260.

Grau, J.A., Roscoe, B.A., and Tabanou, J.R.: "A Borehole Correction Model for Capture Gamma-Ray Spectroscopy Logging Tools," paper SPE 14462 presented at the SPE 1985 Annual Technical Conference and Exhibition.

Hall, J.E., Johnstone, C.W., Baldwin, J.L., and Jacobson, L.A.: "A New Thermal Neutron Decay Logging System—TDT-M," paper SPE 9462 presented at the 1980 SPE Annual Technical Conference and Exhibition.

Hertzog, R.C.: "Laboratory and Field Evaluation of an Inelastic-Neutron-Scattering and Capture Gamma-Ray Spectroscopy Tool," paper SPE 7430 presented at the 1978 SPE Annual Technical Conference and Exhibition, Houston, TX.

Hertzog, R. and Plasek, R.: "Neutron-Excited Gamma-Ray Spectrometry for Well Logging," *Trans.* on Nuclear Science, IEEE (1979) NS-26.

Hicks, W.G.: "Lateral Velocity Variations Near Boreholes," *Geophysics* (July, 1959) **XXIV**, No. 3.

Hicks, W.G. and Berry, J.E.: "Application of Continuous Velocity Logs to Determination of Fluid Saturation of Reservoir Rocks," *Geophysics* (July, 1956) **21**, No. 3.

Kokesh, F.P. and Blizard, R.B.: "Geometric Factors in Sonic Logging," *Geophysics* (Feb., 1959) **24**, No. 1.

Kokesh, F.P., Schwartz, R.J., Wall, W.B., and Morris, R.L.: "A New Approach to Sonic Logging and Other Acoustic Measurements," *JPT* (March, 1965) **17**, No. 3.

Lawson, B.L., Cook, C.F., and Owen, J.D.: "A Theoretical and Laboratory Evaluation of Carbon Logging: Laboratory Evaluation," *SPEJ* (June, 1971) 129-137.

Leslie, H.D. and Mons, F.: "Sonic Waveform Analysis: Applications," *Trans.*, 1982 SPWLA Annual Logging Symposium, paper GG.

Lock, G.A. and Hoyer, W.A.: "Carbon-Oxygen (C/O) Log: Use and Interpretation," *JPT* (Sept., 1974) 1044-1054.

Locke, S. and Smith, R.: "Computed Departure Curves for the Thermal Decay Time Log," CWLS 5th Formation Evaluation Symposium, Calgary (May, 1975); *Trans.*, SPWLA Sixteenth Annual Logging Symposium, New Orleans (June, 1975).

Log Interpretation Charts, Schlumberger, Houston (1988).

Morris, C.F., Little, T.M., and Letton, W.: "A New Sonic Array Tool for Full Waveform Logging," paper SPE 13285 presented at the 1984 SPE Annual Technical Conference and Exhibition.

Nelligan, W.B. and Antkiw, S.: "Accurate Thermal-Neutron Decay Time Measurements Using the Far Detector of the Dual-Spacing TDT—A Laboratory Study," *SPEJ* (Feb., 1979) 59-66.

Olesen, J.R., Mahdavi, M., Steinman, D.K., and Yver, J.P.: "Dual-Burst Thermal Decay Time Logging Overview and Examples," paper 15716 presented at the 1987 SPE Annual Technical Conference and Exhibition.

Pickett, G.R.: "Acoustic Character Logs and Their Applications in Formation Evaluations," *JPT* (June, 1963) **15**, No. 6.

Polyachenko, A.L., Gavrina, T.E., Tseitlin, V.G., and Shaposhnikova, T.A.: "Analysis of Amplitude, Time and Space Characteristics of Gamma Quanta Distribution in Pulsed Neutron Gamma Logging," *Yadern. Geofiz, Tr. Vses. Goekhim.* (1969) **7**, 40-56 (translated by Associated Technical Services, Inc.).

Preeg, W.E. and Scott, H.D.: "Computing Thermal Neutron Decay Time Environmental Effects Using Monte Carlo Techniques," SPE Formation Evaluation 35-42 presented at 56th Annual Technical Conference and Exhibition, San Antonio.

Raymer, L.L., Hunt, E.R., and Gardner, J.S.: "An Improved Sonic Transit Time-to-Porosity Transform," *Trans.*, 1980 SPWLA Annual Logging Symposium, paper P.

Robinson, J.D.: "Neutron Decay Time in the Subsurface: Theory, Experiment, and an Application to Residual Oil Determination," paper SPE 5119 presented at the SPE Annual Meeting, Houston (Oct., 1974).

Schultz, W.E. and Smith, H.D.: "Laboratory and Field Evaluation of a Carbon/Oxygen (C/O) Well Logging System," *JPT* (Oct., 1974) 1103-1110.

Schweitzer, J.S., Manente, R.A., and Hertzog, R.C.: "Gamma-Ray Spectroscopy Tool Environmental Effects," paper SPE 11144 presented at the 1982 SPE Annual Technical Conference and Exhibition, New Orleans.

Scott, H.D., Flaum, C., and Sherman, H.: "Dual Porosity CNL Count Rate Processing," paper SPE 11146 presented at the 1982 SPE Annual Technical Conference and Exhibition.

Segesman, F. and Liu, O.: "The Excavation Effect," *Trans.*, 1971 SPWLA Annual Logging Symposium.

Sherman, H. and Locke, S.: "Effect of Porosity on Depth of Investigation of Neutron and Density Sondes," paper SPE 5510 presented at the 1975 SPE Annual Technical Conference and Exhibition.

Smith, H.D. and Schultz, W.E.: "Field Experience in Determining Oil Saturations from Continuous C/O and Ca/Si Logs Independent of Salinity and Shaliness," *The Log Analyst* (Nov.-Dec., 1974) 9-18.

Steinman, D.K., et al.: "Dual-Burst Thermal Decay Time Logging—Principles," paper SPE 15437 presented at the 1986 SPE Annual Technical Conference and Exhibition.

Tittman, J.: "Radiation Logging," *Fundamentals of Logging*, Univ. of Kansas (1956).

Tixier, M.P., Alger, R.P., and Doh, C.A.: "Sonic Logging," *JPT* (May, 1959) **11**, No. 5.

Wahl, J.S., Nelligan, W.B., Frentrop, A.H., Johnstone, C.W., and Schwartz, R.J.: "The Thermal Neutron Decay Time Log," *SPEJ* (Dec., 1970) 365-379.

Westaway, P., Hertzog, R., and Plasek, R.E.: "The Gamma Spectrometer Tool Inelastic and Capture Gamma-Ray Spectroscopy for Reservoir Analysis," paper SPE 9461 presented at the 1980 SPE Annual Technical Conference and Exhibition, Dallas, TX.

Wyllie, M.R.J., Gregory, A.R., and Gardner, G.H.F.: "Elastic Wave Velocities in Heterogeneous and Porous Media," *Geophysics* (Jan., 1956) **21**, No. 1.

Wyllie, M.R.J., Gregory, A.R., and Gardner, G.H.F.: "An Experimental Investigation of Factors Affecting Elastic Wave Velocities in Porous Media," *Geophysics* (July, 1958) **23**, No. 3.

Youmans, A.H., Hopkinson, E.C., Bergan, R.A., and Oshry, H.L.: "Neutron Lifetime, a New Nuclear Log," *JPT* (March, 1964) 319-328.

4 Completion Evaluation

PRODUCTION LOGGING SERVICES

Production logging provides downhole measurements of fluid parameters on a zone-by-zone basis to yield information on the type of fluid movement within and near the wellbore. These measurements provide the operator with detailed information on the nature and behavior of fluids in the well during production or injection. Major applications of production logging include:

- evaluating completion efficiency
- detecting mechanical problems, breakthrough, coning
- providing guidance for workovers, enhanced recovery projects
- evaluating treatment effectiveness
- monitoring and profiling of production and injection
- detecting thief zones, channeled cement
- single layer and multiple layer well test evaluation
- determining reservoir characteristics
- identifying reservoir boundaries for field development.

A family of production logging tools, designed specifically for measuring the performance of producing and injection wells, is available. The sensors now included are:

- thermometer
- fluid density (gradiomanometer, nuclear)
- hold-up meter
- flowmeter spinners (continuous, fullbore, diverter)
- Manometer (strain gauge, quartz gauge)
- caliper
- noise (single frequency, multiple frequency)
- radioactive tracer
- gravel pack logging.

Many of these sensors can be combined into one tool and recorded simultaneously to measure fluid entries and exits, standing liquid levels, bottomhole flowing and shut-in pressures, pressure losses in the tubing, and the integrity of the gravel pack and hardware assemblies. Since the measurements are made simultaneously, their correlation is less affected by any well instability that might cause downhole conditions to vary over a period of time. The tool string also includes a casing collar locator and a gamma ray tool for correlation and depth control. Figure 4-1 shows a schematic of the sensors in a typical production logging tool string.

Production Logging Applications

A great value of production logs lies in their ability to provide determinations of the dynamic flow patterns of well

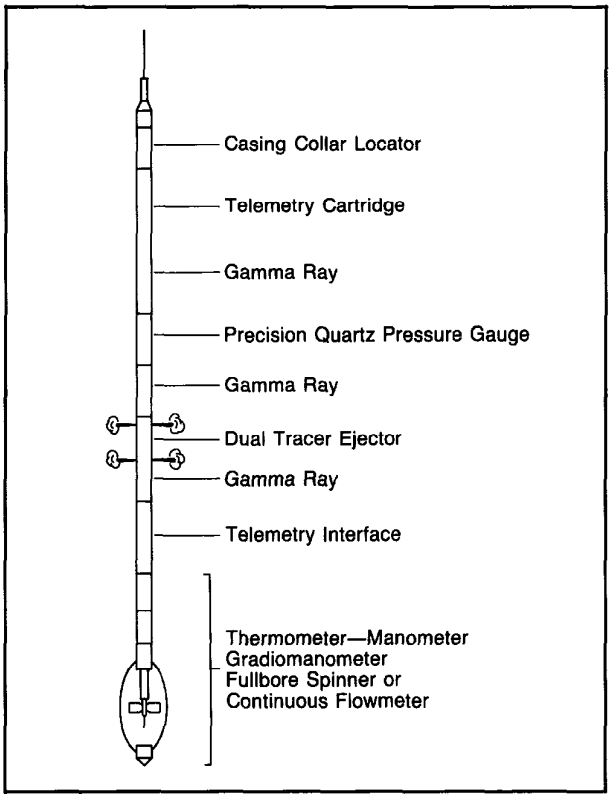

Fig. 4-1—PLT, simultaneous production logging tool

fluids under stable producing or injecting conditions. For a number of reasons production data from other sources may be misleading. Some of these reasons are:

- Surface measurements of pressures, temperatures, and flow rates are not necessarily diagnostic of what is happening in the well.
- Fluid flow outside the presumed paths, such as through cement channels in the annulus, can only be detected by production logs.
- Zone-by-zone measurements of perforating efficiency, impractical except by production logs, are often necessary to identify the actual producing or receiving intervals.
- Zone-by-zone measurements of pressure and flow rate can be used to determine the average pressure and the productivity index of each producing or injected interval.

Production logs therefore have useful application in two broad areas: evaluation of well performance with respect to the reservoir and analysis of mechanical problems.

Well Performance

In a producing well, production logs can determine which perforated zones are giving up fluids, ascertain the types and proportions of the fluids, and measure the downhole conditions of temperature and pressure, and the rates at which the fluids are flowing. If thief zones or other unwanted downhole fluid circulation exist, they can be pinpointed.

Injection wells are especially well adapted to production log analysis because the fluid is monophasic and of a known and controlled type. The objective of logging is to locate the zones taking fluid and to detect lost injection through the casing annulus.

Well Problems

In the absence of knowledge to the contrary, it is assumed that the well has hydraulic integrity, and that the fluids are going where they belong; often, this assumption is wrong. Examples include: casing leaks, tubing leaks, packer leaks, communication through the annulus due to poor cement, and thief zones. Figure 4-2 shows how these conditions can lead to misleading conclusions when well performance data come from surface measurements alone. Solutions to these and other well problems can be found by the integration and interpretation of production log data.

FLOW IN VERTICAL PIPES

Production log analysis must deal with both single- and multiphase flow systems. Single-phase flow is always found in injection wells and may also exist in clean oil- or gas-producers. However, 2-phase conditions always exist near the bottom of the well even when the surface production is

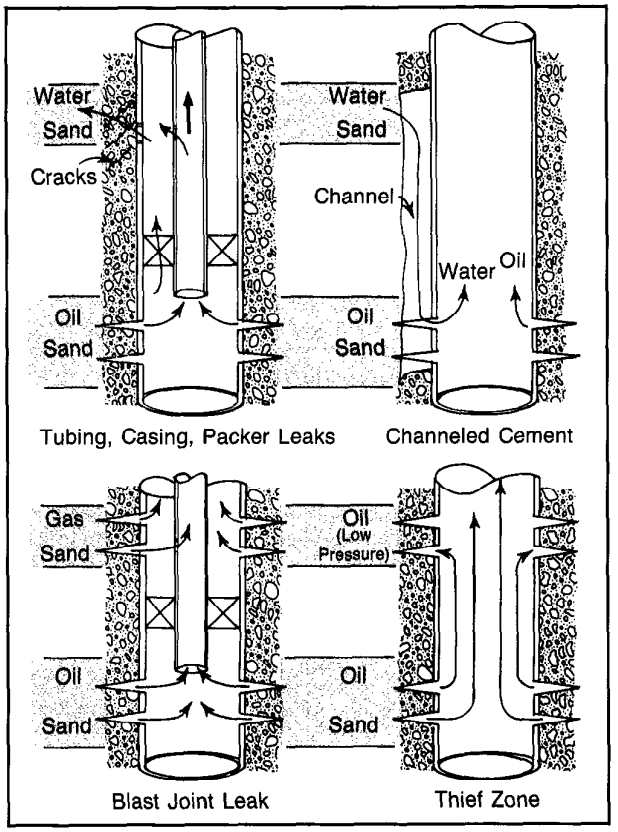

Fig. 4-2—Mechanical well problems

water free. For example, a pumping well producing hydrocarbons at a low rate with a negligible water cut will invariably be filled with water from its total depth up to the tubing shoe, except for the space occupied by the producing oil and gas which takes the form of bubbles rising through almost static water. The case of true, single-phase flow will be considered first.

Single-Phase Flow

Single-phase flow of fluids is divided into two broad classes, laminar and turbulent. The term "laminar" is applied to a streamlined flow pattern in which the fluid may be thought to be divided into infinitesimally thin concentric layers, each layer having a uniform velocity parallel to the hole axis. Adjacent layers flow past each other with slightly different velocities (Fig. 4-3, left). Turbulent flow is characterized by random, irregular, locally circular currents (vortices) throughout the fluid (Fig. 4-3, right).

In laminar flow the fluid adjacent to the surface of the pipe is stationary (assuming the fluid wets the surface) and the maximum velocity is found at the center of the pipe. The profile of velocity across the pipe cross section is parabolic.

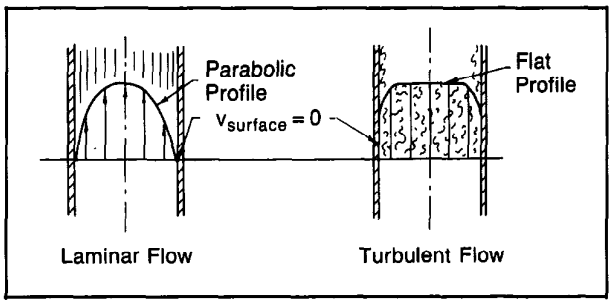

Fig. 4-3—Velocity profiles in laminar and turbulent flow

In turbulent flow the fluid adjacent to the pipe surface is again stationary, and a thin layer in laminar flow exists close to the pipe wall. However, the velocity profile is much flatter than for laminar flow.

Experiments show that the Reynolds Number, N_{Re}, may be used to determine whether the flow will be laminar or turbulent. N_{Re} is a dimensionless number defined as:

$$N_{Re} = \frac{\rho \overline{v} d}{\mu}, \qquad \text{(Eq. 4-1)}$$

where ρ is the density of the fluid, μ the viscosity, d the diameter of the pipe, and $\overline{v}$ is the average (sometimes called superficial) velocity of the fluid given by:

$$\overline{v} = \frac{4q}{\pi d^2} = \frac{q}{A}, \qquad \text{(Eq. 4-2)}$$

where q is volumetric flow rate and A is the internal cross-sectional area of the pipe.

There is a lower limit to the value of N_{Re} below which turbulence will not occur; that value is about 2000. Whether or not turbulence appears for values above 2000 depends upon the degree to which the fluid is free of disturbances, especially in an inlet region. Usually, the flow is fully turbulent for $N_{Re} \geq 4000$.

In either case, the flow rate measured by a flowmeter is most likely to be that near the center of the pipe, and consequently greater than the average flow. This discrepancy is taken into account by means of a velocity correction factor C_v, where $C_v = \overline{v}/v_{flowmeter}$. Where this factor is known from experience, a scale may be constructed to find flow rates. Usually the value will not be known, but using $C_v = 0.83$ has given satisfactory results over a wide range of conditions.

Multiphase Flow

Range of Flow Parameters

Downhole oil viscosities range from 0.2 to 10 cp, and densities from 0.6 to 1.0 gm/cc. Formation-water viscosities range from 0.2 to 1.0 cp, and densities are close to 1.0 gm/cc.

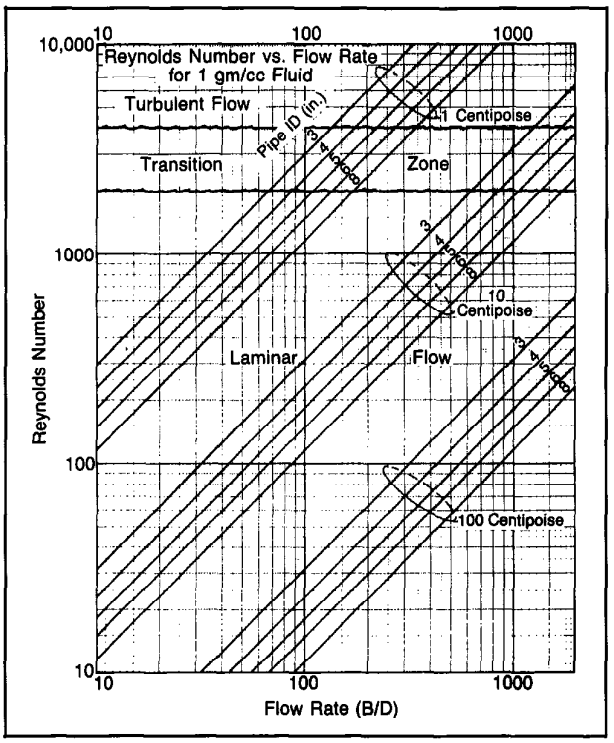

Fig. 4-4—Reynolds Number vs. flow rate for various pipe sizes and fluid viscosities

Gas densities vary from about 0.05 to 0.2 gm/cc downhole, with viscosities from 0.01 to 0.07 cp.

Figure 4-4 shows Reynolds Numbers corresponding to fluids of several viscosities flowing in various diameter pipes vs. flow rate. This figure illustrates that in oil and gas strings turbulent flow is often encountered, at least above the producing zones. On the other hand, laminar flow may be expected in shallow wells producing low-gravity crudes and in wells where water-in-oil emulsions cause the viscosity of the fluids to exceed 100 or even 1000 cp.

Flow Regimes

The geometrical configurations assumed by the gas, water, and oil phases while moving upward in the flow string are classified into several principal patterns or flow regimes.

The flow regime in which a given combination of phases will move depends on several parameters, but is determined chiefly by the relative volumetric flow rates of each phase. Figure 4-5 illustrates the major flow regimes for liquid-gas systems. For water and oil, the flow regime is influenced mainly by the relative production rates. For a liquid-gas mixture, however, the pressure gradient along the flow string becomes important. Consider the case in which the production is oil containing dissolved gas. As the oil moves up the

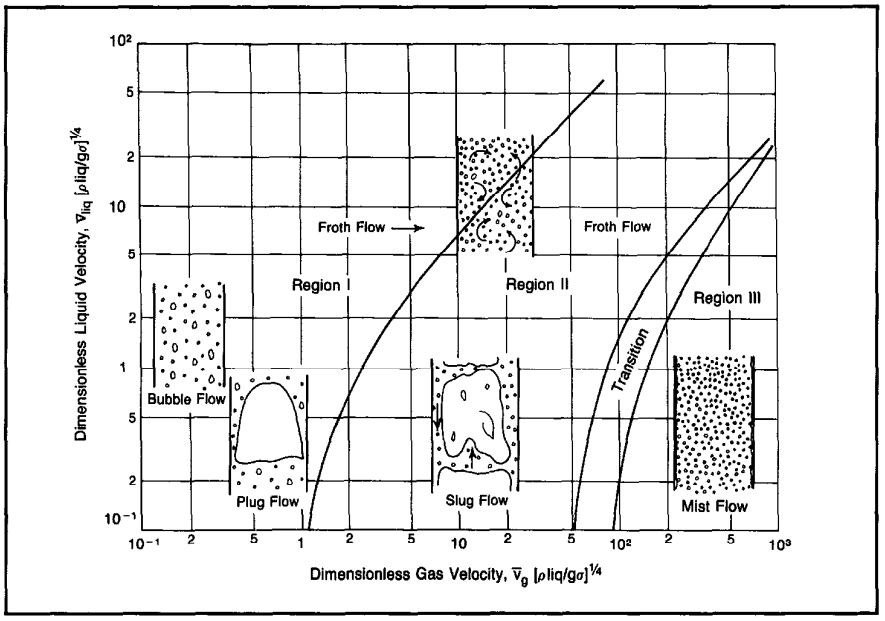

Fig. 4-5—Illustration of fluid configurations in various flow regimes

tubing, the pressure exerted by the fluid column is reduced until the bubblepoint is reached; then gas is released and 2-phase flow begins.

Initially, small bubbles of gas, approximately homogeneously distributed, move upward through the oil at a relative velocity governed by differences between the densities of the gas bubbles and the oil, and by the viscosity of the oil. This flow regime is illustrated on the left of Fig. 4-5 and is called *bubble flow*.

As the fluids rise, the pressure is further reduced. The bubbles expand and new bubbles appear. Large bubbles move upward faster than small ones and aggregate to form larger bubbles, or gas slugs, which reach pipe diameter. This regime is called *slug flow*.

Upon further reduction in pressure, the proportion of gas flow increases. The slugs tend to unite and move up the center of the column. The gas carries some oil droplets, although most of the oil flows up along the pipe walls. This is called *froth flow*.

Additional reduction in pressure will further increase the gas volume and gas flow rate. At very high gas velocities, the flow regime again changes. The oil film on the pipe wall becomes very thin and most of the oil is transported in the form of small droplets approximately homogeneously dispersed in the gas. Therefore, the two phases move at essentially the same velocity. This is called *mist flow*.

In this example, all four regimes are present in one vertical string as a result of gas expansion. However, if the gas volume were increased due to entries downhole, flow could begin with slug, froth, or even mist flow.

Water Holdup and Slip Velocity

Multiphase flow is a much more complex phenomenon than single-phase flow as is shown in Fig. 4-6. The phases move at different velocities. The light phase will move faster than the heavy phase due to the density difference between the two phases. This difference in velocities is called the *slip velocity*. Water holdup is not equal to water cut because of slip velocity. Holdup is the fractional percent by volume (void fraction) and is illustrated in Fig. 4-7.

Several models are available to relate slip velocity to measureable parameters. Schlumberger's Production Log

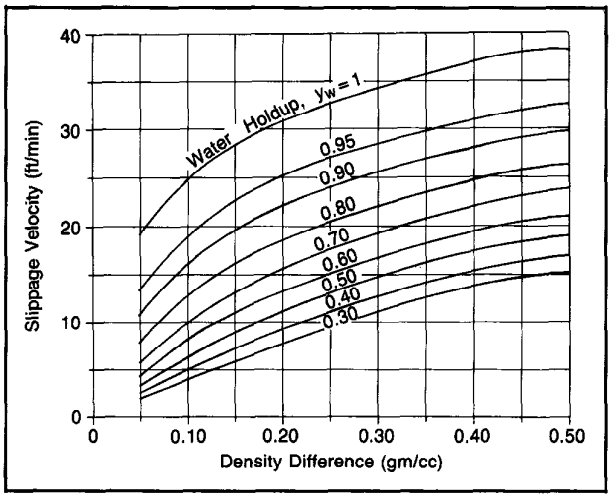

Fig. 4-6—Slippage velocity vs. density difference

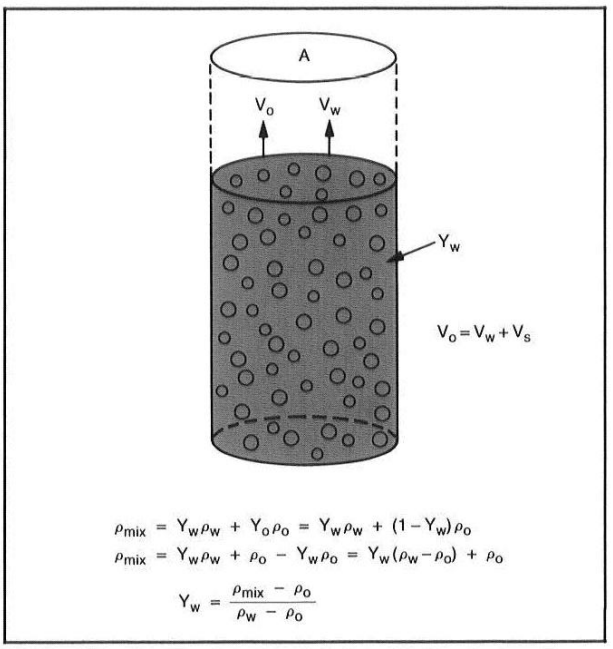

Fig. 4-7—Simplified model illustrating slip velocity

Interpretation Program performs the following pressure drop correlations that account for changes in flow regimes to match the measured pressure data:

- Aziz, Govier, Fogarasi (1972),
- Duns and Ros (1963),
- Orkiszewski (1967),
- Chierici, Ciucci, Sclocchi (1974),
- Beggs and Brill (1973),
- Griffith and Lau (1973), and
- Dukler (1985).

Although these correlations were developed to describe pressure loss in pipes, they include a slip velocity or individual phase flow rates that can be used in production log interpretation.

Deviated Wells

Most of the above pressure-drop correlations are for straight holes. In a deviated well, the fluids will segregate by gravity unless the flow velocity is high enough to ensure complete mixing. Flow loop experiments have shown that a few degrees of deviation can cause significant changes in the flow regime. For example, a flowmeter spinner in segregated flow may exhibit a response resembling downflow. The light phase moving up the high side of the pipe will drag the heavy phase with it and this heavy phase will fall out and flow down the low side of the pipe. This can occur when the heavy phase is water even if no water is being produced at the surface.

The Dukler pressure drop correlation applies to deviated holes.

Fluid Physical Properties

Fluid physical properties affecting production logging interpretation vary with changes in pressure and temperature. Reasons for determining the extent of these changes in fluid properties include:

- the calculation of downhole fluid densities for use in hold-up calculations,
- the conversion of downhole flow rates to surface flow rates and vice versa,
- the correction of sensor response for fluid effects, and
- the prediction of which fluid types will be present downhole while logging.

Meaningful analysis of production log data can only be accomplished when flow rates, viscosities, densities, etc., are converted to downhole conditions. Charts are available in the production logging interpretation books to make these calculations and the conversions are also made in computer interpretation programs. These models are fluid specific, so the use of a PVT model, when available, is recommended. PVT data obtained from fluids sampled at bottomhole conditions is preferred over the use of the conversion charts.

PRODUCTION LOGGING TOOLS AND INTERPRETATION

Flow Velocity

Flowmeter spinner tools and radioactive tracer tools are usually used to measure flow velocity. Under certain conditions, the fluid density and temperature tools can be used to estimate flow rates but their use for this purpose is much less common.

Spinner Flowmeter Tools

Spinner flowmeters all incorporate some type of impeller that is rotated by fluid moving relative to the impeller. The impeller commonly turns on a shaft with magnets that rotate inside a coil. The induced current in the coil is monitored and converted to a spinner speed in revolutions per second. This spinner speed is then converted to fluid velocity (flow rate).

Continuous Flowmeter Tool

The continuous flowmeter tool has an impeller mounted inside the tool, or in some versions, at the end of it. The most common tool diameter is $1^{11}/_{16}$ in. with the spinner being smaller. The continuous flowmeter is most often run in tubing where the fluid velocities are high and the fluids tend to be a homogeneous mixture. The spinner covers a much larger percentage of the cross-sectional flowing area than in casing and tends to average the fluid velocity profile.

Fullbore Spinner Tool (FBS)

The FBS tool is probably the most commonly run spinner tool. The tool collapses to traverse the tubing and opens inside casing for logging purposes. The large cross-sectional area of the spinner tends to correct for fluid velocity profiles and multiphase flow effects. A schematic of the FBS tool, in both the collapsed, through-tubing and opened, below-tubing, configuration is shown in Fig. 4-8.

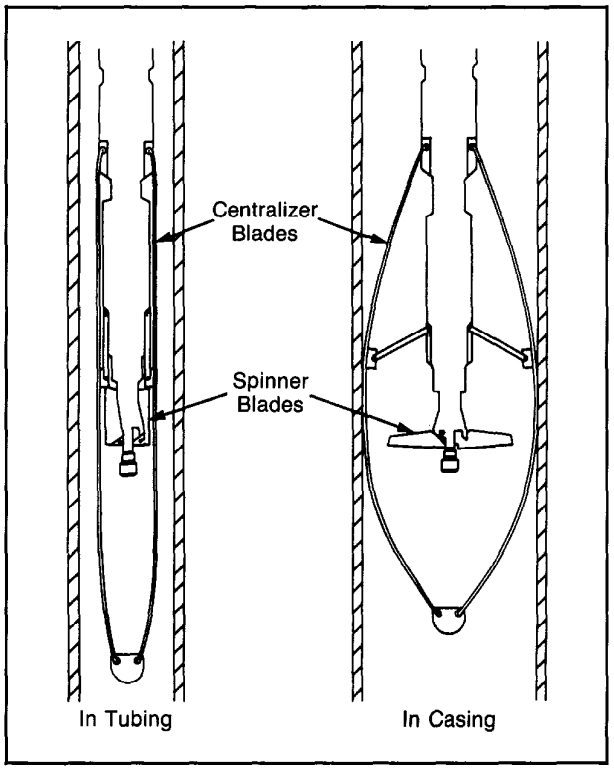

Fig. 4-8—Fullbore spinner flowmeter tool

Inflatable Diverter Tool

The inflatable diverter spinner tool utilizes a fabric diverter with an inflatable ring for use in medium and low flow rate wells. This diverter assembly fits inside a metal cage that is closed and protects the diverter while entering the well. The metal cage is opened and closed on command from the surface and, when open, helps to centralize the tool and deploy the diverter. At the same time, fluid carried with the tool is pumped into the inflatable ring, thus obtaining a seal to the casing. A schematic of the inflatable diverter tool is shown in Fig. 4-9.

Figure 4-10 shows the tool response from flow loop tests in a 2-phase liquid environment. The response is quite linear up to the highest rate tested of 2135 B/D and is quite insensitive to changes in watercut rates. A response slope of approximately 4 rps per 100 B/D is indicated. This compares with a response, for instance, of the fullbore spinner of approximately 0.22 rps per 100 B/D flow rate in a 4-in. ID pipe.

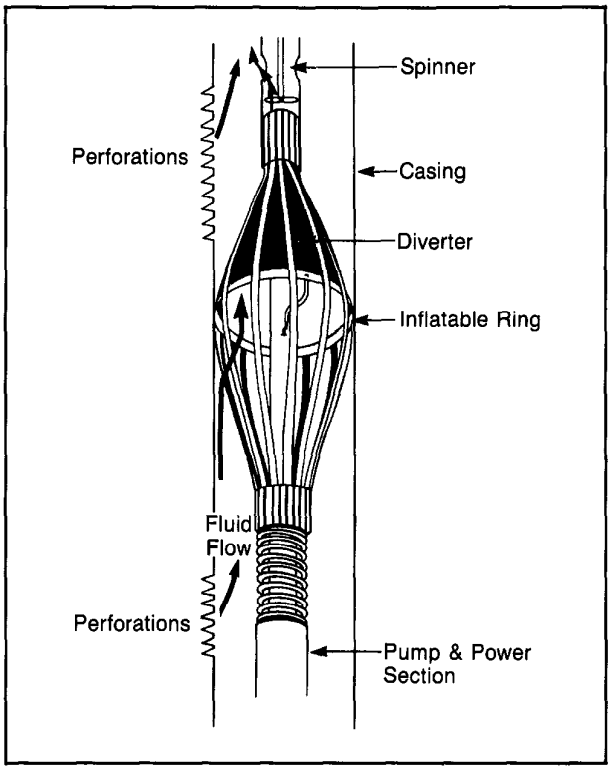

Fig. 4-9—Inflatable diverter tool

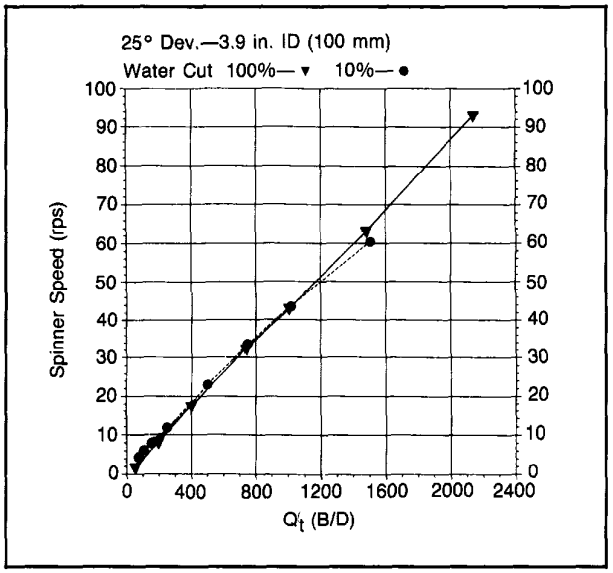

Fig. 4-10—Inflatable diverter tool flow loop response

The inflatable diverter tool has good fluid sampling characteristics since all of the fluids moving through the casing must pass through the spinner section. It is particularly appropriate for multiphase flow since the fullbore spinner measurement can be adversely affected by the downflow of the heavier phase.

The tool can be combined with other production logging sensors (Fig. 4-11) so that both a continuous flow profile and accurate station measurements can be made on the same survey. This is particularly useful for well testing in layered reservoirs.

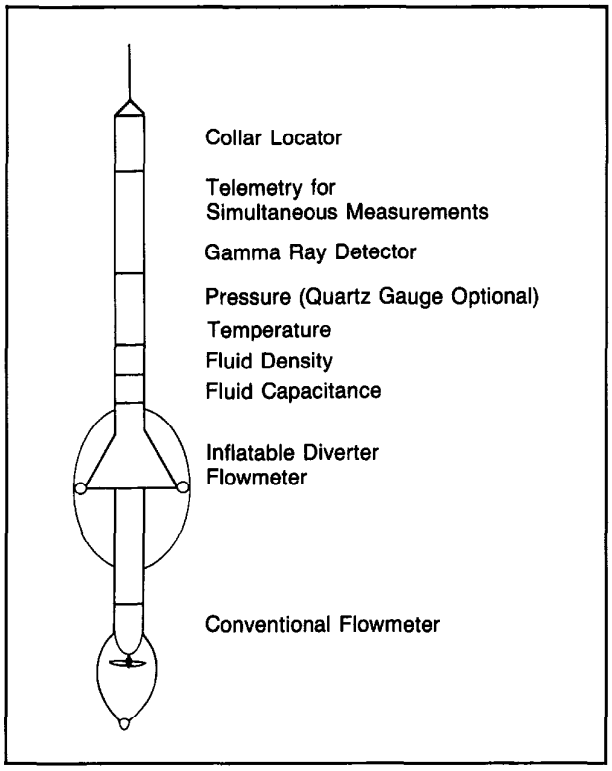

Fig. 4-11—Typical production logging tool string used for testing

Interpretation in Single-Phase Flow

Spinner revolution rate varies with fluid flow rate and the relationship is generally linear for continuous flowmeters, the fullbore spinner tool, and the fluid diverter tool. Therefore, in single-phase flow, the flow profiling interpretation technique is essentially the plotting of spinner data in revolutions per second, such that the percentage flow contribution of each zone can be read directly from the plot. This assumes the fluid density and viscosity are consistent throughout the interval and that the velocity profile does not change. An example showing percentage contributions is shown in Fig. 4-12.

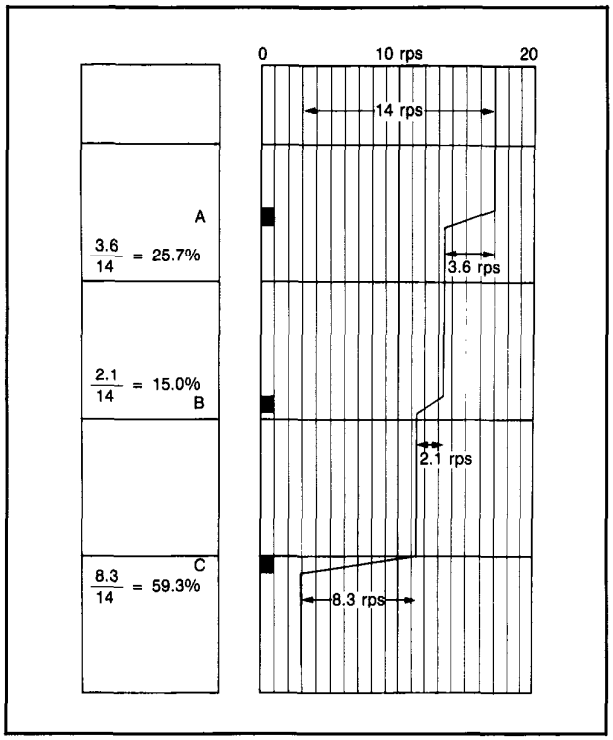

Fig. 4-12—Determining flow rates in single-phase flow

Spinner rate is a function of fluid viscosity, density, and velocity. Care must be taken if absolute flow rates, rather than percentage contributions, are desired from the flowmeter data or if percentage contributions are desired in an interval with varying viscosity or density. Under these conditions, downhole calibrations for continuous data are used for determining absolute flow rates. This is true even for single-phase flow.

A spinner flowmeter device is calibrated against the fluid flow and then with the fluid flow to define the response line of spinner vs. tool speed. Fluid velocity is then obtained from the response line.

Figure 4-13 shows ideal spinner response curve behavior, with only bearing friction and no viscosity effects, and for the real case of mechanical friction and viscosity of the fluid in a stationary fluid. The friction, density, and viscosity effects have split the single ideal spinner response line into two curves offset from each other. The frequency response of the spinner could be given by the equation below, assuming that the friction around the spinner bearings has no viscous component, and that the viscous friction only slows the fluid moving along the blade face.

$$f = av - \frac{b}{\rho v} - c\sqrt{\frac{\mu}{\rho v}}, \qquad \text{(Eq. 4-3)}$$

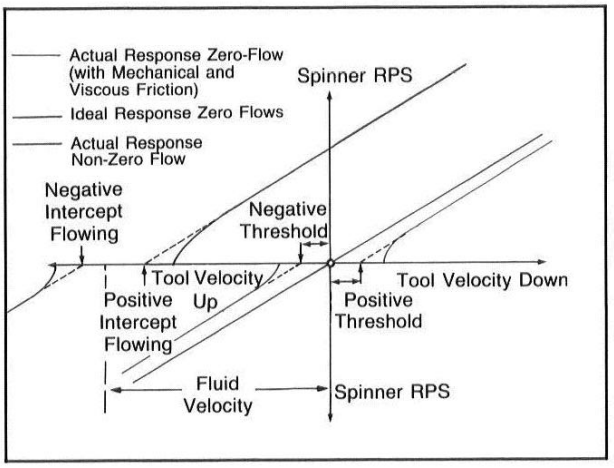

Fig. 4-13—Theoretical response of a spinner flowmeter in monophasic fluid

where:

f = spinner frequency in revolutions per second

v = velocity of the fluid over the spinner blade along the axis of rotation of the blade, i.e., $v = v_t + v_f$

a = constant depending on blade pitch

b = constant depending on the ratio of bearing friction to blade moment of inertia

c = constant depending on the skin friction due to fluids moving along the blade surface

ρ = fluid density

μ = fluid viscosity

v_t = tool velocity (positive direction is downwards)

v_f = fluid velocity (positive direction is upwards in producing wells and downward in injecting wells).

As shown in Fig. 4-13, the extrapolation of the two straight-line portions of higher spinner rotational velocity back to the tool velocity axis determines the positive and negative intercepts. The intercept of the ideal response line should lie between these two and corresponds to the measured velocity, v_m, determined from real intercepts and thresholds. The slope is essentially the constant a and is due to the blade pitch.

Since the viscosity of the fluid creates a velocity profile across the diameter of the pipe (Fig. 4-3), the velocity measured by the spinner should be corrected to give the average velocity.

Figure 4-14 shows a merged flowmeter log with five up passes and four down passes in a water injection well. Six zones of constant spinner response, labeled 0 to 5, were chosen for the interpretation. Spinner response crossplots of both positive and negative spinner rotation vs. tool velocity were made for each of the zones (Fig. 4-15).

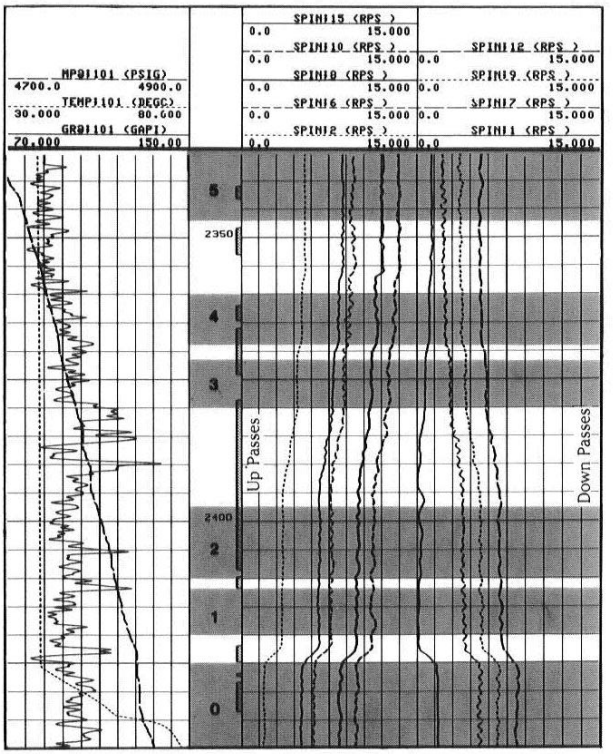

Fig. 4-14—Merged production log passes in an injection well

Figure 4-16 shows the data listing and zone-by-zone flow rate results and Fig. 4-17 shows the CSU wellsite interpretation log. The interpretation results show that the 3 m of perforations between zone 0 and 1 accept 50% of the total injection. Almost all of the remaining water is going into the top of the long perforated interval between zones 2 and 3. The other sensors support the interpretation results. Similar CSU interpretations can be made in 2-phase flow conditions.

2-Pass Technique

The *2-pass technique* can be used to calculate the percent contribution of each zone in varying viscosity conditions, whether from multiphase flow or single-phase flow with multiple viscosities. This technique consists of running several continuous flowmeter passes against the flow direction and with the flow direction. The cable speed must be faster than the fluid velocity on the passes with the fluid flow direction. Two passes, one with and one against the flow, are selected and then normalized to coincide in a region of no-flow (i.e., below all perforations). The amount of separation measured in log divisions between the two passes after normalizing is linearly proportional to fluid velocity. One hundred percent flow is at the point of maximum deflection, which is usually above all perforations. Thief zones complicate the interpretation somewhat, but the principle remains the same.

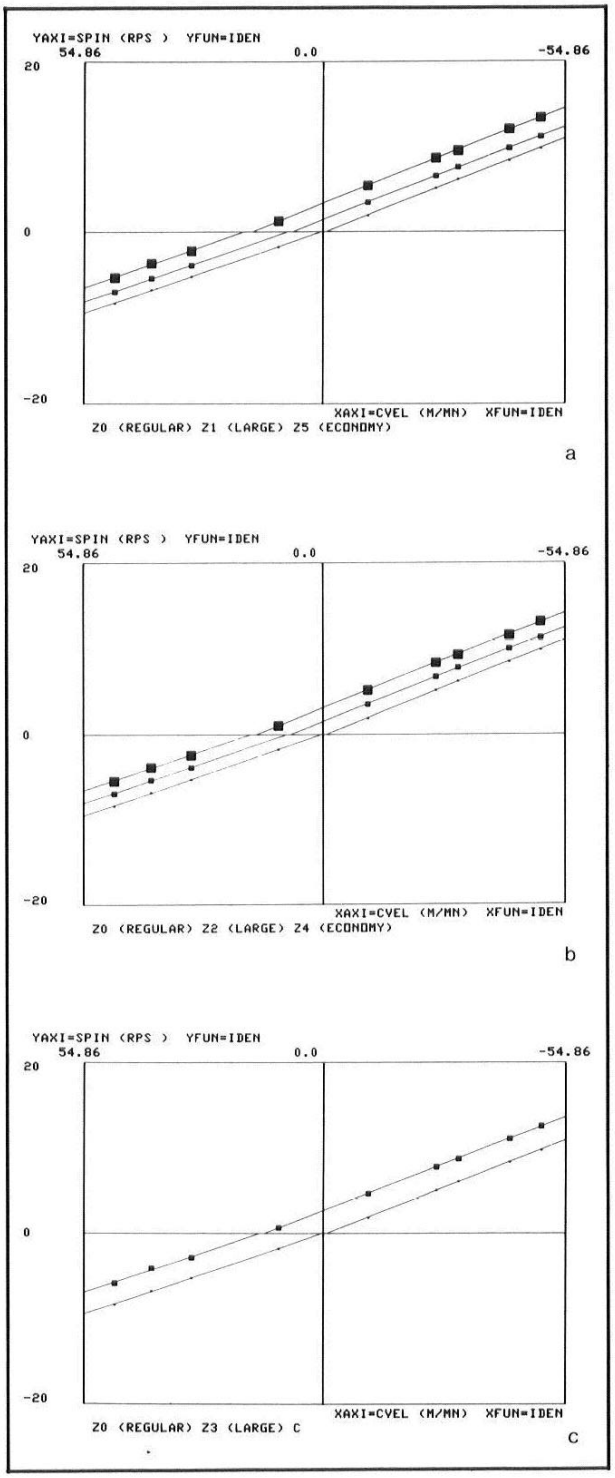

Fig. 4-15—Spinner calibration crossplots

DPL SUMM :

DPL	FILE	CVEL	Z0	Z1	Z2	Z3	Z4	Z5
BZON	0	0.0	2435.00	2419.00	2410.00	2378.00	2366.00	2345.00
TZON	0	0.0	2427.00	2412.00	2400.00	2373.00	2361.00	2335.00
0SPI	1	10.3293	-1.7329	-.08762	-.29530	.682899	1.04657	1.25068
1SPI	7	30.4213	-5.2036	-3.8985	-3.8179	-2.7886	-2.3846	-2.1866
2SPI	9	39.6117	-6.7324	-5.4003	-5.2905	-4.0502	-3.7985	-3.6392
3SPI	12	48.0437	-8.3302	-6.9724	-6.8538	-5.8335	-5.3930	-5.3328
4SPI	2	-10.362	1.87269	3.41894	3.49838	4.74751	5.13757	5.42146
5SPI	8	-42.514	8.39814	9.82338	9.94436	11.1259	11.5534	12.0689
6SPI	10	-49.512	9.81686	11.1931	11.2503	12.5871	13.1071	13.4489
7SPI	15	-25.936	5.10795	6.56242	6.67007	7.85086	8.31250	8.68762
8SPI	6	-30.990	6.16331	7.62067	7.73179	8.78457	9.24537	9.55162
9SPI	0	0.0	0.0	0.0	0.0	0.0	0.0	0.0
GRHD	0	0.0	0.0	0.0	0.0	0.0	0.0	0.0
CSID	0	0.0	4.89200	4.89200	4.89200	4.89200	4.89200	4.67000
PBZD	0	0.0	2440.00	2420.22	2411.22	2379.22	2367.22	2346.22
PTZD	0	0.0	2425.78	2410.78	2398.78	2371.78	2359.78	2335.00

FILE 1 07-JAN-85 15:30
DATA ACQUIRED 00- -00 00:00

QPL SUMM :

QPL	QT	VT	PSLD	PINT	PCC	NSLD	NINT	NCC
Z0	-.00006	-.00000	-.20235	-.86860	-.99987	-.17385	.466176	-.99980
Z1	111.781	6.40147	-.19837	7.07115	-.99989	-.17426	8.23556	-.99927
Z2	116.886	6.69383	-.19822	7.58250	-.99977	-.17209	8.44167	-.99911
Z3	205.379	11.7616	-.19840	13.6240	-.99995	-.17225	14.8364	-.99239
Z4	231.297	13.2458	-.20061	15.3806	-.99991	-.17046	16.7221	-.99822
Z5	228.417	14.3542	-.20417	16.3338	-.99990	-.17822	18.4887	-.99761
Z6	0.0	0.0	0.0	0.0	0.0	0.0	0.0	0.0
Z7	0.0	0.0	0.0	0.0	0.0	0.0	0.0	0.0
Z8	0.0	0.0	0.0	0.0	0.0	0.0	0.0	0.0
Z9	0.0	0.0	0.0	0.0	0.0	0.0	0.0	0.0

Fig. 4-16—Flow rate results listing

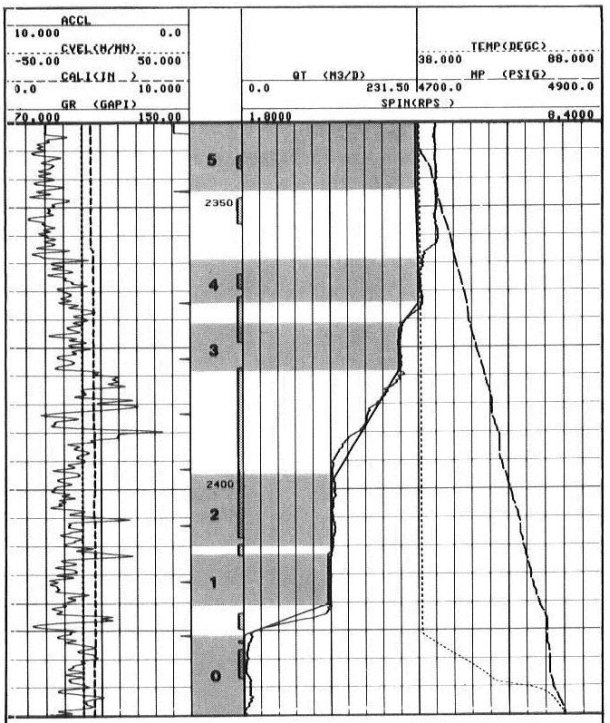

PARAMETERS

NAME	VALUE	UNIT	NAME	VALUE	UNIT
TIRA	.500000		VPCF	.815000	
LPD	0.0		HPD	1.00000	
PTHR	-.868600	M/MN	NTHR	.466176	M/MN
TD	2639.00	M	PCTS	TEMP	
SHT	20.0000	DEGC	BHT	95.0000	DEGC
CSIZ	5.50000	IN	SGSN	0000A-00	
BS	0.50000	IN	BHS	CASE	
PP	NORM		DD	0.0	M

TAPE NOT MADE

Fig. 4-17—CSU PL interpretation log

A distinct advantage of this technique is that it cancels the effect of viscosity changes. These changes are essentially shifts in rps readings in the same amount and direction on both passes. Thus, the separation remains independent of viscosity effects. If the centerline is defined as a line halfway between the two curves, a centerline shift to the right is a viscosity decrease; a centerline shift to the left is a viscosity increase (Fig. 4-18). If absolute fluid velocity is desired from the 2-pass technique, and if multiple calibration passes have been run, it can be computed from the following equation:

$$v_f = 0.83\left(\frac{\Delta rps}{B_u + B_d}\right), \qquad \text{(Eq. 4-4)}$$

where:

B_u = slope of the up calibration line in rps per foot per minute

B_d = slope of the down calibration line in rps per foot per minute

B_u and B_d can, and often will, be slightly different numerically.

Although the foregoing comments focus on fluid viscosity changes, the effects/assumptions regarding fluid density changes are similar but opposite in effect. Fluid velocity can be converted to flow rates in barrels per day with production log chart 6-10 (see Table 4-1).

Radioactive Tracer Tools

Tracer tools can be placed into the following two categories:

- gamma ray tools without downhole ejectors for releasing radioactive material, and
- gamma ray tools with downhole ejectors and multiple gamma ray detectors.

Tools in the first category are standard gamma ray tools that are used for flow profiling with the controlled-time technique. They are also often used for channel detection and treatment evaluation by comparing logging runs made before and after injecting fluids containing radioactive materials into the well. The difference in the two runs will identify where radioactive material is present.

Tracer tools in the second category have multiple gamma ray detectors combined with an ejector. The ejector consists of a chamber that will hold a small amount of radioactive material and a pump that will eject a controlled amount upon command. The detectors monitor the movement of the injected tracer material. The standard tool configuration will consist of three detectors.

If logging an injector well, the tool string will usually consist of one gamma ray detector above the injector and two detectors spaced below. When logging a producing well the configuration will be reversed with one detector below and two detectors spaced above the ejector. The single detector

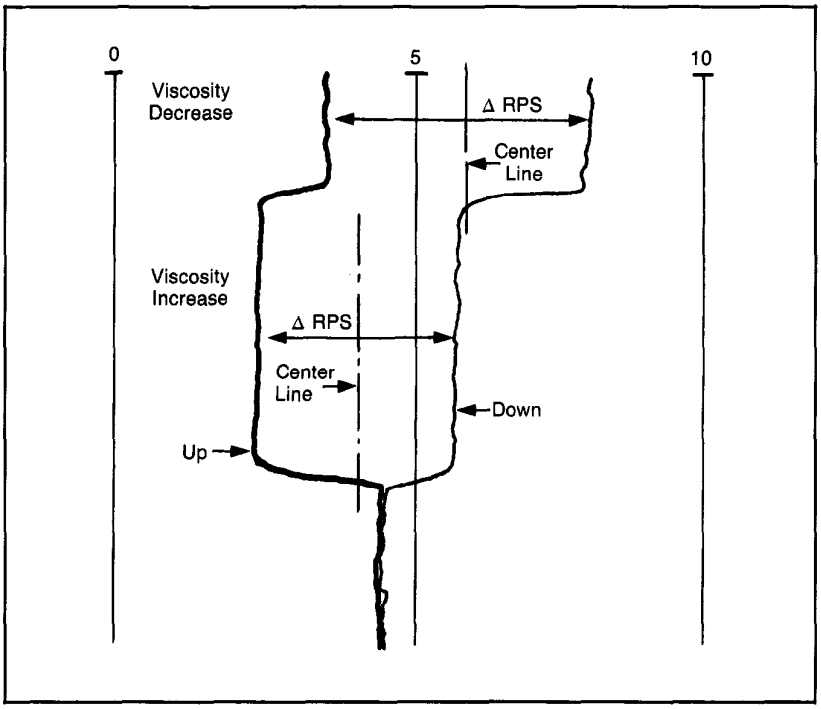

Fig. 4-18—2-pass interpretation technique

Description				Fluid velocity for flow rate of:											
Nom OD	Wt	Int diameter		1,000 B/D			10 cu m/hr			100 cu m/D			1,000 cu ft/D		
in. (mm)	lb/ft	in	mm	m/min	cm/sec	ft/min	m/min	cm/sec	ft/min	m/min	cm/sec	ft/min	m/min	cm/sec	ft/min
4½" (114.3)	9.50	4.090	103.9	13.08	21.8	42.7	19.74	32.9	64.8	8.21	13.7	26.9	2.320	3.867	7.613
	11.60	4.000	101.6	13.44	22.4	44.7	20.40	34.0	66.9	8.49	14.1	27.8	2.426	4.043	7.958
	13.50	3.920	99.6	14.22	23.7	46.6	21.48	35.8	70.5	8.94	14.9	29.3	2.530	4.216	8.299
	15.10	3.826	97.2	15.00	25.0	48.8	22.50	37.5	73.8	9.36	15.6	30.7	2.651	4.419	8.698
5" (127.0)	11.50	4.560	115.8	10.50	17.5	34.4	15.84	26.4	52.0	6.59	11.0	21.6	1.866	3.110	6.123
	13.00	4.494	114.2	10.80	18.0	35.4	16.26	27.1	53.4	6.76	11.3	22.2	1.921	3.202	6.304
	15.00	4.408	112.0	11.28	18.8	36.8	16.98	28.3	55.7	7.06	11.8	23.2	1.997	3.329	6.553
	18.00	4.276	108.6	11.88	19.8	39.1	17.94	29.9	58.9	7.46	12.4	24.5	2.123	3.538	6.964
5½" (139.7)	13.00	5.044	128.1	8.64	14.4	28.1	12.96	21.6	42.5	5.39	8.9	17.7	1.525	2.542	5.004
	14.00	5.012	127.3	8.70	14.5	28.5	13.08	21.8	42.9	5.44	9.1	17.8	1.545	2.575	5.069
	15.50	4.950	125.7	8.94	14.9	29.2	13.44	22.4	44.1	5.59	9.3	18.3	1.584	2.640	5.196
	17.00	4.892	124.3	9.12	15.2	29.9	13.74	22.9	45.1	5.72	9.5	18.7	1.622	2.703	5.320
	20.00	4.778	121.4	9.60	16.0	31.3	14.40	24.0	47.3	5.99	9.9	19.7	1.700	2.833	5.577
	23.00	4.670	118.6	10.02	16.7	32.8	15.12	25.2	49.6	6.29	10.5	20.6	1.780	2.966	5.838
6⅝" (168.3)	17.00	6.135	155.8	5.82	9.7	19.0	8.76	14.6	28.7	3.64	6.1	11.9	1.031	1.719	3.383
	20.00	6.049	153.6	5.94	9.9	19.5	9.00	15.0	29.5	3.74	6.2	12.3	1.061	1.768	3.480
	24.00	5.921	150.5	6.24	10.4	20.4	9.42	15.7	30.9	3.92	6.5	12.8	1.107	1.845	3.632
	28.00	5.791	147.1	6.54	10.9	21.3	9.90	16.5	32.5	4.12	6.8	13.5	1.157	1.929	3.797
	32.00	5.675	144.1	6.78	11.3	22.2	10.20	17.0	33.5	4.24	7.1	13.9	1.205	2.008	3.953
7" (177.8)	17.00	6.538	166.1	5.10	8.5	16.7	7.68	12.8	25.2	3.19	5.3	10.5	.908	1.513	2.979
	20.00	6.456	164.0	5.22	8.7	17.2	7.86	13.1	25.8	3.27	5.4	10.7	.931	1.552	3.055
	23.00	6.366	161.7	5.40	9.0	17.6	8.16	13.6	26.8	3.39	5.6	11.1	.958	1.596	3.142
	26.00	6.276	159.4	5.52	9.2	18.2	8.34	13.9	27.4	3.47	5.8	11.4	.985	1.642	3.233
	29.00	6.184	157.1	5.70	9.5	18.7	8.64	14.4	28.4	3.51	6.0	11.8	1.015	1.691	3.329
	32.00	6.094	154.8	5.88	9.8	19.3	8.88	14.8	29.1	3.69	6.2	12.1	1.045	1.745	3.429
	35.00	6.004	152.5	6.06	10.1	19.8	9.12	15.2	29.9	3.79	6.3	12.4	1.077	1.794	3.532
	38.00	5.920	150.4	6.24	10.4	20.4	9.42	15.7	30.9	3.92	6.5	12.8	1.107	1.846	3.633
7⅝" (193.7)	20.00	7.125	181.0	4.32	7.2	14.1	6.48	10.8	21.3	2.69	4.4	8.86	.764	1.274	2.508
	24.00	7.052	178.4	4.44	7.4	14.5	6.54	10.9	21.5	2.72	4.5	8.94	.786	1.310	2.580
	26.40	6.969	177.0	4.50	7.5	14.7	6.78	11.3	22.2	2.82	4.7	9.23	.799	1.332	2.622
	29.70	6.875	174.6	4.62	7.7	15.1	6.96	11.6	22.8	2.90	4.8	9.48	.821	1.369	2.694
	33.70	6.765	171.8	4.80	8.0	15.6	7.20	12.0	23.6	2.99	4.9	9.81	.848	1.413	2.782
	39.00	6.625	168.3	4.92	8.2	16.3	7.44	12.4	24.4	3.09	5.2	10.2	.884	1.474	2.901
8⅝" (219.1)	24.00	8.097	205.7	3.33	5.55	10.9	5.02	8.38	16.5	2.09	3.5	6.86	.592	.9865	1.942
	28.00	8.017	203.6	3.39	5.66	11.1	5.13	8.55	16.8	2.13	3.6	6.98	.604	1.006	1.981
	32.00	7.921	201.2	3.48	5.81	11.4	5.25	8.75	17.2	2.18	3.6	7.15	.618	1.031	2.029
	36.00	7.825	198.8	3.55	5.92	11.7	5.35	8.93	17.6	2.23	3.7	7.32	.634	1.056	2.079
	40.00	7.725	196.2	3.63	6.05	12.0	5.46	9.10	17.9	2.27	3.8	7.44	.650	1.084	2.134
	44.00	7.625	193.7	3.75	6.25	12.3	5.64	9.40	18.5	2.35	3.9	7.69	.668	1.113	2.190
	49.00	7.511	190.8	3.87	6.45	12.7	5.82	9.70	19.1	2.42	4.0	7.94	.688	1.147	2.257
9⅝" (244.5)	29.30	9.063	230.2	2.66	4.44	8.70	4.00	6.68	13.1	1.66	2.77	5.45	.472	.787	1.550
	32.30	9.001	228.6	2.69	4.49	8.83	4.05	6.75	13.3	1.68	2.80	5.53	.479	.799	1.572
	36.00	8.921	226.6	2.74	4.58	8.98	4.17	6.95	13.7	1.73	2.89	5.69	.488	.813	1.600
	40.00	8.835	224.4	2.80	4.67	9.16	4.23	7.05	13.9	1.76	2.93	5.78	.497	.829	1.631
	43.50	8.755	222.4	2.85	4.75	9.33	4.29	7.15	14.1	1.78	2.97	5.86	.506	.844	1.661
	47.00	8.681	220.5	2.88	4.81	9.49	4.35	7.25	14.3	1.81	3.02	5.95	.515	.859	1.690
	53.50	8.535	216.8	3.00	5.00	9.81	4.51	7.53	14.8	1.88	3.13	6.16	.533	.888	1.748
10¾" (273.0)	32.75	10.192	258.9	2.10	3.50	6.88	3.17	5.28	10.4	1.32	2.19	4.33	.374	.623	1.226
	40.50	10.050	255.3	2.16	3.60	7.08	3.25	5.42	10.7	1.35	2.25	4.45	.384	.641	1.261
	45.50	9.950	252.7	2.20	3.68	7.22	3.33	5.55	10.9	1.39	2.31	4.53	.392	.653	1.286
	51.00	9.850	250.2	2.25	3.75	7.37	3.39	5.65	11.1	1.41	2.35	4.61	.400	.666	1.312
	55.50	9.760	247.9	2.29	3.82	7.51	3.45	5.75	11.3	1.44	2.39	4.70	.408	.679	1.337
	60.70	9.660	245.4	2.34	3.91	7.66	3.52	5.88	11.5	1.46	2.44	4.78	.416	.693	1.364
	65.70	9.560	242.8	2.40	4.00	7.82	3.60	6.00	11.8	1.50	2.49	4.91	.425	.708	1.393
11¾" (298.5)	38.00	11.150	283.2	1.76	2.94	5.75	2.64	4.41	8.66	1.10	1.83	3.60	.312	.520	1.024
	42.00	11.084	281.5	1.77	2.96	5.82	2.67	4.45	8.76	1.11	1.85	3.64	.316	.526	1.036
	47.00	11.000	279.4	1.81	3.02	5.91	2.73	4.55	8.96	1.14	1.89	3.73	.321	.534	1.052
	54.00	10.880	276.4	1.84	3.08	6.04	2.79	4.65	9.15	1.16	1.93	3.81	.328	.547	1.076
	60.00	10.772	273.6	1.88	3.14	6.16	2.83	4.73	9.29	1.18	1.97	3.86	.334	.557	1.097
13⅜" (339.7)	48.00	12.715	323.0	1.35	2.25	4.42	2.04	3.40	6.69	0.85	1.41	2.78	.240	.400	.7875
	54.50	12.615	320.4	1.37	2.29	4.49	2.07	3.46	6.79	0.86	1.44	2.82	.244	.406	.8001
	61.00	12.515	317.9	1.39	2.33	4.56	2.11	3.52	6.92	0.88	1.46	2.87	.248	.413	.8129
	68.00	12.415	315.3	1.41	2.36	4.64	2.13	3.56	6.99	0.89	1.48	2.91	.252	.420	.8261
	72.00	12.347	313.6	1.43	2.39	4.69	2.16	3.60	7.09	0.90	1.49	2.95	.255	.424	.8352
16" (406.4)	55.00	15.376	390.6	0.92	1.54	3.02	1.39	2.32	4.56	0.58	0.86	1.90	.164	.274	.5385
	65.00	15.250	387.4	0.93	1.56	3.07	1.41	2.36	4.63	0.59	0.91	1.92	.167	.278	.5475
	75.00	15.124	384.2	0.95	1.59	3.13	1.44	2.40	4.72	0.60	0.99	1.96	.170	.283	.5566
	84.00	15.010	381.3	0.97	1.62	3.17	1.46	2.44	4.79	0.61	1.02	1.99	.172	.287	.5651
20" (508.0)	94.00	19.124	485.8	0.60	1.00	1.95	0.90	1.50	2.96	0.37	0.62	1.23	.106	.177	.3481

Table 4-1—Average fluid velocity vs. casing size

is used to detect unexpected flow reversals caused by thief zones and for identifying channels behind casing, where flow is opposite of the wellbore fluids. The two adjacent gamma ray detectors are used for flow profiling by measuring the flow time between the two detectors. A typical tool string that included the tracer tool was shown in Fig. 4-1.

Radioactive tracer surveys are not routinely run in producing wells because of the complications of produced radioactive fluid and multiphase flow effects. Therefore, the main application of this technique is in injection wells.

Velocity Shot Interpretation

The recording of a velocity shot consists of ejecting a small slug of radioactive material into the flow stream and measuring the time between detection by two separate detectors. Usually, the velocity shots are recorded on time drive with the tool stationary in the well. Figure 4-19 shows a 2-detector velocity shot.

The flow rate is computed as follows:

$$q = h \times A/t \ , \qquad \text{(Eq. 4-5)}$$

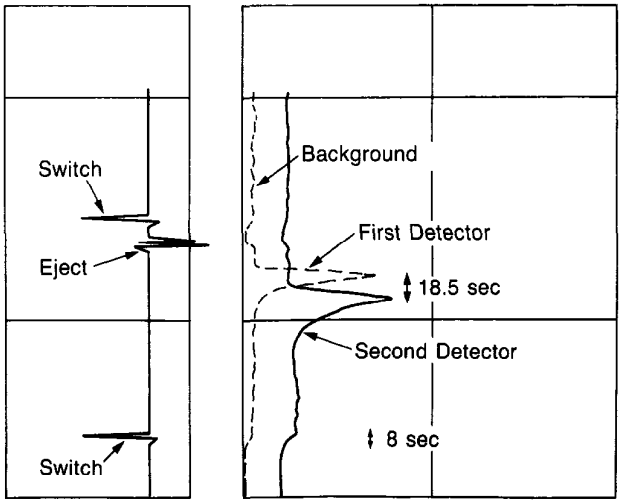

Fig. 4-19—2-detector velocity shot log

where:

h = distance between gamma ray detectors
A = cross-sectional area
t = time.

The flow rate in barrels per day can be calculated from the following equation:

$$q(B/D) = \frac{Spacing\ (in.) \times \frac{1(ft)}{12(in.)} \times \frac{\pi}{4}\ (D^2-d^2) \times \frac{1(sq\ ft)}{144(sq\ in.)} \times 256.5\left(\frac{B/D}{cu\ ft/min}\right)}{Time(sec) \times \frac{1(min)}{60(sec)}} \qquad \text{(Eq. 4-6)}$$

Simplifying,

$$q(B/D) = \frac{6.995\ (D^2-d^2)\chi}{t} \ , \qquad \text{(Eq. 4-7)}$$

where:

6.995 = numerical constant
D = casing inside diameter in inches
d = tool outside diameter in inches
χ = detector spacing in inches
t = time, in seconds, to move X-inches.

The log shown in Fig. 4-19 was run in an injection well with 5½-in., 17-lb casing (ID = 4.892) with a $1^{11}/_{16}$-in. tool, and a 99-in. detector spacing. The flow time between detectors is 18.5 sec. Using Eq. 4-7, the flow rate is 789 B/D.

As a general rule, the flowmeter gives more accurate results in high flow rates and the radioactive tracer technique provides better results in flow rates less than about 100 B/D.

Controlled Time Survey

The controlled time method qualitatively detects the flow of fluids up or down the hole, either in the casing or in the annulus. Figure 4-20 shows an example of the controlled-time Radioactive Tracer Survey. In this case radioactive material was ejected at the bottom of the tubing and successive runs were made with the gamma ray tool. The times of the injection and of each log run were carefully noted. The radioactive slug (points a, c, e, and h) may be seen to move down the casing. After entering the perforations opposite sand 3, a part of the radioactive slug (points f, j, n, and v) channels up the casing annulus to sand 4. After entering at sand 2, part of the radioactive slug (points i and p) channels down the casing annulus to sand 1. Fluid appears to be entering sand 3 because of the stationary readings at points i, m, and q. And finally, some radioactive material is trapped in a turbulence pattern just below the tubing as shown by points b, d, g, and k.

Fluid Density Tools

Downhole fluid density can be determined with the Gradiomanometer* tool, the Pressure-Temperature tool, or from nuclear fluid density tools. In a 2-phase system, knowledge of the downhole density of each phase plus the density of the mixture gives the log analyst the percent holdup of each phase occupying the casing at the point of interest.

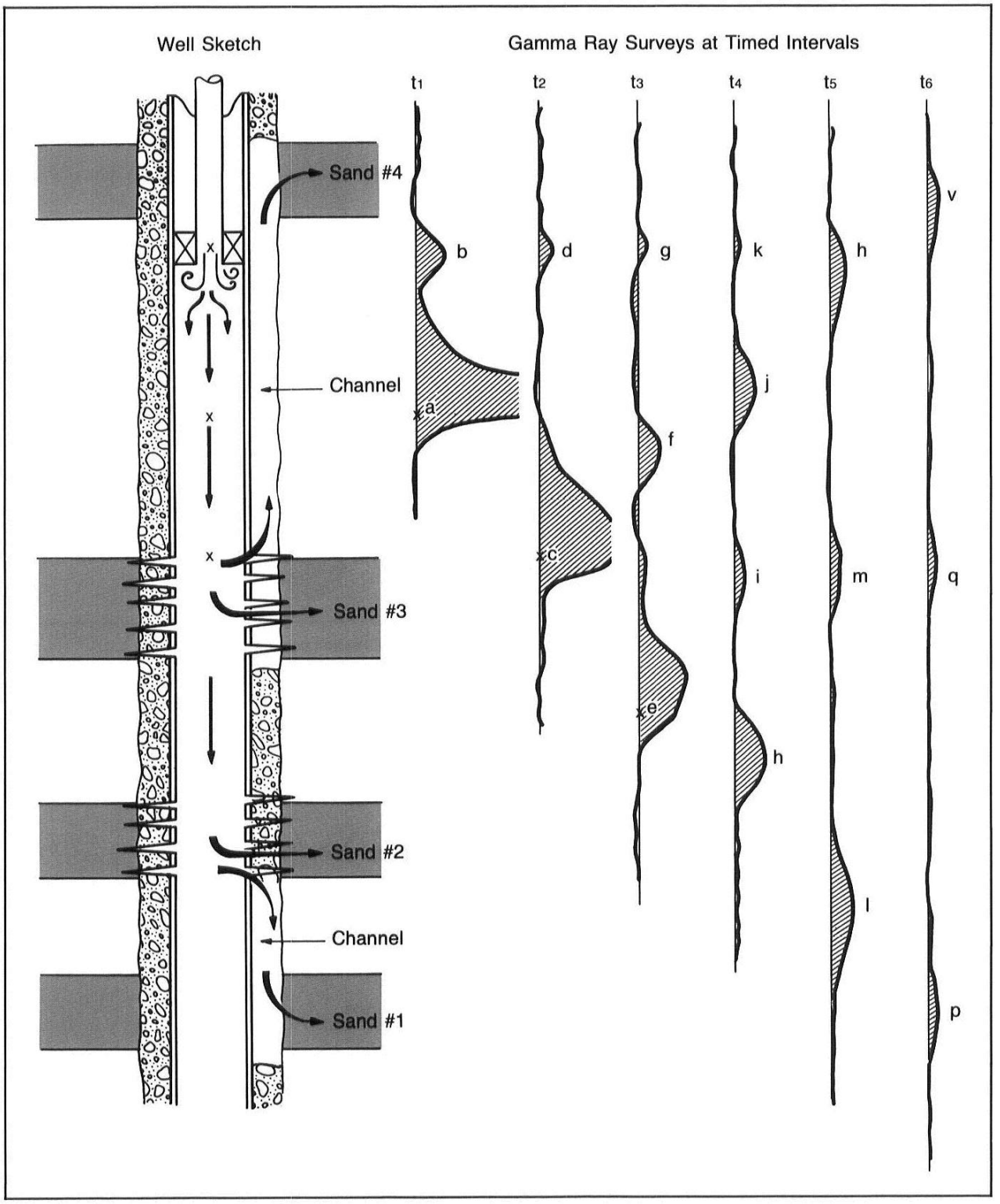

Fig. 4-20—Radioactive tracer survey: timed runs analysis

Once the holdup is determined, it can be used to find the flow rate of each phase, assuming the mixture flow rate and the slip velocity are known. Slip velocity is the difference in the velocity of the two fluids due to the difference in their downhole densities.

Slip velocity determination is one of the important problems of multiphase flow interpretation. The correlations presented earlier include their own model for slip velocity. Liquid-liquid slippage can often be satisfactorily represented by the Choquette correlation shown in Fig. 4-6. Gas-liquid modeling is more complex and often a trial-and-error method has to be used to find an appropriate correlation representing the actual flow.

Holdup, y, of the heavy phase can be determined from the following equation:

$$y_{HP} = \frac{\rho_{LOG} - \rho_{LP}}{\rho_{HP} - \rho_{LP}} , \qquad \text{(Eq. 4-8)}$$

where *HP* and *LP* mean heavy and light phase, respectively.

Gradiomanometer Tool

The Gradiomanometer tool uses the pressure differential between two bellows to infer the density of the fluid between the sensors. A schematic of the bellows tool is shown in Fig. 4-21. The bellows compress with pressure and a rod moves in proportion to the difference in compression between the two sets of bellows. A magnetic plunger on the end of the rod generates a signal proportional to the rod movement in a transducer coil. The coil output is calibrated in terms of fluid density. In deviated wells the Gradiomanometer reading must be divided by the cosine of the deviation angle to correct for the hole deviation effect.

It should be noted that the Gradiomanometer reading is not exclusively a function of fluid density; the true relationship is:

$$\rho_{Gr} = \rho_f (1.0 + K + F) , \qquad \text{(Eq. 4-9)}$$

where K is a kinetic term and F is a friction term. In cases where the flow rate is less than about 2000 B/D, the friction term is negligible. The chart in Fig. 4-22 gives estimated friction corrections over ranges where they are needed.

The kinetic term is observable when the velocity of the fluid across the upper bellows is considerably different from the velocity across the lower bellows. This results in a kick on the Gradiomanometer curve that usually occurs when the tool enters tubing and may be observed at points of fluid entry.

The flowmeter and Gradiomanometer logs shown in Fig. 4-23 were run in the well after it had been acidized. The separation between the up and down flowmeter passes indicates the zones of fluid entry into the casing. The Gradiomanometer log shows a change in fluid density as the tool is moved up the hole. The tool emerges from a column of static water into a flowing column of light gravity oil at the second set of perforations from the bottom. The curve movement through the perforations at 15,400 ft is the kinetic kick caused by the turbulence of the producing fluids at that point. The flowmeter shows this to be the major entry.

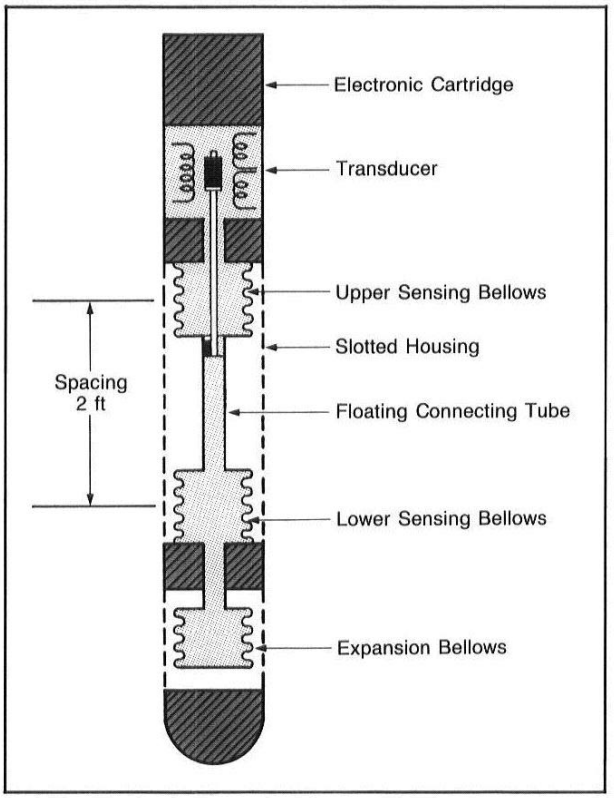

Fig. 4-21—Gradiomanometer fluid density tool

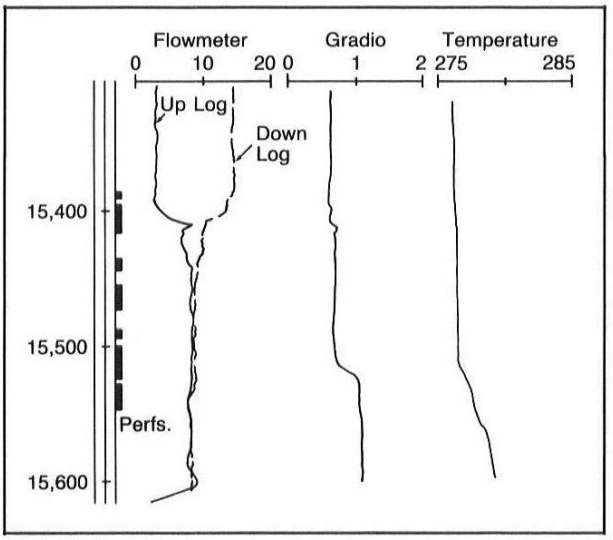

Fig. 4-23—Production logs run after well stimulation

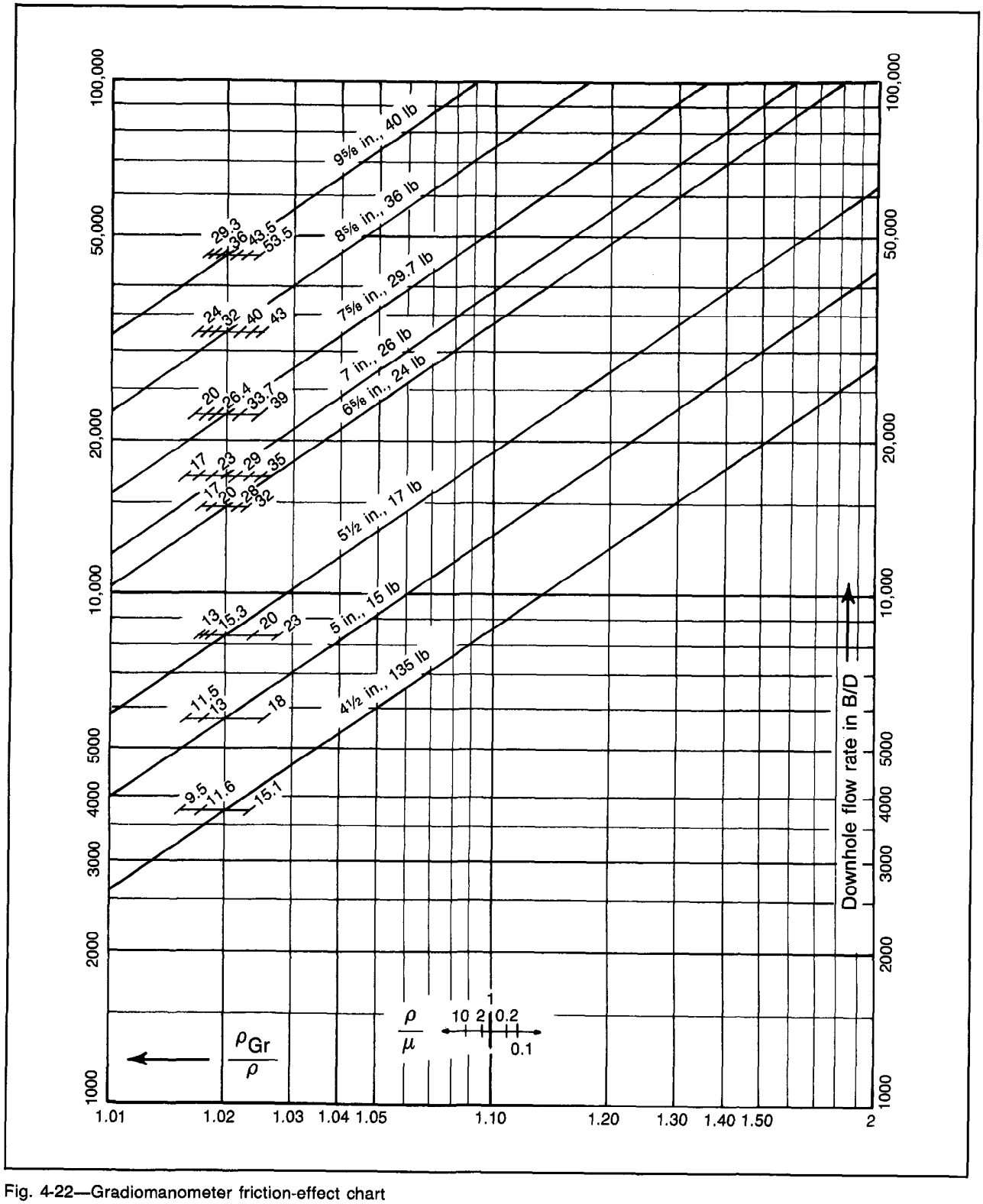

Fig. 4-22—Gradiomanometer friction-effect chart

Nuclear Fluid Density Tool

The Nuclear Fluid Density tool operates on the same principle as openhole density tools. A gamma ray source is positioned with respect to a gamma ray detector so that the wellbore fluid acts as an absorber. Figure 4-24 illustrates the measurement principle. A high count rate indicates a low fluid density and a low count rate indicates a high fluid density.

The advantage of the Nuclear Fluid Density tool over the Gradiomanometer tool is that the measurement is not affected by wellbore deviation or friction effects. However, since the tool relies on radioactive decay, the readings are subject to statistical variations. It should also be noted that the measured value is the average density of the flowing mixture. Therefore, it is subject to the same holdup effects as the Gradiomanometer measurement.

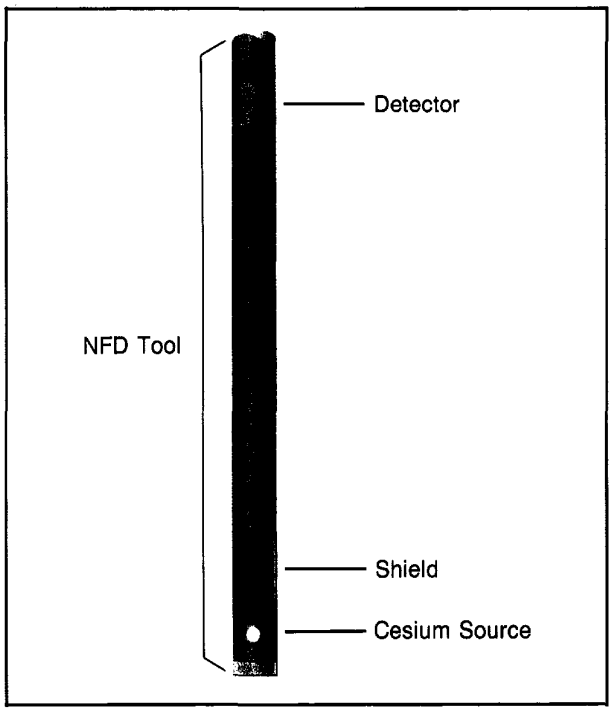

Fig. 4-24—Nuclear Fluid Density tool

Temperature Tools

The varying electrical conductivity of a thin wire that accompanies changes in ambient temperature is the basis of most temperature tool measurements. A tool schematic is shown in Fig. 4-25.

The temperature log has many applications, particularly when run in combination with other sensors. Some of these applications are:

- detection of gas production via the cooling effect of expanding gas (in or behind casing);

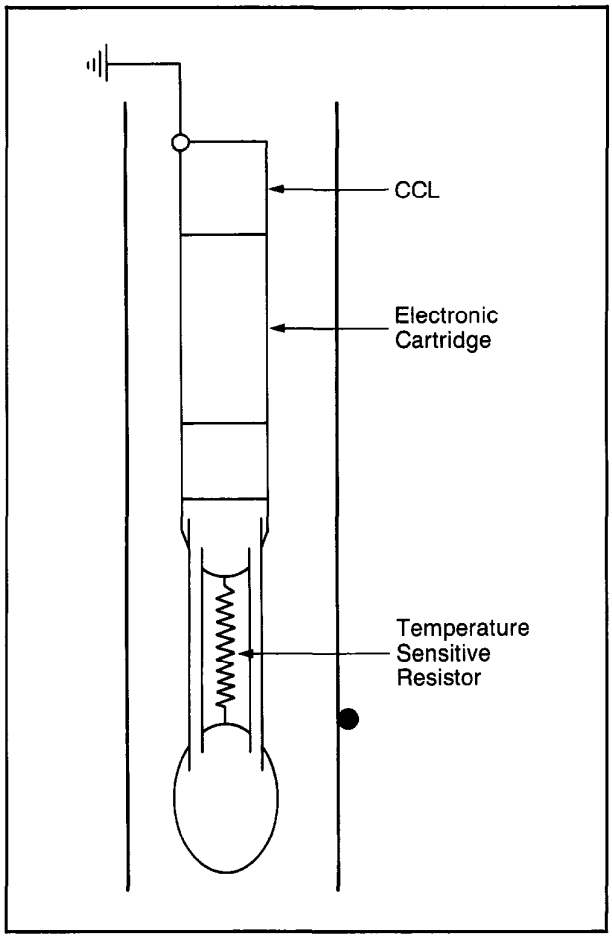

Fig. 4-25—Schematic of temperature tool

- qualitative evaluation of fluid flow as indicated by departures from the geothermal gradient;
- temperature (T) information for PVT equations and charts. Temperature information is critical to the determination of gas expansion/compression, GOR, and oil shrinkage from downhole to surface conditions and vice versa;
- evaluation of fracture treatments; and
- evaluation of the mechanical integrity of a completion.

Temperature log interpretations can also be used to determine flow rates; however, other sensors generally provide better results. The thermometer responds to temperature anomalies produced by fluid flow either within the casing or in the casing annulus, and is thus useful for detecting the latter. Figure 4-26 illustrates the temperature log response in four different situations: liquid flow, liquid flow behind casing, gas flow, and gas flow behind casing.

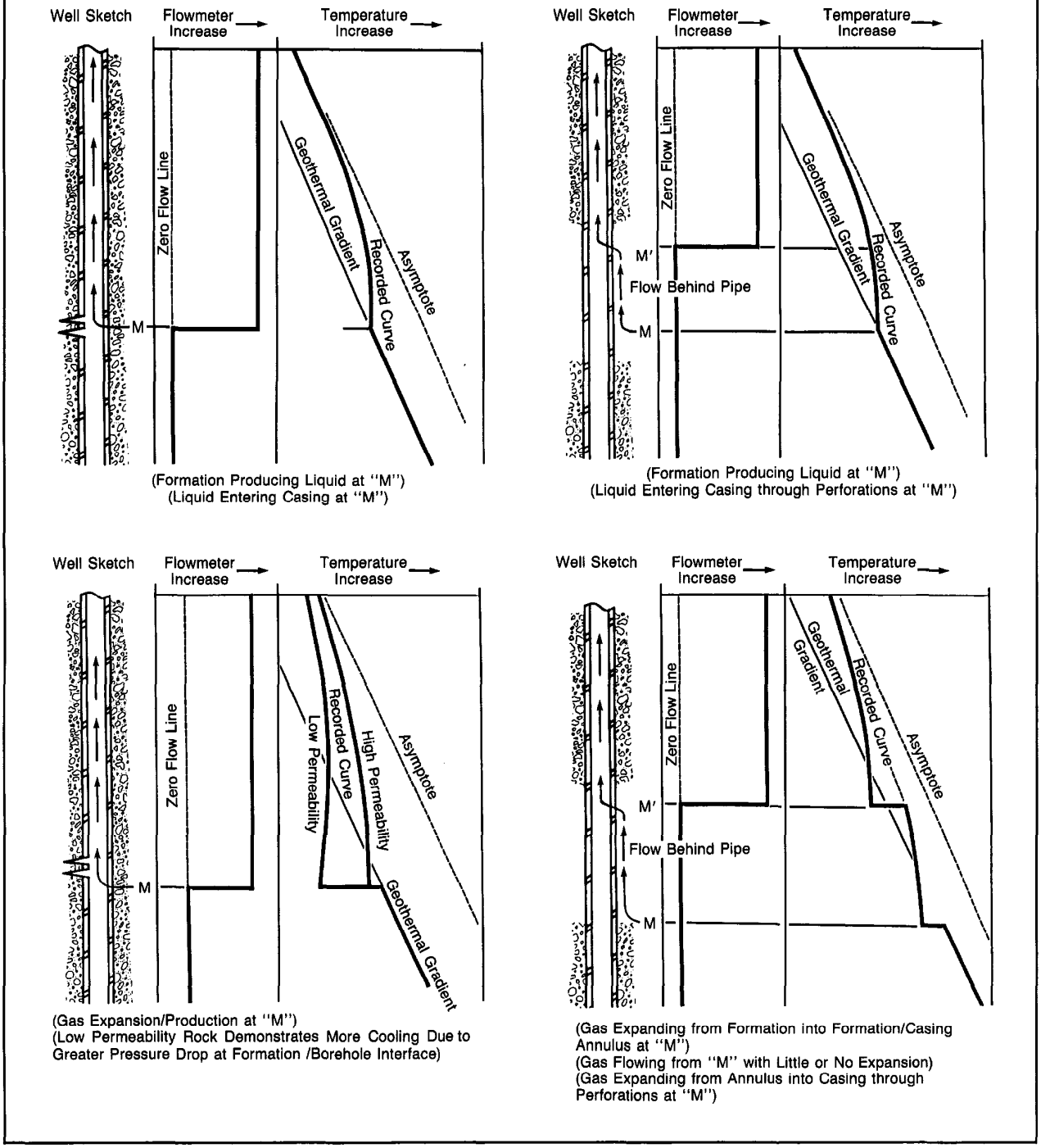

Fig. 4-26—Temperature log responses

The temperature logs shown in Fig. 4-27 were run on a well that was completed as an oil well but soon started producing with a high GOR. Pressure, Gradiomanometer, and flowmeter logs were run with the temperature log to determine if the gas breakthrough was in the completed zone or channeling down behind casing. Both shut-in and flowing passes were recorded. The flowing Gradiomanometer log indicated a drop in density at the top of the perforations and the flowmeter showed a large increase, pinpointing the gas entry into the casing. The temperature pass run with the well flowing on a 24/64-in. choke shows that the gas was channeling down from 3931 m, and possibly from as high as 3923 m as indicated by the temperature slope changes.

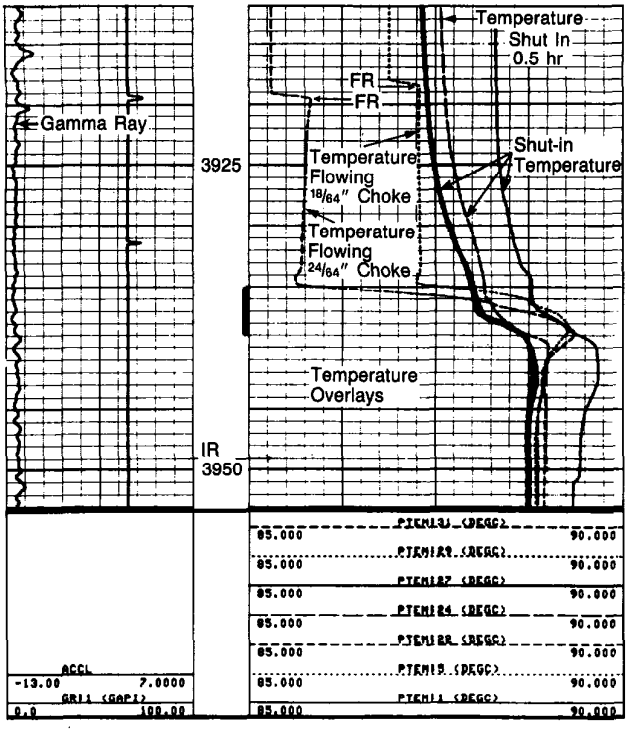

Fig. 4-27—Multiple-pass temperature log overlays

Noise Tools

There are two types of noise tools. The Audio* tool is a single frequency device that is usually run in the continuous mode. Multiple-frequency noise tools record station readings.

A schematic of a typical noise tool is shown in Fig. 4-28. The tool consists of a transducer that converts sound into an electrical signal. The signal is amplified and transmitted up the cable by the electronics cartridge. The tool does not emit any sound energy. It only responds to sound originating in or around the wellbore.

The noise in a well is a function of the acceleration, or

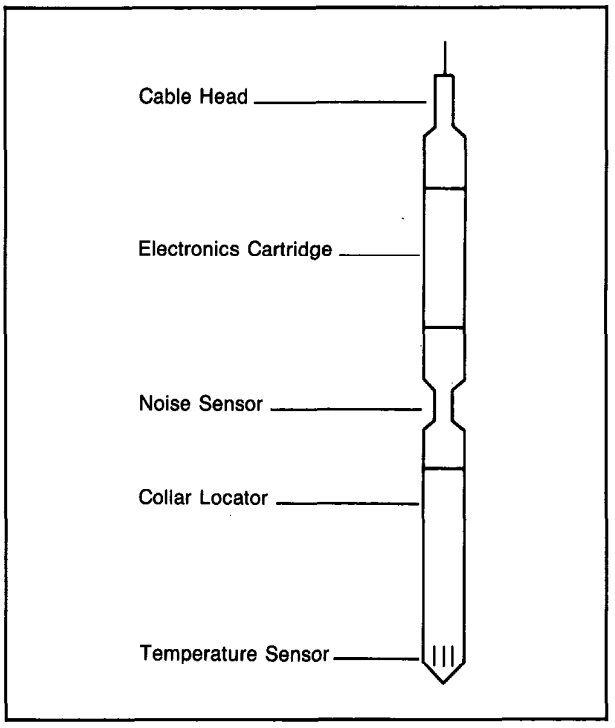

Fig. 4-28—Combination temperature and noise tools

turbulence, of a fluid moving across a pressure differential. By varying the pressure differential, flow rate, or both, various types of noise can be generated. The noises can be characterized and categorized into different groups by examining the frequency spectrum of the total signal. Information from the spectrum can be useful for determining channels behind casing, tubing or casing leaks, and producing perforations.

The noise log may be recorded in a stationary mode so that the tool will respond to wellbore noise without being affected by extraneous noises caused by cable or tool movement. A frequency separation network separates the noise signal into 200 Hz, 600 Hz, 1000 Hz, and 2000 Hz frequency cuts. At each station, a peak mV reading is recorded for each frequency cut. These values are plotted as a set of points on a logarithmic grid.

Figure 4-29 shows a noise log that depicts a gas entry through a set of perforations from 8320 to 8350 ft. Above the perforations the discontinuous phase in the wellbore is gas and the sound attenuates quite rapidly. The sound attenuates much slower in the standing water below the perforations.

The log in Fig. 4-30 illustrates the effectiveness of the noise log at identifying fluid movement behind casing. The log indicates that there is flow behind casing from a group of sands below 9900 ft into a zone at 8700 ft.

Techniques have been developed to calculate flow rates

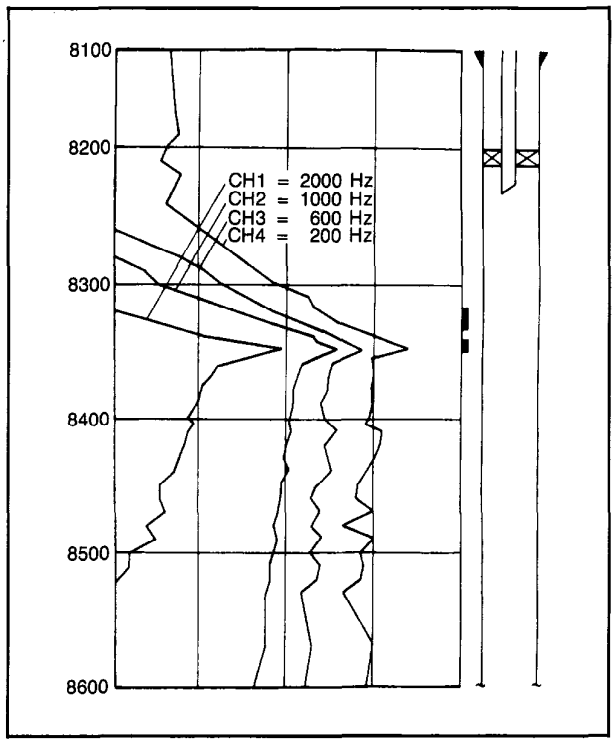

Fig. 4-29—Noise log showing gas entry

from noise logs, but factors such as distance from the noise source, perforation size and condition, tool-to-casing contact, and fluid environment create inaccuracies in the results. Generally, flow rates are best determined by other sensors.

Gravel Pack Logging

Production or injection profiles in gravel-packed wells are influenced tremendously by the distribution of the gravel in the gravel pack assemblies. To fully understand the profile, the integrity of the gravel pack must be evaluated.

The gravel pack logging tool uses a gamma ray source and a single gamma ray detector. The source emits gamma rays radially into the borehole and the surrounding area and is focused upward toward the detector. Figure 4-31 shows a schematic of the tool configuration. Some of the gamma rays are scattered back to the detector. The number of gamma rays returning to the detector is an indication of the density of the material through which they have traveled. High density materials cause more gamma rays to be slowed down and absorbed, and low density materials allow more gamma rays to be detected.

In a gravel-packed well, everything remains constant except the annular space between the casing and the screen or tubing. This space can be totally filled with gravel, partially

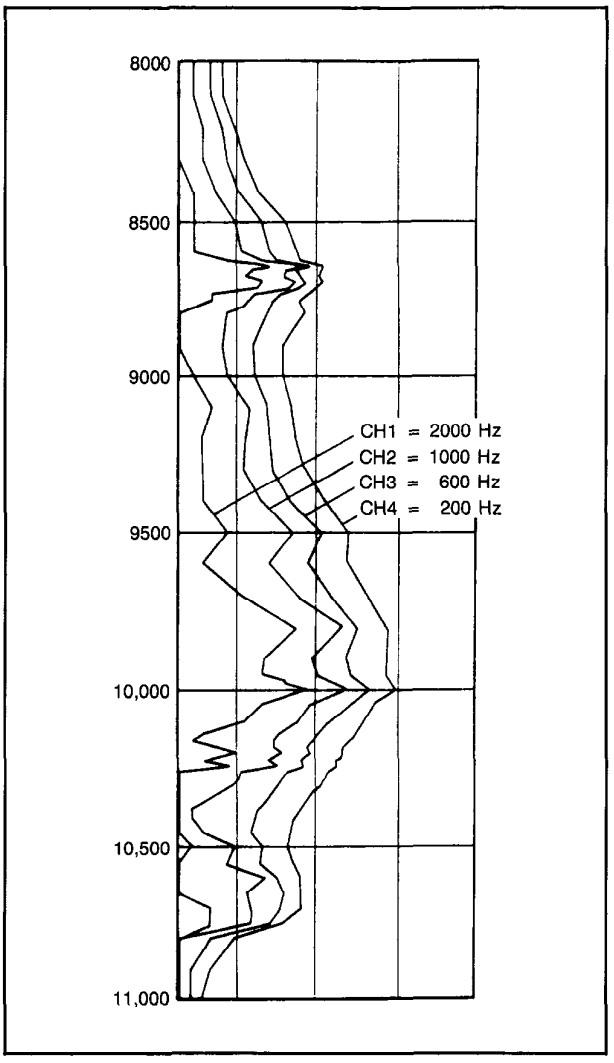

Fig. 4-30—Noise log indicating flow through a channel behind casing

filled with gravel, or have void spaces containing no gravel. In each of these cases, the volume that is not filled with gravel is filled with some type of fluid with known density. Since the density of the gravel is different from the density of the fluid, it is possible to correlate gamma ray count rates to percentage of pack.

A program based on laboratory studies and test well results, and available with the CSU unit, makes these correlations. The results are presented in a gravel pack log as illustrated in Fig. 4-32. This log was run after the well was initially gravel packed and it shows a void from 9800 to 9854 ft. The well was placed on production with no attempt to repair the void. Three undesirable situations could have occurred.

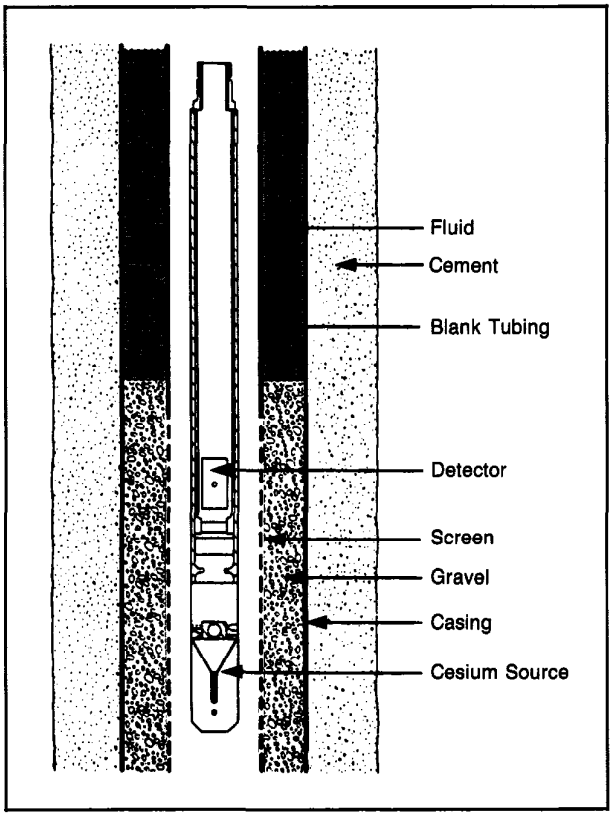

Fig. 4-31—Gravel pack logging tool configuration

- If the void interval produces, the screen could be damaged by sand production and fail.
- The gravel above the void could fall and fill the void section, uncovering the upper portion of the screen.
- Production could move the 2-darcy formation sand into the void, severely reducing the 50-darcy permeability of the gravel pack and, therefore, restricting flow capacity.

The production from the well was not as expected, so production logs were run to determine the problem. Figure 4-33 shows a comparison of the gravel pack log run before production with a log run with the flowmeter and Gradiomanometer sensors. The void section no longer exists but the top of the gravel is at the same depth as it was before production. The flowmeter shows that the well is producing from above the previously void zone and the Gradiomanometer indicates the fluid effect; hence the void section was filled with formation sand.

Gravel Pack Repair

A wireline impulse device (WID) can now be combined with the gravel pack logging tool to repair voids in the gravel pack on one trip in the well. The WID tool contains swab cups

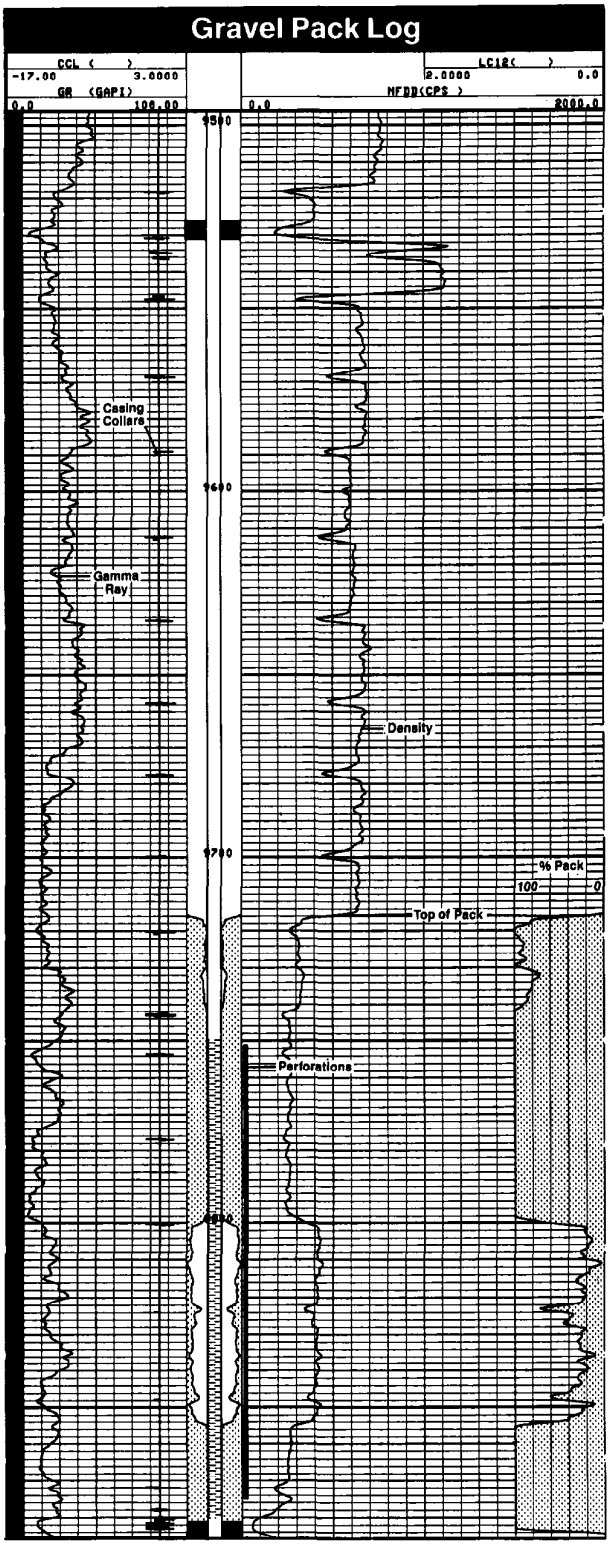

Fig. 4-32—CSU gravel pack log

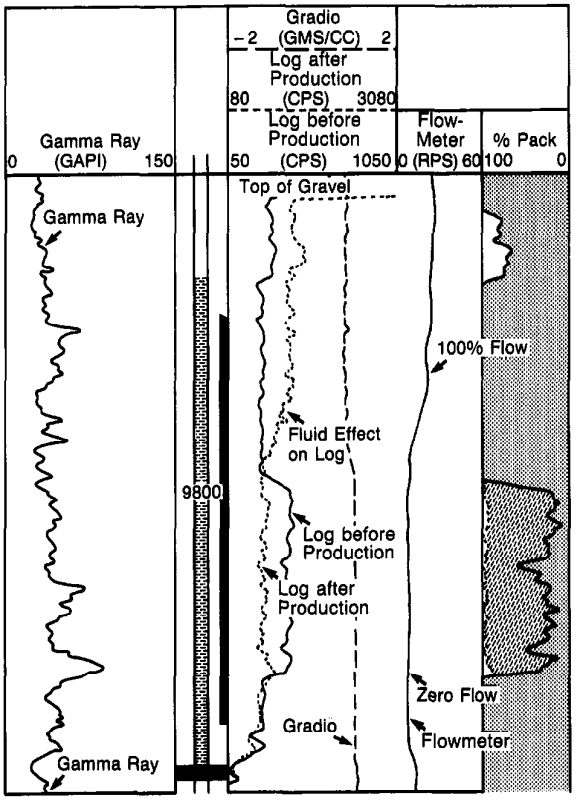

Fig. 4-33—Comparison of gravel pack logs before and after production

to create a turbulence in the wellbore fluid to collapse the gravel bridge and fill the void. Figure 4-34 shows logs before and after repair with the WID tool. In each log, the left track shows percentage of pack as a function of depth; the right track shows gamma ray counts of the gravel pack logging tool; and the middle is a schematic of the tubing, screen, and gravel pack. The initial log (a) shows a large void in the bottom half of the well and smaller voids in the middle. After the first repair attempt (b), gravel from the middle has fallen to the bottom and closed part of the void there. More gravel is pumped into the well (c), closing most of the large voids.

Production Logging Wellsite Quicklook Interpretation Program

Interpretation of production logs using a diphasic model may be made with CSU software at the wellsite. Successive passes of both up and down logs are stored in real time in the computer memory; data present in memory can be viewed at any time in a merged presentation. If for some reason (such as well instability) additional passes are necessary, more data can be acquired and added to memory. An example of merged flowmeter data is shown in Fig. 4-35. Other log examples were shown previously in Figs. 4-14 and 4-27.

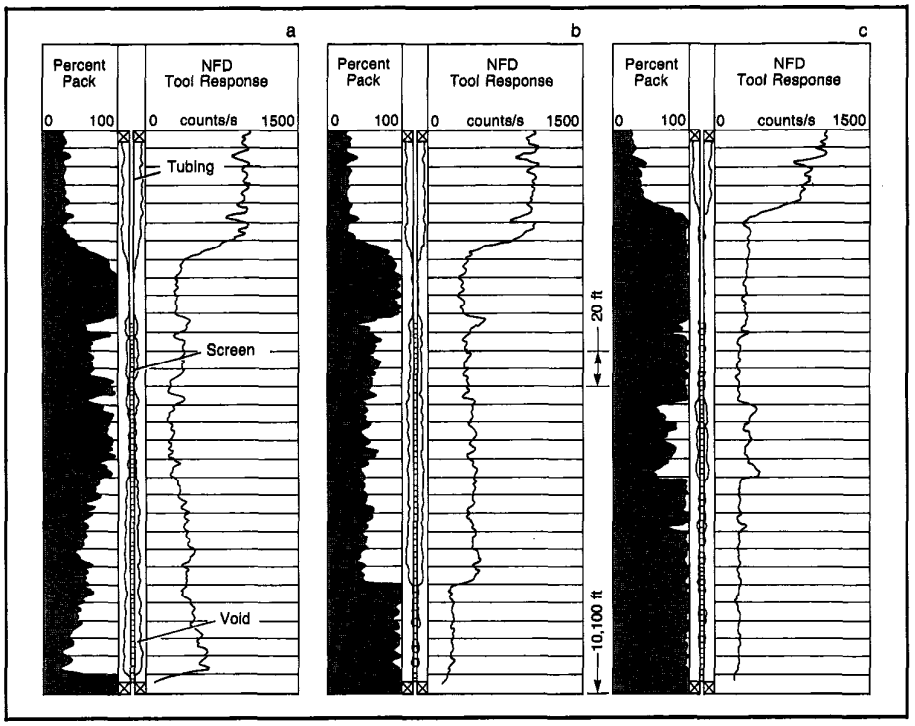

Fig. 4-34—Logs before and after WID repair of a gravel pack

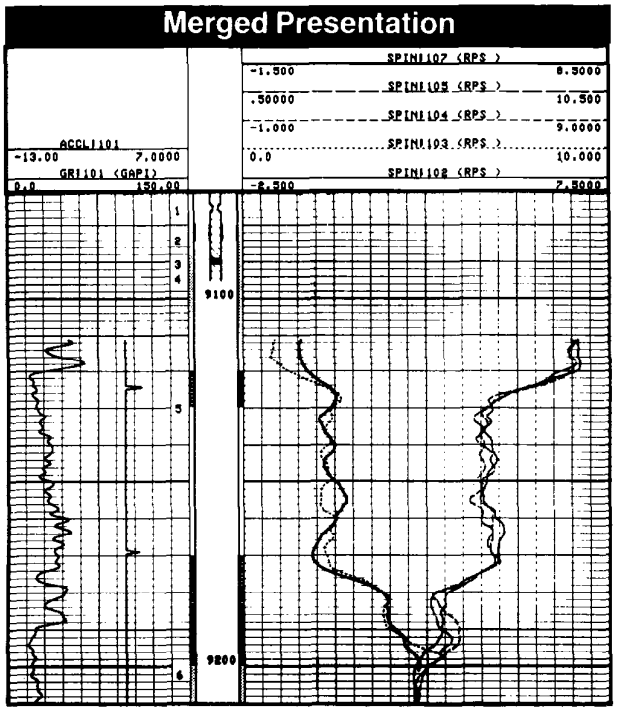

Fig. 4-35—CSU merged flowmeter presentation

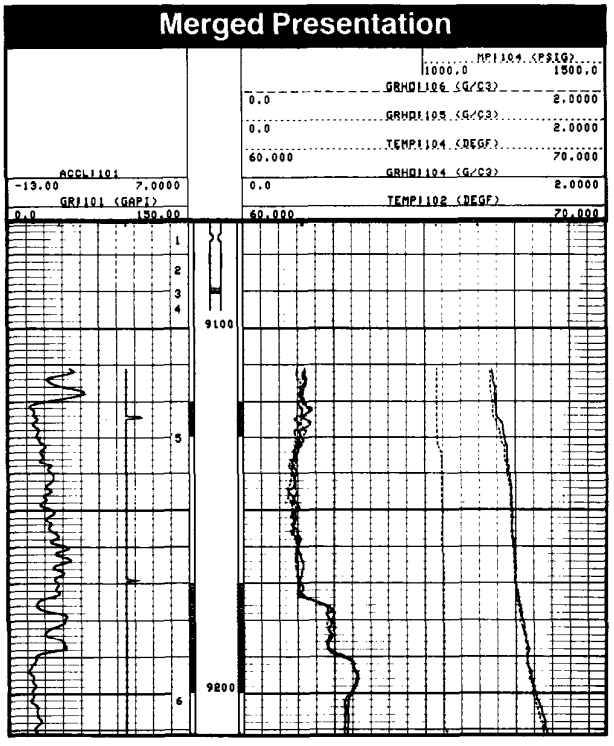

Fig. 4-36—Merged presentation of temperature and Gradiomanometer data

At any stage of the logging operation a flowmeter in-situ calibration plot can be produced as illustrated earlier in Fig. 4-13. Once sufficient accuracy is achieved, total flow rates are computed using the calibration plots.

Gradiomanometer data are interpreted in terms of phase holdup. A slippage velocity algorithm corrected for well deviation, when combined with holdup data, allows computation of 2-phase flow at downhole conditions. An example of merged Gradiomanometer and temperature data is shown in Fig. 4-36.

Downhole fluid properties and interpretation results at surface conditions are automatically calculated using PVT correlations and measured temperatures and pressures. A listing of log data, downhole fluid properties, and interpretation results at downhole and surface conditions is provided as shown in Fig. 4-37. The interpretation results are also presented in a Cyberflow* log (Fig. 4-38).

Job Planning

Planning is the most important facet of a successful production logging job. Close coordination between Schlumberger engineers and well operators is essential.

Planning should start with defining and analyzing the expected downhole injection or production rates, pressures, temperatures, and fluid types. This analysis will determine the tool types and resolutions needed to solve the problem. The presence of H_2S and CO_2 should also be considered. The following information is required to plan the operation:

- a detailed well sketch
- Christmas tree specifications for rigup
- sand or formation fines production
- presence of paraffin or scale deposits
- knowledge of whether the well was hydraulically fractured and/or acidized
- frac balls usage
- reservoir data, reservoir and fluid properties
- production history.

Before the production logging operation is attempted, the operator should verify that the well conditions are acceptable by running a dummy tool (available from Schlumberger) to the bottom to determine if there are any obstacles. Any problems should be remedied before the logging operation is started.

Time allocation is an important consideration for production logging operations—particularly in high pressure operations. Surveys can frequently be run more safely in daylight. This may dictate the use of special lighting equipment for lengthy operations.

All openhole and cased hole logs should be reviewed prior to the logging operation and this data should be available

```
        PRODUCTION LOGGING QUICKLOOK INTERPRETATION LISTING

        LOG DATA

   Z1       Z2       Z3

   TOP OF ZONE DEPTH    (F    )
9110.0   9130.0   9200.0

   BOTTOM OF ZONE DEPTH    (F    )
9120.0   9170.0   9210.0

   DIAMETER OF INTERPRETATION AREA    (IN   )
 4.892    4.892    4.892

   DEVIATION        (DEG )
   0.0      0.0      0.0

   TEMPERATURE      (DEGF)
256.7    257.3    258.3

   PRESSURE         (PSIG)
1033.    1046.    1063.

   FLUID DENSITY      (G/C3)
 .090     .031    1.004

   Z1       Z2       Z3

        DOWNHOLE FLUID PROPERTIES

   1/BG - GAS VOLUME RATIO
 55.9     56.6     57.5

   GAS DENSITY      (G/C3)
 .051     .051     .052

   WATER DENSITY      (G/C3)
1.005    1.004    1.004

   Z1       Z2       Z3

        INTERPRETATION RESULTS AT DOWNHOLE CONDITIONS

   SLIP VELOCITY      (F/MN)
   0.0      0.0      0.0

   WATER PHASE HOLDUP YW
 .04      0.0      1.00

   TOTAL FLOW VELOCITY     (F/MN)
 68.2     45.4      0.0

   CUMULATIVE FLOWRATE GAS     (KF3D)
12.308    8.550     0.0

   CUMULATIVE FLOWRATE WATER     (BB/D)
 94.0     0.0       0.0

   Z1       Z2       Z3

        INTERPRETATION RESULTS AT SURFACE CONDITIONS

   CUMULATIVE FLOWRATE GAS     (KF3D)
  688      484       0.0

   INDIVIDUAL FLOWRATE GAS EACH ZONE  (KF3D)
  203      484       0.0

   PERCENT FLOWRATE GAS EACH ZONE RELATIVE TO TOTAL GAS (%)
29624    70375       0.0

   SPECIFIC PRODUCTION OF GAS EACH ZONE (KF3D/F)
   20       16       0.0

   CUMULATIVE FLOWRATE WATER     (BB/D)
 94.0      0.0       0.0

   INDIVIDUAL FLOWRATE WATER EACH ZONE  (BB/D)
 94.0      0.0       0.0

   PERCENT FLOWRATE WATER EACH ZONE RELATIVE TO TOTAL WATER (%)
100.0      0.0       0.0

   SPECIFIC PRODUCTION OF WATER EACH ZONE (BB/D/F)
  9.4      0.0       0.0

   Z1       Z2       Z3

   INTERPRETATION MODEL =          GAS      AND     GAS WATER

   SUPPLIED DATA              :

   SPECIFIC GAS GRAVITY       :     .750
   WATER SALINITY             :   80000     PPM
```

Fig. 4-37—PL interpretation listing

at the wellsite. In many cases these logs can be used in a NODAL* computer analysis to predict flow profiles for comparison with measured profiles to pinpoint problem areas.

Besides NODAL analysis, the Producibility program is a

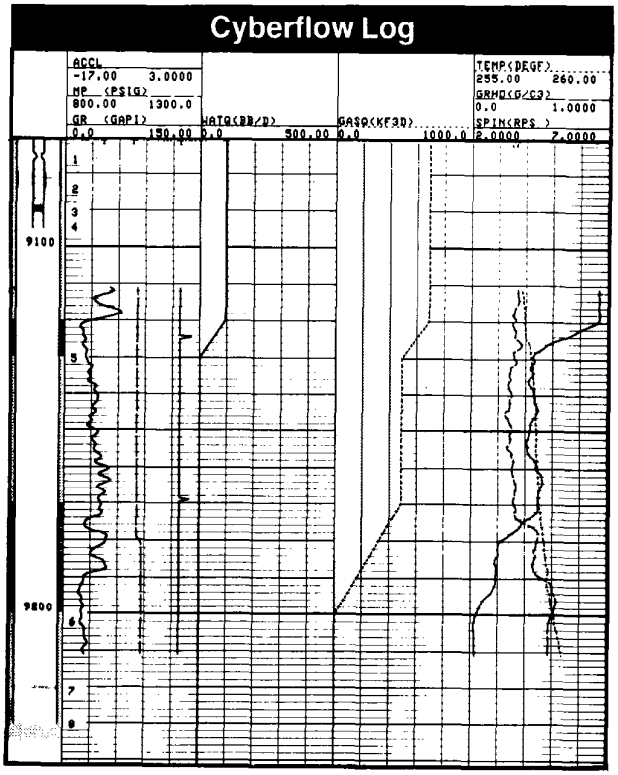

Fig. 4-38—CSU Cyberflow log

useful aid in job planning and subsequent analysis. The program uses permeability estimates from advanced log evaluations and formation pressures from wireline tests, drillstem tests, or production data to predict production performance under various completion designs and conditions. This information can help the completion engineer to design an optimum completion program. It is particularly useful to help evaluate the effectiveness of the completion and identify problem areas. A log presentation is illustrated in Fig. 4-39 and production performance analysis plots of IPR curve and tubing intake curves, differential pressure curves, and perforating shot density curves are shown in Fig. 4-40.

Figure 4-41 illustrates a case in which the well's production rate had decreased. The production problem is defined when the predicted flow profile is compared to the measured profile. The lower two perforated intervals are not producing, as predicted by the Producibility log.

PRODUCTION LOGGING AND WELL TESTING

This section deals with the relationship of production logging to well testing, how downhole measured flow rates can be used to enhance well test interpretation, and the use of computer processing of well test/production logging data.

Pressure transient analysis is one of the most powerful tools

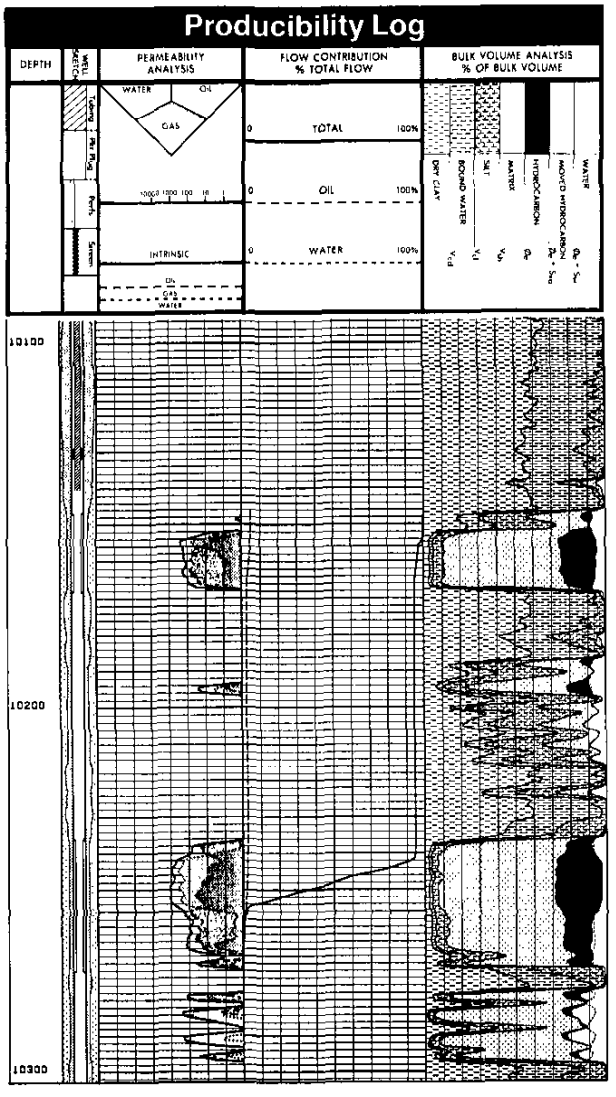

Fig. 4-39—Producibility log

available for determining reservoir characteristics. Rapid developments have occurred in recent years with the advent of downhole measurements, higher resolution pressure gauges, powerful computers, and more sophisticated interpretation and modeling methods.

Well Testing Basics

Production changes, carried out during a well test, induce pressure disturbances in the wellbore and surrounding formation. The pressure changes extend outwards into the formation and are affected in various ways by reservoir features. For example, the pressure disturbance will find difficulty entering a tight zone but pass unhindered through

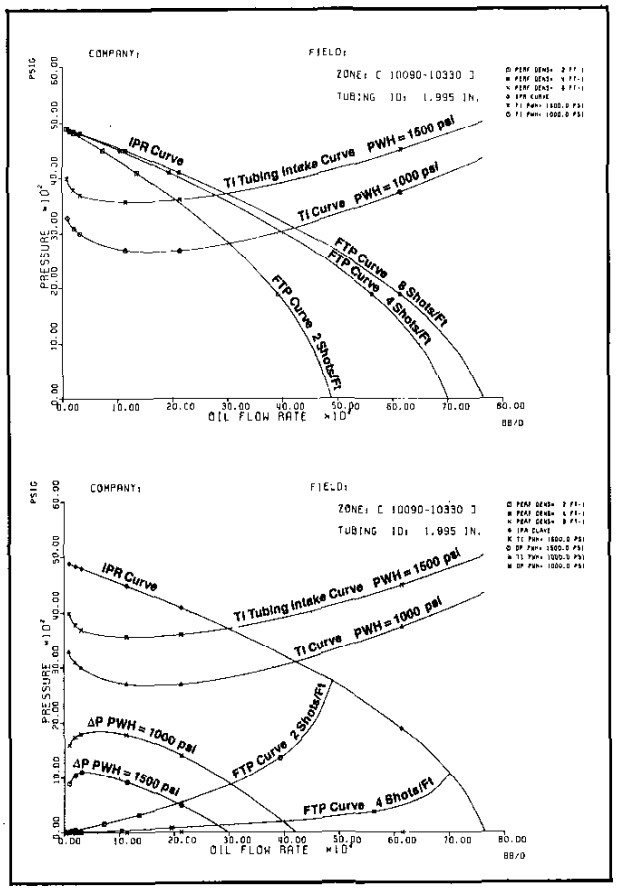

Fig. 4-40—Production performance analysis

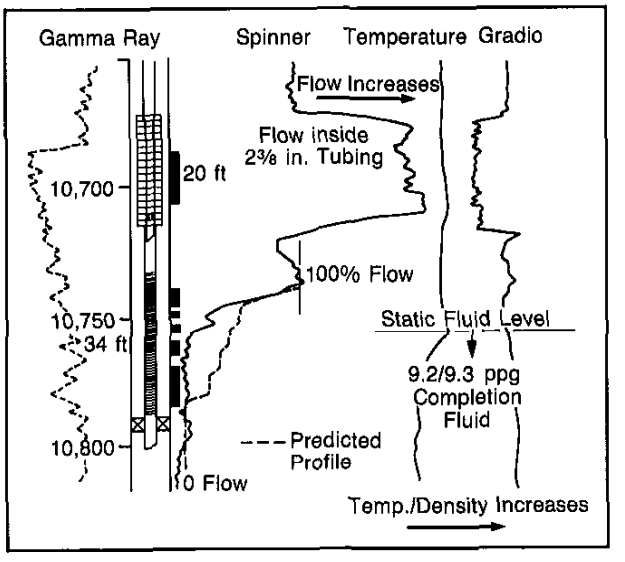

Fig. 4-41—Comparison of predicted profile from Producibility log with the measured flow profile

an area of high permeability. It may diminish or even vanish upon entering a gas cap.

Therefore, a record of wellbore pressure response over time produces a curve whose shape is defined by characteristics of the well and the reservoir. Extracting the information contained in this pressure transient curve is the fundamental objective in well test interpretation. Figure 4-42 shows four types of pressure transients that might occur with various formation characteristics. The points are shown as they appear in a Horner plot, the most common way to present pressure buildup or falloff data. The straight lines on each plot represent the pressure points that would correspond to infinite-acting radial flow, the most readily recognized transient behavior. The top plot shows the type of pressure response seen in a damaged well where skin affects the initial portion of the curve. The abrupt upward trend at the end of the second plot indicates a layered reservoir. The doubling of the slope in the third plot could indicate a well near an impermeable boundary. The last plot shows the effects of a no-flow outer boundary; this plot has no portion representing infinite-acting radial flow.

Analysis of such pressure transient curves probably provides more information about reservoir characteristics than any other single technique. Permeability, average pressure, well damage, fracture length, storativity ratio, and interporosity flow coefficient are just a few of the reservoir characteristics that can be determined. In addition, pressure transient curves can give an indication of the reservoir's extent and geometry.

However, the shape of the pressure transient curve is also affected by the reservoir's production history. Each change in production rate generates a new pressure transient curve which passes into the reservoir and merges with previous pressure effects. The observed pressures at the wellbore will be a result of the superposition of all these pressure changes.

Different types of well tests can be achieved by altering production rates. A buildup test is performed by stopping the flow in a production well, whereas a drawdown test is carried out by putting the well into production. Other forms of well testing, such as multirate, isochronal, and falloff are also possible.

Mathematical models are used to simulate the reservoir's response to changes in production rate. The observed and simulated reservoir responses can then be compared during well test interpretation. By altering model parameters such as permeability or the distance of a fault from the well, a match can be reached between the real and modeled data. The model parameter values are then regarded as a good representation of those of the actual reservoir. Today's computer-generated models add much greater flexibility and improved accuracy to the matching process, making it possible to compare a large number of reservoir models with the observed data.

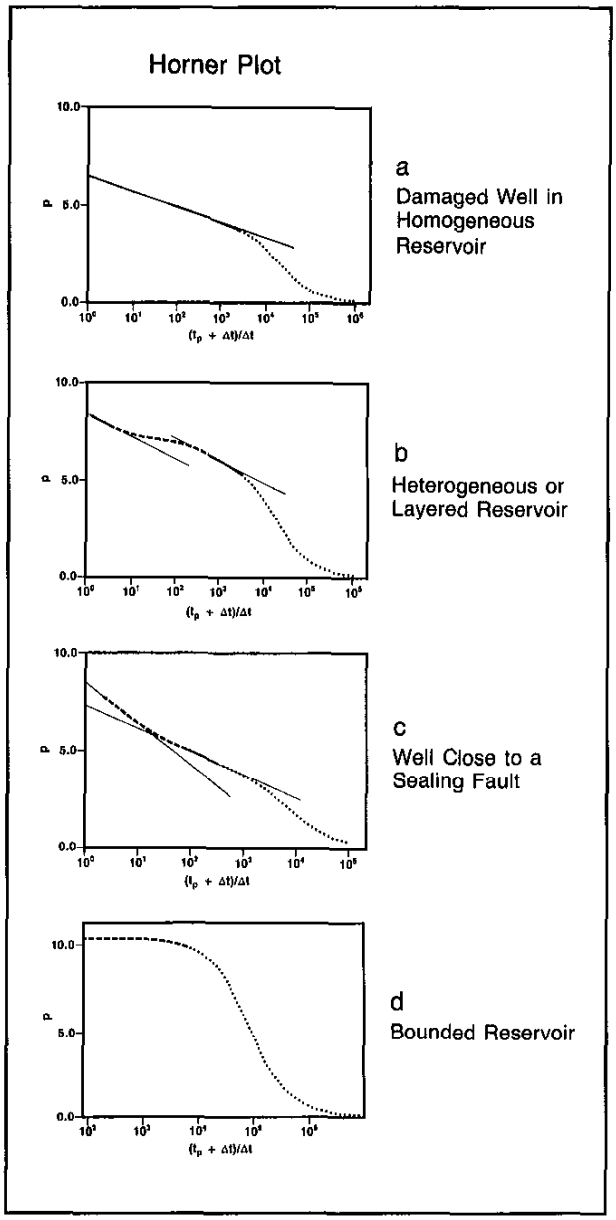

Fig. 4-42—Characteristic pressure transients

Modeling Radial Flow into a Well

A brief review of pressure transient analysis will help to show why advances in technology have had such a dramatic impact on well testing. At the start of production, pressure in the wellbore drops suddenly and fluid near the well expands and moves toward the area of lower pressure. This movement will be retarded by friction against the pore walls and the fluid's own inertia and viscosity. However, as the fluid moves, it will, in turn, create a pressure imbalance and this

will induce neighboring fluid to move toward the well. This process continues until the drop in pressure, created by the start of production, is dissipated through the reservoir.

Most of the fundamental theory of well testing considers the case of a well situated in a porous medium of infinite radial extent. This so-called infinite-acting radial model is illustrated in Fig. 4-43. Flow in the reservoir is modeled by the diffusivity equation and the physical process occurring in the reservoir can be described by this equation:

$$\frac{\partial^2 p}{\partial r^2} + \frac{1}{r}\frac{\partial p}{\partial r} = \frac{1}{\eta}\frac{\partial p}{\partial t}, \qquad \text{(Eq. 4-10)}$$

and $\eta = \phi\mu c_t/k$

where:

p = formation pressure
r = radial distance to the center of the wellbore
t = time
ϕ = porosity
μ = viscosity
c_t = total compressibility
k = permeability
η = diffusivity constant

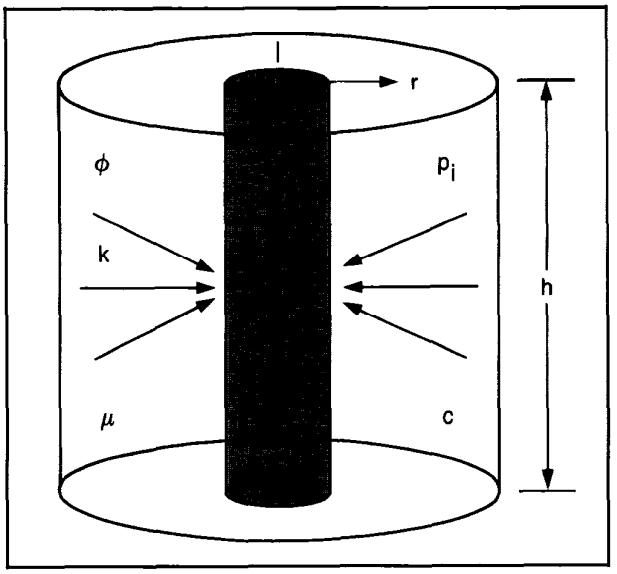

Fig. 4-43—Radial flow model

In order to use the diffusivity equation in modeling, it is first necessary to determine the boundary conditions, such as the reservoir's extent, and initial pressures that prevailed before the change in wellbore flow rate. The equations and conditions which model the reservoir boundary conditions are:

- Initial Condition: Pressures are the same throughout the reservoir and are equal to the initial pressure.

$$p\,(t = 0) = p_i \qquad \text{(Eq. 4-11)}$$

- Condition at the Outer Boundary: Pressures are equal to initial pressure at infinity.

$$p\,(r, t) = p_i \quad \text{as } r \to \infty \qquad \text{(Eq. 4-12)}$$

- Condition at Inner Boundary: From time zero onward the fluid is withdrawn at a constant rate.

$$q_s = \frac{2\pi kh}{\mu}\left(r\frac{\partial p}{\partial r_{r_w}}\right) \qquad \text{(Eq. 4-13)}$$

The approximate solution in its dimensionless form is:

$$p_D\,(t_D) = \frac{1}{2}(\ln t_D + 0.809), \qquad \text{(Eq. 4-14)}$$

where:

t_D = dimensionless time = $\dfrac{0.000264k}{\mu\phi c_t r_w^2}\,t$

p_D = dimensionless pressure = $0.00708\,\dfrac{kh}{q_s\mu}\,(p_i - p_w)$

kh = permeability-thickness product

r_w = well radius.

This shows how the diffusivity equation and boundary conditions can be combined and solved throughout the reservoir to provide a simple model of the radial flow of fluid to a well which has been submitted to an abrupt production rate change. This is called the p_D function or influence function in the literature. Use of the same diffusivity equation, but with new boundary conditions, allows the derivation of other solutions such as the case of a closed cylindrical reservoir or a damaged or stimulated well.

Modeling Departures from Radial Flow

Solutions for reservoirs with regular straight boundaries, such as those which are rectangular or polygonal in shape, and which have a well location on or off center, can be obtained using the same equations as in the infinite reservoir case. This is achieved by applying the principle of superposition in space in the form of method of images. The superposition approach allows analysts to model the effects that features such as faults and variations in reservoir size might have on the pressure response.

The radial flow solution does not account for the drop in pressure which occurs across a localized zone near the well. Instead the term skin is brought into the computations to account for such a drop in pressure. Skin is caused by three

main factors: flow convergence into perforations, viscoinertial flow velocity, and the blocking of pores and fractures during drilling and production. The combined effects of all these factors are estimated and presented in the form of dimensionless skin factors which allow for the comparison of skin effects between wells.

Diagnosing Radial Flow

A plot of pressure versus the log of time will show the radial flow solution as a straight line. This fact provides an easy and seemingly precise graphical procedure for interpretation. The slope and intercept of the portion of the curve forming a straight line is used for permeability and skin factor calculations. Therefore, well test interpretations involve plotting observed pressure measurements on semi-log paper and then determining productivity estimates from the portion of the curve which formed a straight line. Radial flow is assumed to be occurring in this portion of the transient.

An effect which is commonly observed in early time pressure transient behavior is wellbore storage or wellbore phase redistribution. Wellbore storage and skin are modeled by substituting the following for the inner boundary condition given by Eq. 4-13:

$$q = C\,\frac{dp}{dt} + \frac{2\pi kh}{\mu}\,s\,\left(r\,\frac{2p}{2r_{r_w}}\right) . \quad \text{(Eq. 4-15)}$$

This equation assumes that the wellbore storage coefficient, C, is constant. For wellbore phase redistribution, C is not constant.

Often the early portion of the data is distorted by wellbore storage and skin effects. Figure 4-44 shows the effects of wellbore storage and skin on the wellbore pressure response. Radial flow occurs only in the shaded zone. Figure 4-45 illustrates wellbore storage effects. A flowing well of this type always contains a mixture of compressible fluids such as oil, gas, and water. As pressures and temperatures

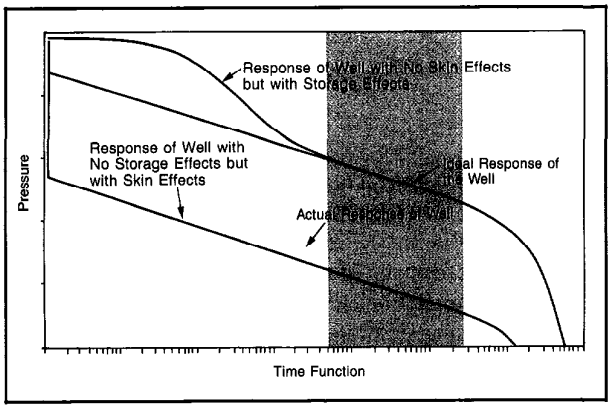

Fig. 4-44—The effects of wellbore storage and skin on the wellbore pressure response

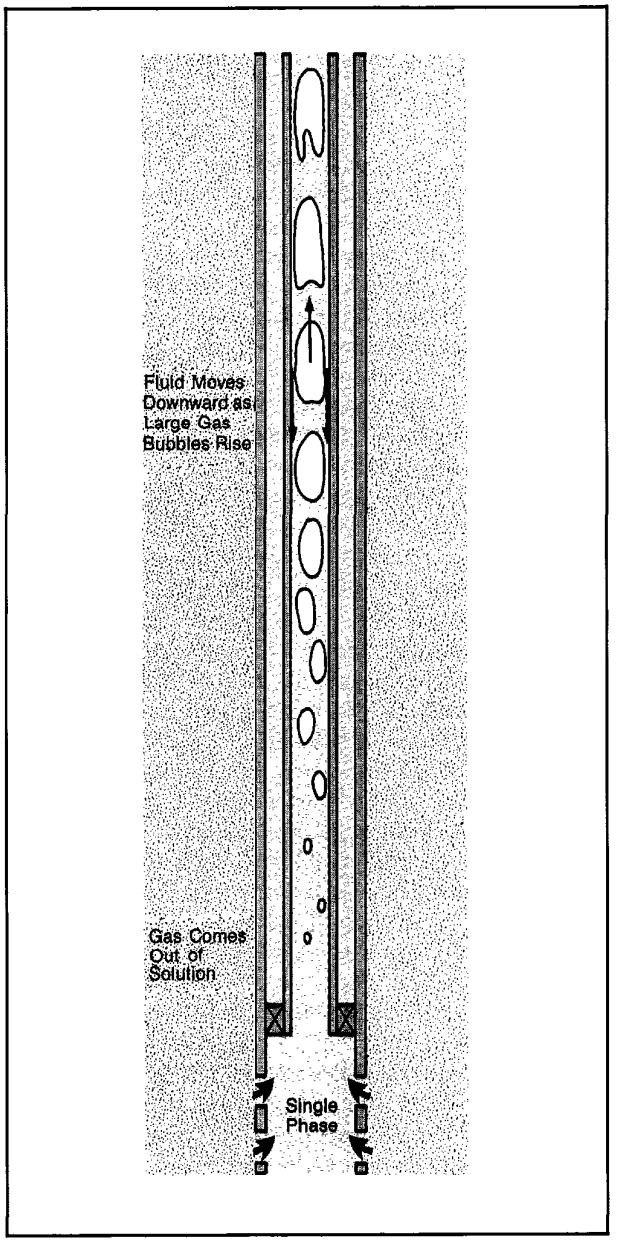

Fig. 4-45—Illustration of wellbore storage

change from the bottom to the top of the well, different flow regimes may develop along the wellbore. If production is suddenly stopped at the surface, complex phenomena develop in which gravitational forces drive fluids to segregate and the pressure buildup compresses the fluids and forces gases back into solution. This creates additional storage space in the well and, as a result, flow from the reservoir does not stop immediately, but continues at a slowly diminishing rate until well pressures stabilize.

Conventional well tests, therefore, are conducted long enough to overcome both skin and wellbore effects to produce a straight line on the plot. But even this approach presents drawbacks. Sometimes more than one apparent straight line appears and analysts find it difficult to decide which one to use. In addition, the choice of plotting scales makes some portions of the pressure response appear straight when, in reality, they should have been curved.

Much of the difficulty in finding the straight line on a semi-log plot which correctly represents radial flow has been alleviated with the use of the log-log diagnostic plot of pressure change and the derivative of pressure with respect to the logarithm of time (or time function). The curves shown in Fig. 4-42 are replotted in the log-log pressure/pressure derivative presentation in Fig. 4-46. Radial flow is characterized on this plot by the flat portion of the derivative. Use of this diagnostic plot greatly reduces the likelihood of analyzing an apparent semi-log line which is not actually representative of radial flow. Further, practice has shown that both near wellbore features (partial penetration, vertical fracture), reservoir heterogeneities (dual-porosity, layering), and boundaries (faults, gas cap) display recognizable characteristic patterns on the diagnostic plot. As such, the pressure/pressure derivative log-log diagnostic plot plays an important part in nearly all types of transient analysis.

The latter portion of the pressure transient can be affected by interference from other wells or by boundary effects such as those that occur when the pressure disturbance reaches the edges of a reservoir. In this case the semi-log pressure transient curve deviates downwards from the straight line as in Fig. 4-42d, and from the pressure derivative plateau as in Fig. 4-46d. Sometimes such disturbances overlap with the early-time effects mentioned previously and can completely mask the all-important straight-line section where radial flow is occurring. In these cases there will be no flat portion in the derivative plot and the analysis can only be done using custom generated type curves. Type curves are also generated using the log-log pressure/pressure derivative presentation. Modern analysis accommodates both interactive matching of data with type curves on the terminal screen and automated type-curve matching using computerized nonlinear parameter estimation. Both of these techniques are greatly improved in effectiveness if the wellbore storage masking early time transients can be eliminated or reduced. One way that wellbore effects are reduced is with the use of downhole shut-in valves; another way to handle the early time transients is to measure sandface flow rate transients and to perform variable flow rate analysis. This is discussed in the next section.

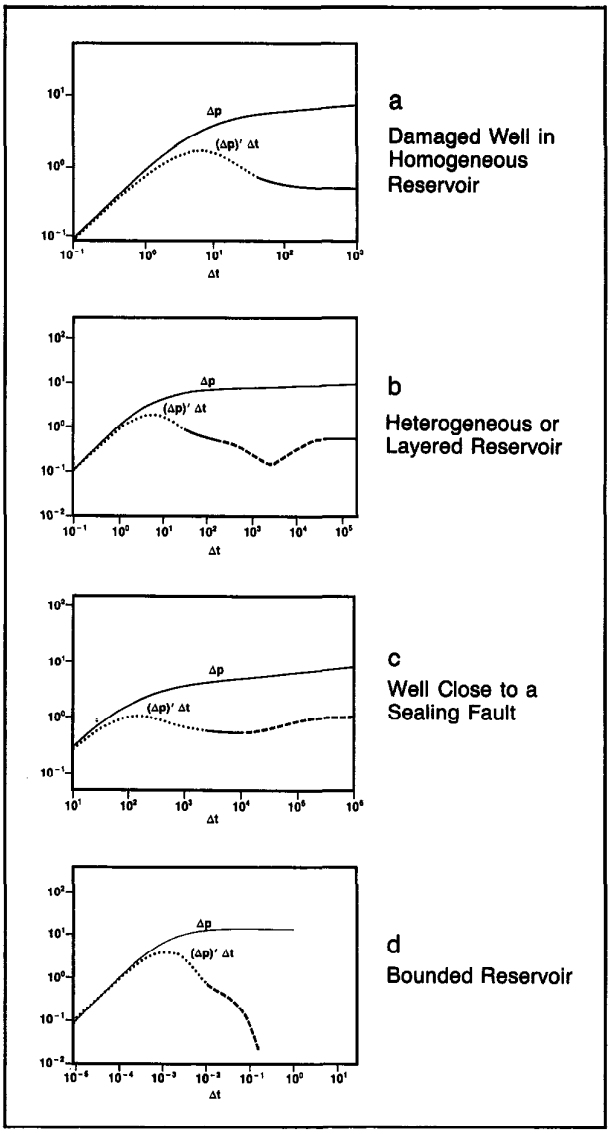

Fig. 4-46—Log-log pressure/pressure derivative presentation of curves shown in Fig. 4-42

Downhole Flow Measurement Applied to Well Testing

Simultaneous measurement of downhole flow rates and pressure with production logging tools has been in existence for some time. However, the use of such measurements for transient analysis in well testing is relatively new. Figure 4-47 shows a schematic of a production logging tool in position to make measurements for a well test. The tool simultaneously measures flow rate, temperature, pressure, and gradient. Combining these downhole measurements with transient drawdown or buildup well tests offers several benefits:

- better early-time analysis. Flow rate information is convolved with the pressure data to perform an accurate early-

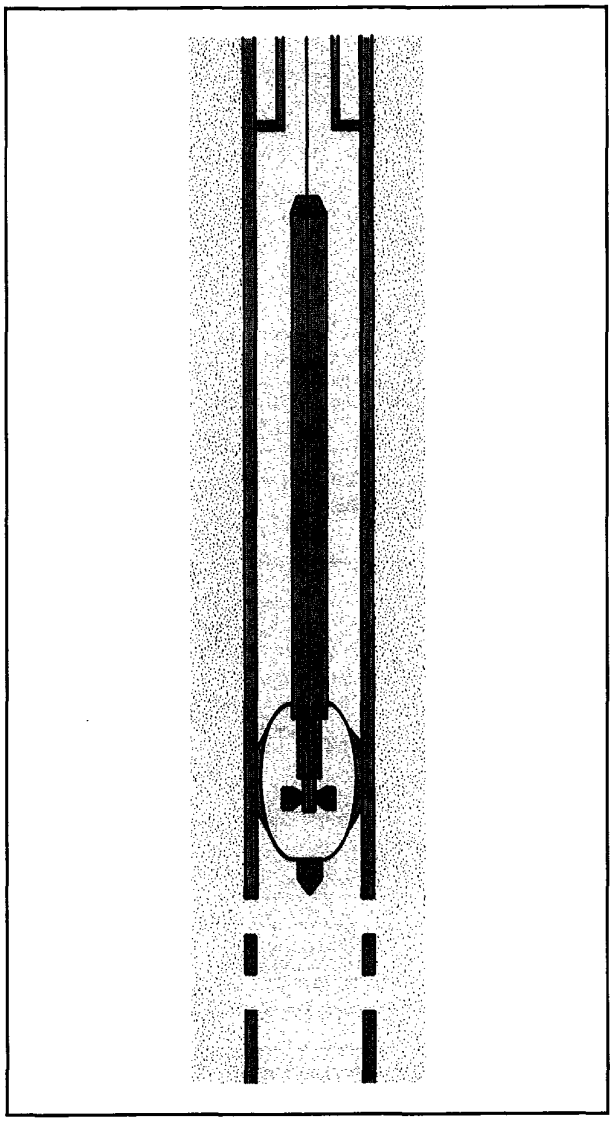

Fig. 4-47—PLT tool in position for a well test

time analysis revealing near wellbore features which would otherwise be masked by wellbore storage. In some cases, the test time can be reduced.

- removing the effect of afterflow. If a boundary is close to the well it may affect pressure behavior before the wellbore storage (afterflow) has died out. In such cases conventional semi-log interpretation techniques cannot be used. Removing the effect of afterflow by convolving the pressure transient data with measured sandface flow rate may reveal the infinite-acting radial flow transients and permit determination of reservoir permeability and skin.
- testing while the well is on production or injection. Because it is difficult to hold the surface rate constant during production or injection, pressure transient tests in flowing wells are often rendered uninterpretable due to small surface rate fluctuations. When sandface flow rates are measured, the convolved pressure data can be easily interpreted. This allows testing without shutting the well in, thus eliminating the loss of production associated with build-up tests and providing more accurately measured downhole flow rates. This strategy can be especially advantageous for reservoir limit testing. In particular, the risk of incorrect reservoir limits evaluation caused by superposition effects or the limits in gauge resolution can be avoided by interpreting the drawdown pressure and sandface flow rate transient data.
- making interpretations above bubblepoint pressure. If the wellbore pressure drops below the bubblepoint pressure of oil during a drawdown, two phases will be present thereafter in the wellbore. This can greatly complicate interpretation if afterflow is still dominating pressure behavior. Using measured sandface flow rates and doing an interpretation on the transients acquired before the wellbore pressure dropped below bubblepoint may provide the desired answers. Further, if downhole pressures during production are about to drop below the bubblepoint pressure, it is possible to reduce the surface rate to avoid 2-phase flow in the reservoir. All of the complications in downhole pressure transients caused by surface rate fluctuations are accounted for when downhole flow rates are recorded along with the pressure.
- quantifying flow rates and distributions. Quantifying flow rates and distributions and perforated-interval thickness is essential when interpreting any well test. If crossflow is occurring before a drawdown, or at the end of a build-up, conventional analysis will be in error. Detecting and quantifying crossflow can be very important for reservoir modeling and description. If the flowing perforated interval thickness derived from the production log flow profile is less than the thickness of the interval derived from the openhole log, then partial penetration effects must be accounted for in the transient analysis.

Simultaneously measured sandface flow rate and pressure provide a direct measure of transients induced by a step change in the surface flow rate. Due to wellbore effects, the sandface flow rate does not represent a step change. However, by measuring the flow rate at the sandface, the effects of the sandface flow rate variations can be rigorously accounted for in the analysis. The most common way to correct for downhole flow rate variations is through the use

of superposition calculations in the form of a convolution. Convolved pressure data can be differentiated for diagnosis analagous to that done with the pressure derivative, and it can be analyzed directly using the straight line on a convolution plot.

By measuring downhole flow rates, radial-type flow can be observed in convolved data at much earlier times than would be seen in just the pressure data. When this regime develops, the convolution derivative becomes flat (as seen in Fig. 4-48) and adequate data for interpretation is available at an earlier time than possible with pressure transients alone. Three curves are overlaid on the same log-log scale to emphasize the utility of the presentation.

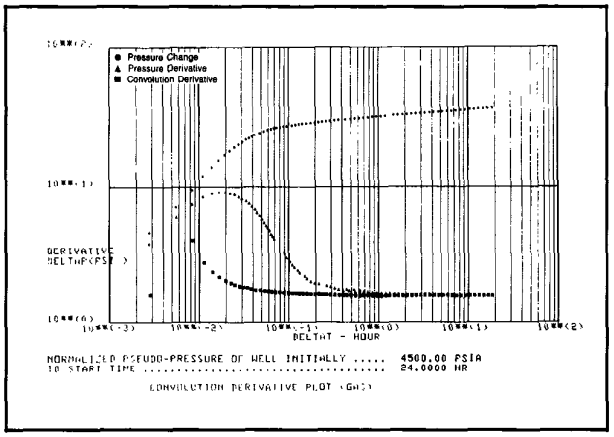

Fi.g 4-48—Wellsite diagnostic plot showing pressure, pressure derivative, and convolution derivative

Figure 4-49 shows an example of downhole flow measurements made during a drawdown test on an oil reservoir. It was felt that this well would not return to normal production without swabbing if a surface shut-in test was carried out. To avoid this, a surface choke valve was used to obtain a step change in production rate during which time downhole pressure and flow rates were measured with a production logging tool. These downhole measurements were analyzed using the sandface rate convolution plot shown in Fig. 4-50 and estimates of the reservoir parameters were obtained. In this sandface rate convolution plot, pressure data, normalized using flow rate data, is plotted against a time function which accounts for all of the observed flow rate changes. This kind of analysis would be impossible without the downhole flow measurements.

In many cases, particularly in thick or layered formations, only a small percentage of the perforated interval may be producing. This can be due to blocked perforations or the presence of low permeability layers. A conventional surface well test might wrongly indicate that there are significant skin effects caused by formation damage throughout the well.

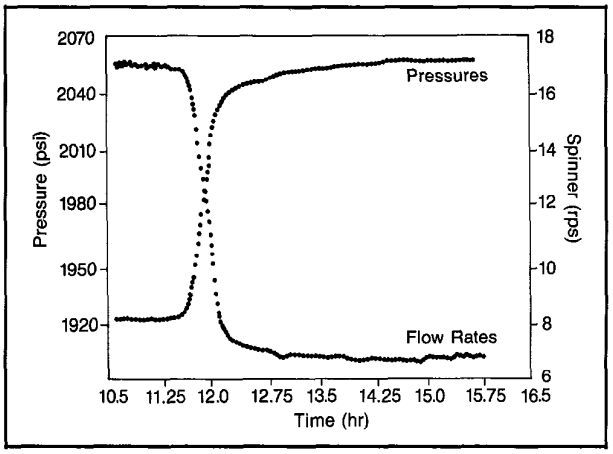

Fig. 4-49—Plot of bottomhole flow rates and pressure recorded during a drawdown test

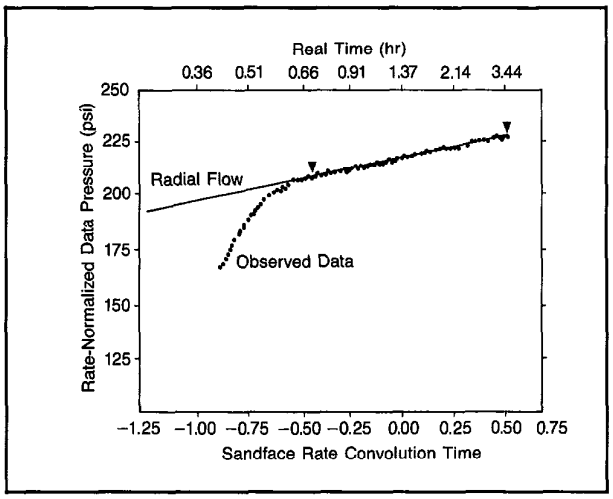

Fig. 4-50—Sandface rate convolution plot

Downhole flow measurements enable reservoir engineers to measure the flow profile in a stabilized well and to calculate the skin effect due to flow convergence. Using this, it is possible to deduce the true contribution that formation damage is making to the overall skin effect.

Optimum production strategies depend on reservoir behavior, and reservoirs that may be classified as geologically homogeneous could in fact possess heterogeneous flow characteristics. Figure 4-51 shows a rate-convolved analysis for an 8-hr buildup test using the convolution derivative approach. The objective of the test was to determine if nonhomogeneous character was evident. The circles and squares represent pressure change and its derivative respectively, while the asterisks denote the convolution derivative using the measured sandface flow rates. Note that the convolution derivative

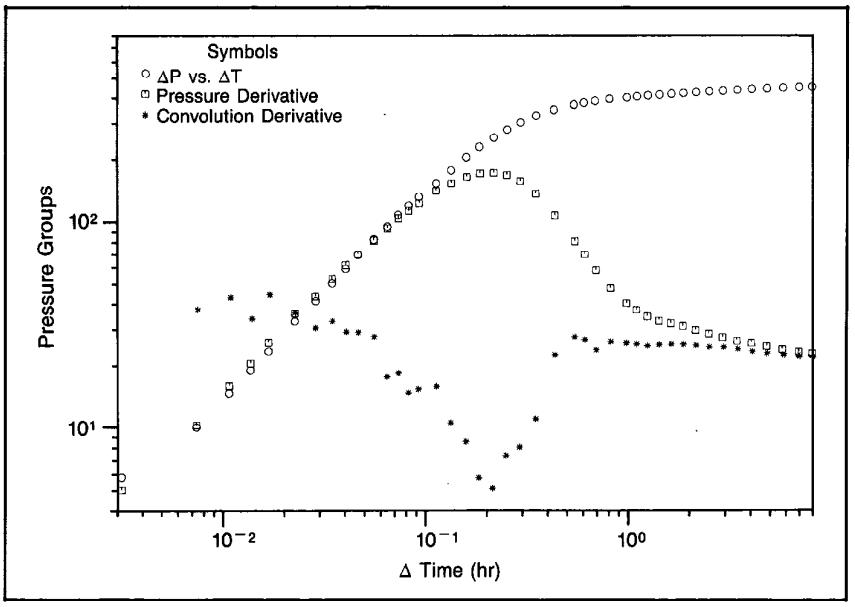

Fig. 4-51—Pressure, pressure derivative, and convolution derivative analysis plot

bears the characteristic dip of a heterogeneous formation (as in Fig. 4-46b) while the pressure data alone does not show this feature. In other words, the heterogeneous behavior apparent in the convolution derivative is masked by the afterflow effects in the pressure data and its derivative. Therefore, diagnosis of reservoir flow behavior based solely on pressure information would have been much less conclusive.

Layered Reservoir Testing

The fundamental theories of well testing can be applied to multilayered reservoirs provided that each layer is tested separately. These kinds of tests are particularly useful on new wells, as they provide an invaluable amount of information about the reservoir.

In production wells where simple estimates of productivity are required, testing by isolating each layer might be unnecessarily costly. A new technique which allows several well-defined layers to be tested simultaneously has recently been introduced. While there are a wide variety of layered reservoirs, this discussion will be limited to those whose layers communicate only through the wellbore. In such reservoirs, the pressure in each layer is often different.

Figure 4-52 shows the difference in pressures between well-defined layers in an oilfield. The plot was computed using Repeat Formation Tester (RFT*) data and log information. Two well-defined permeable layers are clearly indicated in the illustration as is the intervening low permeability zone which is a barrier to vertical flow.

If this reservoir is subjected to a step change in production, a split pressure transient will be produced which will

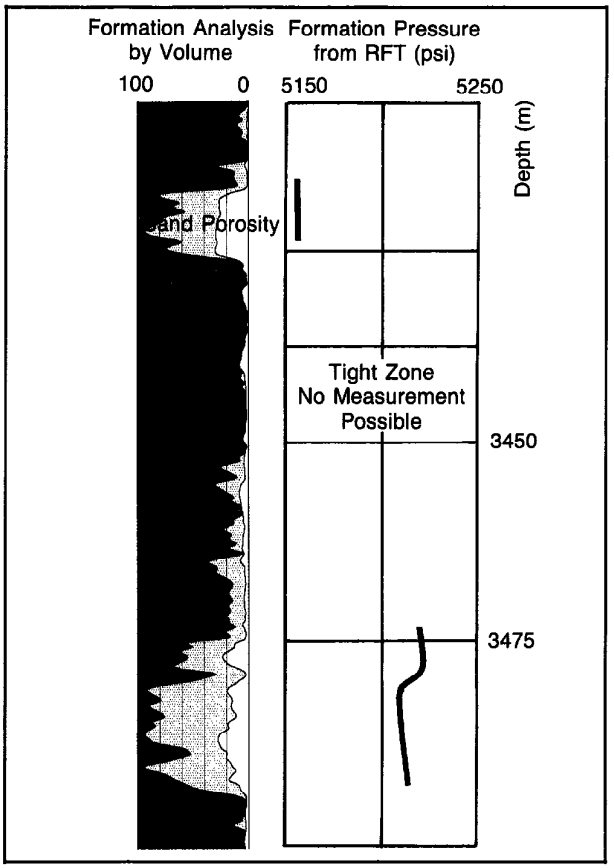

Fig. 4-52—Log and RFT pressure data showing layered reservoir

propagate into the reservoir along each of the permeable layers (Fig. 4-53). The transient is better developed in the upper layer, which has the greatest permeability. In the lower layer, however, the transient also propagates horizontally and both layers must be taken into account during test analysis. Pressure contour plots like the one in Fig. 4-53 are usually made prior to testing to assist in the test design. They provide an indication of the radius of investigation in each layer.

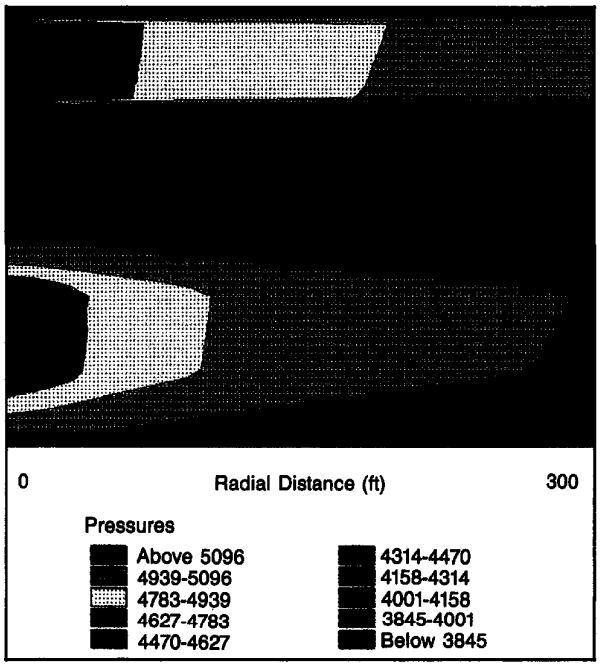

Fig. 4-53—Plot of pressure change within the reservoir following a step change in production

Figure 4-54 shows the steps needed to perform such a well test in a 2-layered case. Once the well has been stabilized the test is carried out using two distinct types of measurements:

- flow profile measurement. A measurement of the stabilized flow rates per layer is made at the beginning of the test, and before each change in the surface flow rate.
- transient measurement. This is achieved by positioning the Production Logging Tool (PLT*) at the top of a perforated interval and then changing the surface production rate while simultaneously measuring flow and pressures. This is done for each of the layers to be tested.

The test produces a nearly continuous record of wellbore pressure.

During interpretation of this kind of test, a well simulation model is forced to track the shape of the pressure response and, from this simulation, theoretical production rates are computed. If these rates do not match the observed

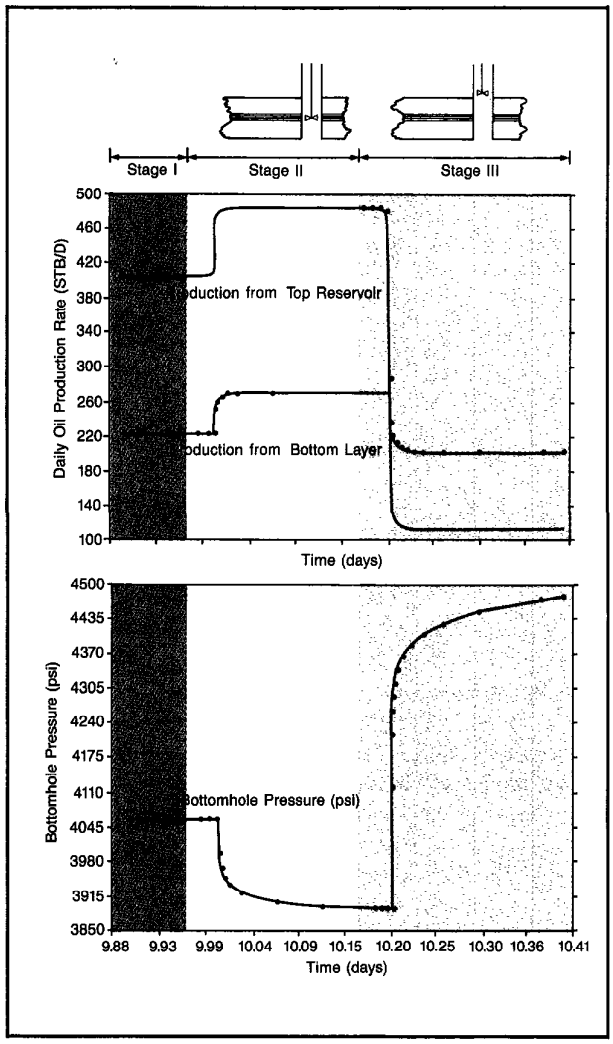

Fig. 4-54—Layered reservoir test stages

flow rates, the model parameters need to be adjusted until the modeled and measured responses match. It is then assumed that the model parameters are representative of the actual formation. Figure 4-55 illustrates a match between computed and measured flow rates.

Computerized Acquisition and Interpretation Features

The use of downhole shut-in for buildup or falloff tests, and the measurement of downhole flow rates represent major advances in acquisition techniques. One or both of these acquisition strategies may be recommended, depending on test objectives. Often openhole log and RFT data are utilized in designing an appropriate test string and measurement sequence.

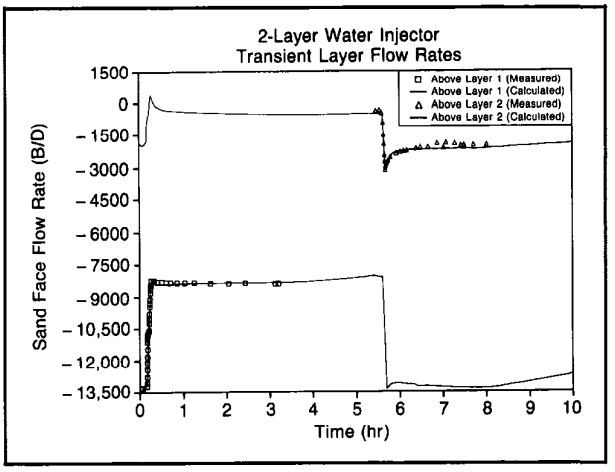

Fig. 4-55—Typical example of forward modeling

TIME DD:HH:MM:SS	DELTAT HOURS	PRESSURE HPGP-PSIA	DELTAP PSI	HORNER	SPINNER SPIN-RPS	DENSITY GRHO-G/C3
20:29:15	.0050	4700.43	96.49	4.079	11.88	.227
20:29:14	.0047	4692.78	88.84	4.104	11.98	.228
20:29:13	.0044	4685.16	81.22	4.130	12.07	.227
20:29:12	.0042	4677.56	73.62	4.159	12.19	.227
20:29:11	.0039	4670.04	66.10	4.188	12.30	.228
20:29:10	.0036	4662.63	58.69	4.221	12.37	.228
20:29: 9	.0033	4655.34	51.40	4.255	12.47	.228
20:29: 8	.0031	4648.19	44.25	4.293	12.52	.228
20:29: 7	.0028	4641.28	37.34	4.335	12.59	.228
20:29: 6	.0025	4634.60	30.66	4.380	12.67	.228
20:29: 5	.0022	4628.26	24.32	4.431	12.79	.227
20:29: 4	.0019	4622.43	18.49	4.490	12.82	.226
20:29: 3	.0017	4617.15	13.21	4.556	12.91	.226
20:29: 2	.0014	4612.49	8.55	4.636	12.98	.225
20:29: 1	.0011	4608.51	4.57	4.732	13.02	.226
20:29: 0	.0008	4605.79	1.85	4.857	13.07	.225
20:28:59	.0006	4604.55	.61	5.034	13.13	.226
20:28:58	.0003	4604.09	.15	5.333	13.13	.226
20:28:57	0.0	4603.94	-.00		13.17	.225
20:28:56	-.0003	4603.88	-.06		13.17	.226
20:28:55	-.0006	4603.85	-.09		13.17	.226
20:28:54	-.0008	4603.86	-.08		13.17	.226
20:28:53	-.0011	4603.86	-.08		13.20	.226
20:28:52	-.0014	4603.85	-.09		13.23	.225
20:28:51	-.0017	4603.85	-.09		13.23	.226
TIME DD:HH:MM:SS	DELTAT HOURS	PRESSURE HPGP-PSIA	DELTAP PSI	HORNER	SPINNER SPIN-RPS	DENSITY GRHO-G/C3

Fig. 4-56—Example of wellsite listing

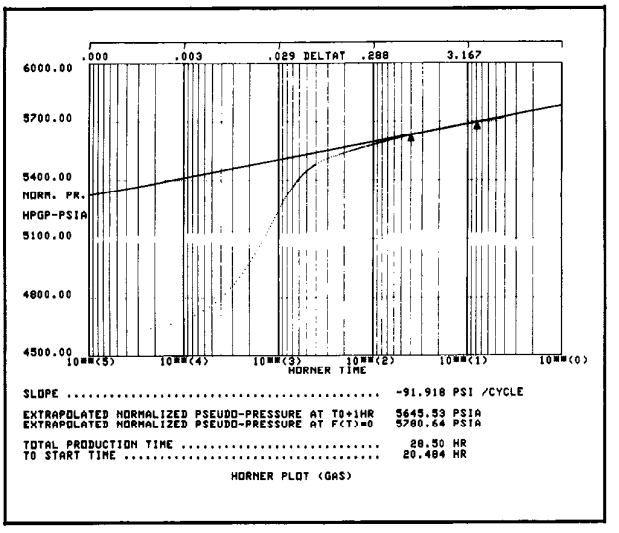

Fig. 4-57—Example of wellsite data plot

During acquisition, the data may be recorded either downhole or at the surface. Real-time data acquisition offers the capability to plot the transient data and monitor the progress of the test. Adjustments in the surface flow rate sequence in the position of the downhole sensors can be made during the test to improve the quality of the data. Also, the real-time plots can be used to determine when there is sufficient data to terminate the test. When measurements are made with downhole recording sensors, it is necessary to pull the tool string out of the hole at specified times to retrieve the data, verify its quality, and determine whether the data is sufficient to satisfy the test objectives. Downhole recording sensors are recommended only when it is preferred not to run electric wireline into the hole for safety reasons.

At the wellsite, the data are validated using a wellsite computer. For testing with the standard Production Logging Tool the wellsite computer is the CSU, which is equipped with Well Test Quicklook (WTQL) software. Other tests may be required with the CAS or CAS/CIS computers, which provide interpretation using the Interpretation Software System (ISS). Both WTQL and ISS offer considerable interpretation capabilities, including most of the standard presentations such as the Horner plot, MDH plot, and deliverability analysis, as well as diagnosis and type-curve matching with the combined pressure derivative/convolution plots using an extensive catalog of reservoir models. The objective of the validation is to demonstrate that the data are interpretable and contain the necessary information to achieve the test objectives. Samples of the CSU wellsite data listing and/or data plot are shown in Figs. 4-56 and 4-57.

For a more complete interpretation, the data are analyzed at the data service centers (also known as Field Log Interpretation Centers). There, analysts use the Schlumberger Transient Analysis and Report (STAR) system for interpretation of single-layer transient tests, and the Well Modeling System (WMS) for analysis of multilayer tests. These systems provide analysis with models not available at the wellsite, automated type-curve and history matching, improved interactive graphics capabilities, and the ability to integrate the well test data with openhole log and RFT data, single well numerical models, and NODAL sensitivity analysis. Table 4-2 illustrates the considerable variety of reservoir conditions, models, and parameter combinations supported by the STAR and WMS programs. Figures 4-58 and 4-59 show examples of interactive graphics displays available in STAR and WMS.

The NODAL analysis is a systematic approach to the optimization of oil and gas well deliverability via thorough evaluation of the complete producing system. The technique establishes flow rate versus pressure drop relationships for

Inner Boundary Condition	Well Condition	Reservoir Model	Outer Boundary Condition	Fluid Type
Constant Flow Rate Constant Pressure	Unfractured Wellbore Storage Skin Vertical Fracture • Infinite Conductivity • Uniform Flux • Finite Conductivity Partial Penetration/ Limited Entry	Homogeneous Double Porosity • Pseudosteady State • Transient Two-Layered • Vertical Interference • Horizontal Interference • Crossflow • Commingled N-Layered (Commingled)	Infinite System No-Flow (Rectangle, Circle) Constant Pressure (Circle) Mixed Boundary Rectangle Single and Intersecting Sealing Faults	Liquid Gas Gas Condensate Solution Gas

Table 4-2—Reservoir condition, model, and parameter combinations supported by the STAR program

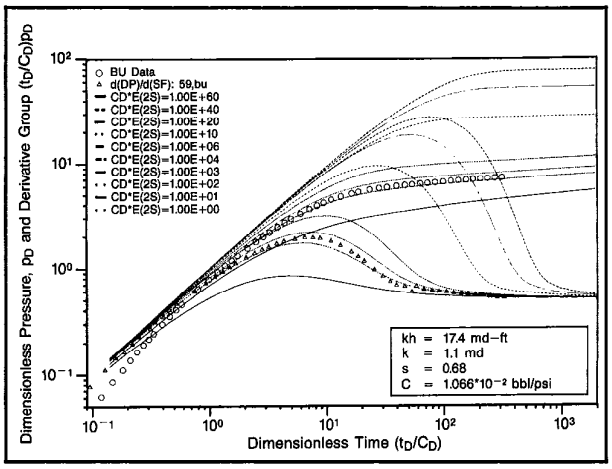

Fig. 4-58—Example of interactive graphics display

each component of the producing system including the reservoir near wellbore completion.

The pressure transient analysis shown in Fig. 4-60 is from an offshore well that had been producing at 1200 BOPD, which is far below the neighboring well's 5000 BOPD in the same reservoir. Formation damage was suspected to be the cause of the low productivity and the well was tested. Interpretation of the data identified a severely damaged well with a skin factor larger than 200. The NODAL analysis was used to study the effect of damage removal on production performance. The results (Fig. 4-61) suggested that the flow rate could be increased by a factor of five at the same wellhead pressure if the impending damage around the wellbore could be removed. This could be achieved by an acid treatment without jeopardizing the integrity of the gravel pack. The well was treated with an acid injection program and a

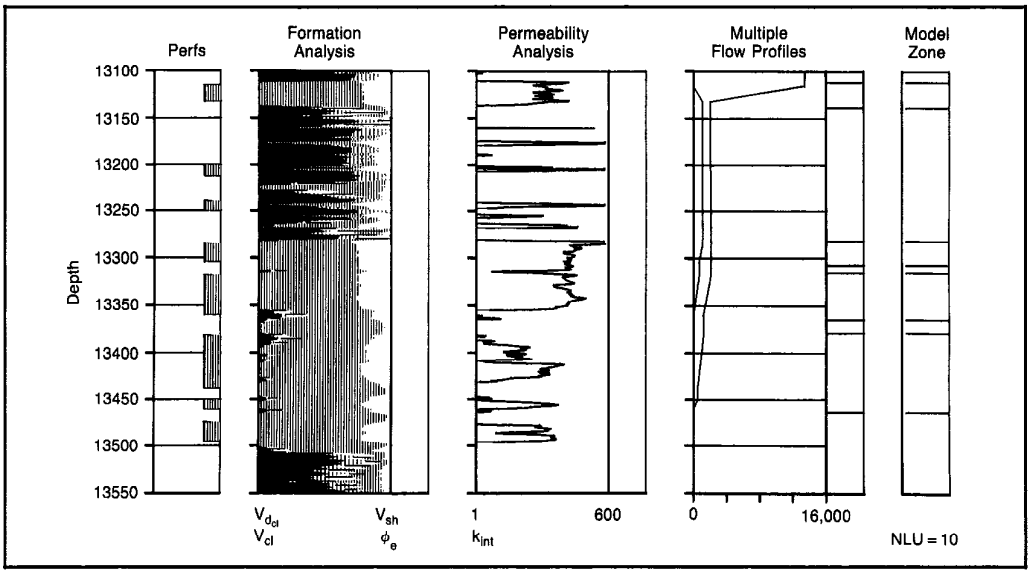

Fig. 4-59—Example of interactive graphics display

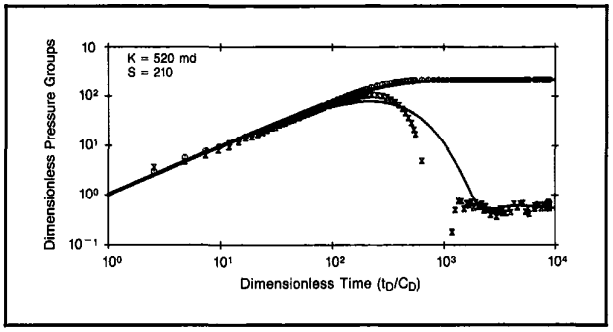

Fig. 4-60—Pressure transient analysis

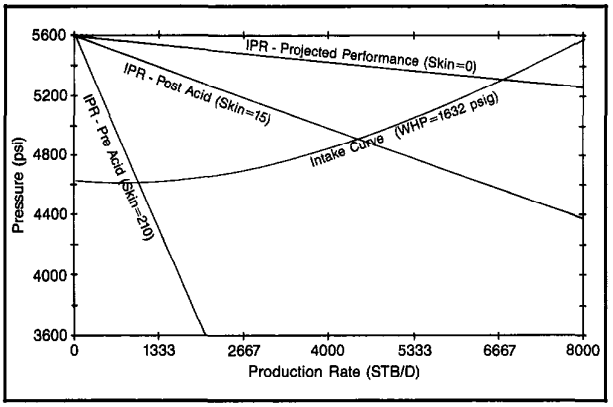

Fig. 4-61—NODAL analysis plot

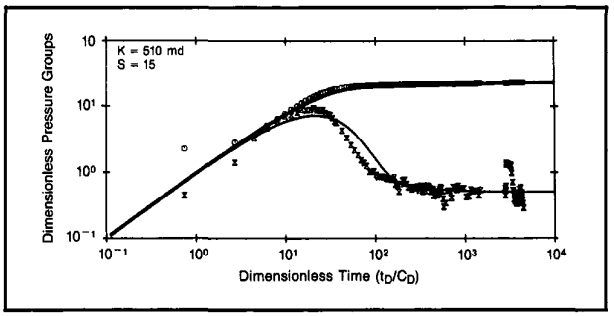

Fig. 4-62—Post-acid pressure analysis

post-acid well test was conducted to evaluate the effectiveness of the treatment. Interpretation of the post-acid well test (Fig. 4-62) showed that the skin was reduced to +15 from the preacid value of about +210. The final stabilized rate of 4300 BOPD was in agreement with the predictions made by the NODAL analysis.

REFERENCES

Ahmed, U., Kucuk, F., and Ayesteran, L.: "Short Term Transient Rate and Pressure Build-up Analysis of Low Permeability Wells," paper 13870 presented at the SPE/DOE Joint Symposium on Low Permeability Reservoirs in Denver, CO, 1985.

Bourdet, D. et al.: "A New Set of Type Curves Simplifies Well Test Analysis," *World Oil* (May, 1983) 95-106.

Bourdet, D.: "Pressure Behavior of Layered Reservoirs with Crossflow," paper SPE 13628 presented at the 1985 SPE California Regional Meeting, Bakersfield, March 27-29.

Boyce, R. and Carroll, J.F.: "Mathematical Modeling of a Gravel-Pack Logging Tool," paper 13138 presented at the SPE 59th Annual Technical Conference and Exhibition in Houston, TX, 1984.

Brown, K.E. and Beggs, H.D.: *The Technology of Artificial Lift Methods*, PennWell Books (1972).

Brown, K.E. and Lea, J.F.: *NODAL System Analysis for Oil and Gas Wells*, Flopetrol Johnston (1985).

Curtis, M.R.: "Flow Analysis in Production Wells," paper 1908 presented at the 1967 Fall Meeting of SPE of AIME, Houston.

Downhole Testing Services - Downhole Tools for DST's and Production Tests, Schlumberger International Coordination, Houston (1987).

Earlougher, R.D., Jr.: *Advanced Well Test Analysis*, Monograph Series, SPE, Dallas (1977).

Ehlig-Economides, C.A. and Joseph, J.A.: "A New Test for Determination of Individual Layer Properties in a Multilayered Reservoir," paper 14167 presented at the 60th Annual Technical Conference and Exhibition in Las Vegas, NV, 1985.

Ehlig-Economides, C., Joseph, J., Erba, M., and Vik, S.A.: "Evaluation of Single-Layer Transients in a Multilayered System," paper 15860 presented at the SPE European Petroleum Conference in London, England, 1986.

Fetkovich, M.J. and Vienot, M.E.: "Rate Normalization of Build-Up Pressure Using Afterflow Data," paper 12179 presented at the SPE 1983 Annual Technical Conference and Exhibition, San Francisco.

Fluid Conversions in Production Log Interpretation, Schlumberger, Houston (1974).

Guillot, A.Y. and Horn, R.N.: "Using Simultaneous Flow Rate and Pressure Measurements to Improve Analysis of Well Tests," paper 12958 presented at the European Petroleum Conference, London, 1984.

Hasan, A.R. and Kabir, C.S.: "A Study of Multiphase Flow Behavior in Vertical Oil Wells Part 1," paper 15138 presented at the 56th California Regional Meeting in Oakland, CA, 1986.

Hasan, A.R. and Kabir, C.S.: "A Study of Multiphase Flow Behavior in Vertical Oil Wells Part 2," paper 15139 presented at the 56th California Regional Meeting in Oakland, CA 1986.

Hill, A.D. and Oolman, T.: "Production Logging Tool Behavior in Two-Phase Inclined Flow," paper 10208 presented at the SPE 1981 Annual Technical Conference and Exhibition in San Antonio, TX.

Leach, B.C., Jameson, J.B., Smolen, J.J., and Nicolas, Y.: "The Full Bore Flowmeter," paper 5089 presented at the SPE 1974 Annual Fall Meeting in Houston, TX.

Meunier, D., Tixier, M.P., and Bonnet, J.L.: "The Production Combination Tool - A New System for Production Monitoring," *JPT* (May, 1971).

Meunier, D., Wittmann, M.J., and Stewart, G.: "Interpretation of Pressure Buildup Test Using In-Situ Measurement of Afterflow," paper 11463 presented at the Middle East Oil Technical Conference in Manama, Bahrain, 1983.

McKinley, R.M.: "Production Logging," paper 10035 presented at the International Petroleum Exhibition and Technical Symposium in Beijing, China, 1982.

Middle East Well Evaluation Review, Schlumberger Technical Services, Dubai, UAE (1987) 2-3.

Modern Well Testing, Schlumberger Educational Services, Houston (1988).

Neal, M.R. and Carrol, J.F.: "Quantitative Approach to Gravel Pack Evaluation," paper 12477 presented at the 6th SPE Formation Damage Symposium at Bakersfield, CA, 1984.

Noik, S.P. and Poupon, A.: "Production Logging Interpretation in Diphasic Flow," SPE Circular Letter (April, 1966).

Piers, G.E., Perkins, J., and Escott, D.: "A New Flowmeter for Production Logging and Well Testing," paper 16819 presented at the SPE 62nd Annual Technical Conference and Exhibition in Dallas, TX, 1987.

Poupon, A. and Loeb, J.: "Temperature Logs in Production and Injection Wells," 27th Meeting of the European Association of Exploration Geophysicists, Madrid, May, 1965.

Production Log Interpretation, Schlumberger, Houston (1973).

Production Services Catalog, Schlumberger, Houston (1986).

Repeat Formation Tester, Schlumberger Educational Services, Houston (1987).

Ros, N.C.J.: "Simultaneous Flow of Gas and Liquid as Encountered in Well Tubing," *JPT* (October, 1961).

Shah, P.C., Karakas, M., Kucuk, F., and Ayestaran, L.: "Estimation of the Permeabilities and Skin Factors in Layered Reservoirs Using Downhole Rate and Pressure Data," paper 14131 presented at the SPE International Meeting in Beijing, China, 1986.

Sollee, S.S.: "Gravel-Pack Logging Experiments," paper 14163 presented at the SPE 60th Annual Technical Conference and Exhibition in Las Vegas, NV, 1985.

Stewart, G., Wittmann, M.J., and Meunier, D.: "Afterflow Measurement and Deconvolution in Well Test Analysis," paper 12174 presented at the SPE 1983 Annual Technical Conference and Exhibition, San Francisco, CA.

Well Evaluation Conference - China, Schlumberger, Paris (1985).

5 Cement Evaluation

CEMENTING TECHNIQUE

The successful cementation of casings and liners is a difficult operation which requires proper planning of the job as a function of well conditions and a working knowledge of the pressure mechanisms involved during the placement of the cement slurry. Causes of poor cement jobs can be classified in two broad categories:

- flow problems of mechanical origin. This is the case of poorly centralized pipes in deviated wells, washed out holes, inefficient preflush, and incorrect flow regime. These conditions are characterized by an incomplete mud removal in the cement annulus (Fig. 5-1).

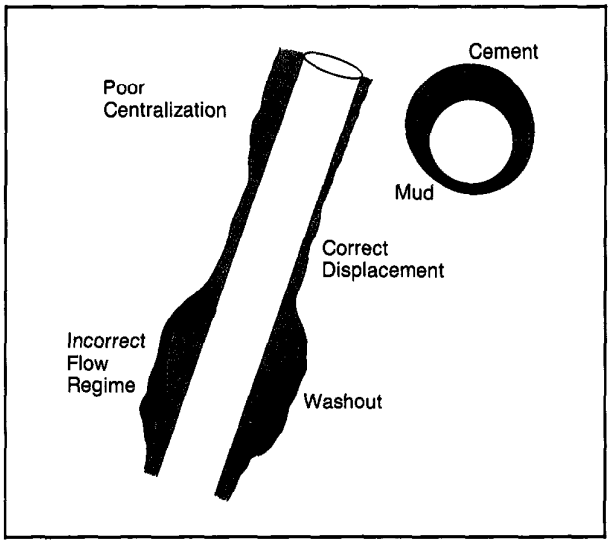

Fig. 5-1—Cement slurry displacement problems

- degradation of the cement slurry during the curing stage. Laboratory experiments confirmed by field tests have shown that the differential pressure between the cement pore pressure and the formation pressure is the cause of many cement failures. Figure 5-2 shows the history of the cement pore pressure during setting and demonstrates how a standard slurry can be invaded by formation fluid or gas at the time of hydration, when the slurry loses water and starts shrinking. This is accompanied by a pressure drop such that when the pore pressure becomes smaller than the formation pressure, the cement can be polluted by formation fluids or, worse, by inflow of gas.

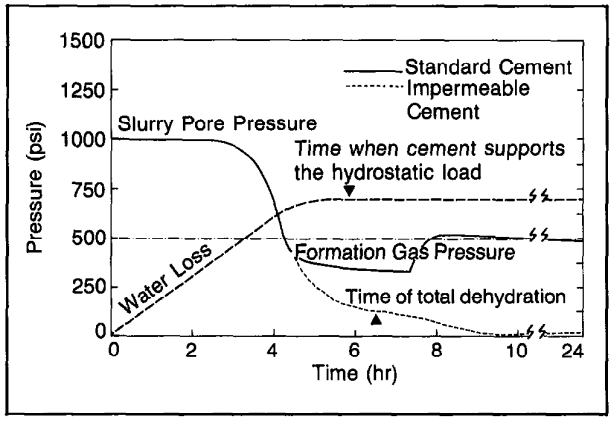

Fig. 5-2—Pressure drop in cement setting

Laboratory measurements have shown that a well cured cement typically has a permeability on the order of 0.001 md, with a pore size below 2μ and a porosity around 35%. However, when gas is allowed to migrate within the slurry before complete curing, the pore structure is partially destroyed and gas generates a network of tubular pores which can reach 0.1 mm in diameter and lead to permeabilities as high as 1 to 5 md. This "gaseous" cement, although supporting the casing, is unable to provide a proper seal to the formation gas. Certain additives are now available which prevent this mechanism and ensure a proper zone isolation of gas-bearing intervals.

Whether the causes of poor cement jobs are of mechanical or pressure origin, the result will affect the hydraulic isolation between formations, which is the main function of primary cementation.

A comprehensive cement evaluation program should then be able to determine not only the quality of the cementing operation or the need for repair jobs, but also to analyze the causes of failures in order to improve the cementing program of future wells in the same field. Some field examples will illustrate how this can be done using the combination of the Cement Evaluation Tool (CET) and CBL-VDL services and the Cement Evaluation Quicklook (CEQL) wellsite interpretation program. First the principles of these measurements are reviewed.

CBL-VDL MEASUREMENT

The cement bond log (CBL), later combined with the Variable Density (VDL) waveform, has been for many years the primary way to evaluate cement quality. The principle of the measurement is to record the transit time and attenuation of a 20 kHz acoustic wave after propagation through the borehole fluid and the casing wall.

The CBL measurement is the amplitude in mV of the casing first arrival E1 at the 3-ft receiver. It is a function of the attenuation due to the shear coupling of the cement sheath to the casing. The attenuation rate depends on the cement compressive strength, the casing diameter, the pipe thickness, and the percentage of bonded circumference (Fig. 5-3).

The longer 5-ft spacing is used to record the VDL waveform for better discrimination between casing and formation arrivals. The VDL is generally used to assess the cement to formation bond and helps to detect the presence of channels and the intrusion of gas.

It has been shown through experiments that a linear relationship exists between the logarithm of E1 (the amplitude of the first peak of the CBL waveform) and the percentage of pipe circumference not cemented, all other conditions remaining constant (Fig. 5-4).

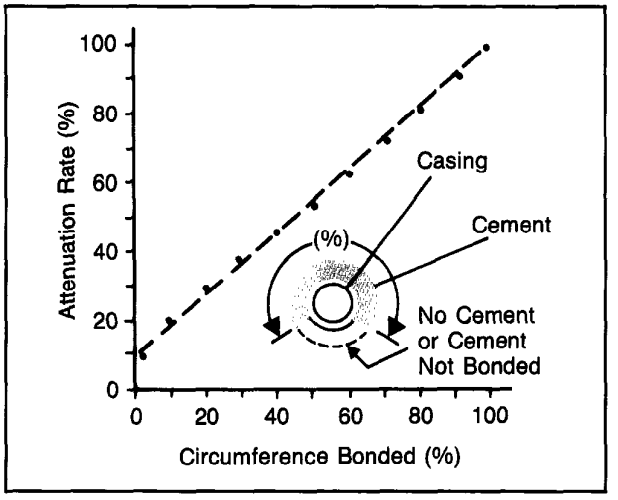

Fig. 5-4—CBL tool response in channels

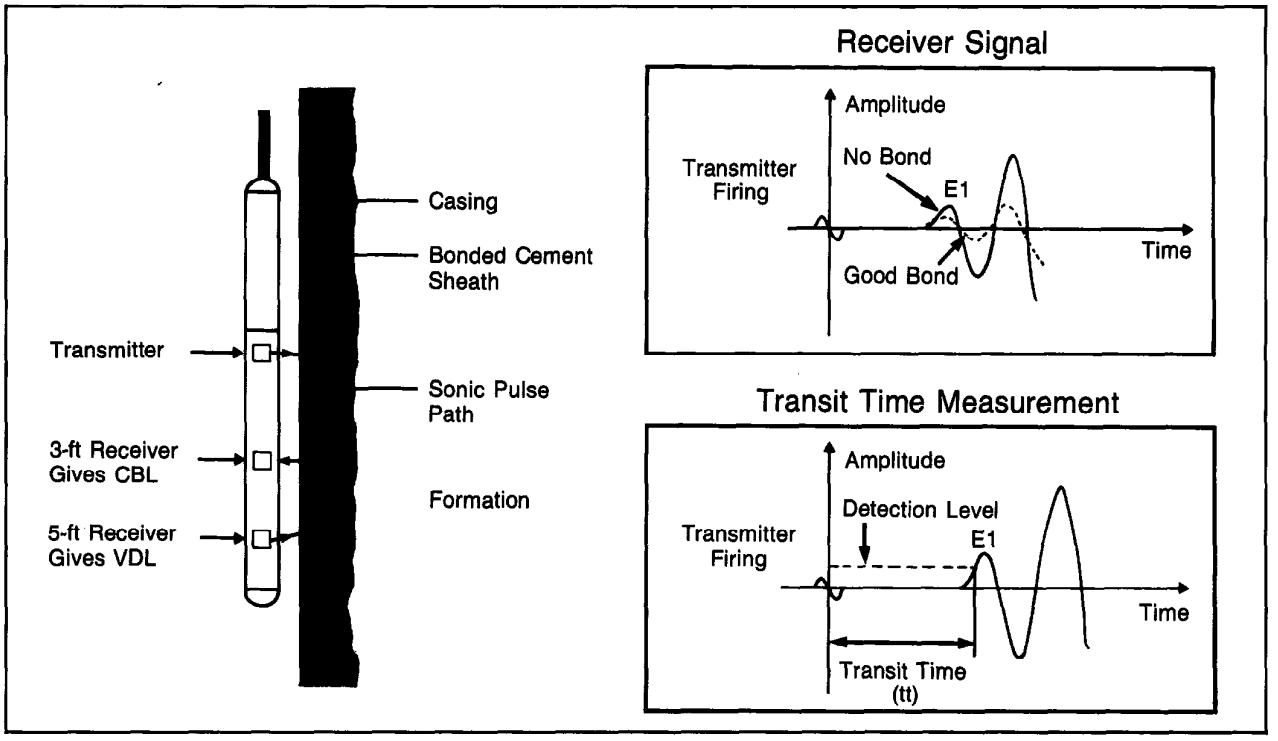

Fig. 5-3—CBL measurement

In addition, when the pipe circumference is fully covered by at least ¾ in. of cement, there is a relationship between E1 amplitude and the cement compressive strength. These relations were used to build the nomogram of Fig. 5-5 which derives from the CBL amplitude in mV and the percentage of pipe circumference bonded by cement. This is also referred to as the "Bond Index".

The determination of E1 amplitude in free pipe and bonded pipe is valid for a tool calibrated in fresh water. Recent field experiments have shown that in other fluids (heavy completion brines, muds) a correction is needed (Fig. 5-6).

A Bond Index of 0.8 or greater over a minimum interval, which varies with the casing diameter (Fig. 5-7), has been found to be a good indicator of hydraulic isolation. This cutoff is used in the Bond Index quicklook presentation. An example of a CBL-VDL log recorded in a 7-in. casing,

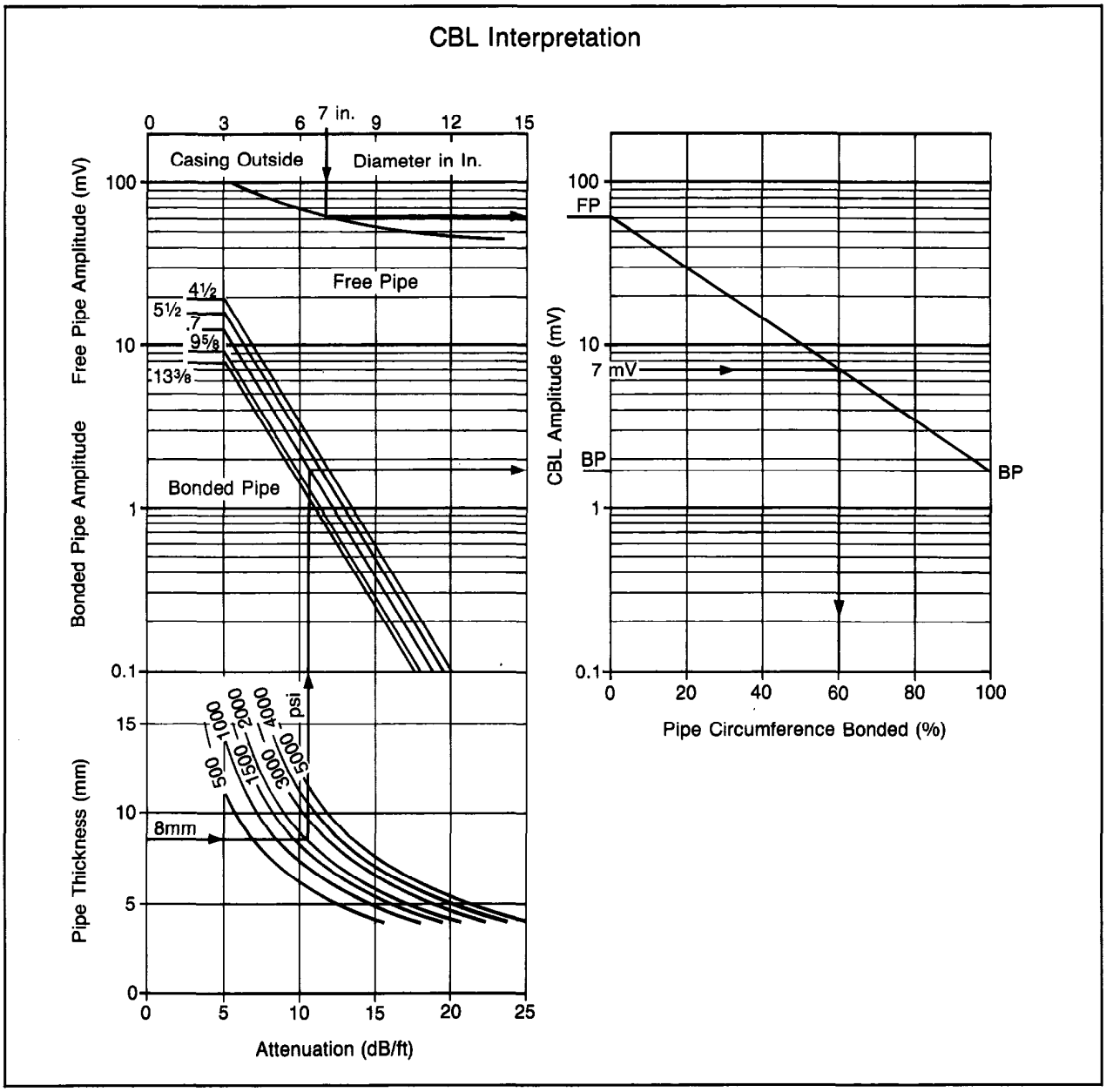

Fig. 5-5—CBL log interpretation nomogram

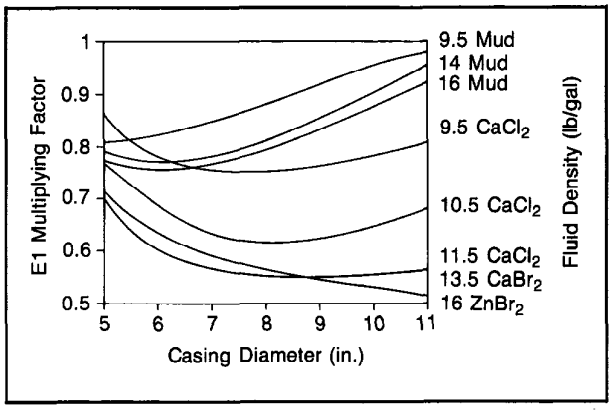

Fig. 5-6—CBL tool response in borehole fluids

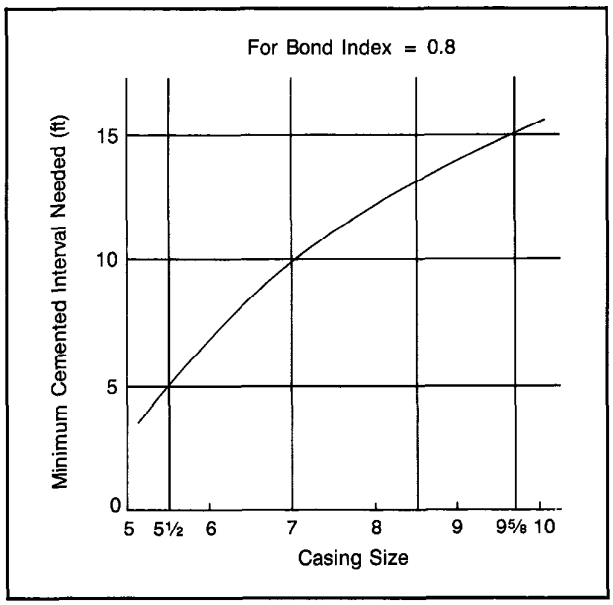

Fig. 5-7—Length of cemented interval needed for zone isolation (for Bond Index = 0.8)

cemented over a sand/shale sequence, is shown on Fig. 5-8.

Zone A is a well bonded section where the Bond Index shows that hydraulic isolation can be expected. Strong formation arrivals confirm a good cement to formation bond. Although the Bond Index is above 0.8, in zones B, C, and D the intervals cemented are too short to guarantee a hydraulic seal.

The Bond Index evaluation is valid when:

- the sonde is properly centralized,
- there is no microannulus,
- there is no change in compressive strength,
- E1 is measured correctly and in particular is not affected by fast formation arrivals or cycle skipping, and

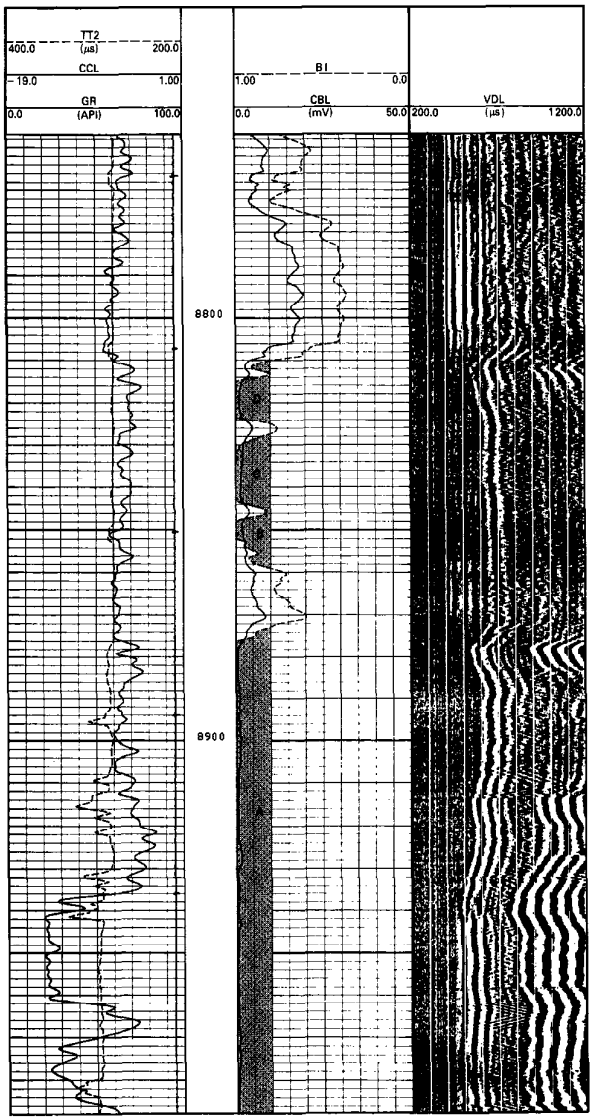

Fig. 5-8—CBL-VDL log with Bond Index

- the correction for borehole fluid impedance and attenuation is correctly done.

These limits have led to the design of two other types of measurements which are described later.

COMPENSATED CEMENT BOND TOOL

The Cement Bond Tool (CBT) is a 2¾-in. diameter sonic tool designed specifically for cement bond logging. The CBT tool features two transmitters and three receivers which provide 2.4-ft and 3.4-ft spacings allowing the computation of a borehole compensated attenuation curve, a 5-ft spacing to

record a VDL waveform, and a short spacing of 0.8 ft which provides a cement bond evaluation in the presence of fast formations affecting the standard 3-ft spacing CBL (Fig. 5-9). The sonde, being light and rigid, can be efficiently centralized by means of in-line centralizers and flex joints, providing a good quality CBL measurement in highly deviated wells.

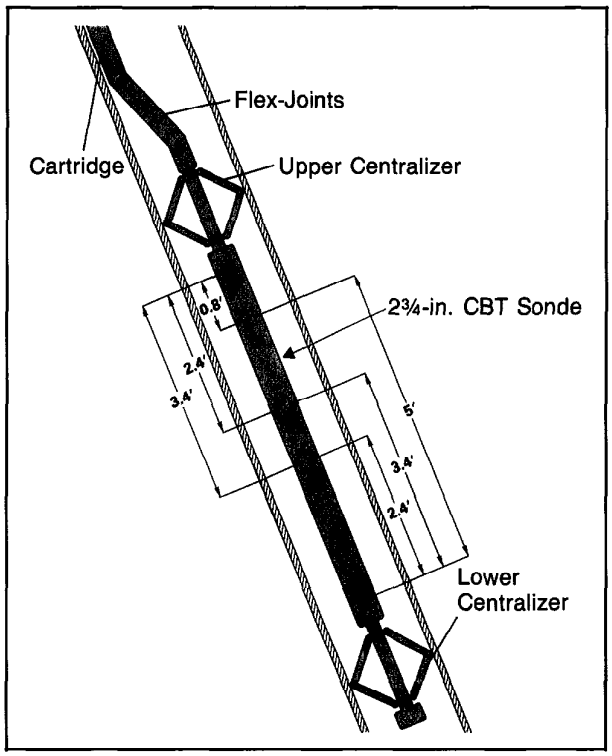

Fig. 5-9—CBT tool and measurement principle

The principle of the measurement consists of recording the two sets of 2.4-ft and 3.4-ft receiver amplitudes and computing their ratio, α. This ratio is then used to compute attenuation.

$$\alpha = \log \frac{A_{U3}\, A_{L2}}{A_{U2}\, A_{L3}}, \qquad \text{(Eq. 5-1)}$$

where:

A_{U2} = amplitude of E1, at receiver 2 from upper transmitter firing

A_{U3} = amplitude of E1, at receiver 3 from upper transmitter firing

A_{L2} = amplitude of E1, at receiver 2 from lower transmitter firing

A_{L3} = amplitude of E1, at receiver 3 from lower transmitter firing

It can be shown that the attenuation rate calculated from this ratio technique is independent of receiver sensitivity, transmitter strength, borehole fluid attenuation, and in addition is much less affected by the eccentralization of the sonde than the conventional CBL log. For comparison with a CBL log, the output of a 2.4-ft receiver can be represented on a CBL-like scale in mV (SA2N) and as an attenuation in dB/ft (CATT). Figure 5-10 shows a CBT-VDL log recorded in the same well as the CBL/VDL log of Fig. 5-8. The attenuation rate (BATT) is expressed in dB/ft. Transit times TT1 and TT2, corresponding respectively to the 2.4-ft and the 3.4-ft spacing, are presented in track 1. The 0.8-ft spacing amplitude (SAG) or the attenuation (SSAT) is useful in the presence of fast formations. The 5-ft VDL from the lower transmitter-receiver R1 waveform is displayed in track 3.

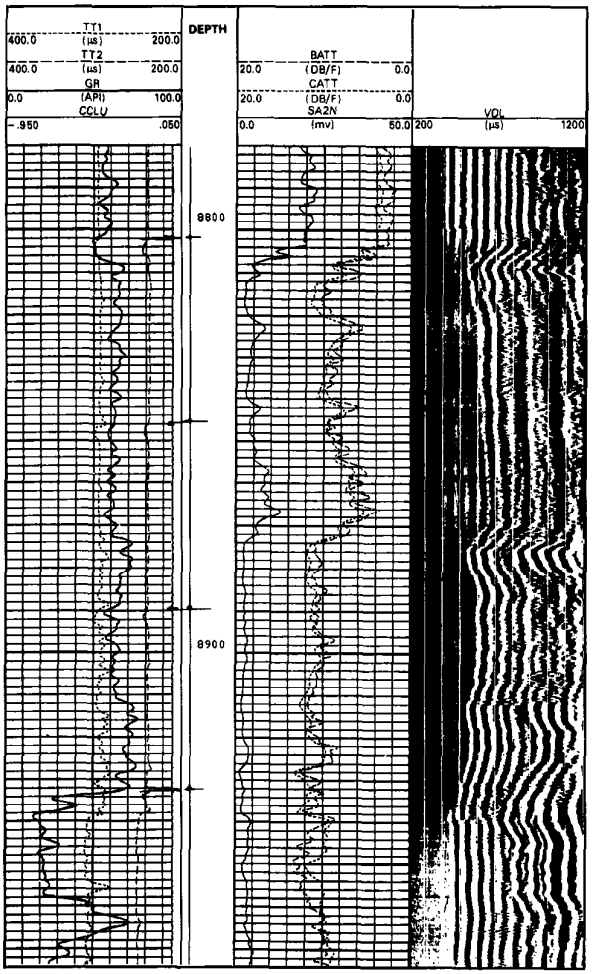

Fig. 5-10—CBT log example

CEMENT EVALUATION TOOL

The Cement Evaluation Tool (CET) was designed to evaluate the quality of cementation in eight directions, 45° apart with a very fine vertical resolution. While conventional cement bond logging tools measure the attenuation of a sonic plane wave propagating axially along the casing, the CET tool uses the casing resonance in its thickness mode. The ultrasonic transducers, both emitters and receivers, emit a short pulse of acoustic energy and receive the echo from the casing.

The transducers are arranged in a 2-ft helical array on the sonde body. A ninth transducer at the bottom of the sonde is used as a reference to measure the transit time and attenuation in the borehole fluid (Fig. 5-11). A built-in pendulum references the radial position of each transducer to the high side of the pipe in deviated wells.

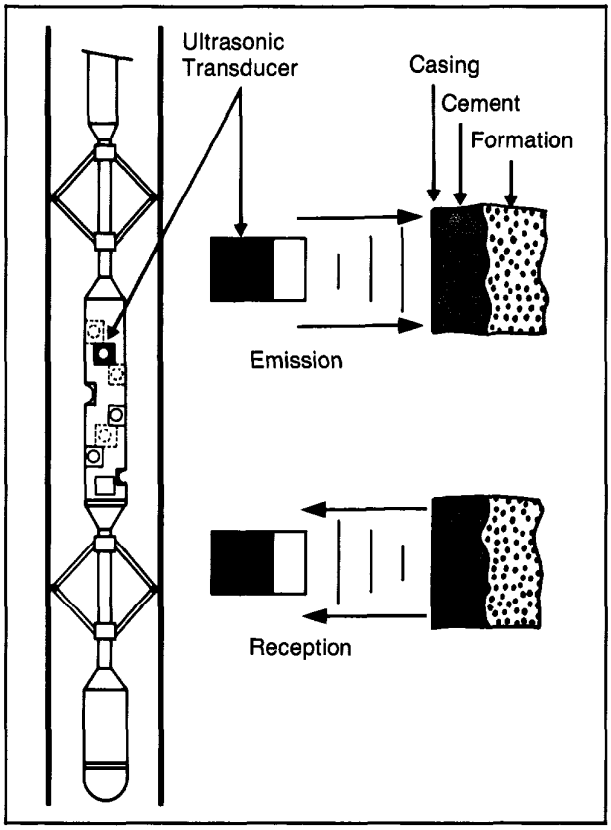

Fig. 5-11—Principle of CET measurement

Each transducer is positioned about 2 in. from the casing wall and repeatedly sends a short high frequency pulse toward the casing. This frequency is a compromise between good impulse response and mud attenuation effects. The transmitter bandwidth, from 270 kHz to 650 kHz, covers the usual range of resonant frequencies for casing thickness from 5 to 15 mm (0.2 to 0.6 in.). The reverberation of energy within the casing is controlled by the local acoustic impedance of the mud column, the casing and the cement, or fluid in each sector of the annulus (Fig. 5-12). The reverberating energy leaks out of the casing to the annulus medium and back to the transducer. The decay of the echo is practically exponential and the rate of decay is controlled by the acoustic impedance of the cement. The transducer response is thus a succession of impulses, separated by twice the travel time through the steel wall. In case of free pipe with mud on both sides, the decay is slow. With cement behind the casing the decay is fast due to the larger acoustic impedance of the cement. The actual transducer response is the convolution of the transducer-emitted pulse plus the impulse response (Fig. 5-13).

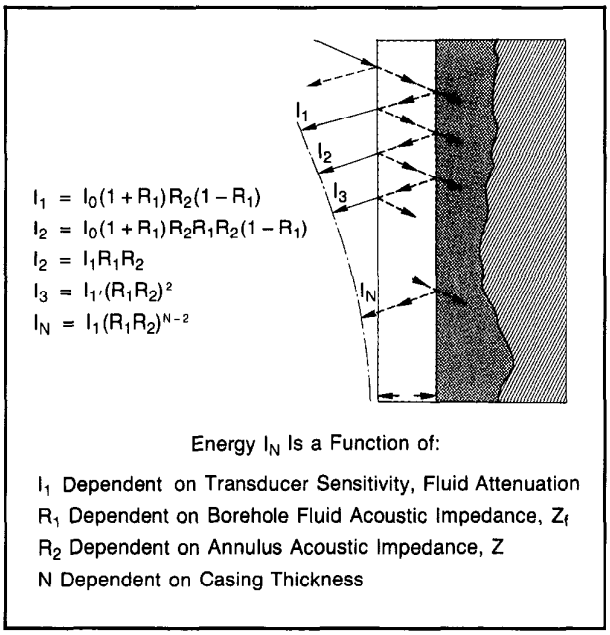

Fig. 5-12—Factors influencing the exponential decay

In order to measure the acoustic impedance of the annulus medium, a gate or window, W_2, is opened to measure the energy of the decaying signal. The attenuation due to the fluid inside the casing is compensated by referring the W_2 amplitude to the peak value of the first echo W_1. Further normalization for casing size is done by reference to the value in free pipe (W_{2FP}) expected when water is on both sides of the casing wall. The final output of each transducer "i" is a value WW_{Ti}. WW_{Ti} is a normalized W_2/W_1 ratio, equal to 1 in free pipe surrounded by water:

$$WW_{Ti} = \left(\frac{W_2}{W_1}\right)_i \times \frac{1}{W_{2FP}} . \qquad \text{(Eq. 5-2)}$$

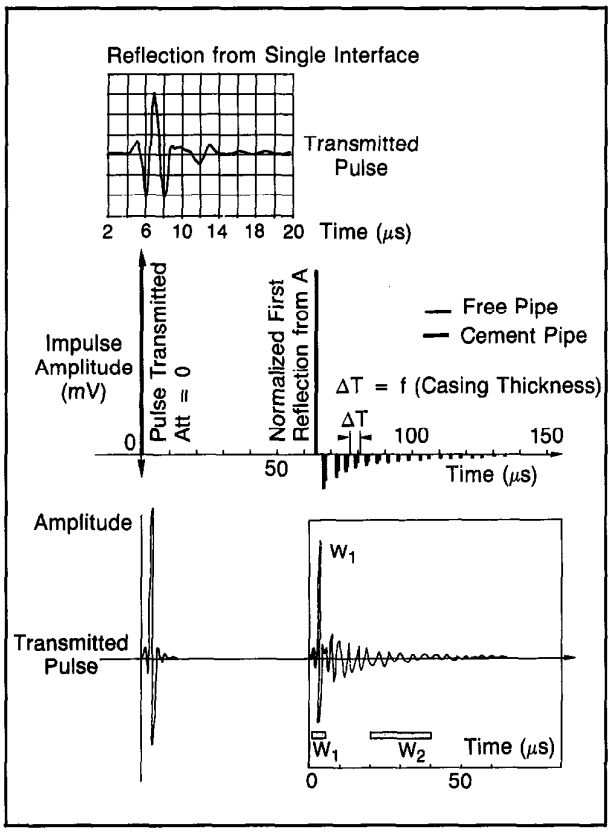

Fig. 5-13—CET transducer response to an interface casing annulus

This output is a function of the acoustic impedance, Z, of the medium behind casing and the casing thickness. The acoustic impedance ($Z = \rho \times v$) of cement has been shown to be empirically related to compressive strength, the relationship being linear for neat cements and foam cements (Fig. 5-14). The above discussion assumed an infinite medium behind the casing. The real case is more complex and three major effects should be considered.

MICROANNULUS

Microannulus is a small water gap between casing and cement generally caused by releasing the pressure inside the casing before the cement is set. Typically a 7-in., 23 lb/ft casing expands by 0.1 mm (0.004 in.) for 1000 psi added pressure. The theoretical and experimental response to this effect is shown on Fig. 5-15 and demonstrates that below 0.1 mm, the CET tool will continue to see cement, as such length is a small fraction of the acoustic wavelength (λ/30). If this gap is water-filled, the hydraulic seal should normally be maintained. However, in gas wells such a gap will not prevent gas migration.

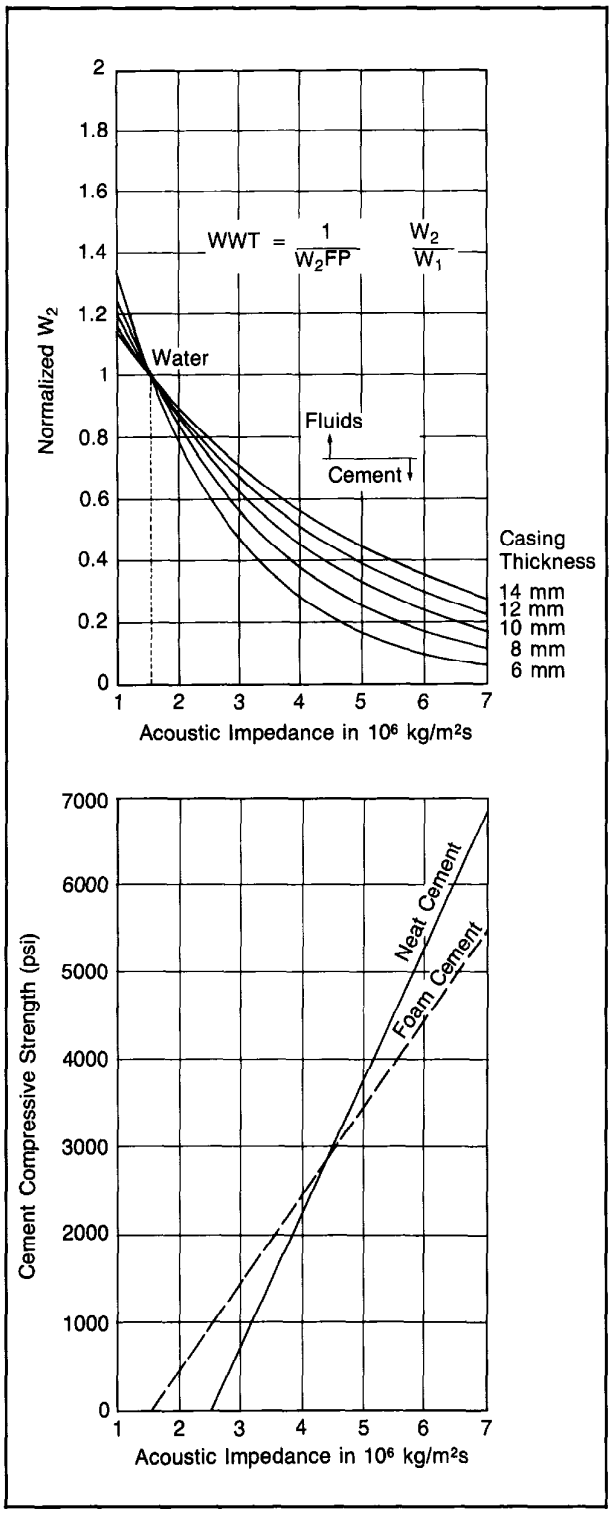

Fig. 5-14—Relationship between W_2, Z, and compressive strength

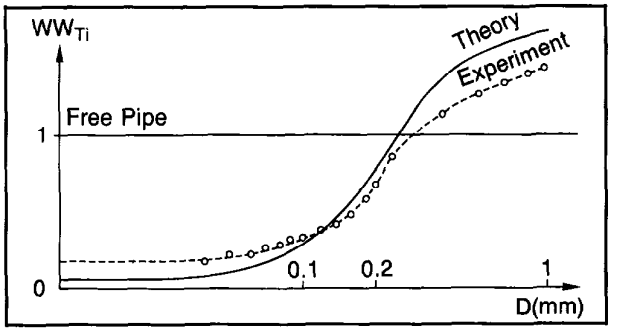

Fig. 5-15—Relationship between normalized W_2 (WW_{Ti}) and thickness of microannulus

THIRD INTERFACE REFLECTIONS

The typical thickness of the cement sheath is 25 mm (1 in.). Part of the acoustic energy is transmitted through the cement sheath. If the interface between cement and formation offers a high reflection coefficient, part of the energy will be reflected back to the transducer and will superimpose on the normal energy, giving a nonexponential decay and increasing the value of W_2, which leads to an apparent decrease in cement quality. This is typically the case of well cemented casings, in thin annulus, in front of in-gauge tight formations, or in double casing strings. To detect these spurious reflections, a third measure gate W_3 is opened shortly after the end of W_1 and has a short duration to avoid being affected by the reflections (Fig. 5-16). The W_3 measurement is normalized by W_1 and a constant W_{3FP} in the same way as W_2. The combination of W_2 and W_3 measurements is used to detect a nonexponential decay.

The presence of third interface reflections is coded on the log and implies little attenuation through the annulus, thus the presence of high quality cement. This concept is enhanced by a crossplot of W_2 versus W_3 (both normalized to read 1 in free pipe). Computer simulations of the tool response have shown that the relationship between W_2N_i and W_3N_i, in the case of an infinite annulus medium, is independent of that medium, the borehole fluid, the casing size, and its thickness. This relationship between W_2N_i and W_3N_i is represented on Fig. 5-17 and has been verified in laboratory and on field data. On this graph, vertical departures [W_2N_i higher than $F1$ (W_3N_i)] occur if echoes from the cement formation interface are received by the transducer. The acoustic impedance of the annulus medium can therefore be obtained from W_2 or W_3 information. Window 2 integration is normally used due to its better resolution, but whenever spurious reflections are detected, Window 3 is retained as it is not affected.

From the estimation of the acoustic impedance it is then fairly simple to locate the presence of cement in the annulus,

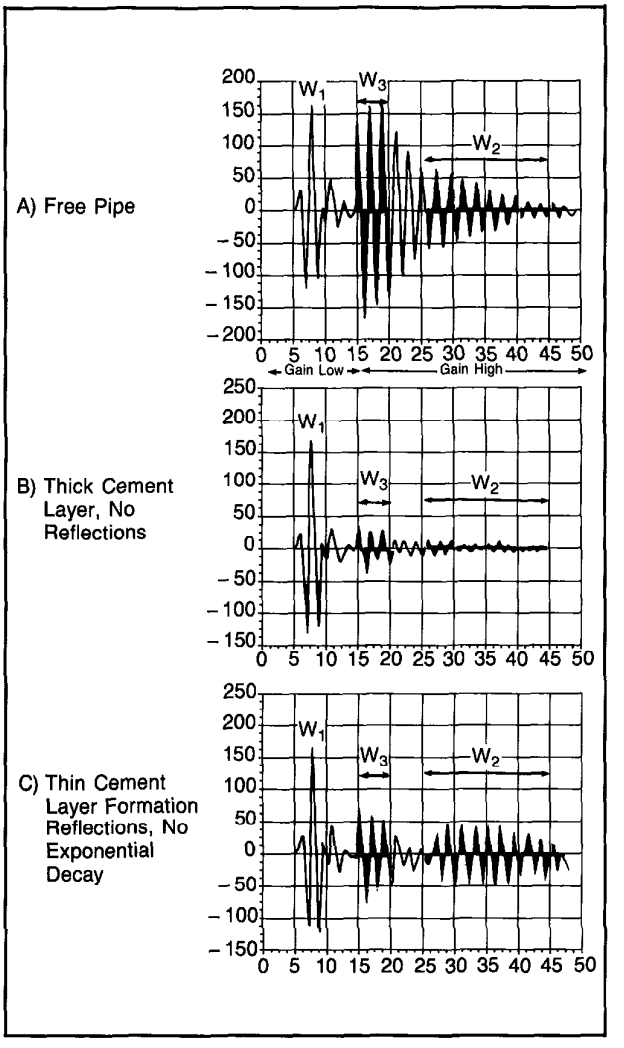

Fig. 5-16—Detection of reflections

whatever the type of cement. Some typical acoustic impedances are listed in Table 5-1. It shows that a mud of density 1.6 gm/cc (13.3 lb/gal) has a Z of 2.4 x 10^6 kg/m^{2}s, which is below that of poor quality cement. Since light cements such as foam, microspheres, or pozzolana cements are usually associated with light drilling fluids (of lower Z), their discrimination is also possible.

GAS EFFECT

Gas under pressure can be identified as it has an acoustic impedance of about 0.1 x 10^6 kg/m^{2}s. We have seen previously that under certain conditions, the cement slurry can be invaded by gas during the curing phase. The crossplots of CBL attenuation versus the CET outputs W_2N and W_3N

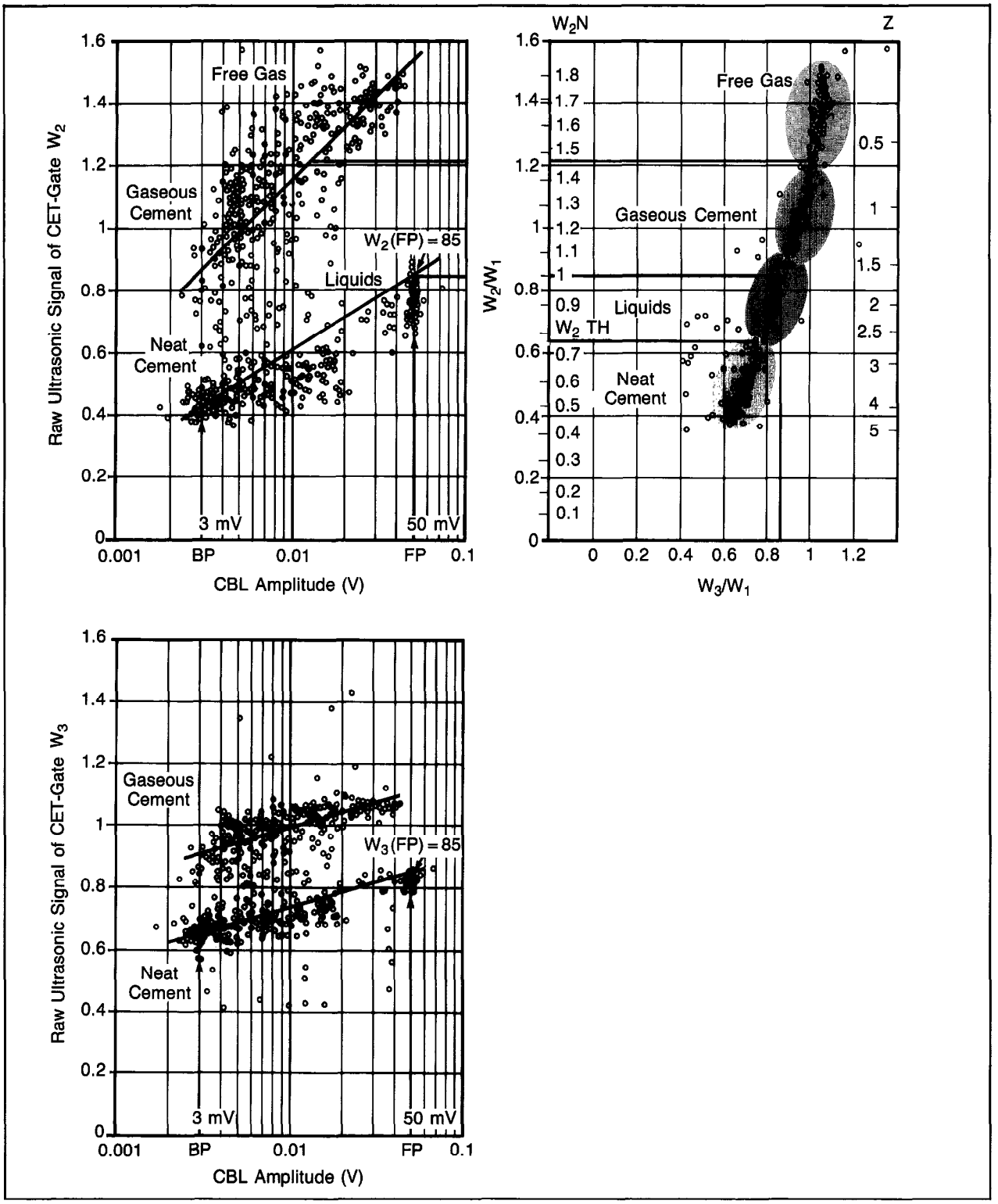

Fig. 5-18—CET response in gas

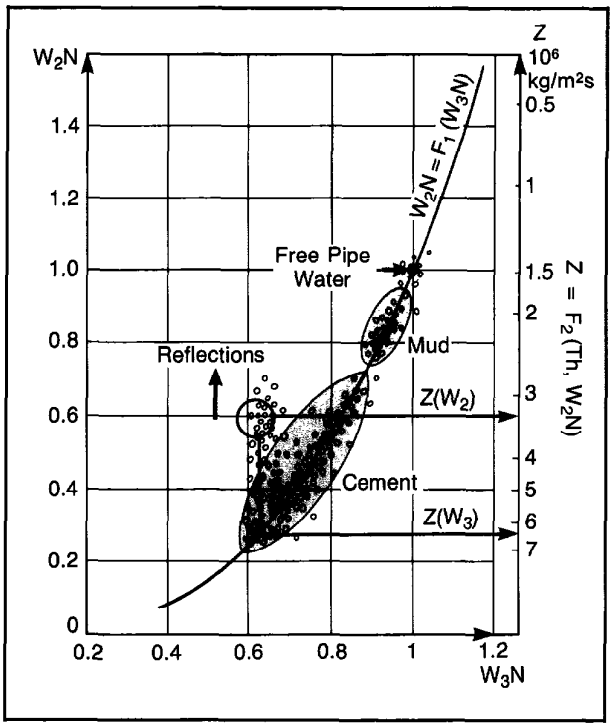

Fig. 5-17—Relationship between W_2N and W_3N

Medium	Acoustic Impedance Z(10^6 kg/m²s)
Gas	0.1
Fresh Water	1.5
Brine (12 lb/gal)	2.2
Mud (14 lb/gal)	2.4
Cement Slurry (not set)	2.6
Cement (CS = 4000 psi)	5.0
Sandstone	7.0
Steel	≃40

Table 5-1—Acoustic impedance of common materials

show (Fig. 5-18) that free gas can be distinguished from cement invaded by gas. The latter provides mechanical support to the pipe but is permeable to gas. The previous analysis is the basis of the CSU wellsite interpretation program (CEQL) which will be discussed later in this section.

FIELD EXAMPLES

An example of a CET log is shown on Fig. 5-19. It has been recorded in the same well as the CBT log of Fig. 5-10 and shows clearly a zone of free pipe above a well cemented section. In track 1, the following data is presented:

- CALU, the average of the four high-resolution diameters from the eight transducer transit times
- OVAL, the ovalization or difference between the largest and smallest diameters
- ECCE, the eccentralization of the sonde as a quality-control check
- CCLU, an ultrasonic casing collar locator derived from CALU
- GR, a standard gamma ray log for correlation.

Track 2 shows a quantitative interpretation of the cement quality:

- CSMX, the maximum compressive strength shown by two consecutive transducers (averaged over 2 ft)
- CSMN, the minimum compressive strength shown by two consecutive transducers (averaged over 2 ft)
- WWM, the mean ratio over 360° of the eight WW_{Ti} (which should be close to 1 in free pipe). It may be as low as 0.8 in case of heavy mud in the annulus.

It is also possible to output directly an averaged acoustic impedance and an averaged cement compressive strength.

Track 3 is an image of the cement placement in the annulus. Low WW_{Ti} (high compressive strength cement) is displayed in black and high WW_{Ti} (fluid or gas) in white. Different shades of gray cover intermediate values. It is possible to orient the display such that the low side of the pipe is at the center of the track. On the far right, eight small tracks are used to display codes of third interface reflections (black bars) and gas detection flags (thin lines). The relative bearing curve is superimposed to indicate the position of Transducer 1 with respect to the low side of the casing.

The evaluation of the cement quality with the CET tool is very often enhanced by a study of the openhole logs, in particular caliper logs to spot washouts and Litho-Density-CNL logs to predict gas problems.

The log example in Fig. 5-20 shows an acute channeling problem. The sonde rotation has been corrected to show the low side of the pipe at the center of the display. A channel spiraling around the casing 11 times in 100 ft is apparent. A look at the LDT-CNL log and in particular at the $\Delta\rho$ curve gives the explanation. The correction $\Delta\rho$ is very sensitive to accumulations of mudcake and it shows that the hole had a corkscrew shape. Since the mudcake could not be swept efficiently by the preflush, this unusual channel was created in the cement column.

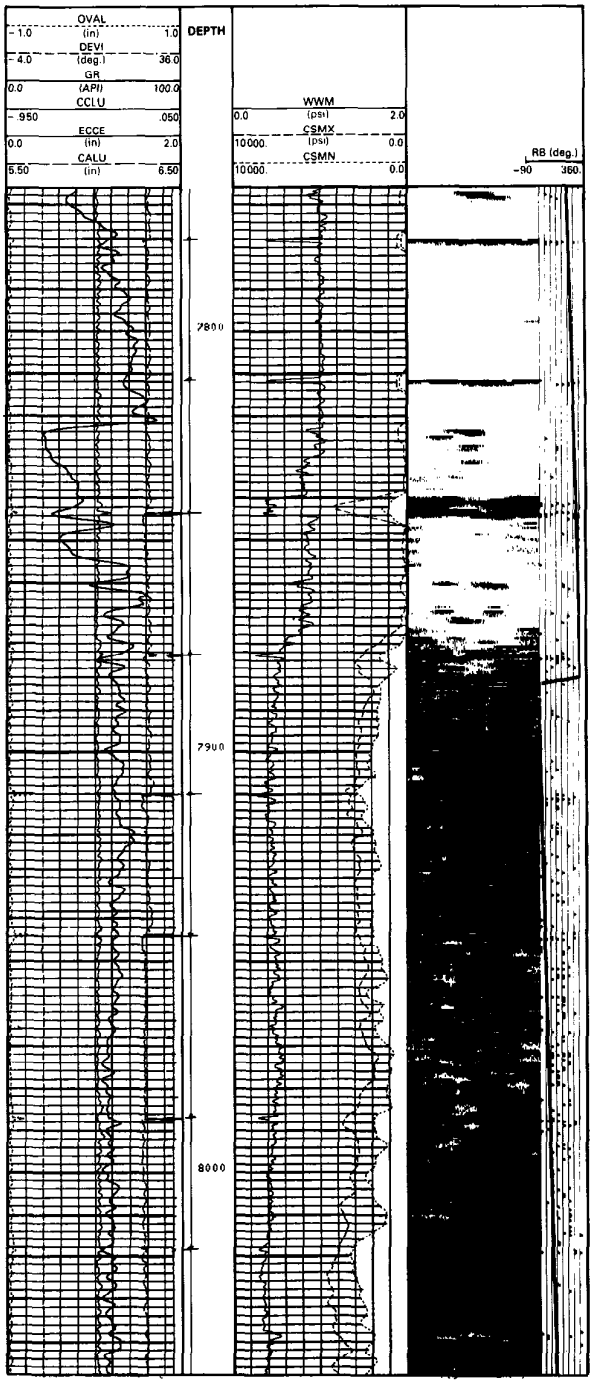

Fig. 5-19—CET log over cement top section

CEMENT EVALUATION PROGRAM

In many cases the objectives of cement quality evaluation are to identify the causes of poor cementing jobs and evaluate repair possibilities. Often both CET and CBL (or CBT) logs are required since the CET and CBL-type measurements have different responses in the presence of:

- microannulus
- thin cement sheaths
- gas or air
- fast formations
- double strings of casing
- heavily corroded casings
- inside deposits (cement, rust), and
- very attenuative muds.

In many ways the two measurements complement each other. The need for an interpretation method using both measurements has been identified and a computer interpretation program (CEQL) is now available at the wellsite.

The principle of the CEQL program is to use the CET interpretation model to map the fluids and solids in the annulus between casing and formation and to provide compatible outputs to merge the CET and CBL-VDL data. The conventional CET log presentation is sensitive to the validity of the empirical relationship between W_2N and compressive strength and it does not allow a rapid discrimination between acceptable and unacceptable cement quality. A sharper cutoff is needed.

The CEQL approach makes a clear cut between the presence of solids (cement) and fluids (liquids or gas) and provides an independent CBL-VDL interpretation to confirm or complement the analysis. Since the CET tool signal can be converted accurately to acoustic impedance once the casing thickness is known, the computed impedance, Z, is used to define the medium behind casing through the interpretation model shown in Fig. 5-21. Using 10^6 kg/m^{2}s as the unit of impedance, $Z = 2.6$ corresponds to both a very heavy mud and a neat cement of less than 500 psi compressive strength. It is usually chosen to discriminate cement from liquids. However, this threshold has to be reduced (down to 2.0) when dealing with low acoustic impedance cements such as foam or light cements. This threshold is called Z_{CEM}.

It was shown previously that the CET allows the detection of gas and that, under certain conditions, a low CBL amplitude demonstrates the presence of cement invaded by gas. The passage from gaseous cement to free gas usually occurs around an acoustic impedance of 0.1 to 0.3 unit.

This second threshold is called Z_{GAS}. To determine if a measurement of acoustic impedance between Z_{GAS} and Z_{CEM} should be interpreted as a liquid (brine or mud) or a gaseous cement, a "gas logic" is used which looks at the statistical

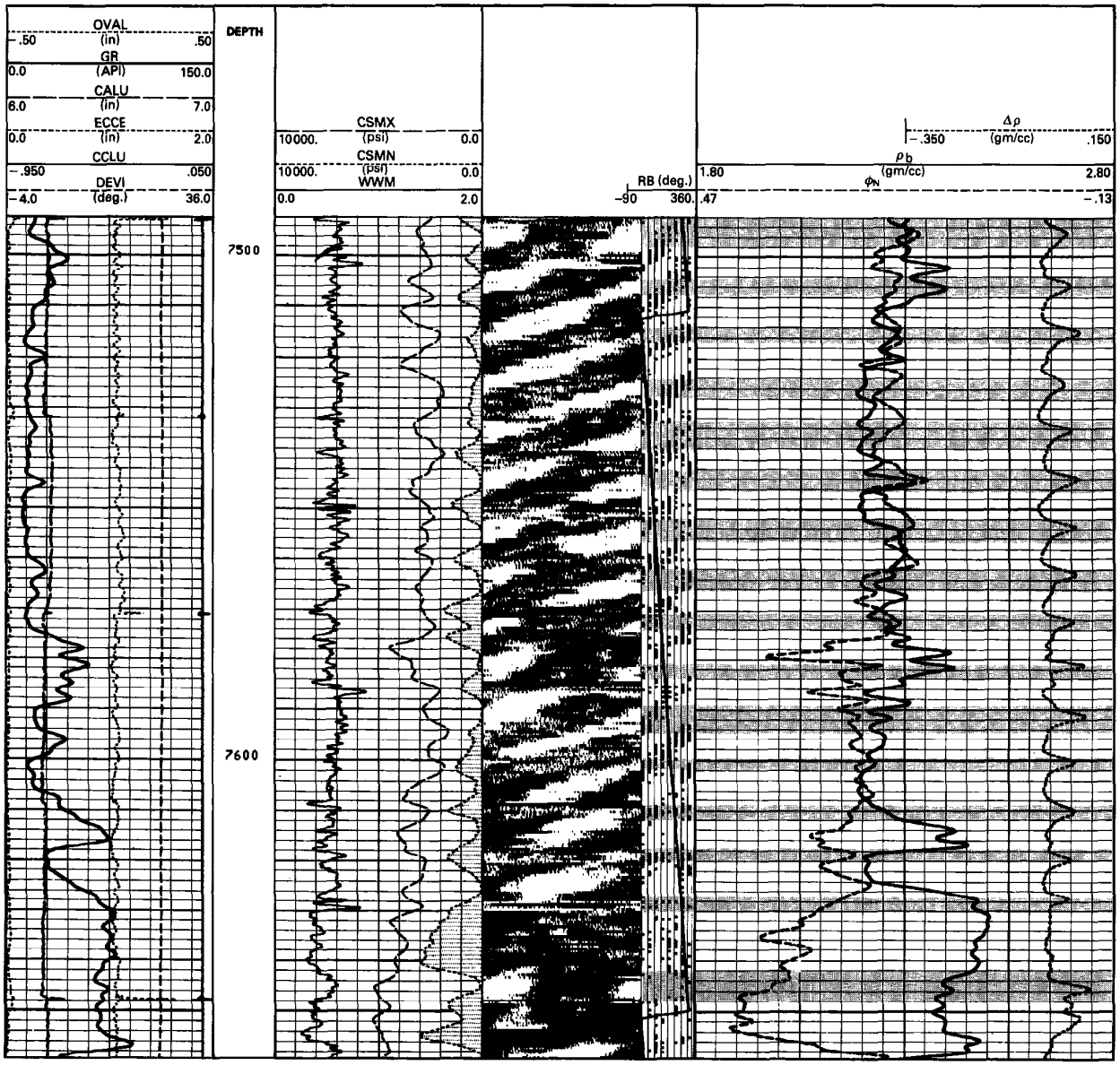

Fig. 5-20—Example of cement channeling

occurrence of gas detection on nearby transducers and switches the gaseous cement coding above a certain threshold (gas ratio GRAT). These thresholds then allow a simple coding of the eight individual transducer responses:

- black if $Z > Z_{CEM}$ (CEMENT)
- white if $Z_{CEM} > Z > Z_{GAS}$ and GAS LOGIC NEGATIVE (LIQUID)
- light gray if $Z < Z_{GAS}$ (GAS)
- dark gray if $Z_{CEM} > Z > Z_{GAS}$ and GAS LOGIC POSITIVE (GASEOUS CEMENT).

The computation of compressive strength, *CS*, is done using the empirical relationships between *Z* and *CS* for neat or light cements, but it is done only for transducers detecting cement.

From the threshold discrimination, derived curves are expressed in percentage of pipe circumference (Fig. 5-22):

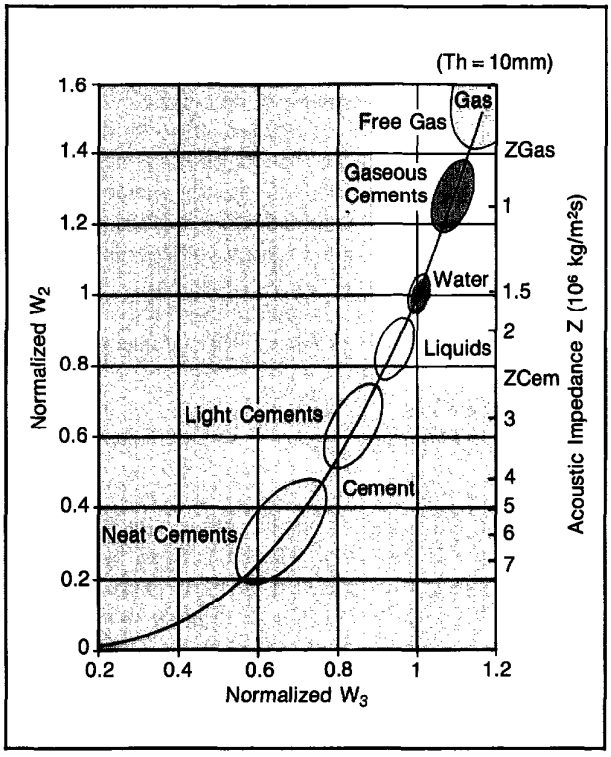

Fig. 5-21—CET interpretation model

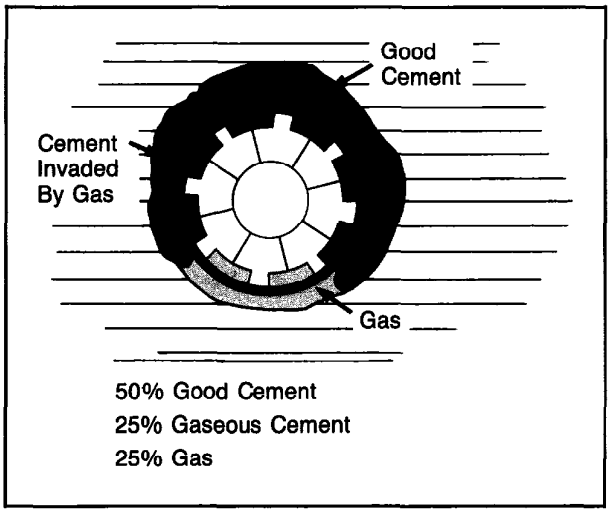

Fig. 5-22—Casing circumference mapping

- The percentage of acceptable cementation is obtained by counting radially the number of transducers that show a response such that $Z > Z_{CEM}$ and dividing that number by eight.
- The percentage of free gas at casing interface is obtained in a similar way for $Z < Z_{GAS}$.

The complement (up to 100%) will either be the percentage of liquid (or unset slurry) in the "normal logic" or the percentage of gaseous cement in the "gas logic".

The CBL log can also be interpreted in terms of percentage of well-bonded pipe circumference if it is assumed that cement compressive strength does not vary much in the same well over a given interval. In normal conditions, when gas is absent and none of the conditions listed previously are present, the CBL Bond Index curve should overlay on the CET curve representing the percentage of acceptable cement. When gaseous cement is present, the CBL Bond Index will overlay the CET curve representing the sum of good cement and gaseous cement percentages. In summary, the difference in reading between the CBL and CET curves allows for the solution to some common evaluation problems:

- gas detection and discrimination of gas-filled cement from impermeable cement,
- detection of miroannulus,
- correct cement evaluation in front of fast formations,
- detection of thin cement sheaths as the CET log is almost insensitive to cement thickness, and
- backup in adverse conditions (local deposits, corrosion).

The VDL display is an important input which can either prove or disprove the resultant hypothesis and is the only indicator of cement to formation bonding.

Figure 5-23 shows a typical 3-track CEQL presentation. Track 1 contains the cement map defined from the eight transducers with a black and white coding (no gas in this case) defined with the threshold $Z_{CEM} = 2.6$.

The left-hand side column is used to represent the occurrence of third interface reflections on a map of the eight transducers. Strong reflections are coded black and no reflections, white. The bottom interval shows large formation reflections in front of a carbonate section.

Track 2 shows on the right-hand side the two percentage curves from the CET and the CBL tool, which overlay most of the interval considered. The pipe is well cemented from bottom to 10,070 ft, then a small channel starts developing from 10,042 ft upwards, enlarging at 10,005 ft.

Track 3 contains four log quality control curves. At each depth the computation of the median W_{2L} of the three smallest W_2N_i is made as well as the median W_{2H} of the three largest W_2N_i. The same is done for W_3N_i data to obtain W_{3L} and W_{3H}. The curves W_{2L} and W_{2H} should respectively overlay with the curves $F1(W_{3L})$ and $F1(W_{3H})$ to verify the quality of the normalization. They should read close to 1 in free pipe. Departure is expected over sections with formation reflections (see bottom interval). The average acoustic

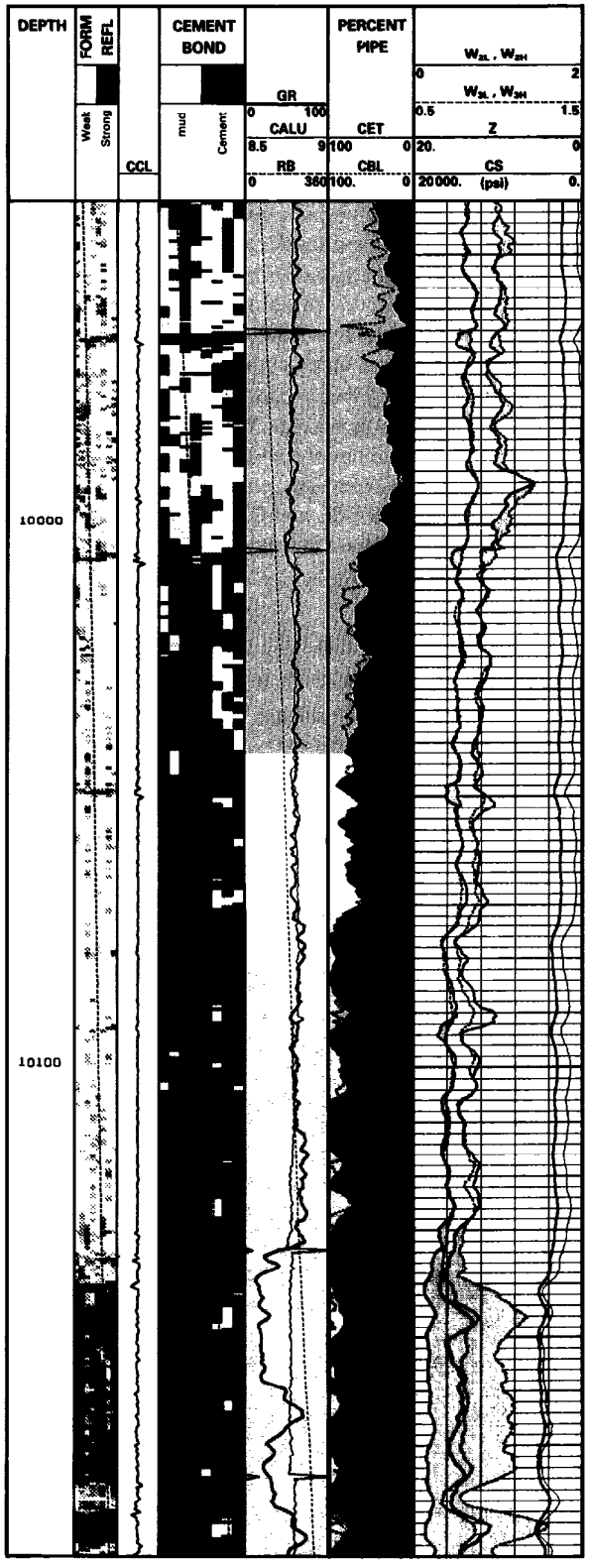

Fig. 5-23—CEQL display presentation

impedance of cement is represented on the Z curve computed from W_{2L}. The compressive strength of cement is shown as CS on a reduced scale of zero to 20,000 psi.

Figure 5-24 shows an example of microannulus. The CET cement map over interval A (8200 to 8240 ft) indicates a well cemented casing but the CBL log shows practically free pipe. This type of discrepancy is usually characteristic of a microannulus. Pass 2, recorded while pressuring the casing to 1000 psi, shows a good agreement between CET and CBL curves and confirms the interpretation.

Figure 5-25 illustrates the application of the CEQL program to a gas invasion problem. The parameters chosen were:

- cement threshold = 2.60,
- gas threshold = 0.20, and
- gas ratio = 30%.

The gas logic has been switched on over two intervals, 8500 to 8518 ft and 8420 to 8468 ft. This is confirmed by the LDT-CNL openhole logs presented in track 4. There is a good correlation between the two top gas-bearing sands and the indications of gas and gaseous cement on the CEQL display. This indicates that the slurry did not prevent gas inflow except over the bottom gas sand below 8524 ft, possibly at a lower pressure. Some gas migration can also be seen across a small shale interval at 8452 to 8462 ft, although the VDL (from the CBT) shows more cement. From the CET, it is interpreted as gas-invaded cement.

The larger shale intervals above 8424 ft and between 8464 and 8500 ft are shown as well cemented by both the CET and the CBT. The VDL displays some formation arrivals and confirms the good hydraulic seal between the two gas sands.

Finally, the CEQL processing can be used to perform the quality control of a remedial cementing job. The CEQL display on the left-hand side of Fig. 5-26 shows two intervals of poor cement quality, A and B, in front of producing sands as shown by the openhole logs. It is likely that this poor cement quality is of pressure origin as it is very localized and adjacent intervals are well cemented.

The lack of cement was confirmed by circulation obtained between the two perforations 1 and 2. Cement was squeezed and a second CET-CBL run proved the success of the repair job as shown by the CEQL display on the right side of Fig. 5-26.

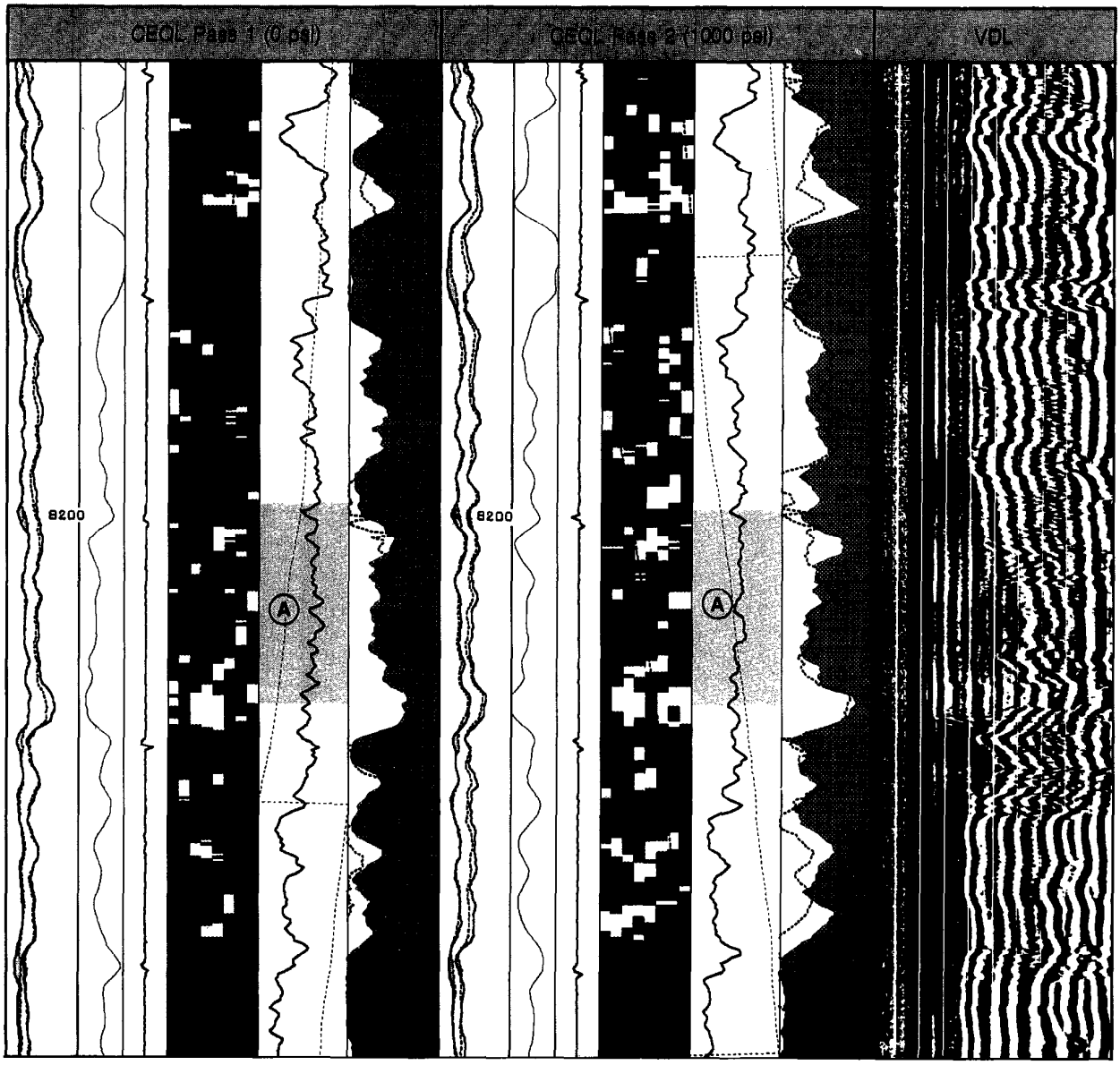

Fig. 5-24—Example of microannulus

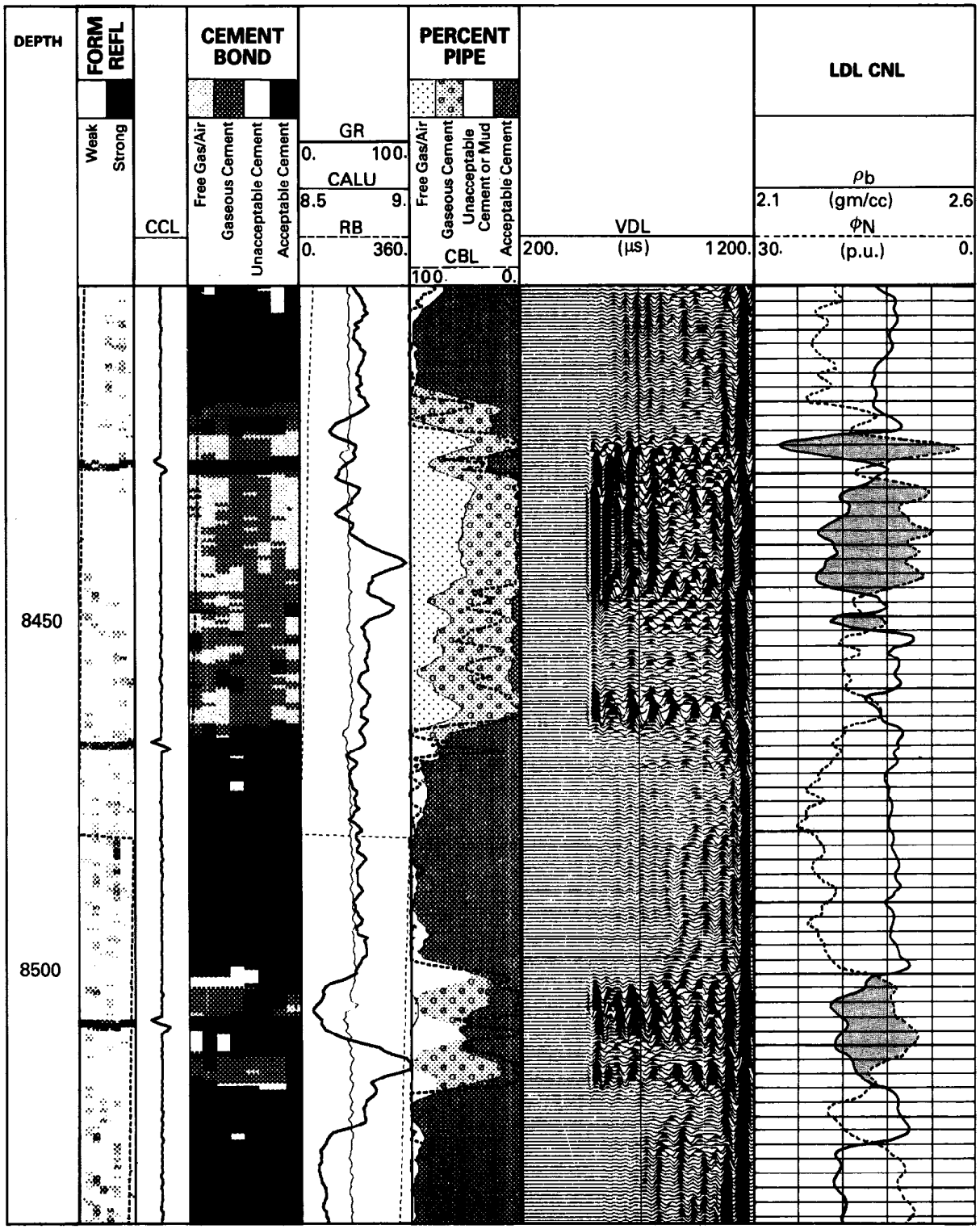

Fig. 5-25—Example of gas invasion

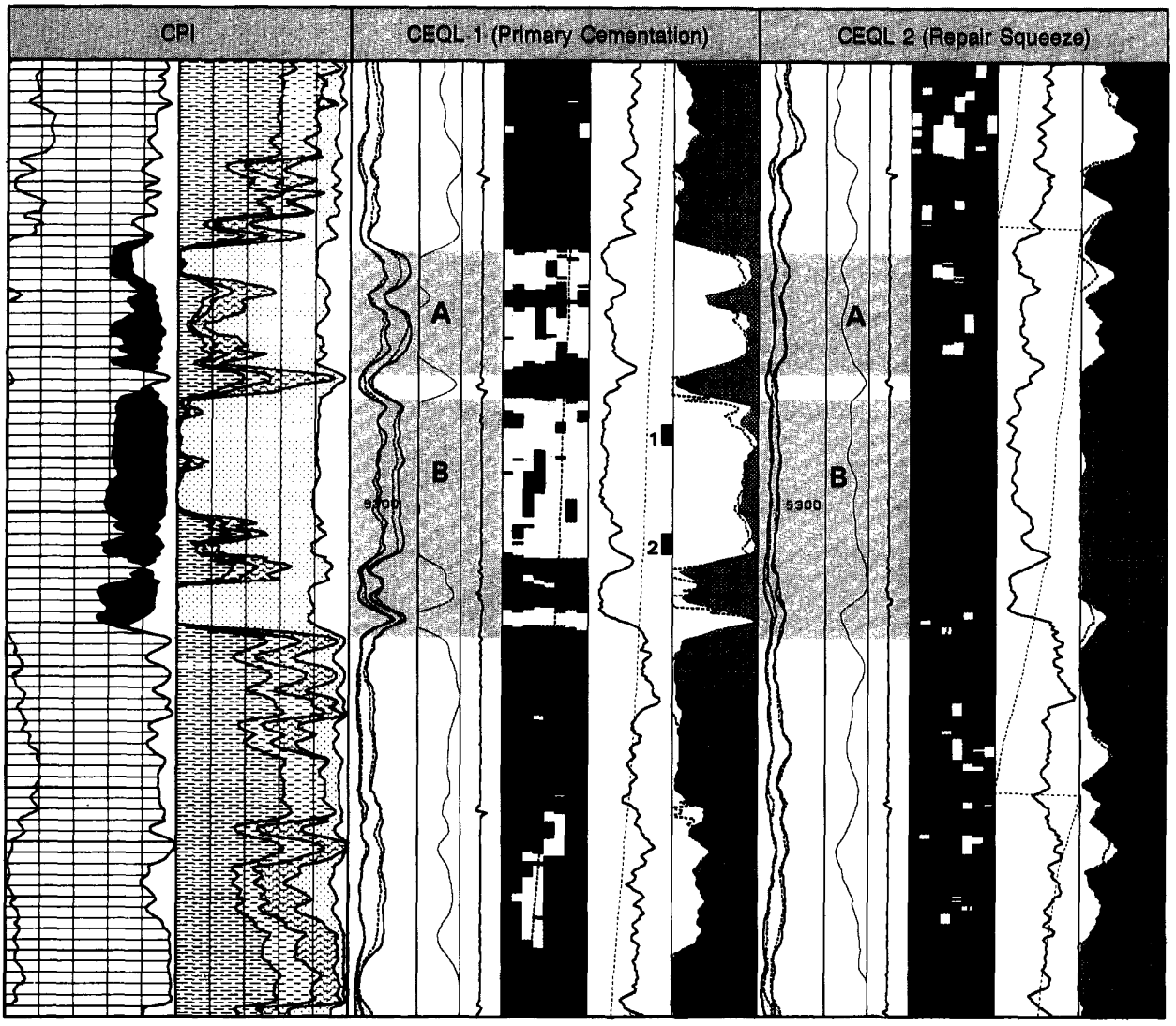

Fig. 5-26—CEQL logs before and after squeeze job

REFERENCES

Brown, H.D., Grijalva, V.E., and Raymer, L.L.: "New Developments in Sonic Wavetrain Display and Analysis in Cased Holes," *The Log Analyst* (Jan.-Feb., 1971).

Carter, L.G. and Evans, G.W.: "A Study of Cement-Pipe Bonding," *JPT* (Feb., 1964).

Catala, G.N., Stowe, I.D., and Henry, D.J.: "A Combination of Acoustic Measurements to Evaluate Cementations," paper 13139 presented at the 1984 SPE Annual Technical Conference and Exhibition, Houston, TX.

Cementing Technology, Dowell Schlumberger, Houston (1984).

Cheung, P.R. and Beirute, R.: "Gas Flow in Cements," paper 11207 presented at the 1982 SPE Annual Technical Conference and Exhibition, New Orleans, LA.

Cooke, C.E., Jr., Kluck, M.P., and Medrano, R.: "Field Measurements of Annular Pressure and Temperature During Primary Cementing," *JPT* (August, 1983).

Dumont, A., Patin, J.B., and le Floch, G.: "A Single Tool for Cement Evaluation and Corrosion Analysis," paper 13140 presented at the 1984 SPE Annual Technical Conference and Exhibition, Houston, TX.

Fredrickson, A.G. and Bird, P.B.: "Non-Newtonian Flow in Annuli," *Industrial and Engineering Chemistry* (March, 1958) **2**, No. 3.

Froelich, B., Pittman, D., and Seeman, B.: "Cement Evaluation Tool - A New Approach to Cement Evaluation," paper 10207 presented at the 1981 SPE Annual Technical Conference and Exhibition, San Antonio, TX.

Grosmangin, M., Kokesh, F.P., and Majani, P.: "The Cement Bond Log - A Sonic Method for Analyzing the Quality of Cementation of Borehole Casings," paper 1512 presented at the 1960 SPE Annual Technical Conference and Exhibition, Denver, CO.

Iyoho, A.W.: "An Accurate Shot-Flow Model for Non-Newtonian Fluid Flow Through Eccentric Annuli," paper 9447 presented at the 1980 SPE Annual Technical Conference and Exhibition, Dallas, TX.

Jutten, J., Guillot, D., and Parcevaux, P.: "Cement Job Evaluation Through Cased Hole Log Interpretation," *Drilling and Pumping Journal* (April, 1988) 41.

Leigh, C.A., Finlayson, C.G., van der Kolk, C., and Staal, J.: "Results of Field Testing of the Cement Evaluation Tool," 1984 SPWLA Logging Symposium, New Orleans, LA.

Log Interpretation Charts, Schlumberger Educational Services, Houston (1989).

McLean, R.H., Manry, C.W., and Whitaker, N.W.: "Displacement Mechanics in Primary Cementing," paper 1488 presented at the 1966 SPE Annual Technical Conference and Exhibition, Santa Barbara, CA.

Nayfeh, T., Wheelis, W., and Leslie, H.: "The Fluid Compensated Cement Bond Log," paper 13044 presented at the 1984 SPE Annual Technical Conference and Exhibition, Houston, TX.

Nigerian Well Evaluation Conference, Schlumberger, Nigeria (1985).

Nwokoye, D.N.: "Prediction and Assessment of Concrete Properties from Pulse-Velocity Tests," *Magazine of Concrete Research* (March, 1973) **25**, No. 82.

Parcevaux, P., Piot, B., and Vercamer, C.: "Annual Flow: A Hazard Free Solution," *Petrol Information* (1983).

Parcevaux, P.: "Pore Distribution of Portland Cement Slurries at Very Early Stage of Hydration," *Journal of Cement and Concrete Research* (1984) **14** No. 3.

Pardue, G.H., Morris, R.L., Gollwitzer, L.H., and Moran, J.H.: "Cement Bond Log - A Study of Cement and Casing Variables," *JPT* (May, 1963).

Rao, P.P., Sutton, D.L., Childs, J.D., and Cunningham, W.C.: "An Ultrasonic Device for Nondestructive Testing of Oilwell Cements at Elevated Temperatures and Pressures," *JPT* (Nov., 1982).

6 Corrosion Evaluation of Casing and Tubing

Wireline evaluation services may be used to save money throughout the life of a well. It has been estimated that 1 % of the total operating costs of the petroleum industry could be saved by correct application of existing corrosion protection technology. Corrosion control is particularly cost effective for deep or remote wells, those expected to have a long lifetime, or for wells producing CO_2 or H_2S.

By predicting problem areas, corrosion prevention budgets may be spent wisely. It is worthwhile to monitor for weak points, since corrosion or damage prevention is cheaper than repair. Finally, precise identification of failure can be used to minimize repair expense.

Electrochemical corrosion can occur when a metal is immersed in a conductive medium (Fig. 6-1). Galvanic or bimetallic corrosion occurs when two metals in contact are immersed in the same fluid (the most obvious example being a battery in which the two metals are very different). Slight differences between casing joints, defects, and impurities can also trigger galvanic action. Concentration cell corrosion occurs when the same metal is immersed in a fluid, the composition of which varies from one point to another. The change in composition may be due to differences in pH or in the concentrations of dissolved gas (e.g., oxygen) or dissolved salts. Galvanic and concentration cells exist on scales ranging from kilometers to millimeters or smaller. Other corrosion processes which can cause problems downhole are stress corrosion, hydrogen embrittlement, and chemical corrosion.

In addition, noncorrosive metal loss can be caused by abrasion from produced fluids and solids or by mechanical wear. The nature of corrosive attack can be relatively uniform, as in general corrosion, or highly localized as in pitting, where penetration can be very rapid.

Hydrogen sulphide, carbon dioxide, oxygen, and chloride ions are known to promote corrosion, though the mechanisms by which they act are very different. The effects of corrosion can be reduced (and in some cases eliminated) by using resistant metals, inert protective coatings, or by introducing chemical inhibitors into the fluid. Corrosion can be controlled by electrochemical means via the application of cathodic protection. This can be achieved by placement of sacrificial anodes, but more commonly a DC current is impressed on the casing from a rectifier and groundbed.

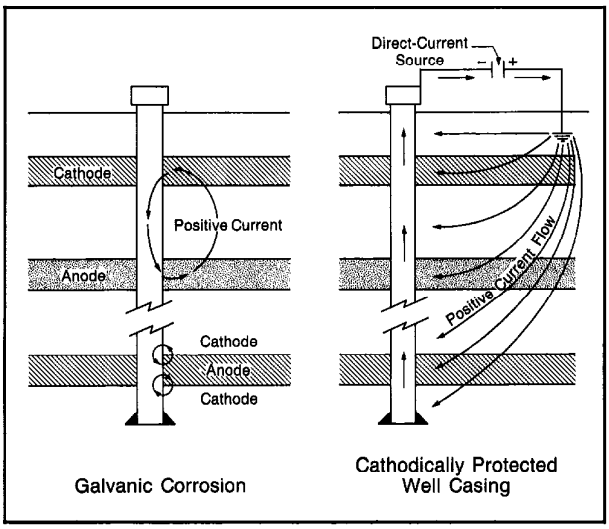

Fig. 6-1—Schematic of galvanic corrosion and its prevention with cathodic protection. The casing surface, in contact with the formations, acts as anode and cathode.

PREDICTING CORROSION

Corrosion from electrochemical action is commonly attacked by using cathodic protection systems which drive current onto and up the entire length of the casing. Spontaneous currents may exist within cells a few inches or several thousand feet long. The impressed current cancels and overrides the corrosion currents.

Cathodic protection is effective, but expensive. This expenditure can be minimized by analyzing surveys of naturally existing electrical potentials in new wells and of current patterns in protected wells.

Such surveys are made with casing potential logging tools which measure the potential difference between electrodes

in contact with the casing (Fig. 6-2). The log shows which sections of casing are losing current (corroding) and which are taking current.

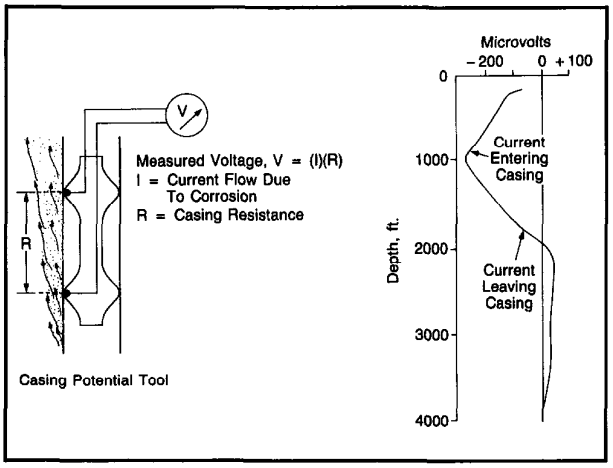

Fig. 6-2—A casing potential tool (left) and a casing potential profile (right). When the slope is negative, current is leaving the casing and corrosion is taking place.

Corrosion and Protection Evaluation Tool (CPET*)

The Corrosion and Protection Evaluation Tool has four sets of measurement electrodes spaced at 2-ft intervals. With each voltage measurement, the CPET tool also measures contact resistance and casing resistance directly.

A schematic of the tool is shown in Fig. 6-3. It contains four hydraulically actuated sets of three electrodes, radially spaced at 120° to each other. Electrode sets are separated vertically by 2 ft.

Casing resistance is measured by passing current between electrode sets A3-D3 and A2-D2 in turn, and measuring the voltage drops between D, C, B, and A. Contact resistance is obtained by injecting a small current between the pairs and measuring the potential difference across them at the same time. Measurements are made while stationary; it is possible to survey 1800 ft of casing per hour with 2-ft vertical resolution.

In-situ measurement of the casing and contact resistance provides more accuracy and reliability than with previous systems. The electrodes are designed to work in any wellbore fluid. Fast thermal stabilization and hydraulic operation give quick survey times.

Log Example

The log in Fig. 6-4 shows a decrease in current above 5700 ft, which indicates active corrosion. A sharp increase in resistance at 5686 ft was evidence of a hole in the casing, a fact which was confirmed by electromagnetic casing

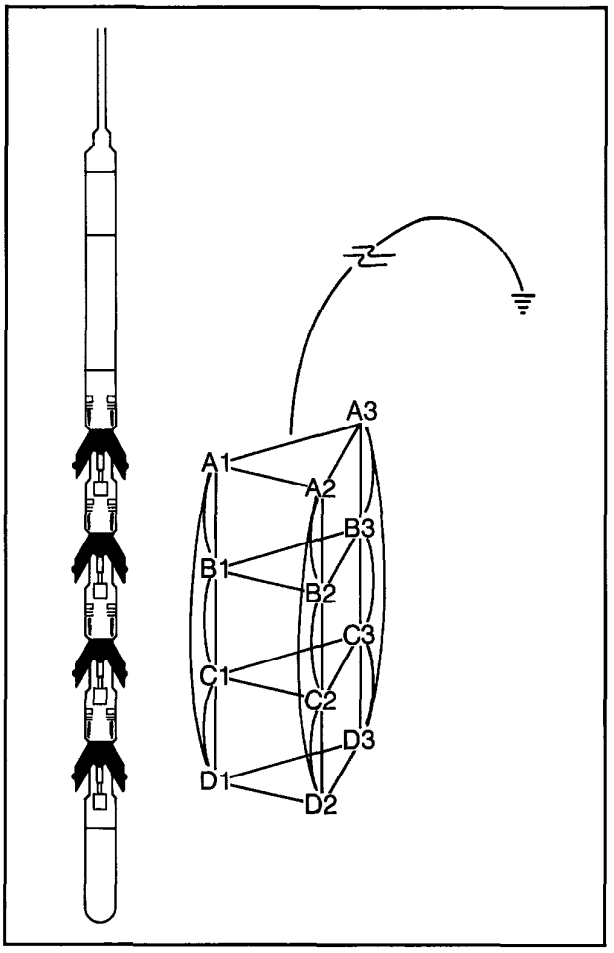

Fig. 6-3—The CPET tool contains four sets of three electrodes. Twelve potential difference, casing resistance, and contact resistance measurements are made.

inspection logs. The average casing resistance is fairly uniform and shows the casing collar joints.

On the right side of Fig. 6-4, another presentation of the same log shows the individual station stops recorded in the depth track. As before, axial current (measured along the borehole axis) and casing resistance are presented. In addition, radial current (between electrodes of a set) is given. The measured corrosion current may be converted to metal loss or corrosion rate. In this case, corrosion rate is shown in millimeters of metal per year.

MONITORING METAL LOSS

Several techniques may be used to search for weak points by measuring metal thickness. Internal calipers, either mechanical or acoustic, are precise but do not indicate external metal loss. Thickness derived from acoustic resonance

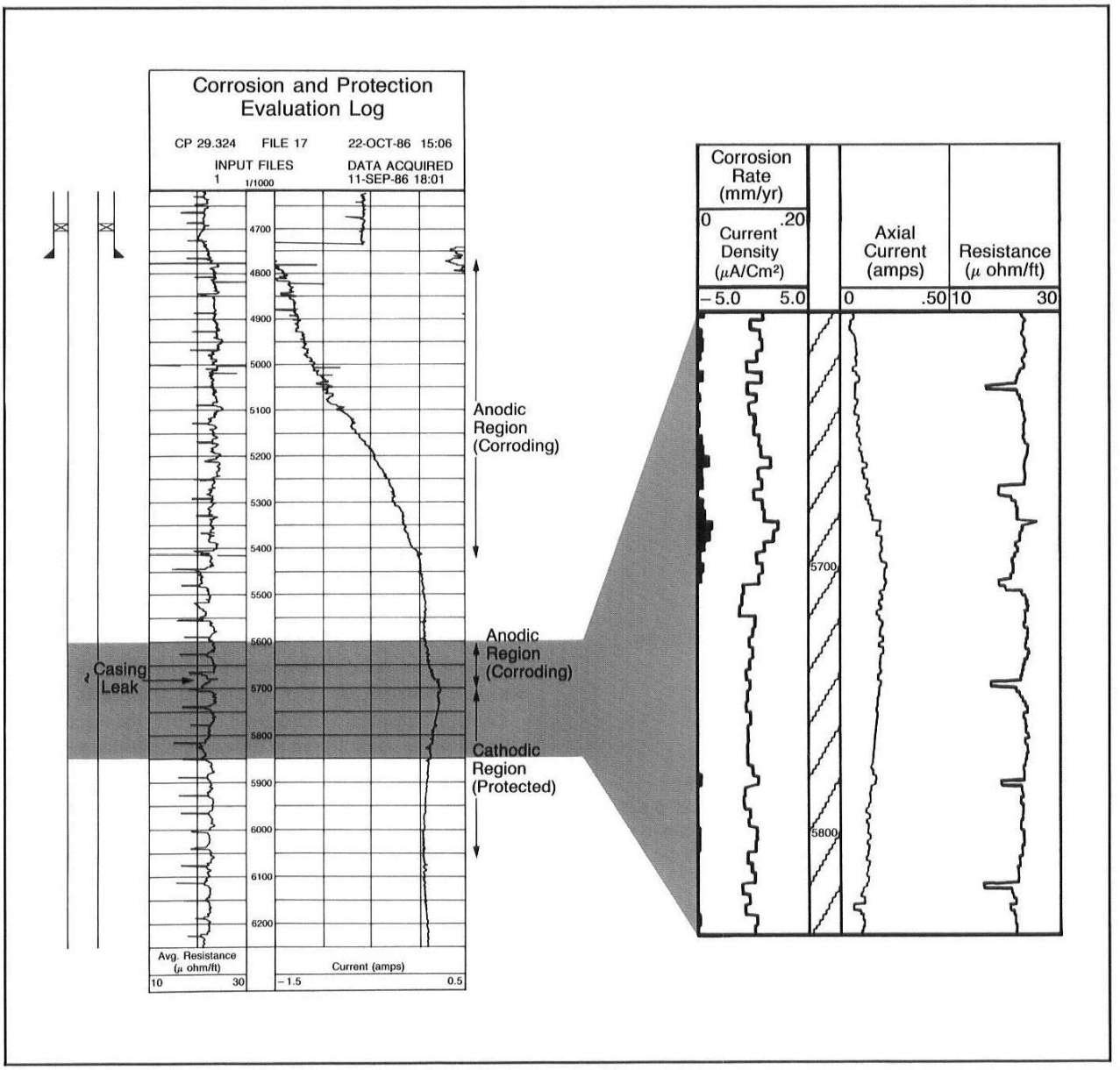

Fig. 6-4—A CPET log showing a hole in casing. The log on the right shows individual station measurements through the zone of concern.

is promising and may be useful in some instances. However, the best indication of general metal loss is derived from measurement of the phase shift of an induced electromagnetic field. This technique is the only method that allows for the determination of metal quality in multiple casings.

Monitoring is usually done with a "time-lapse" approach, where each successive log run over the well's lifetime is compared to previous logs. Time-lapse logging is the most accurate way to quantify metal loss.

Multifrequency Electromagnetic Thickness Tool (METT*)

The METT tool uses nondestructive, noncontact, induction methods to detect areas of metal loss and changes in casing geometry. The tool may be run with any combination of oil, gas, water, or mud in the borehole. The tool is best suited for the detection of large scale corrosion such as thinning,

holes larger than 2 in., and vertical splits. It can also detect metal loss in the outer casing of multiple casing strings.

A coil centered in the borehole generates an alternating magnetic field that interacts with the casing. A second coil measures the field's phase shift. Phase shift is related to three casing properties: magnetic permeability, electrical conductivity, and thickness. If the first two are known, the thickness can be derived.

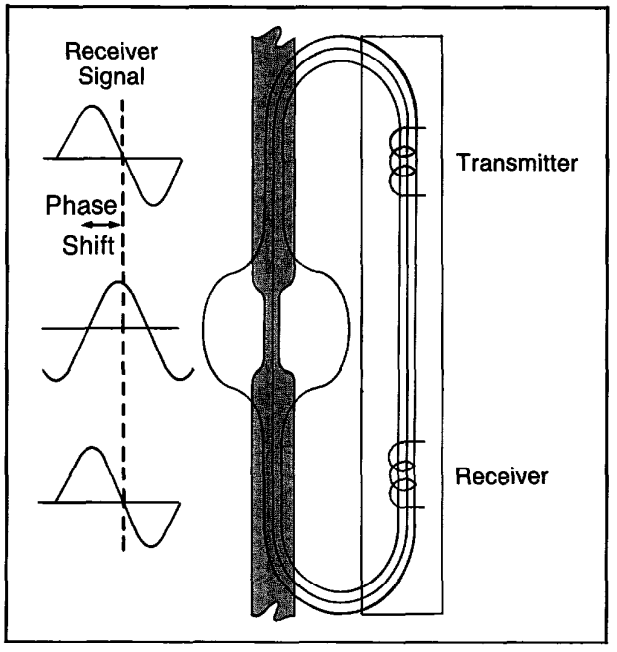

Fig. 6-5—Schematic of electromagnetic phase shift measurement for casing thickness. METT tool has multiple frequency transmitters and several transmitter/receiver pairs.

Coil spacing and operating frequency determine the depth of investigation of the field. A low frequency gives a deeper measurement than a high frequency. The tool makes these electromagnetic measurements at a number of different frequencies, hence the name Multifrequency ETT.

Conductivity is generally constant, but magnetic permeability varies with the type of steel, and will change as the casing ages. The Multifrequency Electromagnetic Thickness Tool was designed to overcome this problem by allowing computation of magnetic permeability.

Three parameters are derived: casing wall thickness, inner diameter, and electromagnetic property ratio (permeability/conductivity). Each of these parameters has a separate measurement system and is averaged around the circumference of the pipe.

Thickness Measurement

The primary measurement is phase shift (PLF, recorded in degrees). Signal amplitude is monitored to determine which of the three selectable frequencies is appropriate.

Phase shift is proportional to the total amount of metal surrounding the tool:

$$\Delta\phi = t\sqrt{2\omega\mu\sigma}\,, \qquad \text{(Eq. 6-1)}$$

where:

ϕ = phase shift
t = thickness
ω = frequency
μ = magnetic permeability
σ = electrical conductivity.

Operating frequency is known, and phase and permeability are measured. Once conductivity is specified, thickness can be computed. Often, an average value of conductivity is used. In this case, the computed thickness is labelled Normalized Thickness (NTSI). Alternatively, a value of conductivity specific to the pipe being investigated can be used in the computation; the thickness output is then labelled THCK.

An internal caliper measurement is made so that any thinning can be defined as being either inside or outside the pipe. This electromagnetic caliper is derived from a high frequency field which penetrates the inner surface less than 0.02 in. The output, corrected for borehole fluid and magnetic properties, is labelled ECID (Casing Internal Diameter).

Unlike mechanical and acoustic calipers, the electromagnetic caliper is not sensitive to mineral scale buildup, provided that the deposited material is nonmagnetic.

Casing Properties Ratio

As mentioned earlier, thickness may be derived from the phase shift measurement if magnetic permeability and electrical conductivity are specified. These two properties are not presented separately, but rather as a ratio: the Casing Properties Ratio (CPR). This ratio is measured at three different frequencies, representing three depths of investigation. The appropriate properties ratio—deep, medium, or shallow—is used to convert phase shift to thickness. The best answer is given by the measurement with the deepest investigation that does not penetrate the outer surface of the casing.

Log Quality

The LRAT curve indicates attenuation of the phase shift measurement. If consistently greater than −10 dB, the log should be repeated at a higher frequency. If LRAT is consistently less than −40 dB, the log should be repeated at a lower frequency. If the lowest frequency has been chosen and LRAT falls below −40 dB the phase measurement is valid as long as the collars are visible and undistorted.

A caliper quality curve, QCID, will indicate eccentering

if it tracks the caliper. The QCID curve should be near zero; internal diameter measurements are considered suspect if QCID exceeds 0.5. Temporary spikes at collars and internal defects are normal.

Log in Test Well

The log shown in Fig. 6-6 was made in a test well and illustrates expected tool response. Looking at the left side of the log, the caliper quality indicator is satisfactory, remaining near zero except for spikes at casing collars. The internal diameter clearly shows the 0.1-in. change between casing of different weight. Casing property ratios (deep, medium, and shallow investigation) are very similar, and in this case are consistent for the three joints of casing shown.

The primary measurement, phase shift, responds to the machined metal loss in the center joint of casing and shows the additional metal of the second string of casing, as well as indicating the buttress couplings. The attenuation monitor falls within acceptable limits.

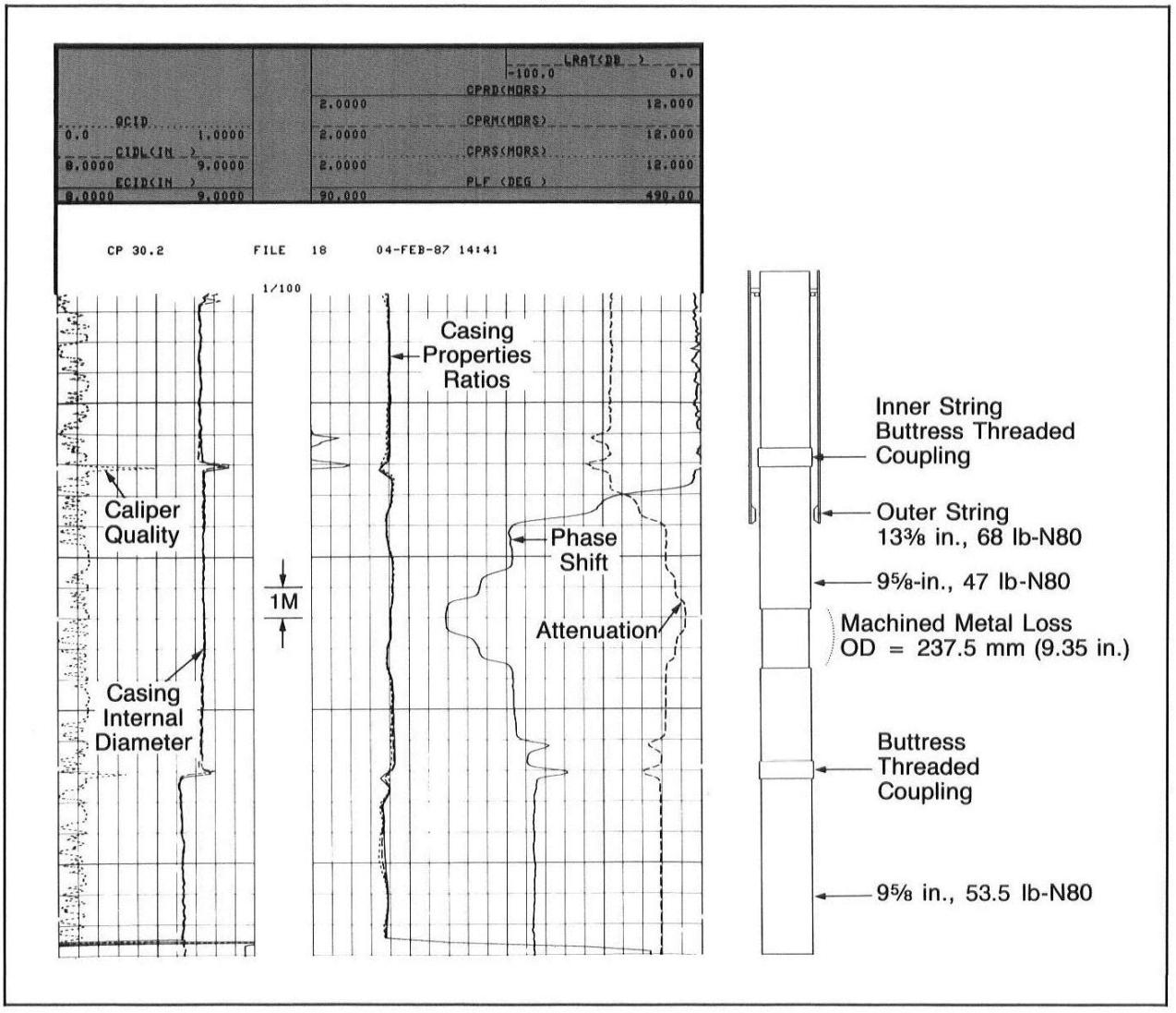

Fig. 6-6—METT log response in test well. The mechanical configuration of the test well is shown on the right side of the figure.

Compensation for Permeability Change

Measured parameters are shown on the log in Fig. 6-7. The casing properties ratio (magnetic permeability divided by electrical conductivity) shows considerable variation between casing joints. Since conductivity is generally constant, the permeability is driving the variation in the properties ratio.

Phase shift is a function of thickness and magnetic permeability; without the independent indication of the variation of magnetic permeability it would not be possible to say if the large changes in phase shift were caused by differences in metal thickness.

Computed outputs from the log in Fig. 6-7 are shown in Fig. 6-8. The thickness computation shows that the casing joints are in fact relatively uniform. Almost all of the variation in the measured phase shift is due to changes in magnetic permeability.

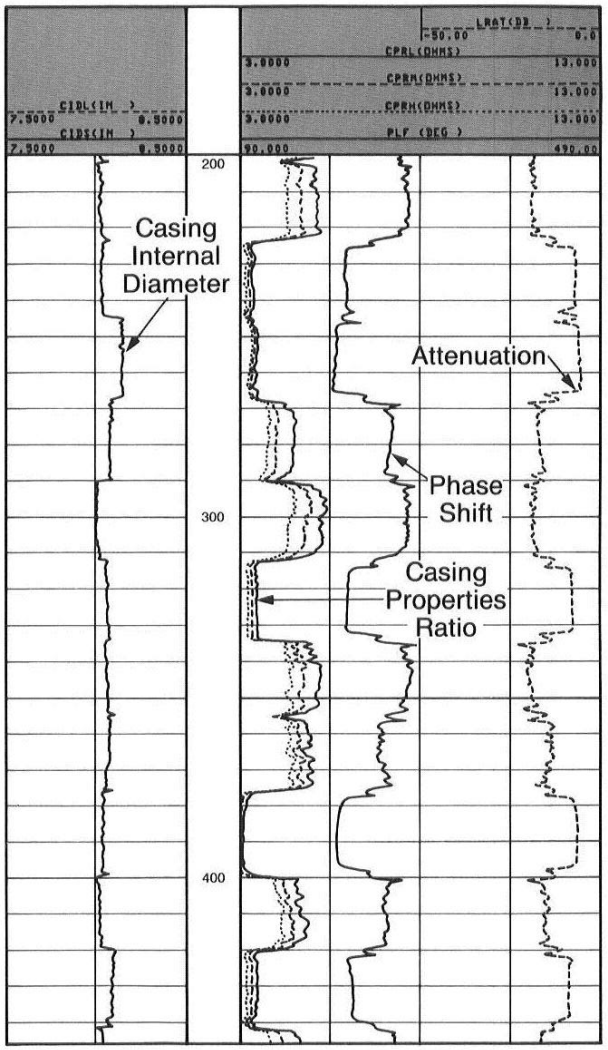

Fig. 6-7—Measured parameters from METT tool

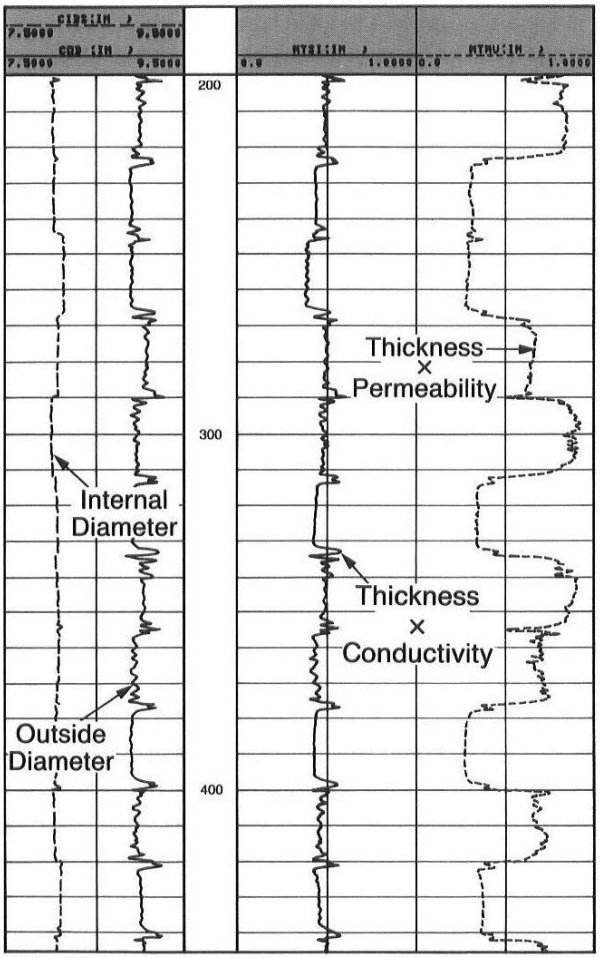

Fig. 6-8—The thickness computation from log in Fig. 6-7

Outside Casing Parted

The field log shown in Fig. 6-9 was made in three concentric strings of casing: 3½ in., 5½ in., and 7 in. The phase shift (PLF) indicates an interval with severe metal loss.

The internal caliper (ECID) shows that the inner casing is intact. Therefore, the change in phase is due to metal loss in one or both of the outer strings of casing.

Split Casing

Many mechanical problems were experienced during drilling and cementing of this well. The log shown in Fig. 6-10 was made in the 9⅝-in. casing upon re-entry nine months after temporary abandonment. The change in phase shift is typical of large holes and vertical splits in the casing.

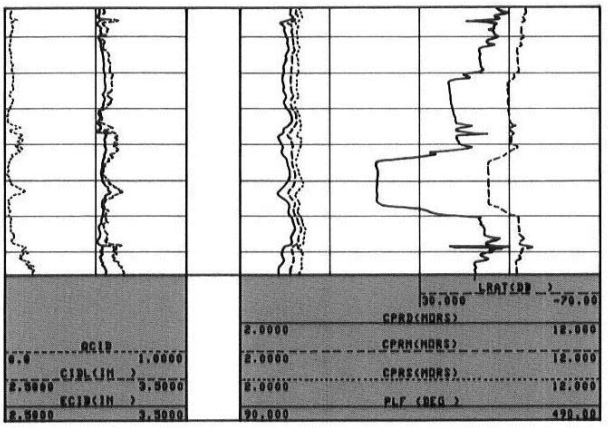

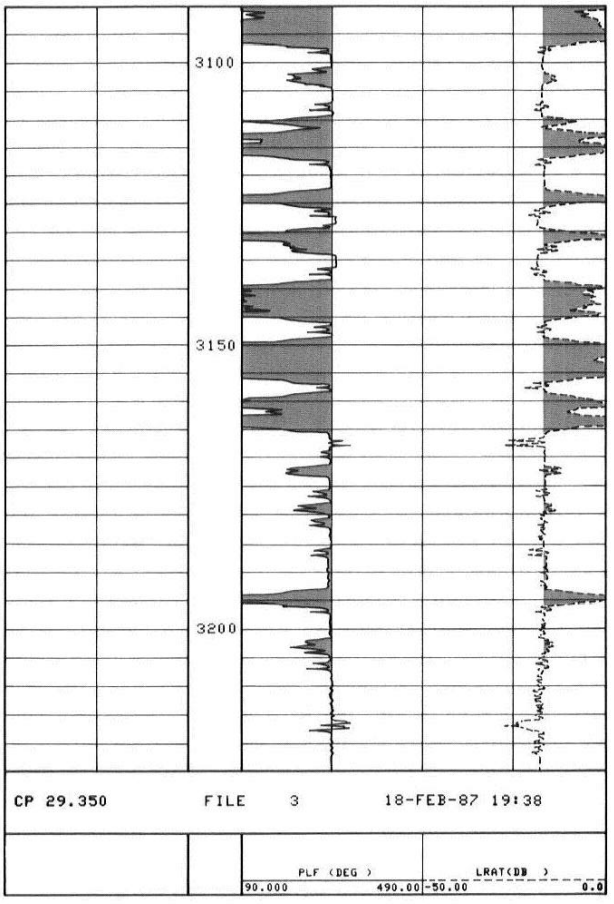

Fig. 6-10—Log example indicating large holes and vertical splits

Triple String

The log shown in Fig. 6-11 was made through 4½-in. tubing, inside 7-in. and 9⅝-in. casings. The tubing-casing annulus was filled with crude oil.

The internal diameter calipers show that the 4½-in. tubing is not completely uniform in weight. In addition, several areas of casing metal loss are seen on the phase shift. It is not possible to say whether it is the 7-in. or 9⅝-in. string that has lost metal.

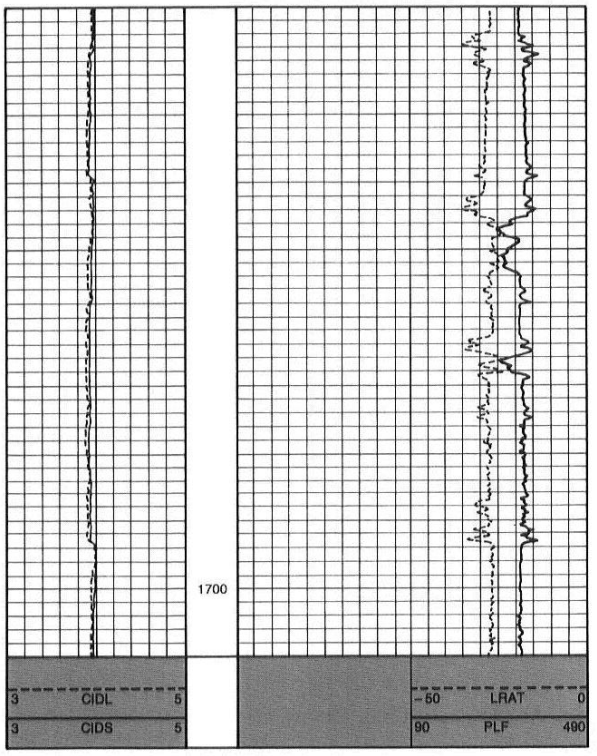

Fig. 6-11—The field log shows different tubing weights and indicates metal loss in the outer casing strings.

Double String

Taken from a well in the same field as in the previous example, this log (Fig. 6-12) was made through 7-in. casing inside 9⅝-in. casing. The phase shift indicates some general metal loss and a severe event at 1682 m (possibly a separation of outer strings). The interval of corrosion is at the same depth as in the other well in the same field.

Cement Evaluation Tool (CET)

The Cement Evaluation Tool monitors casing response to ultrasonic impulses. Bonding is measured from the reflected energy, and internal diameter is calculated using transit

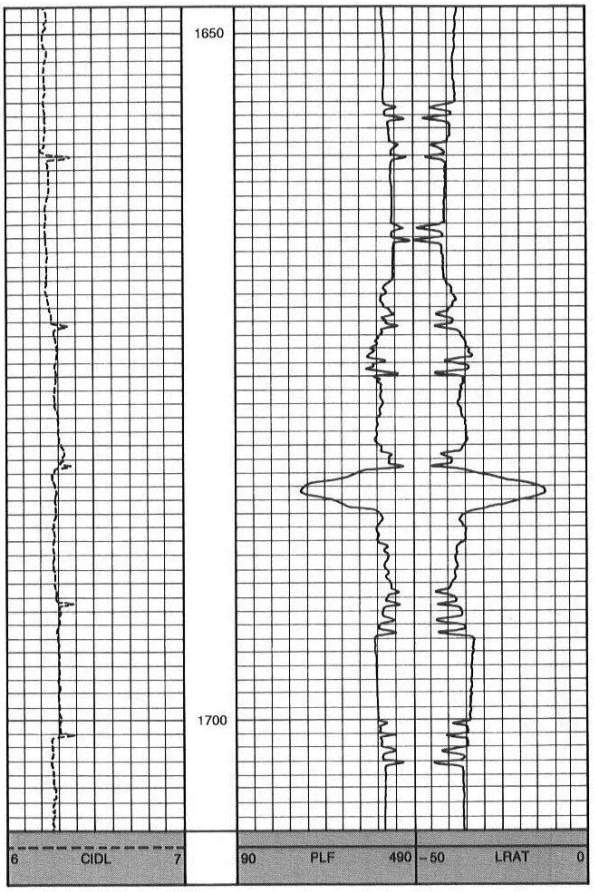

Fig. 6-12—Log from same field as Fig. 6-11. The logs indicate severe metal loss at same depth in both wells.

time. At the same time, casing thickness is derived from resonant frequency.

Eight transducers are arranged in a helix, focused 45° apart (Fig. 6-13). The fixed-position transducers provide 35% to 70% coverage, depending on casing size. This is usually adequate when the problem is general metal loss. Repeat runs can be used to improve coverage.

The tool works in either oil or water. Changes in borehole fluid over the log interval are compensated by using a ninth transducer to measure fluid velocity. Signal response is attenuated by gas, heavy mud, and scale buildup. While the caliper reflects reduction in diameter due to scale deposits, the thickness measurement responds only to metal thickness. This technique is attractive because it allows simultaneous acquisition of casing thickness and cement bond information.

Several different data displays can be made; casing thickness and radius is available for each of the eight transducers. The top of the log in Fig. 6-14 shows a change in casing

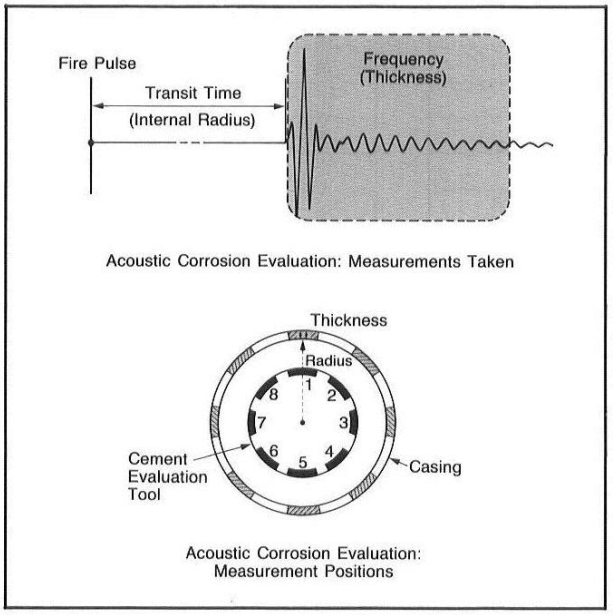

Fig. 6-13—Principle of thickness measurement with CET tool

weight easily seen on the caliper, thickness, and apparent cross-section. In addition, the lighter weight casing is distorted at the bottom of this log interval. Although the internal caliper shows the distortion, the casing is not eroded because the thickness remains constant.

The deformation was caused by perforation of unsupported casing. The casing swelled; however, there was no general metal loss.

Internal and External Corrosion

The color playback shown in Fig. 6-15 was processed in a computing center. The green curve is average casing caliper and the red curve is average casing thickness. Even though the caliper is generally constant, the center interval of the log shows considerable thinning. Therefore, the erosion is on the outside of the casing. The corrosion becomes general towards the bottom of the log.

The color map at right shows the individual response of all transducers, displayed as if the casing were split vertically and unrolled. The color coding has been set so that red indicates original thickness and violet represents 35% metal loss.

Finding Leaks

Often extensive casing damage can be easily located, but a considerable amount of data must be acquired to find small holes. This may be accomplished with multiple repeat logging passes and slow logging speed. Logs should be displayed on an expanded depth scale.

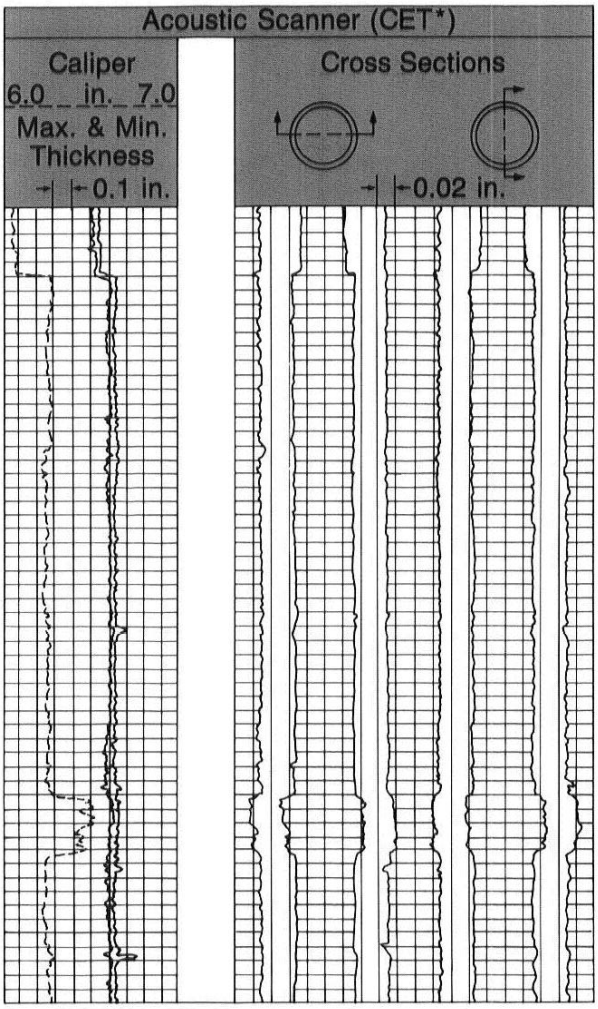

Fig. 6-14—CET thickness presentation

Noise, temperature, and flowmeter logs find a hole by detecting a fluid or gas leak through it. Electromagnetic flux leakage tools respond to magnetic flux anomalies caused by changes in metal volume. Mechanical and acoustic calipers give direct measurement of internal diameter changes caused by pits, holes, and splits. Such acoustic measurements may be acquired at a very high data rate, and presented as a complete image of the casing interior—as with the digital Cement Evaluation Tool (CET) and the Borehole Televiewer (BHTV) tool.

Borehole Televiewer Tool (BHTV)

The Borehole Televiewer tool, like the CET, monitors casing response to high frequency sound pulses. The BHTV tool uses a single transducer which rotates at 3 rps and makes 250 measurements each rotation (Fig. 6-16). Thus, the resolution is essentially limited only by the physical size of the transducer and the data sampling rate.

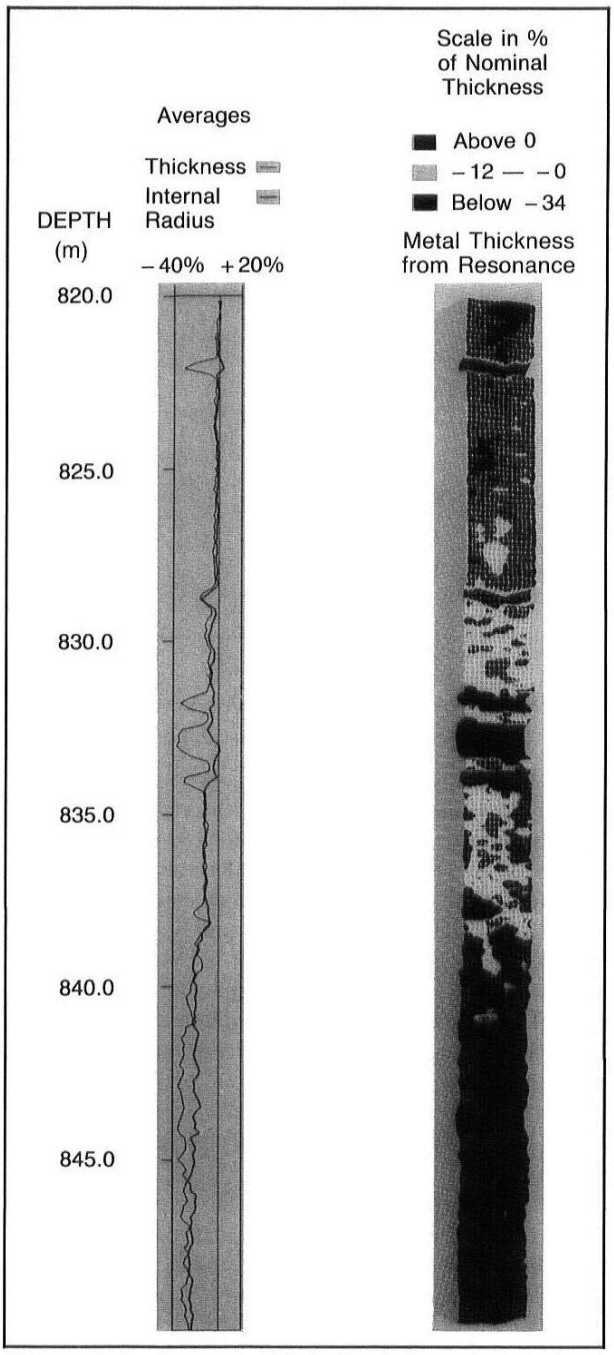

Fig. 6-15—Computed log with color display of CET thickness measurements

Sampling rate (inches of borehole per data sample) translates into logging speed. For example a vertical resolution

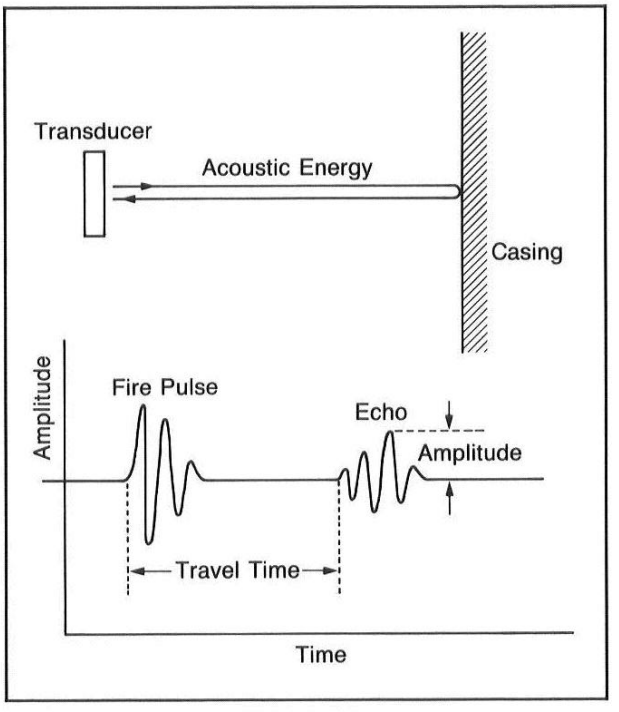

Fig. 6-16—Principle of BHTV measurement

of 3 in. is possible at 2600 ft/hr, or 0.5 in. at 450 ft/hr. Slower logging speeds are not generally available on conventional field units. As with the CET measurements, interpretation is disturbed by scale buildup, fluid changes, and sound-attenuating material such as heavy mud.

Two measurements are presented: the travel time from transducer to the casing and the amplitude of the reflected pulse. Travel time is used to calculate internal diameter, and amplitude is an indication of reflectivity or roughness. These are commonly displayed as maps, as if the casing had been split vertically and unrolled. In addition, the caliper information can be shown for specified depths as a casing cross section.

The two plots in Fig. 6-17 were made for depths selected from a field log. The cross-sectional scale can be specified, and in this case was deliberately exaggerated. The upper section shows that the casing internal diameter is uniform at this depth, as would be expected.

Lower in the well, the internal diameter is enlarged, particularly on the low side of the hole. The wear is believed to be caused by friction from the pump's sucker rod.

Note that although the external diameter is presented, it is for reference only since the BHTV tool can only inspect the *inside* of the casing. Inference of outside erosion can only be made from the electromagnetic thickness measurement or from digital CET resonant frequency measurement.

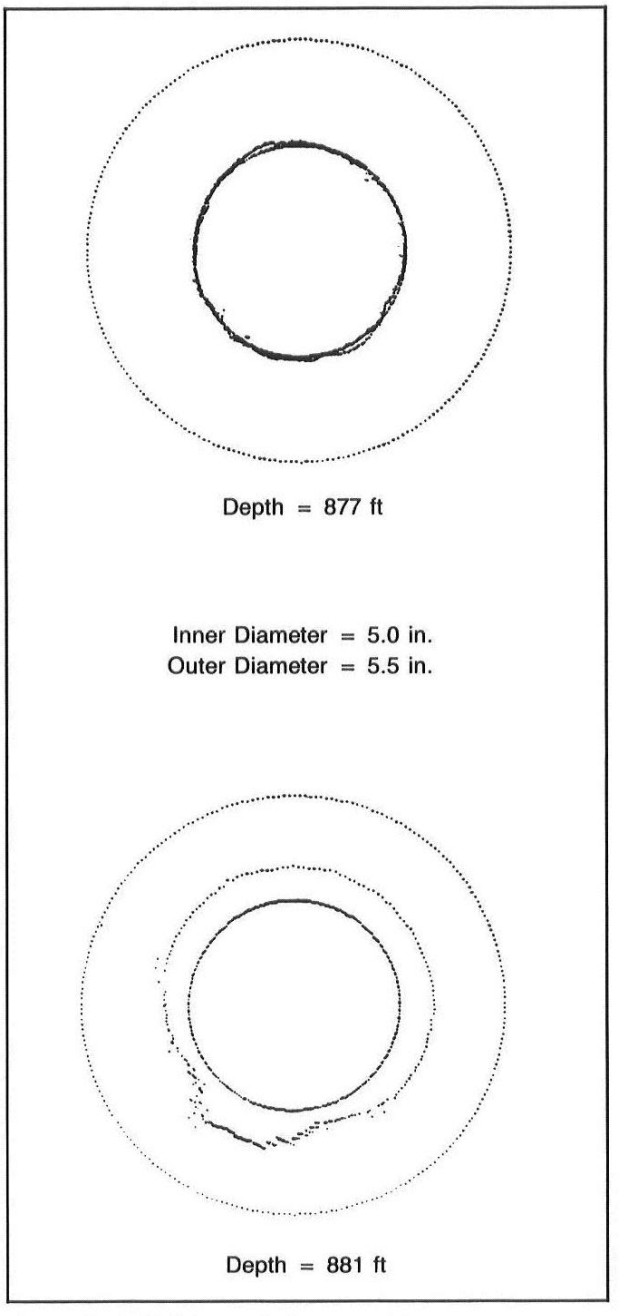

Fig. 6-17—BHTV internal diameter plots

Expanded Depth Scale

As is commonly done when inspecting small features, the log in Fig. 6-18 is presented with an expanded depth scale. Even so, the image is distorted since the vertical scale is different from the horizontal; thus, circular defects tend to appear as flattened ovals. This example was logged in 5-in.

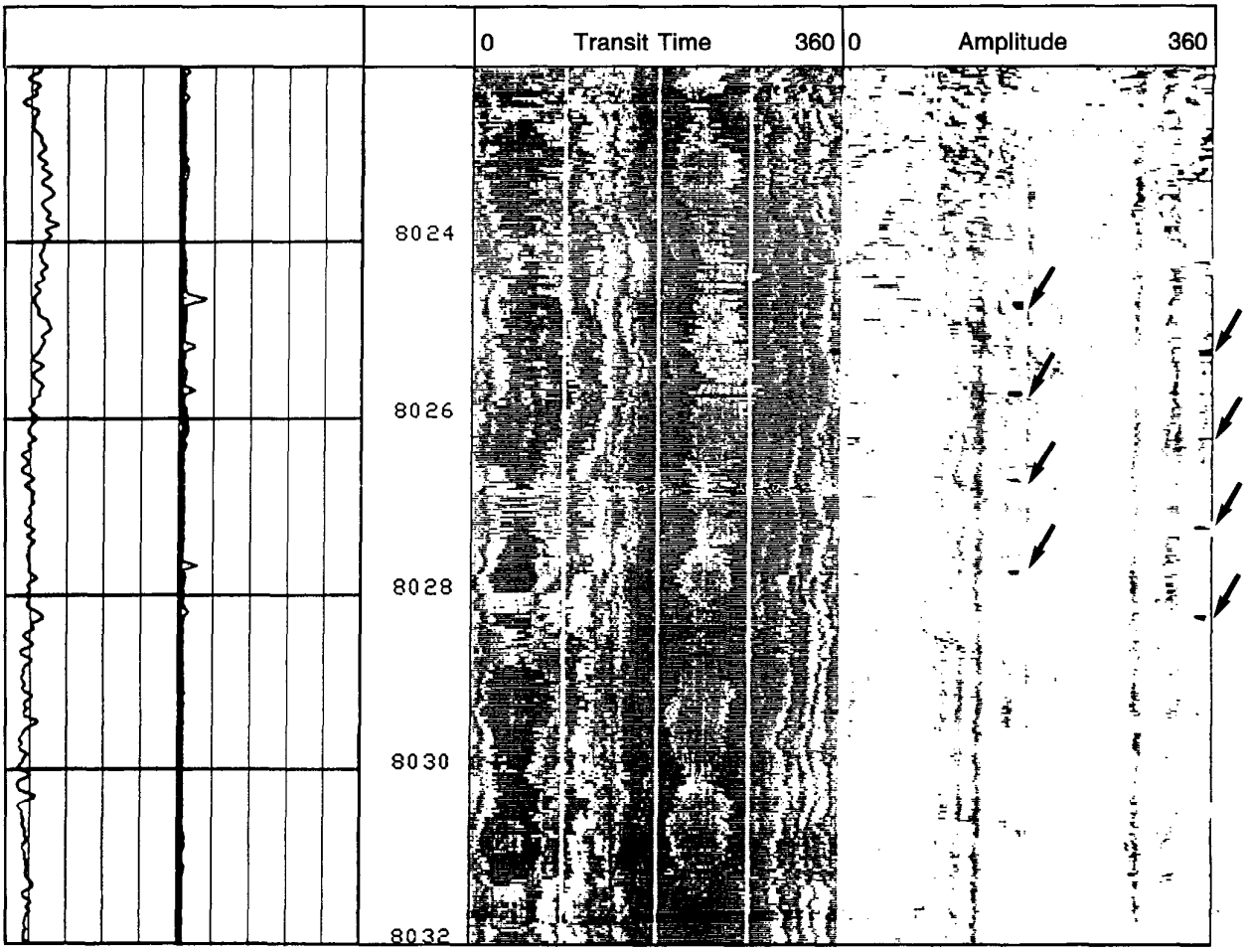

Fig. 6-18—BHTV presentation with expanded depth scale

casing and presented at a depth scale of 1/20, so the image is exaggerated horizontally about three times.

Image maps are conventionally presented so that "nominal" appears white. Increases in diameter and roughness are dark. Here, a series of perforations 0.32 in. across may be seen as dark spots on both transit time and amplitude maps and on the caliper maximum.

This field log illustrates some of the difficulties inherent in any search for small casing anomalies. First, logs must be inspected on an expanded depth scale. If the approximate location of the problem is unknown, this could be a big task, since a well only 5000 ft deep would require a log print 250 ft long for a depth scale of 1/20.

Second, repeat run comparisons are mandatory. On this log, even the very high resolution of the BHTV display missed some known perforations because of erratic tool movement downhole.

The large defect at 2830.5 m on the log in Fig. 6-19 is approximately 30 cm (12 in.) across. Again, the difference between vertical and horizontal log scales appears to flatten it vertically. It is suspected that this 5-in. casing has parted.

In Fig. 6-20 a hole is clearly seen at 666.4 m. Note that the caliper spikes at 665.9 m are normal and are caused by the casing collar. This can be established since the anomaly is present around the entire circumference of the casing on the image maps.

Multifinger Caliper Tool

The mechanical caliper is one of the oldest casing inspection devices. Modern tools have excellent sensitivity (0.004 in.) and multiple measuring fingers to cover pipe sizes from 2⅞ to 13⅜ in. pipe. The log may be run in any borehole fluid, including gas, and the interpretation concept is easy to understand.

The number of fingers vary from 16 to 80, depending on tool size, and many different data presentations are possible.

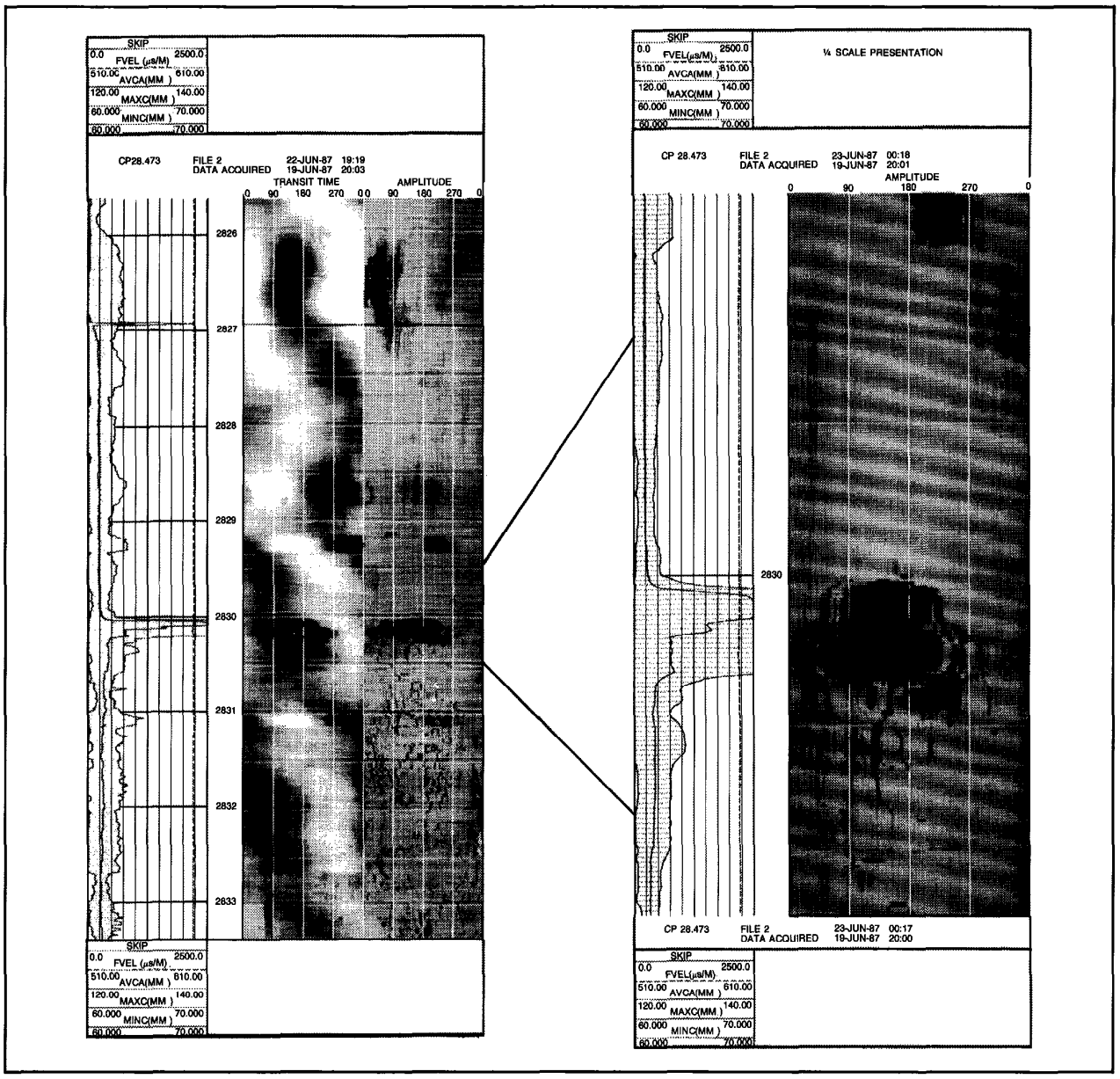

Fig. 6-19—BHTV standard presentation on left and expanded depth scale through zone of interest on right

Often, in order to keep the display simple, only three maximum and minimum caliper readings are output. These represent each of three 120° segments of the casing circumference.

The field log shown in Fig. 6-21 was made in leaking 9⅝-in. casing with the 60-finger caliper. Because the leak was anticipated to be a small hole, data was recorded at the maximum rate of 0.2 in. of borehole per digital sample. The expanded depth scale display shows the hole at 418 ft. The damaged casing was successfully recovered, and is shown in the photograph in Fig. 6-22.

The 16-finger caliper log shown in Fig. 6-23 was used in 3½-in. tubing. The left-hand section of the log displays caliper maximum and minimum, while each individual

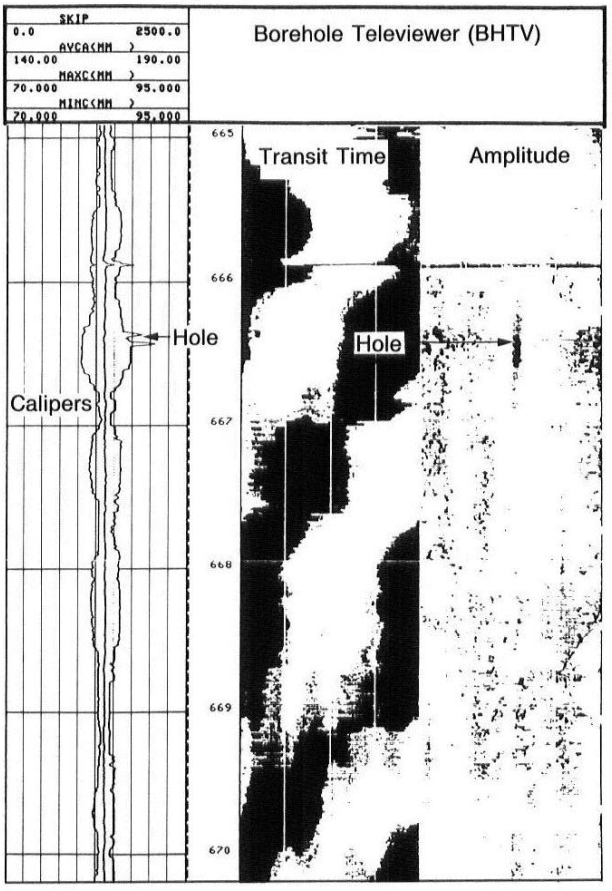

Fig. 6-20—BHTV log showing a small hole in the casing

caliper is mapped at right. The joint-by-joint listing at the bottom of the log gives mean diameter, as well as minimum and maximum change from nominal value. These can be interpreted as scale buildup and pitting, respectively.

Eccentering effects caused by deviated wells can be compensated.

Pipe Analysis Tool (PAT)

Electromagnetic flux leakage tools monitor casing by measuring magnetic flux anomalies close to the casing wall with pad-mounted sensors. A low-frequency background flux is generated from a centrally located electromagnet. In the Pipe Analysis Tool (PAT), a secondary measurement of high-frequency induced eddy current is made to discriminate internal from external defects.

The flux leakage tool response to holes in casing is good; however, such responses are difficult to interpret since similar responses may be generated by corrosion, pits, and holes. Although potential problem intervals can be identified, it may not be possible to determine if holes exist.

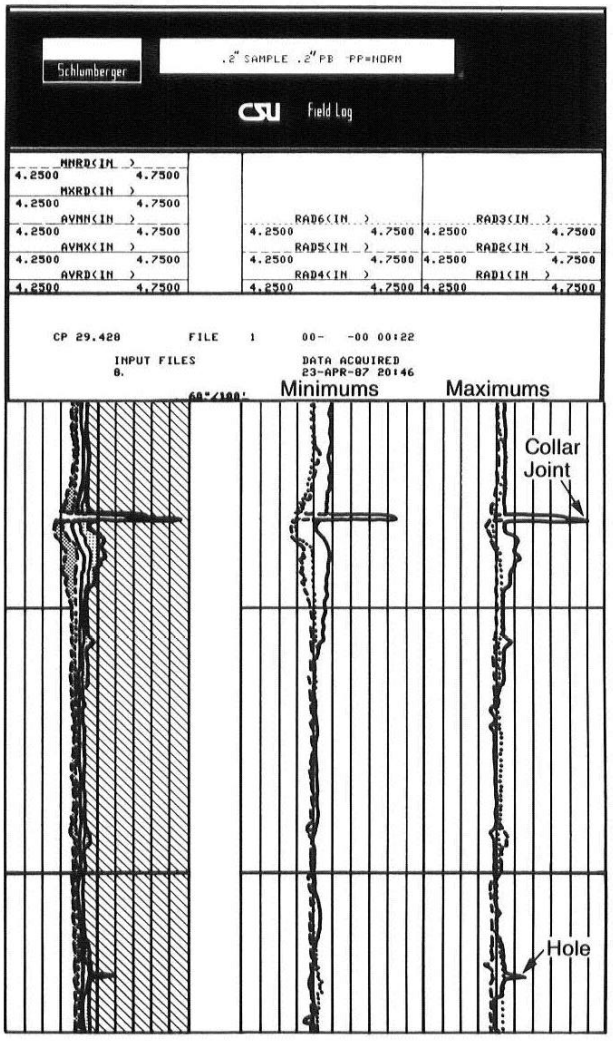

Fig. 6-21—Multifinger Caliper log showing hole in casing

Fig. 6-22—Photograph of recovered casing from well in Fig. 6-21

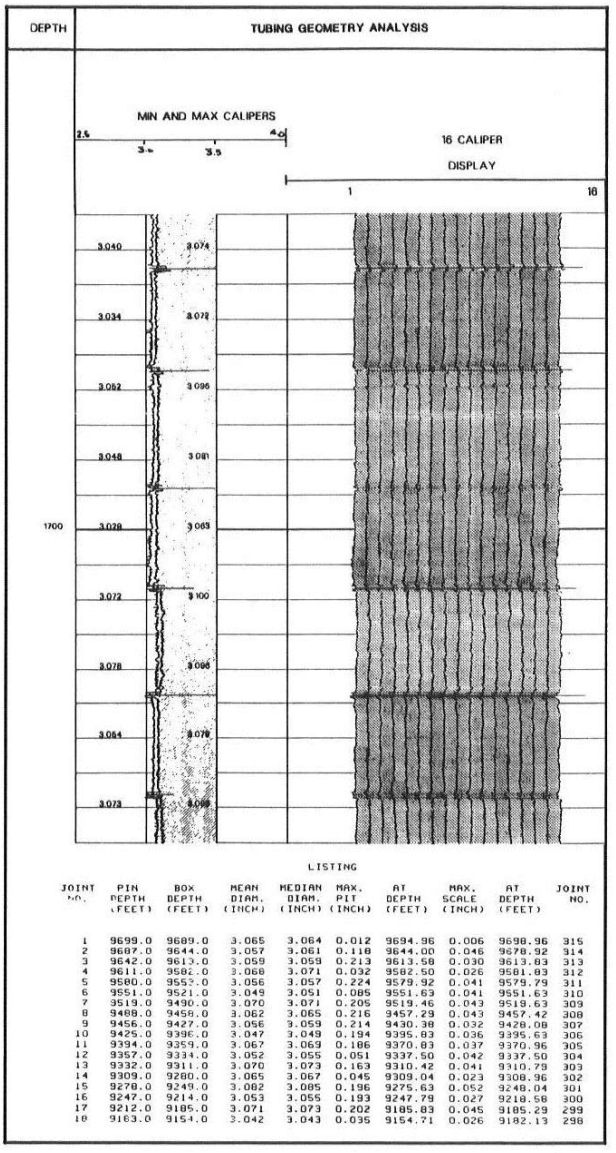

JOINT NO.	PIN DEPTH (FEET)	BOX DEPTH (FEET)	MEAN DIAM. (INCH)	MEDIAN DIAM. (INCH)	MAX. PIT (INCH)	AT DEPTH (FEET)	MAX. SCALE (INCH)	AT DEPTH (FEET)	JOINT NO.
1	9699.0	9689.0	3.065	3.064	0.012	9694.96	0.006	9698.96	315
2	9687.0	9644.0	3.057	3.061	0.118	9644.00	0.046	9678.92	314
3	9642.0	9613.0	3.059	3.059	0.213	9613.58	0.030	9613.83	313
4	9611.0	9582.0	3.068	3.071	0.032	9582.50	0.026	9581.83	312
5	9580.0	9552.0	3.056	3.057	0.224	9579.92	0.041	9579.79	311
6	9551.0	9521.0	3.049	3.051	0.085	9551.63	0.041	9551.63	310
7	9519.0	9490.0	3.070	3.071	0.205	9519.46	0.043	9519.63	309
8	9488.0	9458.0	3.062	3.065	0.216	9457.29	0.043	9457.42	308
9	9456.0	9427.0	3.056	3.059	0.214	9430.38	0.032	9428.08	307
10	9425.0	9396.0	3.047	3.049	0.194	9395.83	0.036	9395.63	306
11	9394.0	9359.0	3.067	3.069	0.186	9370.83	0.037	9370.96	305
12	9357.0	9334.0	3.052	3.055	0.051	9337.50	0.042	9337.50	304
13	9332.0	9311.0	3.070	3.073	0.163	9310.42	0.041	9310.79	303
14	9309.0	9280.0	3.065	3.067	0.045	9309.04	0.023	9308.96	302
15	9278.0	9249.0	3.082	3.085	0.196	9275.63	0.052	9248.04	301
16	9247.0	9214.0	3.053	3.055	0.193	9247.79	0.027	9218.58	300
17	9212.0	9185.0	3.071	3.073	0.202	9185.83	0.045	9185.29	299
18	9183.0	9154.0	3.042	3.043	0.035	9154.71	0.026	9182.13	298

Fig. 6-23—Multifinger Caliper display in 3½-in. tubing

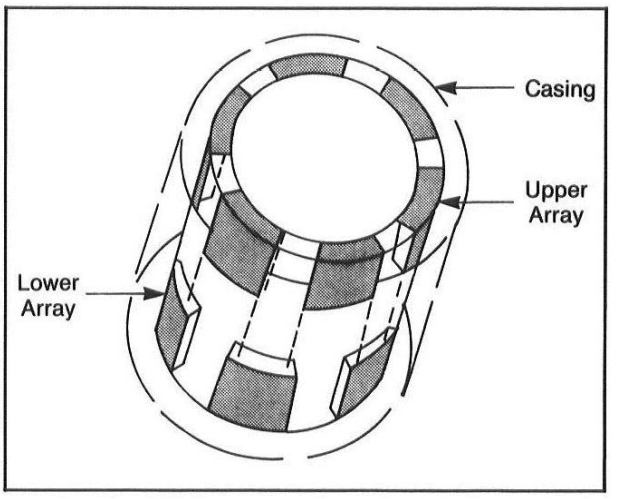

Fig. 6-24—Schematic of the PAT measurement. Sensing coils are pad-mounted in two 6-pad arrays between the poles of a low frequency electromagnet. The two arrays are radially offset for complete coverage.

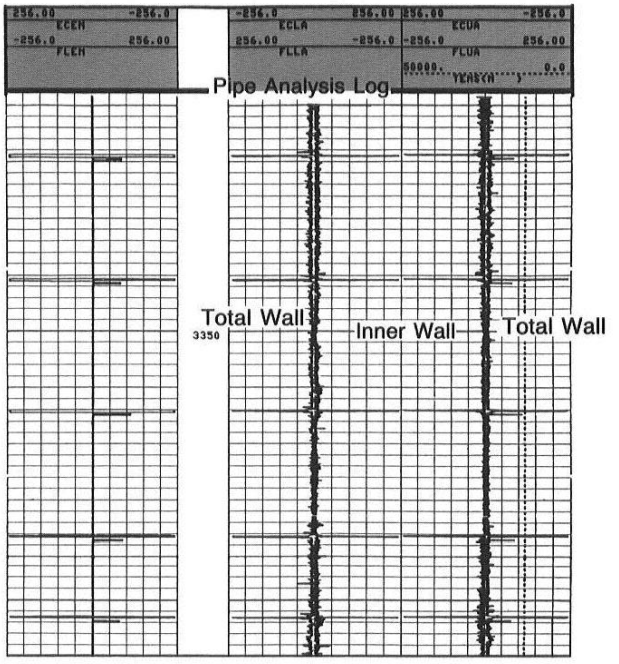

Fig. 6-25—Pipe Analysis log in good casing

The output will respond to logging speed and the casing's magnetic permeability. As noted previously, magnetic permeability varies with steel type and may even change as the metal ages.

The field log in Fig. 6-25 shows two similar pairs of curves to the right of the depth track. The left set is generated by the lower pad array, and the right set by the upper array.

The two eddy current responses (ECLA and ECUA) represent the inner casing wall, and the two flux leakage recordings (FLLA and FLUA) represent the total wall. The log shows very little activity other than the normal large deflections at casing collars.

Figure 6-26 shows a pipe analysis log and a photograph of a section of the recovered casing. The recovered casing verifies the PAT log response showing pits which penetrate

60 to 70% of the casing thickness at a depth of 3570 ft.

The PAT log in Fig. 6-27 indicates even greater corrosion. The recovered casing again verifies the log response showing extreme corrosion with pits penetrating 60 to 90% of thickness, with ½ to 1-in. holes located at 3722, 3728, and 3747.5 ft.

Electromagnetic Thickness

As discussed earlier in the section on metal loss, the electromagnetic thickness technique is best suited for the detection of large scale corrosion such as thinning, holes larger than 2 in., and vertical splits.

However, the quantitative conversion of measured phase shift to thickness makes the Multifrequency Electromagnetic Thickness tool attractive for many general corrosion monitoring problems. Unlike mechanical and acoustic calipers, the METT measurement responds to external as well as internal erosion. In addition, only this method can detect metal loss in the outer casing of multiple strings.

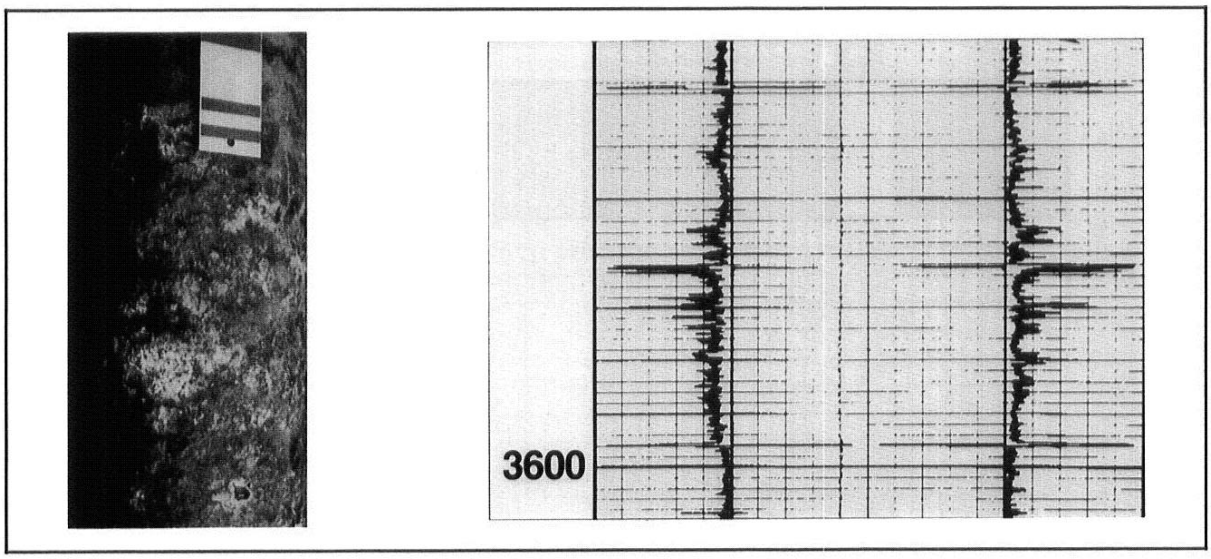

Fig. 6-26—Pipe Analysis log in corroded zone with photograph of recovered casing from same interval

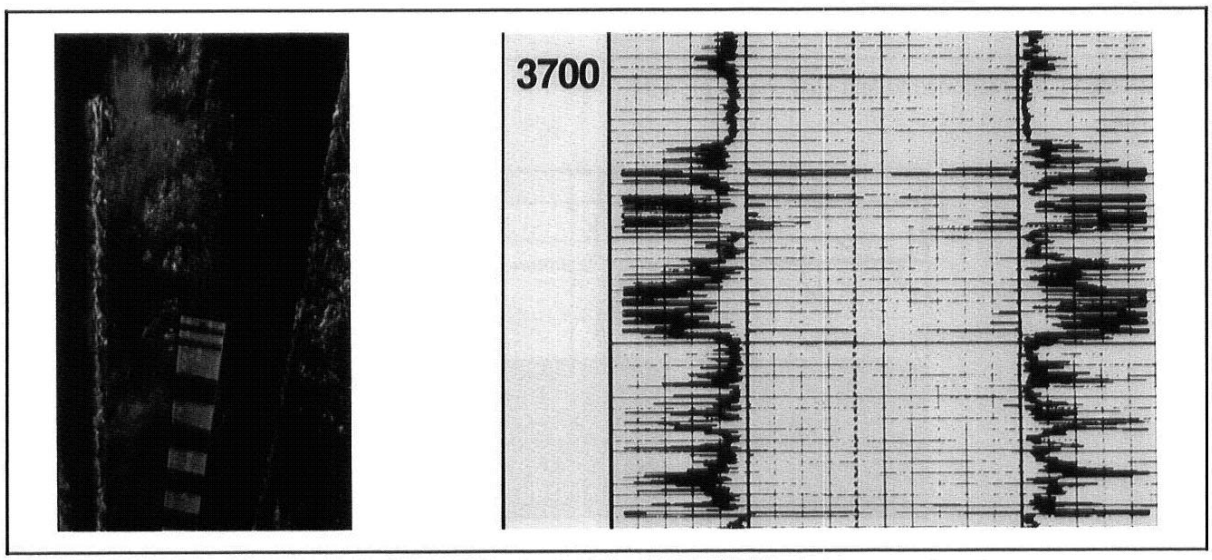

Fig. 6-27—Extreme corrosion shown on the Pipe Analysis log is verified by the recovered casing.

A schematic of a test well and the METT log are shown in Fig. 6-28. It can be seen that although the phase shift measurement clearly indicates a ⅛-in. change in metal thickness in the lower joint, only the largest (2-in.) hole is seen. This is because the tool averages all the metal within the zone of investigation.

Irregular holes and vertical splits have a larger effect on the log than perfectly round holes.

Multiple Casing Strings

The field log shown in Fig. 6-29 covers 3½-in. casing inside 5¼-in. casing. The phase shift output shows two distinct bumps as the two measuring coils pass over a defect. The electromagnetic caliper shows an increase in casing diameter; the defect, which is approximately 1 ft in length, is in the inner casing string.

Casing Hole and Pitting

In Fig. 6-30 the phase shift shows a large hole at 2829.5 m and some metal loss between 2835 to 2840 m. This is confirmed by the flux leakage log made with the pipe analysis tool as shown in Fig. 6-31.

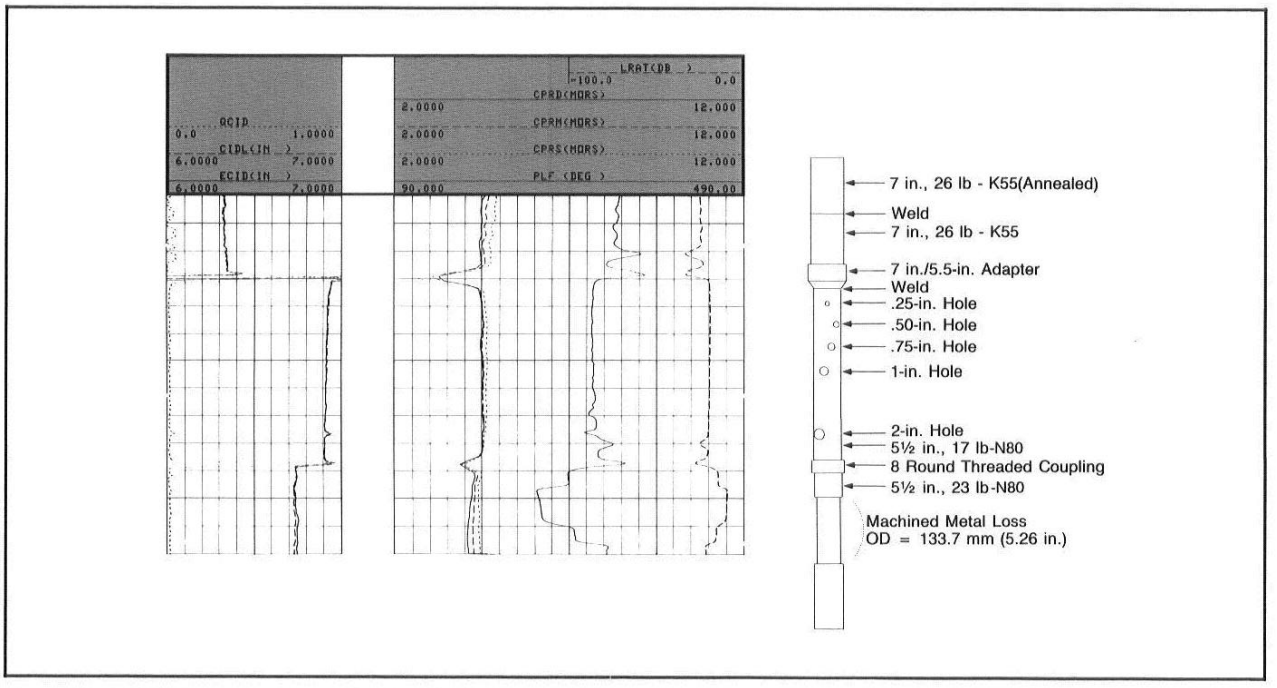

Fig. 6-28—METT log response to text well shown on right

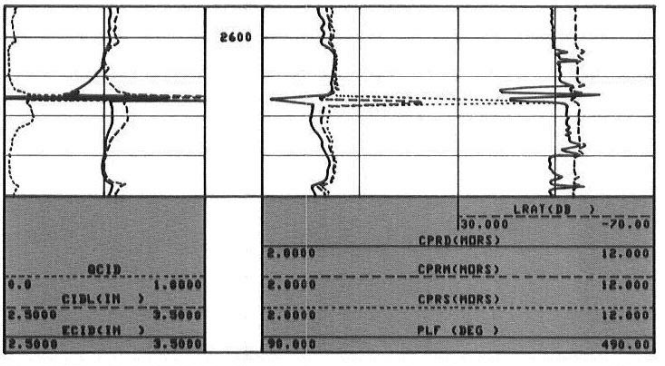

Fig. 6-29—An METT log in dual casing string shows a severe defect in inner string

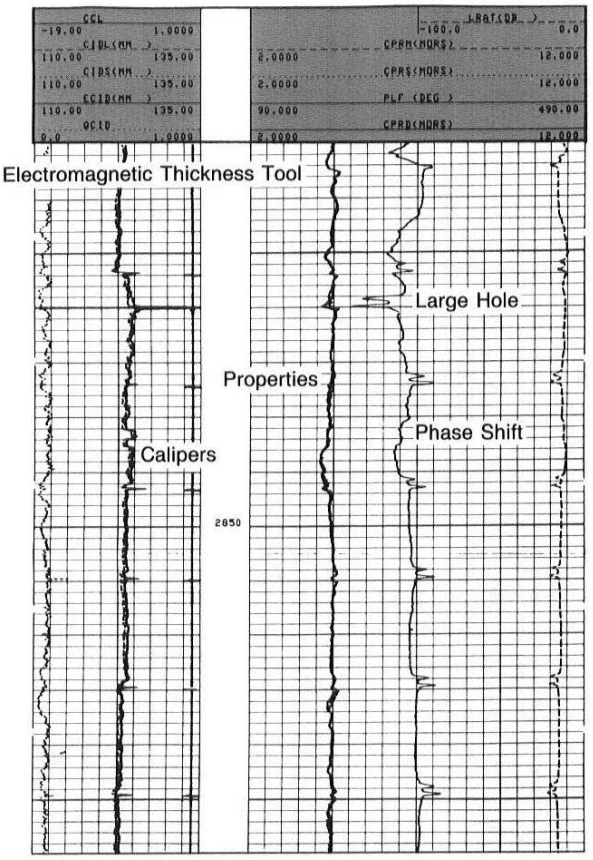

Fig. 6-30—The Electromagnetic Thickness log indicates a large hole in the casing at 2829.5 m.

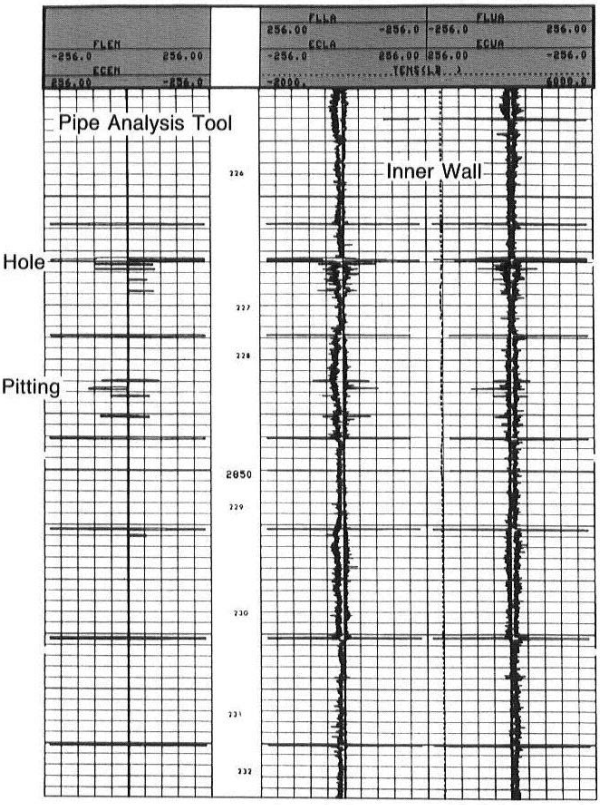

Fig. 6-31—A Pipe Analysis log verifies the large hole indicated in Fig. 6-30.

Corrosion Protection Evaluation Tool

Although the tool was designed to monitor electrical corrosion patterns, it is worth noting that the first example in this chapter (Fig. 6-2) also indicated a casing leak. The casing resistance measurement of the CPET tool can be expected to be fairly uniform. A significant reduction in the amount of metal present will increase the resistance.

MULTIPLE-LOG EXAMPLE

From the previous examples, it can be seen that very often no single log completely describes a problem. Flux-leakage tools (PAT) are sensitive to pits and holes, but phase shift measurements (METT) are more accurate for thickness, and are capable of multistring evaluation. Acoustic monitoring with the BHTV tool provides excellent resolution, but not thickness. Average thickness may be derived acoustically with the CET tool, and cement bonding may also be evaluated. Mechanical calipers may be run in any wellbore fluid, but give only internal information.

Four tools were run in the well in Fig. 6-32. At the left, the flux leakage log from the PAT tool indicates pitting and large holes between 2635 and 2640 m. The thickness, computed from the METT phase shift, shows 100% metal loss from 2638 to 2640 m. The acoustic corrosion evaluation derived from the CET measurement shows that the casing is seriously deformed, and the distortion varies radially. Finally, the expanded scale display of the borehole televiewer data graphically shows the casing damage. Cross-sectional plots of the acoustic calipers show the radial distortion.

Table 6-1 shows the primary applications for the corrosion evaluation tools discussed in this chapter. Table 6-2 shows the vertical and radial resolution for each sensor and Table 6-3 shows the mechanical restrictions for each tool.

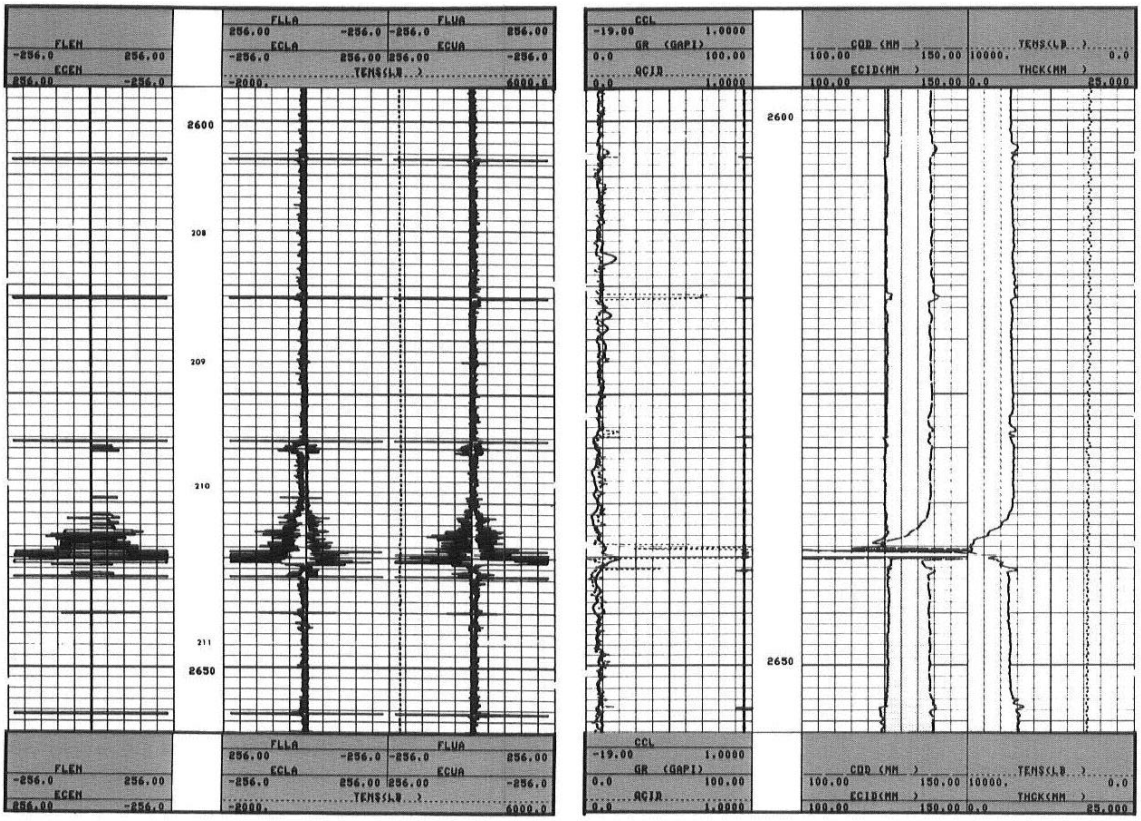

Fig. 6-32—Response of four corrosion tools run in the same well

REFERENCES

Bateman, R.M.: "Casing Inspection in Cased-Hole Log Analysis and Reservoir Performance Monitoring," IHRDC, Boston, 1985.

Corrosion Evaluation, Schlumberger, Houston, 1988.

Davies, D.H., Takeda, J., Niina, and Sasaki, K.: "High Resolution Electrical Measurements for Evaluation of Well Casing Corrosion," paper 372 presented at Corrosion/88, St. Louis, 21-25 March 1988, and the 1988 Annual Conference of National Association of Corrosion Engineers, Houston, Texas.

Dennis, R.: "Casing Corrosion Evaluation Using Wireline Techniques," submitted for presentation to the 1988 Conference of the National Association of Corrosion Engineers.

Dumont, A., Patin, J-B., and LeFloch, G.: "A Single Tool for Corrosion and Cement Evaluation," paper SPE 13140 presented at the 1984 SPE Annual Technical Conference and Exhibition.

Mohamed, S.K., Tongue, R., and Doran, T.: "Leak Detection Using Time-Lapse Technique and Wellsite Computer Processing," paper SPE 11450 presented at the 1983 SPE Middle East Technical Conference, Manama, Bahrain.

Smith, G.S.: "Principles and Applications of a New In-Situ Method for Inspection of Well Casing," paper SPE 9634 presented at the 1981 SPE Middle East Oil Technical Conference, Manama, Bahrain.

Tuttle, R.N.: "Corrosion in Oil and Gas Production," *JPT* (1987) **39**, 756-762.

Watfa, M.: "Take Care of Your Casing," *Middle East Well Evaluation Review* (1986) **1** published by Schlumberger Technical Services, Dubai, UAE, 50-63.

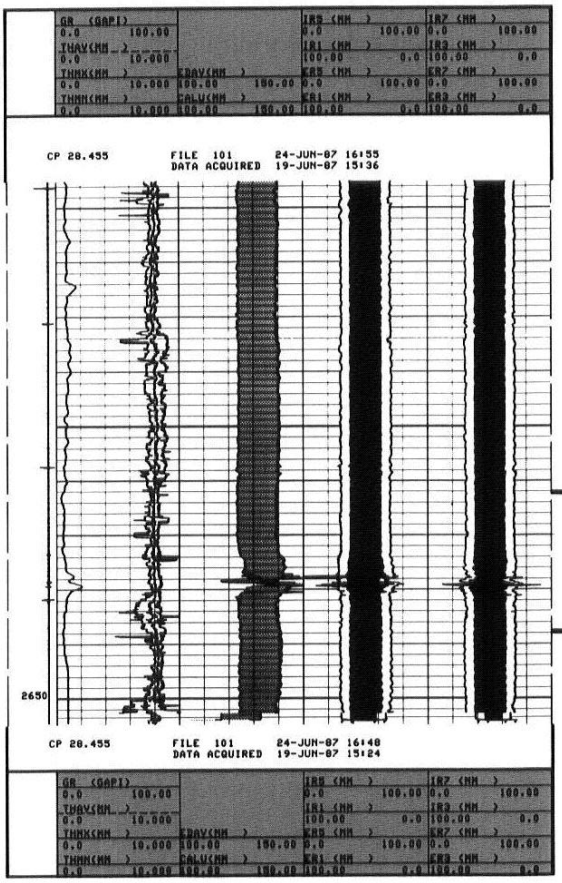

Acoustic Corrosion Evaluation

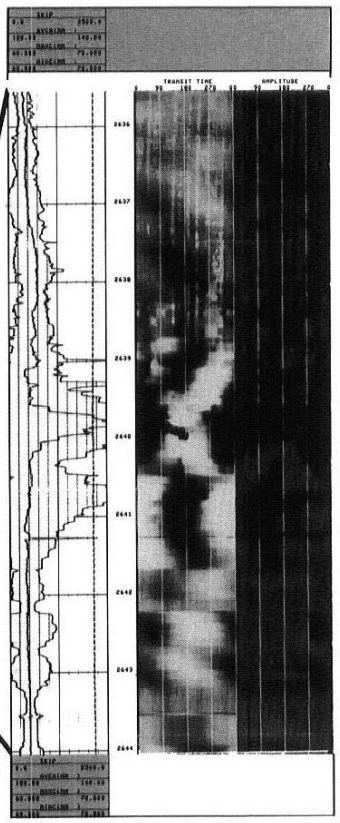

Expanded
Borehole Televiewer

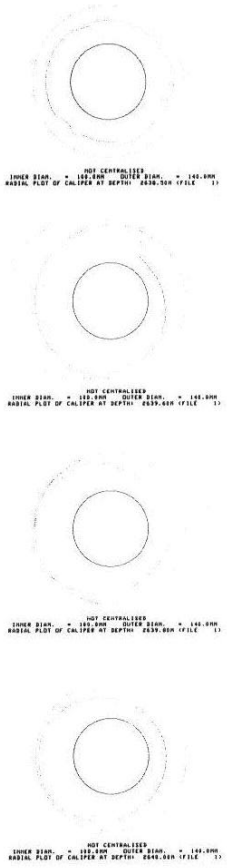

Cross-Section Plots

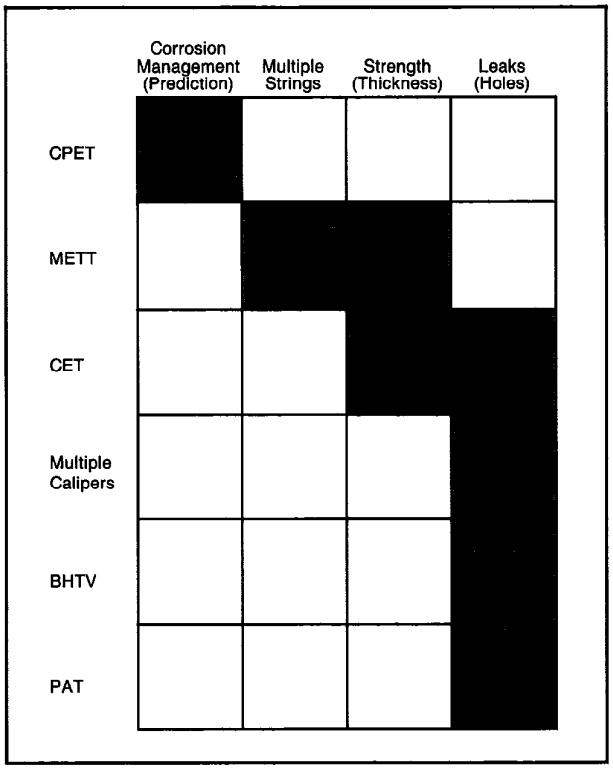

Table 6-1—Primary applications for corrosion evaluation tools

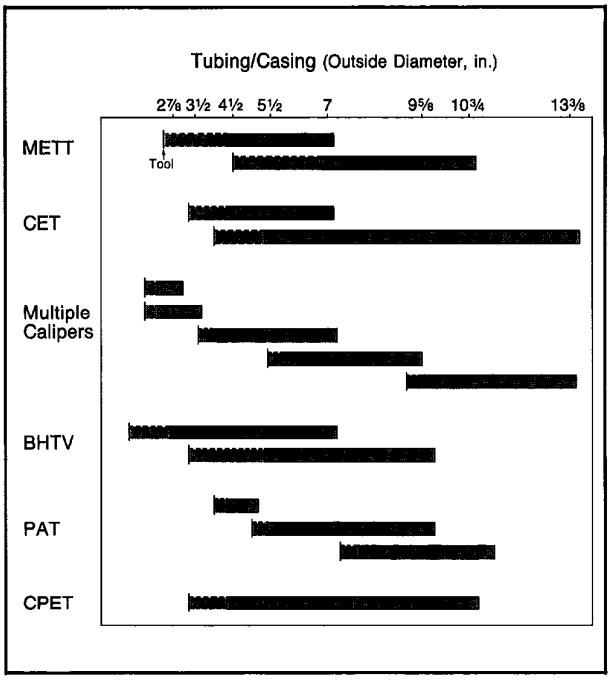

Table 6-3—Mechanical restrictions for corrosion evaluation tools

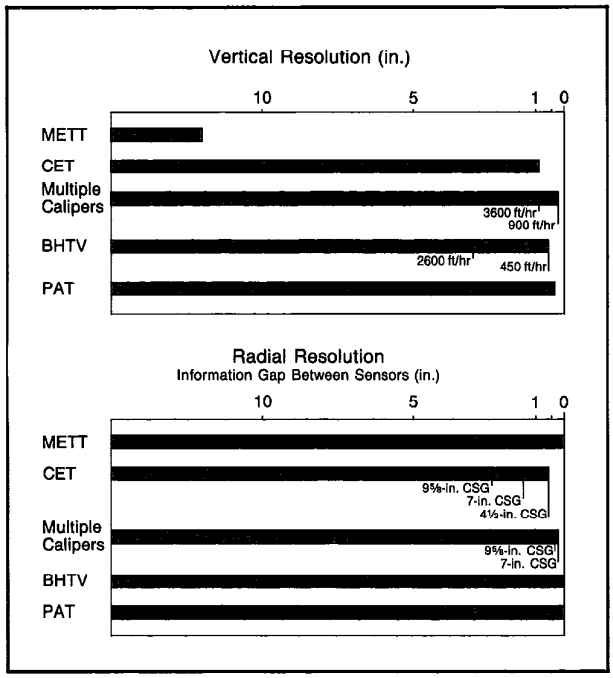

Table 6-2—Vertical and radial resolution for corrosion evaluation sensors

7 Perforating

Perforating technology has evolved from the early mechanical perforators to bullet guns to the shaped charge guns which are used on almost all well completions today. The shaped charge design has also evolved from the early slug-carrying jet into the efficient, high-performance charges currently in use.

Well-completion design is also undergoing a revolution. Three advances—the Perforation Analysis program (SPAN*), the Measurement While Perforating tool (MWP), and the new theory of well testing (Chapter 4)—are contributing to the accurate design and testing of individual well completions.

Technical innovation has transformed Tubing-Conveyed Perforating (TCP) into a very successful well completion system that permits underbalance perforating with large casing guns. In certain areas, it has replaced the wireline-conveyed gun.

SHAPED CHARGE THEORY

In the late 1800s, C.E. Munroe observed that explosives with indentations would imprint on steel plate. Experimenting with different cavities, he managed to achieve penetrations into steel equal to half the cavity's diameter. In the late 1930s, a Swiss, H. Mohaupt, lined a cone-shaped cavity. Enormous penetrations were obtained in solid steel targets. During the second world war the lined shaped charge cavity was developed into a variety of anti-tank weapons.

Shaped charges were first used to perforate oil wells in 1948 and, although many refinements have been made, the same basic technology is employed today.

The shaped charge consists of four basic components: the outer case, explosive powder, primer, and metallic liner. A schematic of a shaped charge is shown in Fig. 7-1.

The outer case is manufactured from a variety of materials depending on the desired mechanical characteristics. Steel and zinc are the most common materials; however, aluminum, ceramics, and glass are also used to form the case. Regardless of the material used to form the case, tight tolerances must be met to ensure correct operation of the shaped charge.

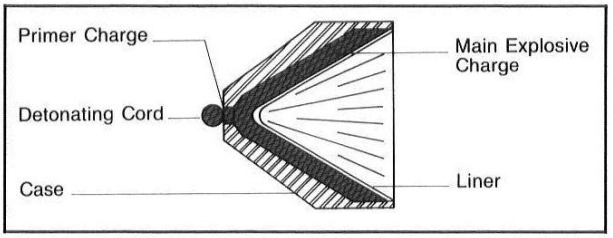

Fig. 7-1—Shaped charge schematic

The selection of explosive material is based on the well temperature and anticipated exposure time at that temperature. RDX, HMX, PSF, HNS, PYX, and TACOT are all explosives used in oil well shaped charges. The temperature versus exposure time curve for each of the explosives commonly used in Schlumberger shaped charges is given in Fig. 7-2. Most wells are within the RDX temperature range and therefore are perforated with shaped charges loaded with RDX. The increase in tubing-conveyed perforating (TCP) has accelerated the development of high temperature shaped charges. Explosives are subjected to elevated temperatures

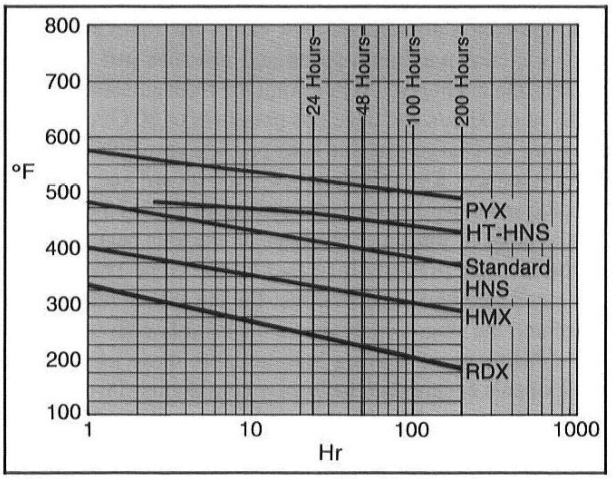

Fig. 7-2—Temperature ratings of explosive systems

for extended periods of time during TCP operations. In the intermediate temperature range shaped charges are manufactured with HMX. For high temperature wells or time consuming completions Schlumberger shaped charges are manufactured with HNS. PSF has been used extensively for wireline applications in the past, however, it is not recommended for TCP applications and is being phased out. PYX shaped charges are under development. The highest temperature rated explosive that has been used in oil well perforators is TACOT. The low volume of production and many steps involved in the manufacture of TACOT result in a very high priced explosive.

The liner is the most important element of the charge. The final performance of the shaped charge is largely dictated by the liner. In the early development of shaped charges solid metal liners were used; however, the slow moving trailing section of the jet, commonly known as the slug, obstructed the perforation. To overcome this problem, a blend of various metallic powders are compressed to form the liner. This allows the slug to disintegrate during the explosion. Liners are formed from mixtures of copper, lead, zinc, tin, or tungsten. The density distribution and dimensions of the liner must be tightly controlled to maintain consistent, high performance.

When the shaped charge is installed in a gun the detonating cord runs along the gun's length and contacts each charge at the primer region. After the gun is positioned correctly in the well the detonating cord is initiated by either applying current to an electric detonating cap or striking a nonelectric detonating cap with a firing pin. The wave front from the detonating cord travels at about 7000 m/s and reaches pressures around 15 to 20 GPa. This wavefront initiates the fine-grained primer explosive that fills the short tunnel connecting the detonating cord with the bulk of the explosive. The detonation accelerates as it enters the main explosive until it attains maximum speed and pressure just before it reaches the liner apex. At this point the front advances spherically at 8000 m/s and develops pressures of 30 GPa. At this pressure the charge case and liner provide very little mechanical resistance. The case is propelled outward and the liner is collapsed inward towards the symmetry axis of the charge. At the point of impact of the liner on the axis near the apex of the liner the pressure increases to 100 GPa. This divides the metal into two axial streams: the jet, which moves forward and the slug, which moves backward, with respect to the collision point. During liner collapse these jet and slug components accumulate to form a continuous, fast-moving stream of metal. The jet tip is moving at about 7000 m/s whereas the rear portion of the jet (the slug) is moving at about 500 m/s. This rapid increase in length due to the velocity gradient between the tip and slug allows the jet to penetrate through the casing and into the reservoir rock to a great depth. The sequence of events is simulated using a computer model shown in Fig. 7-3.

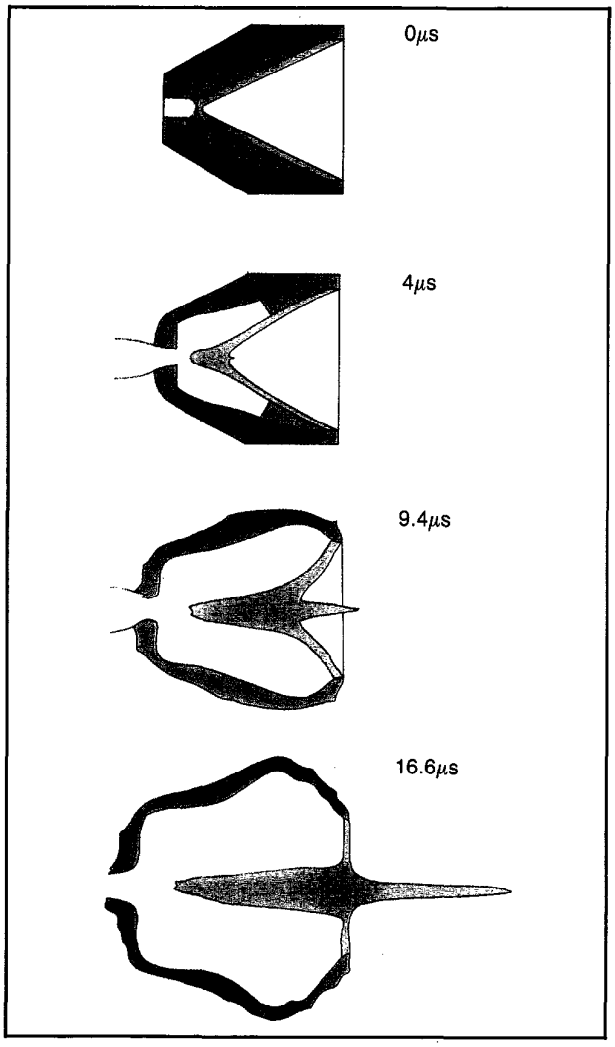

Fig. 7-3—Computer-simulated model

The jet can be considered a high velocity, rapidly stretching rod which strikes the casing and reservoir rock with an impact pressure of 100 GPa. The target material cannot resist the jet's enormous pressure and flows plastically away from the impact point. The target material continues to flow in a radial direction from the path of the jet until the hoop stress around the circumference of the hole is sufficient to stop the growth of the hole. The jet continues to penetrate the formation until the pressure is insufficient to overcome the strength of the target material.

Penetration is accomplished by the high pressure associated with the stream of powdered-metal or solid metal pieces, depending on liner type, forcing the target material aside rather

than through a burning, drilling, or abrasion process. Temperature and explosive gases do not contribute to the penetration process. The simplest theory of metal liner penetration assumes that both jet and rock behave as fluids. Bernoulli's hydrodynamic theory describes the interaction between jet and rock and predicts that total penetration can be increased by using a dense, long jet. The expression for penetration depth for a nonstretching, high velocity, continuous stream of powdered metal particles is:

$$P = \sqrt{\frac{2\rho_{jet}}{\rho_t}}\, L \qquad \text{(Eq. 7-1)}$$

where:

P = penetration
ρ_{jet} = jet density
ρ_t = target density
L = length of jet.

This simple density law formula does not account for the stretching and instability of the jet and does not fully explain the effect of target strength on penetration. For instance, it is much more difficult for a jet to pass through water or air than the density law predicts.

New work suggests that the liner density is more important than predicted by the simple hydrodynamic model. In addition, the jet's velocity profile influences the penetration depth. In a general sense this theory confirms the earlier conclusion that increasing the density and length of the jet will result in increased penetration.

GUN SYSTEM DESIGN

Gun system design begins with the intended end use of the system. Will the gun be used for a natural completion where penetration length is critical or for a gravel pack where the perforation diameter is important? What shot density and phasing are required? The maximum diameter of the gun is limited by the casing and/or tubing size used in the completion.

After these constraints have been defined, the designers optimize the performance of the entire gun system. Performance of the system depends not only on the shaped charge design but also on the positioning of the charge with respect to the carrier wall and adjacent charges. Figure 7-4 illustrates the positioning of the charge within the gun carrier. The charge must be positioned to allow the material near the base of the liner to collapse onto the axis of symmetry before striking the carrier wall.

The oil industry has equated perforating gun performance with the amount of explosive in the shaped charge. Increasing the overall charge size and thereby increasing the amount of explosive does increase performance, however it must be remembered that the charge size is constrained by the gun diameter and shot density. For a given charge size there is an optimum explosive load. Too much explosive may, in fact,

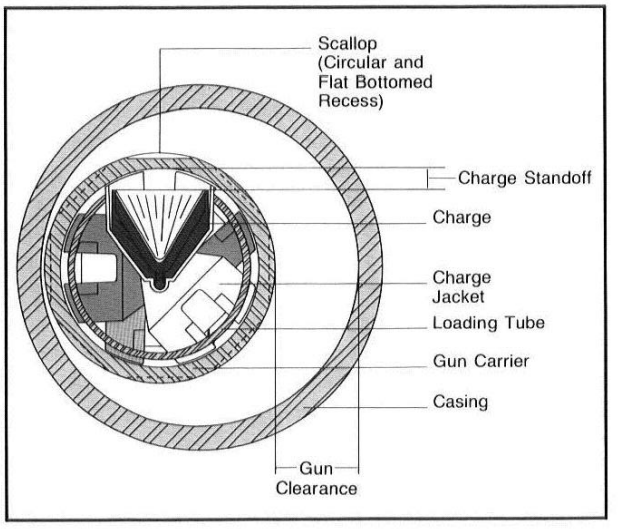

Fig. 7-4—Charge positioning

decrease the perforation performance. In addition, higher explosive loads may contribute to gun splitting or reduced gun life in hollow carrier guns and increased probability of casing damage when perforating with semi-expendable or expendable guns.

In addition to proper positioning of the charge in the gun, the liner geometry and material contribute to the shaped charge performance. Deep penetrating charges usually have narrow cone angles and dense powdered metal liners. Big Hole charges typically have wider cone angles and, in some cases, parabolic rather than conical shaped liners. The various shaped charge parameters are illustrated in Fig. 7-5.

The gun system designer must tune all of these parameters to achieve optimum performance in a particular gun diameter, shot density, and phasing arrangement.

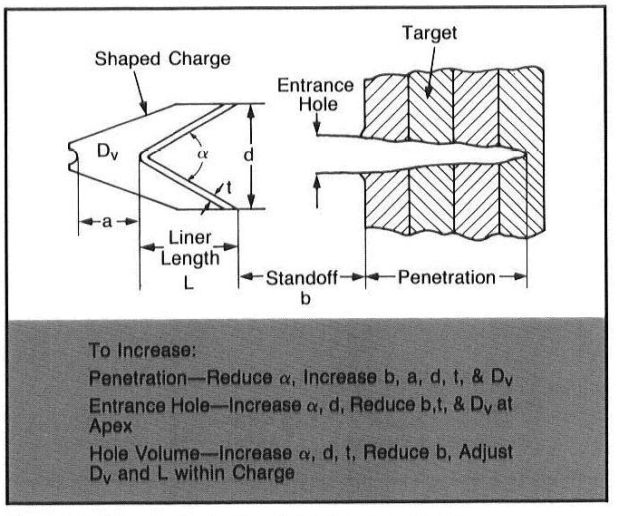

Fig. 7-5—Shaped charge design parameters

INDUSTRY TESTING OF PERFORATING SYSTEMS

The American Petroleum Institute (API) has developed recommended industry test procedures for oil well perforators. These procedures are described in the API RP-43 manual (1985). The recommended practice describes standard test procedures for the evaluation of perforators under surface conditions and under simulated well conditions.

The present API requirement in Section I defines a concrete target (Fig. 7-6) for the evaluation of bullet and jet perforators under multiple-shot, surface conditions. The physical characteristics of the perforation at different clearances, including penetration into concrete, entrance hole diameter in J55 grade casing, and burr height, are evaluated. A regular field gun, equipped with randomly selected charges, is used in the test.

In Section II of the RP-43 test procedure, a laboratory flow test is used to evaluate the perforation characteristics under simulated well conditions. Three single shots are fired into Berea core targets mounted in steel canisters (Fig. 7-7a). Entrance hole diameter in a mild steel face plate and penetration into the Berea cores are measured and averaged. Core flow efficiency as defined in Figs. 7-7b, 7-7c, and 7-7d is derived from the flow measurements. For casing guns the test requires a formation pressure of 1000 psi and a wellbore pressure of 1500 psi. After firing, an additional 200 ml of fluid is pumped into the perforated core before reversing the flow. In the through-tubing gun test, a formation pressure of 1200 psi is simulated with 1000 psi in the wellbore.

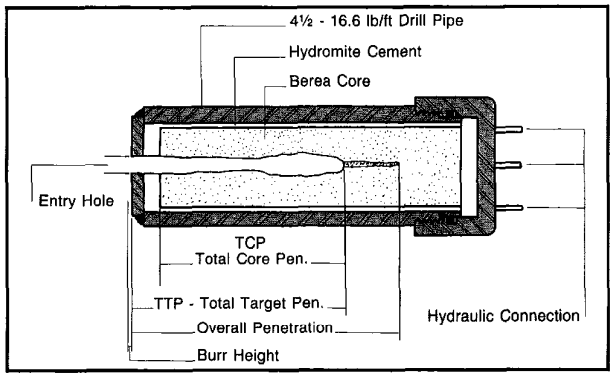

Fig. 7-7a—Shots fired into Berea core target

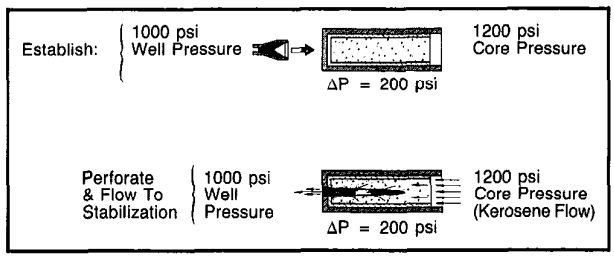

Fig. 7-7b—Through-tubing core flow efficiency in underbalanced condition

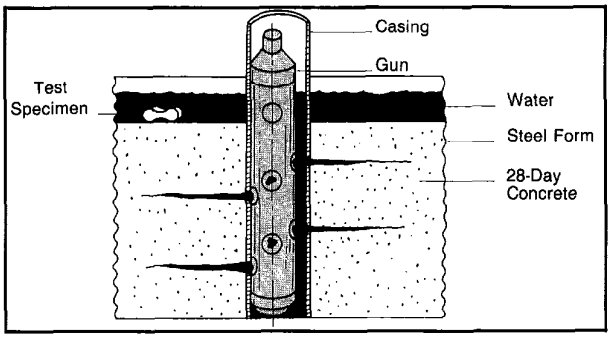

Fig. 7-6—Concrete target

The API Section II test has several limitations. Single shot performance may not reflect actual performance in a multiple perforation gun because of the lack of interaction between shaped charges. The linear nature of the flow through the Berea core results in a strong dependence on the penetration of the perforation and a weak dependence on the permeability impairment around the perforation. Finally, the entrance hole diameter in the mild steel face plate is not representative of the performance in real casings.

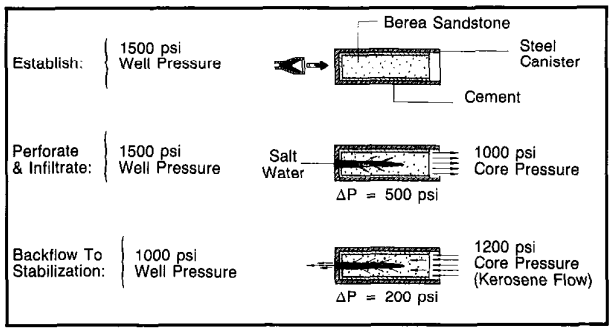

Fig. 7-7c—Casing core flow efficiency in overbalanced condition. Immediately after perforation, salt water flows into the core, followed by backflow with kerosene.

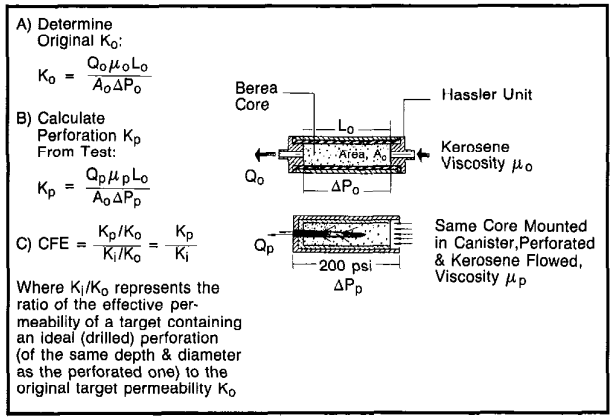

Fig. 7-7d—Core flow efficiency (CFE) determination results in a comparison between a drilled, or ideal, perforation and the actual perforation.

API Section I and II tests are routinely performed on deep penetrating charges. Only Section I tests are performed on Big Hole charges. Shaped charges exceeding 35 g of explosive are exempt from the Section II test because of potential damage to the laboratory apparatus.

GUN SYSTEM PERFORMANCE UNDER DOWNHOLE CONDITIONS

The performance of the gun system under actual downhole conditions is affected by many factors. The overburden stress and formation characteristics affect the penetration achieved by a jet perforator. These effects are discussed in the section on completion design.

In addition to the reservoir characteristics, the perforation penetration and entrance hole diameter are affected by the gun-to-casing clearance, wellbore fluid density and pressure, the casing hardness, and gun wall thickness. Although analytical expressions are not available to correct surface performance data given by API tests, the trend of the corrections is generally known and is covered in this section.

Penetration decreases with increasing gun-to-casing clearance because the jet must expend energy to pass through the completion fluid. As shown qualitatively in Fig. 7-8 deep penetrating charges are affected more than Big Hole charges. For this reason the through-tubing perforating guns are positioned against the casing wall using mechanical or magnetic positioning devices.

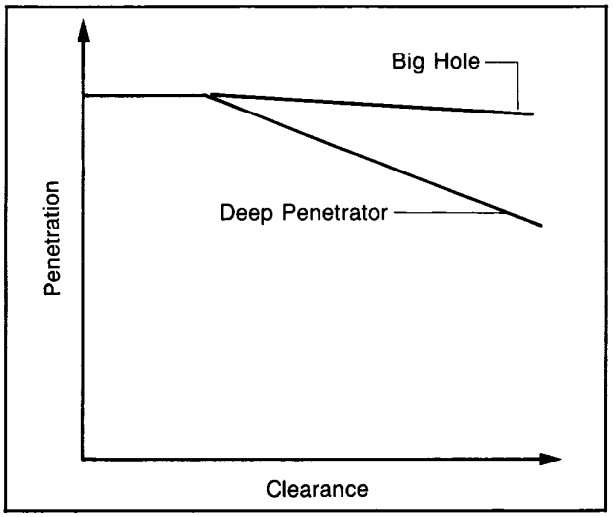

Fig. 7-8—Effect of water layer thickness

Although gun-to-casing clearance has little effect on the penetration performance of a Big Hole charge it has a large effect on the entrance hole diameter. The Schlumberger Ultrapack* charge is designed to provide an optimum entrance hole diameter when the gun is positioned in the center

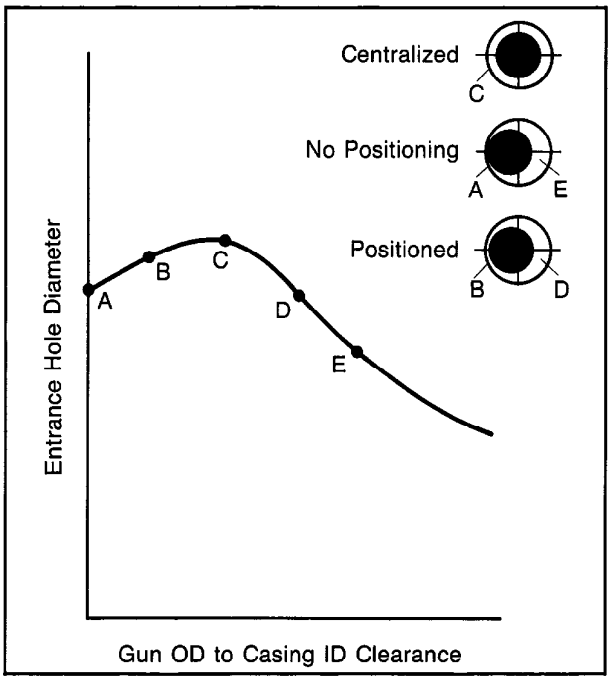

Fig. 7-9—Gun OD to casing ID clearance

of the casing. The entrance hole diameter versus clearance curve is illustrated in Fig. 7-9. Schlumberger Big Hole charges are designed to minimize the energy expended in producing a hole in the gun wall and maximize the entrance hole diameter through the casing and concrete. This design, coupled with the high strength of the HSD carriers, actually produces a relatively small hole in the gun, but a large hole in the casing. If the gun is not positioned it is possible for charges to experience both minimum and maximum clearances resulting in varying entrance hole diameters as illustrated by points A and E in Fig. 7-9. Consistent entrance hole diameters can be obtained by standing the gun off of the casing. The entrance hole diameter ranges between points B and D on the curve with the gun positioned. Schlumberger has positioning devices which stand the gun off of the casing yet allow washover if the guns become sanded in after perforating. The combination of the Ultrapack charges and the positioning devices allows consistent hole diameter and increased total area open to flow.

Wellbore pressure and density have very little effect on entrance hole diameter. However, as the pressure increases, penetration is reduced. This reduction in penetration may be due to the wellbore fluid collapsing onto the rear portion of the jet before it is able to penetrate the formation.

The entrance hole diameter through the casing is affected by the ultimate tensile strength of the casing, not the yield strength, for high-jet-velocity Schlumberger charges. The formula for this correction is given below:

$$\frac{EH_{new}}{EH_{J55}} = \left[\frac{2250 + 4.2\ B_{h(J55)}}{2250 + 4.2\ B_{h(new)}}\right]^{1/2} \quad \text{(Eq. 7-2)}$$

where:

B_h = Brinell hardness.

Equation 7-2 is expressed graphically in Fig. 7-10. As Brinell hardness is not a common field unit, a table is provided showing the equivalence between casing grade, minimum yield, tensile strength, Rockwell, and Brinell hardness.

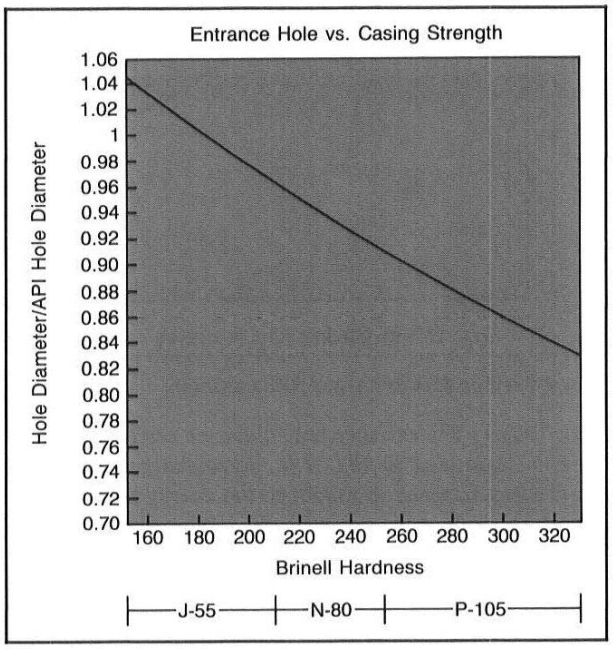

Relationship between Casing Grades and Physical Properties

Casing	Rockwell "B"	Rockwell "C"	Brinell	Minimum Yield (kpsi)	Tensile Strength (kpsi)
H-40	68-87		114-171	40	60-84
J-55	81-95		152-209	55	75-98
K-55	93-102	14-25	203-256	55	95-117
C-75	93-103	14-26	203-261	75	95-121
L-80	93-100	14-23	203-243	80	95-112
N-80	95-102	16-25	209-254	80	98-117
C-95	96-102	18-25	219-254	95	103-117
S-95		22-31	238-294	95	109-139
P-105		25-32	254-303	105	117-143
P-110		27-35	265-327	110	124-154
Y-150		36-43	327-400	150	159-202

Fig. 7-10—Entrance Hole vs. Casing Strength

Many of the Schlumberger high shot density casing guns are equipped with scallops on the outside wall of the carrier (see Fig. 7-4). The scallop serves two purposes. First, on both deep penetrator and Big Hole charges the scallop provides a depression to minimize the height of the burr beyond the outside wall of the carrier. Second, the entrance hole diameter in the casing is decreased when the jet must pass through more steel in the gun wall. The scallops serve to minimize the amount of steel that the jet must pass through before striking the casing. This effect is particularly important for Big Hole charges.

In a deep penetrating charge, most of the penetrating ability of the jet comes from the last 25 to 30% of the liner. Additional steel close to the charge, such as gun wall thickness or additional casing strings, has very little effect on the final penetration depth for large, deep-penetrating shaped charges. If burrs are not a problem, then scallops may be eliminated on the larger guns equipped with deep penetrating charges. On smaller through-tubing guns the effect is more significant and the carriers should always be scalloped.

COMPLETION DESIGN

The perforation must provide a clean flow channel between the producing formation and the wellbore with minimum damage to the producing formation. The ultimate test of the effectiveness of the perforating system, however, is the well productivity (injectivity). The productivity of a perforated completion depends significantly on the geometry of the perforations (Fig. 7-11). The major geometrical factors that determine the efficiency of flow in a perforated completion are:

- perforation length,
- shot density,
- angular phasing, and
- perforation diameter.

The relative importance of each of these factors on well productivity depends on the type of completion, formation characteristics, and the extent of formation damage from the drilling and cementing operations. The next sections explore the relative importance of the geometrical factors on natural, gravel pack, and stimulated completions.

Natural Completions

Isotropy

Productivity analysis of a perforated completion is significantly more complex than an openhole completion due to the 3-dimensional nature of the flow. Comparisons are usually made in terms of the productivity ratio which is defined as the ratio of productivity of a perforated completion to the productivity of an ideal openhole completion.

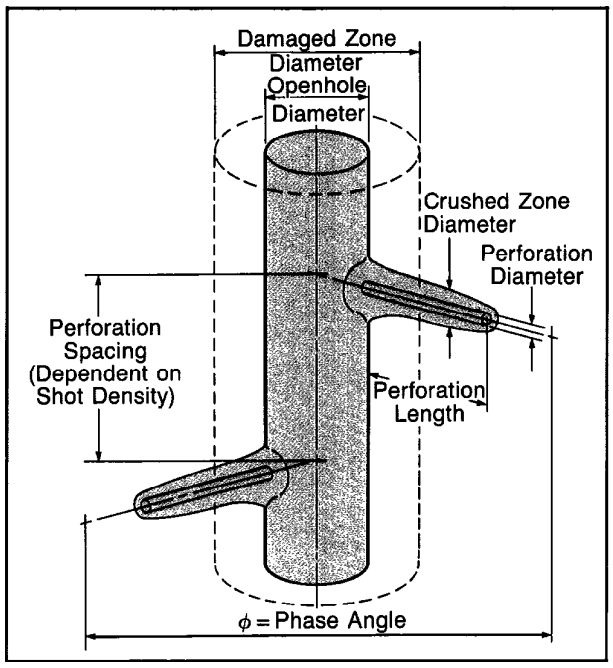

Fig. 7-11—Typical perforation geometry

$$PR = ln(r_e/r_w)/[ln(r_e/r_w) + \text{skin}] , \qquad \text{(Eq. 7-3)}$$

where:

PR = productivity ratio
r_e = drainage radius
r_w = wellbore radius.

Many investigators have studied the effect of perforating parameters on well flow efficiency. Muskat (1943) presented the first analytical treatment of the problem in 1942. McDowell and Muskat (1950), using electrolytic tank experiments, reported productivity results for perforations extending beyond the well casing. They showed the importance of perforation penetration on well productivity and concluded that the analytical treatment given in Muskat's earlier analysis was not accurate.

Harris (1966) and later Hong (1975) studied the productivity of perforated completions using a finite difference method. Although the model provided useful insight into the problem it was limited to wedge-shaped perforations.

Locke (1981) applied the finite element technique to model the full 3-dimensional problem of flow into perforations by properly taking into account the actual geometry of perforations and the spiral nature of their distributions around the wellbore. In a natural completion in a homogeneous, isotropic reservoir, Locke determined that productivity improves with shot density, penetration is much more important than perforation diameter (provided the diameter is greater than 0.25 in.) and penetration through the damaged zone is very important. In addition, an angular phasing of 90° improved productivity significantly when compared to 0° phasing and only slightly when compared to 120° and 180° phasing. The nomograph developed by Locke from his finite element model from which productivity ratios and skin factors can be estimated is shown in Fig. 7-12.

Following is a guide to the use of the productivity ratio nomograph.

1. Enter with perforation length on the upper-left stem. This length can be found from API RP-43 test data, corrected for overburden conditions if applicable. The example case shows 12 in.
2. Proceed horizontally to the appropriate perforation diameter, again obtained from API RP-43 test data. Example: 0.5 in.
3. Go down to the appropriate damaged zone thickness, 6 in. in the example (point a). Now measure along the 6 in. line from the vertical axis to the appropriate K_d/K_u line (line b-c example: 0.4). Transfer distance bc to b′c′, beginning at point a. From point c′, go to step 4. (The results of the nomograph assume that the damaged zone is completely pierced).
4. Go down to the appropriate crushed zone permeability reduction line (K_c/K_u); crushed zone thickness is assumed constant at 0.5 in. K_c/K_u may be estimated on the basis of core-flow efficiency data from API RP-43 or similar tests. A value of 0.2 has been suggested in the literature and as such has been used in this example. Further work is needed to define this parameter under downhole conditions.
5. Cross over to the shot-density (perforations/ft) line.
6. Go up to the angular phasing line. These phasings refer to real perforators: 90° phasing means the shot pattern follows spiral path, each shot offset by 90° from the two adjacent shots.
7. Read right to the productivity ratio (0.88 in the example) and the skin factor figures. These figures, used in conjunction with reservoir producibility calculations, will permit prediction of the production to be expected from a particular well.

The nomograph is drawn for a borehole size of 6 in. However, the effects of varying borehole size are partially compensating, and the nomograph can be used as is with coherent results over a considerable range of borehole sizes. An additional correction for a 12-in. borehole, 160-acre spacing, is shown. At point d, one simply raises the line to the 12 in., 90° line and then continues to the productivity scale (0.87 in the example).

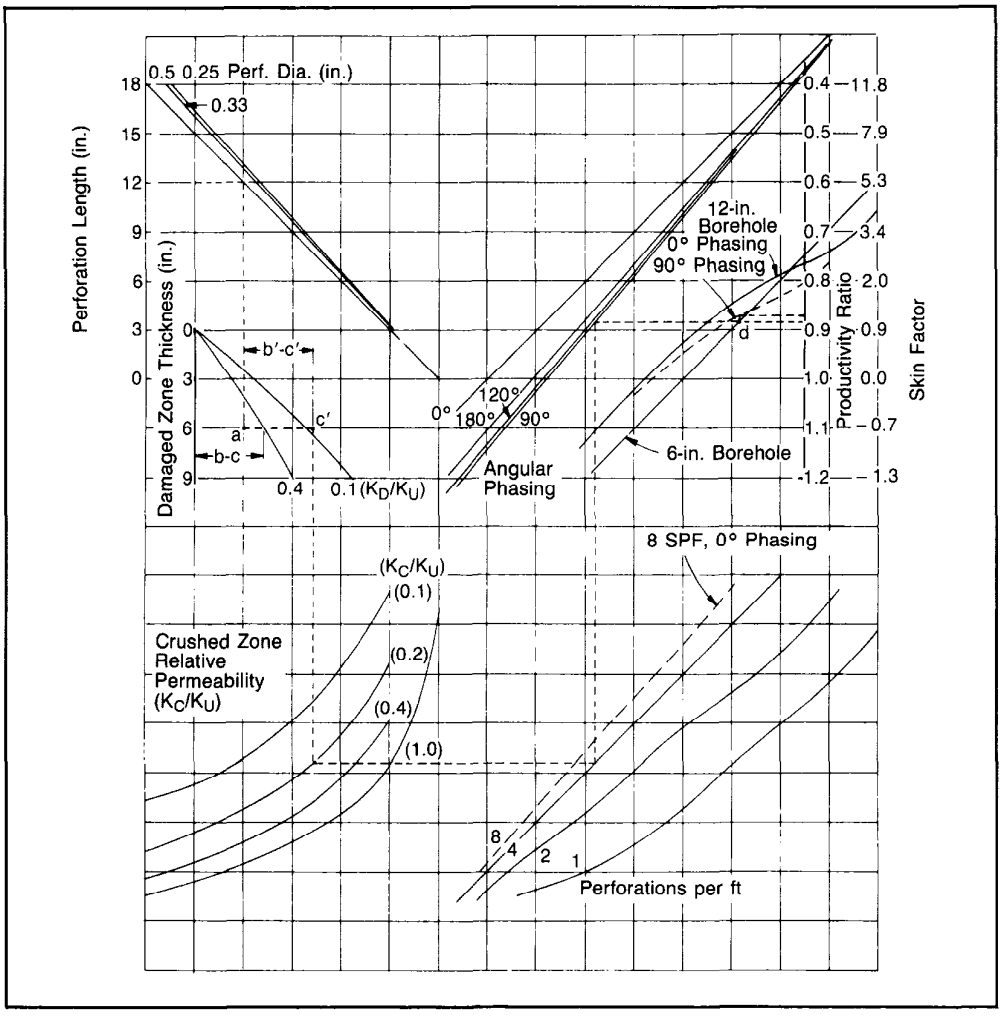

Fig. 7-12—Nomograph for productivity ratio

Tariq (1984), using a finite element model with a carefully chosen mesh size, confirmed Locke's findings qualitatively, but determined that the model was consistently optimistic by 5 to 10%. Figures 7-13 and 7-14 illustrate the effect of penetration length, shot density, angular phasing, and perforation diameter for an ideal case of no crushed zone, no damaged zone, and isotropic formation. Although it is difficult to rank the importance of each of the geometrical factors, it is generally agreed that perforation length, shot density, and angular phasing are significantly more important than perforation diameter in a natural completion.

Turbulent Flow

Tariq considered the case of turbulent flow in the near wellbore region. In high rate oil and gas wells turbulence can cause a reduction in productivity. The effect of turbulence in the near wellbore region is reduced for deep penetration lengths due to the increase in area open to flow. Figure 7-15 illustrates the 90° phasing case. Combining deep penetration lengths with angular phasing between adjacent perforations is an effective way to minimize the effect of turbulence in high flow rate wells.

To determine the optimum perforation geometry, consideration must be given to the characteristics of the reservoir including anisotropy, laminations, natural fractures, formation damage, and underbalance. To assist in designing an effective perforation program all available information from openhole logs, cores, and well tests should be used.

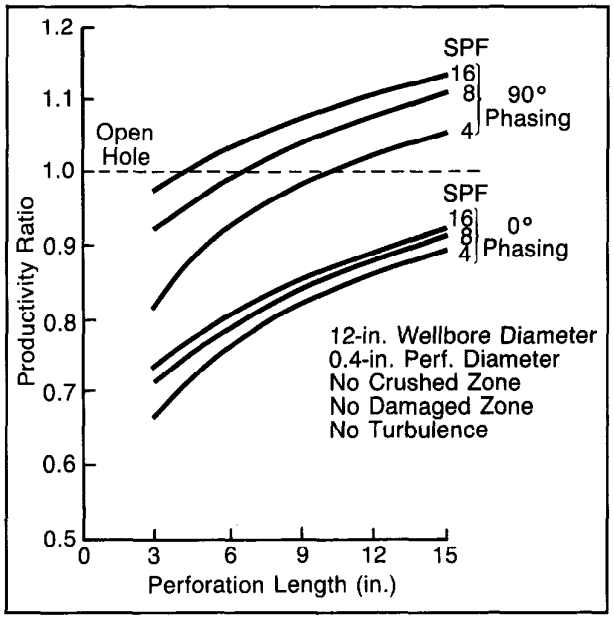

Fig. 7-13—Effect of various perforation parameters on productivity ratio

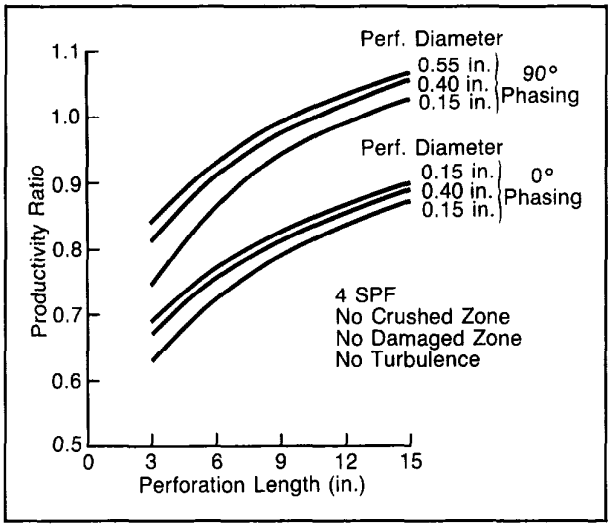

Fig. 7-14—Productivity ratio vs. perforation diameter

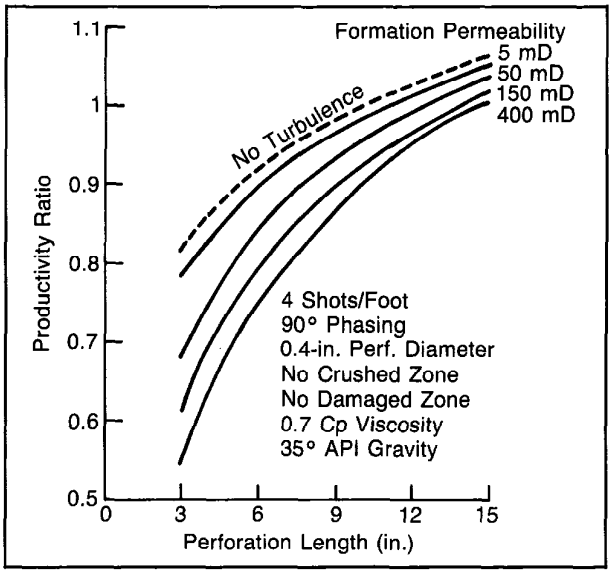

Fig. 7-15—Influence of turbulence on productivity ratio

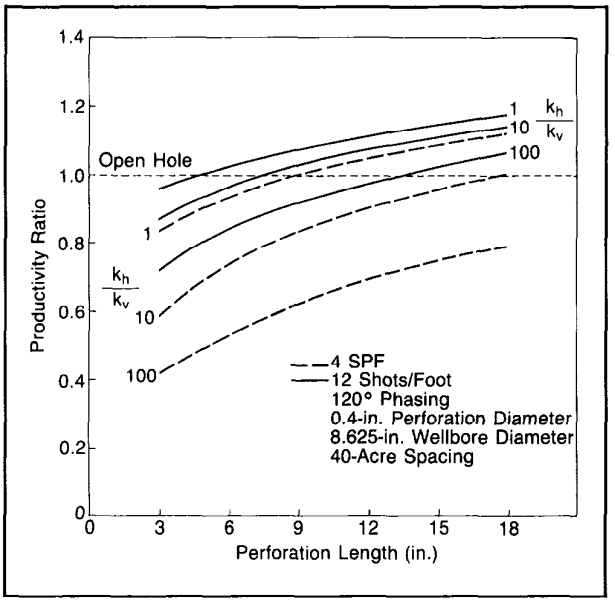

Fig. 7-16—Productivity ratio vs. perforation length—anisotropic case

Anisotropy

Most reservoir rocks have lower vertical permeability than horizontal permeability. Productivity is drastically reduced by the presence of permeability anisotropy. Figure 7-16 illustrates the effect of anisotropy on the productivity ratio. The reduction in productivity is much smaller for high shot densities; therefore, increasing shot density is an effective way of overcoming the adverse effects of anisotropy. At low shot densities the angular phasing between perforations has very little effect in an anisotropic environment as illustrated in Fig. 7-17. Figure 7-18 shows similar results for 12 shots per foot (spf). Similar effects to those described in the low shot density case are seen at a much reduced level.

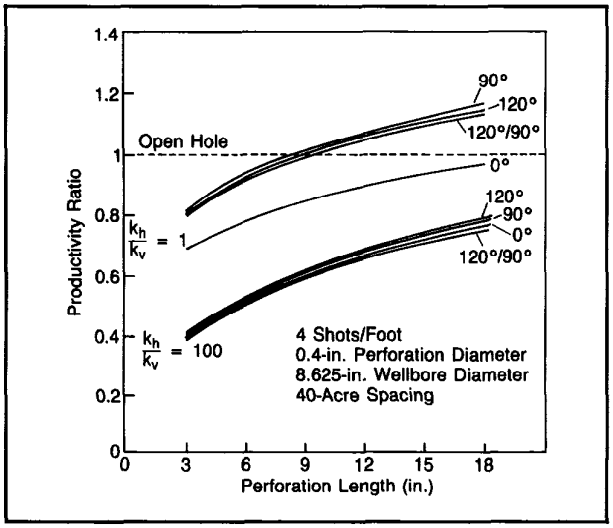

Fig. 7-17—Productivity ratio vs. perforation length—anisotropic case

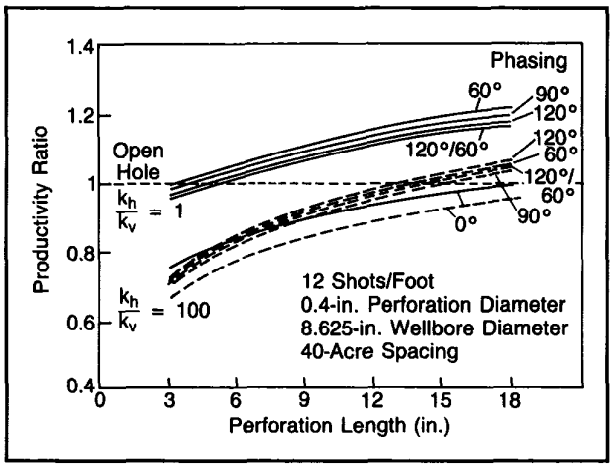

Fig. 7-18—Productivity ratio vs. perforation length—anisotropic case

Shale Laminations

Most sandstone reservoirs contain shale laminations. The presence of shale influences the flow pattern and must be considered during the design of the perforated completion. Research indicates that performance of a laminated formation is essentially independent of perforation location at high shot density. At low shot density the sand/shale distribution controls the performance of the shale laminated formation. Increasing the shot density is an effective way to improve productivity.

Natural Fractures

Productivity of perforated completions in natural fracture systems is highly dependent on the hydraulic communication between perforations and the fracture network, and varies with the type, orientation and interval of natural fractures. Different perforation parameters assume a variety of significances for each type of fracture system; however, perforation length and number of fracture planes seem to be the important parameters.

Formation Damage

During drilling and cementing of casing both mud and cement filtrates invade the formation. This zone of reduced permeability around the wellbore is usually referred to as the damaged zone. Similarly, during the perforating process a zone of reduced permeability referred to as the crushed zone is created around the perforation. These permeability impairments may significantly reduce the flow efficiency of a perforated completion.

Significant reduction in productivity occurs if the perforations do not extend beyond the damage zone. For formations that are suspected to have been damaged substantially the first concern should be the provision of perforation length in excess of the damaged thickness.

Although a crushed zone surrounding the perforation is seen in surface tests there is no conclusive evidence as to the extent of the permeability impairment in this zone. In laboratory experiments the thickness and permeability damage of the crushed zone appears to be determined by the type of shaped charge, the formation type, the underbalance used, and the cleanup conditions. At present, the common practice is to assume a crushed zone of 0.5-in. thickness with reduced permeability of 10 to 20% of the virgin formation.

Underbalance

The importance of shot density in improving productivity, especially in shale laminated formations, has been discussed. This discussion refers to effective shot density or the number of perforations actually producing. Field experience has suggested that underbalanced perforating (lower pressure in the wellbore versus the formation pressure) is an effective method to create open, undamaged perforations. The underbalanced pressure selected must be sufficient to expel debris for improved productivity, yet, at the same time avoid mechanical failure of the formation. If past field experience is not available for selecting the optimum underbalance the guidelines outlined herein should be used.

Guidelines for Selecting Optimum Underbalance

- **Bell's Criteria**

  Based on experiences around the world, Bell (1984) suggested the following criteria for selection of optimum underbalance:

Permeability	Required Underbalance (psi)	
	Oil	Gas
>100 md	200-500	1000-2000
<100 md	1000-2000	2000-5000

- **King's Charts**

  King, et al. (1985) published empirical charts (Figs. 7-19 and 7-20) based on a field study of 90 wells perforated with TCP in sandstone formations. The underbalance was considered sufficient wherever the subsequent acidizing did not improve the well's performance. These charts show the correlation between the underbalance pressure used in perforating, the formation permeability, and the type of reservoir fluid. Both Bell's data and King's correlations suggest that, whatever the fluid content or the formation permeability, the underbalance should be at least 200 psi.

- **Optimum Underbalance Based on Capillary Pressure**

  The underbalance selected should be sufficient to overcome the capillary forces for the removal of invaded mud filtrate. The local capillary pressure can be determined using core analysis. It can also be calculated assuming capillary pressure as a function of the height above the free water level and the difference in fluid densities:

$$P_c = (\rho_w - \rho_{hc}) \times h \times g\,, \qquad \text{(Eq. 7-4)}$$

  where:

  ρ_w = water density
  ρ_{hc} = hydrocarbon density
  h = height above free water level
  g = gravity.

  The underbalance should be approximately twice the capillary pressure as it has to act at some distance in the reservoir. This approach addressed the cleanup of the formation damage by drilling/completion fluids, but it does not consider the cleanup of a perforation through flushing of loose debris and removal of crushed zone around the perforations.

- **Safe Limits of Underbalance**

  From the productivity standpoint, one should strive for the highest value of underbalance. However, there are a number of reasons why one should limit the drawdown imposed on the formation.

  1. The drawdown should not cause mechanical failure of the formation. The Sand Strength Analysis Program* outputs a value of safe underbalance based on the mechanical properties of the formation as estimated from sonic logs.
  2. Excessive drawdown may lead to mechanical deformation of the casing and may cause permeability damage in the near wellbore region due to movement of fines.
  3. Initial spurt rates under high drawdown can be so high as to reach the critical velocity through the completion, i.e., the drawdown is limited by the area open to flow. Imposing higher values of drawdown than is needed to reach critical flow is useless and only endangers the completion mechanically.

- **Schlumberger Perforating and Testing Center Experimental Results**

  A series of experiments (Halleck and Deo, 1987) conducted in Berea sandstone cores of a specific permeability give new insight into the perforation cleanup phenomenon. The cleanup after underbalanced perforating occurs in two stages, first through high transient fluid gradients and, second, by steady-state pressure gradients across the zone of reduced permeability. The first lasts only a short period of time and involves limited flow volumes, while the latter occurs over an extended period of flow. For sufficiently high underbalance (800 to 1000 psi), the initial surge is enough to effectively clean the damage and little, if any, cleanup occurs during post-shot flow. For lower values of underbalance (200 to 600 psi), the post-shot flow does remove some damage, yet a significant amount of damage is locked in place and cannot be cleaned even at subsequent high differential pressures. Figures 7-21 and 7-22 present these results. The results of these experiments confirm in a broad sense both Bell's and King's conclusions that underbalances of 500 to 1000 psi are needed to obtain maximum flow rates in sandstone cores.

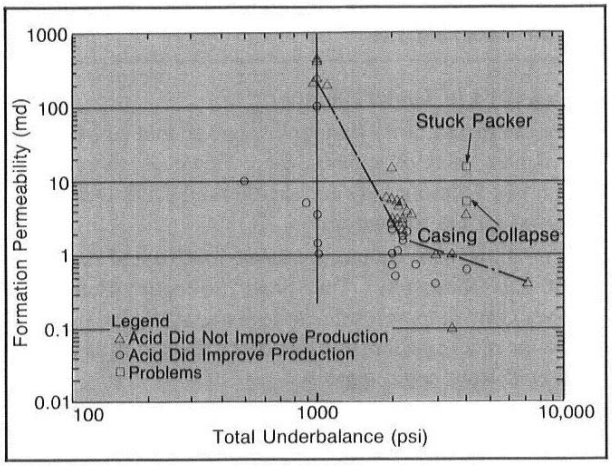

Fig. 7-19—Underbalance pressure used on tubing-conveyed perforating in gas zones in sandstone

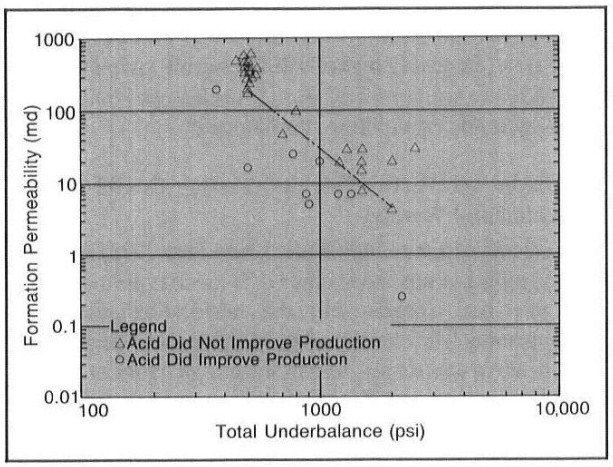

Fig. 7-20—Underbalance used on tubing-conveyed perforating in oil zones in sandstone

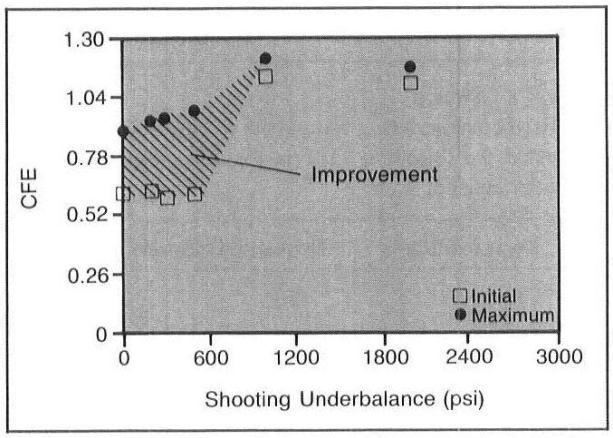

Fig. 7-21—Extent of flow improvement in brine-containing cores. Differences between initial and maximum CFEs show little improvement for shots fired with more than 500 psi underbalance.

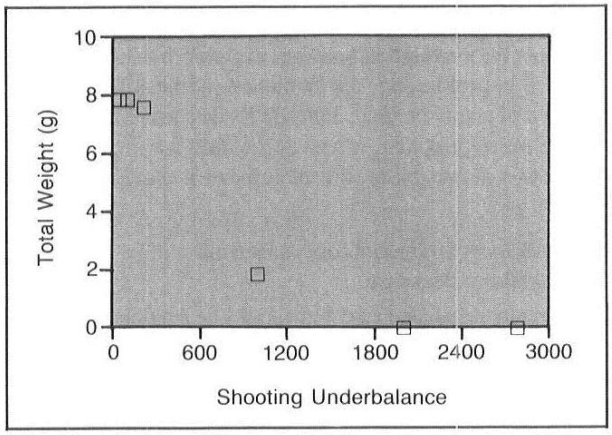

Fig. 7-22—Total weight of debris washed from brine-free cores by postshot flow

Sand Control Completions

In unconsolidated formations the mechanical failure of the formation and subsequent production of sand is a critical problem. Gravel packing is the most common technique for controlling sand production in unconsolidated formations. The technique involves perforating the formation, cleanup of perforations using wash or back-surge and placement of appropriately sized high quality sands called "gravel" between the unconsolidated formation face and the screen. The pressure drop due to liquid flow through a filled perforation tunnel is given by:

$$\Delta P_L = 0.888 \frac{L\mu Q}{kA} + 9.1\,(10^{-13})\,\beta L\rho \left(\frac{Q}{A}\right)^2, \qquad \text{(Eq. 7-5)}$$

where:

ΔP_L = pressure drop, psi
L = length of perforation tunnel, ft
μ = fluid viscosity, cp
k = permeability of tunnel fill material, darcies
Q = flow rate, bpd
A = cross sectional flow area of perforation tunnel, ft^2
ρ = fluid density, lb/ft^3
β = beta factor (inertia coefficient for sandstone), ft^{-1}.

It can be seen from the above equation that the pressure drop across the filled perforation tunnel is dependent on the cross-sectional flow area. For an optimum gravel pack completion large, consistent, perforation diameters and high shot

density are required. The large perforation diameter must be maintained through to the cement/formation interface or the pressure drop will be larger than anticipated. Penetration must be sufficient to reach the formation.

Stimulated Completions

Many low permeability wells will not flow and must be stimulated by acidizing and/or hydraulic fracturing. In some cases, ball sealers may be used to seal off a zone taking fluid, thus permitting pressure to be applied to other zones. This procedure is repeated until all zones are hydraulically fractured. In other cases the hydraulic fracturing operation may be staged. In this case, the first zone is selectively perforated, fractured, and then sealed using a frac plug. The frac plug isolates previously fractured zones from the subsequent stage. This operation is repeated for the remaining stages. After the entire hydraulic fracturing job is completed the frac plugs are retrieved and the well put on production.

For hydraulic fracturing operations the perforation diameter is the crucial parameter. The number and size of perforations are governed by hydraulic horsepower available, formation breakdown pressures, proppant diameter, and flow rates.

SCHLUMBERGER PERFORATION ANALYSIS PROGRAM (SPAN)

General

As can be seen from the preceding discussion, perforated well completion design is a complex problem. Choice of an optimum perforation geometry for a particular formation, constrained by the casing and tubing diameters, is difficult and has in the past largely been accomplished by trial and error. The SPAN program predicts the outcome of any perforating job allowing the completion engineer to compare a variety of alternatives. The program consists of a penetration predictor module and a productivity calculation module.

The penetration module computes the perforation length and diameter for deep penetrator and Big Hole shaped charges for a given completion and formation. The most recent version employs the physics approximated by Allison and Vitali's (1963) 1-dimensional hydrodynamic theory to compute perforation length and diameter for deep penetrator charges. This basic theory of penetration assumes that both jet and rock behave as fluids if the penetration pressure exceeds the rock strength. Theory indicates that penetration depth is dependent on the jet-to-target density ratio as well as the jet length. As described in an earlier section the density ratio is controlled by the selection of liner material.

In the SPAN program penetration for the deep penetrating shaped charges is calculated using the basic theory described above and by using experimental data. Schlumberger is presently developing a new penetration prediction algorithm for deep penetrating charges to improve the accuracy of the predictions.

For each of the Big Hole charges the relationship between penetration and gun-casing clearance has been determined experimentally and is used to predict penetration. The program takes into consideration the type of charge, gun phasing and position, casing specifications and positions, completion fluids, and borehole size.

Entrance Hole Diameter Prediction

The entrance hole diameter estimations are based on experiments using grade J55 steel plates. In addition, for each of the Big Hole charges, the relationship between entrance hole diameter and gun-casing clearance has been determined experimentally and is used to predict entrance hole diameters. In the SPAN program entrance hole diameters are computed as if the casing is grade J55 with an average yield of 65,000 psi. Corrections are then made by the program for other casing grades using the following formula:

$$\frac{EH_{new}}{EH_{J55}} = \left[\frac{2250 + 4.2y}{2250 + 4.2x}\right]^{1/2}, \qquad \text{(Eq. 7-6)}$$

where:

$x = 2.0 \times$ (casing yield, kpsi) + 60

$y = 2.0 \times$ (65 kpsi) + 60 = 190.

where "casing yield" is for the new casing and "65 kpsi" is the yield strength of J55.

Penetration Correction for Formation Characteristics

Perforation penetration is believed to decrease with overburden stress and formation strength. The SPAN program allows perforation penetration to be corrected for these characteristics before estimating productivity by using either of the following methods.

- Thompson's Method (1962), which correlates formation penetration to the compressive strength of the rock according to the following formula:

$$P = P_r\, e(0.086 \times (c_r - c)/1000), \qquad \text{(Eq. 7-7)}$$

where:

P = formation penetration

P_r = penetration in a reference formation

c_r = compressive strength of the reference formation, psi (In the SPAN program reference formation is Berea sandstone with a compressive strength of 6500 psi.)

c = compressive strength of the producing formation, psi.

- Saucier and Lands Method: This involves the use of multiplication factors derived on the basis of experiments for three classes of rock: soft rock represented by Austin limestone, medium hardness rock represented by Berea sandstone, and hard rock represented by Wasson dolomite. These results are shown graphically in Fig. 7-23.

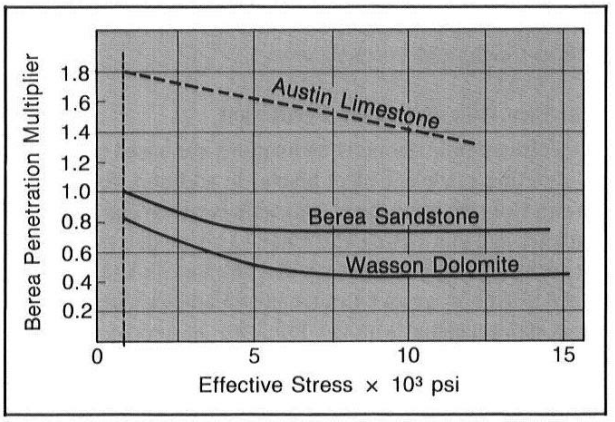

Fig. 7-23—Curves for approximating downhole penetrations after accounting for casing and cement thicknesses

- No Correction: The latest test performed by Schlumberger using large-scale, multiple perforation targets cast serious doubts on the previously observed stress effect. In these tests no significant differences in penetration depths for isotropic stresses up to 8000 psi were observed. More work is underway to resolve this issue. In the meantime, the SPAN program supports a "no correction" option.

The SPAN program performs the penetration computations twice, for the most favorable case when the gun lies in the same eccentered position as the casing and for the unfavorable case when the gun is on the opposite side of the hole.

Figure 7-24 is a typical SPAN plot showing a cross section of the charge penetration. Figure 7-25 is a listing of the perforation geometrical characteristics from SPAN analysis.

Productivity Calculation

In the productivity module the SPAN program uses Locke's and Hong's results to calculate the productivity of the perforated completion using the perforation parameters which are input directly or calculated in the penetration module.

Locke's finite element model was described in an earlier section. Hong also used a numerical technique to study the effects of perforation parameters on productivity. He presented his results in the form of nomographs for simple and staggered perforation patterns. In the SPAN program one has the choice of using either Locke's or Hong's nomograph. Hong's nomograph is less accurate than Locke's data;

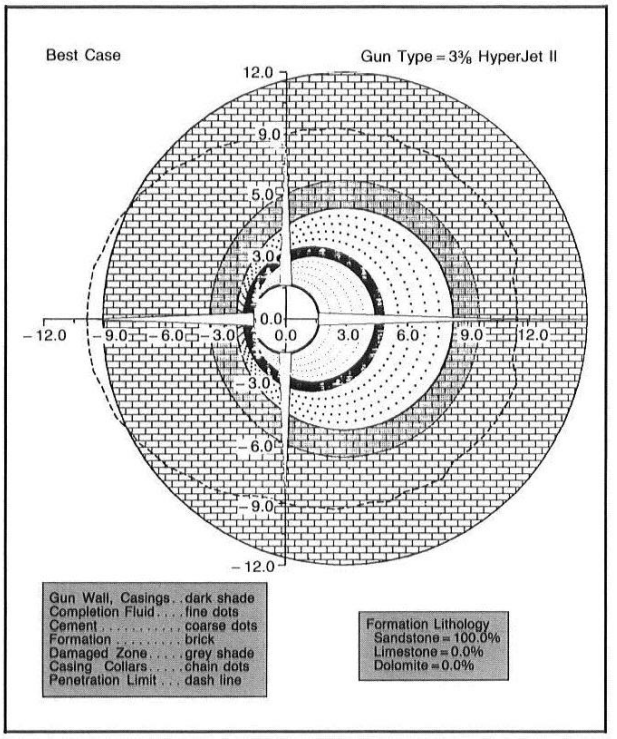

Fig. 7-24—Cross section showing charge penetration depth

Perforation Characteristics			
Best Case			
Orientation	Deg: 0.00	90.00	180.00
Total Penetration	in. : 8.25	7.35	9.88
Formation Penetration (1)	in. : 7.25	4.29	3.08
Entrance Hole Diameter	in. : 0.37	0.31	0.24
Worst Case			
Orientation	Deg: 0.00	90.00	180.00
Total Penetration	in. : 8.14	8.02	9.49
Formation Penetration (1)	in. : 4.35	3.94	5.39
Entrance Hole Diameter	in. : 0.24	0.31	0.37
API Section II			
Overall Penetration	in. : 11.30		
Total Target Penetration	in. : 10.85		
Entrance Hole Diameter	in. : 0.38		

1) Penetration corrected for lithology using the algorithm of Lands-Saucier correction factor = 0.73

Fig. 7-25—Perforation characteristics

however, it covers a broader range of perforation parameters and anisotropy.

Figures 7-26 and 7-27 show typical outputs of the productivity module of the SPAN program. Again the best and worst case corresponds to the position of the gun.

The productivity module also includes a skin analysis. The three skin factors included in the analysis are skin due to partial penetration for the pay zone, skin due to well

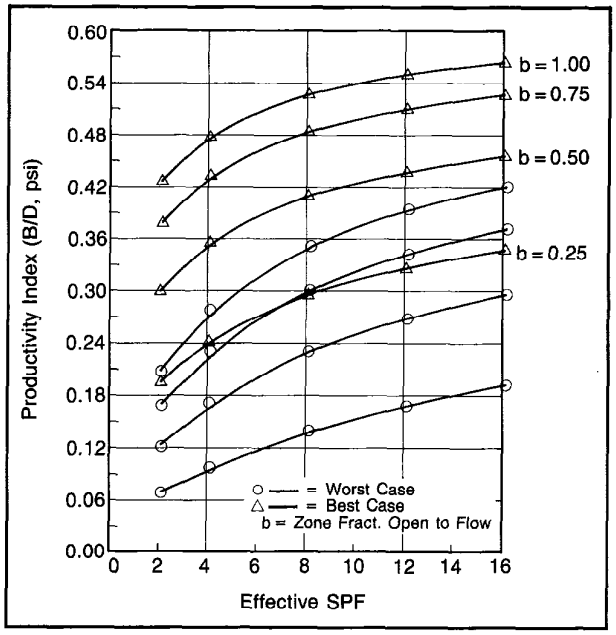

Fig. 7-26—Productivity index

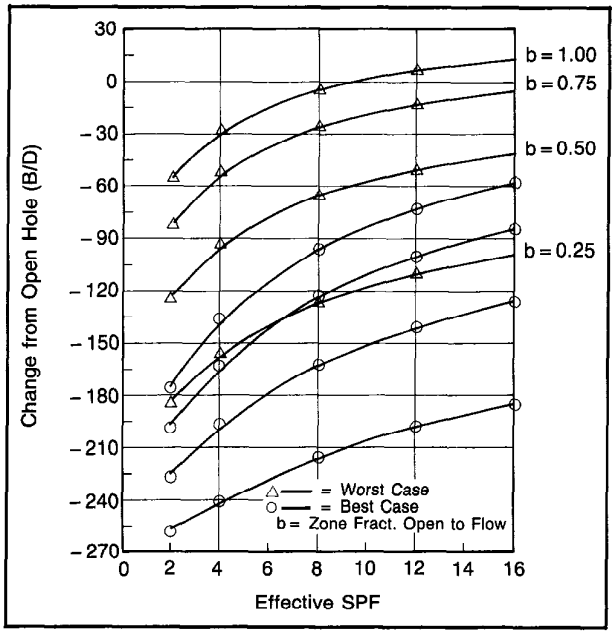

Fig. 7-27—Change from openhole production

deviation, and skin due to invasion damage. A listing of the variation of the total skin with different parameters is also included in the output (Fig. 7-28).

WELL COMPLETION TECHNIQUES

There are three basic techniques employed today to perforate

Shot Density per ft		2.0	4.0	8.0	12.0	16.0
Total Skin						
1. Best Case	b = 0.25	12.25	8.28	5.60	4.44	3.76
	b = 0.50	5.44	3.46	2.12	1.54	1.20
	b = 0.75	2.93	1.61	0.71	0.33	0.10
	b = 1.00	1.77	0.78	0.10	-0.18	-0.35
	b = 1.00(3)	1.77	0.78	0.10	-0.18	-0.35
Worst Case	b = 0.25	46.56	30.56	19.44	14.98	12.47
	b = 0.50	23.58	14.60	9.04	6.81	5.55
	b = 0.75	15.02	9.04	5.33	3.84	3.01
	b = 1.00	10.83	6.35	3.57	2.45	1.82
	b = 1.00(3)	10.83	6.35	3.57	2.45	1.82
Productivity Ratio						
2. Best Case	b = 0.25	0.38	0.48	0.58	0.63	0.67
	b = 0.50	0.58	0.69	0.78	0.83	0.86
	b = 0.75	0.72	0.83	0.91	0.96	0.99
	b = 1.00	0.81	0.91	0.99	1.02	1.05
Worst Case	b = 0.25	0.14	0.20	0.28	0.34	0.38
	b = 0.50	0.24	0.34	0.46	0.53	0.58
	b = 0.75	0.34	0.46	0.59	0.67	0.72
	b = 1.00	0.41	0.55	0.68	0.76	0.81

b = Fraction of pay zone open to flow
1) Total skin is computed by the method of Saidikowski with Odeh's correction factor
2) Production ratio is computed for steady state flow
3) Skin due to perforations and damage only

Fig. 7-28—Output showing variation of total skin using different parameters

a well. Although the variations are virtually endless, the following discussion is limited to a basic description of the three techniques.

Wells can be perforated using casing guns conveyed on wireline, through-tubing guns, and tubing-conveyed guns. These methods are illustrated in Fig. 7-29. Because each method has advantages and limitations, the completion engineer must choose the most appropriate technique for each well.

Wireline Casing Gun Technique

Perforating with a casing gun conveyed on wireline has been a standard technique for many years. Before the tubing and wellhead are put in place, a hollow carrier casing gun is lowered into the well on wireline, positioned opposite the productive zone, and detonated. The main advantages of this system are as follows:

- The diameter of the gun is limited only by the ID of the casing; therefore, large, high performance shaped charges can be conveyed in a multiphase, high shot density carrier.
- The casing gun offers high reliability because the blasting cap detonating cord and shaped charges are protected from the wellbore environment and the carrier is mechanically strong.

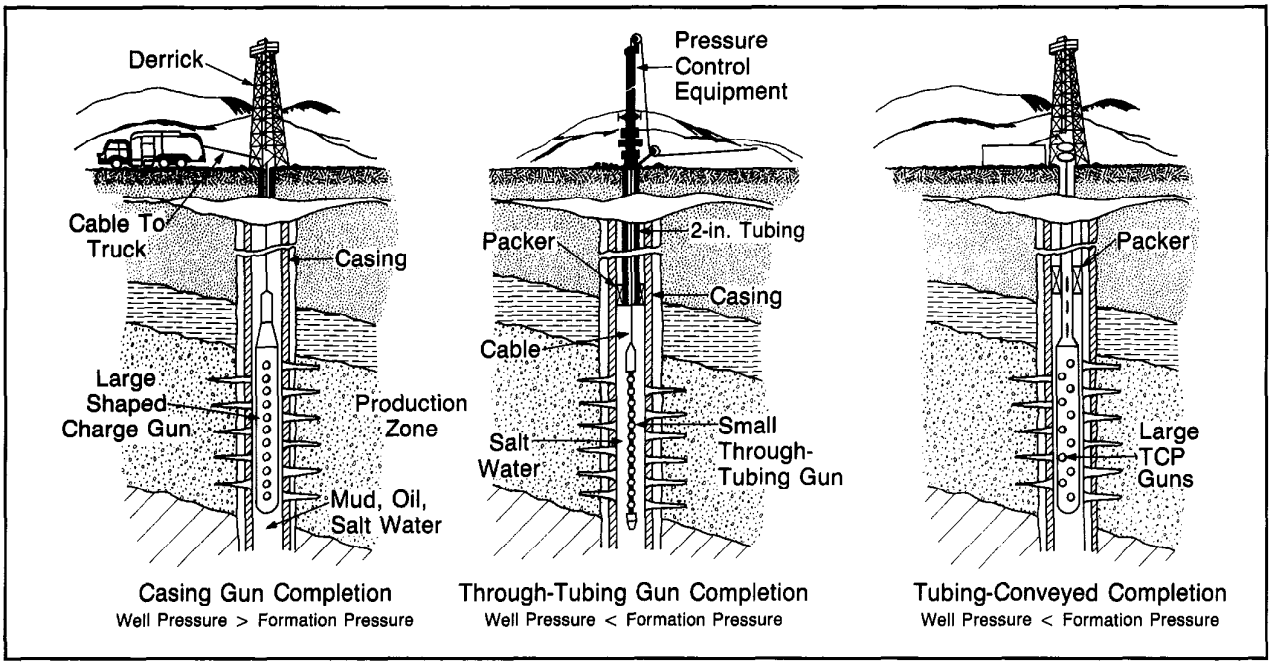

Fig. 7-29—Well completion techniques

- Selective firing is available between guns.
- Guns are accurately positioned opposite the zone of interest using a casing collar locator.
- No damage occurs to the casing and virtually no debris is left in the well.

There are two main limitations to this method:

- As a general practice, the well must be perforated with the wellbore pressure greater than the formation pressure. This pressure differential may prevent optimum cleanup of the perforations. The situation is aggravated when perforating in drilling mud. The mud plugs are difficult to remove even when subjected to high reverse pressure. Perforating in clean liquids such as salt water is recommended.
- The strength of the wireline and the weight of the casing guns limits the length of the assembly which can be run on each trip into the well.

  Schlumberger offers a family of hollow carrier, steel, port plug casing guns in diameters ranging from 3⅜ to 5 in. with a maximum shot density of 4 spf and an angular phasing of 90°. In addition there is a family of high shot density guns which may be conveyed on wireline ranging in diameter from 2⅞ to 7¼ in. with shot densities from 5 to 12 spf.

Through-Tubing Perforating Technique

In 1953, Humble Oil and Refining Co. pioneered the permanent-type well completion. This technique involves setting the production tubing and wellhead in place and then perforating the well with small diameter guns capable of running through tubing. The main advantages of this technique are as follows:

- The well may be perforated with the wellbore pressure below the formation pressure allowing the reservoir fluids to instantly clean up the perforating debris.
- Completion of a new zone or a workover of an existing zone does not require the use of a rig.
- A casing collar locator allows for accurate depth positioning.

The main limitations of this method are as follows:

- To allow the gun to run through tubing, smaller shaped charges, with reduced penetrations, must be used. To achieve maximum penetration with through-tubing perforators the gun is usually positioned against the casing to eliminate the loss of performance when perforating through the liquid in the wellbore. This arrangement restricts the gun to 0° phasing.
- In an effort to improve the penetration performance, gun system designers eliminated the hollow steel carrier and placed pressure tight capsule charges on a strip or wire. These guns are called expendable or semi-expendable depending on whether the wire or strip is retrieved. Removing the steel carrier allows a larger charge to be used;

however, charge case debris is left in the well after perforating and the casing may be damaged by the detonation.

- The charges are exposed in the expendable and semi-expendable systems restricting these guns to less severe well environments and lower running speeds.

Schlumberger offers a line of hollow carrier HyperDome* guns in diameters ranging from 1⅜ to 2⅞ in. The Enerjet* gun is a high performance, semi-expendable gun offered in 1 11/16-in. and 2⅛-in. diameters.

Tubing-Conveyed Perforating Technique

Although various attempts were made to convey perforating guns into the well on tubing it was not until the early 1980s that widespread use of the service began. The basic technique involves assembling hollow carrier steel casing guns vertically with a firing head on top. There are several types of firing heads including drop bar, differential pressure, direct pressure, and electrical wet connect. On top of the firing head is a sub used to allow reservoir fluids to flow into the tubing. A production packer is attached above the fluid communication sub. This entire assembly is then lowered into the well on the end of the tubing string. The string is depth positioned usually with a gamma ray survey. After the guns are positioned, the packer is set, and the well is readied for production. This includes establishing the correct underbalance condition in the tubing. The guns are then fired and the surge of reservoir fluids is used to clean up the perforations. Depending on the situation the guns may be retrieved or dropped to the bottom of the well. Many variations of the procedure described above are in use today. The main advantages of this technique are as follows:

- The well can be perforated with large diameter, high performance, high shot density casing guns with the wellbore pressure lower than the formation pressure (underbalanced) allowing instantaneous cleanup of the perforations.
- The wellhead is in place and the packer is set before the guns are fired.
- Large intervals can be perforated simultaneously on one trip into the well.
- Highly deviated and horizontal wells can be perforated by pushing the guns into the well.

The main limitations of the technique are as follows:

- Unless the guns are withdrawn from the well it is difficult to confirm whether the entire gun fired. Effective shot detection systems may overcome this limitation.
- Explosives degrade when exposed to elevated temperatures, reducing shaped charge performance. It takes many times longer to run a TCP string into the hole than a wireline gun. To compensate, a more expensive and, in some cases, less powerful explosive must be used on TCP operations.
- Selective perforating options with TCP are limited. Limited entry perforating may not be economical with TCP.
- Accurate depth positioning of the gun string is more difficult and time-consuming than wireline depth positioning.

Schlumberger offers a family of high performance TCP guns ranging in diameter from 2⅞ to 7¼ in. with shot densities ranging from 5 to 12 spf.

COMPLETION EVALUATION

After the well has been perforated the completion engineer is interested in verifying the initial productivity prediction. Completion evaluation has always been expensive and time consuming, involving at least a few days of well testing and production logging. For this reason it is often bypassed. To assist the completion engineer in evaluating the perforated completion to determine formation permeability, reservoir pressure, and skin, Schlumberger has developed a Measurement While Perforating (MWP) tool to measure downhole pressure and temperature immediately after perforating. If a high positive skin is calculated, the completion engineer may elect to reperforate the formation or perform additional remedial treatments such as acidizing or fracturing.

The Measurement While Perforating tool can be used to fire both wireline and tubing-conveyed guns. Before the guns are fired, the pressure sensor on the MWP tool can be used to verify that the correct underbalance condition has been established. Figure 7-30 illustrates downhole pressure and temperature recordings versus time before and after perforation. Before the guns were fired the pressure gauge registered 3308 psi, equivalent to the head of the brine cushion filling the tubing. After perforating, formation fluids surged into the well and pressure increased, eventually reaching reservoir pressure.

The well test program (Chapter 4) is used to provide on-site basic well test analysis in real time. Data can be analyzed while the test is in progress, ensuring that interpretable data is collected. The capabilities of the WTQL Well Test Program include: Horner, MDH, $t^{1/2}$, convolution spherical plots, and multirate buildup/drawdown/falloff. Results of the analysis for the example described above appear in Fig. 7-31. The slope of the line on the pressure versus convolution time plot is inversely proportional to the formation permeability multiplied by the bed thickness. The intercept of the pressure axis gives a measure of the skin. A conventional well test confirmed the permeability value but indicated a much lower value of skin. It appears that the perforations had been cleaned up between the two tests.

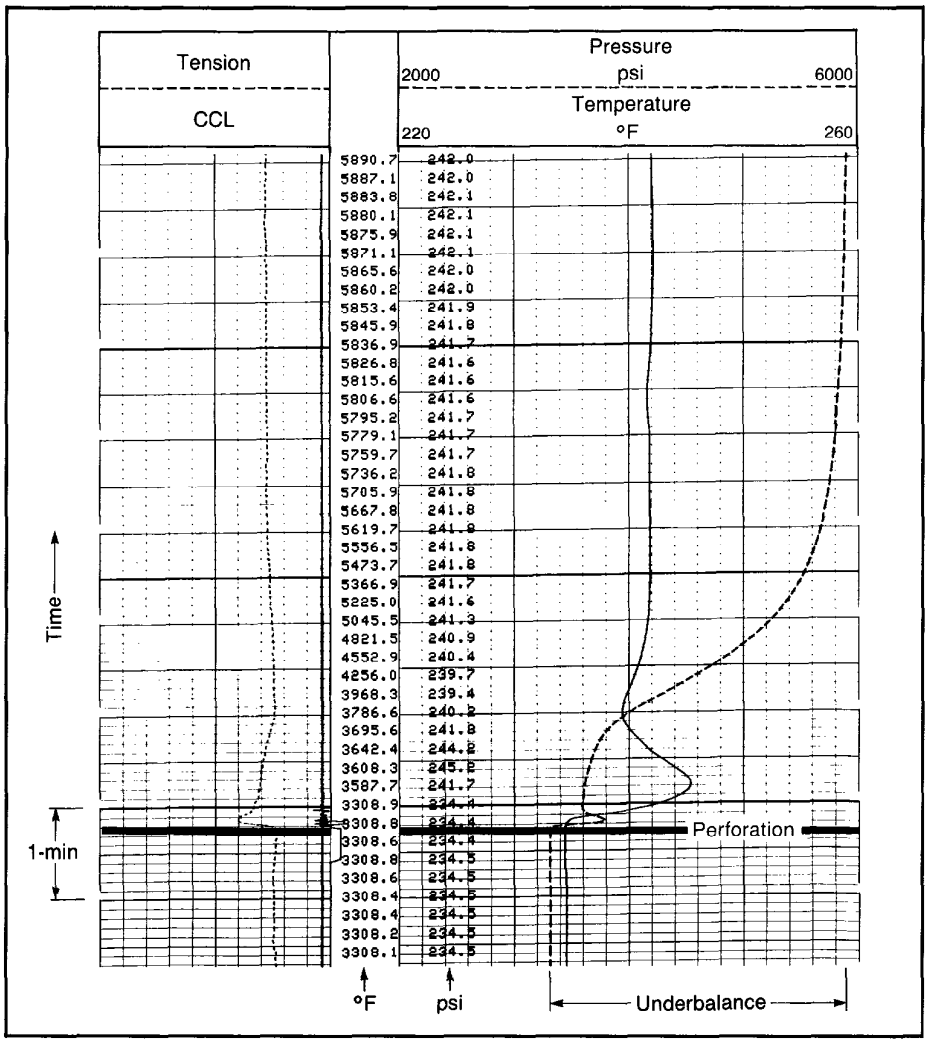

Fig. 7-30—Temperature and pressure vs. time measured by the MWP system while perforating a Texas gas well

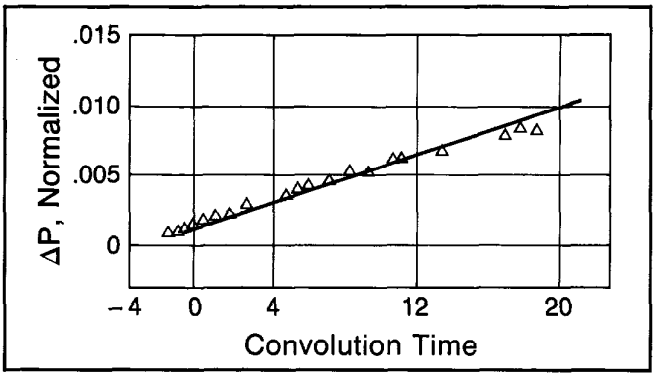

Fig. 7-31—Convolution analysis results in a special plot where the test data assume a linear trend. The line's slope gives permeability and the ordinate intercept gives skin.

REFERENCES

Allison, F.E. and Vitalli, R.: "A New Method of Computing Penetration Variables for Shaped Charge Jets," Ballistic Research Laboratory Report (1963) 1184.

"API Recommended Practice Standard Procedure for Evaluation of Well Perforators," *API RP-43*, Fourth Edition (August, 1985).

Behrmann, L.A. and Halleck, P.M.: "Effects of Wellbore Pressure on Perforator Penetration Depth," paper 18243 presented at the 1988 SPE Annual Technical Conference and Exhibition, Houston.

Behrmann, L.A. and Halleck, P.M.: "Effect of Concrete and Berea Strengths on Perforator Performance and Resulting Impact on the New API RP43," paper 18242 presented at the 1988 SPE Annual Technical Conference and Exhibition, Houston.

Bell, W.T.: "Perforating Underbalance - Evolving Techniques," *JPT* (October, 1984) 1653-1662.

Halleck, P.M. and Deo, M.: "The Effect of Underbalance on Perforation Flow," paper 16895 presented at the 1987 SPE Annual Technical Conference and Exhibition.

Harris, M.H.: "The Effect of Perforating on Well Productivity," *JPT* (April, 1966) 518-528; *Trans.*, AIME, 237.

Hong, K.C.: "Productivity of Perforated Completions in Formations With or Without Damage," *JPT* (August, 1975) 1027-1038; *Trans.*, AIME, 259.

Ichara, M.J. and Cannon, D.E.: "The Effects of Perforating on the Performance of Shale-laminated and Crossbedded Formations," paper 16205 presented at the SPE Production Operations Symposium, Oklahoma City.

Karakas, M. and Tariq, S.: "Semi-Analytical Productivity Models for Perforated Completions," paper 18247 presented at the 1988 SPE Annual Technical Conference and Exhibition, Houston.

King, G.E., Anderson, A., and Bingham, M.: "A Field Study of Underbalance Required to Obtain Clean Perforations Using Tubing-Conveyed Perforating," paper 14321 presented at the 1985 SPE Annual Technical Conference and Exhibition, Las Vegas.

Locke, S.: "An Advanced Method for Predicting the Productivity Ratio of a Perforated Well," *JPT* (December, 1981) 2481-2488.

McDowell, J.M. and Muskat, M.: "The Effect of Well Productivity of Formation Penetration Beyond Perforated Casing," *Trans.*, AIME (1950) **189**, 309-312.

Muskat, M.: "The Effect of Casing Perforations on Well Productivity," *Trans.*, AIME (1943), 175-187.

Saucier, R.J. and Lands, Jr., J.F.: "A Laboratory Study of Perforations in Stressed Formation Rocks," paper 6758 presented at the 1977 SPE Annual Technical Conference and Exhibition, Denver.

Tariq, S.M.: "Evaluation of Flow Characteristics of Perforations Including Nonlinear Effects with the Finite Element Method," paper 12781 presented at the 1984 SPE Annual Technical Conference and Exhibition.

Tariq, S.M., Ichara, M.J., and Ayestaran, L.: "Performance of Perforated Completions in the Presence of Common Heterogeneities: Anisotropy, Laminations, or Natural Fractures," paper 14320 presented at the 1985 SPE Annual Technical Conference and Exhibition, Las Vegas.

Thompson, G.D.: "Effects of Formation Compressive Strength on Perforator Performance," *Drilling and Production Practice* (1962) 191-197.

Tubing-Conveyed Perforating, Schlumberger, Houston (1988).

8 Mechanical Rock Properties vs. Completion Design

The theoretical foundation for many well completion designs lies in rock mechanics — the science of how rocks respond to stress. Of particular importance is a subsection of rock mechanics. Rock-failure mechanics figures largely in two well completion services: hydraulic fracturing, the pumping of special fluids into a well to fracture the reservoir and increase hydrocarbon yield, and sanding control, which prevents the collapse and flow of loosely consolidated rock or sand near the wellbore during production.

Hydraulic fracturing was introduced in 1947. By 1955 the procedure had been performed in more than 100,000 wells, and today is used in more than half of the wells drilled. Success of a hydraulic fracture treatment is dependent on the created fracture geometry, which in turn is related to the mechanical properties of the formation and bounding layer rocks.

Formation collapse into a producing well presents a different problem. When proration ended in the U. S. Gulf Coast in 1970, well production rates were increased. In some wells unconsolidated sands could not withstand the increased production rates and flowed with the oil into the well, resulting in wrecked completion hardware and eventually a blocked-up well. Several techniques were used in an attempt to alleviate the problem. These included perforating the casing with many small-diameter holes to encourage the sand grains to bridge and form an arch around each perforation, injecting plasticizer through the perforations to strengthen the formation, and gravel packing. Today, the most prevalent remedy is the gravel-pack completion, which blocks the influx of loose sand with specially selected gravel held in place by screens.

Well completion design theory used in rock mechanics is grounded in fundamental work by Coulomb and Lame', Otto Mohr, and Karl Terzaghi. Today, the use of computers has propelled rock-mechanics theory into the domain of 3-dimensional models that account for variables that were unmanageable only 15 years ago. Rock mechanics influences every aspect of completion design, helping to determine whether to perforate or gravel pack, or which zones to hydraulically fracture.

The following sections include a discussion of the various elastic constants required to characterize rock strength. These elastic constants are used to define parameters that control fracture geometry and wellbore failure. Finally, wellbore failure mechanisms and fracture geometry modeling are presented.

ELASTIC CONSTANTS

The mechanical properties derived from testing rock samples in the laboratory, such as the measurement of the strain for a given applied stress, are *static* elastic constants. *Dynamic* elastic constants are derived from the measurement of elastic wave velocities in the material. Array-Sonic logging and waveform analysis provide the means for obtaining continuous measurements of compressional and shear velocities. These data, in conjunction with a bulk density permit the in-situ measurement and calculation of the mechanical properties of the rock. The elastic mechanical properties, in terms of elastic wave velocities (or transit times) and bulk density, are shown in Table 8-1.

The standard practice is to use measured values of compressional travel time (t_c) and shear travel time (t_s). When shear travel time cannot be measured (i.e., in soft formations or poor cement jobs), predictions based on Poisson's Ratio and elastic moduli are not recommended. However, t_s data may be replaced with synthetic shear travel times computed from lithological models, using compressional travel times and bulk density that have been corrected for hydrocarbon effect. It should be noted that even though the hydrocarbon corrections are applied for the lithological model inputs for synthetic t_s computations, hydrocarbon corrections are not made when the raw data are used for the elastic properties computation.

The classic relationships in Table 8-1 do not account for the influence of fluid type on the sonic log responses. Generally this makes little difference in the case of carbonates, which have a large surface area of contact through solution welding or mineralization. Although minimal in low porosity sandstones, the effect should not be ignored, particularly

DYNAMIC ELASTIC PROPERTIES			
ν	Poisson's Ratio	$\frac{\text{Lateral strain}}{\text{Longitudinal strain}}$	$\frac{\frac{1}{2}(t_s/t_c)^2 - 1}{(t_s/t_c)^2 - 1}$
G	Shear Modulus	$\frac{\text{Applied stress}}{\text{Shear strain}}$	$\frac{\varrho_b}{t_s^2} \times a$
E	Young's Modulus	$\frac{\text{Applied uniaxial stress}}{\text{Normal strain}}$	$2G(1+\nu)$
K_b	Bulk Modulus	$\frac{\text{Hydrostatic pressure}}{\text{Volumetric strain}}$	$\varrho_b\left(\frac{1}{t_c^2} - \frac{4}{3t_s^2}\right) \times a$
C_b	Bulk Compressibility (with porosity)	$\frac{\text{Volumetric deformation}}{\text{Hydrostatic pressure}}$	$\frac{1}{K_b}$
C_r	Rock Compressibility (zero porosity)	$\frac{\text{Change in matrix volume}}{\text{Hydrostatic pressure}}$	$\frac{1}{\varrho_g\left(\frac{1}{t_{ma}^2} - \frac{4}{3t_{sma}^2}\right) \times a}$
α	Biot Elastic Constant	Pore pressure proportionality	$1 - \frac{C_r}{C_b}$

Note: coeff. a = 1.34×10^{10} if ϱ_b in g/cm³ and t in μs/ft.

Table 8-1—Dynamic elastic properties

when the reservoir fluids are highly compressible. An example would be when free gas is present at reservoir conditions.

The effect of fluid can be mathematically modeled. The ratio t_s/t_c, derived from the expressions for bulk modulus and shear modulus, is as follows:

$$t_s/t_c = (4/3 + K/G)^{1/2} . \qquad \text{(Eq. 8-1)}$$

If the rock were fluid-free, i. e., the pores contained a vacuum, K and G would be equal to the dry frame moduli, K_{dry} and G_{dry}. Since in-situ pores do contain a fluid, a stiffening term K_p should be included, so that $K = K_{dry} + K_p$. At low sonic frequencies, G and G_{dry} can be assumed equal. The shear/compressional ratio can then be expressed as:

$$t_s/t_c = \left(4/3 + \frac{K_{dry} + K_p}{G_{dry}}\right)^{1/2}, \qquad \text{(Eq. 8-2)}$$

where K_p (according to both Biot and Gassman theory) is a function of porosity, bulk modulus of both the dry frame and the grains, and the fluid compressibility. Assuming that $G_{dry} = G = \rho_b/t_s^2$, and knowing the parameters required for K_p, the derivation of the dry frame bulk modulus and Poisson's Ratio is straightforward.

INHERENT STRENGTH COMPUTATIONS AND THEIR RELATIONSHIP TO FORMATION COLLAPSE

To determine whether a formation will collapse under normal drawdown conditions it is first necessary to predict the critical wellbore pressure at which a cavity cannot maintain a stable shape. When the wellbore flowing pressure falls below the critical pressure, the failure of the cavity becomes "catastrophic" and results in formation collapse. Several criteria have been introduced that control the collapse phenomenon. The Mohr-Coulomb and extended Griffith failure criterions are by far the most widely applied and are used in the Sand Strength Analysis Program. Recent works by Morita et al have combined tensile failure with shear slippage in formation collapse modeling.

Stresses around a Producing Cavity

The effective principal stresses acting on an element at the surface of a cavity around a producing perforation are σ_r', σ_θ', and σ_ϕ' (Fig. 8-1). Radial stress due to the wellbore pressure is σ_r', while σ_θ' and σ_ϕ' are tangential to the cavity surface. The three principal stresses are orthogonal. The pore pressure at the surface of the cavity is equal to the well pressure, p_w. The total stresses at the cavity surface are:

$$\sigma_r = \sigma_r' + \alpha p_w = p_w \qquad \text{(Eq. 8-3a)}$$

$$\sigma_\theta = \sigma_\theta' + \alpha p_w \qquad \text{(Eq. 8-3b)}$$

$$\sigma_\phi = \sigma_\phi' + \alpha p_w , \qquad \text{(Eq. 8-3c)}$$

where:

$\alpha = 1 - (C_r/C_b)$

C_r = compressibility of rock matrix

C_b = bulk compressibility in psi^{-1}.

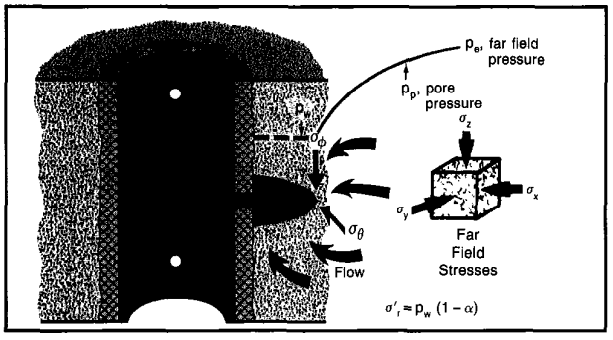

Fig. 8-1—Sanding model diagram

A radial pore pressure differential ($p_p - p_w$) extends from the surface of the cavity to the far field where the reservoir pressure is p_e.

Far field vertical stress can be assumed to be equal to the overburden:

$$\sigma_z = p_{ob} . \qquad \text{(Eq. 8-4)}$$

The effective vertical stress is, therefore, the overburden minus the effect of pore pressure:

$$\sigma_z' = p_{ob} - \alpha p_p . \qquad \text{(Eq. 8-5)}$$

In the absence of a tectonic component, the minimum horizontal stress can be defined as:

$$\sigma_x = \left(\frac{\nu}{1-\nu}\right)(p_{ob} - \alpha p_p) + \alpha p_p \ , \quad \text{(Eq. 8-6)}$$

or, rearranging,

$$\sigma_x = p_{ob}\left(\frac{\nu}{1-\nu}\right) + \alpha p_p \left(1 - \frac{\nu}{1-\nu}\right) . \quad \text{(Eq. 8-7)}$$

Solution to the "Collapse" Problem

The total hydrostatic stress, $\overline{S}$, is defined as:

$$\overline{S} = \frac{1}{3}[\sigma_z + \sigma_x + \sigma_y] \quad \text{(Eq. 8-8)}$$

assuming horizontal stresses are equal (isotropic), $\sigma_x = \sigma_y$.

Therefore, from Eqs. 8-7 and 8-8:

$$\overline{S} = \frac{1}{3}\left[p_{ob} + 2p_{ob}\left(\frac{\nu}{1-\nu}\right) + 2\alpha p_p \left(\frac{1-2\nu}{1-\nu}\right)\right] \quad \text{(Eq. 8-9)}$$

The conceptual basis for determining formation collapse is founded on the stability of a cavity surrounding a producing perforation. The shape of a producing cavity is at its most stable form when the tangential stresses at the surface of the cavity are equal, i.e., when $\sigma_\theta = \sigma_\phi$. Therefore, the total hydrostatic stress at the cavity surface is:

$$\overline{S} = \frac{1}{3}[\sigma_r + \sigma_\theta + \sigma_\phi] \ . \quad \text{(Eq. 8-10)}$$

The stresses at the surface of a cavity with $\overline{S}$ applied and p_w in the wellbore are:

$$\sigma_r = p_w \ ,$$

and from Eq. 8-10,

$$\sigma_\theta = \sigma_\phi = \frac{3}{2}\overline{S} - \frac{1}{2}p_w \ . \quad \text{(Eq. 8-11)}$$

Tangential stress is reduced by $\Delta\sigma_\theta$ due to the radial pore pressure differential:

$$\sigma'_\theta = \sigma_\theta - \Delta\sigma_\theta - \alpha p_w \ ,$$

where the superposed tensile stress is:

$$\Delta\sigma_\theta = \alpha(p_p - p_w)\left(1 - \frac{\nu}{1-\nu}\right)$$

$$\sigma_\theta' = \frac{3}{2}\overline{S} - \frac{p_w}{2} - \alpha(p_p - p_w)\left(1 - \frac{\nu}{1-\nu}\right) - \alpha p_w \ . \quad \text{(Eq. 8-12)}$$

Effective principal stresses on element at surface of stable cavity are:

$$\sigma'_\theta = \frac{3}{2}\overline{S} - p_w\left(\frac{1}{2} + \alpha\right) - \alpha(p_p - p_w)\left(1 - \frac{\nu}{1-\nu}\right) \quad \text{(Eq. 8-13)}$$

when

$$\sigma'_\phi = \sigma'_\theta$$

$$\sigma'_r = p_w(1 - \alpha) \ . \quad \text{(Eq. 8-14)}$$

Griffith Failure Criterion

The Griffith failure envelope for the element at the surface of the cavity, extended to three dimensions by Murrell (Fig. 8-2) is:

$$(\sigma'_\phi - \sigma'_\theta)^2 + (\sigma'_\phi - \sigma'_r)^2 + (\sigma'_\theta - \sigma'_r)^2 = 24T_o(\sigma'_\theta + \sigma'_\theta + \sigma'_r), \quad \text{(Eq. 8-15)}$$

where T_o = tensile strength.

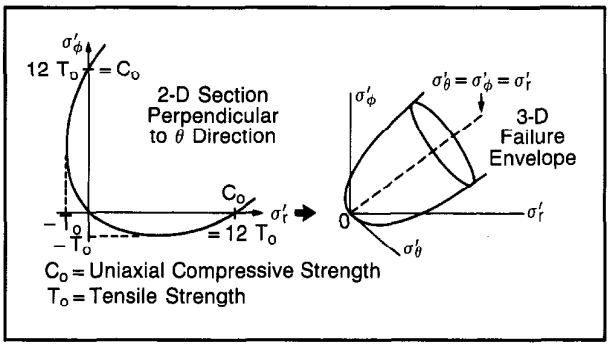

Fig. 8-2—The Griffith Failure Envelope extended to three dimensions by Murrell

σ'_ϕ, σ'_θ, and σ'_r are substituted in the Griffith equation to solve for p_w. The value of p_w predicted to produce unstable conditions is designated p_c, the critical wellbore pressure for shear failure.

In Fig. 8-3, the pore pressure is shown on the left of track 1 scaled in psi/ft representing p_p/TVD. Anticipated drawdown is depicted by a band between p_p and the flowing well pressure p_w. Whenever p_w is less than p_c, the area between the curves is shaded to represent zones of potential failure. The interval 2873 to 2977 m is perforated over one of the zones predicted to fail. Sand production from this interval is confirmed by the cavity log recorded with a 2¾-in. density tool. The perforated interval 2887 to 2889 m has also caved. The other weak zones were avoided in the perforation program.

The mathematical properties of the Griffith Failure Criterion in Eq. 8-15 are such that if two out of the three stresses are set to zero, the third stress, being at the critical condition,

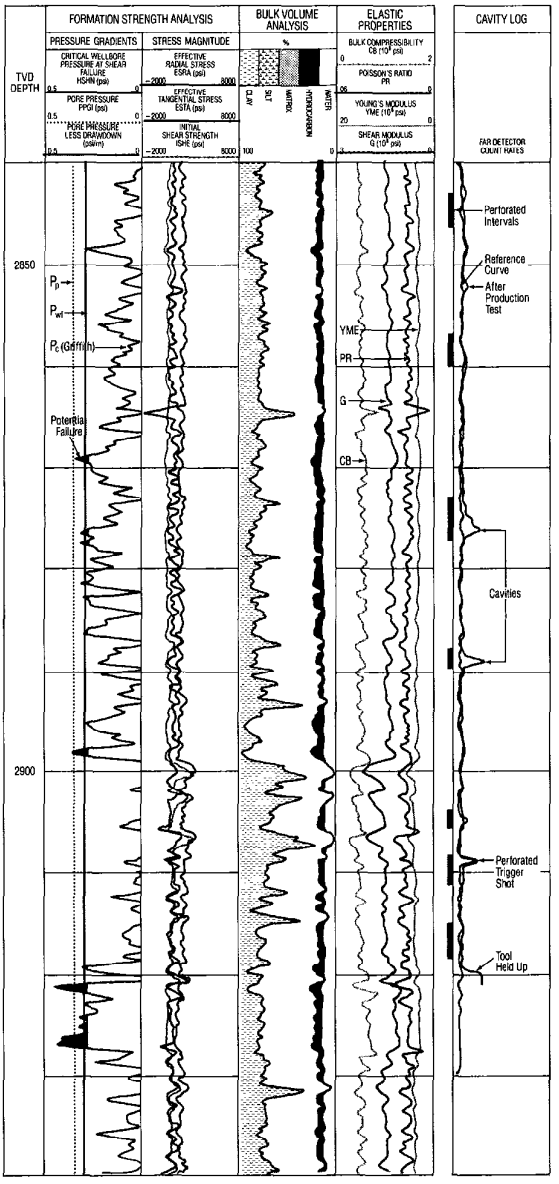

Fig. 8-3—Formation Strength Analysis log

must be equal to the uniaxial compressive strength, C_o. Thus, $C_o = 12\ T_o$. By knowing C_o, the failure envelope is fully defined.

Mohr-Coulomb Failure Criterion

The Mohr-Coulomb Failure Criterion was used in the Sand Strength Analysis program prior to the introduction of the Griffith Model (Coates and Denoo, 1980 and 1981). Its application to sanding problems has been described in detail by Edwards et al (1983). In general, it differs from the 3-D Griffith Model in that an element on the borehole wall is examined rather than the cavity shape.

σ_x and σ_y are far field total stresses. σ_x is derived as shown in the next section. σ_y is the maximum horizontal stress and is equal to σ_z multiplied by the tectonic unbalance factor, σ_y/σ_x, which will be described later. Only two principal stresses on the element in the borehole wall are noted; effective radial stress, σ_r', and effective tangential stress, σ_θ'.

In the case of a "step" pore pressure profile, effective stresses on the element of borehole wall are:

$$\sigma_r' = p_w - \alpha p_p \qquad \text{(Eq. 8-16)}$$

and

$$\sigma'_\theta = 3\sigma_x - \sigma_y - p_w - \alpha p_p\ . \qquad \text{(Eq. 8-17)}$$

Mohr's Circle is a graphic representation of the variation in shear stress along a plane and the normal stress across the plane, as γ (the angle that the direction of the normal stress makes with the greater principal stress) changes from 0° to 90° (Fig. 8-4). The shear stress is:

$$\tau = \frac{1}{2}(\sigma_\theta' - \sigma_r')sin\ 2\gamma\ . \qquad \text{(Eq. 8-18)}$$

The normal stress is:

$$\sigma_n' = \frac{1}{2}(\sigma_\theta' + \sigma_r') + \frac{1}{2}(\sigma_\theta' - \sigma_r')cos\ 2\gamma\ . \qquad \text{(Eq. 8-19)}$$

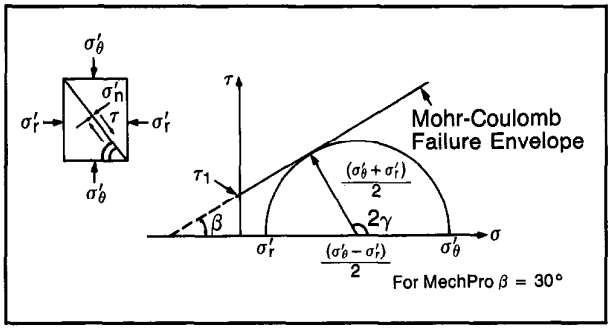

Fig. 8-4—Mohr's circle showing 30-degree failure-envelope line

The initial shear strength, τ_i, is derived from an empirical model based on Deere and Miller's work (1969) and elaborated by Coates and Denoo (1981):

$$\tau_i = \frac{0.026E}{C_b \times 10^6}[0.008V_{clay} + 0.0045(1 - V_{clay})]\ , \qquad \text{(Eq. 8-20)}$$

where:

E = Young's Modulus in psi

C_b = bulk compressibility in psi^{-1} and
V_{clay} = the volume of clay.

A formation collapses due to shear failure when the induced shear stress exceeds an amount depicted by the failure envelope. If the Mohr's Circle just intercepts the failure line, the point of contact identifies both the critical shear stress and the angle γ between the normal to the shear plane and the direction of the maximum stress.

The Coulomb failure line is a linear approximation of the Mohr failure envelope. It is depicted as follows:

$$\tau = \tau_i = \sigma \cos \beta \ , \qquad \text{(Eq. 8-21)}$$

where β = angle of friction.

The condition of instability occurs when:

$$\frac{\sigma'_\theta - \sigma'_r}{2} = \left[\tau, \cos \beta - \frac{\sigma'_r - \sigma'_\theta}{2}\right] \sin \beta \ . \qquad \text{(Eq. 8-22)}$$

By substituting σ'_θ and σ'_r from Eq. 8-16 and Eq. 8-17 in Eq. 8-22, a solution for p_w is provided.

The model is more representative of producing conditions by allowing for a radial pore pressure gradient from the wellbore to the far field. Critical wellbore pressure, p_c, using the Mohr-Coulomb Criterion becomes:

$$p_c = \frac{1.5\sigma_x - 0.5\sigma_y - 0.5\alpha p_p\left(\frac{1-2\nu}{1-\nu}\right) - 1.732\tau_i}{1 - 0.5\alpha\left(\frac{1-2\nu}{1-\nu}\right)}$$

(Eq. 8-23)

Experience has shown that the results are pessimistic in competent sands, but closely match the Griffith results in unconsolidated formations.

In an example from a chalk reservoir in the North Sea (Fig. 8-5), the well pressure desired by the operator is compared with the critical well pressure estimated to cause failure. Intervals where well pressure is lower than the critical pressure (blue) were considered susceptible to failure.

Producing the well at the desired production rate would cause most of the upper oil-bearing zone to collapse, a catastrophe that had previously occurred in other wells. In this case the weak zones were sealed, zones below them were perforated, and communication was re-established to the producing horizons through hydraulically-induced fractures.

STRESS ANALYSIS IN RELATION TO HYDRAULIC FRACTURING

A known regional overburden gradient can be used in the computation. However, the MechPro program has the capability for integrating openhole density log and pseudodensity data to the surface to obtain the cumulative weight or to extrapolate from density log data along predefined trends (Fig. 8-6).

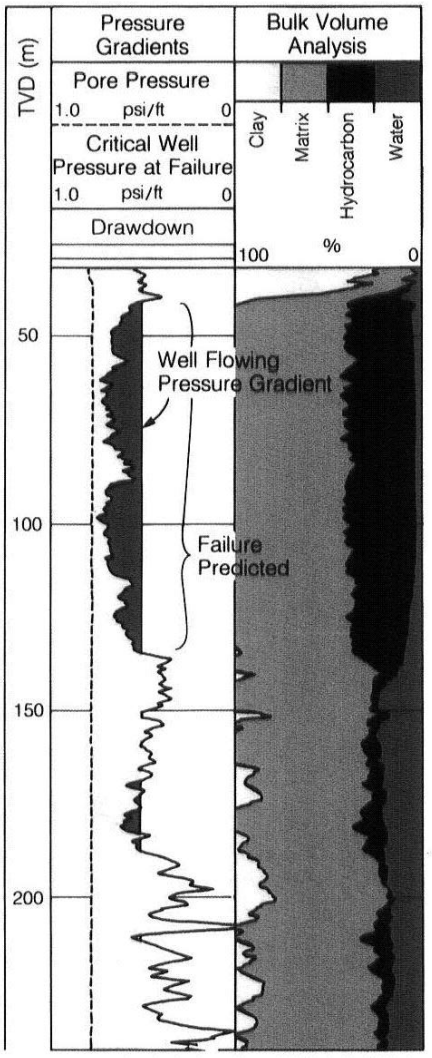

Fig. 8-5—MechPro failure prediction example from a well drilled into a North Sea chalk formation

The vertical stress, σ_z, is assumed to be equal to the overburden pressure:

$$\sigma_z = p_{ob} \ . \qquad \text{(Eq. 8-24)}$$

The minimum horizontal stress, σ_x, is obtained assuming a horizontally constrained elastic model. Three options are available:

- the classical or Terzaghi equation:

$$\sigma_x = \frac{\nu}{1 - \nu}(p_{ob} - p_p) + p_p \ . \qquad \text{(Eq. 8-25)}$$

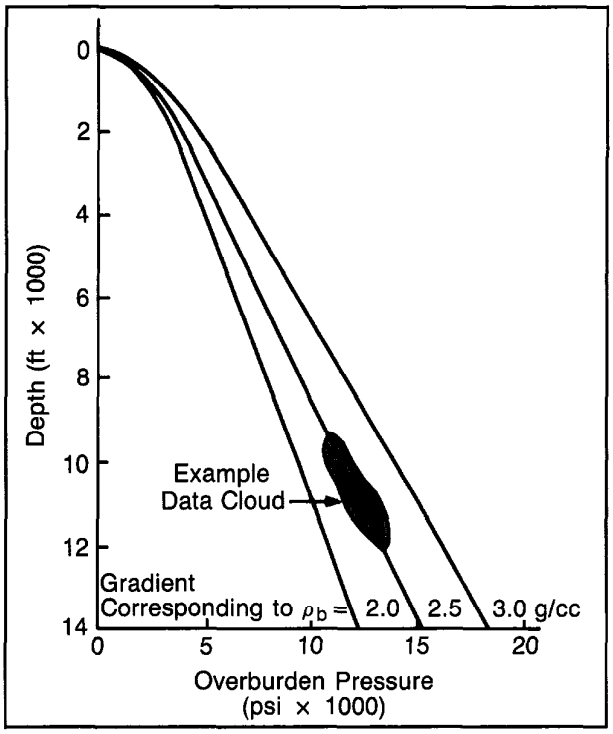

Fig. 8-6—Overburden pressure extrapolation

- A modified version for anisotropically stressed formations with unidirectional microcracks is currently under investigation. Termed "hard rock", the experimental equation simplifies to:

$$\sigma_x = \frac{\nu}{1-\nu}(p_{ob} - \alpha p_p) + p_p \quad \text{(Eq. 8-26)}$$

- The equation to derive the radial and tangential stress inputs to the Griffith and Mohr-Coulomb Failure Criteria is:

$$\sigma_x = \frac{\nu}{1-\nu}(p_{ob} - \alpha p_p) + \alpha p_p \quad \text{(Eq. 8-27)}$$

All three equations ignore the magnitude of the tectonic stress. For simplicity, the term "tectonic component" is used to represent that part of the horizontal stress which is not due to overburden. In the minimum horizontal stress direction the magnitude is T_x.

The tectonic component can still be present in seismically inactive areas. It is assumed that for a given structure, T_x is constant. The three equations are examined on a plot of the Poisson's Ratio term $\frac{\nu}{1-\nu}$ against minimum horizontal stress (Fig. 8-7). Equations 8-25 and 8-26 intercept the stress axis at the pore pressure, p_p. Equation 8-27 intercepts the stress axis at αp_p, and is, therefore, highly influenced by the ratio of rock grain compressibility to framework compressibility. As C_r/C_b approaches one, α approaches zero.

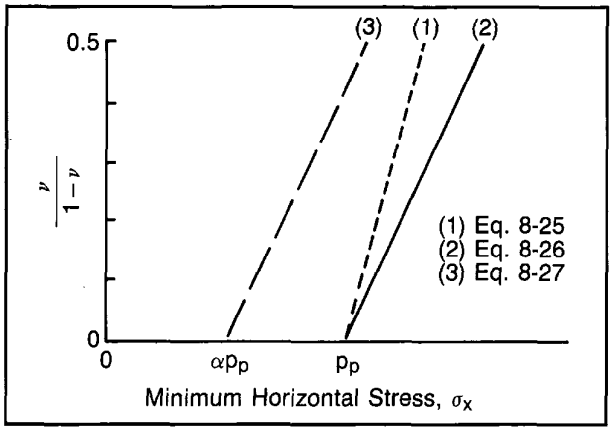

Fig. 8-7—Determination of "tectonic component"

If a tectonic component T_x exists, all three relationships should move an amount equivalent to T_x along the stress axis. The slope is equal to the effective overburden stress, $p_{ob} - \alpha p_p$. In the Terzaghi case α is one.

Calibration with Mini-Frac Data

Analysis of downhole pressure and spinner flow rate during a mini-frac operation can help to determine the minimum horizontal stress. A mini-frac is a series of pumping tests carried out to determine parameters required to plan a hydraulic fracture operation. It is preferably conducted with the same fluid specifications that will be used in the full hydraulic fracture treatment, but without the proppant. The operation consists of:

- pumping at stepped rates and measuring the downhole pressure for fracture initiation, extension, and reopening.
- shut-in by instantaneously switching off the pumps and measuring the falloff in downhole pressure and spinner response.

Several plotting techniques are available to help identify the wellbore pressure which exactly balances the minimum horizontal stress at the point when the fracture closes. This is called the closure pressure (or stress) and is deemed to be equal to the minimum horizontal stress at the fracture interval (Nolte, 1979). A recent innovation by A. Amin (1984) accounts for wellbore storage effects by examining the downhole spinner response following shut-in. This technique is derived from the investigations into "after-flow analysis" by Meunier et al (1983).

The procedure for calibrating the log-derived results is to plot the computed effective minimum horizontal stress against $\frac{\nu}{1-\nu}$. Points representing the effective closure stress obtained from the mini-frac pressure analysis, plotted against the computed $\frac{\nu}{1-\nu}$, should be marked on the same plot.

The calibration technique can be improved by conducting the mini-frac in several intervals with straddle packers. Ideally, the mini-frac tests should be in zones of different Poisson's Ratio to give sufficient range on the crossplot to derive a scaling factor.

The calibration method is illustrated in Fig. 8-8. The most appropriate equation is selected, considering the tectonic nature of the region. The effective closure stress is obtained by subtracting the pore pressure component. For Eq. 8-25 or Eq. 8-26:

$$\sigma_x' = \sigma_x - p_p \,, \qquad \text{(Eq. 8-28)}$$

or for Eq. 8-27:

$$\sigma_x' - \sigma_x - \alpha p_p \,, \qquad \text{(Eq. 8-29)}$$

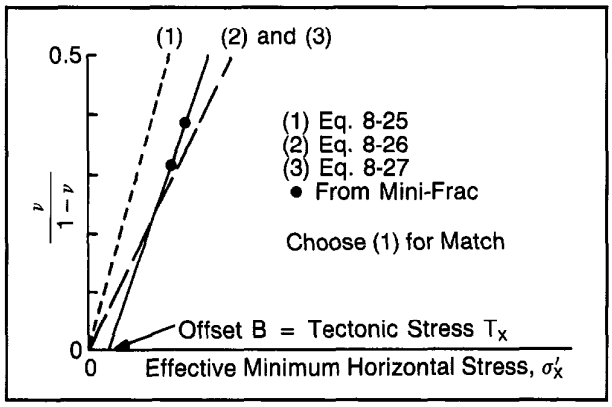

Fig. 8-8—Calibration of closure stress

a scaling factor A and offset B are selected to obtain the best match with the test data. Calibrated closure stress, σ_x, can now be defined:

$$\sigma_x' \text{ (calibrated)} = A\,\sigma_x' + B \,. \qquad \text{(Eq. 8-30)}$$

For the Terzaghi case:

$$\sigma_x \text{ (calibrated)} = A\,(\sigma_x - p_p) + B + p_p \,. \qquad \text{(Eq. 8-31)}$$

The offset B is considered to represent the tectonic component, T_x.

Figure 8-9, from a study by Draxler and Edwards (1984), shows that the minimum computed σ_x value, within the frac test interval, was about equal to the test value, indicating a negligible T_x component.

Fracture Pressure Computations

Fracture initiation pressure, or formation breakdown pressure, p_b, is a function of:

$$p_b = 3\sigma_x - \sigma_y - \alpha p_p + T_o \,, \qquad \text{(Eq. 8-32)}$$

where:

σ_x = minimum horizontal stress
σ_y = maximum horizontal stress
p_p = pore pressure
α = Biot poroelastic constant
T_o = tensile strength.

Models for σ_x computations were shown in the previous section. σ_y is usually defined in terms of the tectonic unbalance factor σ_y/σ_x. This factor is elusive in current oil industry practice, though frequently measured in mining engineering and indirectly obtained in geological and geophysical survey holes. The existence of tectonic unbalance can be inferred from borehole deformation tests or from breakout identification from multiple-diameter caliper logs. Pore pressure is obtained from wireline formation tests or from pressure buildup tests.

Alpha is made unity whenever the Terzaghi or "hard rock" relationship for σ_x is used, simplifying the calculation of fracture initiation to:

$$p_b = 3\sigma_x - \sigma_y - p_p + T_o \,. \qquad \text{(Eq. 8-33)}$$

To compute the fracture reopening pressure, p_{fr}, the tensile strength, T_o, is made zero:

$$p_{fr} = 3\sigma_x - \sigma_y - p_p \,. \qquad \text{(Eq. 8- 34)}$$

In a naturally-fractured zone, an interval selected for hydraulic fracturing would be intersected by many joints. Although individual pieces of rock could possess a high tensile strength, the interval as a whole would have negligible tensile strength. In such a case, the reopening pressure would be the same as the initiation pressure.

After fracture initiation, continual pumping would result in the fracture propagating in a plane parallel to the maximum stress and perpendicular to the minimum stress. Fracture extension pressure is lower than the reopening pressure, but must exceed the minimum horizontal stress. It is a function of the minimum horizontal stress, pump rate, hydraulic fluid characteristics, leakoff due to microfissures, and matrix permeability.

HYDRAULIC FRACTURE GEOMETRY ANALYSIS

Hydraulic stimulation has proven to be a dominant factor in the success of marginal wells in low-permeability, low-porosity, dense rocks. Twenty percent or more of the total well cost can be involved in fracturing; proper treatment design is a must if low-production wells are ever to reach payout. The treatment design is critical. Too small a fracture treatment may result in such inadequate drainage of the reservoir that the well remains unprofitable. Conversely, too large a treatment can be an unnecessary waste of completion funds

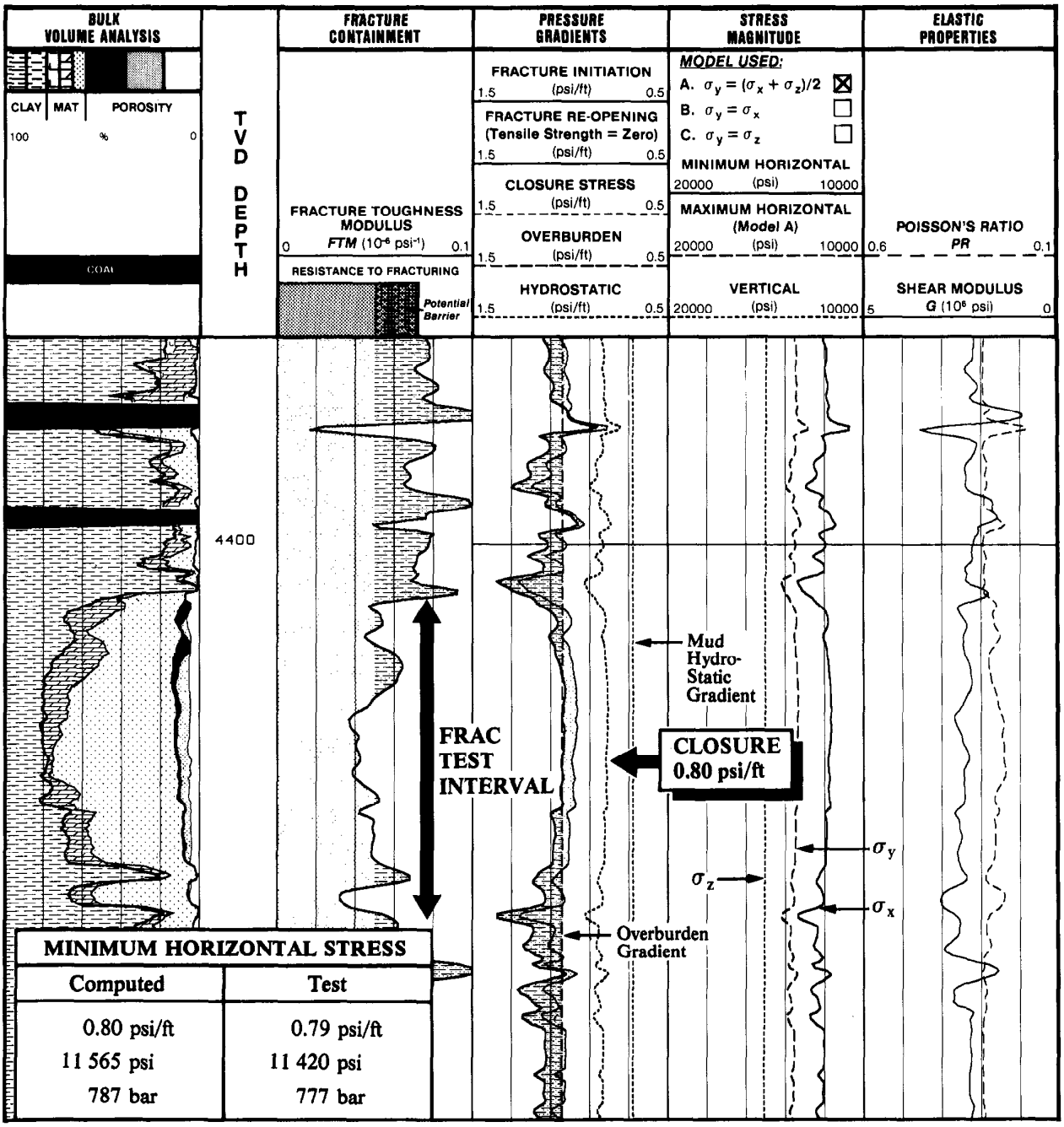

Fig. 8-9—Example showing a negligible T_x component within the frac test interval

and render the well unprofitable; worse, the fracture may migrate into a nearby aquifer.

Fracture Height

When pressure is increased in the borehole, rupture occurs in the plane that is perpendicular to the direction of least compressive stress (σ_x or σ_y). The pressure required to induce this fracture is called the initial or breakdown pressure. Once a fracture has been initiated, the pressure necessary to hold the fracture open (in the case of a vertical fracture) will be

equal to the minimum total horizontal stress, Ahmed (1988). This stress is often referred to as closure stress. In tectonically relaxed areas, the least principal stress is generally horizontal. Fracturing should therefore occur along vertical planes.

Hydraulic fracture design depends on two sets of variables: the distribution and magnitude of in-situ minimum horizontal stress in the producing and surrounding formations, and the flow behavior of the fracturing fluid. These variables determine:

- the direction and geometry (height, length, and width) of the created fracture,
- whether multiple zones should be fractured one at a time, in groups, or simultaneously,
- design parameters of hydraulic fracturing, such as horsepower, pumping pressure, and proppant transport, and
- the fracturing fluid flow behavior and efficiency.

During a fracturing job, the fracture fluid creates tension. In a vertical fracture, its pressure counteracts the earth's compressive horizontal stress. The fracture grows vertically if the stress-intensity factor, K, top or bottom, exceeds the formation's fracture toughness, K_{Ic}. Predicting vertical propagation therefore depends on calculating the stress-intensity factor at the fracture's vertical extremities.

The crucial variables in this calculation are fracture height, fluid pressure in the fracture, and the magnitude of minimum horizontal stress, which varies with depth, z. Several theorists have proven the fundamental result as follows:

$$K_{top} = \frac{1}{\pi\sqrt{2h}} \int_{-h}^{h} (S_H(z) - p_{wf}) \frac{\sqrt{h - z}}{h + z} dz , \qquad \text{(Eq. 8-35)}$$

and

$$K_{bot} = \frac{1}{\pi\sqrt{2h}} \int_{-h}^{h} (S_H(z) - p_{wf}) \frac{\sqrt{h + z}}{h - z} dz .$$

K_{top} and K_{bot} are the stress-intensity factors at the top and bottom of the fracture. The fracture height, $2h$, is normal to the minimum horizontal stress.

Disregarding friction losses in the fracture, fluid pressure is assumed equal to borehole fluid pressure, p_{wf}. Determining whether a vertical fracture extends is a matter of calculating K_{top} and K_{bot}, and determining where fracture toughness is exceeded, if at all. Each time the fracture extends, stress-intensity factors must be recalculated.

The FracHite* Program

The FracHite program calculates the fracture's vertical extension using the continuous horizontal-stress values from the MechPro program and an approximation to the integrals, which includes the fluid-gravity effects within the created fracture. It does this for a sequence of increasing pumping pressures. The FracHite log also provides a picture of the fracture geometry, assuming a 2-dimensional, wedge-shaped fracture. If more than one zone is being fractured simultaneously, the program calculates the percentage of fracturing fluid that enters each fracture, based on zone thickness and material balance, and provides a picture of each fracture's geometry.

Figure 8-10 shows FracHite log results for an East Texas well with two producing zones. Both zones were fractured simultaneously. The left track shows the expected vertical propagation as fracture pressure increases in 300-psi steps. The middle track depicts the vertical and horizontal extent of each fracture. The right track is a lithologic analysis from openhole logs. According to the program, fracture-initiation pressure in the top zone is 600 psi lower than in the bottom zone. FracHite results predict the consequence of this difference. The top zone opens first and takes most of the fracturing fluid. This is exactly what happened during the fracture job with the fracturing fluid pumped at 900 psi.

To monitor the vertical extent of the fracture, the proppant was tagged with a radioactive marker and gamma ray logs were run before and after the fracture operation. Increased radioactivity, indicating successful fracture initiation, was noted in the vertical intervals predicted by the FracHite log for borehole fluid at 900 psi. Production logs show that only the top zone contributed to production as predicted by the FracHite log. A second FracHite result (Fig. 8-11) shows what would have happened had the zones been fractured independently.

Fracture Propagation Azimuth

In areas where the overburden exceeds the minimum horizontal stress, the hydraulic fracture plane would tend to be vertical and to propagate normal to the minimum stress direction.

The minimum stress direction can be inferred from the breakout orientation (Fig. 8-12). Programs now exist to help in the task of identifying breakouts and their azimuth from multiple-diameter, oriented caliper logs. Fig. 8-13 shows an example of a breakout orientation log computed from a 4-arm dipmeter tool.

In very shallow holes, the least principal stress would likely be the vertical stress. Therefore, fracturing would tend to be horizontal and the fracture pressure would be sufficient to lift the overburden.

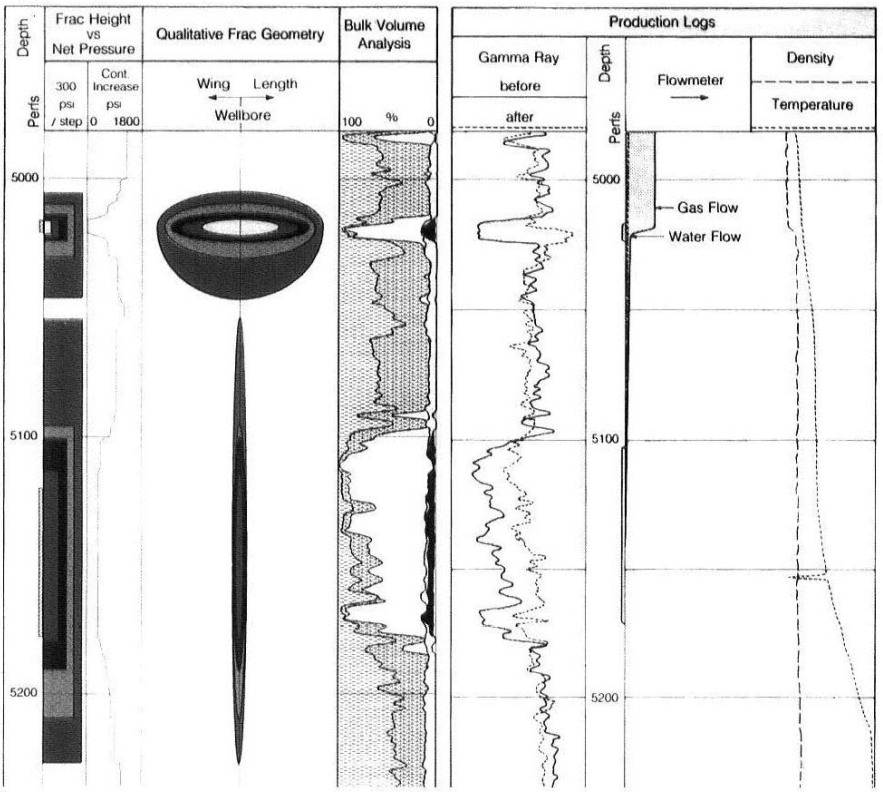

Fig. 8-10—FracHite log and production logs showing the results from fracturing both zones simultaneously

REFERENCES

Ahmed, U.: "Fracture Height Prediction," *JPT* (July 1988) 813-815.

Ahmed, U., Newberry, B.M., and Cannon, D.E.: "Hydraulic Fracture Treatment Design of Wells with Multiple Zones," paper 13857 presented at the 1985 SPE/DOE Low Permeability Gas Reservoirs Symposium.

Anderson, R.A.: *A Review of the Elastic Solution for Fracture Pressure*, American Society of Mechanical Engineers (1976).

Anderson, R.A., Ingram, J.S., and Zanier, A.M.: "Fracture Pressure Gradient Determination from Well Logs," paper 4135 presented at the 1972 SPE Annual Meeting.

Anderson, R.A., Edwards, D.P., and Ormerod, L.: "Log Interpretation Techniques to Evaluate Formation Collapse in the North Sea Chalk, paper presented at the Symposium on North Sea Chalk, Stavanger (1985).

Coates, G.R. and Denoo, S.A.: "Mechanical Properties Program Using Borehole Stress Analysis and Mohr's Circle," *Trans.*, 1981 SPWLA Annual Logging Symposium.

Hottman, C.E. and Johnson, R.K.: "Estimation of Formation Pressures From Log-Derived Shale Properties," *JPT* (June 1965).

Massa, P., Ruhland, M., and Thowvenin, J.: *Structure et fracturation du champ d'hass: Nessaiyd (Algeria)*, Revuede 1 I.F.P., **XXII** (1972).

Morita, N., Whitfill, D.L., Fedde, O.P., and Lovik, T.H.: "Parametric Study of Sand Production Prediction," paper 16990 presented at the 62nd Annual SPE Fall Technical Conference, 1987.

Murrell, S.A.F.: "A Criterion for Brittle Fracture of Rocks and Concrete under Triaxial Stress and the Effect to Pore Pressure on the Criterion," *Rock Mechanics: Proceedings of the 5th Symposium on Rock Mechanics* (May, 1962) 563-577.

Newberry, B.M., Nelson, R.F., and Ahmed, U.: "Prediction of Vertical Hydraulic Fracture Migration Using Compressional and Shear Wave Slowness," paper 13895 presented at the 1985 SPE-DOE Low Permeability Gas Reservoirs Symposium.

"Rock Mechanics," *The Technical Review*, Schlumberger Educational Services (October 1986) **34,** No. 3.

Tixier, M.P., Loveless, G.W., and Anderson, R.A.: "Estimation of Formation Strength from the Mechanical Properties Log," paper 4532 presented at the 1973 SPE Annual Meeting.

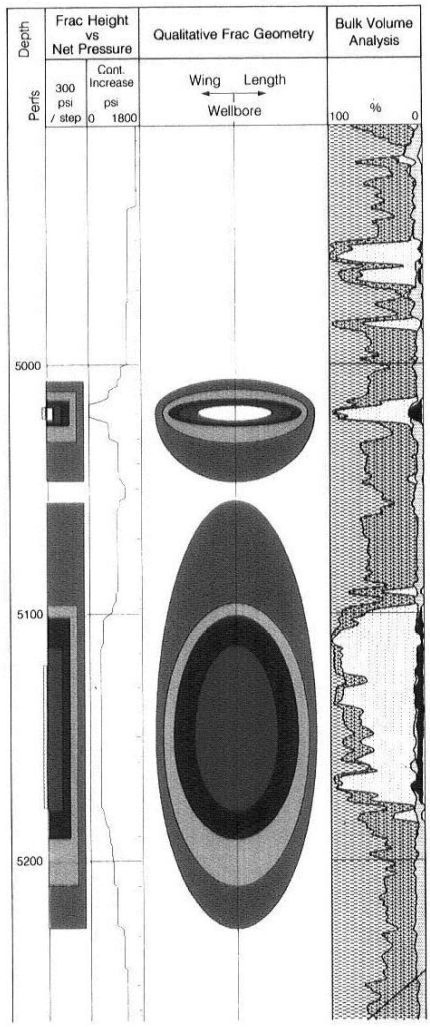

Fig. 8-11—FracHite log predicting results of fracturing each zone separately

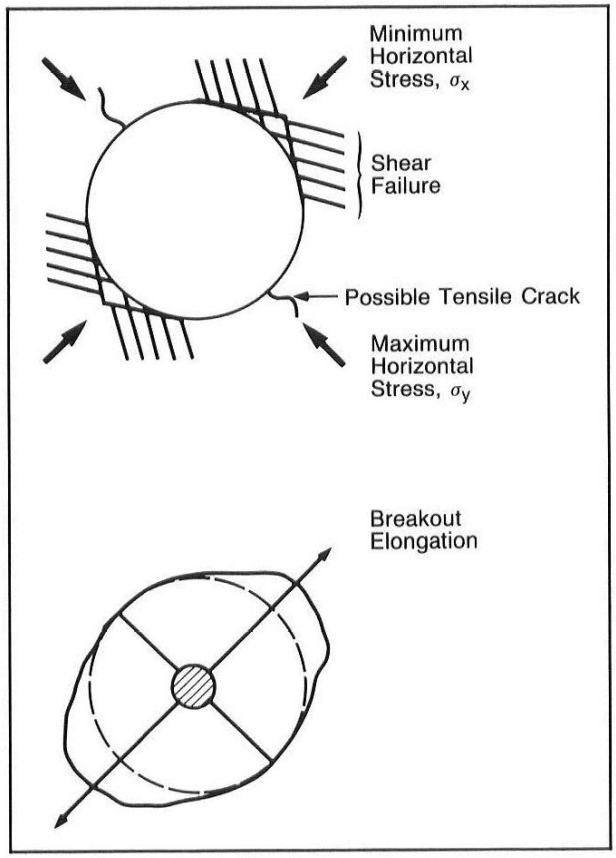

Fig. 8-12—The breakout mechanism in borehole elongation

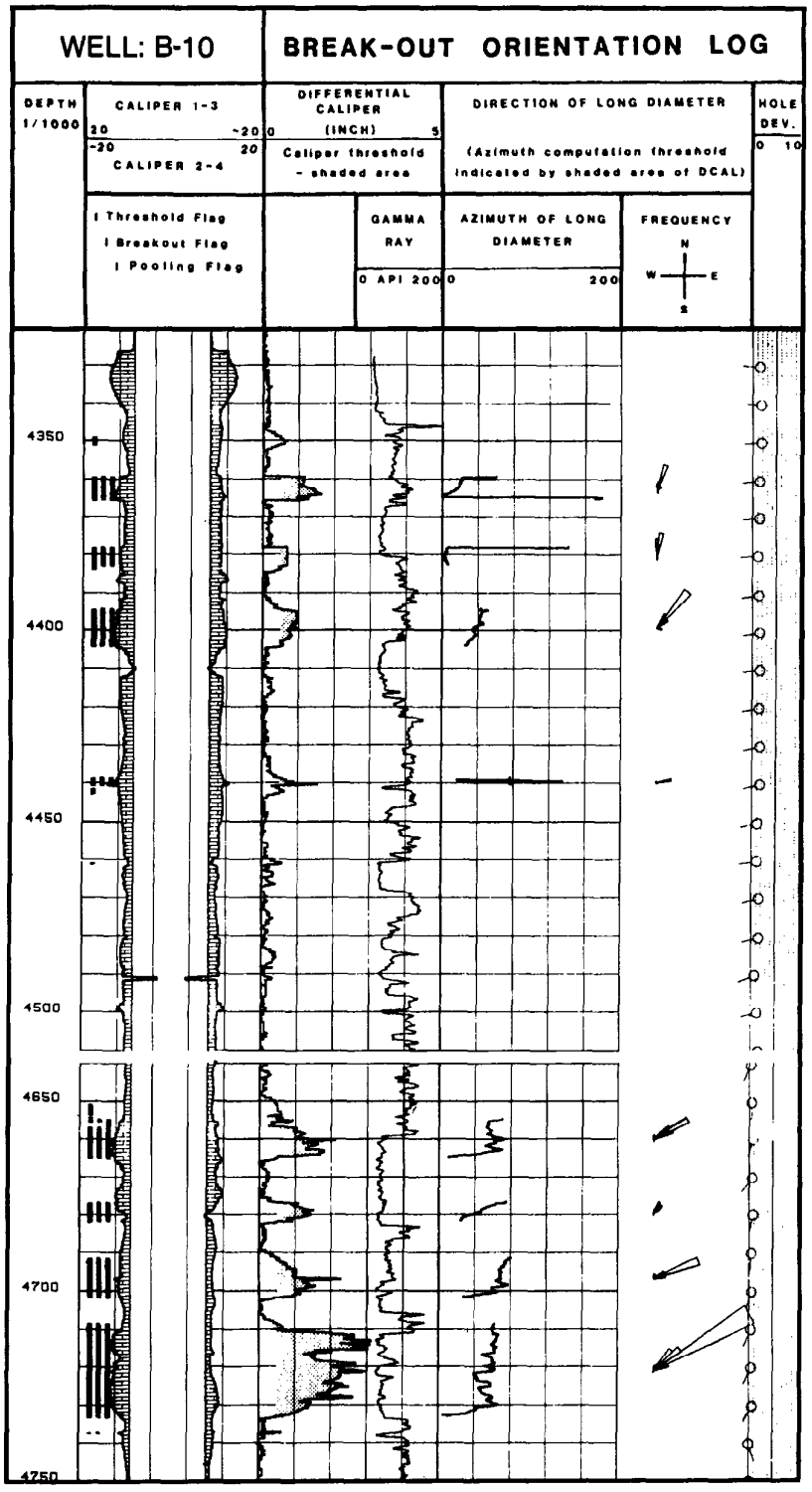

Fig. 8-13—Breakout orientation log computed from a 4-arm dipmeter tool

9 Cased Hole Seismic

In the early stages of planning exploration and development in a new area, surface seismic surveys are used extensively to delineate prospective structural or stratigraphic traps. Recent improvements in digital filtering and processing techniques have led to high-quality results under favorable conditions. The resolution of surface seismic surveys, however, is still fundamentally limited by low operating frequencies.

When wells are drilled, opportunities exist to improve this situation through the use of well logs. After editing and calibrating against check shots, openhole sonic and density logs can be used to generate synthetic seismograms. If openhole data are not available, in many instances a cased hole sonic log can be recorded for this purpose (see Chapter 3). These synthetics are extremely valuable in verifying reflection events in a seismic section and relating seismic features to geological structures. Velocity anomalies, which may cause exploration wells to be drilled off-structure, can be resolved.

A more recent geophysical application of wireline logging measurements involves the preparation of a vertical seismic profile (VSP). In this technique, an air gun vibroseis, or other seismic source on the surface generates the input signal that is detected by a downhole geophone. As the sound energy travels only once through the weathered surface layers, the resultant profile has much better resolution than the surface seismic around the borehole, and, in favorable cases, can identify reflectors far below the total depth of the well.

Unlike many wireline services, openhole and cased hole seismic results are similar since the casing typically does not affect the seismic signal. In fact, cased holes eliminate some of the openhole operational problems associated with poor hole conditions and highly deviated wells. Also, special multisensor array tools for VSP acquisition can be used in cased holes that are not practical for openhole operations.

CASED HOLE SEISMIC EQUIPMENT

The equipment shown in Fig. 9-1 consists of a downhole tool with geophones, the CSU surface recording system, offset shooting equipment, and an air gun system.

The most commonly used energy source offshore is the air gun. Its safety, reliability, cost, broad spectrum, simple signature, and transportability make the air gun a convenient seismic source. An array of synchronized air guns can be used if a large power output for deeper penetration is needed. The air gun firing chambers may incorporate a waveshaping kit that significantly reduces the bubble effect and provides a clean signal. The air compressor and air storage bottles provide an adequate air supply for fast, uninterrupted operations. Other sound sources, such as vibroseis units, are routinely used in the field depending on specific applications and local conditions.

When using an impulsive source such as an air gun, the source signal is recorded at the surface by a hydrophone. This allows a precise determination of the time break and permits continuous monitoring of the gun signature. The recorded source signature is used to enhance the signals recorded by the geophone in VSP processing.

The data are recorded digitally on magnetic tape with the CSU system. The seismic waveforms can also be stacked to improve the signal-to-noise ratio.

The downhole tools currently in use are the Well Seismic Tool (WST*), the Seismic Acquisition Tool (SAT*), and the Downhole Seismic Array tool (DSA*). The WST tool has four uniaxially stacked geophones that are primarily sensitive to movement in the vertical direction. The SAT tool has three mutually orthogonal geophones (which may also be gimbal-mounted for use in deviated wells) for 3-dimensional operation. This arrangement provides an x, y, z system of reference where each arriving ray can be represented by a vector. Among other applications, the ability to record and process signals in three axes allows the recording and interpretation of shear waves, salt proximity surveys, and long-offset VSP surveys. The DSA tool (Fig. 9-2) uses eight sensor packages (shuttles) which are positioned along an insulated multiconductor bridle cable at intervals of up to 50 ft. The sensor package contains a vertical geophone for signal acquisition, a magnetic clamping device to secure the package to the casing, a shaker element to generate mechanical vibrations for reference, and electronic circuitry to transmit

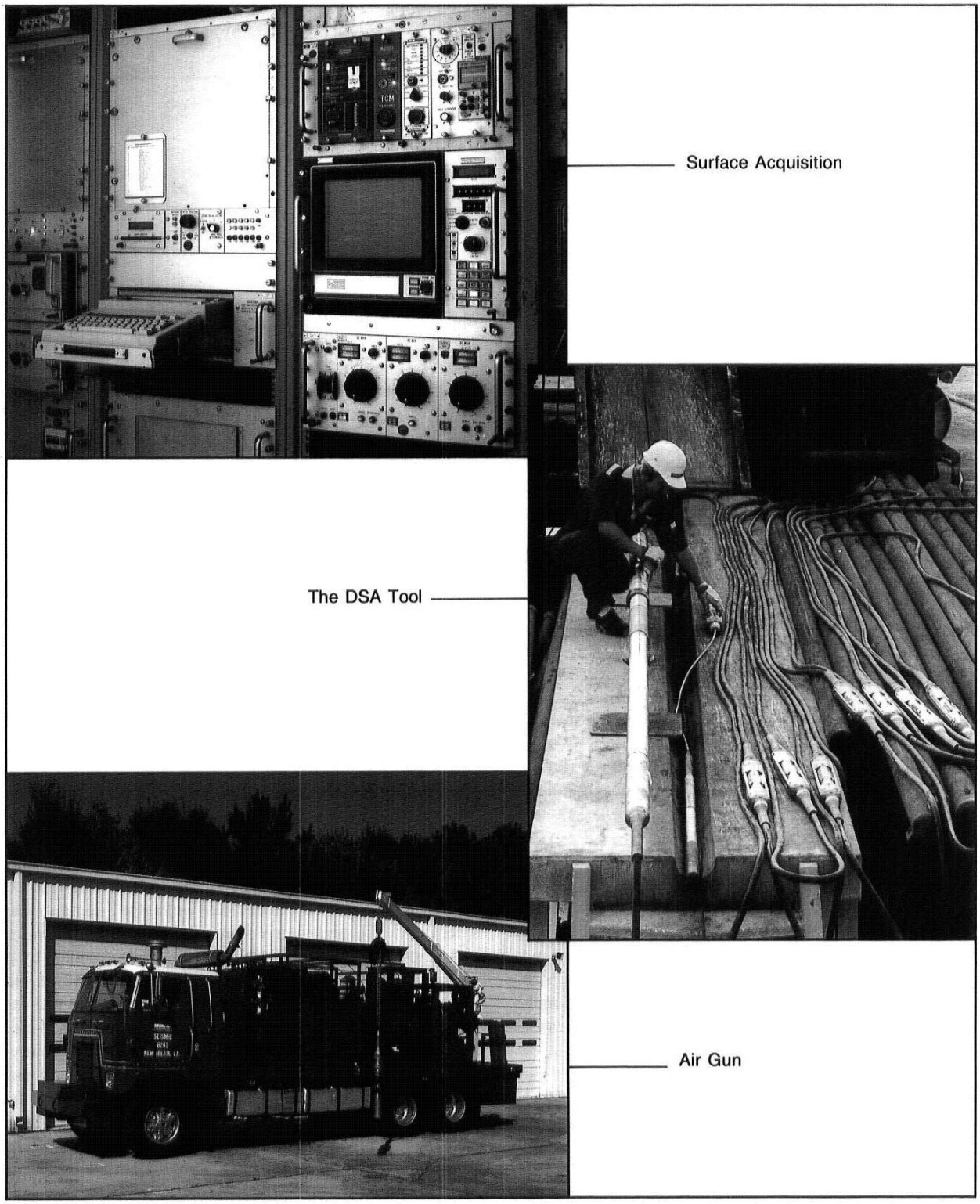

Fig. 9-1—Well seismic tool hardware

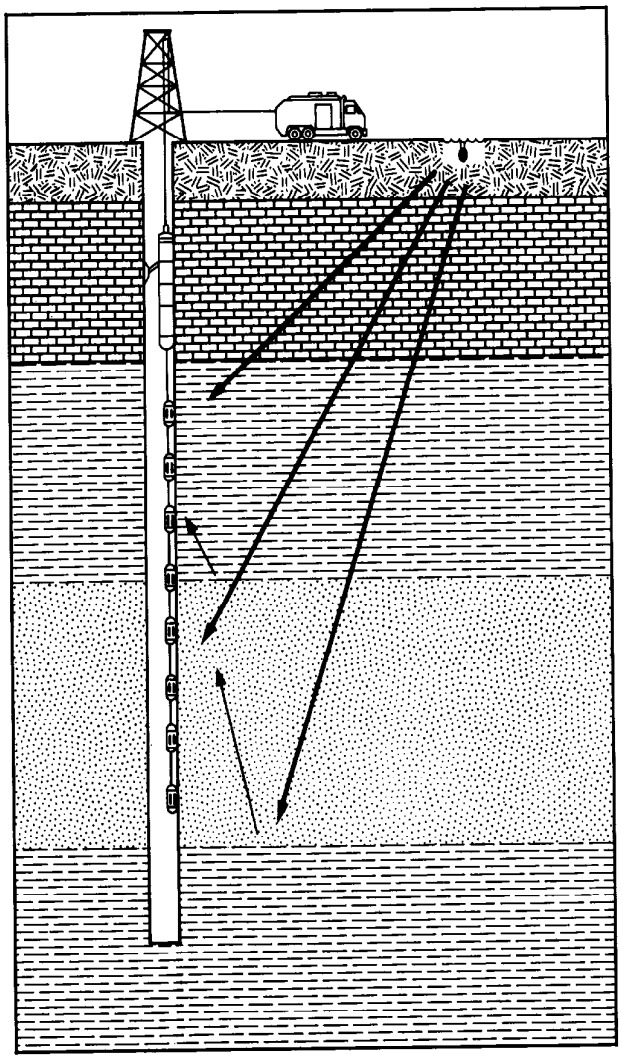

Fig. 9-2—Schematic of DSA tool in operation

signals to the cartridge. In the cartridge, the signals pass through antialiasing filters, sample-hold circuits, and multiplexers, and are then digitized and telemetered to the surface. The tool can be combined with a casing collar locator for depth control.

DIGITAL CHECK-SHOT SURVEY

At each depth, the interval velocity of the formations between the source and the borehole geophone is measured. With an air gun source, the hydrophone monitors the signature and timing of the source signal, and the downhole geophone records the direct and reflected arrivals.

Transit time is measured from the first break of the hydrophone (surface) recording to the first break of the geophone (downhole) recording. Several shots are usually made at the same level and stacked in order to improve the signal-to-noise ratio.

If the hole is deviated or if there is a significant source offset, the transit times obtained must be converted to true vertical depth (TVD) transit times. Correction to the seismic reference datum (SRD) is also necessary if the source is above or below the seismic datum. The corrected, stacked magnetic tape data can then be converted to a standard SEG-Y tape format.

TIME-TO-DEPTH CONVERSION AND VELOCITY PROFILE

Check-shot surveys are used to correct the velocities obtained by the integration of the sonic interval transit times. The adjusted sonic may then be used for the translation of surface seismic time into depth and in the calculation of formation acoustic impedance necessary for the generation of a Geogram* synthetic seismogram and for other applications.

Formation velocities obtained by the integration of sonic logs may differ from those obtained by surface and check-shot surveys for the following reasons:

- Because of velocity dispersion with frequency, seismic velocities (measured at roughly 50 Hz) may be as much as 6% lower than sonic velocities (measured at 20,000 Hz).
- Borehole effects, such as those caused by formation alteration, may decrease the apparent sonic log velocities.
- The sonic transit time measurement is fundamentally different from the surface seismic measurement. The sonic log velocity is measured in a continuous manner alongside the borehole, while the seismic waves reaching the geophone(s) take the most direct acoustic (shortest) path.

The long-spaced (LSS) or Array-Sonic tools are required for cased hole logs and provide better data than BHC sonics in open holes. However, all recorded sonic logs should be edited to correct for borehole effects. To adjust a sonic log correctly, check shots are required. Check shots should be made at the SRD, at the tops of significant formations, at the top of the sonic log, and spaced not greater than 500 ft apart.

Seismic time is normally referenced from the check shots, and sonic log measurements are adjusted accordingly. The adjustment consists of computing the raw drift, selecting the drift curve, adjusting the sonic log, and checking the validity of the result.

Raw drift is defined as the correct shot time minus the integrated sonic time. The selected drift curve is derived from the raw drift values. The knees of the selected drift curve are usually located at changes in lithology, borehole conditions, sonic log character, and the drift data. The correction determined by the selected drift curve is distributed to the sonic transit times over the interval defined by consecutive

knees. The check of the adjusted sonic is made by ensuring that the integrated sonic time and the corrected shot time agree at each shooting level within the accuracy of the shot time. Obviously, the more check shots, the more accurately this can be done.

A section of a sonic calibration log is shown in Fig. 9-3. The uncalibrated transit time, calibrated transit time, and gamma ray curve are displayed along with bulk density, spontaneous potential, and differential caliper data from open-hole logs. In the left track, vertical depth, shot numbers, corrected shot times, uncorrected 1-way integrated sonic times, and corrected 2-way integrated sonic times are displayed.

In addition to providing data for sonic calibration, check shots allow a time-to-depth conversion to be made when no sonic log has been recorded. A similar, related application is the determination of the weathering correction and the thickness of the weathered zone.

GEOGRAM PROCESSING

The seismic waveforms propagating through the earth are affected by each lithologic bed boundary. Specifically, at the interface of two formations of contrasting acoustic impedances, part of the energy will be transmitted across the interface and some will be reflected. The amount of seismic energy transmitted and reflected depends on the acoustic impedance contrast between the two formation beds. The acoustic impedance of a formation, Z_a, is given as:

$$Z_a = \rho v \ , \qquad \text{(Eq. 9-1)}$$

where ρ is the formation density and v is its interval velocity.

The amount of reflected energy between two adjacent beds depends on the relative impedances of the two beds. The reflection coefficient, R, is defined as:

$$R_{1,2} = \frac{Z_{a_2} - Z_{a_1}}{Z_{a_2} + Z_{a_1}} \ , \qquad \text{(Eq. 9-2)}$$

where Z_{a_2} and Z_{a_1} are the acoustic impedances of layers 2 and 1.

The subsurface can be approximated for seismic purposes by a series of layers having specific acoustic impedances, which can be used to produce a series of reflection coefficients at the boundaries (Fig. 9-4). Since a sonic log measures acoustic velocity and a density log measures bulk density, the sonic and density logs can be used to compute the reflectivity series, which can then be convolved with a suitable wavelet. The result is a Geogram display (synthetic seismogram).

Geogram processing produces an ideal seismic trace only if the sonic and density logs have been properly recorded, edited, and adjusted to represent the subsurface undisturbed by drilling. Special programs allow the recomputation of sonic velocities and bulk densities, taking into account the

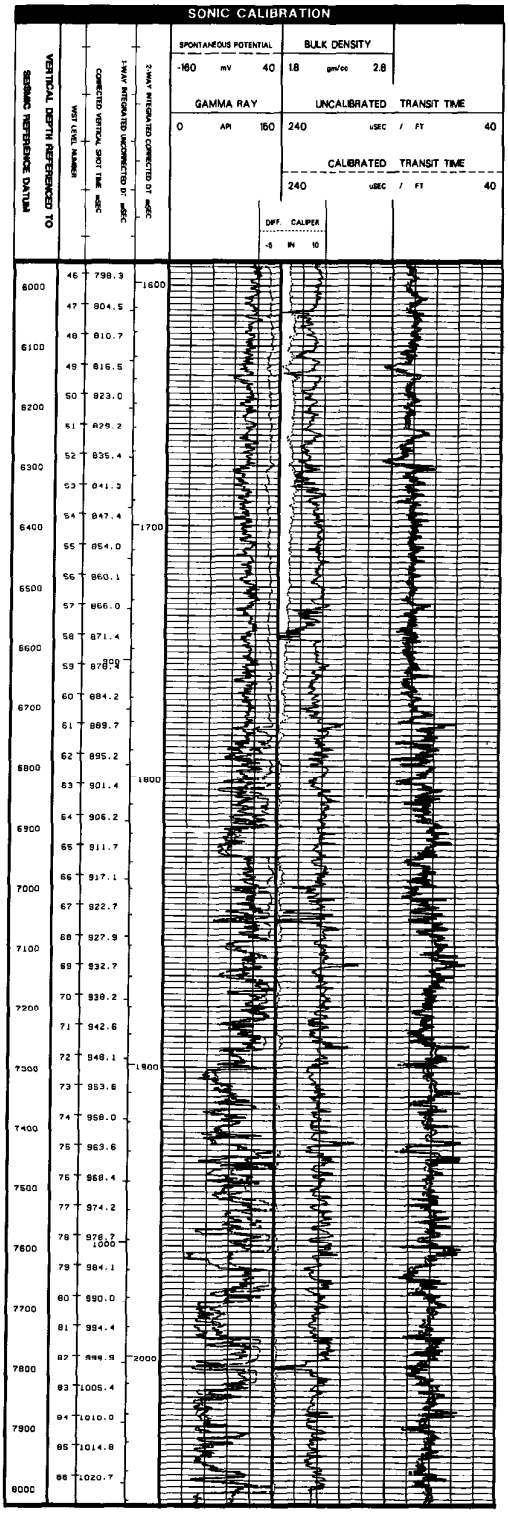

Fig. 9-3—Sonic calibration log

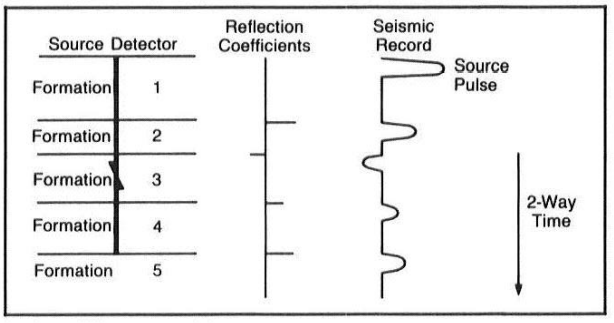

Fig. 9-4—Ideal seismic record giving position (in time) of reflector and value (amplitude) of reflection coefficient

effect of the invaded zone; this is particularly important in gas-bearing formations. Geogram processing enables qualitative correlations as well as quantitative evaluations of seismic data to be made.

The Geogram processing sequence is shown in Fig. 9-5. The first two steps, which involve editing and sonic adjustments, are normally made during the time-to-depth conversion. Once the reflectivity series and transmission losses have been computed, the decision must be made on what type of wavelet to use for convolution. In order to give the best approximation of the actual source signature, several wavelets are available. These include Ricker minimum- or zero-phase, Klauder, spike with Butterworth filter, or other user-defined operators.

The Geogram display can be made with or without multiples and/or transmission losses, and with any desired frequency or band of frequencies. A typical Geogram display is shown in Fig. 9-6.

The structural dip, as interpreted from a dipmeter survey, can be incorporated into the presentation to permit the Geogram results to be projected away from the well (Fig. 9-7).

A Geogram display can help in the qualitative evaluation of the seismic sections by providing the following:

- an ideal seismic trace as a reference for the surface seismic data
- time-to-depth conversions
- detection of multiples
- seismic character correlation
- direct correlation with log intervals.

Seismic modeling can also be enhanced and processing time decreased by assuming a realistic model based on the Geogram computation. The original log data can be modified and used to generate new synthetic seismic traces. Other applications are inverse modeling and the design of the deconvolution operator. Furthermore, any log data, raw data, or

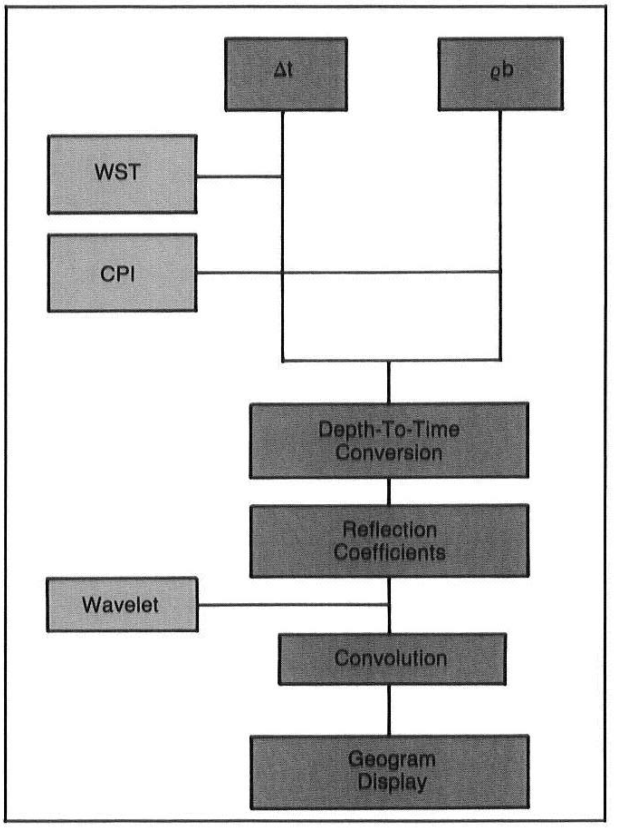

Fig. 9-5—Geogram processing chain

processed data can be presented on a time scale for correlation with the seismic data.

VERTICAL SEISMIC PROFILE

Vertical seismic profiling is a technique of simultaneously recording the upgoing and downgoing wavetrains (Fig. 9-8). This represents a major advantage over the conventional surface reflection seismic technique, which records only the upgoing waves. By recording a sufficient number (50 or more) of fairly regularly spaced levels in the well, the upgoing and downgoing wavefields can be separated by computer processing. An analysis of the upgoing and downgoing components permits the detailed study of the change of the seismic wavetrain with depth. The acoustic properties of the earth can then be directly linked to and interpreted in terms of the subsurface lithology. The use of downhole sensors reduces the signal distortion caused by the low-velocity shallow layers since the signal passes only once through the surface layers.

The total wavefield recorded at the detector in the borehole consists of signals arriving from above the tool

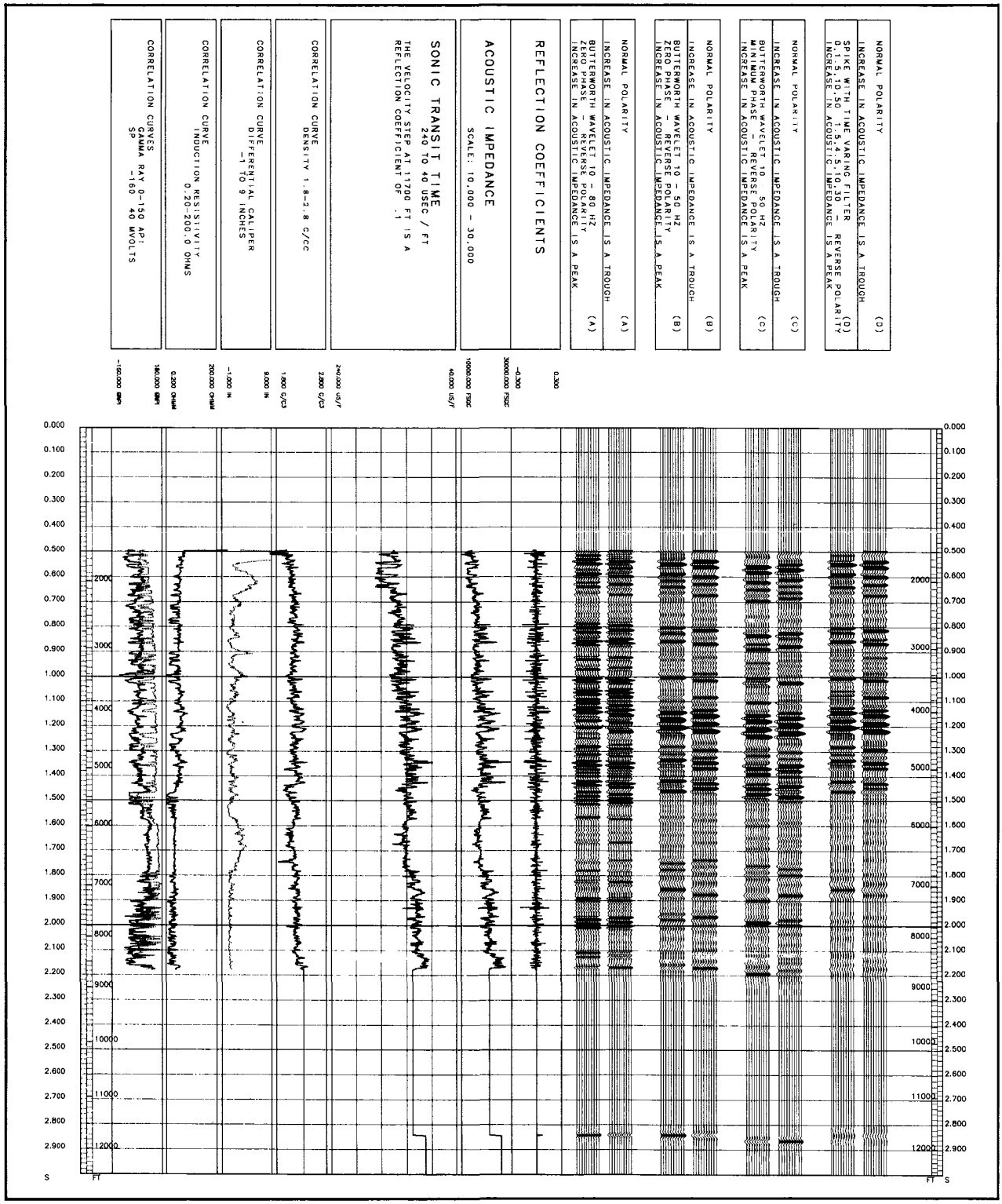

Fig. 9-6—Typical Geogram presentation

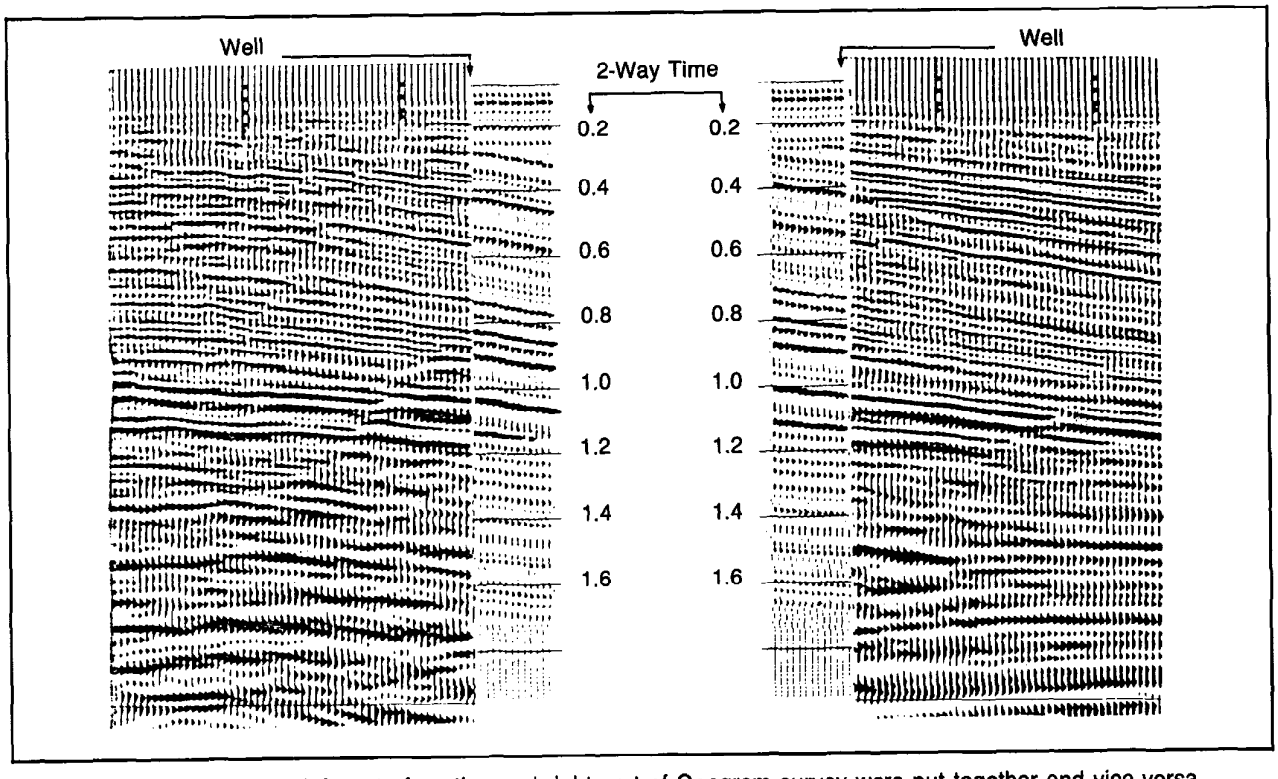

Fig. 9-7—Dip extrapolation: left part of section and right part of Geogram survey were put together and vice versa

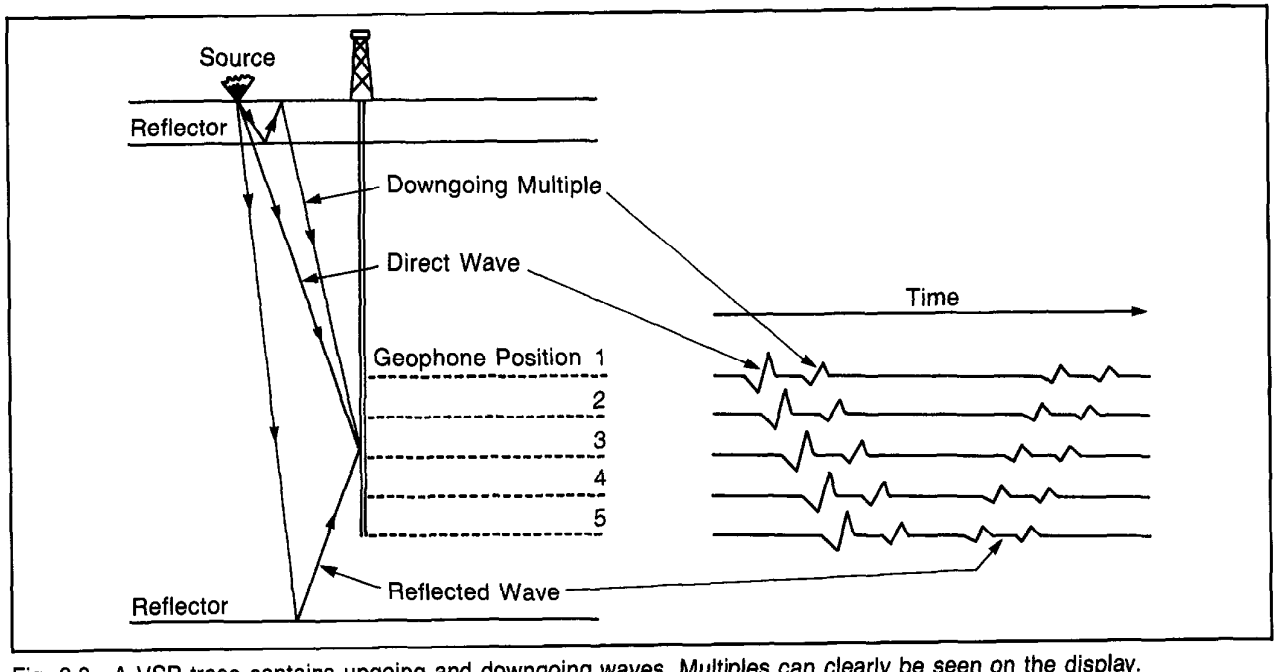

Fig. 9-8—A VSP trace contains upgoing and downgoing waves. Multiples can clearly be seen on the display.

(downgoing) and the signals arriving from below the tool (upgoing). The downgoing signals are the direct (first) arrivals and the downgoing multiples. The upgoing signals consist of the direct reflections and the upgoing multiples.

Advantages of the vertical seismic profile technique include:

- recording a real seismic trace in the borehole rather than relying on a synthetically generated seismogram
- measuring the spectral content of the downgoing seismic signal as a function of depth
- establishment of a precise link between the surface seismic results and well logs, since the VSP is a high-resolution measurement
- the recording of signals with an improved high-frequency content, since they cross the highly absorptive low-velocity layers near the surface only once
- improved seismic resolution of subtle stratigraphic features around the well, such as faults or pinchouts
- the recording of deep reflector signals that are not received at surface; this is particularly useful in structurally complex areas
- an excellent record of the band-limited reflection coefficient series through deconvolution of the VSP.

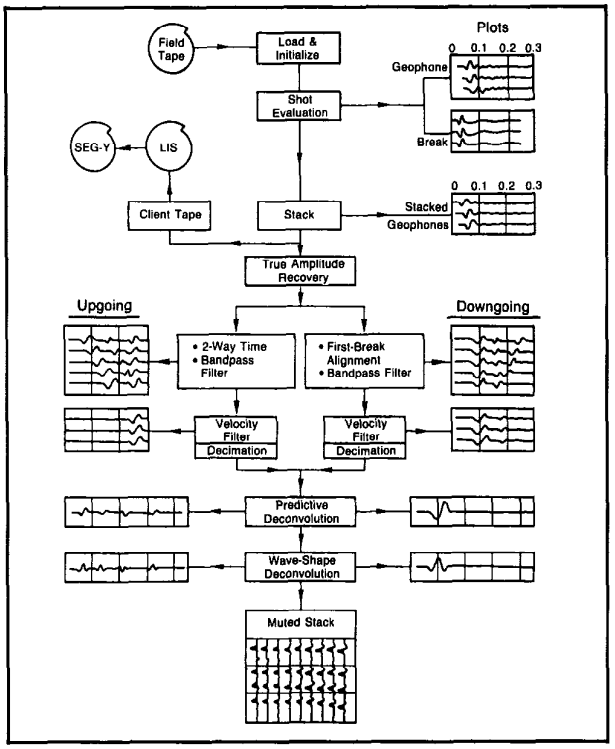

Fig. 9-9—Processing of VSP's involves three major steps: data editing for optimized shot quality, upgoing and downgoing wavetrain separation, and deconvolution.

VSP PROCESSING

The VSP processing sequence (Fig. 9-9) usually includes most of the following steps:

- shot selection by an analyst to reject the noisy, poor-quality shots
- consistency check of the surface hydrophone signal
- median stacking of shots
- check of coherence between a reference level and all others
- monitoring of phase shifts and acoustic impedance at all levels
- bandpass filtering to eliminate noise and remove aliased frequencies
- filtering to help eliminate tube waves
- true amplitude recovery by a time-variant function to compensate for spherical spreading
- velocity filtering to separate the upgoing and downgoing components of the total wavefield
- autocorrelation of the downgoing wave after filtering for selection of the proper deconvolution parameters using the downgoing wave field as a deterministic model
- predictive deconvolution to remove source signature effects and to improve resolution
- time-variant filtering to match the surface seismic data
- corridor stacking: summing all the upgoing waves recorded in a window following the first break.

A vertical seismic profile display using data from the Downhole Seismic Array tool is shown in Fig. 9-10. The corridor stack from this presentation is shown superimposed on the surface seismic section in Fig. 9-11.

OFFSET VERTICAL SEISMIC PROFILE

A normal VSP survey in a vertical borehole with horizontal bedding gives very limited lateral information. However, with dipping reflectors, a normal VSP survey can provide some information on the updip features (Fig. 9-12).

An offset VSP (Fig. 9-13), however, offers the possibility of large lateral coverage. Lateral coverage of up to one-half of the source offset distance can be achieved in the direction of the source. Profiling of a feature can be done by using a fixed offset source position some distance from the well and moving the geophone(s) in the well, or by having the geophone(s) fixed and moving the source.

WALKAWAY SURVEYS

A walkaway survey provides a 2-dimensional seismic picture of the formations on either side and below a well. This

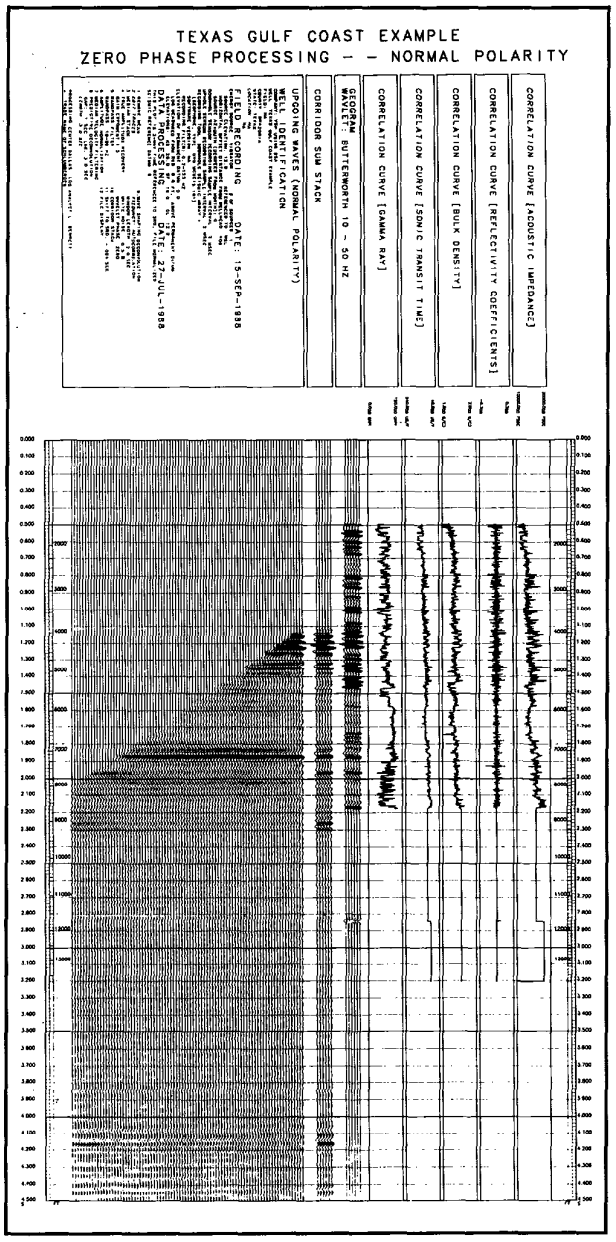

Fig. 9-10—VSP using DSA tool

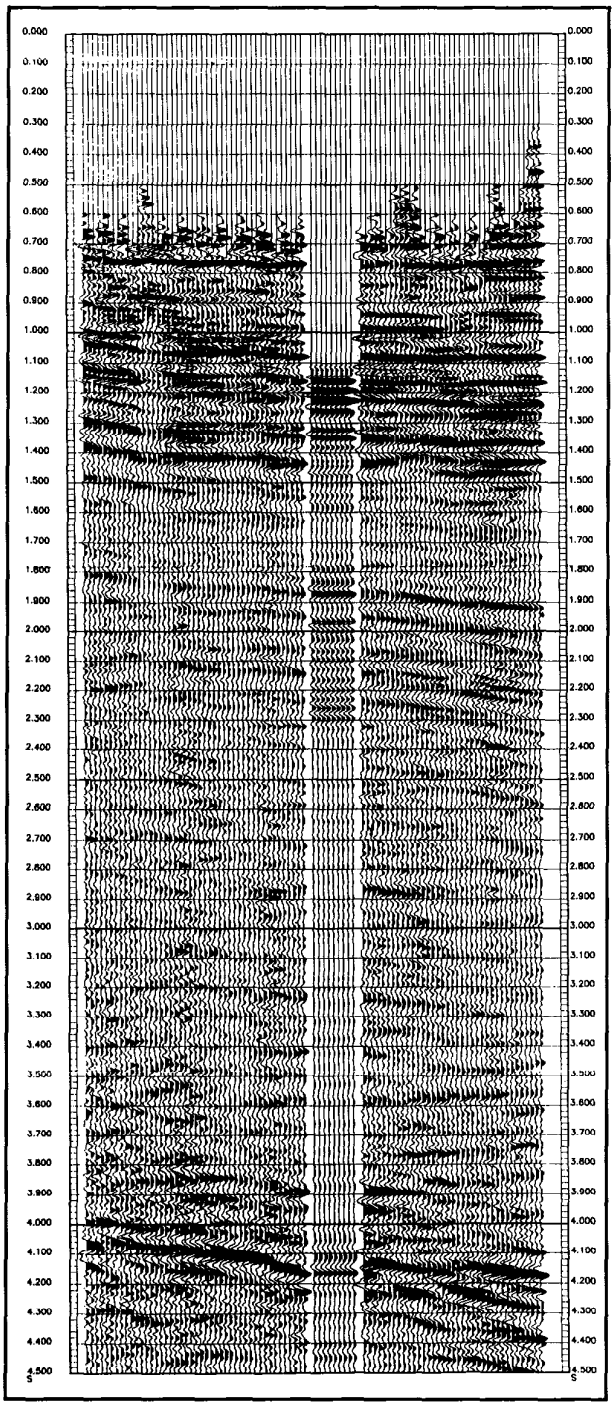

Fig. 9-11—VSP corridor stack from Fig. 9-10 superimposed on surface seismic section

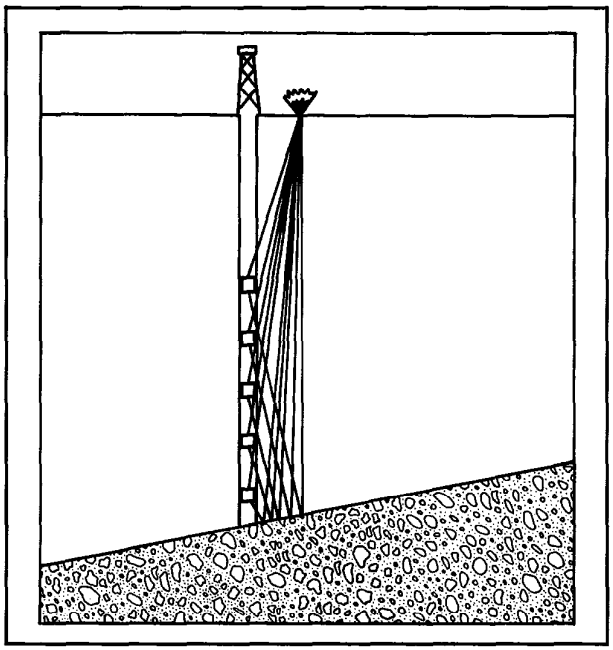

Fig. 9-12—VSP: stationary source, moving receiver

is achieved by using survey techniques developed from Zero Offset VSP (ZVSP) and Offset VSPs (OVSP). Walkaway surveys are unique, however, in that they always employ a multiple source and single receiver arrangement.

A typical offshore walkaway survey would be carried out by a boat with the energy source, moving at a constant speed and direction along a 3 km line that passes close to the well. Seismic shots would be generated with an air gun at 30 m intervals along this line and a downhole geophone would monitor the arrivals. Each pass of the boat would generate 100 seismic wave traces at each geophone position. Accurate navigation fixes are obtained for each shot position along the survey line by placing navigation equipment on both the rig and boat. The seismic wave pattern created by this multi-source/single receiver arrangement is particularly useful in investigating complex formations.

The following illustrations show the family of borehole seismic surveys and the development of a walkaway survey. The first illustration (Fig. 9-14) shows the results of a check-shot survey. The impedance log (sonic × density) has been corrected with the check shot times to match the seismic times and a Geogram display computed from the data. Both logs are superimposed on the surface seismic section to allow correlation of the log data with the surface seismic events.

Figure 9-15 illustrates a ZVSP. In the ZVSP survey, the events beyond the check shot's first arrivals are recorded and interpreted, providing a time and depth record of upgoing reflected events. To obtain quality reflected data, a higher density of receiver positions is used than in the check-shot survey. A corridor stack of the VSP data is shown superimposed on the surface seismic section to allow correlation of depth and time.

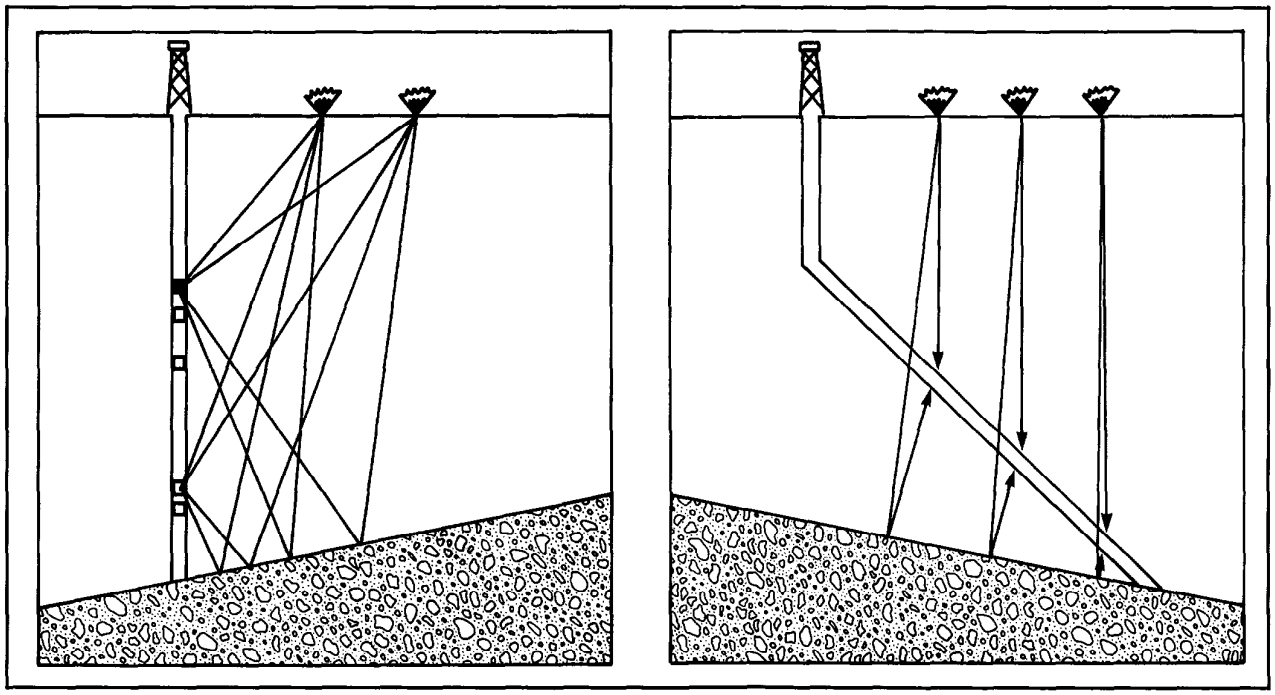

Fig. 9-13—Offset VSP: moving source, stationary receiver

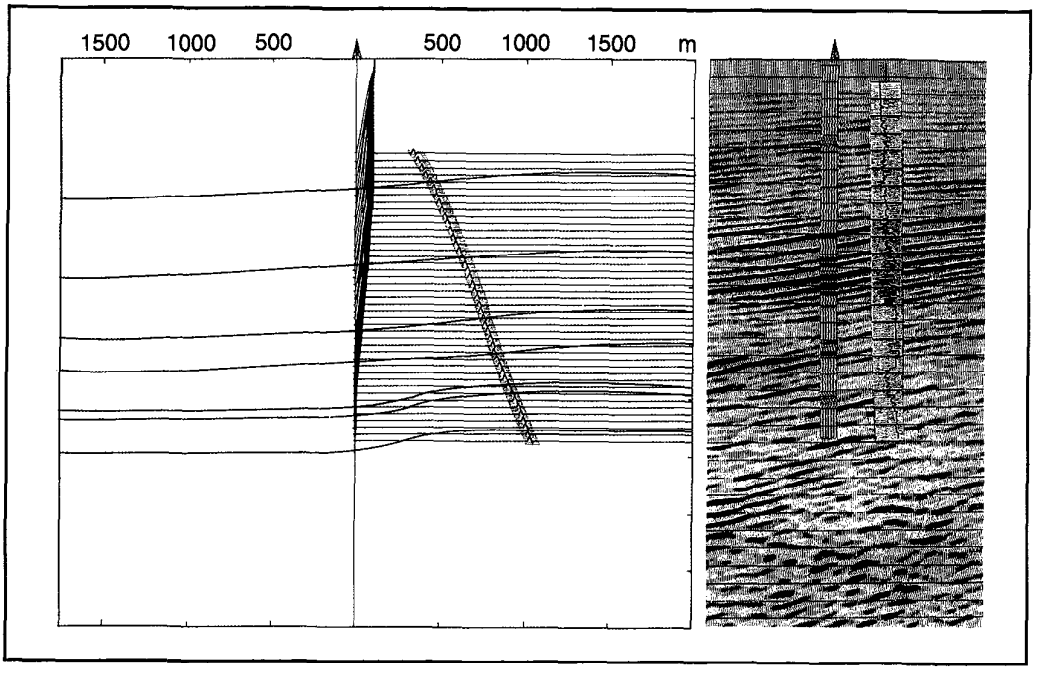

Fig. 9-14—An impedance log and Geogram log are shown superimposed on the surface seismic section

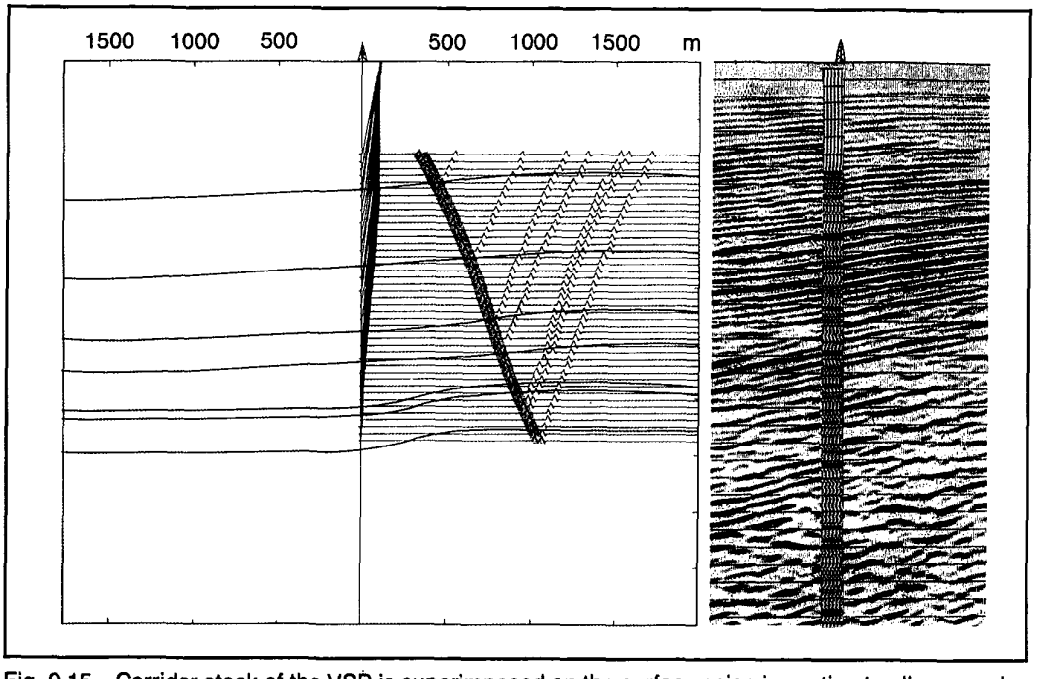

Fig. 9-15—Corridor stack of the VSP is superimposed on the surface seismic section to allow correlation of depth and time

The same data from the previous acquisition has been processed with 2-dimensional model data to extend the offset position of reflection points on the dipping horizons (Fig. 9-16).

The OVSP is illustrated in display (a) of Fig. 9-17. In this case, the source is substantially offset from the well. This shifts the reflection points away from the well and produces coverage of an extended area around the well. This is

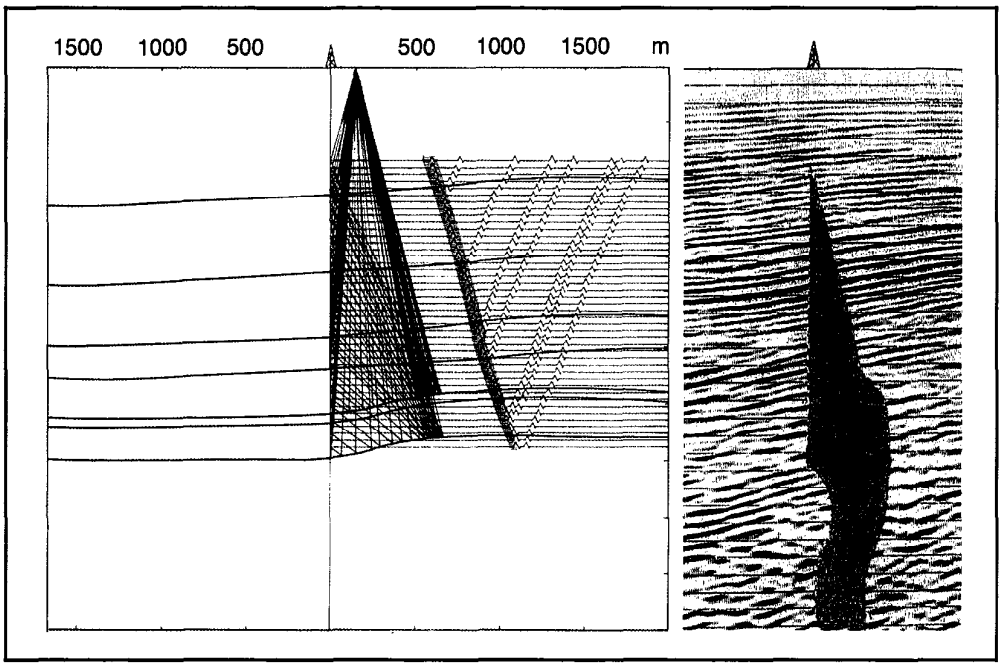

Fig. 9-16—Same data as Fig. 9-15, processed with 2-dimensional model data to extend the offset position of reflection points on the dipping horizons

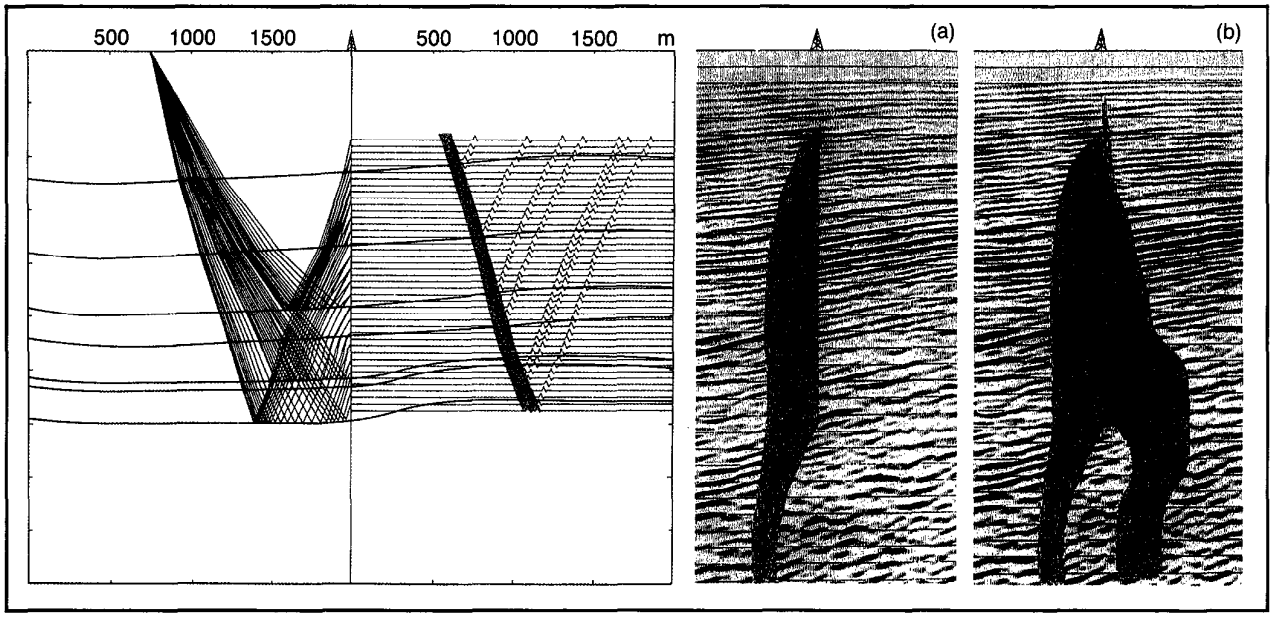

Fig. 9-17—The (a) display shows the Offset VSP events superimposed on the surface seismic section. The (b) display shows the combined results of the OVSP and modeled VSP data.

particularly useful for detection of faults and formation pinchouts. The OVSP events are shown superimposed on the appropriate part of the surface seismic data. The display (b) shows the combined results of the OVSP and modeled VSP data.

Note that there is no reflector coverage below total depth of the well. A particular attraction of walkaway surveys is that they provide better continuity and more complete coverage, especially below the bottom of the well.

The use of the Downhole Seismic Array tool to acquire the data can significantly reduce the acquisition time and improve the consistency of the seismic signal from level to level in the well. Figure 9-18 shows a schematic of the operational setup for a walkaway VSP job on land. Two vibrators, in radio contact with the logging unit, were used as the energy source. The shot points were located at 75 m intervals and were moved out 3 km from the well in each of the four orthogonal directions. At each shot position, eight levels were recorded with the DSA tool.

The east-west walkaway VSP results are shown on the left in Fig. 9-19. Faults, nearby and intersecting the well, were determined from this seismic section. The north-south walkaway section is shown on the right.

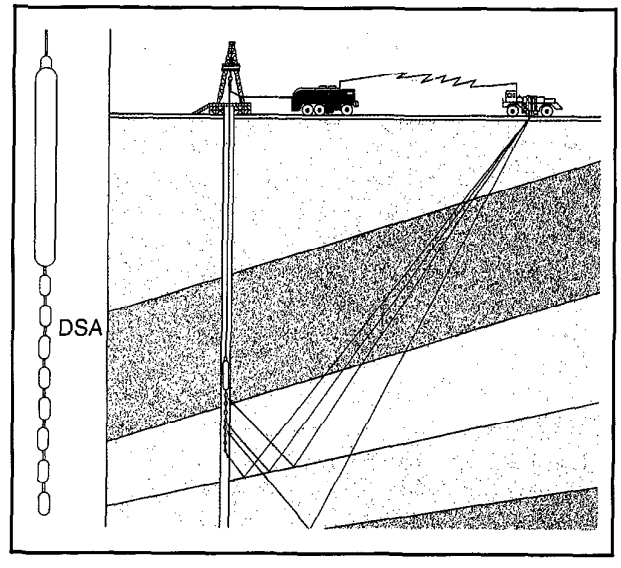

Fig. 9-18—Schematic of operational setup for a walkaway VSP job on land

DSA TOOL FOR VSP ACQUISITION

The Downhole Seismic Array tool, with its eight single-axis geophone array configuration, provides several advantages over single level tools for VSP acquisition in cased holes:

- time savings. One obvious advantage is the savings in time since eight levels are recorded at each firing of the energy source.

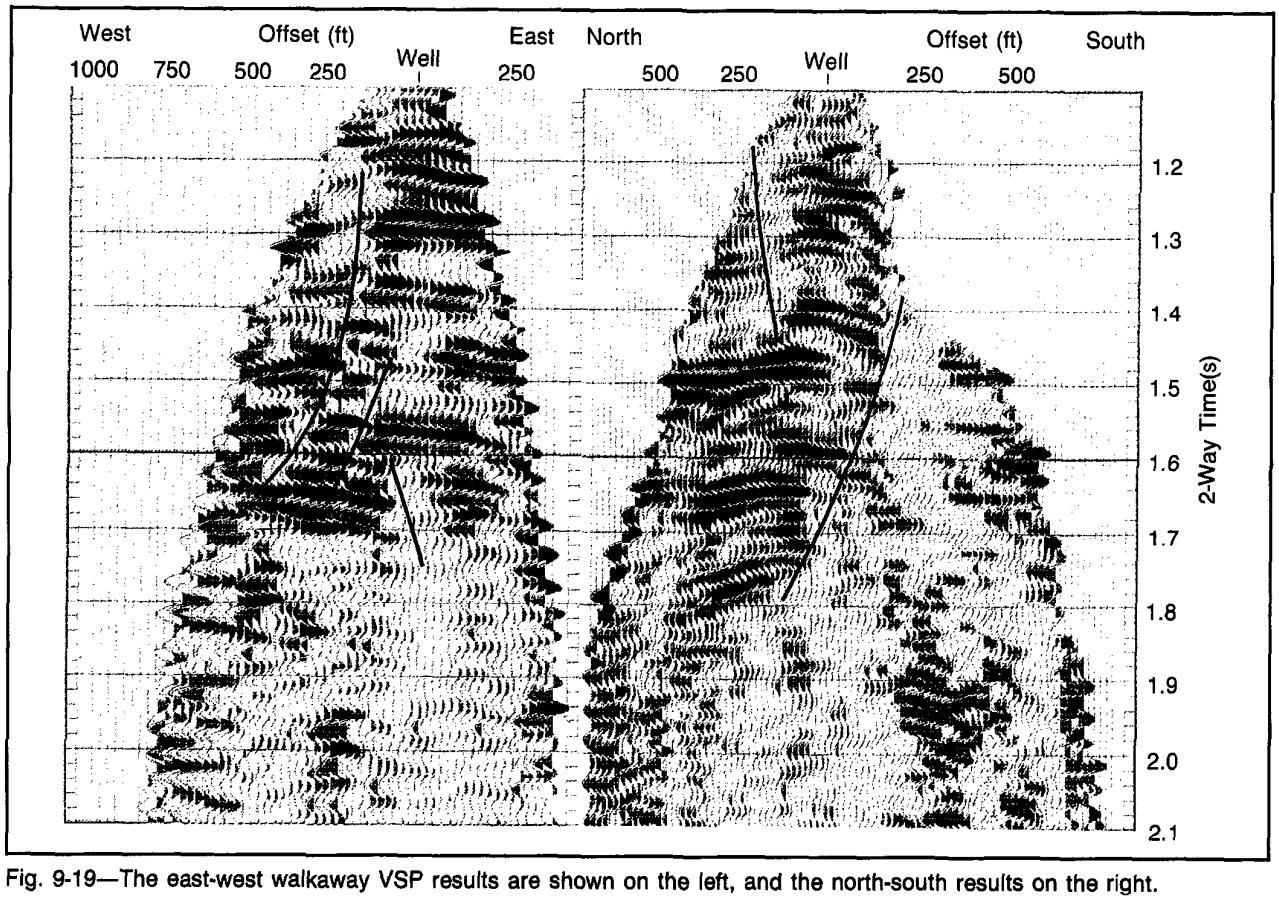

Fig. 9-19—The east-west walkaway VSP results are shown on the left, and the north-south results on the right.

- reduction in tube-wave effects. The DSA tool provides some advantages in areas where strong tube-waves may contaminate the waveform data. The strong clamping force, the small cross-sectional area, and the streamlined shape of the shuttle help to reduce the effect of tube-waves on the seismic data.
- reduction of navigation errors in walkaway VSP operations. In offshore multioffset operations, the seismic source is moved by a boat at a constant speed. The DSA tool acquires signals from eight levels while the boat is making a single path, reducing navigational errors over single level tools.
- reduction of effects of source signature changes. The effects of source signature changes due to such things as changes in gun pressure, gun pit alteration, or tide levels, are reduced because the eight shuttles receive signals which originate from the same shot.
- accurate transit times between levels. Since the DSA geophones are equally spaced on a cable, potential distance errors are eliminated.

PRIMARY USES OF THE VSP SURVEY

The enhanced resolution of the VSP makes it possible to verify or deny the presence of reflections that are indistinct or doubtful on seismic sections near the well. The VSP is particularly well suited to determine the conditions existing below the well's total depth. Overpressured zones, gas sands, and deep reflectors can be verified or recognized.

Since the downgoing wavefield is recorded, multiple reflections can be identified and removed. The same downgoing wave information can be used to reprocess surface seismic profiles traversing the vicinity of the well.

Perhaps the most common use for the VSP is a link between reflections observed on a surface seismic profile and specific petrophysical properties measured in the borehole. The correlation role of the VSP is important for reservoir development applications.

Finally, by positioning the seismic source a significant distance from the well, structural and stratigraphic features from hundreds to thousands of feet from the well can be delineated and verified against the surface seismic.

PROXIMITY SURVEY INTERPRETATION

Proximity surveys have been used for many years to define the shape of salt domes. Now a program is available to entirely mechanize the interpretation process. After a well has been drilled on the flank of a salt dome, a downhole sensor is lowered into the hole and anchored at numerous depths. An energy source is positioned directly over the top of the structure. A travel time is measured from the source to each of the downhole sensor locations. From prior knowledge of salt velocities, velocities of formations encountered in the well, and at least one salt tie point, distances from salt to sensor positions can be calculated, and the shape of the salt flank determined.

Given the layer velocities and the source and receiver locations, the transit times to each receiver are measured by ray tracing. Next, an initial model is generated on the computer containing the known source and receiver locations and the layer velocities. The program then calculates, for each source-receiver pair, all the possible travel paths the acoustic energy could have taken with the total time equal to the measured time. A line through all the refraction points contains all the possible locations for the salt interface calculated from one receiver. The resulting oval is called an aplanatic surface (Gardner, 1949). The computation can be performed for combinations of source and receiver, and will result in a series of aplanatic surfaces. The best fitting line, tangent to all the ovals, is the final solution for the location of the interface.

The technique is illustrated in a well in the Gulf of Mexico. Using accurate source-receiver travel times and the source-receiver positions, the initial model was generated. The salt was a known distance from one receiver, which enabled the use of the refraction oval technique for the determination of the salt top. The formation velocities adjacent to the salt were determined from a vertical check shot and the aplanatic surfaces were generated, as shown in Fig. 9-20. The salt flank was interpreted as the common tangent line illustrated in Fig. 9-21.

The mechanized proximity interpretation gives results consistent with the interpretation made with wavefront charts, but is much less time consuming.

REFERENCES

Anstey, N.A.: *Seismic Interpretation: The Physical Aspects*, IHRDC, Boston (1977).

Ausburn, B.E.: "Well Log Editing in Support of Detailed Seismic Studies," *Trans.*, 1977 SPWLA Annual Logging Symposium.

Gardner, L.W.: "Seismograph Determination of Salt Dome Boundary Deep on the Dome Flank," *Geophysics* (1949) **46**, 268-287.

Goetz, J.F., Dupal, L., and Bowler, J.: *An Investigation Into Discrepancies Between Sonic Log and Seismic Check-Shot Velocities*, Schlumberger Technical Services (1977).

Landgren, K.M. and Deri, C.P.: *A Mechanized Process for Proximity Survey Interpretation*, Schlumberger Offshore Services (1986).

McCollum, B. and LaRue, W.W.: "Utilization of Existing Wells in Seismograph Work," *Bull.*, AAPG (1931) **15**, 1409-1417.

Miller, D.E.: "Arrival Times and Envelopes - Inverse Modeling for Subsurface Seismics," 53rd Annual International SEG Meeting, Sept., 1983, Las Vegas, Expanded Abstracts, 449-467.

Mons, F. and Babour, K.: Vertical Seismic Profiling, SAID Quatrieme Colloque Annuel de Diagraphies (Oct., 1981).

Musgrave, A.W., Wooley, W.C., and Gray, H.: "Outlining of Salt Masses by Refraction Methods," *Geophysics* (1960) **25**, 141-167.

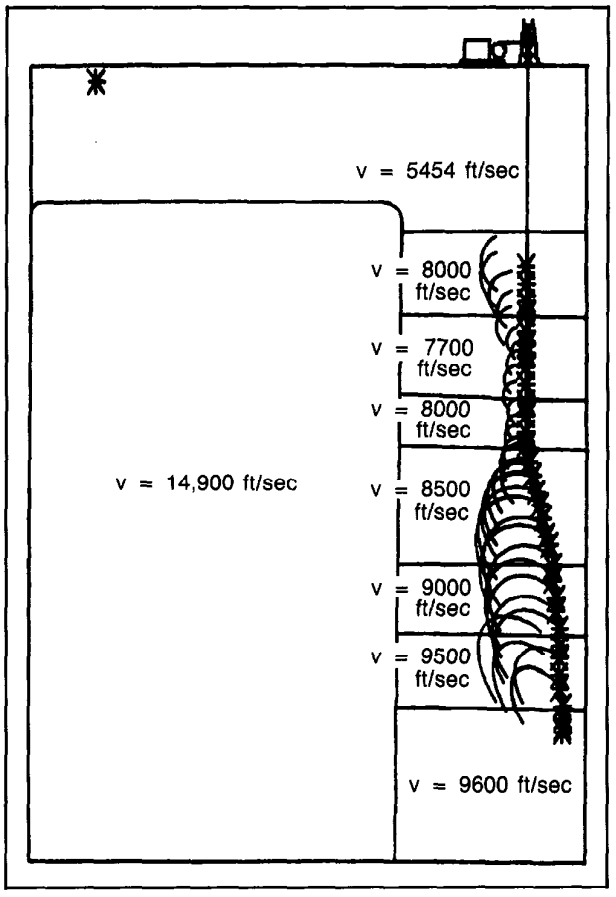

Fig. 9-20—Proximity Survey interpretation: refraction ovals

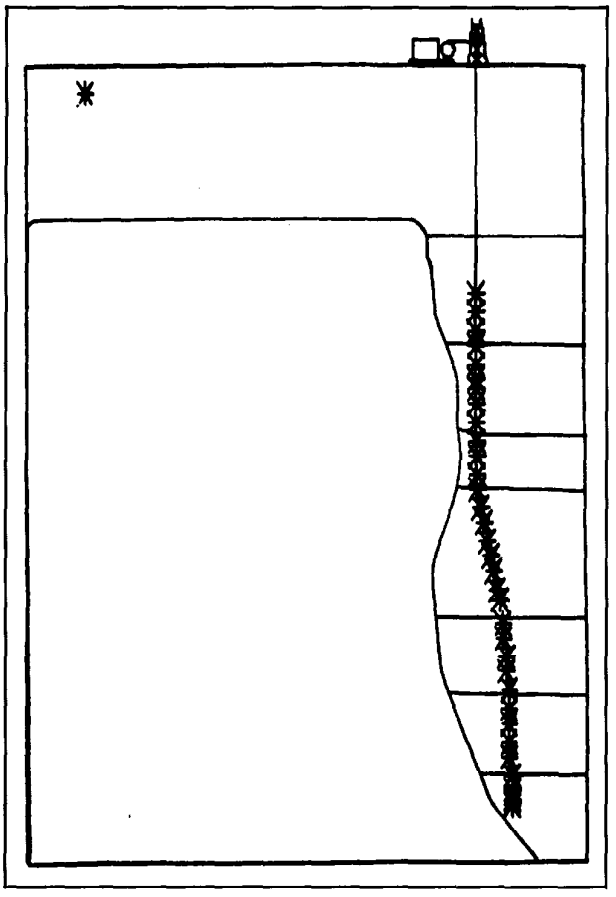

Fig. 9-21—Proximity Survey interpretation: final solution

Robinson, E.A. and Treitel, S.: *Geophysical Signal Analysis*, Prentice-Hall Inc., New Jersey (1980).

Schlumberger Middle East Well Evaluation Review "Borehole Seismics", Schlumberger Technical Services, Paris (Autumn 1988).

Schlumberger West Africa Well Evaluation Conference, Schlumberger Technical Services, Paris (1983).

10 Other Cased Hole Services

This chapter is a discussion of several cased hole services that were not covered in previous chapters. The Guidance Continuous (GCT*) tool for directional measurements, the Freepoint Indicator tool and backoff service, the PosiSet* mechanical plug back tool for through-tubing bridge plug operations, the wireline formation tester, the CERT electromagnetic fishing tool, and the Formation Subsidence Monitor Tool (FSMT) are all examples of cased hole services designed to meet important special requirements.

GUIDANCE CONTINUOUS TOOL (GCT)

The Guidance Continuous tool provides a highly accurate, continuous gyroscopic directional measurement in cased holes. The measurement is based on a 2-axis gyroscope whose spin axis is maintained in the horizontal direction and is aligned towards the north. The position of the gyro is sensed by an accelerometer and a gyro-axis position resolver. This information is combined with data from another accelerometer to derive the azimuth and inclination of the hole.

Knowledge of the precise bottomhole location of a well and the well trajectory is required in several situations, principally including:

- cluster drilling operations on multiwell platforms,
- exact location of both the blowout well and the relief wells,
- precise targets within reservoirs for infill drilling,
- precise location of old wells in secondary recovery projects, and
- lease boundary, regulatory, and unitization requirements.

A 3-dimensional well trajectory schematic is shown in Fig. 10-1. The position of the target is defined by:

- the bottomhole coordinates which are the north and east departures of the projection of the bottom of the well on a horizontal plane. The coordinate system is formed by the north/south and east/west axis centered on the wellhead;
- the True Vertical Depth (TVD) which is the actual depth of the well measured along the vertical axis; and
- the azimuth of the hole with respect to geographic north, the inclination, and the well depth. The north/south departure, east/west departure, and TVD are then computed from these measurements.

The accuracy of the cased hole GCT measurement is also illustrated in Fig. 10-1. In the 4000-m well with a 2000-m departure, the bottomhole position will be determined with a maximum error of ± 10.4 m in the horizontal plane.

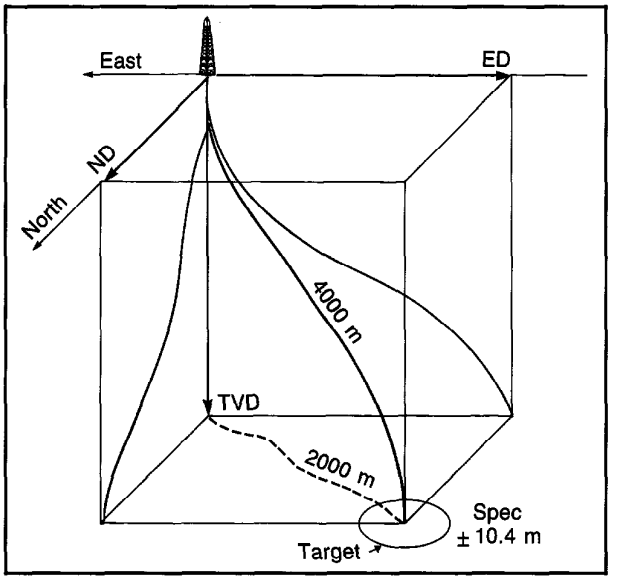

Fig. 10-1—Representation of a 3-dimensional well trajectory

The GCT tool is composed of a 3⅝-in. sonde containing the gyroscope, an electronic cartridge, a telemetry cartridge, an auxiliary measurement sonde for temperature and downhole head tension measurements, and an anchoring device for wellsite calibrations. The measurement is based on a 2-axis gyroscope whose spin axis is maintained in the horizontal direction and aligned to north (or to a fixed known direction). The principle of the measurement is shown in Fig. 10-2.

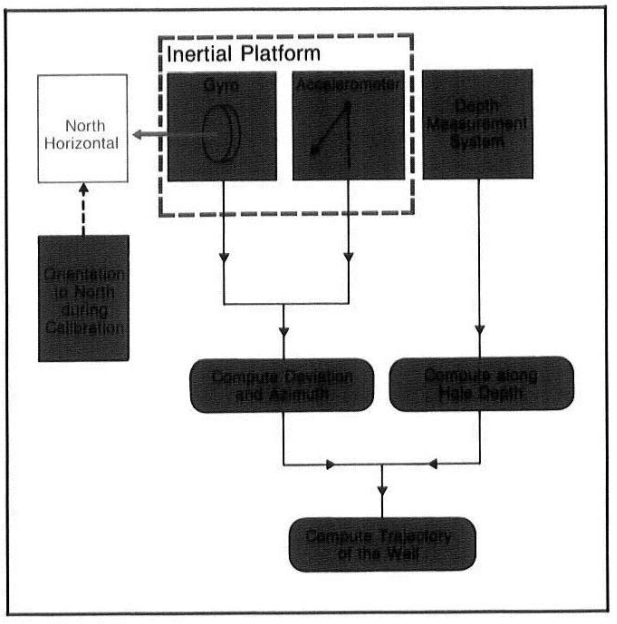

Fig. 10-2—Principle of the GCT measurement

The gyroscope and a 2-axis accelerometer are mounted on an inertial platform. Their measurements are combined to derive the azimuth and the inclination along the hole (Fig. 10-3). The well trajectory is computed from the azimuth and deviation information combined with the measured depths.

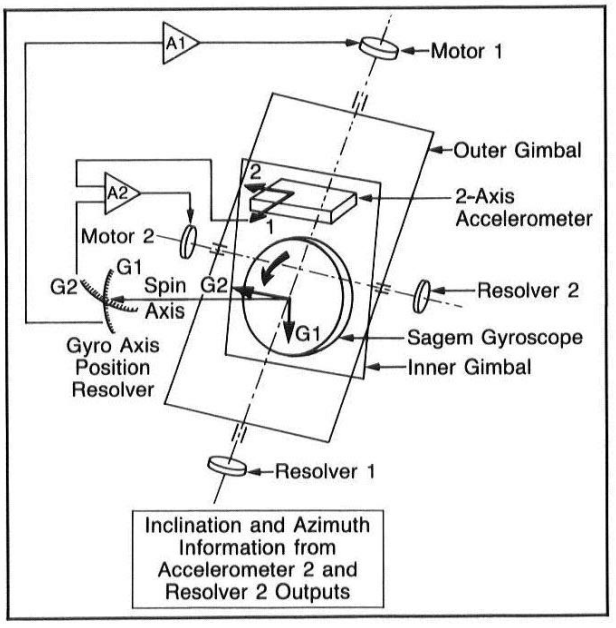

Fig. 10-3—The GCT measurement system

The tool position is compared to a reference defined by:

- the horizontal plane (accelerometer measurement) and
- a known direction (gyro information).

The initial orientation of the gyro to a fixed direction is performed at the tool calibration phase.

MEASUREMENT THEORY

The gyroscope is composed of a disk, rotating at high speed, held by a system of gimbals which allows the frame of the gyro to move in any position while the gyro spin axis remains fixed (Fig. 10-4). The fast rotational speed of the flywheel tends to keep the gyro axis pointed in a fixed direction. This direction is used as a reference for the guidance tool. The gyro disk (flywheel) when submitted to a torque due to external forces (earth rotation, mechanical unbalance) moves at a right angle to the applied torque and starts a precessional movement. The torque applied to the gyro can be estimated by measuring the precession speed.

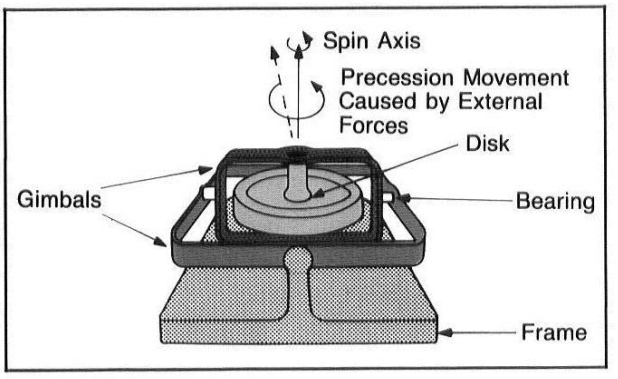

Fig. 10-4—GCT gyroscope

The gyroscope in the GCT tool contains a servomechanism composed of two position sensors and two torquing motors. These are used to cancel the torque created by external forces. This technique is used to counterbalance the torque due to the mechanical imperfections of the gyro and to measure the precessional speed movement caused by the earth's rotation. This speed is proportional to the earth's rotation component along the gyro axis and depends on the angle between north and the gyro spin axis. The detection of the precessional movement allows the computation of this angle.

The accelerometer is a type of pendulum which detects and measures any acceleration (Fig. 10-5). This movement is proportional to the acceleration of gravity which created it. The accelerometer used in the GCT tool works along two orthogonal axes, and, therefore, measures two orthogonal components of gravity.

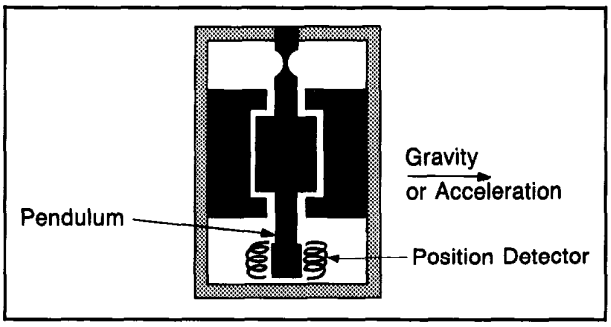

Fig. 10-5—Schematic of an accelerometer

Calibration

Mechanical imperfections and gain and offset of the sensors are two parameters that are characteristic of each particular tool and they are determined during the shop calibration as follows:

- Mechanical imperfections of the gyro and the accelerometer: Gyro imperfections such as gyro mass imbalance, aerodynamic friction, and colinearity error between spin axis and accelerometer X-axis are measured so that compensations can be made.
- Gain and offset of the tool sensors: The gain and offset of accelerometer and gyro position sensors are measured for use in the tool response computation.

At the wellsite a calibration is performed to:

- position the gyro axis and align it to north;
- position the gyro axis in a chosen direction. After seeking north, the orientation of the gyro may be changed. The best choice of orientation is the average hole azimuth;
- compute the correction necessary to compensate for the effect of the earth's rotation. A correction is applied, through the servomechanism, to the inertial platform.

The wellsite calibrations are performed with the tool anchored inside the casing so that the tool is fixed in respect to the earth, providing a stable reference position during gyrocompassing seeking north.

Log Quality Control

After the calibration, the tool is pulled back to the surface and the survey started. The log is normally recorded both in and out of the hole so that the results can be compared for closure. Closure is defined as the distance between the top of the well as originally recorded and the top of the well as recorded by the GCT tool after the survey. Tool measurement errors are cumulative; therefore a small closure indicates a good log. The well trajectory, deviation, and curvature of the up and down runs are compared and must repeat.

Accuracy

The accuracy of the measurement is assured for operations in cased holes with an uncentralized tool. The north-seeking accuracy of the gyro is better than 0.1°, and the drift, after applying the correction computed during calibration, is less than 0.1°/hr.

The accuracy of the tool measured in terms of horizontal errors in the north and east direction is:

$$\text{N or E} = 0.4\% \times (\cos 45°)/(\cos L) \times H + 0.06\% D, \quad \text{(Eq. 10-1)}$$

where:

H = horizontal departure
D = tool depth
L = latitude.

These specifications can also be defined with respect to the axis passing through the top and the bottom of the well, and the axis perpendicular to it. Then the error on the azimuth (0.4% H), which affects only the reading perpendicular to the hole direction, can be removed from the error in the other directions:

Δ (along axis top/bottom of well) = 0.06% D
Δ (axis orthogonal) = 0.4% H + 6% D.

Equation 10-1 shows that errors on departures become too large for geographical latitudes higher than 70°. This is due to the difficulties in finding the north direction with a gyro in high latitudes. Gyrocompassing uses the horizontal component of the earth's angular speed and this component becomes too small near the pole. Optical sighting may eventually overcome this problem.

The accuracy of the bottomhole position is, at least, better than half of the closure between the up and down runs (Fig. 10-6). The closure specification is:

$$\text{Closure } (\Delta x, \Delta y) < 2\left(0.4\% \frac{\cos 45°}{\cos L} H + 0.06\% D\right). \quad \text{(Eq. 10-2)}$$

An after-survey calibration is also performed with the tool anchored in the casing. A new north is found and compared to the north found before the survey to determine any gyro orientation error.

Wellsite Processing

The data is processed in real time by the CSU logging unit. The information required includes:

- shop calibration data tape
- latitude of the well
- "grid angle departure" (GAD parameter), which is the

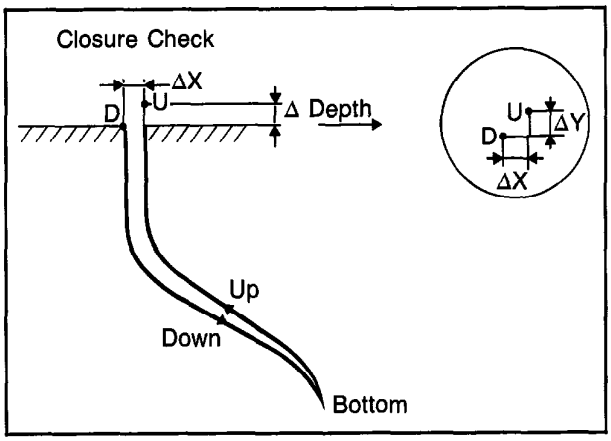

Fig. 10-6—Illustration of the closure check

angle between geographic north and client north, positive in the NE direction

- coordinates of the origin of the log if they are different from zero (see Fig. 10-7).

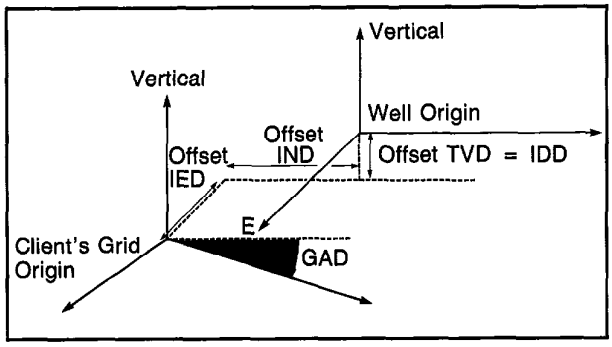

Fig. 10-7—Illustration showing offset of the origin

The CSU software:

- computes the earth rotation components to keep the gyro in a fixed direction in the earth's reference field using calibration data and latitude
- computes stretch on the cable and provides corrected depths using uphole and downhole tension measurements
- uses calibration data to correct for mechanical imperfections of the inertial platform.

The program uses accelerometer data to compute the azimuth and deviation and depth data to integrate the trajectory along the borehole. Computations are made every 10 sec.

Presentation of Results

Presentations available at the wellsite include well trajectory plots and a listing of the results.

A tabular listing of results is shown in Fig. 10-8. The listing

DEPTH	NORTH	EAST	DOG-LEG	AZIMUTH	DEVIATION
9868.83	- 617.70	2094.89	2.0	123.73	11.70
9868.81	- 617.69	2094.88	2.0	123.74	11.70
9868.59	- 617.67	2094.85	2.0	123.73	11.69
9867.34	- 617.53	2094.64	2.0	123.69	11.67
9864.81	- 617.25	2094.21	.6	123.64	11.65
9862.35	- 616.97	2093.79	.6	123.58	11.64
9859.90	- 616.70	2093.38	.8	123.50	11.65
9857.50	- 616.43	2092.98	1.5	123.44	11.68
9855.01	- 616.15	2092.56	1.2	123.39	11.71
9852.47	- 615.87	2092.13	.9	123.38	11.73
9850.07	- 615.60	2091.72	.3	123.43	11.74
9847.57	- 615.32	2091.29	.6	123.48	11.75
9845.14	- 615.04	2090.88	1.0	123.57	11.75
9842.76	- 614.78	2090.48	1.1	123.69	11.75
9840.29	- 614.50	2090.06	1.7	123.76	11.73
9837.27	- 614.16	2089.55	1.1	123.79	11.69
9837.06	- 614.13	2089.51	7.8	123.83	11.66
9836.31	- 614.05	2089.39	7.8	123.70	11.64
9829.41	- 613.28	2088.23	1.6	123.35	11.65
9821.75	- 612.43	2086.93	.9	123.17	11.72
9814.15	- 611.58	2085.63	.6	123.33	11.77
9806.60	- 610.73	2084.35	.7	123.55	11.80
9797.99	- 609.75	2082.88	2.0	124.08	11.82
9788.72	- 608.68	2081.31	.9	124.29	11.82
9779.47	- 607.62	2079.74	1.8	124.37	11.86
9770.17	- 606.52	2078.16	.8	124.62	11.89
9760.78	- 605.43	2076.58	1.2	124.58	11.90
9751.28	- 604.31	2074.95	.4	124.47	11.95
9741.89	- 603.21	2073.35	1.2	124.55	11.99
9732.25	- 602.07	2071.70	.6	124.59	12.03
9722.21	- 600.88	2069.97	.6	124.29	12.02
9712.01	- 599.69	2068.21	.3	124.12	12.05
9701.93	- 598.51	2066.47	.4	124.21	12.08
9691.68	- 597.30	2064.69	.1	124.26	12.10
9681.56	- 596.10	2062.94	.4	124.25	12.13
9671.46	- 594.90	2061.18	.4	124.28	12.18
9661.29	- 593.69	2059.40	.4	124.39	12.19
9651.19	- 592.48	2057.64	1.0	124.42	12.24
9640.98	- 591.26	2055.85	.3	124.25	12.29

NAME	VALUE	UNIT	NAME	VALUE	UNIT
NRA	106.000	DEG	GAD	0.0	DEG
IED	0.0	F	IDD	61.0000	F
LATD	70.3200	DEG	IND	0.0	F
GRAV	9.82612	M/S2	ALTI	40.0000	F
TTRB	4.00000	DEGC	HTEM	120.000	DEGC
BHS	CASE		ENVT	FIEL	
DO	0.0	F	BS	8.50000	IN

PARAMETERS

Fig. 10-8—Listing of GCT results

includes depth, north departure, east departure, true vertical depth, dogleg severity, azimuth, and deviation. The insert shows the parameters that were input by the engineer:

ALIT = altitude of the wellhead
GRAV = gravitation
LATD = latitude
GAD = grid angle departure
IDD = initial depth departure
IND = initial north departure
IED = initial east departure
NRA = angle between geographic north and the spin position chosen for navigation.

Several well trajectory plots can be made by the CSU system in the playback mode. Fig. 10-9 shows the projection of the well on a N-S vertical plane. In this example the well origin is not at zero on the crossplot.

The well projection is shown on a vertical E-W plane in Fig. 10-10. Projection can be made on any other vertical plane if desired. The well projection on a horizontal plane is shown in Fig. 10-11.

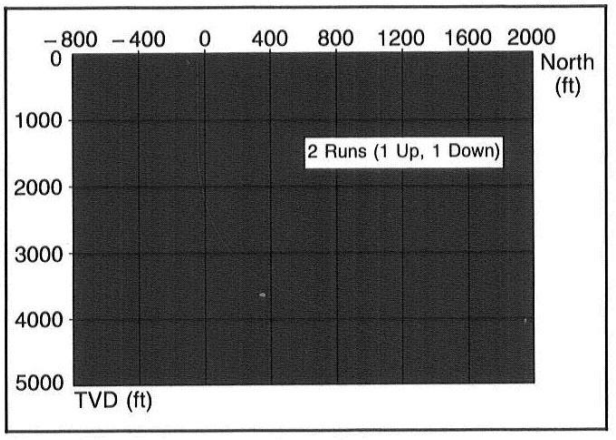

Fig. 10-9—Well projection on a vertical N-S plane

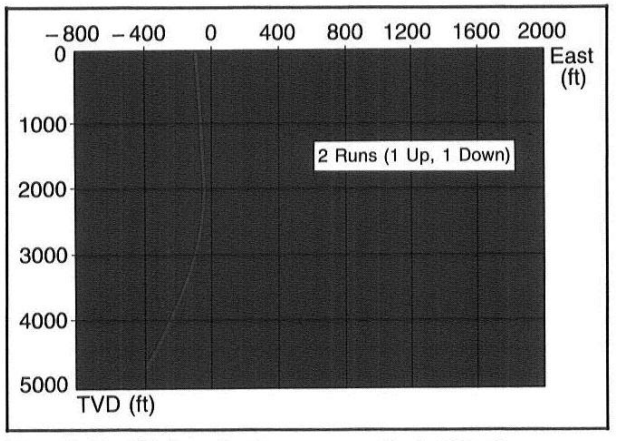

Fig. 10-10—Well projection on a vertical E-W plane

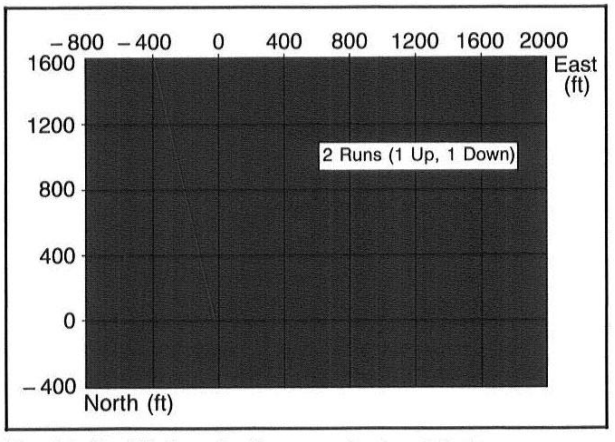

Fig. 10-11—Well projection on a horizontal plane

Fig. 10-12 shows a plot of well curvature (dogleg severity) versus true vertical depth. Dogleg severity is measured in degrees per 10 m or 100 ft. The tool can handle rather

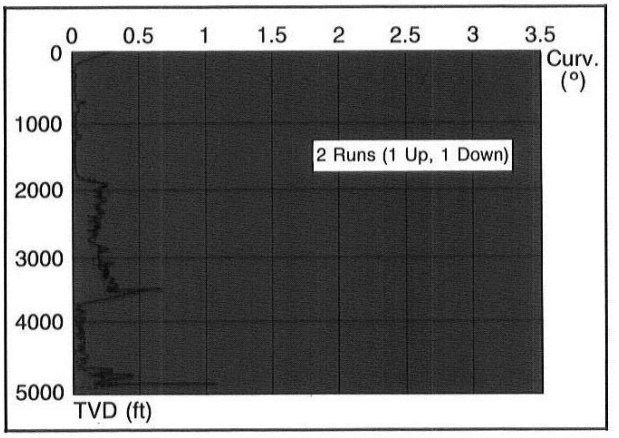

Fig. 10-12—Plot of well curvature

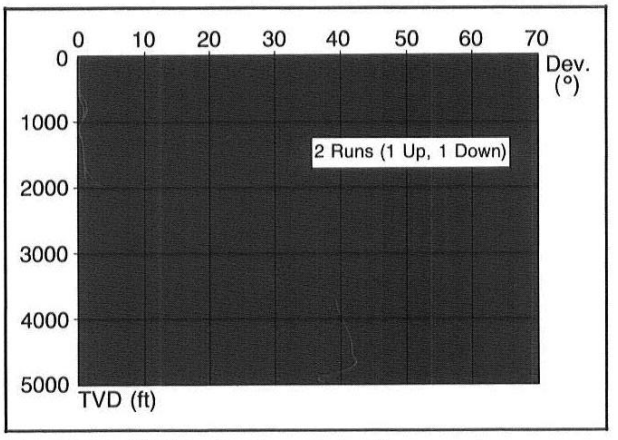

Fig. 10-13—Well inclination vs. depth

rapid hole direction changes; azimuth shifts up to 10°/sec and inclination variation of up to 10°/100 m.

The well inclination versus true vertical depth plot is shown in Fig. 10-13. Both down and up runs are shown for comparison.

FREEPOINT INDICATOR (FPIT) TOOL

Some of the major causes of stuck pipe are:

- differential sticking caused by heavy mud and/or highly deviated holes
- keyseated pipe caused by doglegs
- unconsolidated formations collapsing around the pipe
- sloughing or swelling shales.

Once the pipe is stuck, attempts to free it are usually made by jarring and by circulating a friction reducer. If these attempts are unsuccessful, a wireline service is usually run to locate the deepest free point of the stuck pipe and then the

pipe is backed off just above this point. After the free pipe is recovered, a common procedure is to washover the stuck section of pipe and reconnect with a jar near the stuck section for retrieval.

By using stretch and torque measurements, the Freepoint Indicator tool accurately determines the free point in any string of pipe stuck in the hole including drillpipe, drill collars, tubing, and casing.

The FPIT tool, shown in Fig. 10-14, consists of two anchors and a sonde. A backoff can be successful only if the desired backoff joint is free in both stretch and torque. The FPIT sonde contains two sensors, one which detects stretch and is not affected by torque, and one which detects only torque. With measurements from both sensors, the interpretation of the results is completely reliable.

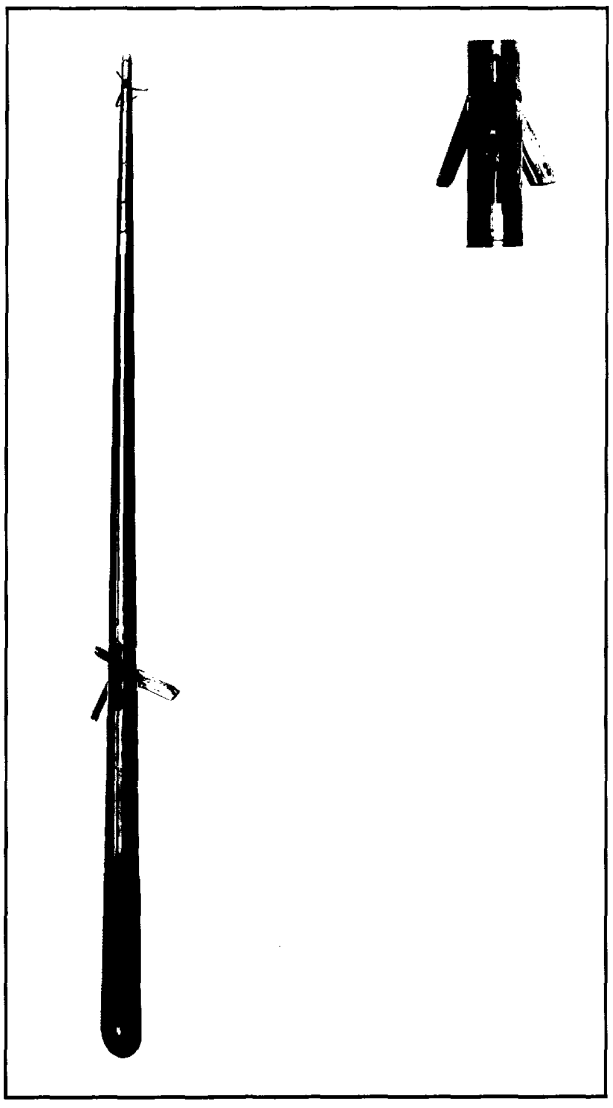

Fig. 10-14—Freepoint Indicator tool

The torque sensor can measure both right- and left-hand torque, giving the added capability of showing that applied left-hand torque has reached the point to be backed off. This is particularly useful in deviated wells where torque has to be worked down. These measurements can be read directly on the bar graph display on the FPIT module in the CSU unit.

In most cases, the FPIT tool can be combined with the backoff shot allowing the backoff to be made immediately after the detection of the deepest free point. This results in a very high success rate in backing off at the first attempt.

The CSU program allows the full integration of the drillers' parameters and pipe string configuration (such as weight before sticking, pipe dimensions and depths) to provide a computation of the required pull and torque to be applied for optimum sensor readings. Once the survey has been completed, the program gives the estimated stuck point and the recommended number of primacord strands to be used for the backoff shot on a summary listing (Fig. 10-15). If more than seven strands of primacord are required, the backoff shot must be run separately. A log is also presented as shown in Fig. 10-16 that provides a pipe sketch and displays the stretch and torque measurements.

DSC SUMMARY LISTING

EL.#	TOP DEPTH	LENGTH	TYPE	OD (INCH)	ID (INCH)	WEIGHT (LBS/F)	MAT
9	-51.00	45.00	KELL	6.50	2.76	92.07	STEE
8	-6.00	30.00	DP	4.50	3.00	32.30	STEE
7	24.00	30.00	HWDP	4.50	2.75	33.73	STEE
6	54.00	30.00	JAR	5.00	2.70	47.08	STEE
5	84.00	3.00	XOVR	5.00	2.50	49.85	STEE
4	87.00	30.00	DC	6.00	2.25	82.25	STEE
3	117.00	10.00	STAB	6.00	2.25	82.25	STEE
2	127.00	30.00	DC	6.00	2.25	82.25	STEE
1	157.00	3.00	SUB	6.00	2.25	82.25	STEE
0	160.00		BIT				

DRILLER PARAMETERS

WEIGHT GOING-UP BEFORE STICKING: 30.00 TON
WEIGHT GOING-DOWN BEFORE STICKING: 20.00 TON
MAX SAFE PULL 60.00 TON
WEIGHT OF TRAVELLING BLOCK: 10.00 TON
MAX RH # OF TURNS 2
MAX LH # OF TURNS 1

SIT LOG PARAMETERS

WEIGHT IN MUD 15.35 TON
OVERPULL MINI: 5.98 TON
OF TURNS MINI: 0.01
RECOMMENDED STARTING POSITION: 33.00 TON
RECOMMENDED RELEASE POSITION: 20.00 TON

BACK-OFF PARAMETERS

AT DSPO: 150.0 F 1 # OF PRIMACORD STRANDS: 4

0

FILE

MEASUREMENTS SUMMARY LISTING

STATION NUMBER	STATION DEPTH	TYPE OF PIPE	LINEAR WEIGHT (LBS/F)	PERCENT FREE IN STRETCH	PERCENT FREE IN TORQUE
5	85.03	XOVR	49.85	94	99
4	95.03	DC	82.25	76	82
2	105.0	DC	82.25	38	45
1	125.0	STAB	82.25	7	15

Fig. 10-15—Freepoint Indicator summary listing

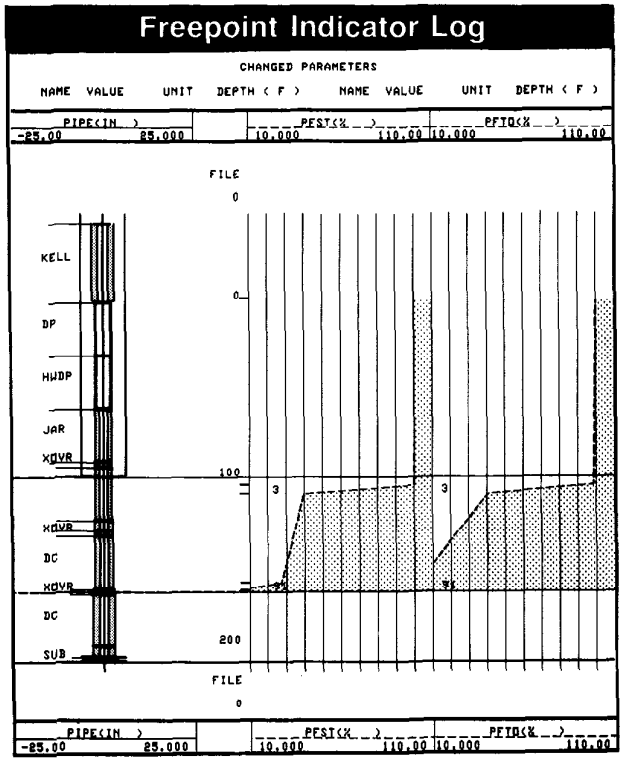

Fig. 10-16—Freepoint Indicator log

HYDRAULIC SEALING

The need for hydraulic isolation of selected portions of the wellbore became more important with the introduction of cemented casing strings and wireline gun perforating. Baker Oil Tools developed a setting tool in the 1940s that would allow sealing devices to be run in the well and set with wireline. Today, all commercially available wireline sealing devices such as production packers, cement retainers, bridge plugs, and tubing stops can be accurately set with depth control provided by a casing collar locator and a Gamma Ray log.

Through-Tubing Bridge Plug (Plus Plug*)

The need for a device to permanently plug casing without pulling tubing to effect plug backs, water shutoffs, and gas shutoffs was recognized early on. Finding an effective solution to this problem, however, has proven difficult.

The Through-Tubing Bridge Plug (Plus Plug) was introduced in the early 1960s. Although it was considered a breakthrough in bridge plug technology, the Plus Plug still presented problems.

The Plus Plug tool assembly consisting of a positive displacement dump bailer, a vent tube with a mechanically-timed vent valve, and a collapsed packer bag is run in and positioned in the well. The dump bailer is actuated and cement is forced into the packer bag, inflating it to the diameter of the casing. The remaining cement is dumped around the vent tube. Subsequent dump bailer runs place an additional column of cement around the vent tube, which is open to allow the movement of well fluids.

After the cement has set up within the bag and in the column above the vent tube, the timer closes the vent tube and additional cement is dumped to strengthen the plug. The operational sequence is illustrated in Fig. 10-17.

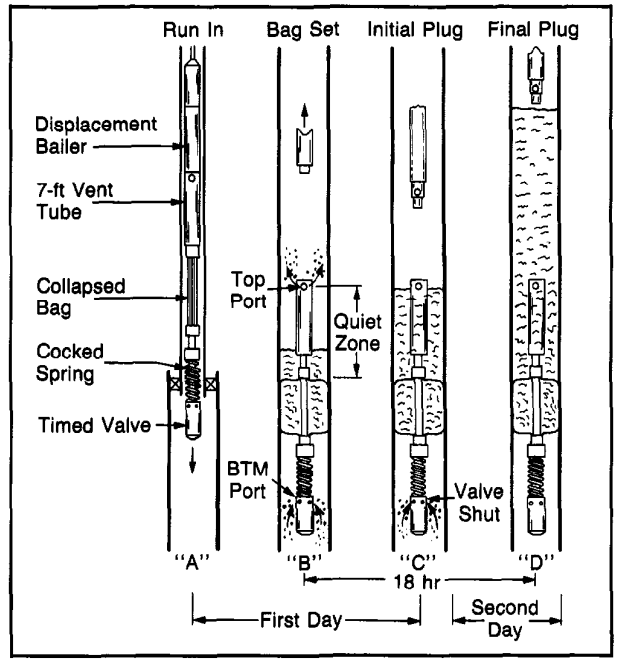

Fig. 10-17—Plus Plug operational sequence

The Plus Plug has several design features to enhance the success rate:

- The expanding cement that is forced into the bag is never in contact with the well fluids and remains free from contamination.
- The packer bag effects a hydraulic seal between the vent tube and the casing. Therefore, the vent hole through the plug permits the well fluids to move through the plug without contaminating the cement around the vent tube.
- The mechanically timed shutoff valve prevents the movement of well fluids through cement dumped on the final run.

While the Plus Plug was probably the best through-tubing bridge plug available, it has been plagued with a variety of problems over the years. In many cases it worked just as designed, even under extreme conditions; other times it failed under seemingly ideal conditions. The basic problem is the

mixing of cement in small quantities for use under various downhole conditions. A project to develop a mechanical plugback tool that does not require cement for hydraulic integrity has been under development for several years.

PosiSet Mechanical Plugback Tool

The recently introduced PosiSet through-tubing bridge plug satisfies the same basic need for a simple, cost effective, through-tubing system to facilitate plugback and reperforating operations in wells with water production or depleted zone problems. The operational sequence is shown in Fig. 10-18.

The PosiSet plug is illustrated in Fig. 10-19 in both the running in the well and after setting configurations. The plug consists of:

- upper and lower anchors,
- metal backup elements, and
- elastomeric seal elements.

The seal elements are constrained within specially treated plastic sleeves when running in through the small diameter tubing. Positioned at the desired depth, the setting sequence begins. Activation of the setting tool energizes the top anchor first and then the bottom anchor and the elastomeric seal elements. The constraining sleeves around the seal elements are burst as the elements are compressed. The metal backup elements are also flattened, forming an antiextrusion system for the seal elements. The mandrel lock serves as a restraining ratchet system during the setting process. With the seal and backup elements fully compressed, the anchor arms "bite" into the casing to lock the plug against

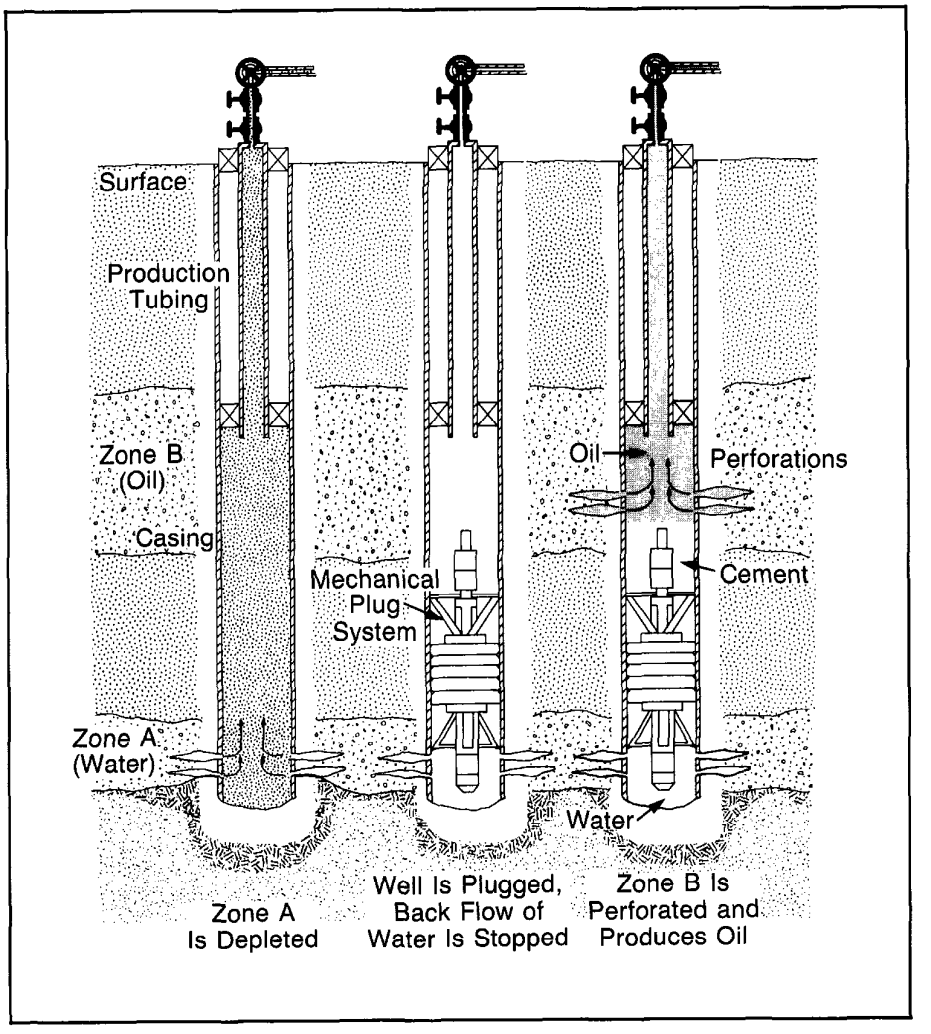

Fig. 10-18—PosiSet mechanical plugback tool operational sequence

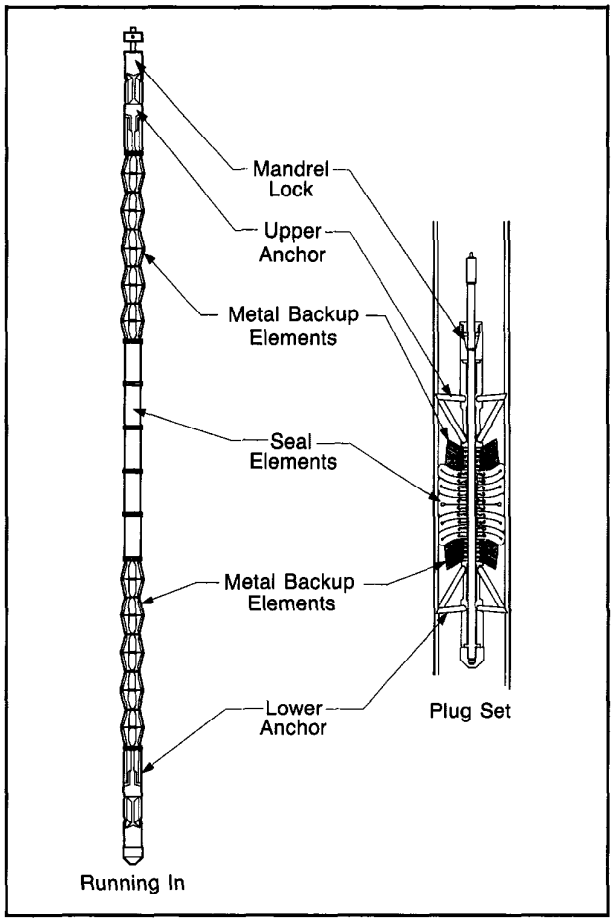

Fig. 10-19—Schematic of PosiSet through-tubing plug operation

differential pressure forces. Finally, a tension stud in the rod system breaks, allowing the tool string to separate from the plug.

The setting tool is powered by a downhole hydraulic motor. During the setting process, the motor-pump-intensifier system pumps in a high volume mode until the pressure demand increases. The intensifier is then activated to break out the seal elements, compress the backup elements, and shear the tension stud. This allows a relatively fast setting time (25 to 60 min) depending on the casing size.

An emergency release system provides separation of the plug assembly from the rest of the tool string in the unlikely event the plug hangs up.

The main advantage of the mechanical plugback tool is that no cement is required in the setting operation. Of course, the plug can be, and normally is, used as a platform for supplementary cement, depending on the pressure rating requirements. Another important feature is that the setting action is independent of hole deviation.

CASED HOLE WIRELINE FORMATION TESTER

The wireline formation test tools provide a safe, economical, and reliable method for testing potential producing zones behind casing. The applications in cased hole are the same as those in openhole testing. These include the measurement of formation pressure, the determination of formation fluid, the determination of oil and gas ratios and oil gravity, and the location of gas-oil or oil-water contacts.

One of the primary applications for cased hole wireline testing is pre-abandonment testing in old wells. Before the well is plugged and abandoned, a TDT log (or GST log depending on the conditions) is run to identify other potential pay zones. Starting at the bottom of the well and working up, the potential zones are tested with the wireline tester. If the test results indicate a producer, a bridge plug is set and the zone perforated for production. If not, the process is repeated on the next potential pay zone up the hole.

Wireline testing in cased holes offers the following technical advantages:

- The tests are made through clean perforations sealed from the borehole fluid.
- For safety, the well may stay under complete hydrostatic fluid control during the testing operation.
- Invasion is generally not a problem so interpretation of the results is straightforward.
- There are usually no packer seal problems in casing.
- Precise depth positioning is provided by gamma ray and casing collar logs.

One condition is essential for cased hole wireline testing: a good seal in the casing/formation annulus must exist. A log for cement evaluation before testing is recommended, even though conclusive tests can often be obtained above the cement top because formation sloughing and mud hydration create the necessary seal between casing and formation.

Cased Hole Wireline Tester Tools

Two types of formation tester tools are currently in use. Both the Formation Interval Tester (FIT) tool and the recently introduced Dual Shot Repeat Formation Tester (RFK-V) tool are available in limited areas.

FORMATION INTERVAL TESTER (FIT)

With the FIT tool, a hydraulic multiplier system actuates a backup shoe which pushes the tool against the casing and causes sealing of the small circular packers. One or two holes are perforated through the casing within the area sealed by the packers. An initial shut-in pressure measurement is recorded and then the sample chamber is opened to flow. A recording of flowing pressure is made and when the chamber is filled with formation fluids a final shut-in pressure is

recorded and the chamber sealed. The tool is then returned to the surface and redressed for the next test.

DUAL SHOT KIT WITH REPEAT FORMATION TESTER

The RFK-V kit modifies the openhole RFT* tool. The probe block contains two shaped charges that can be fired independently, allowing two samples or pressure tests per trip in the well. Operationally, the tool is similar to the RFT tool in that the tool may be set as many times as necessary and the packer seal integrity can be checked before the casing is perforated.

Interpretation

Interpretation of fluids recovered in cased hole tests is somewhat more meaningful than openhole recoveries, particularly in old wells. Since the invaded zone generally disappears within a few weeks or months after casing is set, the cased hole test recovers virgin formation fluids and therefore is indicative of expected production.

Fig. 10-20 shows logs on a well that was tested with the FIT tool. The primary objective of the cased hole evaluation was to identify the fluid type and to determine productivity.

The openhole neutron-density logs do not indicate free gas, but it was thought that the gas effect might have been masked by excessive filtrate invasion. The cased hole CNL log, which should be free from invasion effects, overlays the openhole log, confirming that free gas is not present.

The FIT tool recovered 1650 cc oil, 15 cu ft gas (GOR 1440 cu ft/bbl), and no water, in 23.5 min of sampling time. Pressures recorded with an Amerada gauge measured 583 to 864 psi flowing and 4476 psi shut-in.

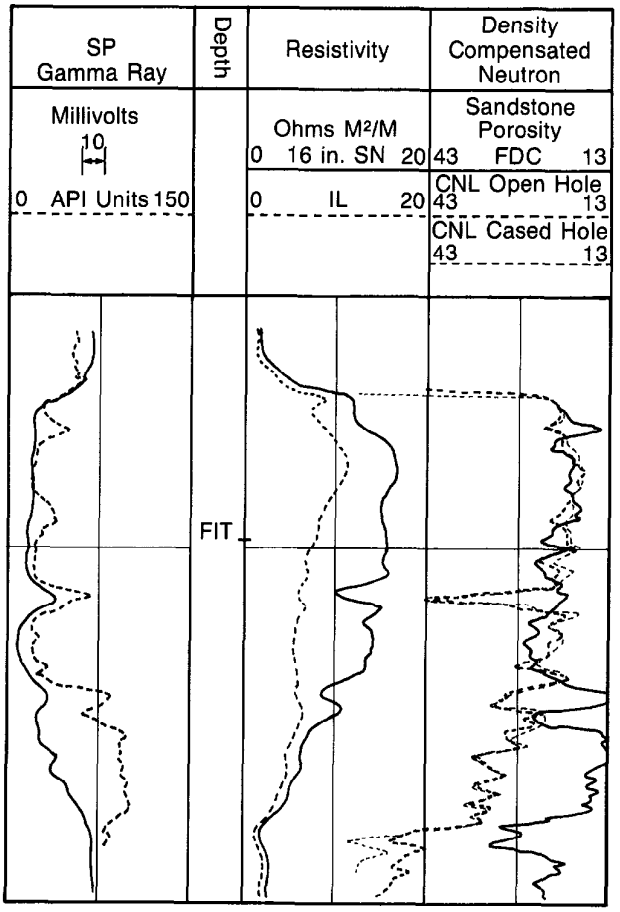

Fig. 10-20—FIT test confirms the openhole and cased hole CNL interpretation

CORRELATED ELECTROMAGNETIC RETRIEVAL (CERT) TOOL

The CERT tool is a wireline electromagnetic fishing device designed to retrieve metallic junk in cased or open holes. It offers the following advantages over permanent magnet-type fishing tools:

- The tool is nonmagnetic when the power is off so it will not disrupt navigational instruments during transport to the well.
- The tool is not activated until fishing depth is reached so that a clean surface is maintained for maximum lifting capacity.
- Casing collar and gamma ray logs can be run with the CERT tool for positive depth control.
- A "fish detector" circuit provides an indication of fish contact and/or loss so that the progress can be monitored all the way to the surface.

The CERT electromagnet is five times more powerful than a permanent magnet of the same size, a fact which greatly enhances the chance of a successful fishing job. The 5-in. CERT tool has a flat plate lifting capacity of 1000 lb compared to 200 lb for a permanent magnet. Fig. 10-21 shows a plot of vertical lift force versus distance for a 5-in. CERT tool and permanent magnet. The $1^{11}/_{16}$-in. CERT tool has a flat plate lifting capacity of 120 lb.

Tools are available for various tubing and casing sizes. Nonmagnetic guide shoes, matched to the casing size, prevent the tool from bypassing the fish and direct it toward the CERT tool's contact area.

SUBSIDENCE MONITORING

Introduction

Terrain subsidence caused by hydrocarbon production has been a major concern in some areas for many years.

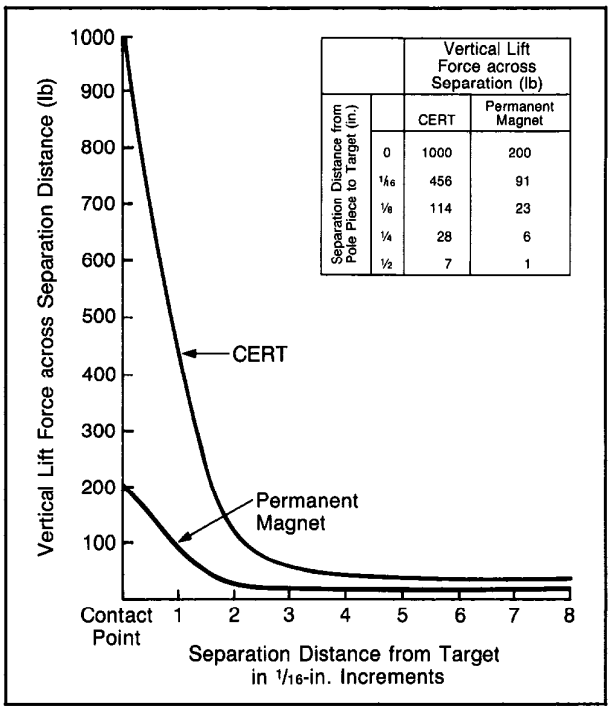

Fig. 10-21—Plot of vertical lift force vs. distance

Reservoir compaction can be modeled with laboratory-measured rock compressibility and pressure decline. However, results show that the process is far more complex than this and downhole compaction measurements are the only practical way to monitor subsidence for accurate modeling.

In the United States, production from the overpressured Wilmington Oil Field had caused widespread subsidence in the City and Port of Long Beach. Newsreels in the late 1940s showed wellheads standing 15 ft above ground. Total subsidence reached as much as 30 ft in some areas before further sinking was halted by water injection. A monitoring of compaction has been performed in several wells since 1949.

In the Bolivar Coast field of the Maracaibo Basin, Venezuela, compaction measurements have been made since 1956. In this field, production casings were being damaged and, in addition, surface facilities were sinking below lake level, necessitating the construction of dikes. The solution, as at Long Beach, was to identify the contracting zones, so that water injection could be effectively applied.

Of the other subsidence projects throughout the world, the Groningen program in the Netherlands has probably been the most publicized. Compaction measurements were started there in 1967. A large part of the land surface of the Groningen field lies on the average between 0 and 1 m above sea level, so it was very important to get an early understanding of the ultimate degree of subsidence.

Subsidence Measurement Techniques

Two subsidence measurement techniques have been used throughout the years. One uses a multiple casing collar tool to calculate the compaction of the lengths of individual casing joints and then relates this to formation subsidence. The other uses a multidetector gamma ray tool to monitor the movement of radioactive markers in the formation itself. Most subsidence monitor projects use one, or a combination, of these techniques.

Assuming a good cement bond between the formation and casing, the casing collar technique may be a good measure of formation compaction during the early stages of subsidence. However, when casing shortening exceeds the maximum elastic deformation of the casing, collar movement will probably no longer be representative of formation movements. The measurement of fixed radioactive markers placed in the formation should then provide a better measurement of compaction.

THE FORMATION SUBSIDENCE MONITOR TOOL (FSMT)

A new Formation Subsidence Monitor Tool (FSMT) is now available in limited areas for compaction measurements. The FSMT tool has four gamma ray detectors for accurate measurements of radioactive bullets placed at spacings between 9 and 12 m apart in the formation (Fig. 10-22). The detectors are mounted at precise spacings, defined by invar spacers, to minimize changes in detector spacing from temperature variations. The temperature inside the tool is also recorded for computation of residual changes in detector spacings.

The tool is centralized by two 4-arm Teflon®-covered centralizers to reduce uneven tool movement. An accelerometer in the central housing measures any speed variations during logging so that corrections can be applied.

Cable Motion Measurement

The movement of the logging cable is measured with a dedicated integrated depth wheel (IDW) measuring device. This device is identical to the standard cable measuring device; however, the IDW device is mounted at the wellhead to eliminate depth errors induced by sheave motion or cable sag. The absolute accuracy of the IDW is 3 parts in 10,000. Therefore, the errors induced in the measurement between adjacent peaks by adjacent detectors should be negligible. The IDW emits depth pulses every 0.1 in.

® Teflon is a registered trademark of E.I. Du Pont De Nemours and Company

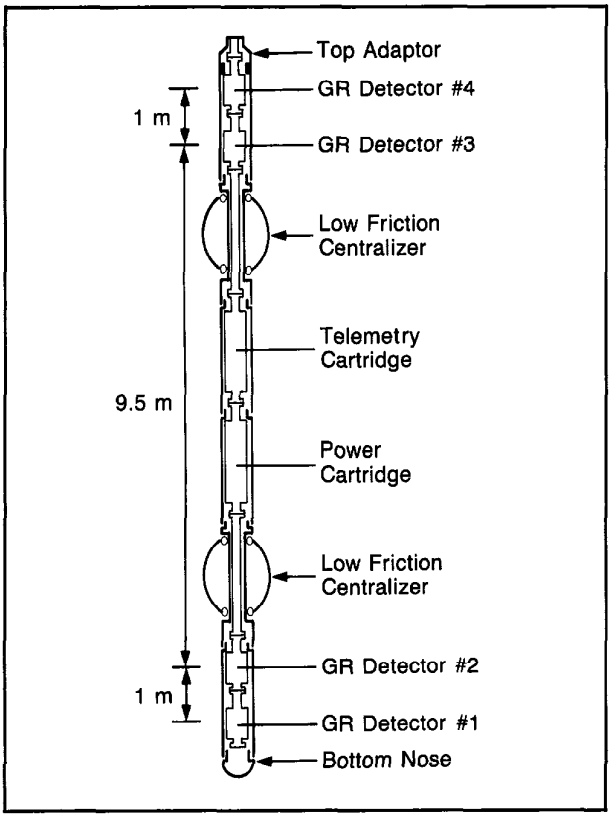

Fig. 10-22—A schematic of the FSMT tool

Radioactive Bullet Placement

Each bullet contains 100 microcuries of Cs 137, emitting monoenergetic gamma rays of 663 keV. The radioactive material is encapsulated in a sealed stainless pellet, which in turn is sealed in the hardened steel bullet body.

The bullets are shot into the formation by a special select fire gun, either in open hole before casing is set or through casing. The explosive load is tailored to place the bullet into the formation far enough so that it will not be affected by any relative movement of the casing/cement with reference to the formation, but not so far that the radioactive peak is not seen clearly by the FSMT detectors.

Measurement Theory

It is possible to measure the distance between radioactive markers with a single detector gamma ray tool, but not with the accuracy required for subsidence measurements. The simplest practical tool would be one with two gamma ray detectors separated by a distance approximately equal to the spacing between the bullets. With this technique, the cable will only move a short distance for the detection of adjacent markers by upper and lower detectors. Only this short distance is subject to errors in the cable measurement system. The closer the match between the spacing of the bullets and detectors, the better the accuracy.

2-Detector Tool

In the ideal case for a 2-detector tool (illustrated in Fig. 10-23) the initial gamma ray log will have both peaks at the same depth. However, after subsidence, $S2$ will be less than $S1$ and the peaks no longer coincident:

$$S2 = b2 - S\,, \qquad \text{(Eq. 10-3)}$$

where S is measured by the depth measuring system. Therefore, subsidence is determined as follows:

$$S = S1 - S2 = b1 - b2 + S\,. \qquad \text{(Eq. 10-4)}$$

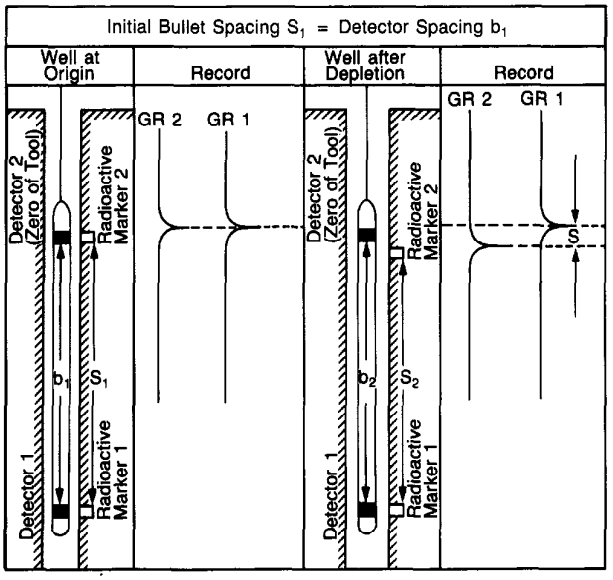

Fig. 10-23—An ideal case for a 2-detector tool

The errors in measurement will come from errors in measuring detector spacings $b1$ and $b2$, in cable measurement errors, and tool yo-yo effects. Since subsidence monitoring is usually performed with dedicated tools and since temperature and pressure conditions are likely to be about the same on all log runs, $b1$ will likely equal $b2$.

In practice, the spacing between radioactive bullets will not be exactly 10 m, but will vary within a 9.5 to 11.5 m range. Figure 10-24 illustrates such a case. At the initial measurement, $S1 = b1 - X1$. Any error in measuring $S1$ stems from tool calibration and the measuring system. The smaller the value of $X1$, the smaller the error.

Following subsidence, $S2 = b2 - X2$, and the subsidence can be calculated.

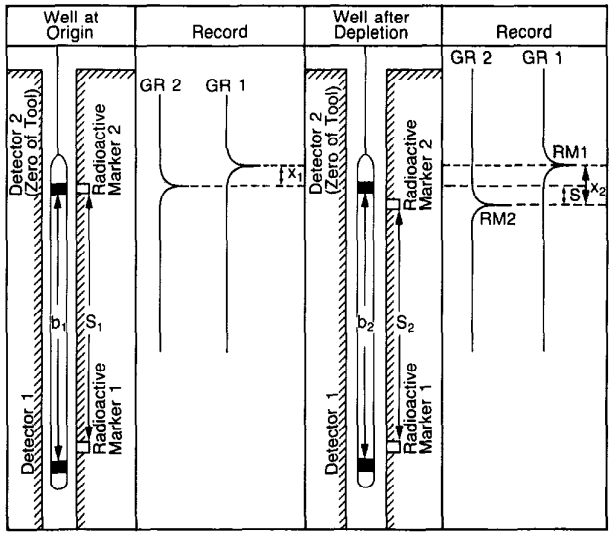

Fig. 10-24—A normal case for a 2-detector tool

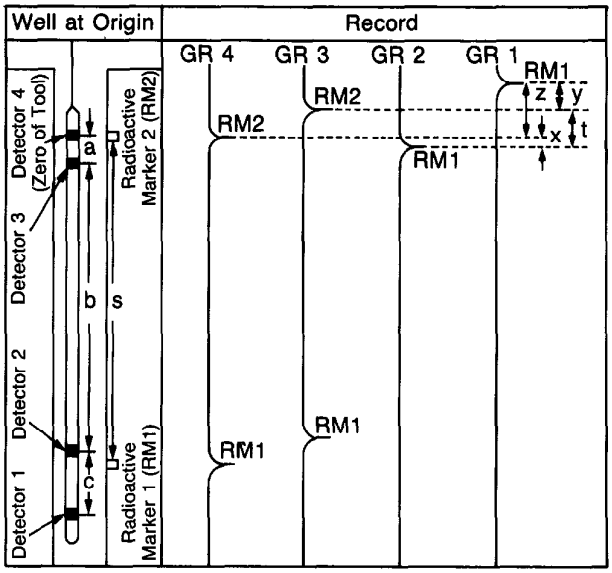

Fig. 10-25—A normal case for a 4-detector tool

Subsidence $S = S1 - S2$

$= bl - X1 - (b2 - X2)$

or $b1 - b2 - (X1 - X2)$. (Eq. 10-5)

The sources of error are now:

- measurement of detector spacing on both runs,
- measurement of cable movement on both runs, and
- variations of tool movement relative to cable movement at surface.

4-Detector Tool

A 4-detector tool brings two major advantages to the measurement. First, four independent measurements of each bullet pair spacing are made. Second, the possibility of a detector pair spacing being close to the bullet pair spacing is greatly increased, reducing the errors from uneven tool movement and cable measurement. A 4-detector measurement schematic is shown in Fig. 10-25.

The distance, S, between radioactive markers can be obtained from the four following relationships:

$$S = (a + b) - X \quad \text{(Eq. 10-6)}$$

$$S = (a + b + c) - Z \quad \text{(Eq. 10-7)}$$

$$S = (b + c) - Y \quad \text{(Eq. 10-8)}$$

$$S = b - t\,. \quad \text{(Eq. 10-9)}$$

In each case, S (the distance between adjacent bullets) is equal to the spacing between any two gamma ray detectors less the displacement of the peaks recorded by these two detectors of the adjacent bullets. The displacement of peaks is considered positive when the peak on the lower detector log corresponding to the lower bullet is recorded higher than the peak on the upper detector from the upper bullet. If the peak on the lower detector log is lower, it is given a negative sign.

Therefore, a 4-detector measurement, a downhole accelerometer for compensation of tool yo-yo effects, more accurate cable movement measurements, digital recording, and digital processing provides improved accuracy.

FSMT Tool Calibrations

The primary calibrator for the FSMT tool is a solid invar bar in which radioactive markers have been placed at precise intervals as shown in Fig. 10-26. Each calibrator has been certified by the Bureau des Mesures in Paris.

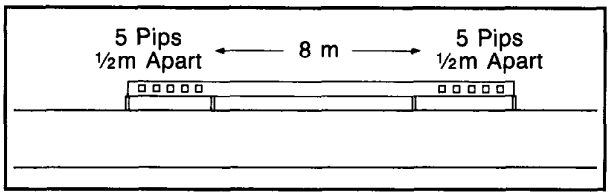

Fig. 10-26—Primary calibrator for the FSMT tool

The bar is clamped to the outside of a riser pipe at a distance sufficient to make the peaks on the gamma ray log from the calibrator about the same as the peaks from the radioactive bullets in the formation. After logging the riser pipe, the calibrator's radioactive marker positions are calculated

using the exact computation routines that are used in normal logging, and are compared to the certified values. This comparison yields a conversion factor, from measured to true distance, which eliminates errors introduced by detector spacing measurements and the cable measurement device. Multiple passes are made to ensure that the conversion factors are coherent. A typical FSMT surface calibrator log is shown in Fig. 10-27.

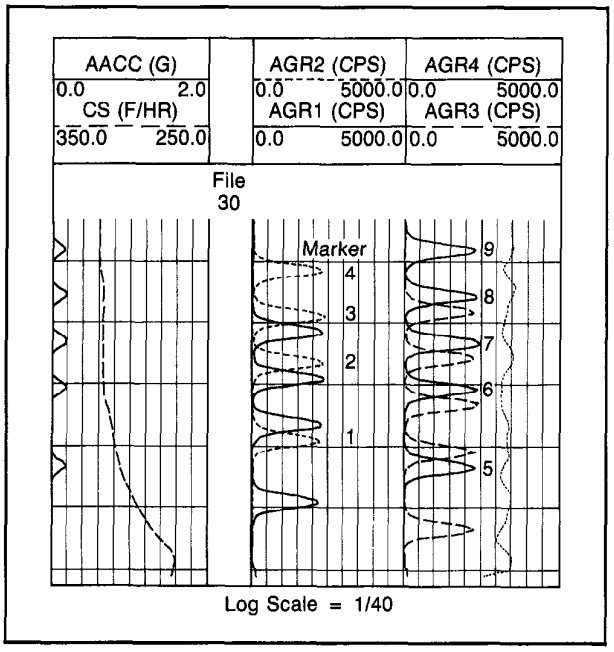

Fig. 10-27—FSMT tool surface calibrator log

Logging Procedure

Following calibration, at least three logging runs are made over the zone containing the radioactive markers at a speed of 1.5 m/min (300 ft/hr). Data from the four gamma ray detectors and the accelerometer are recorded on tape every 0.1 in. of cable movement.

Log Data Processing

After the gamma ray data are filtered and normalized, the marker positions are calculated. First the gamma ray peaks are identified using a simple threshold detection. Then the approximate center of the peak is detected using a center of gravity technique. This center point depth is corrected for variations in tool motion using input from the accelerometer. The true marker position is then determined as a function of the position of the points of inflection on the filtered gamma ray curve on either side of the rough marker position and the slope of the tangent through these points of inflection.

Presentation of Results

A computation of results is available at the wellsite with the CSU field unit; however, a more complete computation is usually made at a Schlumberger computing center. The results include a calibration summary and a results summary for each marker, relative to the previous (lower) marker. A results summary example is shown in Fig. 10-28. The summary table combines the marker spacing results for three runs, interpreted both with and without accelerometer compensation.

The heading line gives the interval number, tool number, logging date, and well name. The main section of the summary is divided into three columns, one for each run. The reference depth of the interval is given for each run. The upper portion of the listing contains the results from the processing with accelerometer compensation and can be explained as follows:

- RELATIVE PEAK POSITIONS show where the program has found the peak to be, relative to the GR 1 peak. The first figure is always zero.
- MARKER PRECISION is an indication of how accurately the peak was defined. A low value here implies a good peak profile.
- MARKER SPACINGS ACCELEROMETER are the spacing results from the four possible equations. Their order, in terms of the relative peak spacings used as inputs, is S41 S31 S42 S32. The average of these four is given on the next line.
- S12-L12 and S34-L34 are quality indicators. In the perfect case, tool travel downhole is equal to the cable travel measured at surface and the values will be zero.
- The standard deviation of the four marker spacings from each pass is listed on the last line of this section.
- On the extreme right of the table, the results from all three log passes are evaluated in the overall average and standard deviation. If all results from all passes are used, then the NO. USED indicator will be 12.

The lower half of the summary lists the results calculated without using accelerometer data.

Graphical Summary

The graphical summary below the main table (Fig. 10-29) is a plot of the marker spacing results. The distance scale is indicated across the top of the plot. Again, the upper half is for results with accelerometer data and the lower half without.

The four results from each run are plotted with a number 1, 2, 3, or 4 corresponding to the equation number. The average for each run is X and the overall average of all the logging runs is A.

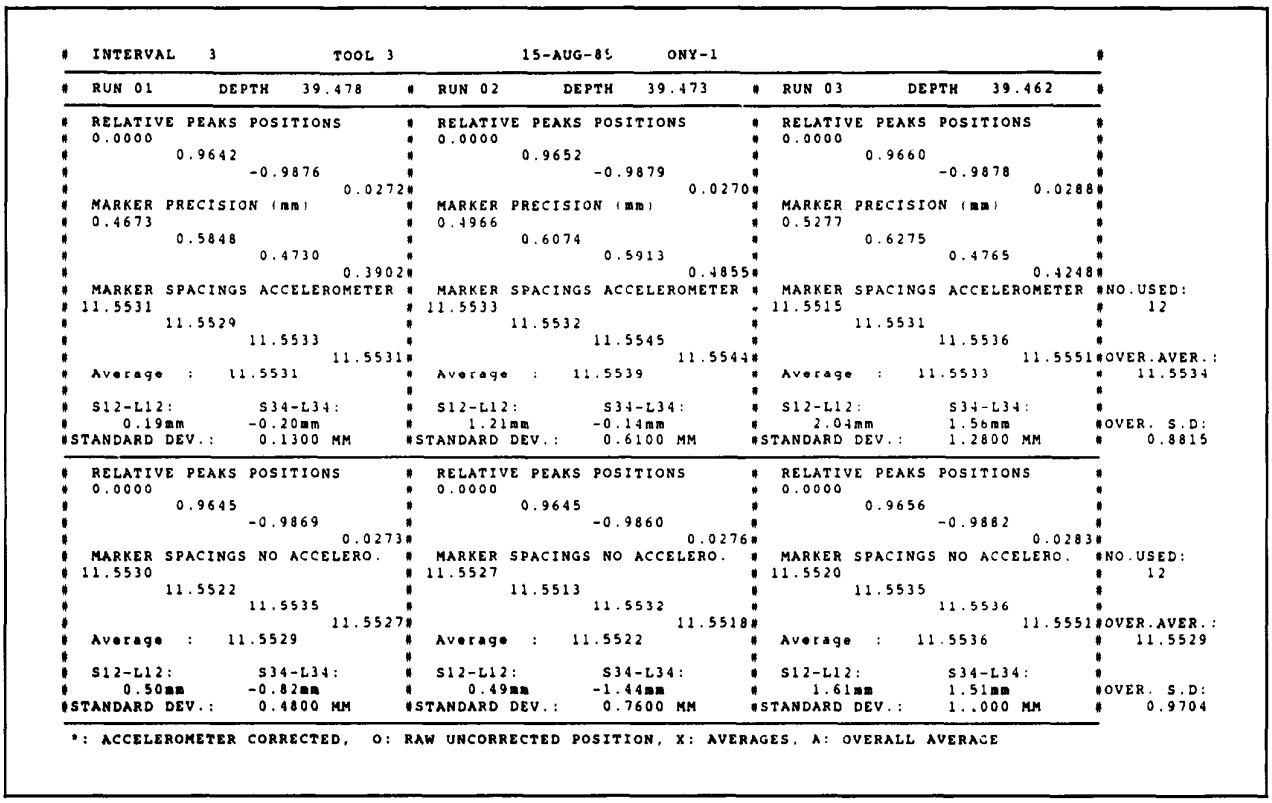

```
#  INTERVAL   3            TOOL 3            15-AUG-85      ONY-1                                  #

#  RUN 01       DEPTH   39.478   #  RUN 02       DEPTH   39.473   #  RUN 03       DEPTH   39.462   #

#  RELATIVE PEAKS POSITIONS      #  RELATIVE PEAKS POSITIONS      #  RELATIVE PEAKS POSITIONS      #
#  0.0000                        #  0.0000                        #  0.0000                        #
#           0.9642               #           0.9652               #           0.9660               #
#                    -0.9876     #                    -0.9879     #                    -0.9878     #
#                             0.0272#                          0.0270#                          0.0288#
#  MARKER PRECISION (mm)         #  MARKER PRECISION (mm)         #  MARKER PRECISION (mm)         #
#  0.4673                        #  0.4966                        #  0.5277                        #
#           0.5848               #           0.6074               #           0.6275               #
#                    0.4730      #                    0.5913      #                    0.4765      #
#                             0.3902#                          0.4855#                          0.4248#
#  MARKER SPACINGS ACCELEROMETER #  MARKER SPACINGS ACCELEROMETER #  MARKER SPACINGS ACCELEROMETER #NO.USED:
# 11.5531                        # 11.5533                        # 11.5515                        #    12
#           11.5529              #           11.5532              #           11.5531              #
#                    11.5533     #                    11.5545     #                    11.5536     #
#                             11.5531#                         11.5544#                         11.5551#OVER.AVER.:
#  Average  :   11.5531          #  Average  :   11.5539          #  Average  :   11.5533          #   11.5534
#                                #                                #                                #
#  S12-L12:        S34-L34:      #  S12-L12:        S34-L34:      #  S12-L12:        S34-L34:      #
#     0.19mm       -0.20mm       #     1.21mm       -0.14mm       #     2.04mm       1.56mm       #OVER. S.D:
#STANDARD DEV.:    0.1300 MM     #STANDARD DEV.:    0.6100 MM     #STANDARD DEV.:    1.2800 MM     #    0.8815

#  RELATIVE PEAKS POSITIONS      #  RELATIVE PEAKS POSITIONS      #  RELATIVE PEAKS POSITIONS      #
#  0.0000                        #  0.0000                        #  0.0000                        #
#           0.9645               #           0.9645               #           0.9656               #
#                    -0.9869     #                    -0.9860     #                    -0.9882     #
#                             0.0273#                          0.0276#                          0.0283#
#  MARKER SPACINGS NO ACCELERO.  #  MARKER SPACINGS NO ACCELERO.  #  MARKER SPACINGS NO ACCELERO.  #NO.USED:
# 11.5530                        # 11.5527                        # 11.5520                        #    12
#           11.5522              #           11.5513              #           11.5535              #
#                    11.5535     #                    11.5532     #                    11.5536     #
#                             11.5527#                         11.5518#                         11.5551#OVER.AVER.:
#  Average  :   11.5529          #  Average  :   11.5522          #  Average  :   11.5536          #   11.5529
#                                #                                #                                #
#  S12-L12:        S34-L34:      #  S12-L12:        S34-L34:      #  S12-L12:        S34-L34:      #
#     0.50mm       -0.82mm       #     0.49mm       -1.44mm       #     1.61mm       1.51mm       #OVER. S.D:
#STANDARD DEV.:    0.4800 MM     #STANDARD DEV.:    0.7600 MM     #STANDARD DEV.:    1..000 MM     #    0.9704

 *: ACCELEROMETER CORRECTED,  O: RAW UNCORRECTED POSITION, X: AVERAGES, A: OVERALL AVERAGE
```

Fig. 10-28—FSMT log results summary table

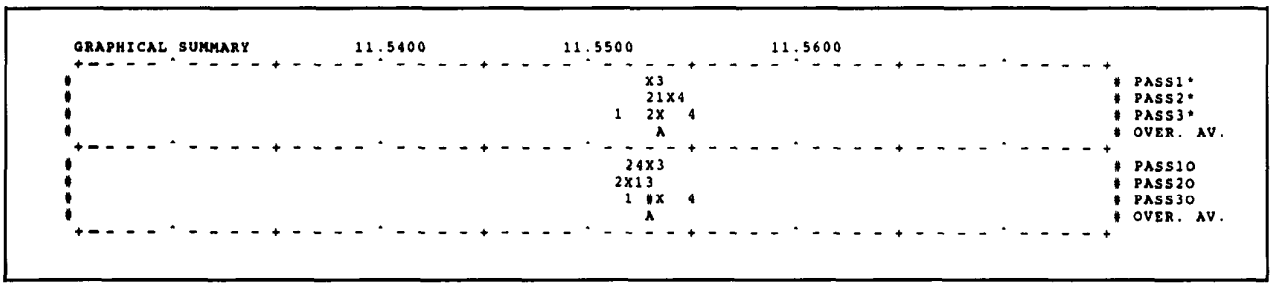

```
 GRAPHICAL SUMMARY          11.5400          11.5500          11.5600
 +-----*-----+-----*-----+-----*-----+-----*-----+-----*-----+-----*-----+
#                                    X3                                  # PASS1*
#                                   21X4                                 # PASS2*
#                                1  2X  4                                # PASS3*
#                                    A                                   # OVER. AV.
 +-----*-----+-----*-----+-----*-----+-----*-----+-----*-----+-----*-----+
#                                   24X3                                 # PASS1O
#                                  2X13                                  # PASS2O
#                                   1 #X  4                              # PASS3O
#                                    A                                   # OVER. AV.
 +-----*-----+-----*-----+-----*-----+-----*-----+-----*-----+-----*-----+
```

Fig. 10-29—Graphical summary of FSMT log results

REFERENCES

De Loos, J.M.: "In Situ Compaction Measurements in Groningen Observation Wells," *Verhandelingen Kon. Ned. Geol. Mijnbouwk. Gen.* (1973) **28**, 79-104.

Overboom, E.J.M., Peeters, M., and Milloy, G.: "Precise Distance Measurements with Gamma-Ray Tools To Monitor Compaction (PDM)," paper presented at the SPWLA 22nd Annual Logging Symposium, June, 1981.

Production Services Catalog, Schlumberger (1986).

Repeat Formation Tester, Schlumberger (1987).

Well Evaluation Conference - Nigeria, Schlumberger (1985).

Schlumberger Wireline & Testing

SMP-7025